

Deciphering petrological signatures of reactive
melt stagnation and cooling in the oceanic mantle
underneath ultraslow-spreading ridges

Dissertation

zur Erlangung des Grades

„Doktor der Naturwissenschaften“

am Fachbereich

Chemie, Pharmazie und Geowissenschaften

der Johannes Gutenberg Universität Mainz

vorgelegt

von

ANETTE VON DER HANDT

geboren in Düsseldorf

Mainz, 2008

A dissertation submitted to the
Geosciences Institute of the Johannes Gutenberg University Mainz
in fulfillment of the requirements for the degree of

Doctor rerum naturalium

Dekan: Peter Langguth

1. Berichterstatter:

2. Berichterstatter:

3. Berichterstatter:

Tag der mündlichen Prüfung: 18.06.2008

D77

Ich versichere hiermit, die vorliegende Arbeit selbständig verfasst zu haben und alle benutzten Hilfsmittel und Quellen in der Arbeit angegeben zu haben. Diese Arbeit wurde an keiner anderen Fakultät als Dissertation eingereicht.

ABSTRACT

The global mid-ocean ridge system creates oceanic crust and lithosphere that covers more than two-thirds of the Earth. Basalts are volumetrically the most important rock type sampled at mid-ocean ridges. For this reason, our present understanding of upper mantle dynamics and the chemical evolution of the earth is strongly influenced by the study of mid-ocean ridge basalts (MORB). However, MORB are aggregates of polybarically generated small melt increments that can undergo a variety of physical and chemical processes during their ascent and consequently affect their derivative geochemical composition. Therefore, MORB do not represent “direct” windows to the underlying upper mantle. Abyssal peridotites, upper mantle rocks recovered from the ocean floor, are the residual complement to MORB melting and provide essential information on melt extraction from the upper mantle. In this study, abyssal peridotites are examined to address these overarching questions posed by previous studies of MORB: How are basaltic melts formed in the mantle, how are they extracted from the mantle and what physical and chemical processes control mantle melting?

The number of studies on abyssal peridotites is small compared to those on basalts, in part because seafloor exposures of abyssal peridotites are relatively rare. For this reason, abyssal peridotite characteristics need to be considered in the context of subaerially exposed peridotites associated with ophiolites, orogenic peridotite bodies and basalt-hosted xenoliths. However, orogenic peridotite bodies are mainly associated with passive continental margins, most ophiolites are formed in supra-subduction zone settings, and peridotite xenoliths are often contaminated by their host magma. Therefore, studies of abyssal peridotites are essential to understanding the primary characteristics of the oceanic upper mantle free from the influence of continental rifting, subduction and tectonic emplacement processes.

Nevertheless, numerous processes such as melt stagnation and cooling-induced, inter-mineral exchange can affect residual abyssal peridotite compositions after the cessation of melting. The aim of this study is to address these post-melting modifications of abyssal peridotites from a petrological-geochemical perspective.

Recent results have shown that the style of accretion at ultraslow-spreading (<20 mm/yr full rate) mid-ocean ridges is fundamentally different from that at faster spreading centers, and that the influence of melting style becomes more important at slower spreading rates. Low melt production and low melt-to-rock interaction tend to preserve the geochemical signature of processes generated at the onset of melting and melt-rock reaction.

The samples in this study were dredged along the axis of the ultraslow-spreading Gakkel Ridge in the Arctic Ocean within the “Sparsely Magmatic Zone”, a 100 km ridge section where only mantle rocks are exposed. During two expeditions (ARK XVII-2 in 2001 and ARK XX-2 in 2004), exceptionally fresh peridotites were recovered. The boulders and cobbles collected cover a range of mantle rock compositions, with most characterized as plagioclase-free spinel peridotites or plagioclase- spinel peridotites.

This thesis investigates melt stagnation and cooling processes in the upper mantle and is divided into two parts. The first part focuses on processes in the stability field of spinel peridotites (>10 kb), while the second part investigates processes in the stability field of plagioclase peridotites (< 10 kb). The dissertation chapters are organized to follow the

theoretical ascent of a mantle parcel upwelling beneath the location where the samples were collected.

Chapter 1 gives a general introduction to melting processes at mid-ocean ridges with emphasis on slow- to ultraslow-spreading ridges.

Chapter 2 describes the characteristics of spinel peridotites from major and trace element mineral compositions indicate that refractory spinel peridotites were affected by melt refertilization at high temperature and pressure. Clinopyroxene trace element composition suggests that this melt was produced by near-solidus melting in some samples. The spinel peridotites are assumed to represent the starting composition for the processes investigated in subsequent chapters.

Chapter 3 studies the temperature-dependent lithophile trace element diffusive exchange between clinopyroxene and orthopyroxene. Despite lower trace element abundances, orthopyroxene is very sensitive to inter-pyroxene trace element redistribution during cooling. Temperature-dependent partition coefficients and zoning profiles in orthopyroxene can be used to quantify timescales of cooling and uplift. Based on opx compositional zoning, a new geospeedometer for mantle rocks is proposed.

Chapter 4 is a study of cation diffusion in orthopyroxene. Orthopyroxene zoning in spinel peridotites allows the determination of the relative diffusivities of 14 trace elements in orthopyroxene. The systematic behavior of cation diffusion in silicate minerals in general permits inferences on the cation distribution in the orthopyroxene crystal lattice.

Chapter 5 represents the first chapter of the second part of the thesis. This chapter investigates the change in major and trace element composition that accompanies the formation of plagioclase peridotites. Plagioclase peridotites are a major lithology among the oceanic ultramafic rocks, but their origin is still a matter of debate. Different models are tested and a new theory on the formation of plagioclase peridotites and reactive melt-rock reaction is proposed.

Chapter 6 focuses on the characteristics of spinel compositions found in plagioclase peridotites. Spinel composition is very sensitive to many geochemical processes and is therefore a valuable petrogenetic indicator. This chapter investigates the role of melt composition and residual rock composition in determining the final spinel composition. It is shown that changes in silica activity and oxygen fugacity are an important factor in controlling spinel composition.

Chapter 7 elaborates on the outcomes of chapter 5 and 6 regarding the importance of melt migration models in the mantle. Models of melt transport and melt-wall rock reaction in the mantle are generally based on the assumption of at least an instantaneous equilibrium process between melt and mineral surfaces. The strong compositional heterogeneities and preserved disequilibrium conditions in plagioclase peridotites suggest that disequilibrium is widespread in melt migration processes in the uppermost mantle beneath mid-ocean ridges.

Chapter 8 presents a synthesis of the entire dissertation.

ZUSAMMENFASSUNG

Im Bereich der mittelozeanischen Rücken wird die ozeanische Kruste gebildet, die mehr als zwei Drittel der Erde bedeckt. Basalte stellen dabei die volumetrisch bedeutendste Gesteinsgruppe dar, die infolgedessen die Hauptgrundlage unseres Wissens über geodynamische und geochemische Prozesse im Erdmantel bilden. Basalte von mittelozeanischen Rücken (MORB) unterliegen während ihrer Bildung und beim Transport zur Oberfläche einer Vielzahl von Prozessen, die ihre geochemische Zusammensetzung modifizieren können. Daher erlauben MORB keine direkten Einblicke in Mantelprozesse. Tiefsee-Peridotite, also Mantelgesteine, die direkt am Ozeanboden aufgeschlossen sind, repräsentieren das Komplementärgestein zu den MORB-Basalten und sind daher mindestens ebenso wichtig für die Erforschung von Schmelzprozessen und Schmelzmigration im Mantel. Infolgedessen werden zentrale Fragen von Schmelzbildung und -transport im ozeanischen Mantel anhand von Tiefsee-Peridotiten untersucht.

Die Zahl der wissenschaftlichen Untersuchungen an Tiefsee-Peridotiten ist noch vergleichsweise gering, was zum Teil an der relativen Seltenheit liegt, dass Tiefsee-Peridotite direkt am Ozeanboden aufgeschlossen sind. Unser Wissen über Mantelgesteine beruht auf Studien an Ophioliten, alpinotypen Peridotiten, und an Xenolithen, die daher auch immer im Kontext betrachtet werden müssen. Allerdings sind erstere häufig durch Obduktionsprozesse und letztere durch die sie transportierenden Schmelzen modifiziert. Weiterhin ist ein Großteil der Ophiolite in Back-Arc Becken entstanden, während alpinotype Peridotite mit der Entstehung an kontinentalen Rändern in Zusammenhang gebracht werden. Daher erlauben sie keine direkten Einblicke in Mantelprozesse an mittelozeanischen Rücken. Dies macht die Erforschung von Tiefsee-Peridotiten umso wichtiger.

Allerdings werden auch Tiefsee-Peridotite nach Beendigung des Aufschmelzungsprozesses noch weiteren Prozessen, wie z.B. Abkühlung und Schmelzrefertilisierung unterworfen. Ziel dieser Doktorarbeit ist es, diese Prozesse aus petrologisch-geochemischer Perspektive zu untersuchen.

Neuere Erkenntnisse haben gezeigt, dass die sogenannten ultra-langsam spreizenden mittelozeanischen Rücken eine fundamental andere Dynamik aufweisen, als ihre schneller spreizenden Äquivalente. Geringe Magmenproduktion, typisch für langsam spreizende Rücken, und damit einhergehende niedrigere Verhältnisse von Schmelzen zu Umgebungsgestein erlauben die detaillierte Studie von Modifikationsprozessen der Zusammensetzung von residuellen Peridotiten.

Die Proben für diese Arbeit stammen aus der Amagmatischen Zone (Sparsely Magmatic Zone) am Gakkel-Rücken, der das langsam spreizende Endglied im System der mittelozeanischen Rücken darstellt. Der zentrale Bereich des Gakkel-Rückens wird von einem 100 km langen Abschnitt gebildet, an dem nur Mantelgesteine direkt am Ozeanboden aufgeschlossen sind. Am westlichen Ende dieses Bereiches wurden am gleichen Ort in zwei aufeinanderfolgenden Expeditionen (ARK XVII-2 im Jahre 2001 und ARK XX-2 im Jahre 2004) ausserordentlich frische Mantelperidotite gedredgt, die die Grundlage dieser Studie darstellen.

Diese Arbeit ist thematisch in zwei Teile gegliedert. Der erste Teil untersucht Prozesse im Stabilitätsbereich der Spinelperidotite (>10 kbar), während der zweite Teil sich mit Prozessen bei niedrigeren Drücken (<10 kbar) im Stabilitätsbereich der Plagioklasperidotite befasst. Die

Reihenfolge der Kapitel folgt einem theoretischen Aufstiegsfad von Mantelgesteinen unter einem mittelozeanischen Rücken.

Kapitel 1 gibt eine allgemeine Einführung in die Prozesse an mittelozeanischen Rücken mit Schwerpunkt auf langsam und ultra-langsam spreizende Rücken.

Kapitel 2 untersucht die Haupt- und Spurenelement-Zusammensetzung der Spinelperidotite der Probenlokation. Die refraktären Spinelperidotite dieser Probenlokation erfuhren alle eine Refertilisierung unter hohen Temperaturen und Drücken. Die Spurenelementzusammensetzung von Klinopyroxenen zeigt, dass die Refertilisierung teilweise mit Schmelzen erfolgte, die nah am Peridotit-Solidus gebildet wurden. Die Spinelperidotite stellen mit großer Wahrscheinlichkeit das Ausgangsmaterial für die in den folgenden Kapiteln beschriebenen Prozesse dar.

Kapitel 3 untersucht den Einfluss von Abkühlungsprozessen auf den Spurenelementaustausch zwischen Klinopyroxen und Orthopyroxen. Das niedrige Spurenelement-Budget von Orthopyroxenen führt zur Ausbildung von Zonierungen während der Abkühlung. Auf der Basis von temperaturabhängigen Klinopyroxen-Orthopyroxen-Spurenelementverteilungskoeffizienten und der Spurenelement-Zonierung im Orthopyroxen wird ein neues Geospeedometer vorgestellt, das das Abschätzen von Abkühlungsraten von Mantelgesteinen ermöglichen soll.

Kapitel 4 stellt eine Studie der Diffusionssystematik von Spurenelementen in Orthopyroxen dar. Spurenelement-Zonierungen in Orthopyroxenen von Spinelperidotiten erlauben es, die relativen Diffusionsgeschwindigkeiten von 14 Spurenelementen zu bestimmen. Desweiteren kann auf der Basis der bekannten Diffusionssystematik in Silikaten eine Zuordnung auf die Kationenverteilung im Orthopyroxen-Kristallgitter durchgeführt werden.

Kapitel 5 ist der Beginn des zweiten Teils, der sich mit Prozessen im Stabilitätsbereich von Plagioklasperidotiten befasst. Dieses Kapitel ist eine Detailstudie der Haupt- und Spurenelementveränderungen der Silikate in Plagioklasperidotiten, die im Zusammenhang mit der Entstehung von Plagioklasperidotiten stehen. Trotz ihrer relativen Häufigkeit an mittelozeanischen Rücken wird die Entstehung von Plagioklasperidotiten immer noch kontrovers diskutiert. Innerhalb dieses Kapitels werden diskutierte Modelle zu ihrer Entstehung überprüft und eine neue Theorie zur Entstehung von Plagioklasperidotiten postuliert.

Kapitel 6 befasst sich mit der Zusammensetzung von Spinellen in Plagioklasperidotiten. Spinel ist ein wichtiges petrogenetisches Mineral, das sehr empfindlich auf viele Prozesse im Mantel reagiert. In diesem Kapitel wird gezeigt, dass nicht nur die Zusammensetzung der reagierenden Schmelze von grosser Bedeutung für seine Zusammensetzung ist, sondern auch die Ausgangszusammensetzung. Darüberhinaus wird seine Zusammensetzung massgeblich durch Änderungen der Silika-aktivität und Sauerstoff fugazität bestimmt.

Kapitel 7 stellt die Ergebnisse der Kapitel 5 und 6 in Bezug zu Modellen der Schmelzmigrationsprozesse im oberen Erdmantel. Die ausgeprägte Variabilität in Haupt- und Spurenelementen in Plagioklasperidotiten weist auf die Bedeutung von Ungleichgewichtsprozessen in Schmelzmigrationsprozessen zumindest in niedrigen Druckbereichen hin.

Den Abschluss bildet Kapitel 8, das eine Synthese der Ergebnisse der vorangegangenen Kapitel gibt.

ACKNOWLEDGMENTS

It is probably impossible to adequately thank all the people, who helped me to reach the point of finishing this thesis, but I will try...

First, I want to thank my advisors Eric Hellebrand and Jonathan Snow, who pulled me into the fascinating world of mid-ocean ridges and peridotites. Through them, I've sailed if not the seven but at least two seas, had my share of polar bear sightings and sea sickness, and described one mid-ocean ridge, one (presumably) ocean-continent transition zone and one very long section of gabbro. I enjoyed working with you very much.

I would also like to thank Eric especially, for his constant patience, help and sometimes challenge. For the amount of time, he invested in my projects and all the discussions we had; also, the hospitality that he always offers in his usual selfless way. And let's not forget that he got me a job in paradise!

Al Hofmann runs a fantastic institute that provided me with everything, I needed for the success of my projects. He always had time for discussion and his door was always open. He also agreed to become my supervisor in the final stages of this thesis, and just acted fantastic all along. Furthermore, he provided me with many commas, even though there may be still some missing. I only hope I can continue to learn from him.

I am very grateful to Prof. Richard White for accepting the supervision on an external thesis, not foreseeing what he got himself into.

Over the course of my PhD time, I had the chance to discuss with many great people who I met at conferences, workshops and expeditions. All their input was of great help and helped me to get along with my projects, or just taught me something important. Specifically I would like to thank (in totally random order): Monique Seyler, Giovanni Piccardo, James van Orman, Elisabetta Rampone, Ron Frost, Greg Hirth, Arjan Dijkstra, Jean Bedard, Dave Christie, Laurence Coogan, Julian Pearce, Günter Suhr and Jürgen Köpke.

I also want to thank my fellow students at the Institute in Mainz: Stefanie Brückner, Zoran Jovanovic, Yongjun Gao, Joachim Krause.

I do not know how my time in Mainz would have been without Stefanie Brückner, in particular; she is not just a fellow student, but also a good friend and the most altruistic person in the world. She always provided me with everything: from coffee breaks, papers, spirit boxes, inspirational emails, scientific discussions to chocolate in times of crisis. She is also the most knowledgeable person in the world. Her knowledge of mineral structures and all things petrological is just astounding and came very helpful.

Zoran Jovanovic was my partner in peridotite crime in this institute. I had many stimulating discussions with him and hope there will be many more to come.

My former office mates: Anne-Desiree Schmidt, Marlina Elburg and Sylvain Pichat, even though they all moved on, they still were part of the process. It was a great time.

Sebastian Fischer started as a great student aid, and became an even more fantastic part of the group and a friend in record time. He is the calm sea in times of thunderstorms and

saved me many times. He also forced me to socialize once in a while, for which I want thank him especially.

Rosemarie Gross and Karin Geiger were a constant source of help, Andreas Zimmer always could get hold of even the rarest publications, Heinz Feldmann was the keeper of the software and the guardian of all things electronic. I also regret that I had not more time to go to the ballet with Rosemarie.

The unlimited access to machines and hence to collect a wealth of data for my projects were one of the great aspects of my time in Mainz. I could not have done without the support from Peter Hoppe and Elmar Gröner at the ion probe; Nora Groschopf and Dr. Schulz-Dobrick at the electron microprobe and Brigitte Stoll and Kristin Herwig at the LA-ICP-MS.

Dieter Dettmar from Bochum produces the best thin sections in the world that gave me a fantastic ground to work on.

The projects were made possible by the tireless efforts of the ship's crew and captain as well as the students on both cruises to Gakkel Ridge.

I also want to thank my friends that they still remember me and continued to keep in contact during the final stages of this thesis, in particular Micha, Wiebke and Merle. Thank you.

Last but not least, I want to thank my family without their constant support, I could not have done it.

... and of course Oskar, who always has a purr for me.

TABLE OF CONTENTS

CHAPTER 1: GENERAL INTRODUCTION AND REGIONAL SETTING

1.1 Introduction	1
1.2 Gakkel Ridge	4
1.2.1 Morphology of Gakkel Ridge	5
1.2.2 Petrology of Gakkel Ridge	8
1.2.2.1 Basalts	8
1.2.2.2 Peridotites	10
1.2.2.3 Gabbro	11
1.2.3 Petrology and tectonics of the Gakkel 3°E 'amagmatic' segment	11
1.2.3.1 Dredging results	11
1.2.4 Sample locations: dredge hauls PS66-238 and PS59-235	13
1.3 Outline of the thesis	15
1.4 References	17

CHAPTER 2: NEAR-SOLIDUS MELTING AND MELT REFERTILIZATION IN THE SPINEL STABILITY FIELD: EVIDENCE FROM THE ULTRASLOW-SPREADING GAKKEL RIDGE

2.1 Introduction	21
2.2 Petrography and methods	22
2.2.1 Petrographic and microtextural features	23
2.2.2 Methods	26
2.3 Results	26
2.3.1 Major elements	26
2.3.2 Trace elements	29
2.4 Discussion	30
2.4.1 Melting conditions	30
2.4.2 Melt refertilization	33
2.4.2.1 Refertilization of PS66-238 peridotites	34
2.4.2.2 Refertilization of PS59-235 peridotites	36
2.4.3 Implications for low degree partial melting at Gakkel Ridge	37
2.5 Summary	39
2.6 References	40

CHAPTER 3: TEMPERATURE-DEPENDENT TRACE ELEMENT EXCHANGE IN MANTLE MINERALS
- TOWARD A NEW GEOSPEEDOMETER FOR ULTRAMAFIC ROCKS

3.1 Introduction	48
3.1.1 Thermal structure of mid-ocean ridges	49
3.1.2 Geospeedometry	51
3.2 Sample description and methods	53
3.2.1 Petrography	53
3.2.2 Methods	55
3.3 Results	57
3.3.1 Major elements	57
3.3.2 Temperatures from major element geothermometers	57
3.3.3 Trace elements	61
3.3.4 Temperatures from trace element geothermometers	65
3.4 Discussion	67
3.4.1 Temperature dependence of mineral-mineral trace element exchange	67
3.4.1.1 Cooling-dependent trace element re-distribution between cpx and opx	68
3.4.1.2 Cooling-dependent trace element re-distribution between olivine and opx	70
3.4.2 Cooling rates: toward a new geospeedometer	72
3.4.2.1 Trace element zoning profiles and cooling rates	72
3.4.2.1.1 Model parameters	72
3.4.2.1.2 Model results	75
3.4.2.1.3 Model results for PS66-238	77
3.4.2.2 Closure temperature profiles and cooling rates	80
3.4.2.2.1 Model parameters	81
3.4.2.2.2 Model results	82
3.5 Summary	85
3.6 References	87

CHAPTER 4: CATION DIFFUSION IN ORTHOPYROXENE

4.1 Introduction	120
4.1.1 Diffusion in silicates	120
4.1.2 Diffusion in orthopyroxene	123
4.1.3 REE diffusion in orthopyroxene and silicates	125
4.2 Methods and results	126
4.3 Discussion	130
4.3.1 Diffusion of rare earth elements in orthopyroxene	130
4.3.2 Diffusion systematics and crystal site positions in orthopyroxene	133
4.3.3 Differences between diffusion in orthopyroxene and clinopyroxene	135
4.3.4 REE diffusion in orthopyroxene: experimental data and results from Gakkel Ridge peridotites	137
4.4 Summary	140
4.5 References	141

CHAPTER 5: PLAGIOCLASE PERIDOTITES FROM GAKKEL RIDGE: ON STAGNANT REACTIVE
POROUS FLOW AND SILICA ACTIVITY

5.1 Introduction	144
5.1.1 Significance of the spinel to plagioclase phase transformation	145
5.1.2 Significance of melt migration and melt stagnation processes	146
5.2 Sample description and methods	147
5.2.1 Modal analyses	147
5.2.2 Petrography	148
5.2.3 Methods	154
5.3 Results	155
5.3.1 Spinel	155
5.3.2 Clinopyroxene	157
5.3.3 Orthopyroxene	164
5.3.4 Plagioclase	165
5.3.5 Olivine	167
5.4 Models	168
5.4.1 Closed-system breakdown	169
5.4.2 Melt impregnation	179
5.4.2.1 Trapped melt model	181
5.4.2.2 Fractional crystallization model	186
5.5 Discussion	189
5.5.1 Parental melts to plagioclase peridotites – ambiguous	190
5.5.2 Coupled flow and reaction in the mantle – a conceptual model for the formation of plagioclase peridotites and melt-rock reaction in the mantle	192
5.5.2.1 Silica activity in the mantle	192
5.5.2.2 Melt-rock reaction and the silica activity space	194
5.5.2.3 Phase relations in systems of variable silica activity	195
5.5.2.3.1 Reaction toward lower silica activity	197
5.5.2.3.2 Reaction toward higher silica activity	199
5.5.2.4 Evidence from experiments and nature: melt-rock reaction and crystal dissolution	200
5.5.2.4.1 Textures	201
5.5.2.4.2 Reaction progress: dissolution reactions and their influence	203
5.5.3 Mineral compositions in plagioclase peridotites	205
5.5.4 Differences to current models of melt-rock reaction processes	207
5.5.5 Origin of silica-rich melts in the oceanic mantle	209
5.6 Summary	210
5.7 References	211
A5-1: Results of the experimental study of Kushiro and Yoder (1966)	227
A5.1.1 The system enstatite and anorthite in the ratio 2:1	227
A5.1.2 The system forsterite and anorthite in the ratio 2:1	227
A5.1.3 The system forsterite and anorthite in the ratio 1:1	228
A5-2: Results of the experimental study of Green and Ringwood (1967)	230
A5-3: Results of the experimental study of Bultitude and Green (1970)	232

CHAPTER 6: SPINEL AS PETROGENETIC INDICATOR: INFLUENCE OF REACTIVE MELT-ROCK REACTION AND THE ROLE OF OXYGEN FUGACITY

6.1 Introduction	246
6.2 Methods and petrography	248
6.2.1 Sample description and petrography	248
6.2.2 Modal proportions	249
6.2.3 Methods	250
6.3 Results	251
6.3.1 Spinel compositions	251
6.3.2 Spinel zoning	253
6.3.3 Sample systematics	256
6.3.4 Oxygen fugacities	258
6.4 Discussion	260
6.4.1 Gakkel Ridge plagioclase peridotites - variation between spinel composition and plagioclase abundance	261
6.4.2 The role of melt-rock reaction	265
6.4.3 Oxygen fugacity	269
6.4.3.1 Reactive melt-rock reaction and oxygen fugacity – evidence for oxidation?	270
6.4.3.2 The effect of closed-system breakdown of spinel	275
6.5 Summary	277
6.6 References	277

CHAPTER 7: SPINELS IN PLAGIOCLASE PERIDOTITES AS RECORDER OF DISEQUILIBRIUM MELT MIGRATION

7.1 Introduction	285
7.2 Discussion	286
7.3 References	289

CHAPTER 8: SYNTHESIS AND OUTLOOK

8.1 Introduction	292
8.2 Melt extraction at Gakkel Ridge	293
8.3 Mantle heterogeneity at Gakkel Ridge	294
8.3.1 Pre-existing heterogeneity	294
8.3.2 Heterogeneity at Gakkel Ridge: produced by melt-rock reaction	295
8.4 Melt production at Gakkel Ridge	296
8.5 Heterogeneity of melts	297
8.6 Cooling below Gakkel Ridge	298
8.7 Summary	299
8.8 References	299

APPENDIX	302
A: Partial melting	302
B. Trapped melt model	303
C: Fractional crystallization	304
D: Transition from spinel to plagioclase facies condition	305
Table A-1	307
References	308
CURRICULUM VITAE	310

CHAPTER 1

GENERAL INTRODUCTION AND REGIONAL SETTING

1.1 INTRODUCTION

The mid-ocean ridge system is the site of creation of the oceanic crust and lithosphere that covers more than two-thirds of the Earth. Basalts are volumetrically the most important rock type sampled on mid-ocean ridges and provide the bulk of compositional information that exists about the processes of melt generation, transport and crystallization. However, mid-ocean ridge basalts (MORBs) represent the end product of melting at oceanic ridges and have seen a long series of geochemical processes during their ascent. They are known to be produced by polybaric melting (O'Hara, 1985, Klein and Langmuir, 1987, McKenzie and Bickle, 1988), followed by a multistage history of pooling, interaction with the wall-rock and differentiation during their migration to the surface (e.g. Langmuir et al., 1992). Studies on melt inclusions show that primary melts have widely varying compositions (Sobolev and Shimizu, 1993). The effects of porosity, type of melt transport (porous versus channelized flow) and extent of melt-rock interaction during melt percolation are still a matter open to discussion. Abyssal peridotites, mantle rocks found on the ocean floor, represent the residual complement to MORBs and therefore play a key role for understanding mantle melting and melt extraction.

The style, in which new oceanic crust is formed, depends on the spreading rate of the mid-ocean ridge. Mid-ocean ridges have been divided into fast-, intermediate-, and slow-spreading types, each with distinctive morphologic characteristics (Macdonald, 1982).

Slow-spreading ridges (< 55 mm/year full spreading rate) have deep rift valleys with highly variable relief from 400 m to 2500 m and rough rift mountain topography weakly correlated to spreading rate.

CHAPTER 1

Fast-spreading ridges (80– 180 mm/year) have low (400 m) axial highs, sometimes with small linear depressions (less than 100 m wide and less than 10 m deep) at their crests, and minimal rift mountain topography uncorrelated to spreading rate.

Intermediate-spreading ridges (55–70 mm/year) have long alternating sections with either slow- or fast-spreading ridge morphology.

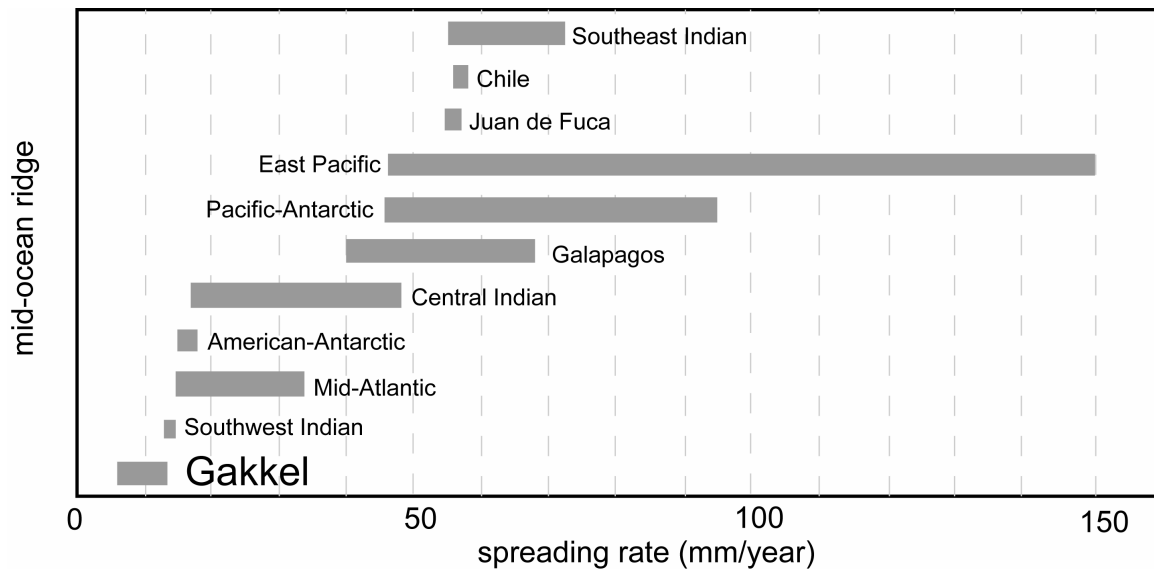


Figure 1-1: Spreading rates compared by mid-ocean ridge, Gakkel Ridge represents the end-member in the world ridge system (from Cochran et al., 2003).

Mid-ocean ridges, spreading at less than 20 mm/year, comprise 20000 km of the 55000 km global ridge system, but until recently have been little studied (Dick et al., 2003). Observations show that the crustal architecture and the processes responsible for its creation differ substantially from fast- to slow-spreading ridges. Fast-spreading ridges display a homogeneous, layered crust of more or less constant thickness that is formed with high melt supply and a relatively stable magmatic system (i.e., near-continuous axial magma chamber, frequent eruptions, etc.). In contrast, slow-spreading ridges show a wide range of crustal composition, structure and thickness, with variations both regionally and along individual segments. This complexity arises from a discontinuous mode of magma emplacement, and from a wide variation in the magma supply to the ridge axis, ranging from extension by pure stretching of the mantle lithosphere (Dick et al., 2003), to well-developed and magmatically

robust ridge segments that locally have crustal thicknesses exceeding 8 or 9 km (Cannat et al., 1999, Escartin et al., 2001, Searle and Escartin, 2004).

Slow-spreading ridges show a wide range of crustal composition, structure and thickness, with important variations both regionally and along individual segments. The differences between ultraslow- and slow-spreading ridges are as great as those between slow- and fast-spreading ridges (Dick et al., 2003). The ultraslow-spreading ridges usually form at full spreading rates less than about 12 mm/year, though their characteristics are commonly found at rates up to approximately 20 mm/year. The ultraslow-spreading ridges consist of linked magmatic and amagmatic accretionary ridge segments.

Models for magma production by decompression melting of passively upwelling mantle predict a rapid decrease in crustal thickness at total spreading rates of less than 15 mm/year (Reid and Jackson, 1981, Bown and White, 1994). However, many of their data for slow spreading rates came from areas at the onset of spreading or from dying ridges (Jha et al., 1994, Coakley and Cochran, 1998). In contrast, crustal thickness is very variable at slow-spreading ridges. Numerical and laboratory experiments showed that buoyancy-driven, dynamic mantle flow is an important element in the geodynamics of mid-ocean ridges (Kincaid *et al.*, 1996, Magde *et al.*, 1996). Buoyant flow is driven by density contrast from (i) melt depletion, (ii) melt retention and (iii) thermal expansion. When buoyant upwelling is important, crustal thickness is relatively independent of spreading rate (Jha et al., 1994). Active upwelling by buoyancy effects in relation to passive upwelling is more important at slow-spreading ridges compared to fast-spreading ridges (Jha et al., 1994). With decreasing spreading rate and mantle viscosity, mantle flow undergoes a transition from two-dimensional, sheet-like, to three-dimensional, plume-like, mantle flow. In the 3D case, upwelling is segmented into isolated melting centers spaced along axis (Barnouin-Jha et al., 1997).

Furthermore, slow-spreading ridges have thick lithospheric lids, depressing the top of the melting column and further limiting melt production (e.g. White et al., 2001). Deep conductive cooling also promotes the crystallization of significant amounts of melt in the mantle. It has been suggested that up to 25% gabbro is intruded into the peridotite at slow-spreading ridges (Cannat, 1996).

At slow-spreading ridges, in areas of low melt production, lower crustal and mantle rocks are often emplaced directly on the ocean floor (Bonatti, 1968, Aumento and Loubat, 1971, Auzende et al., 1989, Dick, 1989). These “deeper” rocks are most commonly found at the ends of slow-spreading segments and at inside corners, where the geophysically defined crust is thinner, and where tectonic processes appear to be more effective in exposing deeper lithologies (Searle and Escartin, 2004).

Peridotite outcrops are not restricted to segment ends or ridge discontinuities only, but may also be found along the segment centers of magma starved sections of slow-spreading ridges (Dick, 1989, Cannat, 1993, Cannat and Casey, 1995, Cannat et al., 1997, Seyler et al., 2003).

1.2 GAKKEL RIDGE

Gakkel Ridge extends over 1800 km across the Arctic Ocean from the northeastern corner of Greenland to the Laptev Shelf. On its western end, it is connected via the oblique-spreading Lena Trough and the Molloy Fracture Zone to the Knipovich Ridge, the northernmost part of the Mid-Atlantic Ridge; its eastern end runs into the continental margin of the Laptev Sea, where rifting continues (Figure 1-2).

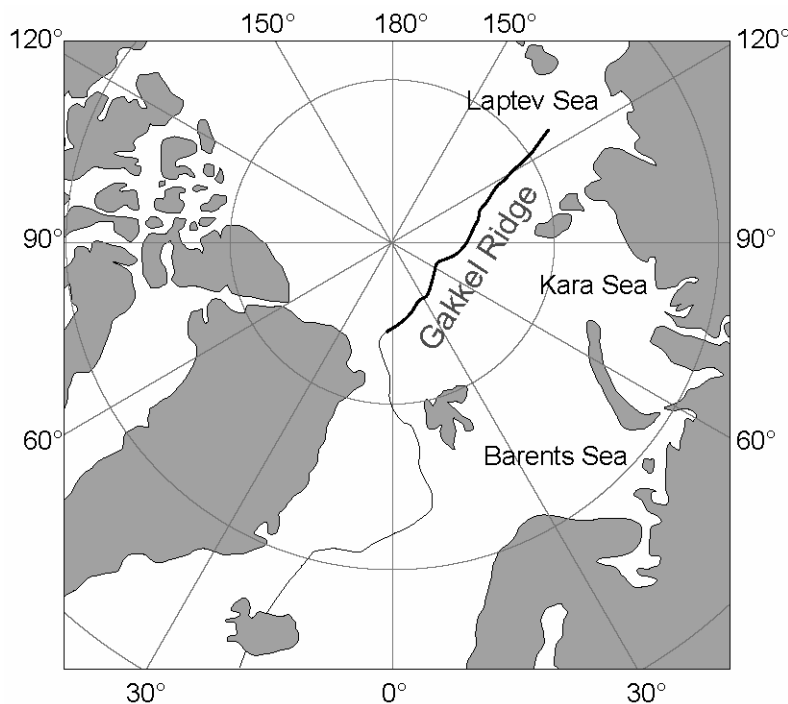


Figure 1-2: Overview map of the Arctic Ocean with the location of Gakkel Ridge.

Gakkel Ridge is an orthogonally-spreading mid-ocean ridge that is the slow-spreading end-member in the global mid-ocean ridge system. Its spreading rate decreases from 15.5 mm/year at the Greenland end to 6.3 mm/year at the Eastern end in the Laptev Sea.

Gakkel Ridge was the last unstudied mid-ocean ridge. It was virtually unsampled before the AMORE (Arctic Mid-Ocean Ridge) expedition in 2001, but for three samples found in a core catcher in 1987 (Mühe et al., 1993, Mühe et al., 1997). Prior to AMORE, the SCICEX (Science Ice Exercises) program carried out a bathymetry and gravity survey in 1996 (Coakley and Cochran, 1998) and sidescan survey in 1999 (Edwards et al., 2001). Gravity data from Gakkel Ridge predicted thin or absent crust and that large areas of the ridge had mantle peridotites outcropping at the sea floor (Coakley and Cochran, 1998). Sidescan data revealed fresh basaltic flows (Edwards et al., 2001).

The AMORE expedition plan was to obtain more precise bathymetry in conjunction with a small-spaced sampling program. Goals were to study the relation between volcanism and spreading rate and the nature of the oceanic mantle not modified by high degrees of partial melting. Furthermore, low degree melts expected at Gakkel Ridge are difficult to study in laboratory experiments. The AMORE expedition studied the ridge between 8° W and 85° E.

1.2.1 Morphology of Gakkel Ridge

The Gakkel Ridge rift valley is continuous without transform faults. The rift axis is exceptionally deep and is located within a 20 km wide rift valley (Cochran et al., 2003). Axial depths between 20°E and 70°E lie generally between 4600 and 4800 m below sea level, but locally exceed 5000 m (Coakley and Cochran, 1998). A short portion of the rift axis farther west near 0°E shows axial depths of 4000 – 4350 m (Jokat et al., 1995). The Gakkel Ridge axial depths are consistently deeper than those observed on the Mid-Atlantic Ridge where maximum depths usually lie within 3500 – 4000 m, only rarely reaching 4500 m (Cochran et al., 2003).

Gakkel Ridge flanks lie at depths of about 3200 m, also several hundred meters deeper than typically observed at faster-spreading ridges (e.g. Small, 1994). The ridge flanks are characterized by a linear fabric of ridge-parallel abyssal hills. The abyssal hills are large and

CHAPTER 1

blocky reflecting the importance of tectonic extensional processes. Large scarps with relief of up to 1400 m are common, both in the axial valley and on the ridge flanks. Fault-bounded troughs with relief of over 1000 m and reaching depths of over 4000 m are observed on the ridge flanks (Coakley and Cochran, 1998).

The ridge axis to the west of 60°E is segmented into 50 – 100 km intervals by non-transform discontinuities of less than 20 km offset. The rift valley morphology is very asymmetric within individual segments. These bends are reflected in the morphology of the Lomonosov Ridge and are evidently inherited from the initial breakup (Brozena et al., 2003). Outside corners are deep with low slopes and do not get much shallower than 3600 m. Inside corner highs are well developed with steep slopes and up to 3 km relief (Coakley and Cochran, 1998).

Gakkel Ridge is divided into three distinct morphotectonic regions (Michael et al., 2003) (Figure 1-3):

1 7°W – 3°E: Western Volcanic Zone (WVZ):

This region is characterized by three well-developed magmatic swells in the ridge axis that are composed of hundreds of small volcanic cones. Lower crustal lithologies are tectonically exposed in between these magmatic upwelling centers.

2 3°E – 30°E: Sparsely Magmatic Zone (SMZ):

At 3°E, the ridge suddenly goes through an offset that appears similar to an overlapping spreading centre but with a purely amagmatic tectonic eastern limb. The valley to the east lies 1000 m deeper than the adjacent magmatic ridge. The ridge continues as a series of lenticular basins interrupted twice by a tectonic septum and twice by volcanically constructed magmatic centres.

3 30°E – 85°E: Eastern Volcanic Zone (EVZ):

The frequency and magnitude of magmatic constructional features increases in this region despite the declining spreading rate. Magmatic saddles arise in the rift valley at 31°E, 33°E, 37°E, 42°E, 55°E, 61°E, and large volcanic centers are observed at 69°E and 85°E. Very little to no peridotite is found in this region, suggesting that fault throws are short and

CHAPTER 1

magmatism has increased and produced a thicker lithosphere. The shape of the valley is largely unchanged but the rift walls are steeper than those of the WMZ.

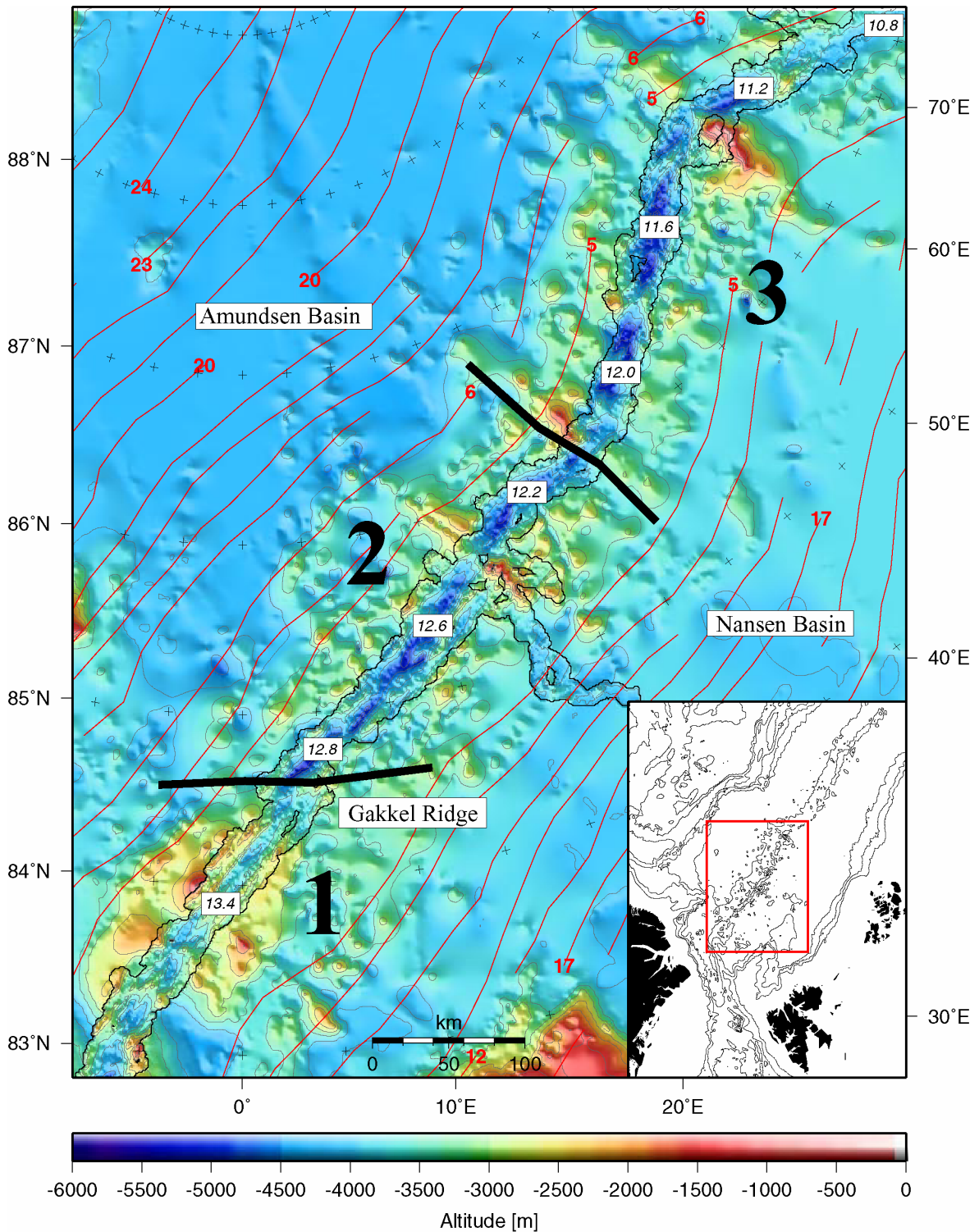


Figure 1-3: Bathymetric map of the western portion of Gakkel Ridge. Small numbers in the axial valley report spreading rates in mm per year, red contours represent lines of same age. The subdivision of the ridge into three regions is added, explanations see text (modified from Jokát et al., 2003).

1.2.2 Petrology of Gakkel Ridge

Gakkel Ridge was virtually unsampled before the AMORE-expedition in 2001; only two basalt and one peridotite samples were incidentally found in a core catcher during an expedition in 1987 (Mühe et al., 1991). During the AMORE-expedition, 18 tons of samples were recovered, mainly basalts (70%), 20% peridotites, 5% gabbros and 5% other lithologies such as sulfides, greenstones etc. The ARK XX-2 expedition returned in 2004 to the SMZ for more intense sampling and higher bathymetric coverage in the 3° E region.

1.2.2.1 Basalts

Abundant phyric basalts can be found at Gakkel Ridge, suggesting the presence of magma chambers. Plagioclase phyric lithologies always contain olivine, suggesting that the rocks remain primitive, as olivine remains on their liquidus. Basalts found on the Gakkel Ridge are unusual in their vesicle content, approaching in places 10% and more, which is much higher than usual.

Radiogenic isotopes (Pb-Sr-Nd) show significant differences between the WVZ and the EVZ with a sharp boundary in the SMZ at 14° E (Goldstein et al., 2006). Lavas of the EVZ sample depleted mantle that is isotopically similar to the Atlantic-Pacific mantle. Axial lavas of the WVZ show high $^{208}\text{Pb}/^{204}\text{Pb}$ ratios and a steep negative correlation between Sr- and Pb-isotopes similar to the 'DUPAL anomaly' of the Southern Hemisphere. The boundary between these two isotopic provinces occurs in the middle of the SMZ within 20 km without overlap. The WVZ lavas are explained by contribution of sublithospheric continental mantle from Spitsbergen to the western Gakkel asthenospheric mantle (Goldstein et al., 2006). (Goldstein *et al.*, 2006)

Trace element and volatile composition of basalts corroborate this interpretation (Michael et al., 2006). All basalts from the WVZ are enriched in Ba and H₂O at a given level of mantle enrichment (i.e. La/Sm) compared to the EVZ and global MORB. Trace element ratios suggest participation of amphibole, minor phlogopite and another unconstrained phase in the melting of the WVZ-MORB source. However, the transition between WVZ and EVZ is not as sharp for trace element and volatile ratios as it is for isotopic ratios.

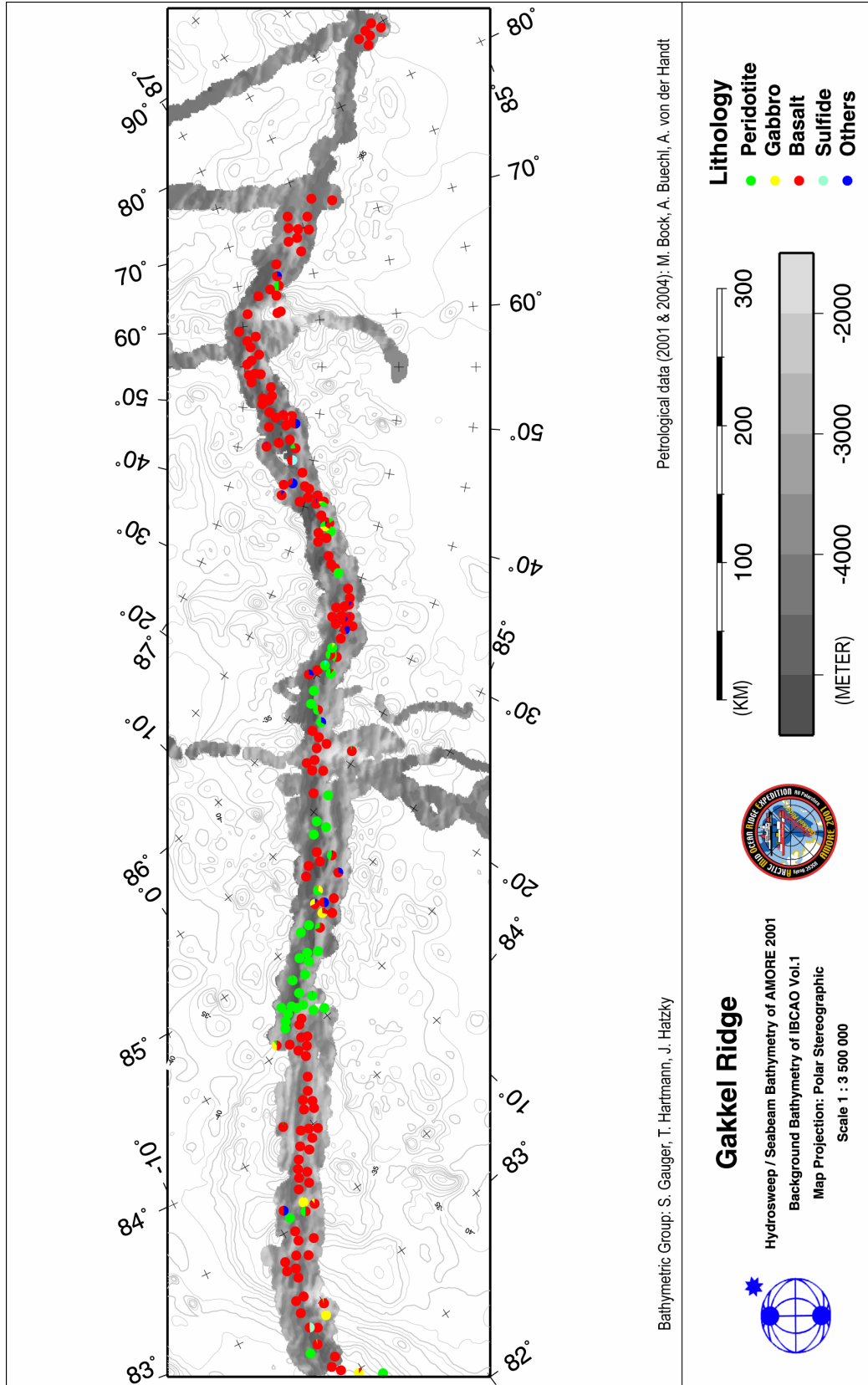


Figure 1-4: Map of Gakkel Ridge. The combined dredged lithology statistics from 2001 and 2004 expeditions are shown as pie charts.

1.2.2.2 Peridotites

Peridotites were recovered primarily between 3°E and 30°E from the centre and walls of the axial valley and from off-axis scarps. Most samples underwent moderate to strong sea-floor serpentinization but frequently preserve fresh cores of the primary phases.

Gakkel Ridge peridotites show a wider variety in mineral compositions than ever observed on a mid-ocean ridge. Spinel Cr-number (molar Cr/(Cr+Al)); an indicator for the degree of melting) vary from the lowest (0.07) to the highest (0.65) yet found at a mid-ocean ridge. Beside these variations in spatial distribution, dredge statistics show a huge variation in composition.

In the region between 3°E and 20°E, peridotite compositions record low degrees of near-fractional melting but require increasing amounts of reactive melt migration going eastwards (Hellebrand et al., 2006). This reactive melt transport is superimposed on the near-fractional 'background' melting, and must have been restricted to focused melt transport channels and confined infiltration zones; otherwise the LREE-depleted signature in the modally fertile lherzolites would have been easily overprinted. The easternmost part of this region consists exclusively of virtually cpx-free harzburgites and dunites (4 dredges, n=11, 40 km). The change in peridotite compositions is abrupt (<20 km). Spinel Cr-numbers between 0.53 and 0.63 are among the most depleted on the ocean floor, and not at all consistent with a spreading-rate dependent degree of melting. Most cpx REE patterns are LREE-enriched, one dunite is LREE-depleted, and two harzburgites have hump-shaped cpx REE patterns. The distribution of breccia-hosted spinels (n=113) show a similar range in spinel Cr-numbers (0.50-0.65), confirming that there is no fertile peridotite relict preserved in the locally exposed upper mantle. This signature can only be preserved if degrees of melting are low, suggesting that a strong depletion prior to upwelling underneath Gakkel Ridge is required (Hellebrand et al., 2006). This is corroborated by an Os-isotopic study on Gakkel Ridge peridotites that found very old depletion ages (~2.2 Ga) in two harzburgites (Liu et al., in press).

Plagioclase peridotites could be identified in about half of the dredges in the SMZ but only a small percentage of the samples actually contain plagioclase.

1.2.2.3 Gabbro

Gabbros are virtually absent from this ridge compared to basalts and peridotites, implying that shallow magma chambers are small or non-existent. Seismic refraction data also show no or no resolvable Layer 3 (Jokat et al., 2003, Jokat and Schmidt-Aursch, 2007).

1.2.3 Petrology and tectonics of the Gakkel 3°E ‘amagmatic’ segment

Between 3°E and 8° E, an ‘amagmatic’ segment within the ‘Sparsely Magmatic Zone’ occurs. There, the axial valley plunges 2000 m deeper from a magmatically robust area at 3000 m depth by an oblique crossing high. This area was investigated twice by dredging operations, during the AMORE expedition in 2001 and during ARK XX-2 in 2004.

1.2.3.1 Dredging results

Overall, ten dredge hauls were carried out in the 3°E amagmatic area of Gakkel Ridge in the course of ARK XX-2 (Figure 1-5), which adds to the information obtained during the AMORE- expedition in 2001. Dredging of the axial high brought, both in 2001 (PS59-234) and 2004 (PS66-232), altered basalts which suggest that this high was not magmatically active for some time.

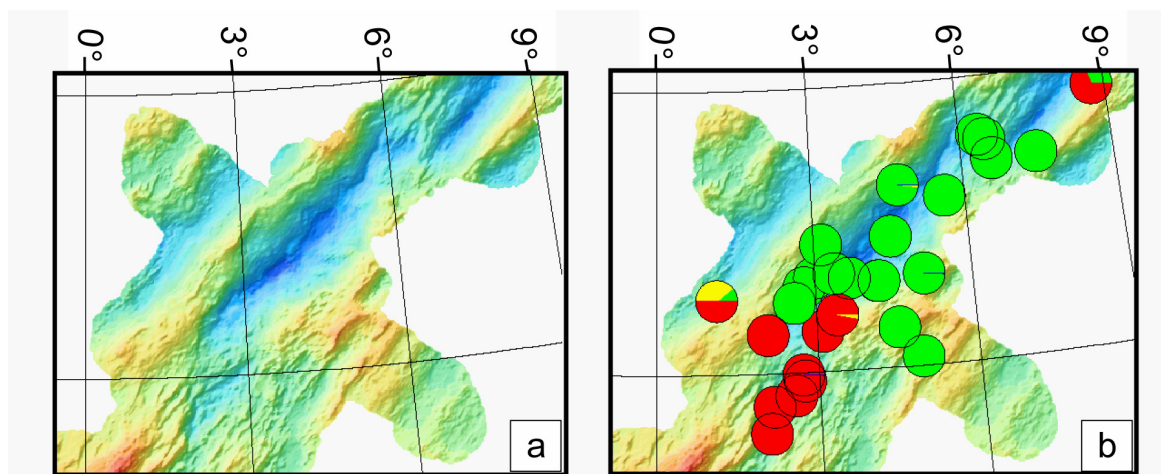


Figure 1-5: 3°E region of Gakkel Ridge showing the (a) bathymetry and (b) distribution of lithologies; see Figure 1-4 for legend.

CHAPTER 1

Further east along the rift axis, no other evidence for the creation of a magmatic crust can be found except in dredge haul PS66-241, off-axis of the Northern wall that recovered 3.4 kg gabbro and 2.3 kg basalts. Seven out of ten dredge hauls contain plagioclase-bearing peridotites, ranging from plagioclase lherzolites to plagioclase-enstatite-dunites. The modal content of plagioclase and distribution seems to be correlated with the stratigraphic level; peridotite samples with less plagioclase occur in the deeper parts of the valley and higher modal contents are found in most samples in the higher structural levels (PS66-234 and PS66-238). Additionally to the plagioclase-bearing lithologies, some dredge hauls contain few vein-bearing peridotites with both gabbro (PS66-234) and pyroxenite (PS66-236) veins.

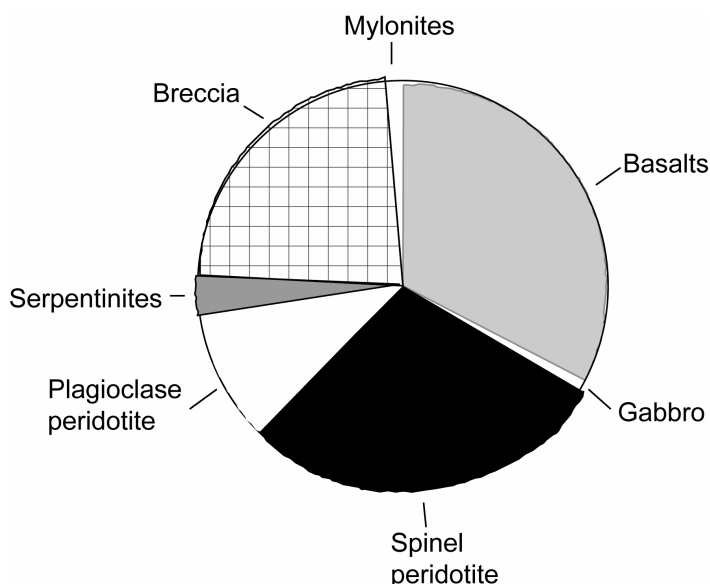


Figure 1-6: Overview of lithologies recovered by dredging at 3°E at Gakkel Ridge during ARK XX-2 based on onboard descriptions.

For the interpretation of the tectonic history of this area the degree of deformation was noted for each sample. Peridotites recovered from the bottom of the flanks show signs of intense deformation on both sides of the flank. The two dredge hauls of the northern flank both show deformation where PS66-233 consists only of low-temperature brittle cataclasites, two also with a high modal content of plagioclase, whereas PS66-235 mainly consists of breccias whose clasts show intense deformation. On the opposite side of the rift valley, dredge haul PS66-236 consists of mylonites and other deformed samples. Unfortunately, most of them also show a high degree of alteration.

The two dredge hauls that lie at a higher level on either side of the rift valley show some deformation but considerably weaker than the ones previously mentioned. Samples from

dredge haul PS66-234 at the western wall have aligned minerals and even some protomylonitic samples. The dredge haul on the other side of the rift (PS66-238) shows a similar degree of deformation. Dredging on off-axis highs on the southern side of the ridge valley recovered only peridotites as well. There, the peridotites of dredge haul PS66-239 showed abundant mylonitic features.

1.2.4 Sample locations: Dredge hauls PS66-238 and PS59-235

Peridotites from dredge hauls PS59-235 (AMORE 2001) and PS66-238 (ARK XX-2), from the western edge of the sparsely magmatic area are extremely fresh; their degree of alteration rarely exceeds 20%, and some samples show no hydrous alteration at all. Fresh peridotites from the ocean floor are extremely rare. Hence, PS66-238 was an attempt to repeat the dredging track of PS59-235 (Table 1-1) and ended successfully with the recovery of 275 kg of the freshest abyssal peridotites known.

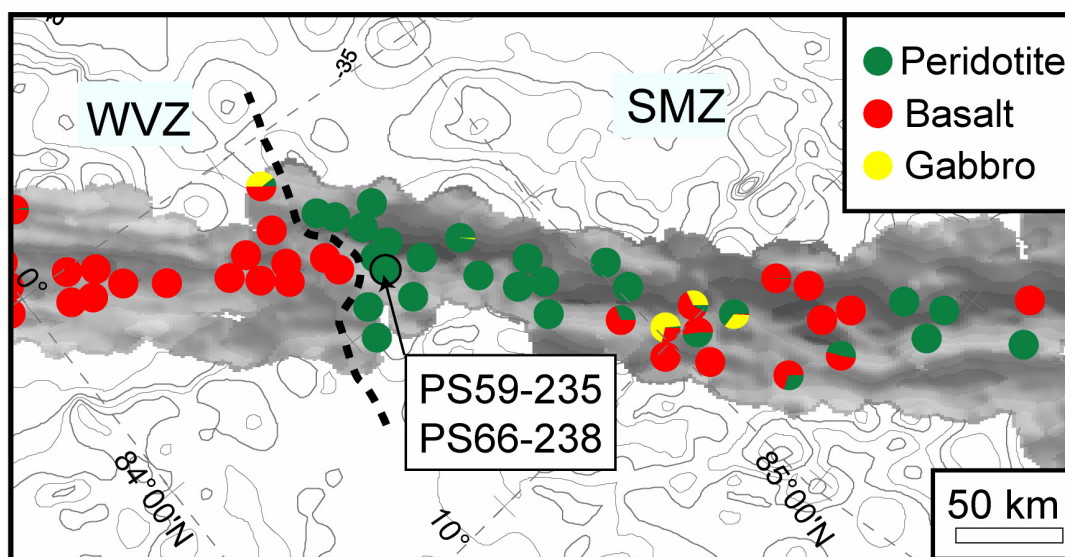


Figure 1-7: Bathymetric map of the central portion of Gakkel Ridge at the transition of the Western Volcanic Zone (WVZ) to the Sparsely Magmatic Zone (SMZ). Dredge results from expedition ARK XVII-2 (2001), and ARK XX-2 (2004), are shown as pie charts. The samples in this study were collected at the westernmost part of the SMZ where only mantle peridotites have been recovered.

CHAPTER 1

Table 1-1: Dredge positions for PS59-235 and PS66-238.

Station No.	Start			End			Results (kg)	Lithology
	Position		Water Depth (m)	Position		Water Depth (m)		
	Latitude (N)	Longitude (E/W)		Latitude (N)	Longitude (E/W)			
PS59-235	84° 39.2'	004° 11.9' E	4232	84° 37.5'	004° 13.9' E	3370	170.2	Peridotite
PS66-238	84° 39.2'	004° 12.6' E	4151	84° 38.1'	004° 12.2' E	-	274.6	Peridotite

PS59-235 dredge haul consists of 140 fertile spinel and plagioclase peridotites, of which 15 were selected for detailed investigation. No evidence for extrusive or intrusive magmatic products as basalts or gabbros could be identified in the dredge haul.

PS66-238 peridotites show in general a degree of alteration of less than 10% and all major peridotite types (lherzolite, harzburgites, enstatite-dunite) are represented except for orthopyroxene-free dunites. Besides the residual lithologies, almost half of the peridotite samples consist of plagioclase-bearing peridotites whose subgroups mirror the residual ones in matching modal proportions (Figure 1-8). Furthermore, several samples showed distinct modal changes of pyroxene contents in hand specimens as well as diffuse cpx-veins or layering. Two pyroxenite samples were found as well. From this dredge haul, two fresh samples with heterogeneous pyroxene-contents were chosen.

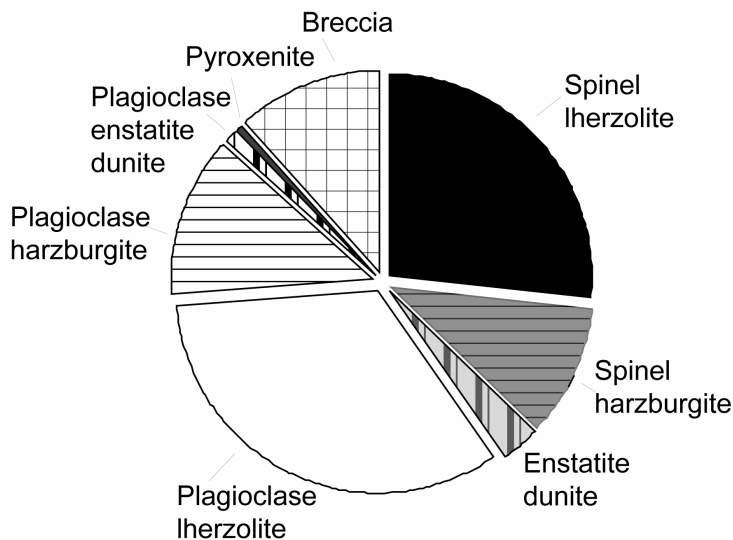


Figure 1-8: Overview of lithologies recovered in dredge haul PS66-238. Total weight of samples is 275 kg.

1.3 OUTLINE OF THE THESIS

The aim of this thesis is to systematically study the different processes that can modify the composition of residual peridotites during their uplift to the ocean floor below mid-ocean ridges.

The following six chapters are ordered to reflect the presumed order of processes occurring during the uplift beneath Gakkel Ridge in P-T space (Figure 1-9). The individual chapters are kept to be as self sustained as possible.

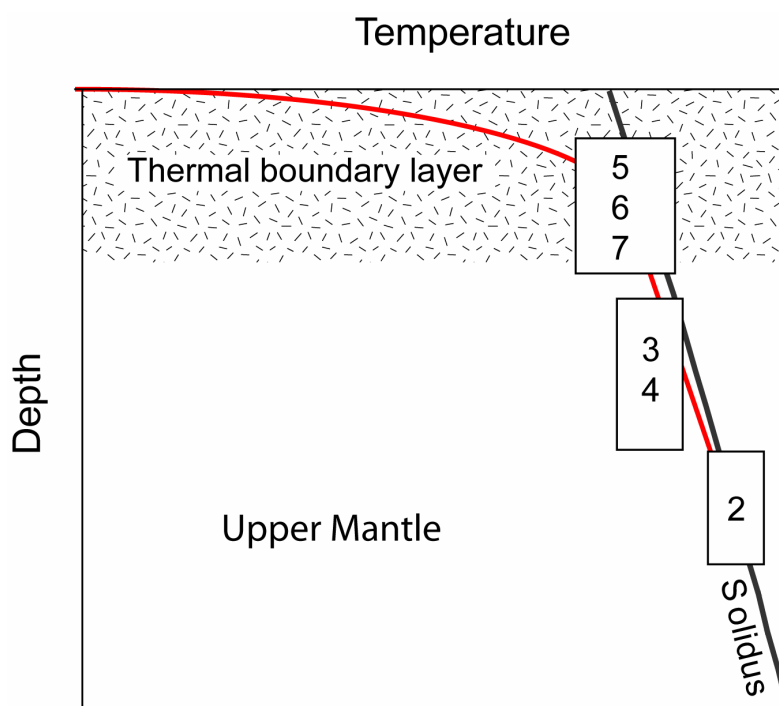


Figure 1-9: Outline of the thesis, numbers denote the respective chapters, red line represents the hypothetical trajectory of the mantle peridotites of this study. Not to scale.

This thesis is structured as follows:

Chapter 1 gave a general introduction to slow- and ultraslow-spreading ridges and on the regional geology of Gakkel Ridge.

Chapter 2 investigates the melting history of the spinel peridotites found in dredge hauls PS59-235 and PS66-238. They are assumed to represent the starting point for most processes that are dealt with in the following chapters. Major and trace element mineral composition in conjunction with microtextures are presented in this chapter.

CHAPTER 1

Chapter 3 investigates the trace element exchange between clinopyroxene and orthopyroxene during subsolidus cooling in mantle peridotites. Based on systematic core to rim trace element zoning in orthopyroxene, a new geospeedometer for mantle rocks is proposed that allows assessing a temperature interval not covered by any other known geospeedometer.

Chapter 4 represents a study on the diffusion systematics of selected trace elements and rare earth elements in orthopyroxene. This is an offshoot of the study presented in Chapter 3 that allows determining the relative diffusivities of 16 trace elements and their cation position within the orthopyroxene lattice. This represents the first comprehensive and internally consistent study with 16 trace elements on cation diffusion in natural orthopyroxene to date.

Chapter 5 presents a major and trace element study on mineral compositions from very fresh plagioclase peridotites from dredge haul PS59-235. Despite the high relative abundance of plagioclase peridotites among dredge abyssal peridotites, data is still scarce from samples from mid-ocean ridges. Different qualitative models for the formation of plagioclase in mantle rocks have been proposed previously, which are tested quantitatively in this chapter by mass balance approach. Furthermore, a new conceptual model of reactive melt stagnation and melt-rock reaction in the oceanic mantle is proposed.

Chapter 6 focuses on the composition of chromian spinels in plagioclase peridotites. Spinel is sensitive indicators of their environment and are widely used as petrogenetic indicators. I will show that their composition is the product of the complex interplay between residual composition, reactive melt interaction and equilibration processes.

Chapter 7 uses the implications of the previous chapter and strengthens the presence of disequilibrium melt migration in the mantle and its implications.

Chapter 8 gives a synthesis and outlook.

1.4 REFERENCES

- Aumento, F. and Loubat, H. (1971). The Mid-Atlantic Ridge near 45°N. Serpentinized ultramafic intrusions. *Canadian Journal of Earth Sciences* 8, 691-663.
- Auzende, J. M., Bideau, D., Bonatti, E., Cannat, M., Honnorez, J., Lagabriele, Y., Malavieille, J., Mamaloukasfrangoulis, V. and Mevel, C. (1989). Direct observation of a section through slow-spreading oceanic-crust. *Nature* 337, 726-729.
- Barnouin-Jha, K., Parmentier, E. M. and Sparks, D. W. (1997). Buoyant mantle upwelling and crustal production at oceanic spreading centers: On axis segmentation and off-axis melting. *Journal of Geophysical Research-Solid Earth and Planets* 102, 11979-11989.
- Bonatti, E. (1968). Ultramafic rocks from the Mid-Atlantic Ridge. *Nature* 219, 363-364.
- Bown, J. E. and White, R. S. (1994). Variation with spreading rate of oceanic crustal thickness and geochemistry. *Earth and Planetary Science Letters* 121, 435-449.
- Brozena, J. M., Childers, V. A., Lawver, L. A., Gahagan, L. M., Forsberg, R., Faleide, J. I. and Eldholm, O. (2003). New aerogeophysical study of the Eurasia Basin and Lomonosov Ridge: Implications for basin development. *Geology* 31, 825-828.
- Cannat, M. (1993). Emplacement of mantle rocks in the sea-floor at midocean ridges. *Journal of Geophysical Research-Solid Earth and Planets* 98, 4163-4172.
- Cannat, M. (1996). How thick is the magmatic crust at slow spreading oceanic ridges? *Journal of Geophysical Research-Solid Earth and Planets* 101, 2847-2857.
- Cannat, M. and Casey, J. F. (1995). An ultramafic lift at the Mid-Atlantic Ridge: successive stages of magmatism in serpentinized peridotites from the 15°N region. In: Vissers, R. L. M. & Nicolas, A. (eds.) *Mantle and lower crust exposed in oceanic ridges and in ophiolites*. 6. Dordrecht/Boston/London: Kluwer Academic Publishers, 5-34.
- Cannat, M., Lagabriele, Y., Bougault, H., Casey, J., deCoutures, N., Dmitriev, L. and Fouquet, Y. (1997). Ultramafic and gabbroic exposures at the Mid-Atlantic Ridge: geological mapping in the 15°N region. *Tectonophysics* 279, 193-213.
- Cannat, M., Rommevaux-Jestin, C., Sauter, D., Deplus, C. and Mendel, V. (1999). Formation of the axial relief at the very slow spreading Southwest Indian Ridge (49°-69°). *Journal of Geophysical Research-Solid Earth and Planets* 104, 22825-22843.
- Coakley, B. J. and Cochran, J. R. (1998). Gravity evidence of very thin crust at the Gakkel Ridge (Arctic Ocean). *Earth and Planetary Science Letters* 162, 81-95.
- Cochran, J. R., Kurras, G. J., Edwards, M. H. and Coakley, B. J. (2003). The Gakkel Ridge: Bathymetry, gravity anomalies, and crustal accretion at extremely slow spreading rates. *Journal of Geophysical Research-Solid Earth and Planets* 108, doi:10.1029/2002JB001830.
- Dick, H. J. B. (1989). Abyssal peridotites, very slow spreading ridges and ocean ridge magmatism. In: Saunders, A. D. & Norry, M. J. (eds.) *Magmatism in the ocean basins*. Geol. Soc. London Spec. Pub. 42. 71-105.

CHAPTER 1

- Dick, H. J. B., Lin, J. and Schouten, H. (2003). An ultraslow-spreading class of ocean ridge. *Nature* 426, 405-412.
- Edwards, M. H., Kurras, G. J., Tolstoy, M., Bohnenstiehl, D. R., Coakley, B. J. and Cochran, J. R. (2001). Evidence of recent volcanic activity on the ultraslow-spreading Gakkel ridge. *Nature* 409, 808-812.
- Escartin, J., Hirth, G. and Evans, B. (2001). Strength of slightly serpentinized peridotites: Implications for the tectonics of oceanic lithosphere. *Geology* 29, 1023-1026.
- Goldstein, S. L., Soffer, G., Langmuir, C., Lehnert, K., Cail, Y. and Michael, P. J. (2006). Isotope geochemistry of Gakkel Ridge basalts and origin of a 'DUPAL' signature. *Ophioliti* 31, 59-60.
- Hellebrand, E., Snow, J. E., Dick, H. J. B. and von der Handt, A. (2006). Inherited depletion in the oceanic mantle inferred from peridotite composition and distribution along Gakkel Ridge. *Ophioliti* 31, 60-61.
- Jha, K., Parmentier, E. M. and Morgan, J. P. (1994). The role of mantle-depletion and melt-retention buoyancy in spreading-center segmentation. *Earth and Planetary Science Letters* 125, 221-234.
- Jokat, W., Ritzmann, O., Schmidt-Aursch, M. C., Drachev, S. S., Gauger, S. and Snow, J. E. (2003). Geophysical evidence for reduced melt production on the Arctic ultraslow Gakkel mid-ocean ridge. *Nature* 423, 962-965.
- Jokat, W. and Schmidt-Aursch, M. C. (2007). Geophysical characteristics of the ultraslow spreading Gakkel Ridge, Arctic Ocean. *Geophysical Journal International* 168, 983-998.
- Jokat, W., Weigelt, E., Kristoffersen, Y., Rasmussen, T. and Schone, T. (1995). New geophysical results from the south-western Eurasian Basin (Morris-Jesup-Rise, Gakkel-Ridge, Yermak-Plateau) and the Fram- Strait. *Geophysical Journal International* 123, 601-610.
- Kincaid, C., Sparks, D. W. and Detrick, R. S. (1996). The relative importance of plate-driven and buoyancy-driven flow at mid-ocean ridges. *Journal of Geophysical Research-Solid Earth and Planets* 101, 16177-16193.
- Klein, E. M. and Langmuir, C. H. (1987). Global correlations of ocean ridge basalt chemistry with axial depth and crustal thickness. *Journal of Geophysical Research-Solid Earth and Planets* 92, 8089-8115.
- Langmuir, C. H., Klein, E. M. and Plank, T. (1992). Petrological systematics of mid-ocean ridge basalts: constraints on melt generation beneath ocean ridges. In: Phipps Morgan, J., Blackman, D. K. & Sinton, J. M. (eds.) *Mantle flow and melt generation at mid-ocean ridges*. Geophysical Monograph 71. Washington: American Geophysical Union, 183-280.
- Liu, C., Snow, J. E., Hellebrand, E., Brüggmann, G., Von der Handt, A., Büchl, A. and Hofman, A. W. (in press). Ancient, highly heterogeneous mantle beneath Gakkel Ridge, Arctic Ocean. *Nature*.

CHAPTER 1

- Macdonald, G. A. (1982). Mid-ocean ridges: fine scale tectonic, volcanic and hydrothermal processes within the plate boundary zone. *Annual Review of Earth Planet. Sciences* 10, 155-190.
- Magde, L. S., Kincaid, C., Sparks, D. W. and Detrick, R. S. (1996). Combined laboratory and numerical studies of the interaction between buoyant and plate-driven upwelling beneath segmented spreading centers. *Journal of Geophysical Research-Solid Earth and Planets* 101, 22107-22122.
- McKenzie, D. and Bickle, M. J. (1988). The volume and composition of melt generated by extension of the lithosphere. *Journal of Petrology* 29, 625-679.
- Michael, P. J., Langmuir, C. H., Dick, H. J. B., Snow, J. E., Goldstein, S. L., Graham, D. W., Lehnert, K., Kurras, G. J., Jokat, W., Mühe, R. and Edmonds, H. N. (2003). Magmatic and amagmatic seafloor generation at the ultraslow-spreading Gakkel Ridge, Arctic Ocean. *Nature* 423, 956-961.
- Michael, P. J., Langmuir, C. H., Goldstein, S. L., Graham, D. W., Ionov, D. A. and Matzen, A. K. (2006). Volatile and trace element constraints on sources of Gakkel MORB. *Ophioliti* 31, 66-67.
- Mühe, R., Bohrmann, H., Garbe-Schonberg, D. and Kassens, H. (1997). E-MORB glasses from the Gakkel Ridge (Arctic Ocean) at 87°N: evidence for the Earth's most northerly volcanic activity. *Earth and Planetary Science Letters* 152, 1-9.
- Mühe, R., Devey, C. W. and Bohrmann, H. (1993). Isotope and trace-element geochemistry of MORB from the Nansen-Gakkel Ridge at 86° North. *Earth and Planetary Science Letters* 120, 103-109.
- Mühe, R. K., Bohrmann, H., Hormann, P. K., Thiede, J. and Stoffers, P. (1991). Spinifex basalts with komatiite tholeiite trend from the Nansen-Gakkel Ridge (Arctic-Ocean). *Tectonophysics* 190, 95-108.
- O'Hara, M. J. (1985). Importance of the shape of the melting regime during partial melting of the mantle. *Nature* 314.
- Reid, M. R. and Jackson, I. (1981). Oceanic spreading rate and crustal thickness. *Marine Geophysical Research* 5, 165-172.
- Searle, R. and Escartin, J. (2004). The rheology and morphology of oceanic lithosphere and mid-ocean ridges. In: German, C. R., Lin, J. & Parson, L. M. (eds.) *Mid-ocean ridges: Hydrothermal interactions between the lithosphere and oceans*. 148. Washington, DC: American Geophysical Union, 63-93.
- Seyler, M., Cannat, M. and Mevel, C. (2003). Evidence for major-element heterogeneity in the mantle source of abyssal peridotites from the Southwest Indian Ridge (52° to 68°E). *Geochemistry Geophysics Geosystems* 4, doi:10.1029/2002GC000305.
- Small, C. (1994). A global analysis of mid-ocean ridge axial topography. *Geophysical Journal International* 116, 64-84.
- Sobolev, A. V. and Shimizu, N. (1993). Ultra-depleted primary melt included in an olivine from the Mid-Atlantic Ridge. *Nature* 363, 151-154.

CHAPTER 1

White, R. S., Minshull, T. A., Bickle, M. J. and Robinson, C. J. (2001). Melt generation at very slow-spreading oceanic ridges: constraints from geochemical and geophysical data. *Journal of Petrology* 42, 1171-1196.

CHAPTER 2

NEAR-SOLIDUS MELTING AND MELT REFERTILIZATION IN THE SPINEL STABILITY FIELD: EVIDENCE FROM THE ULTRASLOW-SPREADING GAKKEL RIDGE

2.1 INTRODUCTION

Mid-ocean ridge basalts (MORB) form by partial melting of adiabatically decompressing mantle beneath spreading mid-ocean ridges (e.g. Allègre et al., 1973, McKenzie and Bickle, 1988). Abyssal peridotites are commonly thought to represent the residual product after the partial melting process in the oceanic mantle (Dick, 1989). Therefore, the study of abyssal peridotites complements MORB studies to unravel melting conditions and dynamics at mid-ocean ridges. Mantle rocks occur on the ocean floor in a variety of tectonic settings such as on the walls of oceanic transform faults (Miyashiro et al., 1969, Aumento and Loubat, 1971), magmatically starved sections of slow spreading ridges (Cannat et al., 1995, Dick et al., 2003, Seyler et al., 2003) and ocean-continent transition zones (Kornprobst and Tabit, 1988).

Several melting models are currently used to explain the chemical variation in abyssal peridotites with fractional and batch melting as end-member models. Fractional melting assumes immediate removal of every infinitesimal increment of melt from the residue which rapidly leads to extreme depletion of highly incompatible trace elements in the residue. Batch melting assumes that melt and residue stay in contact after the melts have formed.

The strong light rare earth element (LREE) depletion in residual clinopyroxene (cpx) shows that melt extraction in the mantle is nearly fractional (Johnson et al., 1990, Johnson and Dick, 1992). Theory and experiments such as the MELT-experiment below the East Pacific Rise suggest that a finite porosity of 1 to 2% is present during mantle melting (Forsyth et al., 1998). At the onset of melting a critical threshold of porosity has to be reached before interconnectivity of the melt can lead to melt migration. This porosity threshold is estimated to be at 0.1% (Faul, 2001). However, modeling using the MELTS-software (e.g. Ghiorso and Sack, 1995) suggests that batch melting is required to explain the major element composition

of abyssal peridotites (Asimow, 1999). As an apparent compromise, a combination of both models, near fractional and batch melting, is envisaged to reconcile the chemical characteristics of abyssal peridotites (Kelemen et al., 1997, Asimow, 1999).

Experiments have successfully been used to constrain melting conditions and phase relations at pressure and temperatures relevant for the mantle (e.g. Kushiro, 2001). However, experimental determination of liquid compositions at low melt fractions are compromised by quenching-related modifications at the end of piston cylinder experiments (Takahashi and Kushiro, 1983). In natural samples, anomalous glass inclusions in mantle minerals, often with $\text{SiO}_2 > 60$ wt%, $\text{Na}_2\text{O} + \text{K}_2\text{O}$ up to 11 wt% and nepheline-normative compositions, have been interpreted as trapped liquids formed at less than 1% of partial melting (Schiano et al., 1998, Draper and Green, 1999).

New experimental techniques such as the diamond aggregate- (Johnson and Kushiro, 1992, Baker and Stolper, 1994, Baker et al., 1995), vitreous carbon sphere- (Pickering-Witter and Johnston, 2000, Wasylenki et al., 2003, Johnston and Schwab, 2004) and the microdike-technique (Laporte et al., 2004) have been developed to separate and analyze small volumes of liquids. However, it has been noted that at very low degrees of melting, the composition of the segregated liquid may deviate from the equilibrium composition (Laporte et al., 2004).

One of the objectives in sampling Gakkel Ridge was to study the nature of partial melting at very slow spreading rates. At such low spreading rates, melting should be restricted to a few percent and hence Gakkel Ridge could serve as a natural laboratory where experimental techniques faced difficulties so far. Although, this thesis does not aim to investigate comprehensively the melting dynamics below Gakkel Ridge, an understanding of the melting conditions of the sample suite is nevertheless important to the discussions presented in the following chapters.

2.2 PETROGRAPHY AND METHODS

Two spinel peridotites each, from dredge hauls PS59-235 and PS66-238 were investigated for their major and trace element composition. While abyssal peridotites are

commonly highly altered, peridotites from these two dredge hauls only show minor alteration, with most samples rarely exceeding 5% modal serpentine. This allowed the verification of the complete absence of plagioclase, both optically and by electron microprobe element mapping. The two samples from PS66-238 are modally heterogeneous in their pyroxene content on sample and thin section scale and grade from almost lherzolitic to dunitic in composition. Accordingly, two thin section blocks (A and B, respectively) were cut each representing the different modal domains. For sample 238-25, both blocks were cut next to each other whereas for 238-62 both blocks are separated about 5cm.

2.2.1 Petrographic and microtextural features

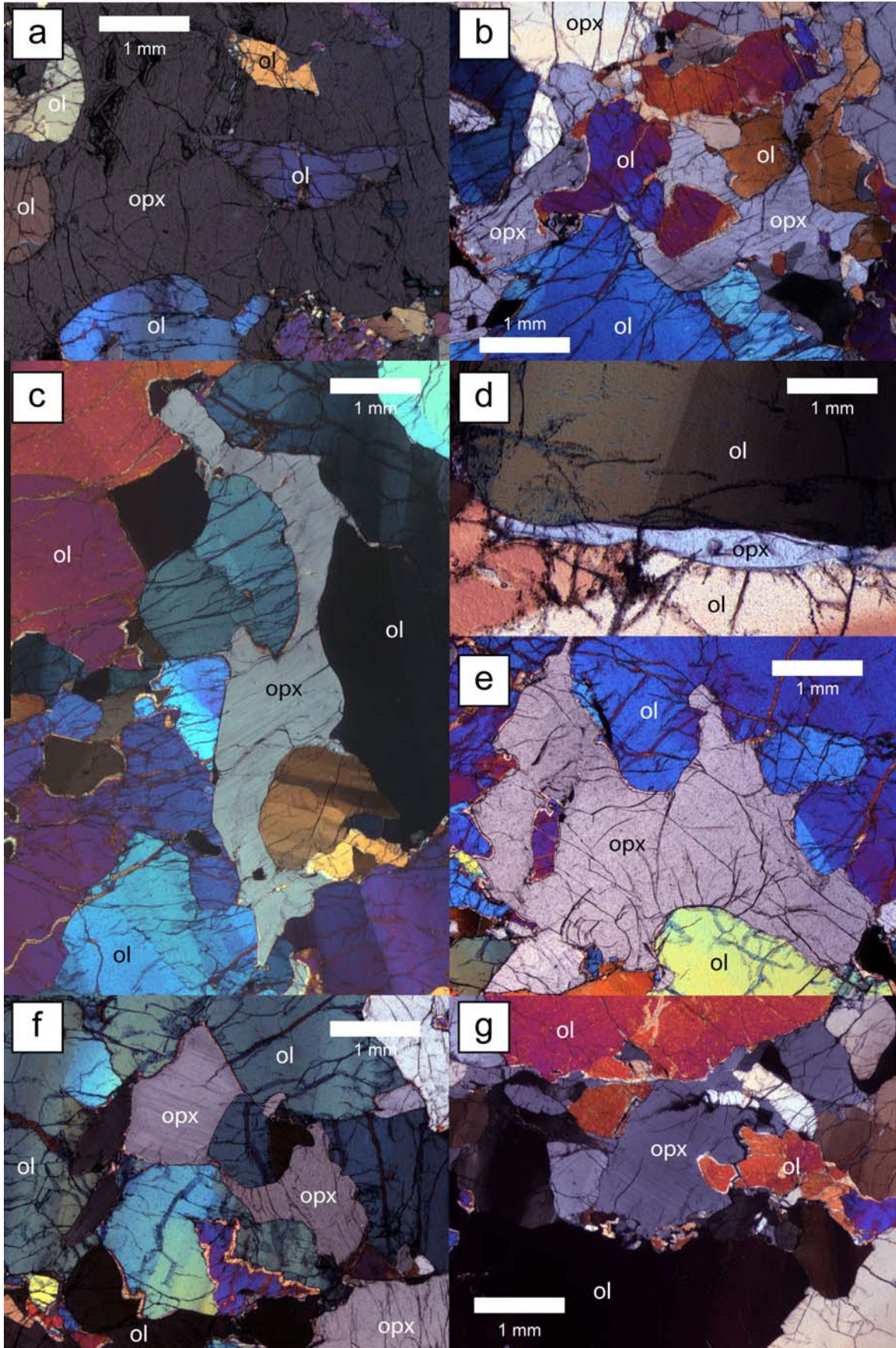
The textures of spinel peridotites from Gakkel Ridge range from coarse-granular to porphyroclastic. Olivine occurs in large grains (up to 1 cm) whereas pyroxenes form mm- to cm-scale porphyroclasts. Spinel is brown, and usually associated with pyroxenes. Pyroxenes show fine exsolution lamellae of the complementary pyroxene. Clinopyroxenes (cpx) rarely form large porphyroclasts but occur mostly disseminated in the matrix along grain boundaries. Orthopyroxenes (opx) form large (up to 1 cm) porphyroclasts with peculiar microstructures.

The most common orthopyroxene microstructures are (Figure 2-1):

- I. Undeformed, very coarse opx crystals with strongly irregular outlines, showing deep embayments against deformed olivine crystals. They often contain “undigested” olivine relicts that sometimes are still in crystallographic continuation with larger olivine grains.
- II. Elongated, mm- sized opx along olivine grain boundaries.

The microstructures suggest pervasive crystallization of opx (and cpx) with corrosion of residual olivine. This observation is in contrast to the commonly expected dissolution of pyroxenes and crystallization of olivine below mid-ocean ridges by either incongruent partial melting of orthopyroxene (Jaques and Green, 1980, Kelemen, 1990, Hirose and Kushiro, 1993), or reactive percolation of an orthopyroxene-undersaturated melt through mantle peridotites (e.g. Kelemen et al., 1995). Dissolution of olivine and crystallization of new orthopyroxene indicates a peritectic reaction of a silica-saturated liquid with mantle olivine.

CHAPTER 2



CHAPTER 2

Figure 2-1: Orthopyroxene microtextures: a) olivine relicts “swimming” in a large opx porphyroblast; b) corroded and “dismembered” mantle olivine replaced by undeformed opx; c) opx along grain boundaries with apophyses extending into the olivine; d) vermicular opx at olivine grain boundary; e) opx replacing olivine with opx apophyses extending into the olivine; c) undeformed opx crosscutting olivine; d) cpx associated with spinel between three opx grains; e) Embayed and corroded olivine replaced by undeformed opx; f) opx along grain boundaries and crosscutting olivine; g) undeformed opx replacing olivine that is still in crystallographic continuation.

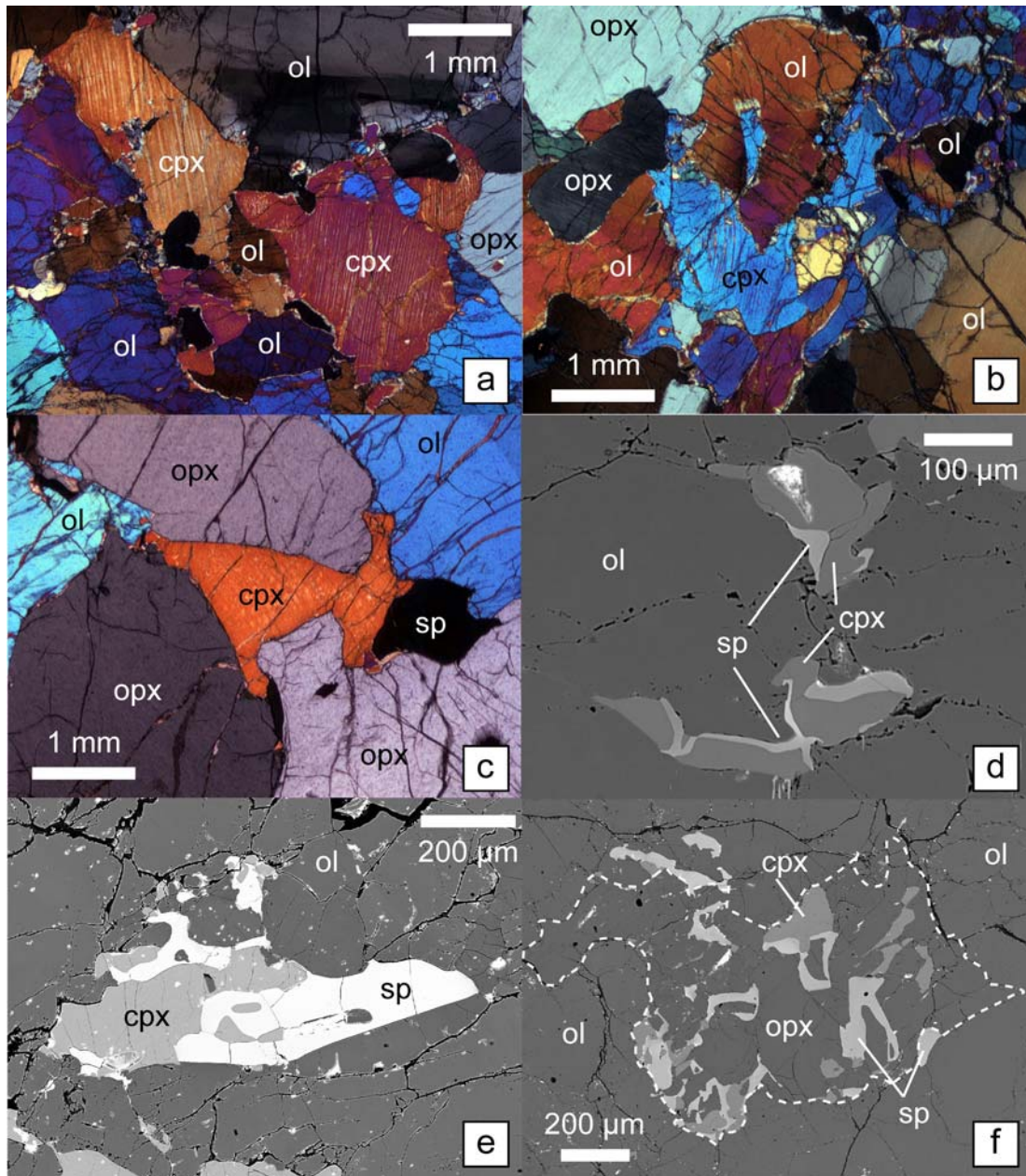


Figure 2-2: Clinopyroxene+spinel textures. a) cpx corroding olivine; b) crystallographic continuous olivine replaced by cpx; c) cpx associated with spinel interstitially between opx; d) cpx associated with spinel in olivine matrix (BSE picture); e) cpx intergrown with spinel in olivine matrix; f) opx-cpx-sp symplectite in olivine matrix (BSE picture).

2.2.2 Methods

Major element compositions of the silicate phases and spinels were analyzed with a five spectrometer electron probe microanalyzer (JEOL Superprobe 8900) at the University of Mainz. For pyroxenes and olivines, an accelerating voltage of 15 kV and a beam current of 12 nA were used. Standard counting times were 15s for Si, Mg, Fe, Ca, Cr, Mn and 20s for Al, Ti, Na, K and Ni. For spinels, an accelerating voltage of 20 kV and beam current of 20 nA were used. Standard counting times were 40s for Ca, Ti; 35s for Mg, Al; 30s for Cr, Fe, Mn, Co, Ni, Zn, and 20s for Si. Beam size was 2 μm for both routines. Natural and synthetic mineral and element standards were employed. Total FeO is assumed to be ferrous except for spinel where the Fe^{3+} content was calculated based on stoichiometry (Droop, 1987).

Clinopyroxenes were analysed in-situ in polished thin sections for selected rare earth elements (REE), and for Ti, Sc, V, Cr, Sr, Zr by secondary ion mass spectrometry (SIMS) using a modified Cameca IMS-3f ion probe at the Max-Planck Institute for Chemistry in Mainz. Ca^{43} was monitored as well to detect mixed analyses of opx and cpx. The primary beam of O^{16-} -ions was focused to a spot of 10 nA corresponding to a spot size of 20 μm . A high energy offset of – 80eV was used to reduce molecular interferences. Additional interference corrections were performed offline, where data were corrected for oxide overlaps at Eu, Gd, Dy, Er and Yb. Each measurement consisted of 6 cycles. Rare earth elements were measured in each cycle for 60s except Ce, Gd, Er and Yb for 40s, Dy, Sr and Zr for 20s, Y for 8s, Ti and Sc for 5s and all of the remaining elements for 1s. Detailed analytical conditions are reported elsewhere (Hellebrand et al., 2002). The overall accuracy is better than 20% for all REE and better than 12% for all other trace elements. Sensitivity factors were monitored by continuous analysis of the MPI-DING glasses GOR132-G and KL2-G (Jochum et al., 2006).

2.3 RESULTS

2.3.1 Major elements

Representative major element compositions of all phases are reported in Table 2-1. All spinel peridotites are homogeneous in terms of major elements in their silicates and spinels.

Spinel in PS66-238 samples show small variation in spinel Cr-numbers (= molar Cr/(Cr+Al)) ranging from 0.18-0.28 and 0.16-0.29, for 238-25 and 238-62, respectively, with TiO₂ contents below 0.15 wt%. This variation is correlated with high Fe₂O₃ concentration that either occurs in highest- or lowest-Cr-number spinels, but the majority of spinel analyses plot around Cr-number 0.21. PS59-235 samples have slightly lower spinel Cr-numbers of 0.14 and 0.16 for 235-17 and 235-20 respectively. TiO₂ concentrations are low and range between 0.05 and 0.09 wt% attesting to their residual nature since spinel-TiO₂ contents in plagioclase-bearing peridotites and dunites are usually high (Dick, 1989). Mg-numbers (= molar Mg/(Mg+Fe)) in spinel lie in-between and follow the trend of abyssal peridotites (Figure 2-3c).

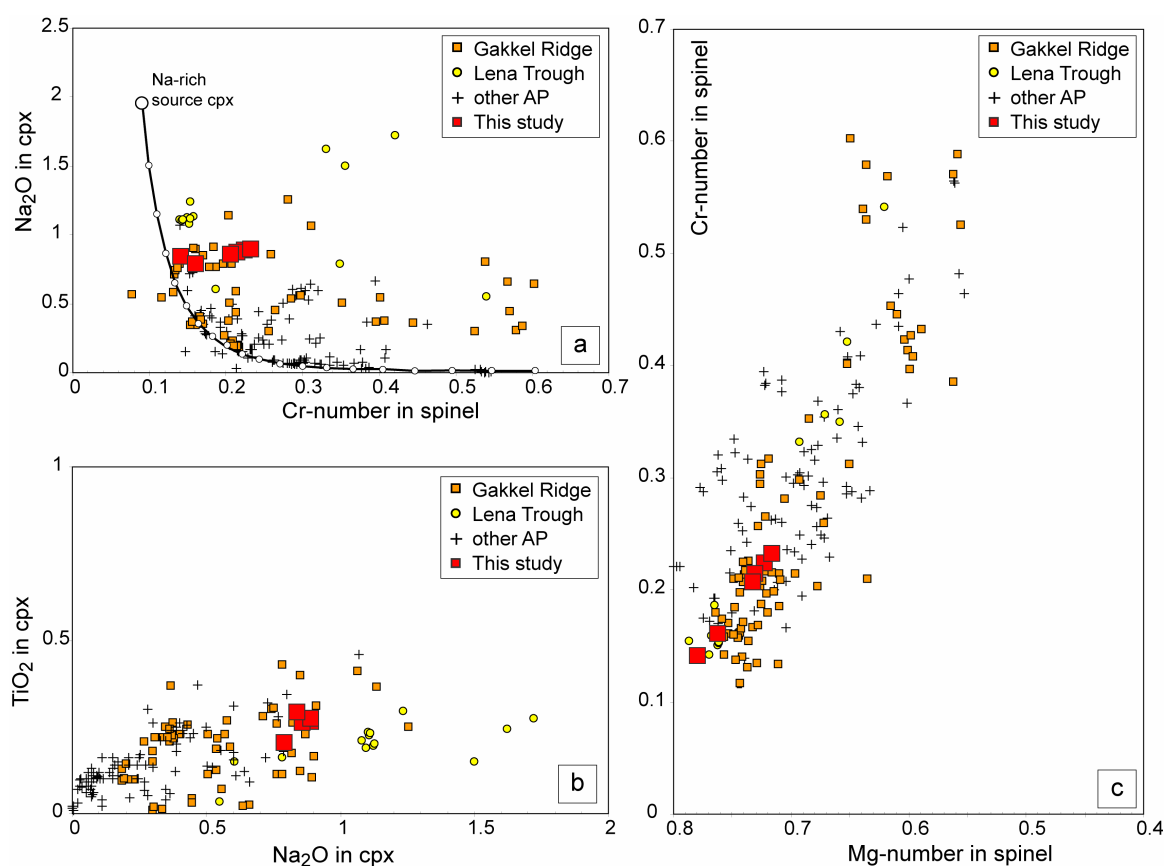


Figure 2-3: Major element composition of spinel peridotites. a) Na₂O in cpx against Cr-number in the associated spinel. All samples are shifted toward higher concentrations than predicted by the fractional melting trajectory. For model details see Hellebrand et al., (2003); b) Na₂O against TiO₂ in cpx. Samples lie within the broad trend defined by abyssal peridotites and plot toward the fertile end of the distribution; c) Mg-number against Cr-number in spinel. The studied samples fall within the field of abyssal peridotites. Additional data from the global mid-ocean ridge system and the Arctic Ridge system is plotted for comparison (global abyssal peridotites: Dick, 1989, Johnson et al., 1990, Juteau et al., 1990, Ghose et al., 1996, Hellebrand et al., 2002); Gakkel Ridge: E. Hellebrand, unpubl. data; Lena Trough: Hellebrand and Snow (2003).

CHAPTER 2

Clinopyroxenes have Mg-numbers (= molar $\text{Mg}/(\text{Mg}+\text{Fe})$) between 0.91 and 0.92, and Na_2O concentrations can reach 1.1 wt% but are 0.85 wt% on average. Clinopyroxenes are slightly shifted toward higher Na_2O concentrations away from the fractional melting trend (Figure 2-3a) suggesting Na_2O addition, though this has not significantly disturbed the correlation with TiO_2 in cpx (Figure 2-3b).

Orthopyroxenes have core CaO concentration of up to 1.34 wt% that decrease to rim concentrations as low as 0.4 wt%. Both pyroxenes have decreasing Al_2O_3 and Cr_2O_3 concentrations towards the rims (Figure 2-4) but constant Cr-numbers similar to the description of Seyler et al, (2007). Olivines show a narrow range in Mg-numbers of 0.908 (± 0.03) and NiO contents of around 0.39 wt%.

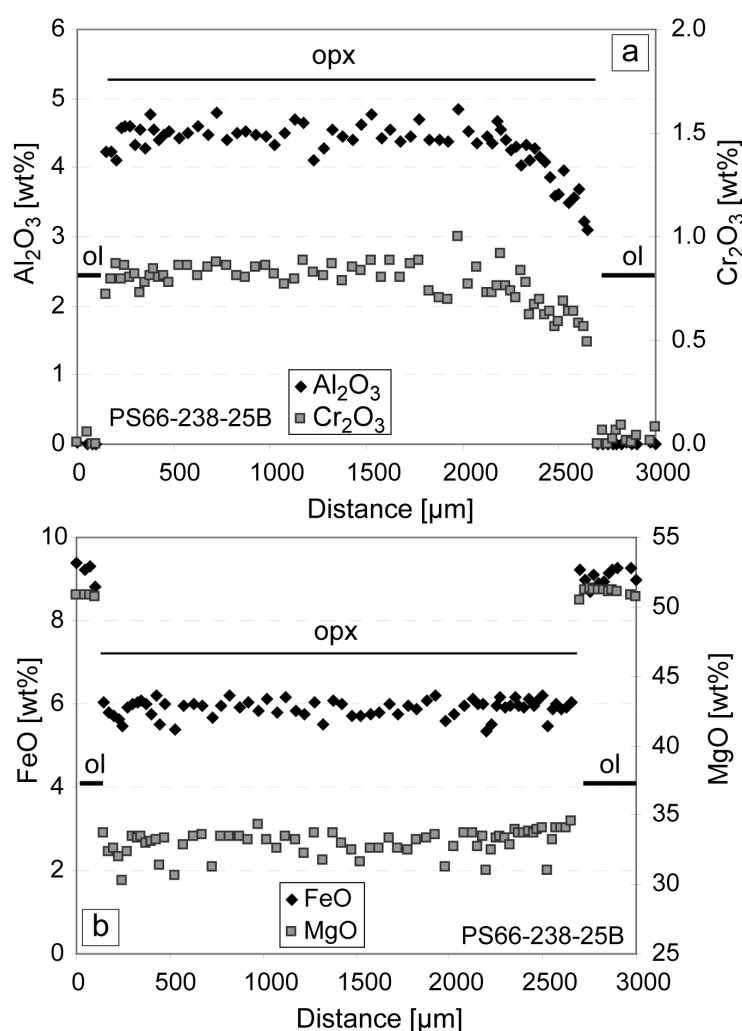


Figure 2-4: Orthopyroxene core-rim zoning in sample PS66-238-25B. Pyroxenes often show a decrease in Cr_2O_3 and Al_2O_3 toward the rim while MgO and FeO stay constant.

The good correlation between spinel, clinopyroxene (Figure 2-5) and orthopyroxene (not shown) indicates equilibrium between the mineral phases.

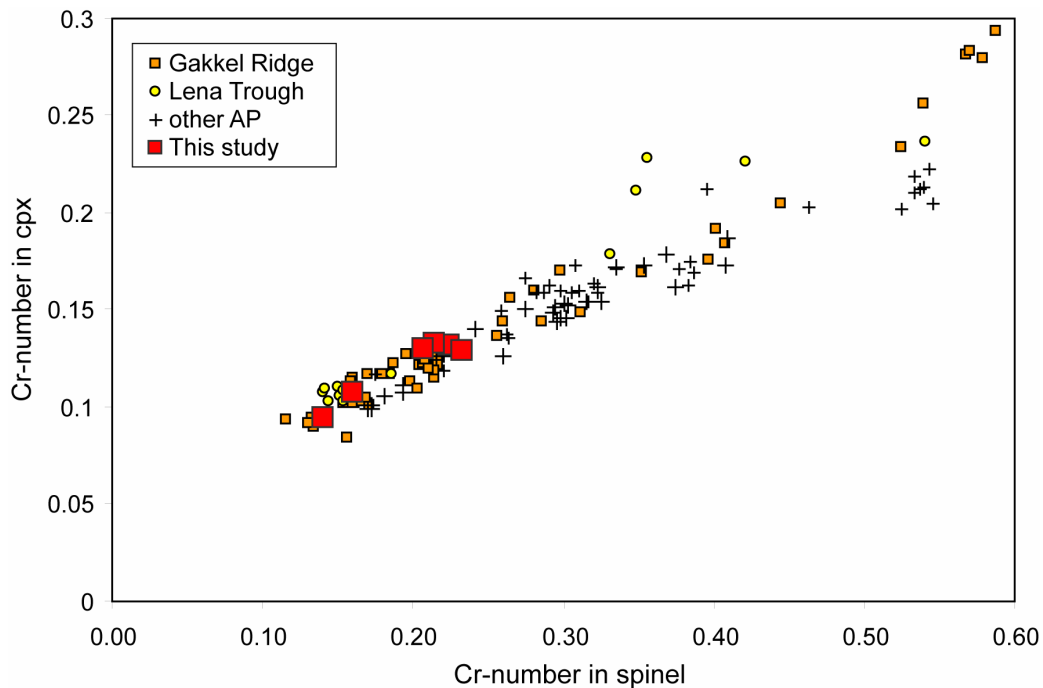


Figure 2-5: Cr-number in spinel against Cr-number in the associated cpx. The samples fall on the trend defined by global abyssal peridotites and from the Arctic Ridge system. Additional data from the global mid-ocean ridge system and the Arctic Ridge system is plotted for comparison (global abyssal peridotites: Dick, 1989, Johnson et al., 1990, Juteau et al., 1990, Ghose et al., 1996, Hellebrand et al., 2002); Gakkel Ridge: E. Hellebrand, unpubl. data; Lena Trough: Hellebrand and Snow (2003).

2.3.2 Trace elements

Trace element compositions of clinopyroxenes are reported in Table 2-2. Clinopyroxenes of PS66-238-25 and -66 show a flat REE-pattern ($(La/Yb)_N$: 0.6-0.9; subscript N denotes CI-chondrite normalized after Anders and Grevesse (1989)) at about 7 x CI, homogeneous within analytical accuracy on thin section scale (Figure 2-6). PS59-235 samples have steeper REE patterns with lower $(La/Yb)_N$ of 0.14 and 0.04 for 235-20 and 235-17, respectively. All clinopyroxenes exhibit a slight negative Sr-anomaly of around 0.8. Negative Ti- and Zr-anomalies typical for clinopyroxenes (Rampone et al., 1991) are more prominent in PS59-235 samples. Clinopyroxenes from individual thin sections of PS66-238-25 and -66 differ slightly in their LREE concentrations.

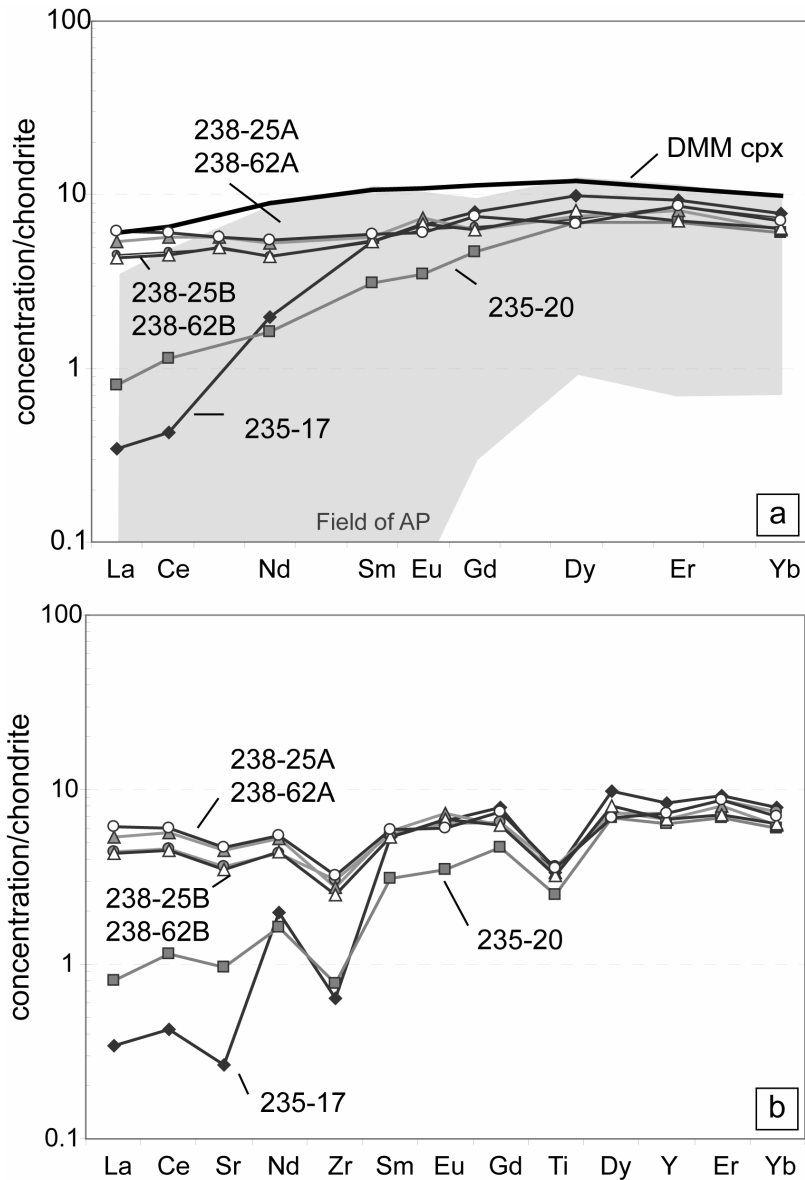


Figure 2-6: Trace element composition of clinopyroxenes; a) REE diagram, b) Trace element diagram. In gray, the field of abyssal peridotite compositions is shown (after Johnson et al., 1990).

2.4 DISCUSSION

2.4.1 Melting conditions

Trace element compositions of residual clinopyroxene [high field strength elements (HFSE) and REE] have been used to evaluate the degree of melting undergone by a mantle source (Johnson et al., 1990, Johnson and Dick, 1992, Hellebrand et al., 2002, Brunelli et al., 2006). Another good melting indicator is the Cr-number in spinel (Dick and Bullen, 1984).

CHAPTER 2

Hellebrand and coworkers (2001) have shown that the heavy rare earth elements (HREE) and the Cr-number in spinel are well correlated (Figure 2-7a), which allows to estimate the degree of partial melting directly from the spinel Cr-number. Based on this method, the absolute degree of melting is 8-9% for PS66-238 peridotites, 4% for PS59-235-17 and 6% for PS59-235-20. This lies at the lower end for Gakkel Ridge peridotites (Figure 2-7a).

However, this method assumes a spinel-facies Depleted Mantel (DMM) composition and does not account for melting in the stability field of garnet peridotite. The fractionation of Cr from Al is weaker during melting in the garnet stability field compared to the spinel stability field (Webb and Wood, 1986). This will lead to an underestimation of the true degree of total melting using the spinel Cr-number (Hellebrand and Snow, 2003). Hence, it is important to assess the amount of melting in the presence of garnet as well.

Heavy rare earth elements are compatible in garnet, and moderately incompatible in cpx (Hart and Dunn, 1993, Hauri and Hart, 1995). Melting in the presence of garnet will therefore produce a residue with higher HREE compared to melting in the spinel stability field. After re-equilibration under spinel facies conditions, cpx will have high HREE abundances and a low MREE/HREE-ratio. Thus, the cpx trace element composition is a useful recorder of garnet field melting (Hellebrand et al., 2002).

Lena Trough, a 300 km long linear, obliquely spreading deep and part of the Arctic ridge system, connects the orthogonal spreading Gakkel Ridge in the North with the amagmatic Molloy Ridge in the South. Peridotites from Lena Trough record the highest extent of garnet field melting relative to their total amount of melting compared to abyssal peridotites worldwide (Hellebrand and Snow, 2003). Spinel peridotites from Gakkel Ridge record much lower amounts of garnet field melting (E. Hellebrand, pers. communication and Figure 2-7b), which is also seen in the samples of this study. PS66-238 samples show no indication of garnet field melting whereas PS59-235 samples plot at 1-2% garnet field melting (Figure 2-7b). The degree of melting estimated from the spinel Cr-number is in good agreement with the results by this method for the individual sample. This suggests that the amount of garnet field melting is negligible and melting started at much shallower depth than in the Lena Trough.

CHAPTER 2

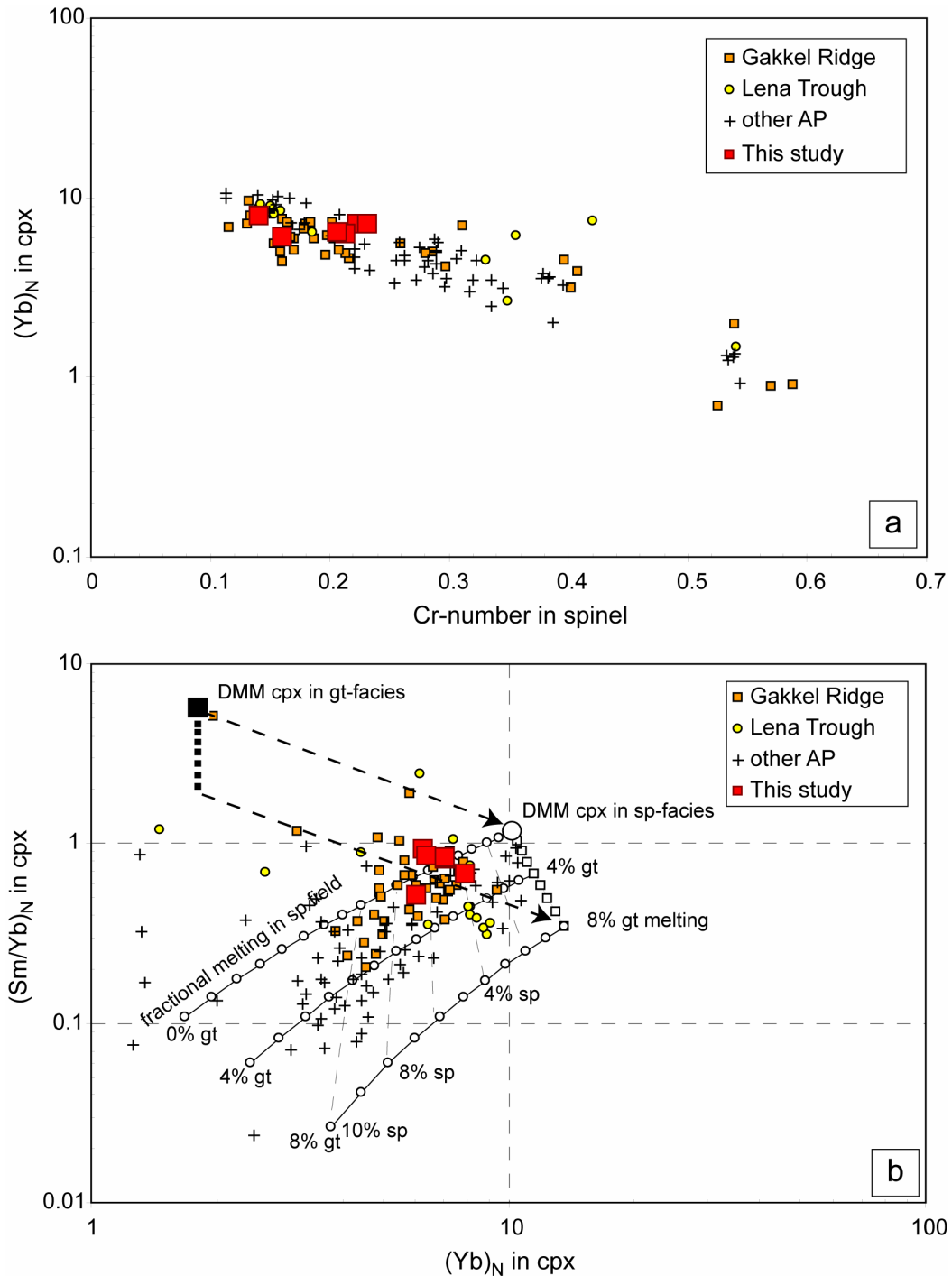


Figure 2-7: a) Cr-number in spinel versus the chondrite-normalized Yb in cpx. The good correlation allows the calculation of the degree of melting F via the empirical correlation $F=10*\ln(Cr\text{-number})+24$ (Hellebrand et al., 2001); b) Chondrite-normalized Yb against (Sm/Yb) in cpx. Superimposed are fractional melting models in the spinel and garnet peridotite field. PS66-238 and PS59-235 peridotites record almost entirely spinel field melting conditions. For a more detailed description of the model see Hellebrand et al. (2002). (data from global abyssal peridotites: Dick, 1989, Johnson et al., 1990, Juteau et al., 1990, Ghose et al., 1996, Hellebrand et al., 2002); data from Gakkel Ridge: E. Hellebrand, unpubl. data; Lena Trough: Hellebrand and Snow (2003).

2.4.2 Melt refertilization

Even though the melting indicators give consistent results for the samples of this study, cpx trace element patterns are inconsistent with a fractional or near-fractional melting process (Figure 2-8). Instead, cpx-REE patterns suggest equilibration with a LREE-enriched melt most likely derived by low degrees of melting. This is corroborated by the replacive textures seen in the samples, which also indicate the presence of an exotic melt.

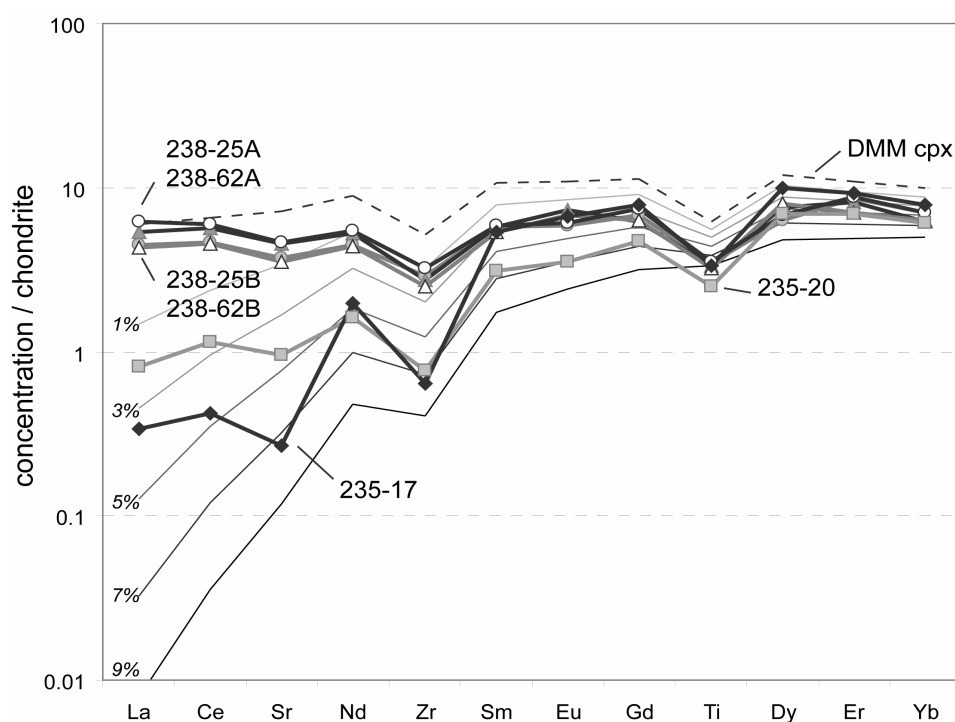


Figure 2-8: PS66-238 clinopyroxene REE concentrations. Gray field denotes the range in composition of clinopyroxene from abyssal peridotites (from Johnson et al., 1990). Superimposed is a cpx in equilibrium with DMM (Workman and Hart, 2005) and residual clinopyroxenes after different degrees of partial melting assuming critical melting of DMM at 1% residual porosity.

Current melt transport models assume that melts segregate from their residues after crossing a porosity threshold and then are rapidly extracted from the surrounding mantle in high-porosity channels without further equilibration with the shallow mantle (Kelemen et al., 1997). Final melt fractions produced at low pressures may also travel by porous flow leading to extensive melt-rock reaction and refertilization at shallow mantle levels (Kelemen et al., 1997, Dijkstra et al., 2003). Many abyssal peridotites show textural and chemical evidence for refertilization such as relative enrichment of highly incompatible trace elements in

clinopyroxene (Hellebrand et al., 2002, Brunelli et al., 2006) and also characteristic interstitial cpx microtextures (Seyler et al., 2001).

In the following, a two-stage model is applied to reconcile the different observations and match the cpx trace element compositions of the samples. The details of the procedure and model parameters of these calculations are reported in the Appendix.

The model assumes that the good correlation between HREE and major element indicates that no significant modification occurred to both after melting. Accordingly, the degree of partial melting estimated from the spinel Cr-number can be used to reconstruct the residual trace element composition of the cpx. Near-fractional melting is commonly accepted to be the most realistic melting process to explain trace element systematics beneath mid-ocean ridges and is therefore applied here. As the first step, a critical melting model (Maaloe, 1982) is used to calculate residual bulk and melt compositions. This model includes finite residual melt porosities that hold back minor amounts of melt in the residue. Melt porosities in mantle peridotite are varied between 0.1 to 2%, a range presumably typical for partial melting below mid-ocean ridges (e.g. Forsyth et al., 1998, Brunelli et al., 2006). Starting composition for all models is the Depleted Mantle (DMM) composition from Workman and Hart (2005). The new bulk composition is calculated for the melting increment indicated by the spinel Cr-number. As the second step, a trapped melt model assumes the infiltration of the residual peridotite by a melt that crystallizes completely in different modal proportions. Trace elements are then re-distributed between the new and the residual phases attaining full equilibrium. The results of these models are very sensitive to the model parameters, allowing only narrow variability of these model parameters. The model results are reported in Table 2-3 and in Figures 2-9 and 2-10.

2.4.2.1 Refertilization of PS66-238 peridotites

PS66-238 peridotites are identical in their major element composition and only differ slightly in their cpx trace element composition. Clinopyroxenes are homogeneous and show a very flat REE-pattern with $(La/Yb)_N$ of around 0.8. Spinel Cr-numbers of 0.21 indicate about

CHAPTER 2

8% melting in the spinel stability field for both samples following the procedure of Hellebrand et al. (2001). Eight percent of near-fractional melting at 1% residual porosity will produce a LREE-depleted bulk with a cpx with a (La/Yb)_N-ratio of about 0.01. In order to match the REE-patterns of the cpx, entrapment of a LREE-enriched melt is then required to increase the LREE to MREE concentrations relative to the residual cpx. Fractional crystallization of cumulus-cpx alone is not capable of achieving this (not shown). The observed cpx compositions can be reproduced by trapping 3-3.5 % of a low-degree melt (1-1.5% of accumulated melt after critical melting at 1% porosity) in the residual peridotite, followed by complete equilibration of all phases. The trapped melt completely crystallized cpx, which is a simplification, as the addition of opx is required by the microtextural observation. However, model results are not significantly affected by crystallization of opx because of its relatively low REE concentration.

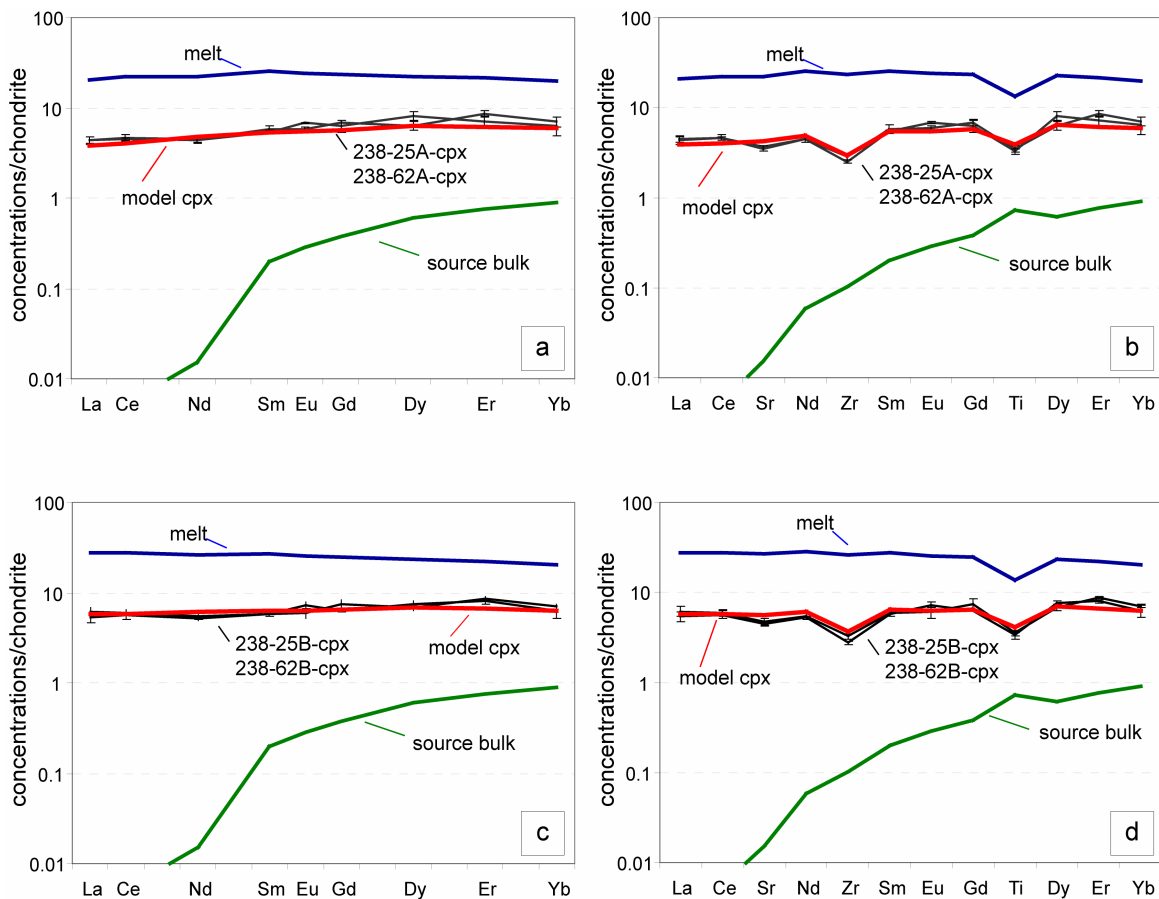


Figure 2-9: Refertilization model for clinopyroxenes of PS66-238-25 and 62. Error bars denote one standard deviation. Model parameters and results are shown in table 2-3.

2.4.2.2 Refertilization of PS59-235 peridotites

Spinel peridotites from PS59-235 are characterized by lower spinel Cr-numbers and lower cpx-TE abundances compared to PS66-238 spinel peridotites. This indicates that the residual peridotite was more fertile but the impregnating melt more depleted compared to PS66-238 peridotites.

Starting point for the model for PS59-235-17 and -20 is a residual peridotite after 4% and 6% critical melting, respectively, from a DMM composition. The relatively fractionated pattern of 235-17 requires a relatively depleted melt and/or lower residual porosities. A good match for the steep cpx- pattern is achieved by assuming a lower porosity of 0.5% for both bulk depletion as well as melt production. Three percent of an instantaneous melt at 7% of critical melting are trapped in the residual peridotite. In contrast, the flatter cpx-pattern of 235-20 requires higher relative porosities of 1.5% and a more fertile melt of 4%; only 1.5% of melt are trapped. Again, only cpx is crystallized. However, the strongly negative Ti- and Zr-anomalies in PS59-235 cpx strongly suggest that the impregnating melt fractionated opx prior to the entrapment.

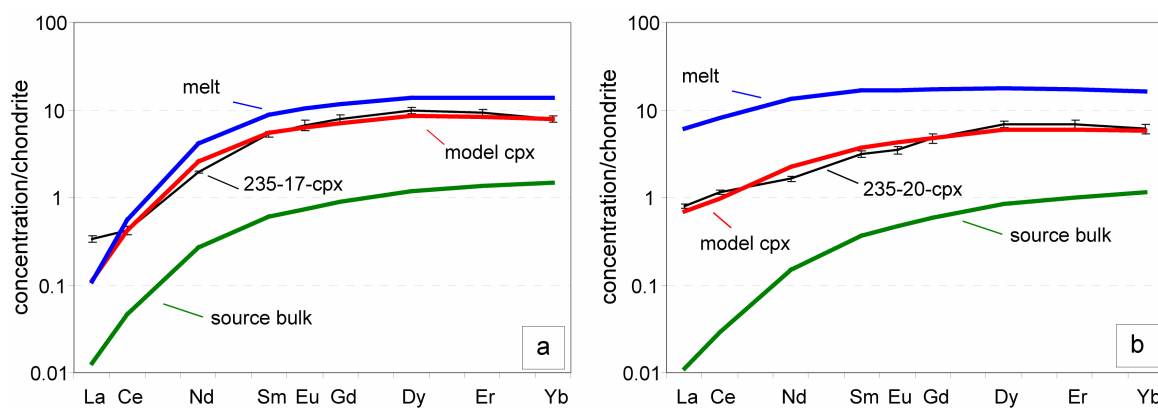


Figure 2-10: Refertilization model results for (a) PS59-235-17 clinopyroxenes and (b) PS59-235-20 clinopyroxenes. Error bars denote one standard deviation. Model parameters and results are shown in Table 2-3.

The calculations require a variable source rock depletion followed by entrapment of variable, generally more fertile, melt increments of critical melting at variable porosities. This suggests that this process occurred over a wide interval where the peridotites remained at or close to the solidus. Nevertheless, the refertilization of spinel peridotites must have occurred at

CHAPTER 2

temperatures sufficiently high for porous flow and at a long enough time scale to allow equilibration between the different phases, since cpx crystals are devoid of TE zoning. Furthermore, Na₂O concentrations in cpx deviate slightly from the partial melting trend and are shifted toward higher values (Figure 2-4a). The $D^{cpx/l}$ for Na is pressure dependent and decreases from ~0.5 at 3 GPa to values less than 0.2 at the top of the melting column (Blundy et al., 1995). Therefore, high pressure crystallization of cpx will lead to higher Na₂O concentrations than estimated from melting models. This is further evidence that pyroxene crystallization in the spinel peridotites occurred at high pressures and temperatures.

Table 2-3: Model parameters and results.

Sample	Residual porosity	Bulk depletion	Near-fractional melting increment	% trapped melt
238-25A/238-62A	1%	8%	1.5%	3%
238-25B/238-25B	1%	8%	1%	3.5%
235-20	1.5%	6%	4%	1.5%
235-17	0.5%	4%	7%	3%

2.4.3 Implications for low degree partial melting at Gakkel Ridge

The distinctive petrographical signature of these samples is the orthopyroxene reactive texture. In general, the opposite process, dissolution of orthopyroxene and crystallization of olivine, is expected either by incongruent melting (Jaques and Green, 1980, Kelemen et al., 1990, Hirose and Kushiro, 1993) or reactive melt migration (Kelemen et al., 1995, Kelemen et al., 1997). Olivine dissolution and (ortho-)pyroxene addition has been rarely noted in the mantle peridotites except in plagioclase-bearing peridotites from ophiolites (Dijkstra et al., 2003, Piccardo et al., 2004) but, in contrast, pyroxene porphyroclasts show systematic major element heterogeneity between core and rim. They are interpreted as the low pressure crystallization product of a melt that reached silica-saturation by reactive percolation through the mantle column (Piccardo et al., 2004). Melt impregnation as seen in this study must have occurred at high temperatures to allow complete equilibration between all phases in terms of major and trace elements unlike the emplacement in the thermal boundary layer (Dijkstra et al., 2003, Piccardo et al., 2004). Erupted MORB, produced by a DMM mantle and low pressure crystallization are usually silica-undersaturated and do not have opx on the solidus (Kinzler

and Grove, 1992). Ultracalcic melts produced by a more depleted mantle composition also never have multiple saturation of ol+opx+cpx near or at the solidus in melting experiments (Medard et al., 2004).

In contrast, all liquids produced in low degree partial melting experiments to date are high-silica relative to MORB, irrespective of the starting composition of the experimental mix. Experiments on low degree melts were carried out on fertile (MM3, Baker et al., 1995) and depleted spinel mantle composition (Depma, Laporte et al., 2004) as well as on a garnet peridotite (Johnson and Kushiro, 1992). Liquids produced from the refractory mantle composition, Depma, by Laporte et al. (2004) are lower in SiO₂ by two percent at a given MgO compared to fertile mantle, MM3, experiments but are relatively more silica-saturated because of lower Na₂O contents (Laporte et al., 2004). All Depma experiments produce hypersthene-normative liquids and in one experiment, opx+cpx+sp formed as crystallization product. The new phases do not show significant differences in major element composition to their residual counterparts in the experiment-mix. Because of the small experimental charges, no trace element analyzes exist for these experiments. Therefore, it is unknown if near-solidus trace element partition coefficients differ significantly from partition coefficients estimated from batch melting experiments as suggested by Baker et al. (1995) for HFSE.

Trace element modeling for PS66-238 peridotites requires entrapment of a low degree melt; PS59-235 peridotites, on the other hand, require interaction with more refractory melts. Nevertheless, they show the same olivine dissolution textures as PS66-238 peridotites. This corroborates the results of low degree melting experiments that near-solidus melts will have very distinctive silica-rich compositions. High-silica melts have a much higher viscosity relative to MORB-type melts (Baker et al., 1995) and may never reach the surface below mid-ocean ridges. They will probably travel only short distances, then react out and refertilize residual peridotites on their ascent. Ultraslow-spreading ridges such as Gakkel Ridge may be the only location to study this process. This sample collection provides the opportunity to study melting processes and trace element partitioning at near-solidus conditions.

2.5 SUMMARY

Four spinel peridotites from Gakkel Ridge were studied for their major and trace element composition. All samples show no traces of alteration giving the rare opportunity to investigate their composition in context with their microtextures.

Overall, the characteristics of the spinel peridotites are consistent with infiltration and stagnation of low degree melts. In summary:

- Mineral compositions of spinel peridotites from PS59-235 and PS66-238 are homogeneous and well correlated in their major elements indicating full equilibration of all phases.
- Spinel peridotites show reactive microtextures of olivine dissolution and orthopyroxene addition, opposite to what is normally expected for melting and reactive processes below mid-ocean ridges.
- Trace element characteristics of clinopyroxene require refertilization of variably depleted residual peridotites by variable amounts of instantaneous melts, produced at variable degrees of melting.
- Thus, melt refertilization occurred at high pressures and temperatures over a large interval during the uplift close to or at the solidus.
- Microtextures found in the samples corroborate that at low degrees of melting, silica-rich melts will form, irrespective of source composition, while trace elements will reflect source fertility.
- This sample set may provide a unique opportunity to study trace element partitioning at near-solidus conditions.

2.6 REFERENCES

- Allègre, C. J., Montigny, R. and Bottinga, Y. (1973). Cortège ophiolitique et cortège océanique, géochimie comparée et mode de genèse. *Bulletin De La Societe Geologique De France* 15, 461-477.
- Anders, E. and Grevesse, N. (1989). Abundances of the elements - meteoritic and solar. *Geochimica Et Cosmochimica Acta* 53, 197-214.
- Asimow, P. D. (1999). A model that reconciles major- and trace-element data from abyssal peridotites. *Earth and Planetary Science Letters* 169, 303-319.
- Aumento, F. and Loubat, H. (1971). The Mid-Atlantic Ridge near 45°N. Serpentinized ultramafic intrusions. *Canadian Journal of Earth Sciences* 8, 691-663.
- Baker, M. B., Hirschmann, M. M., Ghiorso, M. S. and Stolper, E. M. (1995). Compositions of near-solidus peridotite melts from experiments and thermodynamic calculations. *Nature* 375, 308-311.
- Baker, M. B. and Stolper, E. M. (1994). Determining the composition of high-pressure mantle melts using diamond aggregates. *Geochimica Et Cosmochimica Acta* 58, 2811-2827.
- Blundy, J. D., Falloon, T. J., Wood, B. J. and Dalton, J. A. (1995). Sodium partitioning between clinopyroxene and silicate melts. *Journal of Geophysical Research-Solid Earth and Planets* 100, 15501-15515.
- Brunelli, D., Seyler, M., Cipriani, A., Ottolini, L. and Bonatti, E. (2006). Discontinuous melt extraction and weak refertilization of mantle peridotites at the Vema Lithospheric Sections (Mid-Atlantic Ridge). *Journal of Petrology* 47, 745-771.
- Cannat, M., Mevel, C., Maia, M., Deplus, C., Durand, C., Gente, P., Agrinier, P., Belarouchi, A., Dubuisson, G., Humler, E. and Reynolds, J. (1995). Thin crust, ultramafic exposures, and rugged faulting patterns at Mid-Atlantic Ridge (22°- 24°N). *Geology* 23, 49-52.
- Dick, H. J. B. (1989). Abyssal peridotites, very slow spreading ridges and ocean ridge magmatism. In: Saunders, A. D. & Norry, M. J. (eds.) *Magmatism in the ocean basins*. Geol. Soc. London Spec. Pub. 42. 71-105.
- Dick, H. J. B. and Bullen, T. (1984). Chromian spinel as a petrogenetic indicator in abyssal and alpine-type peridotites and spatially associated lavas. *Contributions to Mineralogy and Petrology* 86, 54-76.
- Dick, H. J. B., Lin, J. and Schouten, H. (2003). An ultraslow-spreading class of ocean ridge. *Nature* 426, 405-412.
- Dijkstra, A. H., Barth, M. G., Drury, M. R., Mason, P. R. D. and Vissers, R. L. M. (2003). Diffuse porous melt flow and melt-rock reaction in the mantle lithosphere at a slow-spreading ridge: A structural petrology and LA-ICP-MS study of the Othris Peridotite Massif (Greece). *Geochemistry Geophysics Geosystems* 4, doi:10.1029/2001GC000278.
- Draper, D. S. and Green, T. H. (1999). P-T phase relations of silicic, alkaline, aluminous liquids: new results and applications to mantle melting and metasomatism. *Earth and Planetary Science Letters* 170, 255-268.

CHAPTER 2

- Droop, G. T. R. (1987). A general equation for estimating Fe^{3+} concentrations in ferromagnesian silicates and oxides from microprobe analyses, using stoichiometric criteria. *Mineralogical Magazine* 51, 431-435.
- Faul, U. H. (2001). Melt retention and segregation beneath mid-ocean ridges. *Nature* 410, 920-923.
- Forsyth, D. W., Scheirer, D. S., Webb, S. C., Dorman, L. M., Orcutt, J. A., Harding, A. J., Blackman, D. K., Morgan, J. P., Detrick, R. S., Shen, Y., Wolfe, C. J., Canales, J. P., Toomey, D. R., Sheehan, A. F., Solomon, S. C. and Wilcock, W. S. D. (1998). Imaging the deep seismic structure beneath a mid-ocean ridge: The MELT experiment. *Science* 280, 1215-1218.
- Ghiorso, M. S. and Sack, R. O. (1995). Chemical mass-transfer in magmatic processes .4. A revised and internally consistent thermodynamic model for the interpolation and extrapolation of liquid-solid equilibria in magmatic systems at elevated temperatures and pressures. *Contributions to Mineralogy and Petrology* 119, 197-212.
- Ghose, I., Cannat, M. and Seyler, M. (1996). Transform fault effect on mantle melting in the MARK area (Mid- Atlantic Ridge south of the Kane transform). *Geology* 24, 1139-1142.
- Hart, S. R. and Dunn, T. (1993). Experimental cpx-melt partitioning of 24 trace-elements. *Contributions to Mineralogy and Petrology* 113, 1-8.
- Hauri, E. H. and Hart, S. R. (1995). Correction to "Constraints on melt migration from mantle plumes: a trace element study of peridotite xenoliths from Savai'i, Western Samoa". *Journal of Geophysical Research-Solid Earth and Planets* 100, 2003.
- Hellebrand, E. and Snow, J. E. (2003). Deep melting and sodic metasomatism underneath the highly oblique-spreading Lena Trough (Arctic Ocean). *Earth and Planetary Science Letters* 216, 283-299.
- Hellebrand, E., Snow, J. E., Dick, H. J. B. and Hofmann, A. W. (2001). Coupled major and trace elements as indicators of the extent of melting in mid-ocean-ridge peridotites. *Nature* 410, 677-681.
- Hellebrand, E., Snow, J. E., Hoppe, P. and Hofmann, A. W. (2002). Garnet-field melting and late-stage refertilization in 'residual' abyssal peridotites from the Central Indian Ridge. *Journal of Petrology* 43, 2305-2338.
- Hirose, K. and Kushiro, I. (1993). Partial melting of dry peridotites at high-pressures - determination of compositions of melts segregated from peridotite using aggregates of diamond. *Earth and Planetary Science Letters* 114, 477-489.
- Jaques, A. L. and Green, D. H. (1980). Anhydrous melting of peridotite at 0-15 kb pressure and the genesis of tholeiitic basalts. *Contributions to Mineralogy and Petrology* 73, 287-310.
- Jochum, K. P., Stoll, B., Herwig, K., Willbold, M., Hofmann, A. W., Amini, M., Aarburg, S., Abouchami, W., Hellebrand, E., Mocek, B., Raczek, I., Stracke, A., Alard, O., Bouman, C., Becker, S., Dücking, M., Bratz, H., Klemm, R., de Bruin, D., Canil, D., Cornell, D., de Hoog, C. J., Dalpe, C., Danyushevsky, L., Eisenhauer, A., Premo, W. R., Sun, W. D.

CHAPTER 2

- D., Tiepolo, M., Vannucci, R., Vennemann, T., Wayne, D. and Woodhead, J. D. (2006). MPI-DING reference glasses for in situ microanalysis: New reference values for element concentrations and isotope ratios. *Geochemistry Geophysics Geosystems* 7, doi:10.1029/2005GC001060.
- Johnson, K. T. M. and Dick, H. J. B. (1992). Open system melting and temporal and spatial variation of peridotite and basalt at the Atlantis-II Fracture-Zone. *Journal of Geophysical Research-Solid Earth and Planets* 97, 9219-9241.
- Johnson, K. T. M., Dick, H. J. B. and Shimizu, N. (1990). Melting in the oceanic upper mantle - an ion microprobe study of diopsides in abyssal peridotites. *Journal of Geophysical Research-Solid Earth and Planets* 95, 2661-2678.
- Johnson, K. T. M. and Kushiro, I. (1992). Segregation of high pressure partial melts from peridotite using aggregates of diamond: A new experimental approach. *Geophysical Research Letters* 19, 1703-1706.
- Johnston, A. D. and Schwab, B. E. (2004). Constraints on clinopyroxene/melt partitioning of REE, Rb, Sr, Ti, Cr, Zr, and Nb during mantle melting: First insights from direct peridotite melting experiments at 1.0 GPa. *Geochimica Et Cosmochimica Acta* 68, 4949-4962.
- Juteau, T., Berger, E. and Cannat, M. (1990). Serpentinized, residual mantle peridotites from the M.A.R. median valley, ODP Hole 670A (21°10'N, 45°02'W, Leg 109): Primary mineralogy and geothermometry. In: Detrick, R. S., Honnorez, J., Bryan, W. B. & Juteau, T. (eds.) *Proceedings of the Ocean Drilling Program, Scientific Results*. College Station: ODP, 27-45.
- Kelemen, P. B. (1990). Reaction between ultramafic rock and fractionating basaltic magma .1. phase-relations, the origin of calc-alkaline magma series, and the formation of discordant dunite. *Journal of Petrology* 31, 51-98.
- Kelemen, P. B., Hirth, G., Shimizu, N., Spiegelman, M. and Dick, H. J. B. (1997). A review of melt migration processes in the adiabatically upwelling mantle beneath oceanic spreading ridges. *Philosophical Transactions of the Royal Society of London Series a-Mathematical Physical and Engineering Sciences* 355, 283-318.
- Kelemen, P. B., Joyce, D. B., Webster, J. D. and Holloway, J. R. (1990). Reaction between ultramafic rock and fractionating basaltic magma II. Experimental investigation of reaction between olivine tholeiite and harzburgite at 1150-1050°C and 5 kb. *Journal of Petrology* 31, 99-134.
- Kelemen, P. B., Whitehead, J. A., Aharonov, E. and Jordahl, K. A. (1995). Experiments on flow focusing in soluble porous-media, with applications to melt extraction from the mantle. *Journal of Geophysical Research-Solid Earth and Planets* 100, 475-496.
- Kinzler, R. J. and Grove, T. L. (1992). Primary magmas of midocean ridge basalts .1. Experiments and methods. *Journal of Geophysical Research-Solid Earth and Planets* 97, 6885-6906.
- Kornprobst, J. and Tabit, A. (1988). Plagioclase-bearing ultramafic tectonites from the Galicia Margin (Leg 103, Site 637): comparison of their origin and evolution with low-pressure ultramafic bodies in Western Europe. In: Boillot, G. & Winterer, E. L. (eds.)

CHAPTER 2

- Proceedings of the Ocean Drilling Program, Scientific Results*. 103. College Station, Texas: Ocean Drilling Program, 253-268.
- Kushiro, I. (2001). Partial melting experiments on peridotite and origin of mid-ocean ridge basalt. *Annual Review of Earth and Planetary Sciences* 29, 71-107.
- Laporte, D., Toplis, M. J., Seyler, M. and Devidal, J. L. (2004). A new experimental technique for extracting liquids from peridotite at very low degrees of melting: application to partial melting of depleted peridotite. *Contributions to Mineralogy and Petrology* 146, 463-484.
- Maaloe, S. (1982). Geochemical aspects of permeability controlled partial melting and fractional crystallization. *Geochimica Et Cosmochimica Acta* 46, 43-57.
- McKenzie, D. and Bickle, M. J. (1988). The volume and composition of melt generated by extension of the lithosphere. *Journal of Petrology* 29, 625-679.
- Medard, E., Schmidt, M. W. and Schiano, P. (2004). Liquidus surfaces of ultracalcic primitive melts: formation conditions and sources. *Contributions to Mineralogy and Petrology* 148, 201-215.
- Miyashiro, A., Shido, F. and Ewing, M. (1969). Composition and origin of serpentinites from the Mid-Atlantic ridge near 24° and 30° north latitude. *Contributions to Mineralogy and Petrology*, 117-127.
- Piccardo, G. B., Müntener, O., Zanetti, A., Romairone, A., Bruzzone, S., Poggi, E. and Spagnolo, G. (2004). The Lanzo South peridotite: Melt/peridotite interaction in the mantle lithosphere of the Jurassic Ligurian Tethys. *Ophioliti* 29, 37-62.
- Pickering-Witter, J. and Johnston, A. D. (2000). The effects of variable bulk composition on the melting systematics of fertile peridotitic assemblages. *Contributions to Mineralogy and Petrology* 140, 190-211.
- Rampone, E., Bottazzi, P. and Ottolini, L. (1991). Complementary Ti and Zr anomalies in orthopyroxene and clinopyroxene from mantle peridotites. *Nature* 354, 518-520.
- Schiano, P., Bourdon, B., Clocchiatti, R., Massare, D., Varela, M. E. and Bottinga, Y. (1998). Low-degree partial melting trends recorded in upper mantle minerals. *Earth and Planetary Science Letters* 160, 537-550.
- Seyler, M., Cannat, M. and Mevel, C. (2003). Evidence for major-element heterogeneity in the mantle source of abyssal peridotites from the Southwest Indian Ridge (52° to 68°E). *Geochemistry Geophysics Geosystems* 4, doi:10.1029/2002GC000305.
- Seyler, M., Lorand, J. P., Dick, H. J. B. and Drouin, M. (2007). Pervasive melt percolation reactions in ultra-depleted refractory harzburgites at the Mid-Atlantic Ridge, 15° 20' N: ODP Hole 1274A. *Contributions to Mineralogy and Petrology* 153, 303-319.
- Seyler, M., Toplis, M. J., Lorand, J. P., Luguet, A. and Cannat, M. (2001). Clinopyroxene microtextures reveal incompletely extracted melts in abyssal peridotites. *Geology* 29, 155-158.
- Takahashi, E. and Kushiro, I. (1983). Melting of a dry peridotite at high-pressures and basalt magma genesis. *American Mineralogist* 68, 859-879.

CHAPTER 2

- Wasylenki, L. E., Baker, M. B., Kent, A. J. R. and Stolper, E. M. (2003). Near-solidus melting of the shallow upper mantle: partial melting experiments on depleted peridotite. *Journal of Petrology* 44, 1163-1191.
- Webb, S. A. C. and Wood, B. J. (1986). Spinel-pyroxene-garnet relationships and their dependence on Cr/Al ratio. *Contributions to Mineralogy and Petrology* 92, 471-480.
- Workman, R. K. and Hart, S. R. (2005). Major and trace element composition of the depleted MORB mantle (DMM). *Earth and Planetary Science Letters* 231, 53-72.

Table 2-1a: Major element composition of clinopyroxenes in [wt%]

Sample	PS66-238			PS59-235		
	238-25A 41	238-25B 82	238-62A 70	235-17 13	235-20 22	
n						
SiO ₂	51.6 ± 0.7	51.7 ± 0.5	51.9 ± 0.6	50.7 ± 0.4	51.6 ± 0.3	
TiO ₂	0.26 ± 0.05	0.27 ± 0.04	0.26 ± 0.04	0.29 ± 0.05	0.20 ± 0.03	
Cr ₂ O ₃	1.15 ± 0.20	1.17 ± 0.17	1.10 ± 0.24	0.96 ± 0.12	1.08 ± 0.09	
Al ₂ O ₃	5.0 ± 0.7	5.1 ± 0.6	4.9 ± 0.8	6.2 ± 0.6	6.0 ± 0.4	
FeO	2.5 ± 0.2	2.5 ± 0.1	2.5 ± 0.1	2.8 ± 0.2	2.8 ± 0.2	
MgO	16.3 ± 0.5	16.1 ± 0.4	16.1 ± 0.5	15.9 ± 0.5	16.3 ± 0.6	
MnO	0.09 ± 0.03	0.09 ± 0.03	0.09 ± 0.03	0.09 ± 0.03	0.04 ± 0.06	
CaO	21.9 ± 0.5	22.1 ± 0.4	22.3 ± 0.3	21.4 ± 0.3	21.6 ± 0.8	
NiO	0.05 ± 0.03	0.04 ± 0.03	0.05 ± 0.04	0.04 ± 0.03	0.04 ± 0.04	
Na ₂ O	0.89 ± 0.09	0.87 ± 0.08	0.86 ± 0.08	0.84 ± 0.06	0.79 ± 0.07	
K ₂ O	0.00 ± 0.01	0.00 ± 0.01	0.00 ± 0.01	0.01 ± 0.01	0.01 ± 0.01	
Total	99.8 ± 0.4	99.8 ± 0.4	100.1 ± 0.4	99.3 ± 0.2	100.4 ± 0.3	
Cr-number	0.132 ± 0.009	0.133 ± 0.007	0.130 ± 0.011	0.095 ± 0.004	0.107 ± 0.003	
Mg-number	0.920 ± 0.005	0.921 ± 0.004	0.921 ± 0.005	0.910 ± 0.006	0.913 ± 0.004	

n: number of analyses ±: one standard deviation

Table 2-1b: Major element composition of orthopyroxenes in [wt%]

Sample	PS66-238			PS59-235		
	238-25A 46	238-25B 55	238-62A 31	235-17 10	235-20 11	
n						
SiO ₂	55.0 ± 0.5	55.1 ± 0.5	55.1 ± 0.5	53.6 ± 0.5	55.2 ± 0.4	
TiO ₂	0.08 ± 0.02	0.07 ± 0.03	0.07 ± 0.03	0.07 ± 0.03	0.04 ± 0.02	
Cr ₂ O ₃	0.61 ± 0.11	0.57 ± 0.10	0.61 ± 0.14	0.62 ± 0.09	0.49 ± 0.09	
Al ₂ O ₃	3.7 ± 0.5	3.6 ± 0.5	3.8 ± 0.5	5.1 ± 0.4	4.0 ± 0.4	
FeO	6.0 ± 0.1	6.0 ± 0.1	6.0 ± 0.1	6.2 ± 0.2	6.2 ± 0.1	
MgO	34.0 ± 0.4	33.8 ± 0.4	33.6 ± 0.4	32.5 ± 0.3	33.3 ± 0.4	
MnO	0.14 ± 0.02	0.15 ± 0.03	0.14 ± 0.03	0.14 ± 0.02	0.13 ± 0.05	
CaO	0.80 ± 0.15	0.87 ± 0.18	0.84 ± 0.22	1.23 ± 0.33	0.86 ± 0.32	
NiO	0.08 ± 0.03	0.09 ± 0.04	0.08 ± 0.04	0.09 ± 0.05	0.13 ± 0.09	
Na ₂ O	0.04 ± 0.02	0.04 ± 0.02	0.04 ± 0.02	0.06 ± 0.02	0.04 ± 0.03	
K ₂ O	0.00 ± 0.01	0.00 ± 0.01	0.01 ± 0.01	0.00 ± 0.01	0.00 ± 0.01	
Total	100.4 ± 0.4	100.3 ± 0.4	100.2 ± 0.4	99.6 ± 0.4	100.4 ± 0.2	
Cr-number	0.099 ± 0.009	0.094 ± 0.009	0.097 ± 0.011	0.076 ± 0.006	0.076 ± 0.007	
Mg-number	0.910 ± 0.002	0.909 ± 0.002	0.909 ± 0.001	0.904 ± 0.003	0.905 ± 0.002	

n: number of analyses ±: one standard deviation

Table 2-1c: Major element composition of olivines in [wt%]

Sample	PS66-238			PS59-235		
	238-25A n	238-25B 20	238-62A 8	235-17 16	235-20 23	
SiO ₂	41.0 ± 0.2	40.8 ± 0.2	40.9 ± 0.2	40.1 ± 0.4	40.9 ± 0.2	
TiO ₂	0.01 ± 0.01	0.00 ± 0.00	0.01 ± 0.01	0.00 ± 0.01	0.00 ± 0.00	
Cr ₂ O ₃	0.03 ± 0.04	0.04 ± 0.05	0.03 ± 0.03	0.05 ± 0.15	0.01 ± 0.00	
Al ₂ O ₃	0.01 ± 0.01	0.01 ± 0.01	0.01 ± 0.01	0.20 ± 0.79	0.02 ± 0.01	
FeO	9.0 ± 0.4	9.0 ± 0.3	8.9 ± 0.3	9.1 ± 1.6	9.0 ± 0.3	
MgO	50.5 ± 0.4	50.6 ± 0.4	50.6 ± 0.2	49.3 ± 3.4	48.6 ± 0.3	
MnO	0.13 ± 0.03	0.14 ± 0.04	0.14 ± 0.03	0.15 ± 0.03	0.13 ± 0.01	
CaO	0.04 ± 0.02	0.03 ± 0.02	0.02 ± 0.02	0.05 ± 0.03	0.04 ± 0.01	
NiO	0.39 ± 0.05	0.38 ± 0.05	0.39 ± 0.05	0.36 ± 0.08	0.38 ± 0.01	
Na ₂ O	0.01 ± 0.01	0.01 ± 0.01	0.01 ± 0.01	0.02 ± 0.03	0.02 ± 0.02	
K ₂ O	0.01 ± 0.01	0.00 ± 0.00	0.01 ± 0.01	0.01 ± 0.01	0.00 ± 0.00	
Total	101.1 ± 0.4	101.0 ± 0.5	101.0 ± 0.4	99.4 ± 0.4	99.1 ± 0.3	
Fo	0.909 ± 0.004	0.909 ± 0.003	0.909 ± 0.003	0.904 ± 0.002	0.906 ± 0.003	

n: number of analyses ±: one standard deviation

Table 2-1d: Major element composition of spinels in [wt%]

Sample	PS66-238			PS59-235		
	238-25A n	238-25B 131	238-62A 131	235-17 36	235-20 14	
SiO ₂	0.04 ± 0.01	0.04 ± 0.01	0.04 ± 0.01	0.07 ± 0.02	0.09 ± 0.01	
TiO ₂	0.08 ± 0.02	0.08 ± 0.02	0.07 ± 0.02	0.05 ± 0.02	0.05 ± 0.02	
Cr ₂ O ₃	20.2 ± 1.8	19.5 ± 1.8	18.9 ± 1.7	13.3 ± 0.5	15.1 ± 1.2	
Al ₂ O ₃	47.1 ± 2.0	48.1 ± 1.8	48.8 ± 1.8	54.3 ± 0.6	53.1 ± 1.2	
V ₂ O ₅	0.12 ± 0.02	0.11 ± 0.02	0.10 ± 0.02	0.06 ± 0.02	0.10 ± 0.01	
Fe _{ret}	13.7 ± 1.4	13.1 ± 0.6	13.2 ± 0.9			
MgO	17.7 ± 0.6	18.0 ± 0.4	18.1 ± 0.5	19.6 ± 0.3	19.2 ± 0.2	
MnO	0.12 ± 0.02	0.11 ± 0.02	0.11 ± 0.02	0.09 ± 0.01	0.11 ± 0.01	
CaO	0.01 ± 0.02	0.01 ± 0.02	0.01 ± 0.02	0.01 ± 0.01	0.01 ± 0.01	
CoO	0.06 ± 0.01	0.06 ± 0.01	0.07 ± 0.01	0.03 ± 0.01	0.05 ± 0.01	
NiO	0.25 ± 0.03	0.25 ± 0.03	0.25 ± 0.03	0.33 ± 0.02	0.31 ± 0.02	
ZnO	0.22 ± 0.06	0.22 ± 0.05	0.23 ± 0.04	0.18 ± 0.04	0.16 ± 0.04	
Total	99.7 ± 0.3	99.6 ± 0.2	100.0 ± 0.2	99.26 ± 0.25	99.97 ± 0.31	
Cr-number	0.224 ± 0.023	0.214 ± 0.021	0.207 ± 0.021	0.141 ± 0.006	0.160 ± 0.014	
Mg-number	0.723 ± 0.019	0.730 ± 0.013	0.733 ± 0.014	0.780 ± 0.010	0.762 ± 0.006	
FeO*	12.1 ± 0.7	11.8 ± 0.5	11.8 ± 0.5	9.9 ± 0.4	10.6 ± 0.3	
Fe ₂ O ₃ *	1.8 ± 0.9	1.4 ± 0.3	1.6 ± 0.5	1.5 ± 0.4	1.2 ± 0.3	

n: number of analyses ±: one standard deviation

*: FeO and Fe₂O₃ calculated after Droop (1987)

Table 2-2: Average trace element composition of clinopyroxenes in [µg/g]

Sample	PS66-238				PS59-235			
	238-25A		238-25B		238-62A		238-62B	
n	12	4	4	4	4	4	4	5
Na	6403 ± 655	5775 ± 497	5003 ± 231	5829 ± 221	3982 ± 195	4239 ± 260	47.1 ± 3.4	49.8 ± 9.2
Sc	54.0 ± 5.6	51.8 ± 6.3	52.2 ± 5.7	53.3 ± 2.6	1467 ± 96	1087 ± 136	187 ± 8	189 ± 15
Ti	1526 ± 132	1454 ± 122	1418 ± 93	1539 ± 114	5982 ± 270	6177 ± 455	2.1 ± 0.1	7.5 ± 0.5
V	251 ± 16	234 ± 12	230 ± 12	247 ± 10	13.2 ± 0.7	10.0 ± 0.6	2.5 ± 0.1	3.0 ± 0.3
Cr	7846 ± 385	7903 ± 465	7743 ± 387	8141 ± 122	0.07 ± 0.02	0.06 ± 0.04	0.08 ± 0.01	0.19 ± 0.01
Sr	28.9 ± 1.0	35.3 ± 1.3	27.4 ± 1.8	36.5 ± 3.9	0.26 ± 0.03	0.69 ± 0.04	0.89 ± 0.03	0.74 ± 0.05
Y	11.1 ± 0.9	10.6 ± 0.4	10.6 ± 0.5	11.3 ± 0.4	0.79 ± 0.06	0.46 ± 0.04	0.37 ± 0.05	0.20 ± 0.02
Zr	11.4 ± 1.0	10.9 ± 0.4	9.9 ± 0.5	12.8 ± 0.9	1.56 ± 0.17	0.93 ± 0.10	2.40 ± 0.22	1.68 ± 0.14
La	1.04 ± 0.09	1.26 ± 0.17	1.02 ± 0.11	1.45 ± 0.18	1.48 ± 0.12	1.10 ± 0.11	1.28 ± 0.10	0.98 ± 0.11
Ce	2.80 ± 0.21	3.42 ± 0.34	2.74 ± 0.09	3.61 ± 0.30	0.86 ± 0.06	0.86 ± 0.06	0.07 ± 0.02	0.06 ± 0.04
Pr	0.43 ± 0.02	0.50 ± 0.04	0.44 ± 0.02	0.51 ± 0.04	0.34 ± 0.05	0.34 ± 0.05	0.08 ± 0.01	0.19 ± 0.01
Nd	2.02 ± 0.14	2.38 ± 0.10	2.00 ± 0.16	2.47 ± 0.22	0.26 ± 0.03	0.69 ± 0.04	0.26 ± 0.03	0.69 ± 0.04
Sm	0.85 ± 0.09	0.84 ± 0.04	0.79 ± 0.04	0.86 ± 0.06	0.89 ± 0.03	0.74 ± 0.05	0.89 ± 0.03	0.74 ± 0.05
Eu	0.33 ± 0.02	0.41 ± 0.03	0.38 ± 0.01	0.41 ± 0.03	0.79 ± 0.06	0.46 ± 0.04	0.79 ± 0.06	0.46 ± 0.04
Gd	1.34 ± 0.10	1.23 ± 0.01	1.23 ± 0.19	1.47 ± 0.19	0.34 ± 0.05	0.20 ± 0.02	0.37 ± 0.05	0.20 ± 0.02
Dy	1.53 ± 0.18	1.83 ± 0.15	1.95 ± 0.22	1.66 ± 0.13	1.23 ± 0.19	0.93 ± 0.10	1.56 ± 0.17	0.93 ± 0.10
Er	1.36 ± 0.11	1.29 ± 0.09	1.13 ± 0.15	1.38 ± 0.05	1.95 ± 0.22	1.68 ± 0.14	2.40 ± 0.22	1.68 ± 0.14
Yb	1.14 ± 0.14	1.02 ± 0.17	1.03 ± 0.23	1.15 ± 0.05	1.13 ± 0.15	1.10 ± 0.11	1.48 ± 0.12	1.10 ± 0.11

n: number of analyses
±: one standard deviation

CHAPTER 3

TEMPERATURE-DEPENDENT TRACE ELEMENT EXCHANGE IN MANTLE MINERALS - TOWARD A NEW GEOSPEEDOMETER FOR ULTRAMAFIC ROCKS

3.1 INTRODUCTION

Quantifying the thermal history of ultramafic rocks is important to help understand their uplift rates and emplacement mechanisms. The thermal structure of the lithosphere has been subject of many studies in the recent past (e.g. Doin and Fleitout, 1996, Hofmeister, 1999, Honda and Yuen, 2001, McKenzie et al., 2005), and it has been found that individual estimates of such geotherms can vary widely depending on lithospheric structure and age (Figure 3-1).

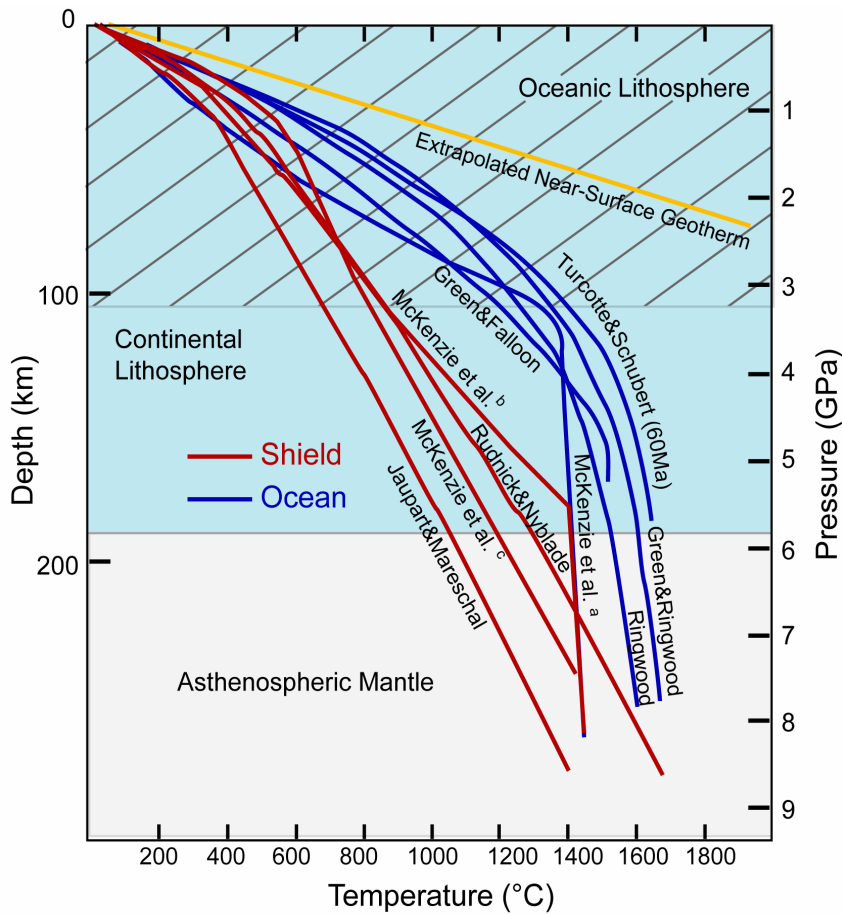
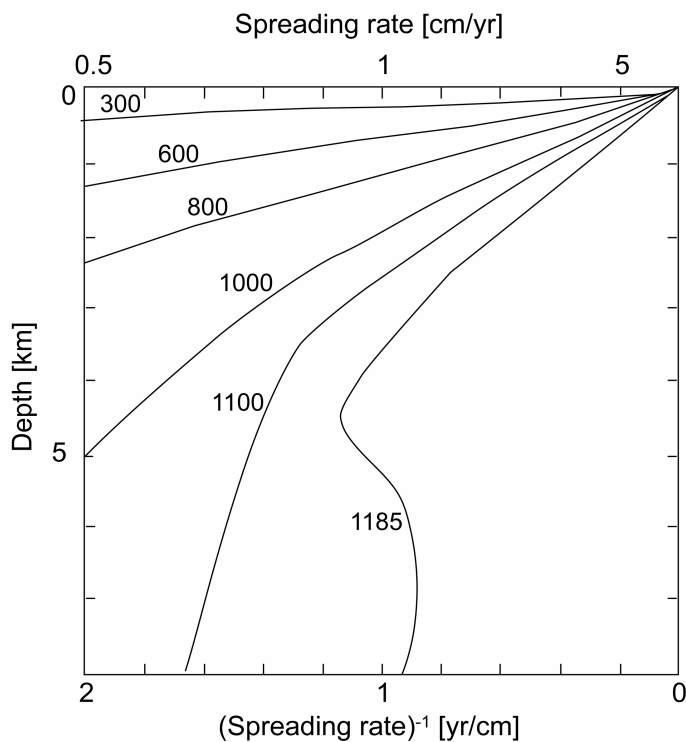


Figure 3-1: Overview of predicted geotherms for oceanic (blue curves) and continental settings (red curves) down to a depth of 300 km. The thickness of mature (> 100 Ma) oceanic lithosphere is hatched and that of continental shield lithosphere is light blue. Data from Green and Falloon (1998); Green & Ringwood (1967); Jaupart and Mareschal (1999); McKenzie et al. (2005): (a) oceanic lithosphere, (b) old continental lithosphere, (c) Udachnaya Kimberlite; Central Siberia; Ringwood (1966); Rudnick and Nyblade (1999); Turcotte and Schubert (2002).

3.1.1 Thermal structure of mid-ocean ridges

The thermal structure of the axial region of mid-ocean ridges consists essentially of an adiabatic upwelling overlain by a conductively cooled lid. The depth at which magmas begin to crystallize beneath the ridge axis is largely controlled by the thermal structure (Shen and Forsyth, 1995). At slow-spreading ridges, both the rate of mantle upwelling and the flux of magma into the lithosphere are lower than at fast-spreading ridges, resulting in a much cooler axial zone. Evidence for this comes from: (1) the occurrence of a steady-state magma chamber at fast-spreading ridges, but only intermittent magma-chambers at slow-spreading ridges (e.g. Detrick et al., 1987, Sinha et al., 1997); (2) the occurrence of deep axial earthquakes at slow- but not at fast-spreading ridges (e.g. Toomey et al., 1988); (3) the occurrence of an axial valley at slow-spreading ridges and an axial high at fast-spreading ridges (e.g. Morgan and Chen, 1993).

Most theoretical studies on the thermal state of the oceanic lithosphere focus on the change in temperatures away from the ridge and the accompanying subsidence with seafloor depth and heat flow as the two primary observational constraints (Parsons and Sclater, 1977, Stein and Stein, 1992, McKenzie et al., 2005). However, the thermal structure directly below a mid-ocean ridge axis is also very variable and influenced by a number of factors.



The axial thermal structure of mid-ocean ridges depends strongly on spreading rates as described above (Figure 3-2). At high spreading rates the temperature is proportional to the inverse of spreading rates (Sleep, 1975).

Figure 3-2: Temperature [$^{\circ}\text{C}$] at the ridge axis calculated for spreading rates greater than 0.5 cm/year and plotted against the inverse of spreading rates (from Sleep, 1975).

CHAPTER 3

Along-axis variations in temperature exist with a colder thermal regime at segment ends close to transform faults relative to segment centers (Niu and Batiza, 1994, Ghose et al., 1996). Figure 3-3 shows a numerical model of the effect of a transform fault on the ridge thermal structure relative to the segment center of a slow-spreading ridge axis (Ligi et al., 2005).

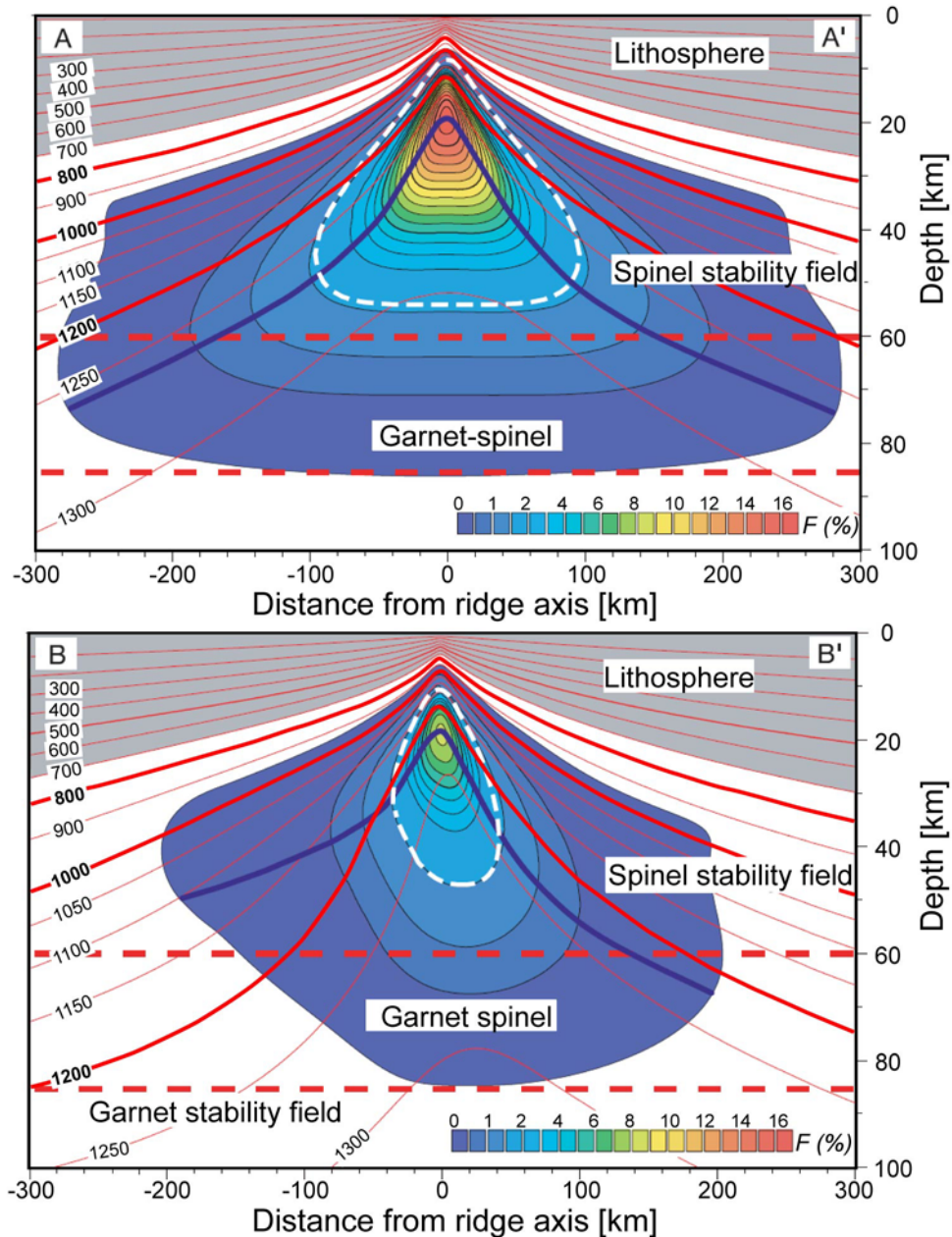


Figure 3-3: Thermal structure and its effect on partial melting at a mid-ocean ridge with half-spreading rate of 16 mm/a (a) at the ridge axis and (b) close to a transform fault (from Ligi et al (2005)). The 800°C, 1000°C and 1200°C isotherms are highlighted to emphasize the difference in thermal structure, especially farther away from the ridge axis.

Furthermore, studies along the Vema Transform, exposing a 20 Ma long record of crust formation at the Mid-Atlantic Ridge, show that temporal and regional variations in the ridge temperature structure occur. Temperatures from mineral equilibria were found to correlate with the degree of melting, oscillating in 3-4 Ma intervals. Superimposed on these oscillation is a steady temperature increase at the Mid-Atlantic Ridge over the past 20 Ma (Bonatti et al., 2003). Similarly, the existence of regional mantle thermal minima, creating so-called “cold spots”, at the Mid-Atlantic Ridge has been suggested (Bonatti et al., 2001). Therefore, it seems that the thermal structure along mid-ocean ridges is very variable in time and space.

The simplest conductive cooling model is the “half-space” model (Turcotte and Schubert, 2002) in which purely conductive cooling takes place in an infinite rigid half-space. While a half-space cooling model usually successfully predicts many phenomena such as the maximum depth of transform earthquakes, it neglects many physical processes that occur in the crust and upper mantle (such as hydrothermal cooling and advective heat transport) (e.g. Behn et al., 2007). Numerical models that incorporate three-dimensional advective and conductive heat transport, indicate that the mantle beneath oceanic transform faults is anomalously cold relative to a half-space model (Phipps Morgan and Forsyth, 1988, Shen and Forsyth, 1992). A recent study that also incorporated brittle weakening into the model, found temperatures similar to the half-space cooling models but with the highest temperatures near the center of the transform (Behn et al., 2007). Thus, testing numerical models against cooling rate estimates from abyssal peridotites and ophiolites will provide further insights into the thermal structure of mid-ocean ridges.

3.1.2 Geospeedometry

There are few methods to directly constrain the thermal history of mantle rocks. Geospeedometry has proved itself in studies of continental orogenic belts (Lasaga and Jiang, 1995, Faryad and Chakraborty, 2005, Chakraborty, 2006), but has rarely been applied in studies of the oceanic lithosphere (Coogan et al., 2005, Demouchy et al., 2006). Geospeedometry comprises a variety of methods used to determine cooling rates in rocks (Lasaga, 1983, Garrido et al., 2001, Stimpfl et al., 2005, Chakraborty, 2006); but only few methods exist for ultramafic rocks (Ozawa, 1983, Redfern et al., 1996, Stimpfl et al., 2005).

CHAPTER 3

Cooling rates can be determined from the relationship between spinel grain sizes and temperatures calculated from the Mg-Fe²⁺ exchange between olivine and spinel (Ozawa, 1984). Zoning in spinel starts to develop at temperatures less than 850°C, so no information from higher temperature histories can be retrieved. Furthermore, the method is still hampered by the lack of data on the effect of trivalent ions on spinel diffusion (Liermann and Ganguly, 2002). Another type of geospeedometer examines order-disorder effects in orthopyroxenes and olivines. However, Fe²⁺-Mg order-disorder between the M2 and M1 site in orthopyroxene only allows calculation of cooling rates below 300°C for slowly cooled rocks (Stimpfl et al., 2005). Metal-cation ordering in olivine can only reliably resolve fast cooling rates such as in volcanic rocks (Redfern et al., 1996). Therefore, no method yet exists to investigate the high-temperature part of the subsolidus cooling of mantle rocks.

The modelling of diffusion-generated concentration profiles in minerals is becoming an increasingly important tool in geospeedometric studies (e.g. Chakraborty, 2006, Watson and Baxter, 2007). Mineral zoning patterns can be used for geospeedometry if two parameters are known: (1) the temperature-dependence of the partition coefficient of an element between two phases and (2) the corresponding diffusion coefficients (Lasaga, 1983, Jiang and Lasaga, 1990, Chakraborty, 2006). Rapid cooling allows for little exchange, and the element distribution records a high closure temperature. Slow cooling allows for extensive diffusive exchange which results in a lower closure temperature. Thus, by comparing the measured distribution of the element in question to modelled distributions, the cooling rate can be calculated.

Subsolidus trace element partitioning between mantle minerals has been studied and found to strongly depend on temperature. Clinopyroxene/orthopyroxene (cpx/opx) partition coefficients ($D^{\text{cpx/opx}}$) increase systematically with decreasing temperature which allows the application of the $D^{\text{cpx/opx}}$ as a geothermometer (Witt-Eickschen and O'Neill, 2005). The change in clinopyroxene (cpx) trace element composition will be less noticeable because of its high relative concentrations. The low relative concentration of trace elements makes orthopyroxene (opx) a viable recorder of cooling-related processes, and its use as a

geospeedometer has been suggested before (von der Handt et al., 2005, Cherniak and Liang, 2007). This allows the calculation of cooling rates in a temperature range that was previously „invisible“.

3.2 SAMPLE DESCRIPTION AND METHODS

Two plagioclase-free spinel peridotites from the ultraslow-spreading Gakkel Ridge were chosen for this study because of their a) high trace element concentrations in cpx allowing good analytical accuracy in associated opx; b) zero amount of alteration, ensuring true rim to rim profiles and c) high pyroxene content.

3.2.1 Petrography

The two samples, PS66-238-25 and -62, were recovered from the Sparsely Magmatic Zone at Gakkel Ridge. They are both very fresh, showing only minute traces of serpentinization. Therefore, the complete absence of plagioclase could be verified optically and by electron microprobe element mapping. The samples are modally heterogeneous in their pyroxene content on sample and thin section scale grading from almost lherzolithic to dunitic in composition (Figure 3-4). Two thin section blocks, representative of cpx-rich and -poor domains were cut from each sample (A and B, respectively). For sample 238-25, the blocks were cut adjacent to each other whereas for 238-62, they are spaced about 5 cm apart.

Both peridotite samples are relatively coarse-grained protogranular spinel peridotites. The degree of deformation is low; undulose extinction is visible in olivines but pyroxenes are unstrained. Microscopic investigations of both opx and cpx show extensive replacive textures (Figure 3-5, and Chapter 2). Both samples have large unstrained opx grains (<0.7 cm), that enclose olivine grains that still show their mantle deformation. Clinopyroxenes and also small opx often occur along grain boundaries. Spinel shows holly-leaf shapes and is mostly associated with either clinopyroxene or small opx.

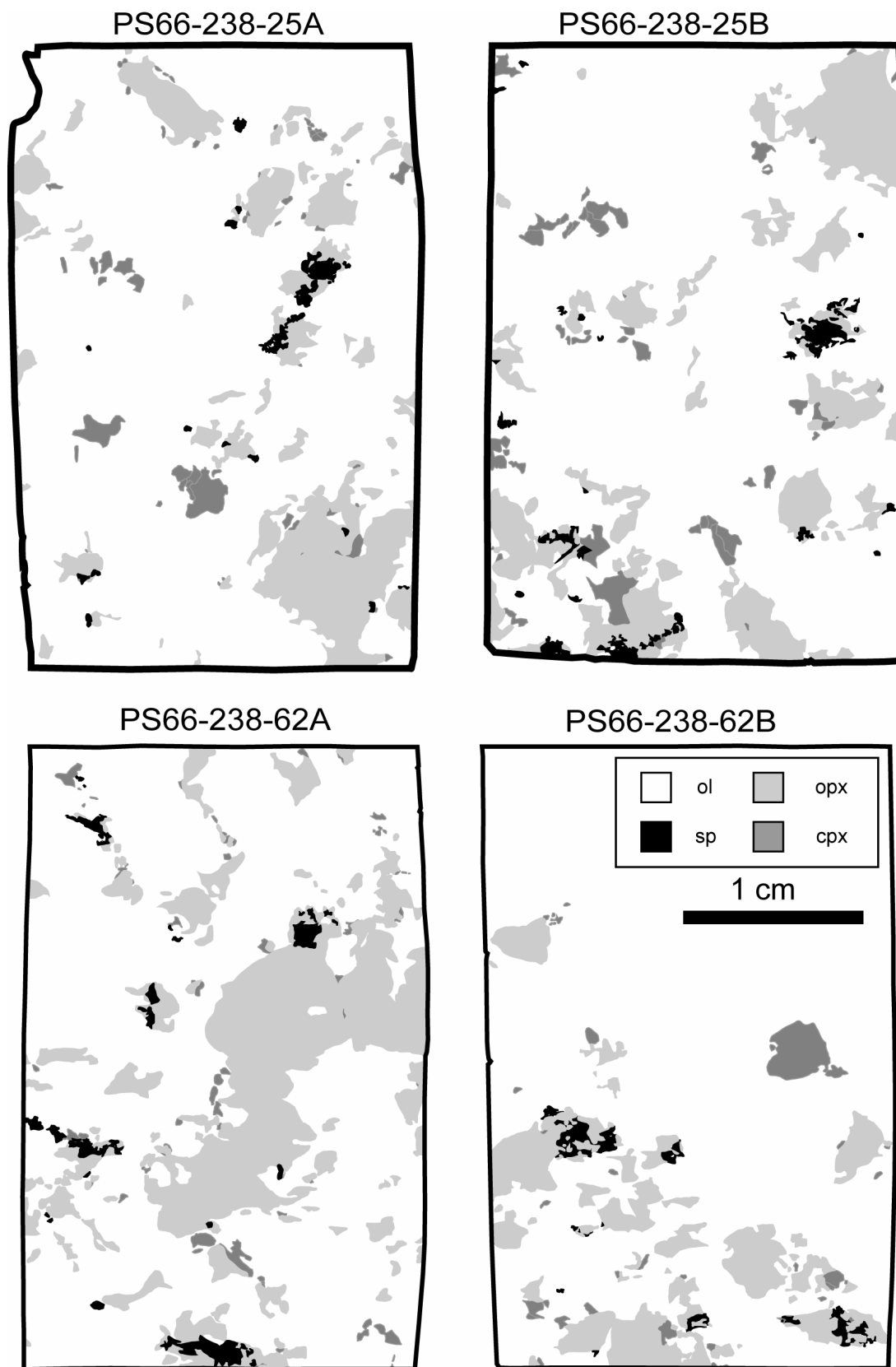


Figure 3-4: Sketches of thin sections from cpx-bearing harzburgites PS66-238-25 and -62. Distribution and contents of pyroxene vary in each thin section; spinel is usually associated with pyroxene.

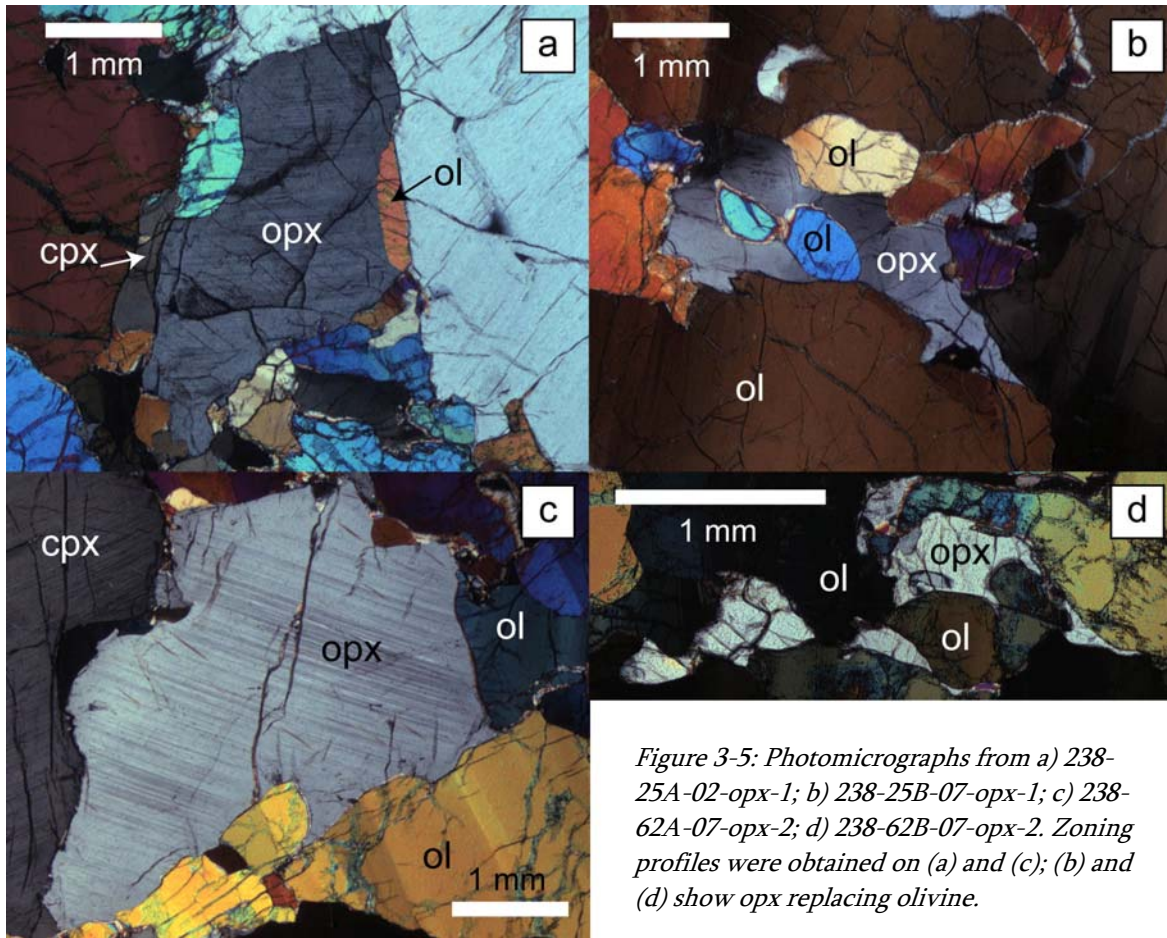


Figure 3-5: Photomicrographs from a) 238-25A-02-opx-1; b) 238-25B-07-opx-1; c) 238-62A-07-opx-2; d) 238-62B-07-opx-2. Zoning profiles were obtained on (a) and (c); (b) and (d) show opx replacing olivine.

3.2.2 Methods

Major element compositions of the silicate phases and spinels were analyzed with a five spectrometer electron probe microanalyzer (EPMA; JEOL Superprobe 8900) at the University of Mainz. For pyroxenes and olivines an accelerating voltage of 15 kV and a beam current of 12 nA were used. Standard counting times were 15s for Si, Mg, Fe, Ca, Cr, Mn and 20s for Al, Ti, Na, K and Ni. For spinels, an accelerating voltage of 20 kV and beam current of 20 nA were used. Standard counting times were 40s for Ca, Ti; 35s for Mg, Al; 30s for Cr, Fe, Mn, Co, Ni, Zn, and 20s for Si. Beam sizes were 2 μm for both programmes. Natural silicates and oxides were employed as standards according to standard practice. Total FeO is assumed to be ferrous except for spinel where the Fe^{3+} content was calculated based on stoichiometry (Droop, 1987).

CHAPTER 3

Clinopyroxenes and orthopyroxenes were analysed in-situ in polished thin sections for selected REE, and for Ti, Sc, V, Cr, Sr, Zr and Ca by secondary ion mass spectrometry (SIMS) using a modified Cameca IMS-3f ion probe at the Max-Planck Institute for Chemistry in Mainz. The primary beam of $^{16}\text{O}^-$ -ions was focused to a spot of 10 nA for cpx and 20 nA for opx analyses, corresponding to spot sizes of 20 and 30 micron, respectively. A high energy offset of -80eV was used to reduce molecular interferences. Additional interference corrections were performed offline, where data was corrected for overlaps at Eu, Gd, Dy, Er and Yb. Each measurement consisted of 6 cycles. Orthopyroxene REE were measured in each cycle for 60s except Ce and Yb for 40s, Sr and Zr for 20s, Y for 8s, Ti and Sc for 5s and all of the remaining elements for 1s. The cpx programme only differed for Gd and Er, which were measured for 40s, and for Dy (20s). Detailed analytical conditions are reported elsewhere (Hellebrand et al., 2002). The overall accuracy is better than 20% for all REE and better than 12% for all other trace elements. Sensitivity factors were monitored by continuous analysis of the MPI-DING glasses GOR132-G and KL2-G (Jochum et al., 2006). Measurements were done in two campaigns. The inter-comparability of the data set was ensured by re-analysis of a cpx analysis and completion of an opx profile. During the measurement of the single grain profiles, analyses were widely spaced (100 μm), and the sample was re-coated several times to prevent surface charging effects due to gold coating damage.

A small subset of clinopyroxenes from both samples was measured in-situ on polished thick sections by laser ablation inductively-coupled plasma mass spectrometry (LA-ICP-MS) using a ThermoFinnigan ELEMENT 2 mass spectrometer coupled to a New Wave UP-213 laser ablation system at the Max-Planck Institute for Chemistry, Mainz. Beam size was 120 μm and dwell time 130s. The MPI-DING reference glasses KL2-G and GOR132-G (Jochum et al., 2006) and the NIST-612 were measured prior and after each sample. ^{43}Ca was used as internal standard to correct for differences in the ablation yield.

The linear distance to rim for opx analyses was measured by an optical microscope using the *analySIS*TM- software v3.0 after calibration with an external scale. The measurements were

repeated three times and the precision is better than 1.5% for distances up to 200 μm and better than 0.5% for distances over 200 μm .

3.3 RESULTS

3.3.1 Major elements

Representative major element compositions of all phases are reported in Table 3-1. The two spinel peridotites from dredge haul PS66-238 are homogeneous in terms of major elements in their silicates but show some variation in spinel Cr-numbers (molar $\text{Cr}/(\text{Cr} + \text{Al})$) ranging from 0.18-0.28 and 0.16-0.29, respectively, with TiO_2 contents below 0.15 wt%. Some spinels have very high Fe_2O_3 concentrations, which either occur in the highest- or lowest-Cr-number spinels. The majority of spinel analyses fall around Cr-number 0.21 and TiO_2 wt% of 0.08 attesting to their dominantly residual nature. Clinopyroxenes have Mg-numbers (molar $\text{Mg}/(\text{Mg}+\text{Fe})$) of 0.92, and NaO concentrations can reach 1.1 wt% but are 0.9 wt% on average.

Orthopyroxenes have core CaO concentrations of up to 1.34 wt%, which decrease to rim concentrations as low as 0.4 wt%. Both pyroxenes have decreasing Al_2O_3 and Cr_2O_3 concentrations towards the rims but constant Cr-numbers similar to the description of Seyler et al. (2007). Olivines show a narrow range in Mg-numbers of 0.908 (± 0.03) and more variable NiO contents of around 0.39 wt%.

3.3.2 Temperatures from major element geothermometers

Results from several spinel peridotite geothermometers based on major element exchange are shown in Table 3-2. A pressure of 10 kbar was assumed for all calculations. This represents a lower limit; hence, all temperatures are minimum estimates. The samples are mostly homogeneous in their major element composition with the most notable exception for CaO in orthopyroxene, and Cr_2O_3 and Al_2O_3 in both pyroxenes. Therefore, also two single-mineral thermometers were used that can monitor these elements.

CHAPTER 3

The results of standard thermobarometric calculations will be discussed in the order of increasing temperatures.

The olivine-spinel thermometer (T_{ol-sp}) is a widely used thermometer for ultramafic rocks. Temperatures of around 700°C are obtained for the samples with the geothermometer of Fabries (1979). Olivine-spinel-based thermometers usually record relatively low equilibrium temperatures, often 100°C lower than pyroxene-based thermometers, and it was suggested that the very fast equilibrium exchange of Mg and Fe between olivine and spinel may account for these low results (Fabries, 1979). However, Li and coworkers (1995) re-evaluated the olivine-spinel thermometer, fitted the original thermometer by Fabries to new experimental data, and obtained a slightly different relationship that resolves the discrepancy. Applying their calibration to the samples yields higher equilibration temperatures of about 815°C. This also represents the upper limit of temperatures that can be obtained by a spinel-based thermometer because of the limitation of fast cation diffusion in spinel (Ozawa, 1983).

The other thermometers used are both two-pyroxene thermometers from Brey and Köhler (1990). T_{BKN} uses the temperature dependent exchange of enstatite component between cpx and opx and gives a slightly higher temperature of about 935°C. The Na-cpx/opx thermometer ($T_{Na-cpx/opx}$) essentially gives the same temperatures, albeit slightly lower, of about 915°C. This corroborates the results of T_{BKN} , because the $T_{Na-cpx/opx}$ thermometer was fitted with the T_{BKN} thermometer and both should agree within $\pm 56^\circ\text{C}$ with each other (Brey and Köhler, 1990).

The olivine-spinel thermometer uses the temperature dependent Fe^{2+} -Mg fractionation between the two minerals, similar to the opx-spinel thermometer. The smaller Fe^{2+} -Mg diffusion coefficient in opx compared to olivine and spinel results in higher temperatures relative to the T_{ol-sp} (Liermann and Ganguly, 2003). Application of the opx-spinel thermometer records on average 990°C.

The Ca-in-opx thermometer of Brey and Köhler (1990) utilizes the fact that the diopside content in opx in equilibrium with cpx is a function of temperature and to a lesser extent of pressure. The thermometer is widely used even though there is some debate over the absolute meaning of the calculated temperatures (Nimis and Trommsdorff, 2001, Paquin and Altherr, 2001). The reproducibility of natural data in the CMS systems is 19°C. This thermometer gives

temperatures of up to 1145°C for orthopyroxene cores and as low as 830°C for rims. The temperature distribution is more or less Gaussian, with an average of about 985°C (Figure 3-6). This thermometer is very sensitive to the quality of the CaO-analyses because 0.1 wt% CaO changes the temperature by 20°C. Orthopyroxenes were analyzed with a focused 2 µm beam at the EPMA. The likelihood exists, as in trace element studies, that clinopyroxene exsolutions smaller than 2 µm result in mixed analyses. This introduces a slight bias towards lower temperature. Temperatures calculated from SIMS analysis represent an integration over a much larger area of 30 µm and shift the calculated temperatures to higher values of around 1030°C (Figure 3-6).

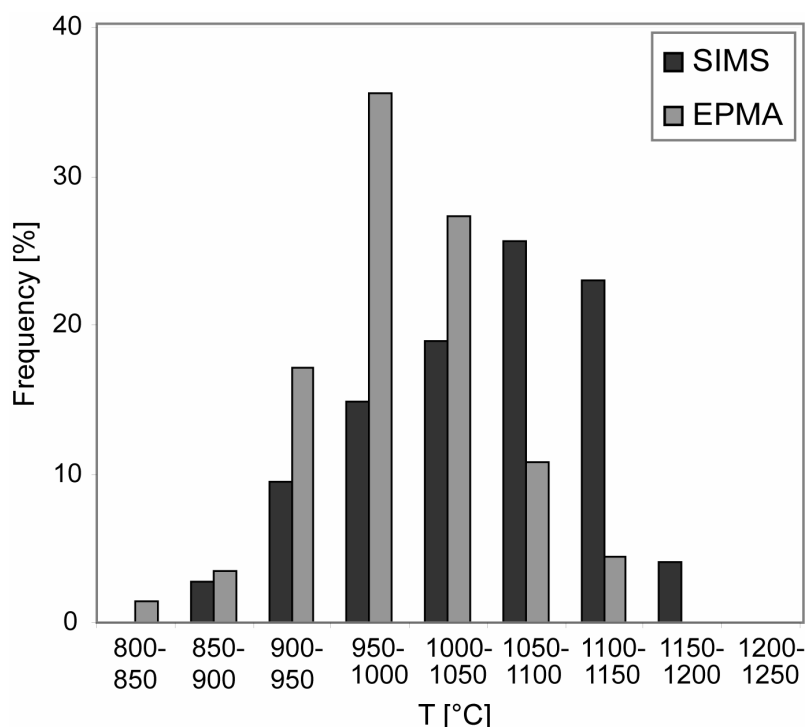


Figure 3-6: Comparison of temperatures calculated from the Ca-in-opx thermometer from Brey and Köhler (1990) from EPMA and SIMS analyses. The temperatures are normalized to the absolute number of analyses for better comparability.

The Cr-Al-in-opx thermometer from Witt-Eickschen and Seck (1991) is a single-mineral thermometer and uses the distribution of Cr and Al (in the M1 site) in orthopyroxene. Similar to the Ca_in_opx thermometer (Figure 3-7a), the distribution of equilibration temperature is Gaussian but shifted slightly towards higher temperatures (Figure 3-7b). Core temperatures are as high as 1150°C and rims as low as 810°C with an average around 1015°C. The shift towards

CHAPTER 3

higher equilibration temperatures can be explained by the more sluggish diffusion of Al compared to Ca in the pyroxenes (Witt-Eickschen and Seck, 1991). Combining all the data, the samples show an average pyroxene equilibration temperature of 965°C.

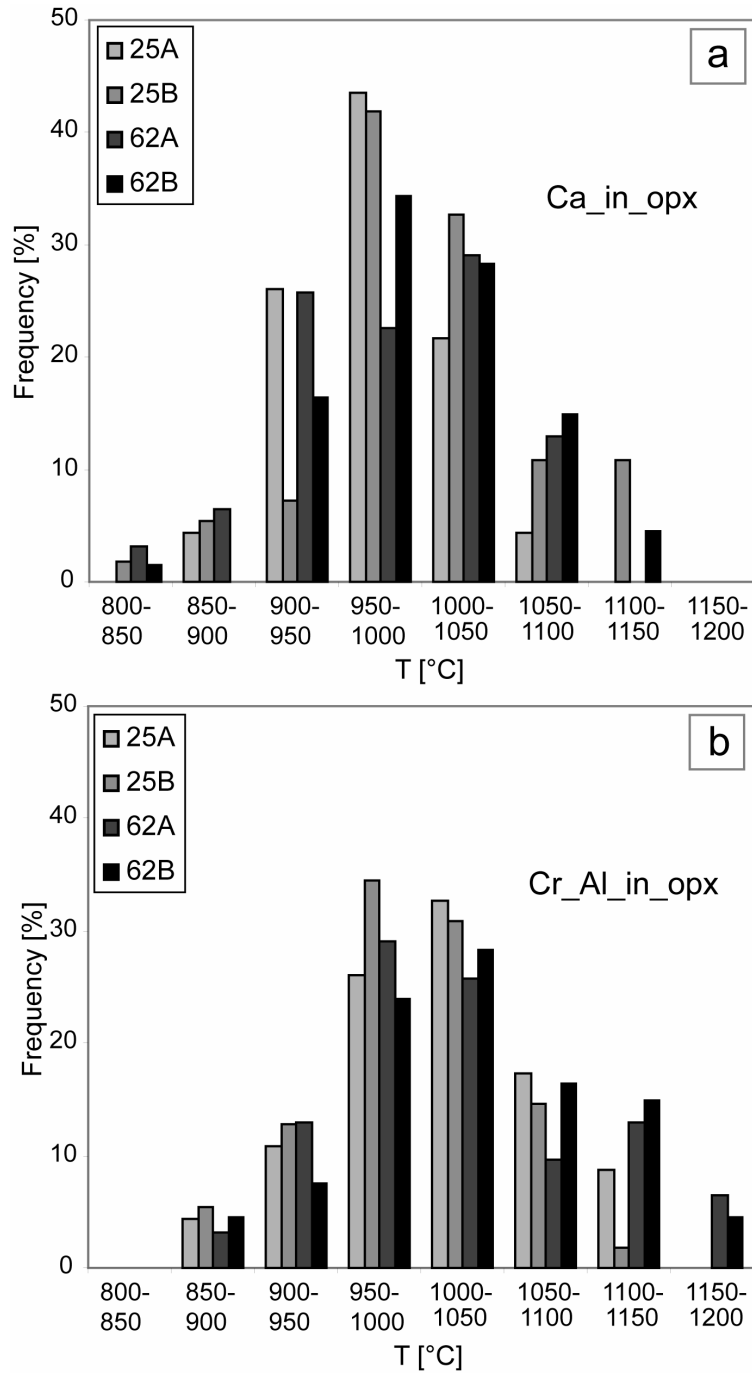


Figure 3-7: Temperatures calculated with the a) Ca-in-opx thermometer (Brey and Köhler, 1990); b) the Cr-Al-in-opx thermometer (Witt-Eickschen and Seck, 1991). The analyses are normalized to the absolute number of points for better comparability.

In comparison with the global array of abyssal peridotites (Figure 3-8), the estimated equilibration temperatures are relatively low and plot at the lower end of temperatures found at mid-ocean ridges. Together with the well developed Ca and Al-Cr zoning in orthopyroxene, this corroborates a long and relatively slow cooling history of these samples.

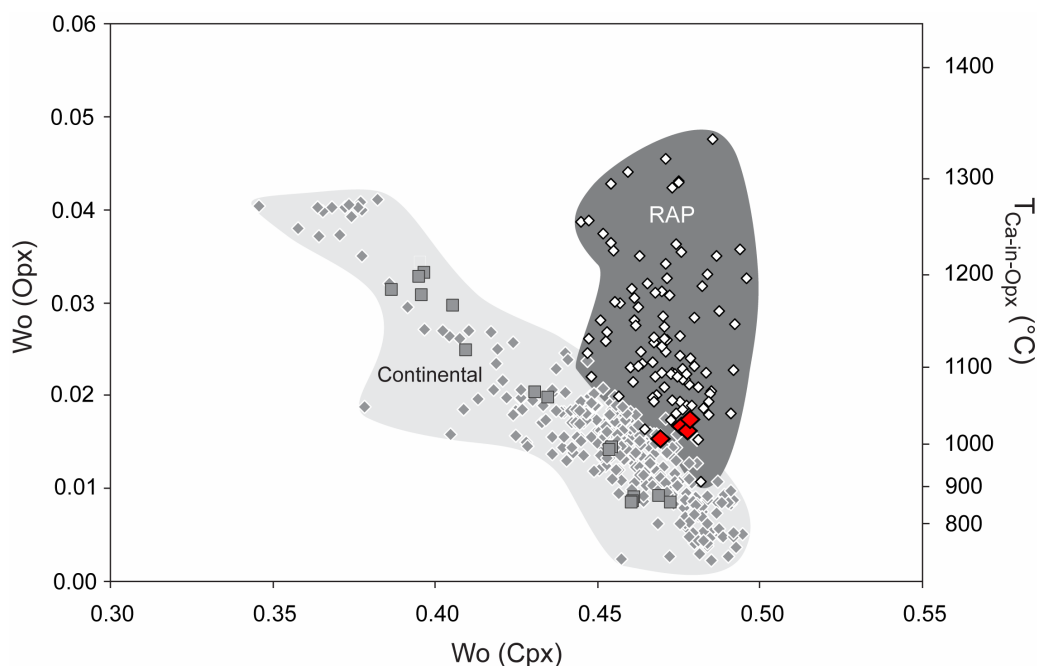


Figure 3-8: Wollastonite content in cpx versus associated opx. Residual abyssal peridotites (RAP) are shifted towards higher wollastonite contents in cpx relative to continental xenoliths, which is the result of preferential measurement of post-exsolution cpx in RAP. Nevertheless, both cover a similar range of temperatures. Samples from this study (red diamonds) plot at the lower end in equilibration temperatures in the range of global abyssal peridotites (modified from Hellebrand et al., 2005).

3.3.3 Trace elements

Trace element compositions of cpx and opx are reported in Table 3-3 and Table 3-4, respectively. Clinopyroxenes in both samples show flat REE-patterns (La/Yb_N : 0.6-0.9; subscript N denotes CI-chondrite normalized after Anders and Grevesse (1989)) at about 7 x CI. The analyses are homogeneous within analytical accuracy on thin section scale (Figure 3-9). All cpx exhibit slight negative Sr-anomalies of around 0.8. This is typical for low-Cr-number spinel peridotites and does not indicate the presence of plagioclase.

Orthopyroxene trace element patterns show large variation (Figure 3-9). La_N concentrations vary by over an order of magnitude while Yb_N shows much less variability.

CHAPTER 3

Large orthopyroxene grains are zoned with highest REE concentrations in the core and lowest at the rim. Smaller opx grains show usually intermediate REE concentrations with respect to the overall range. All opx grains show the typical positive Ti- and Zr-anomalies (Rampone et al., 1991).

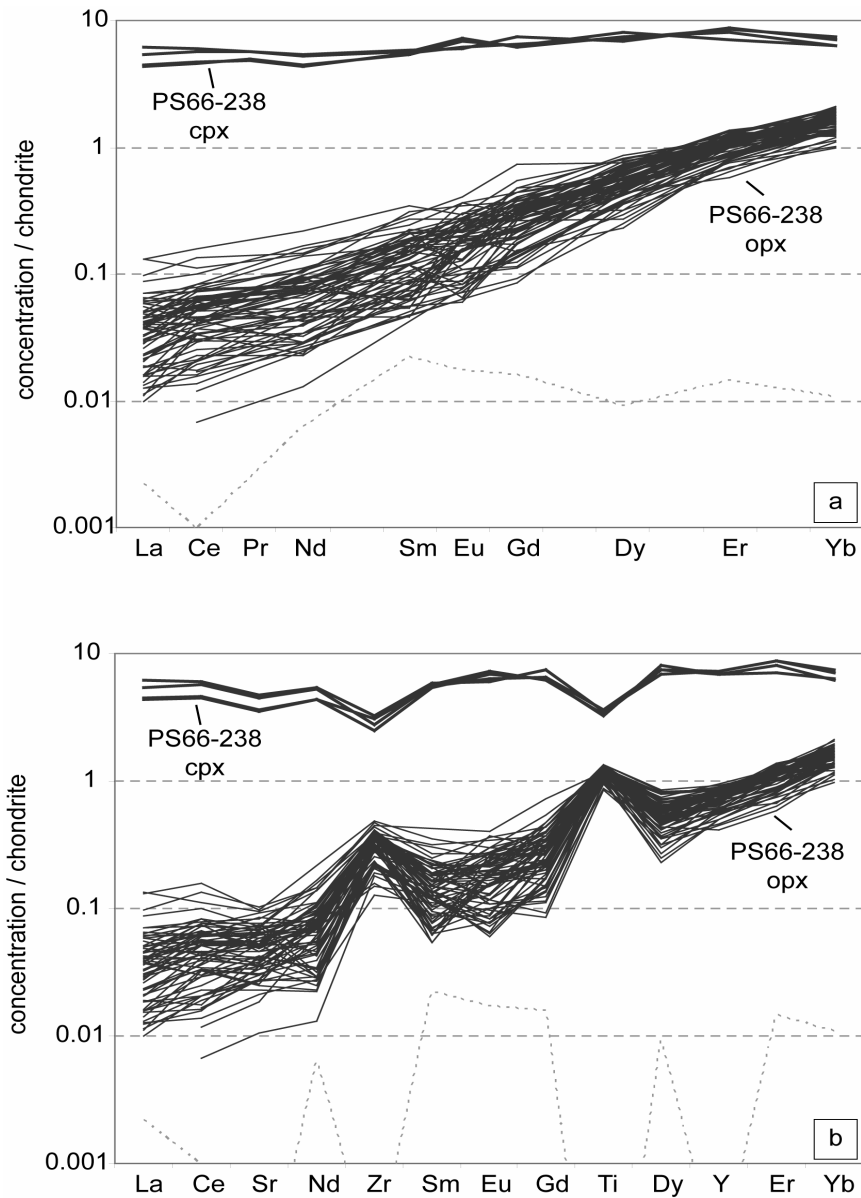


Figure 3-9: Chondrite-normalized REE concentrations in pyroxenes of PS66-238-25 and -62. a) Clinopyroxenes are homogeneous in composition within error on sample scale; only averages are plotted. Orthopyroxene shows a significant concentration range, which decreases systematically from opx core to rim. b) Chondrite-normalized spidergram for both pyroxenes. Clinopyroxenes and orthopyroxenes show complementary Ti- and Zr-anomalies. A weak negative Sr-anomaly exists in clinopyroxenes; Detection limit of SIMS is shown as grey stippled line, CI normalization values taken from Anders and Grevesse (1989).

CHAPTER 3

Calcium was measured by SIMS as well and correlated with microprobe analyses from the same spot. This gave a good correlation (R^2 of 0.99) with the equation $\text{CaO_EPMA [wt\%]} = 0.0001683 \times \text{Ca_SIMS [\mu\text{g/g}]} - 2.0349445$.

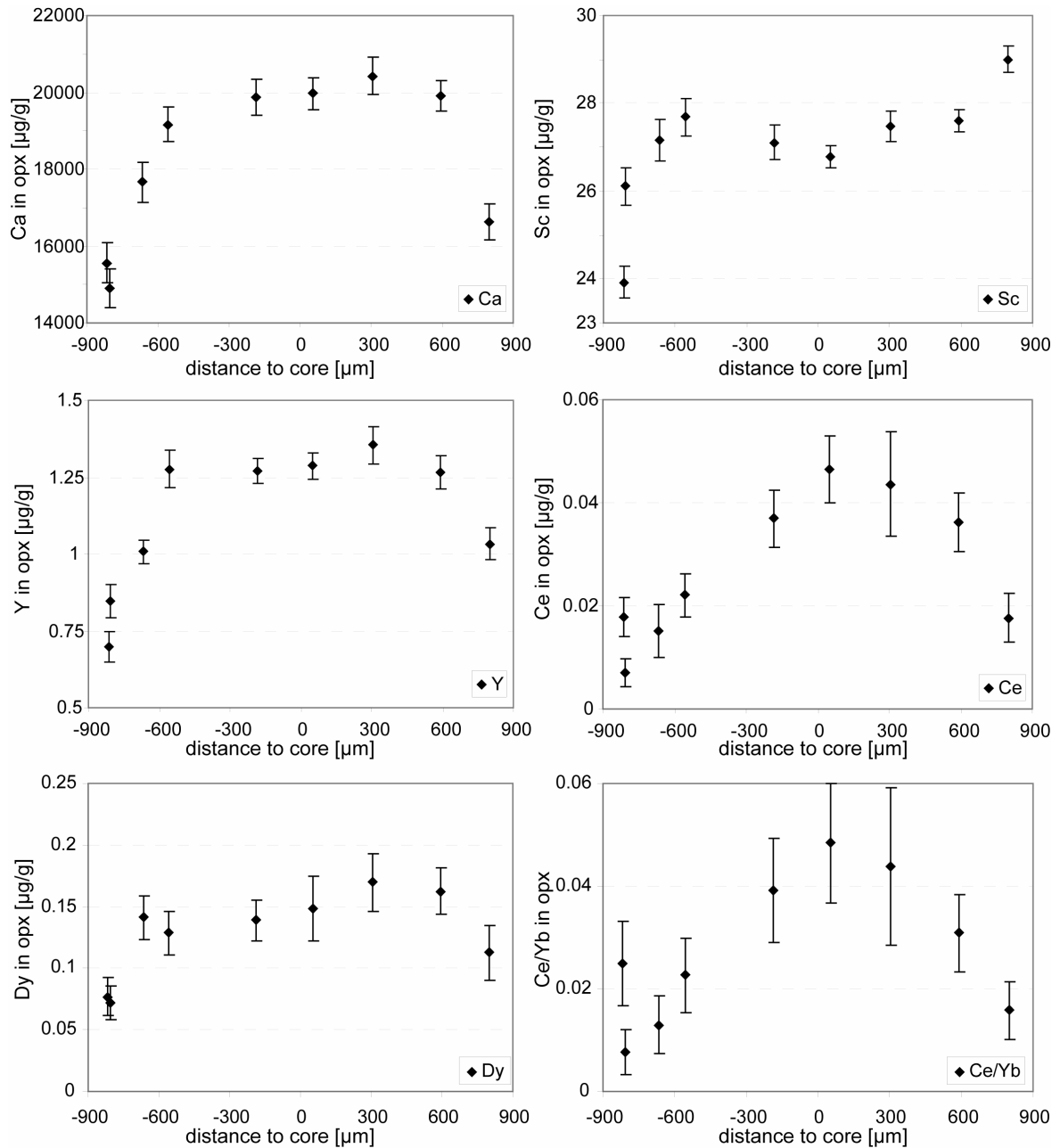


Figure 3-10: Selected trace element profiles from 238-62A-07-opx-2. At the left rim is cpx, at the right rim is olivine in contact. Zoning profiles are slightly asymmetric toward the olivine contact with higher concentrations relative to the cpx contact. Sc is even enriched relative to the core composition. Error bars denote one standard deviation. The complete set for all analyzed elements can be found in the appendix A3.

CHAPTER 3

Three opx grains from the sample set were selected for more detailed analysis of their zoning profiles (238-25A-02-opx-1, 238-25A-12-opx-1 and 238-62A-07-opx-2). For all analysed incompatible elements, concentrations decrease systematically from the core toward the rims (Figure 3-10 and appendix A3). Orthopyroxenes show the characteristic mushroom or bell-shaped concentration profiles that are typical cooling and diffusive-reequilibrium (Lasaga, 1983, Dodson, 1986, Lasaga and Jiang, 1995). Very pronounced core/rim ratios (e.g. LREE: 5.2; HREE: 1.6) occur in opx.

Clinopyroxene/orthopyroxene contacts are not abundant in the samples, and, as shown in Figure 3-4, olivine is the dominant phase in contact with opx. Consequently, no “ideal” opx profile with cpx on both sides could be measured. This effect was initially inferred to be negligible, as grain boundary diffusion might be expected to maintain equilibrium in the sample over a wide temperature range. However, the measured profiles are not perfectly symmetrical but show consistently higher absolute trace element concentration at opx/olivine rims than at opx/cpx rims. Nevertheless, the overall shape is similar on both sides for all analysed elements, except for Sc, Ti and V. These three elements consistently show an increase towards olivine but a decrease towards the cpx contact relative to the opx core.

Interpyroxene partitioning coefficients ($D^{\text{cpx/opx}}$) were calculated by dividing the average cpx composition for each thin section by the individual opx analyses of a given sample (Table 3-5). The accuracy of the reported $D^{\text{cpx/opx}}$ hinges on the assumption that the element-to-Si ratios of cpx can be directly related to those of opx. Careful investigation in a different study, using the same SIMS, showed that the respective Ca/Si ratios are not affected (Hellebrand et al., 2005). However, in the present study, cpx was always measured between opx lamellae or at lamellae free rim areas and arguably does not represent its true solidus composition. Orthopyroxene, on the other hand, generally contains very closely-spaced (5-10 μm) and narrow (1-2 μm) cpx lamellae, and the 30 μm wide beam ensures representative and constant proportions of the opx and cpx lamellae. Accordingly, the calculated $D^{\text{cpx/opx}}$ may theoretically deviate from the pre-exsolution value and its effect needs to be assessed further. Peridotites from Gakkel Ridge, including one sample from the same location were studied for their trace element exchange during exsolution (Hellebrand et al., 2005). It was shown that the mean

volume proportion of opx lamellae in cpx porphyroclasts makes up about 15% of the near-solidus cpx prior to exsolution. This shifts compositions slightly from the uncorrected cpx composition but remains still within the analytical accuracy. Hence, the formation of exsolution should not affect significantly $D^{\text{cpx/opx}}$. As a further confirmation, a subset of cpx analyses from both samples was performed by LA-ICP-MS at the Max-Planck Institute for Chemistry, Mainz. A 120 μm wide spot was used that would integrate the host cpx with its opx lamellae. Clinopyroxenes again have a relatively flat REE pattern (La/Yb_N of 0.6-0.9) at Yb_N of 7.4 and a negative Sr-anomaly of around 0.8. Clinopyroxene compositions from SIMS and LA-ICP-MS are identical within analytical accuracy (see Table 3-3).

3.3.4 Temperatures from trace element geothermometers

The systematic increase of $D^{\text{cpx/opx}}$ for a given element during cooling allows for the calculation of an equilibrium temperature at any opx measurement point with the empirically determined geothermometers of Witt-Eickschen and O'Neill (2005). They are reported in Table 3-6. Figure 3-11 shows the distribution of $D^{\text{cpx/opx}}$ as a function of distance to the opx/mineral interface. The different symbols denote the mineral present at the nearest opx grain boundary, in order to highlight the systematic variations present in the data. No differences between the individual samples could be found.

An almost exponential relationship between $D^{\text{cpx/opx}}$ and corresponding distance to grain boundary is visible for all elements. Calculated equilibrium temperatures show a relatively constant value at distances of more than about 400 μm from the orthopyroxene rim, but they drop considerably close to the opx surface. No systematic difference between the different grain boundary mineralogies is evident, except at distances less than 100 μm to the grain boundary, differences between olivine and pyroxene contacts exist. Orthopyroxene trace element concentrations increase within 100 μm to an olivine contact again, sometimes to almost core values again. This is systematic and is also observable in orthopyroxene zoning profiles. As a result, $D^{\text{cpx/opx}}$ differs significantly between pyroxene and olivine contacts with only minor overlap.

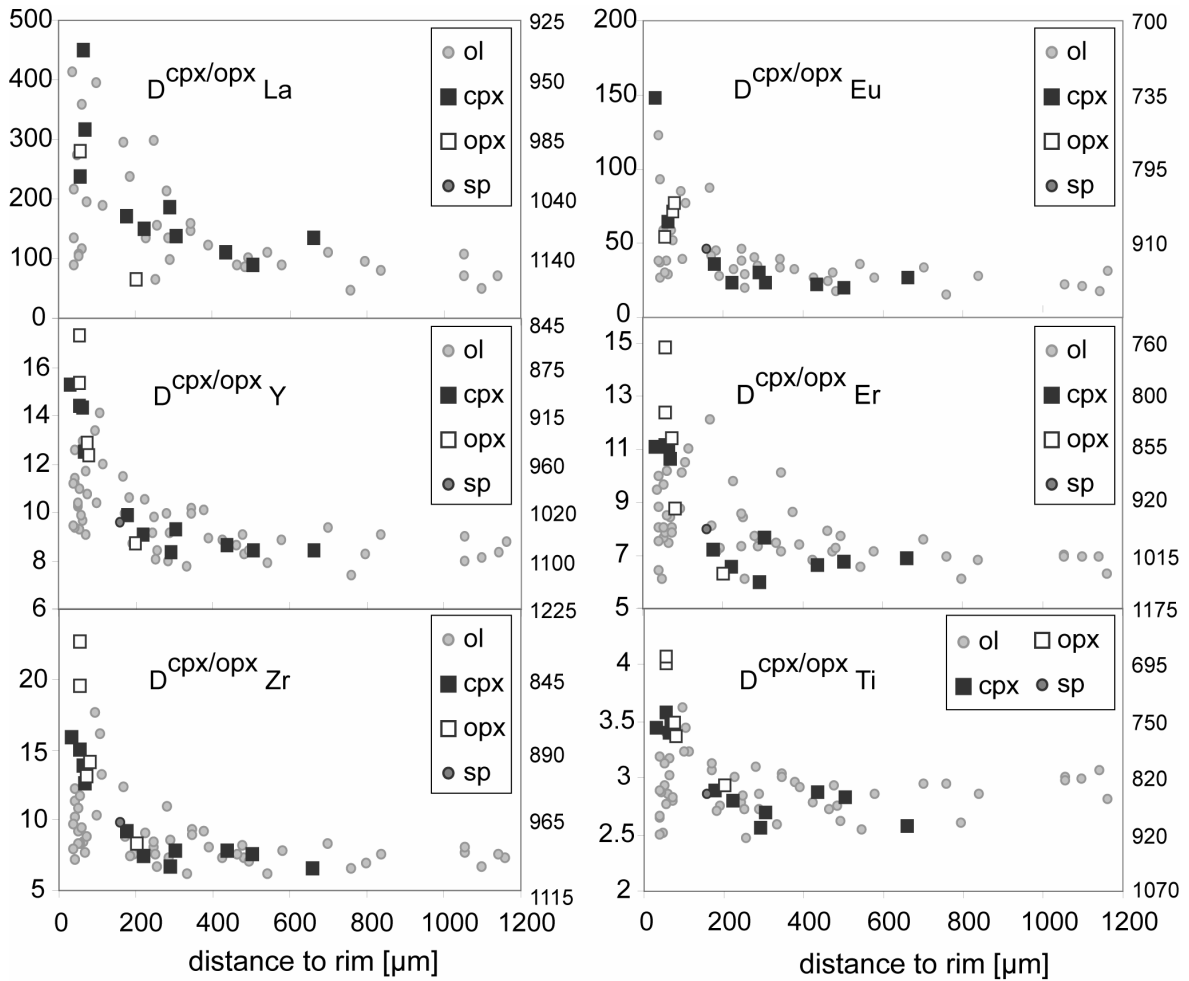


Figure 3-11: $D^{cpx/opx}$ for selected elements versus the distance of the opx analyses to its nearest grain boundary in μm . All orthopyroxene analyses have been normalized to the average clinopyroxene composition of their respective thin section. On the second (right) axis, the corresponding equilibrium temperatures are shown in $^{\circ}\text{C}$. The data are grouped depending on what mineral phase is in contact at the nearest rim. Analyses at distance less than $100\ \mu\text{m}$ from the ol-opx contact differ considerably relative to opx-px contacts. This probably indicates the closure of grain boundary diffusion and the dominance of the $D^{ol/opx}$ on the opx composition.

Equilibration temperatures calculated by $D^{cpx/opx}$ give an individual temperature interval for each element with an overall range of equilibration temperatures from 1380°C down to 760°C (Figure 3-12). The geothermometer of Seitz et al. (1999) was also applied for comparison for Sc, V and Cr and yielded slightly different temperature estimates. This discrepancy was also noted by Witt-Eickschen and O'Neill (2005) who suggested that it is an effect of major element composition on $D^{cpx/opx}$.

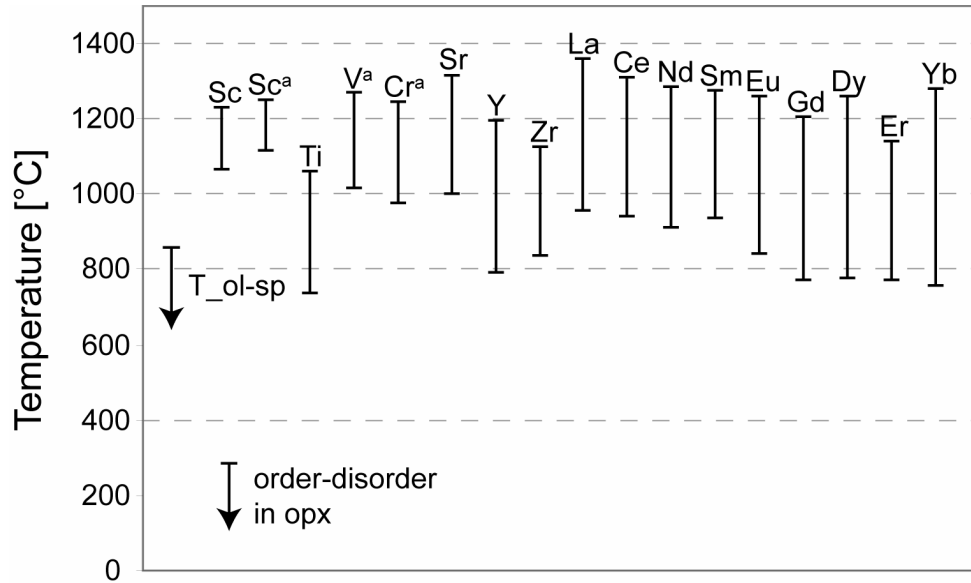


Figure 3-12: Range of equilibration temperatures for the individual elements calculated with the Witt-Eickschen and O'Neill partitioning coefficients, except elements with superscript 'a' are calculated with thermometers of Seitz et al., 1999. For comparison, the olivine-spinel thermometer (T_{ol-sp}) of Ozawa (1984) only records temperatures lower than 850°C; the order-disorder-in-opx method records cooling rates at temperatures lower than 300°C (Stimpfl et al., 2005).

3.4 DISCUSSION

Most geothermometers available for peridotitic and websteritic rocks are based on the partitioning of major elements between the individual mineral phases (Wells, 1977, Fabries, 1979, Hervig and Smith, 1982, Bertrand and Mercier, 1985, Brey and Köhler, 1990, Witt-Eickschen and Seck, 1991, Liermann and Ganguly, 1999). However, most cation diffusion is too fast for the slowly cooled mantle rocks, and major element zoning is rarely reported from abyssal peridotites.

3.4.1 Temperature dependence of mineral-mineral trace element exchange

Few studies have been devoted to the temperature dependence of $D^{cpx/min}$ of trace elements (Seitz et al., 1999, Witt-Eickschen and O'Neill, 2005, Lee et al., 2007). The dependence of $D^{cpx/opx}$ on temperature has been recently studied for a large set of elements on fully equilibrated spinel peridotite xenoliths (Witt-Eickschen and O'Neill, 2005) and was

found to vary systematically in a manner that allows the application of the $D^{cpx/opx}$ as a geothermometer.

The aim of this study is to develop a new geospeedometer using the temperature dependent trace element exchange between orthopyroxene and clinopyroxene.

3.4.1.1 Cooling-dependent trace element re-distribution between cpx and opx

The importance of the subsolidus re-organization of trace elements between different minerals has previously been discussed mostly in the light of the perils of recalculating magmatic compositions from mineral analyses (Treiman, 1996), and applying subsolidus partition coefficients for crystal-liquid calculations (Eggins et al., 1998, Witt-Eickschen and O'Neill, 2005) as well as to study exsolution effects on mineral compositions (Hellebrand et al., 2005). When coexisting minerals equilibrate in the absence of a magma (i.e. subsolidus) the remaining REE are redistributed among the solid phases. Plagioclase-pyroxene re-partitioning that affects parent melt calculations has been observed to play an important role in the evolution of lunar samples (Treiman, 1996). However, in the case for cpx and opx in peridotites, the cooling effect will be less obvious on cpx composition because the relative change in opx concentration can be large, whereas the absolute increase in cpx concentration is negligible. This makes opx an excellent recorder of the continuous cooling history of ultramafic rocks.

The spinel peridotites in this study were refertilized by a low degree melt (see Chapter 2 for discussion), which changed their pyroxene trace element composition to higher concentrations relative to their depleted protoliths. Calculated opx compositions in equilibrium with an average cpx from this sample set at temperatures between 1300°C and 800°C match well the observed range in opx trace element compositions (Figure 3-13). The cpx/opx trace element partitioning data suggest high temperature equilibration between cpx and opx cores at around 1250-1300°C. The fact that the cores of large opx clasts are in high temperature equilibrium with cpx confirms the inference that complete equilibration was attained after refertilization.

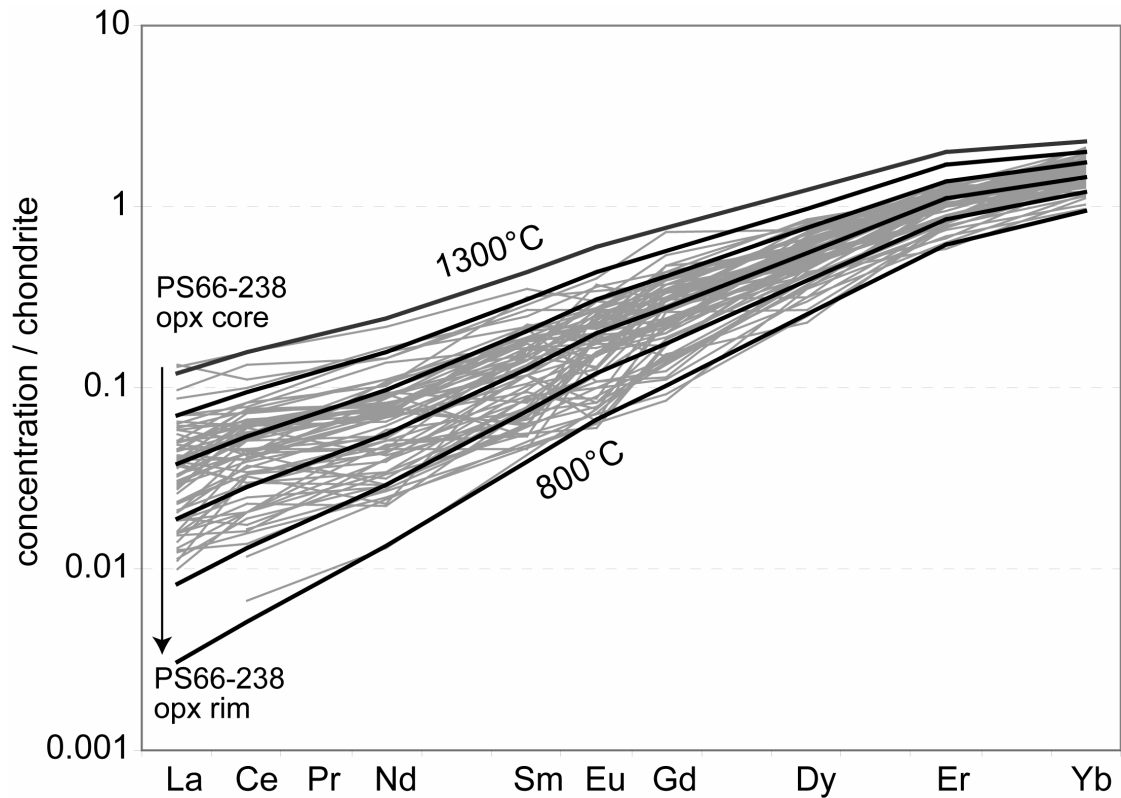


Figure 3-13: Chondrite-normalized REE concentrations in orthopyroxene. Opx compositions in equilibrium with the average clinopyroxene from 238-25 and 238-62 at temperatures from 1300°C to 800°C are superimposed. The range of analyzed orthopyroxenes falls within the calculated data.

Closure temperatures calculated by $D_{\text{cpx/opx}}$ yield smooth correlations with distance to the opx grain boundary. The correlations improve with increasing analytical certainty. Calcium was also part of the measurement sequence. On one hand, it allowed to further verify that the variability in opx composition is not an artifact of the changing contribution of cpx lamellae to the opx composition. It also allowed the use as an independent thermometer. Through correlation with corresponding EPMA analyses, it was possible to construct closure temperature profile for CaO using the Ca_in_opx thermometer of Brey and Köhler (1990).

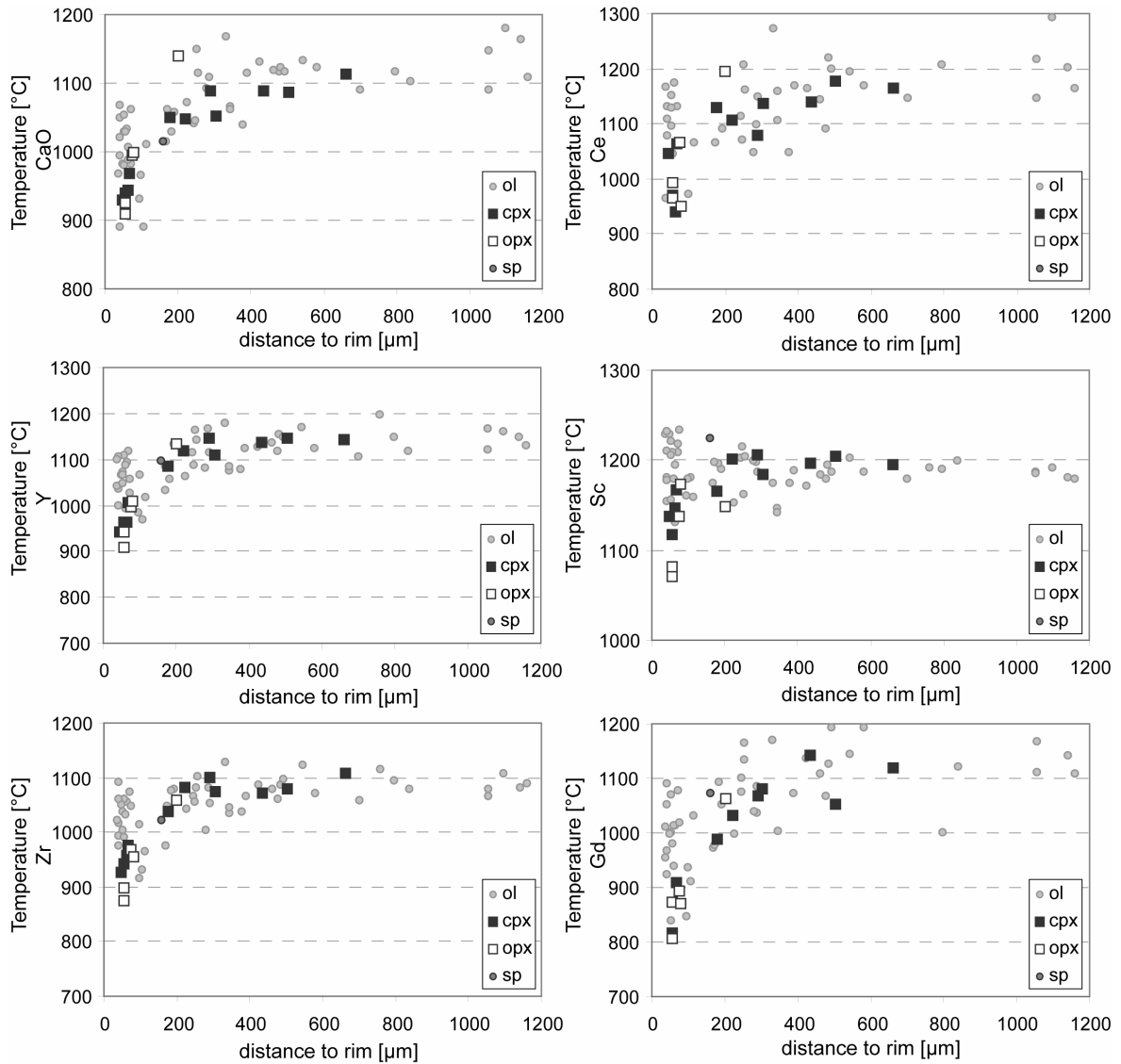


Figure 3-14: Equilibrium temperatures from selected trace elements in opx versus the distance to rim.

3.4.1.2 Cooling-dependent trace element re-distribution between olivine and opx

At distances less than 100 μm from the opx/mineral interface, considerable scatter for analyses next to olivine occurs while opx/cpx and opx/opx interfaces continue the exponential relationship with distance. In general, opx rim concentrations next to olivine are significantly higher relative to pyroxene contacts. In the case for Sc, V and Ti, contact zones next to olivine are even enriched compared to the opx core.

Olivine is known to strongly fractionate REE (McKay, 1986) and its REE composition is also temperature dependent (Zanetti et al., 2004). Interpartitioning between olivine and opx

CHAPTER 3

(Witt-Eickschen and O'Neill, 2005), opx and cpx (Seitz et al., 1999, Witt-Eickschen and O'Neill, 2005), and olivine and cpx (Witt-Eickschen and O'Neill, 2005, Lee et al., 2007) has been studied for a limited set of elements. Sc is one of the elements investigated in all these studies and also shows a pronounced difference in concentration depending on its neighboring mineral in this study. Partitioning of scandium follows the relationship $D^{cpx/ol} > D^{opx/ol} > D^{cpx/opx}$. Using these individual partition coefficients can explain the difference in scandium concentration between olivine and cpx rims of 238-62A-07-opx-2. Thus, if grain boundary diffusion is no longer effective, exchange with olivine can actually have significant impact on opx composition.

This has important implications for cooling rate and temperature calculations based on trace element exchange thermometers. The empirical geothermometer of Seitz et al. (1999) uses the partitioning of transition elements (Sc, Ti, V, Cr, Mn, Co, Ni) between opx and cpx to calculate equilibrium temperatures. Of these elements, Sc, Ti and V show strong “olivine contact effects”, while Cr does not. However, there still exists some variability in chromium concentrations close to the opx rims in the complete data set (see Appendix A3-5), and this may merit further investigation. Mn, Co and Ni were not determined in this study. Furthermore, the asymmetric shape of the zoning profiles suggests a weak “olivine effect” for all other elements as well, being strongest for HREE.

As a result, temperatures obtained from opx/olivine contacts will either obliterate cooling-related zoning in opx or even record an apparent (though false) heating event. Small interstitial, often magmatic, grains that preferentially occur along olivine grain boundaries, will also record higher apparent temperatures relative to larger porphyroclasts. To obtain reliable cooling rates, it will be important to only study data from opx in contact with other pyroxenes.

3.4.2 Cooling rates: Toward a new geospeedometer

Different approaches exist to calculate cooling rates from element zoning profiles. One is the straightforward numerical modelling of element concentrations, the other is to model closure temperature profiles. The temperature dependent partition coefficients from Witt-Eickschen and O'Neill (2005) allow the transfer of opx trace element zoning profiles in this study into closure temperature profiles. Therefore, both methods can be applied in this study.

3.4.2.1 Trace element zoning profiles and cooling rates

Four main parameters can influence the opx zoning pattern: (1) starting temperature T_0 , (2) cooling rate, (3) time, and (4) diffusion coefficients. None of the first three parameters is known accurately, but a best estimate and a probability range for each can be provided.

3.4.2.1.1 Model parameters

Starting temperature: Chapter 2 discussed the high-temperature refertilization event that affected the spinel peridotites. The samples show clear evidence of interaction with a low degree melt that must have occurred at high temperature, most likely close to the onset of melting. Melting beneath normal mid-ocean ridges starts in a narrow depth range close to the spinel-garnet transition zone (Shen and Forsyth, 1995). No unequivocal evidence for melting in the presence of garnet could be found. Therefore, as an upper limit, the starting temperature T_0 is set to be 1400°C which represents the solidus temperature at about 70 km (Hirschmann, 2000). This is approximately in agreement with the upper limit of equilibrium temperatures from trace elements which gives 1377°C.

Cooling rate: Cooling is more rapid near the ridge axis at low spreading rates than at faster spreading rates (Sleep, 1975), thus high cooling rates would be expected for these samples. In contrast, low closure temperatures from major element geothermometers for these samples (Table 3-2) suggest a slow and long cooling history that allowed diffusive element exchange down to low temperatures. Nevertheless, boundary estimates can be made from the knowledge of the sample location. Based on magnetic anomalies, the full spreading rate at the sample location is estimated to be 12.2 mm/a (Jokat et al., 2003). The half-spreading rate equals

CHAPTER 3

the upwelling rate if we assume that only passive upwelling occurs (e.g. Shen and Forsyth, 1995). Thus, an uplift rate of about 6.6 km/Ma is expected. Given the depth and uplift rate, a cooling rate of 30°C/Ma would keep the samples just below the solidus (27°C/Ma) until they reach the surface; this would be the minimal cooling rate. A constant cooling rate of 130°C/Ma would cool the samples down to 0°C at the seafloor, which would be an (unrealistic) maximum. For simplicity, cooling rates will be assumed to be constant even though they will most likely change slightly over a longer temperature-depth interval. However, plagioclase peridotites from the same dredge haul indicate that the dredge haul remained close to the solidus down to relatively low pressure (≈ 10 kbar; see Chapter 5). Therefore, the cooling rate will probably not change significantly and the assumption of a constant cooling rate is reasonable. In addition, it is likely that the cooling rate will be rather close to 30°C/Ma.

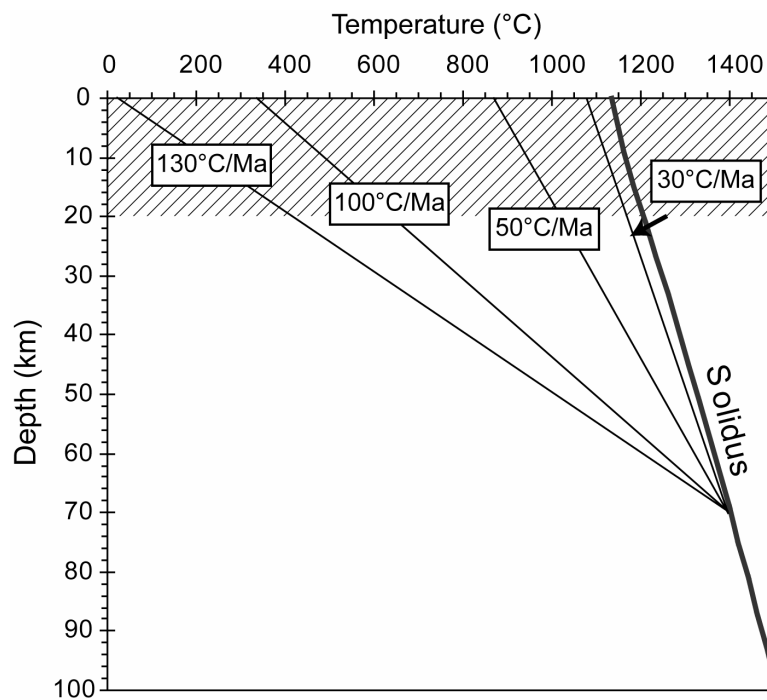


Figure 3-15: Overview of possible cooling rates for Gakkel Ridge assuming an uplift rate of 6 km/Ma and a depth of 70 km at solidus temperatures as a starting point. Grey hatched area indicates the conductively cooled lithospheric lid assumed for Gakkel Ridge.

Time: A starting depth of 70 km and an uplift rate of 6.6 km/Ma would allow for 10.6 million years of continuous cooling to the surface. This is of course a maximum estimate as hydrothermal cooling will increase cooling rates close to the surface.

CHAPTER 3

Diffusion coefficients: While trace element diffusion in cpx is fairly well studied (Sneeringer et al., 1984, Cherniak, 1998, van Orman et al., 1998, Cherniak, 2001, van Orman et al., 2001), experimentally determined cation diffusion data for opx are scarce. The recent experimental study of Cherniak and Liang (2007) determined diffusivities for five REE on a near-endmember enstatite between 850-1250°C and 1 atm. Diffusion coefficients were found to be identical within error for all REE, and Cherniak and Liang used an average over their diffusion data in their models. Their expression of the temperature-dependent diffusion coefficient:

$$D_{\text{REE, Y}} = 1.2 \times 10^{-7} \exp(-369 [\text{kJ mol}^{-1}] / RT) [\text{m}^2 \text{s}^{-1}]$$

will be applied in this study as well.

The general equation for diffusion in a sphere with constant diffusion coefficient D (Crank, 1975) is:

$$\frac{\partial C}{\partial t} = D \left(\frac{\partial^2 C}{\partial r^2} + \frac{2}{r} \frac{\partial C}{\partial r} \right) \quad (3-1)$$

where C is the concentration at position r after time t and r refers to the distance to the sphere center.

Anisotropic diffusion may occur at least for divalent cations in enstatite with the fastest cation diffusion parallel to the c -axis and slowest parallel to the a -axis (Ganguly and Tazzoli, 1994, Schwandt et al., 1998). However, diffusion studies of pyroxene have shown no evidence of significant anisotropy in diopside (Sneeringer et al., 1984, Dimanov et al., 1996, Cherniak, 2001) as well as orthopyroxene (Schwandt et al., 1998, Cherniak and Liang, 2007). All SIMS-profiles were measured subparallel to the [100] direction as evidenced by clinopyroxene exsolutions. Considering the absence of significant anisotropy and the equal orientation of all profiles, diffusion was modelled as a concentration-independent, one-dimensional diffusion in a sphere (e.g. Crank, 1975).

Hence, by setting

$$u = Cr \quad (3-2)$$

we obtain for equation 3-1:

$$\frac{\partial u}{\partial t} = D \frac{\partial^2 u}{\partial r^2} \quad (3-3)$$

Two assumptions were made for the boundary and initial conditions: (1) no pre-existing zoning exists in the opx, so that the grain has a uniform initial concentration distribution for a given element (eq. 3-4), and (2) the opx surface is in equilibrium with cpx during cooling (eq. 3-5).

$$u = r C_i; t = 0; 0 < r < a \quad (3-4)$$

$$u = a \frac{C_{cpx}}{D_{cpx/opx}(t)}; r = a; t > 0 \quad (3-5)$$

, whereby C_i is the initial concentration in the grain, C_{cpx} the composition of the associated cpx, a the radius of the grain and t is the duration time of diffusion.

The initial concentration C_i in opx is calculated to be in equilibrium at T_o with its associated cpx. The surface concentration C_o is calculated in each step by dividing the cpx composition by the $D_{cpx/opx}$ from Witt-Eickschen and O'Neill (2005) in the corrected version of Lee et al. (2007) for the given temperature. Clinopyroxene is treated as an infinite reservoir in this model because of its high concentrations relative to opx and because it does not change its composition significantly. The diffusion equation was then solved with the PDE toolbox from Matlab™.

3.4.2.1.2 Model results

In order to be a good recorder of the thermal history, the shape of element zoning profiles should be sensitive to the details of the thermal history. To illustrate the potential of this geospeedometer and the effects of starting temperature and cooling rate on the shape of diffusion profiles, different models were run for La in opx (Figure 3-16). Starting temperatures are 1200°C and 1100°C, respectively, and cooling rates range between 30°C/Ma and 10°C/Ma. All models cover the same time interval of 10 million years. Starting composition is an opx in equilibrium at near-solidus temperatures with the average cpx composition of this sample set (= average of PS66-238-25 and 62; La concentration of 1.19 µg/g).

CHAPTER 3

Core concentrations and the shape of the “dome” are strongly dependent on the cooling rate. The lower the final temperatures become, either by a lower starting temperature or by faster cooling, the stronger core-rim ratios increase. The increasing sensitivity of $D_{\text{cpx/opx}}$ of REE on temperature with increasing ionic radii makes elements such as the LREE in opx more sensitive to cooling-related interpartitioning than HREE. On the other hand, analytical sensitivity improves with the higher concentrations of the HREE in opx. A good balance between both should be maintained for a given data set.

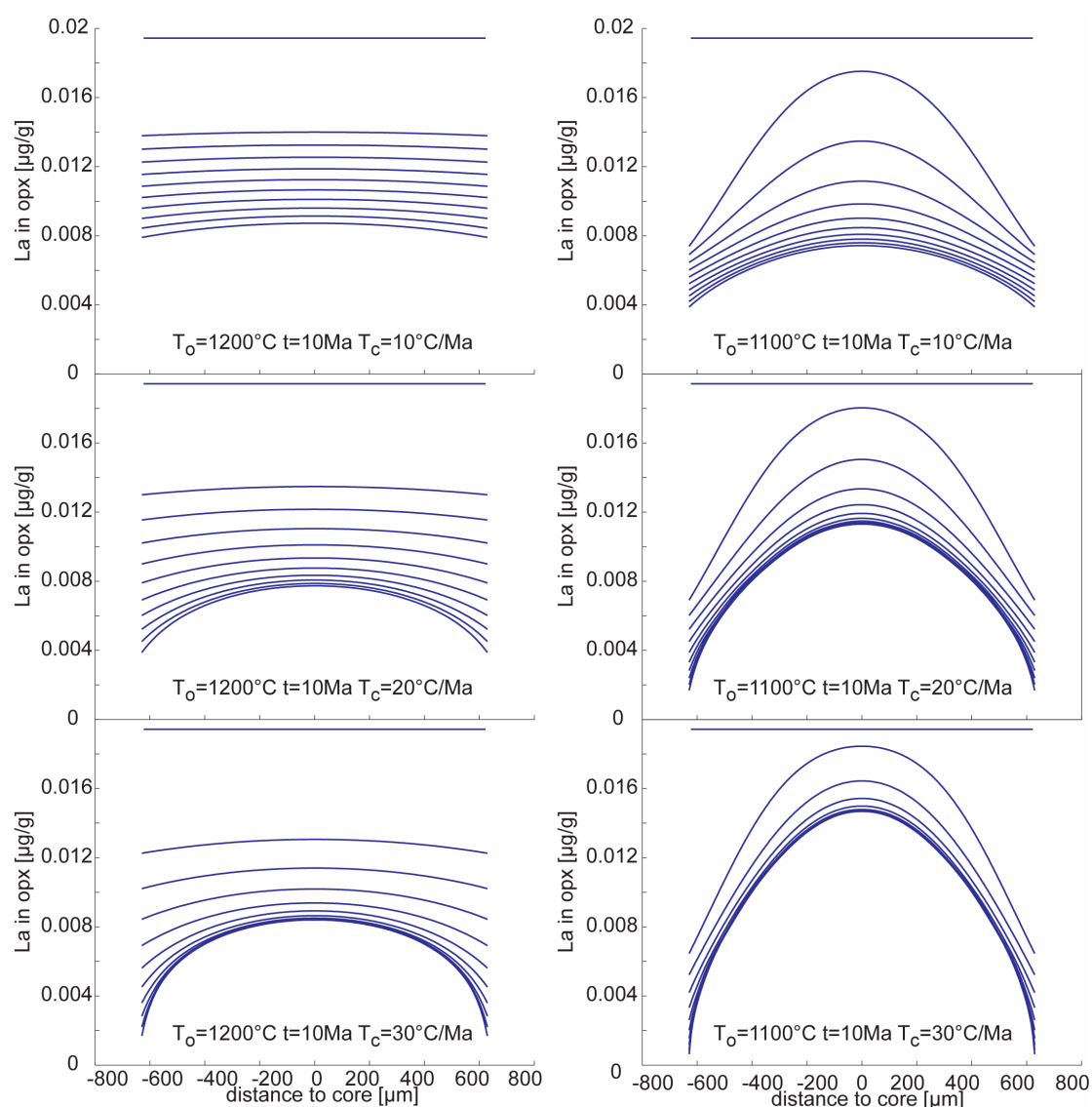


Figure 3-16: Influence of starting temperature and cooling rate on the development of diffusion profiles in orthopyroxenes during cooling. All profiles are calculated for a total duration of 10 million years. Each line denotes a 1 million year increment. Starting point is an orthopyroxene composition in high temperature equilibrium (1250°C) with 238-25A. Grain radius was set to 630 µm, the same as 238-25A-02-opx-1. The exponential change in $D_{\text{cpx/opx}}$ during cooling dramatically influences the shape of the zoning profile.

3.4.2.1.3 Model results for PS66-238

Figure 3-17 shows the model results for the opx profile from PS66-238-62A. Diffusion coefficients are only available for REE and Y in opx, and are the only elements investigated accordingly. The starting composition and the composition after 10 million years are highlighted, which is assumed to represent the maximum time interval possible for this location. In order to check if longer diffusion times could match the profile, the model is run for 15 million years to show the further development of the profile. Cooling rates of 30°C/Ma, representing the minimum estimate, as well as 50°C/Ma and 100°C/Ma were chosen for this model. Another example for a cooling rate of 30°C/Ma is shown in the appendix (Figure A3-6).

Several observations can be made:

Continuous cooling for 10 million years alone at a cooling rate of 30°C/Ma cannot match any of the REE zoning profiles, even though calculated uplift rates suggest that this represents the maximum time interval possible. The models indicate that prolonged cooling for at least another five million years at 30°C/Ma could eventually match at least the La concentrations. In contrast, MREE and HREE not only would need much further cooling to lower temperatures but also require much slower cooling rates. A cooling rate of 30°C/Ma is already a minimum estimate as otherwise the solidus would be crossed again. The HREE zoning can be only reproduced by two contrasting parameters. On one hand, high cooling rates suggested by rim compositions. The range of equilibrium temperatures from opx rim compositions seen by the HREE actually requires cooling to much lower temperatures than 950°C. To stay within a reasonable time frame for the samples, this would implicate high cooling rates in order to reach the temperatures seen by the HREE at the rim (down to 750-800°C). On the other hand, low cooling rates suggested by core compositions. Faster cooling will shut down the effective diffusion at much higher temperatures, and “freeze-in” the cores of the profiles at higher concentrations. This can be seen in Figure 3-18 that shows the model results for cooling rates of 50°C/Ma and 100°C/Ma. While higher cooling rates seem to match rim compositions better, the mismatch for the core compositions becomes even more evident. Again, La suggests much higher cooling rates relative to Nd and Y. This result is also consistent with results from the other zoning profiles (Appendix A3-6).

CHAPTER 3

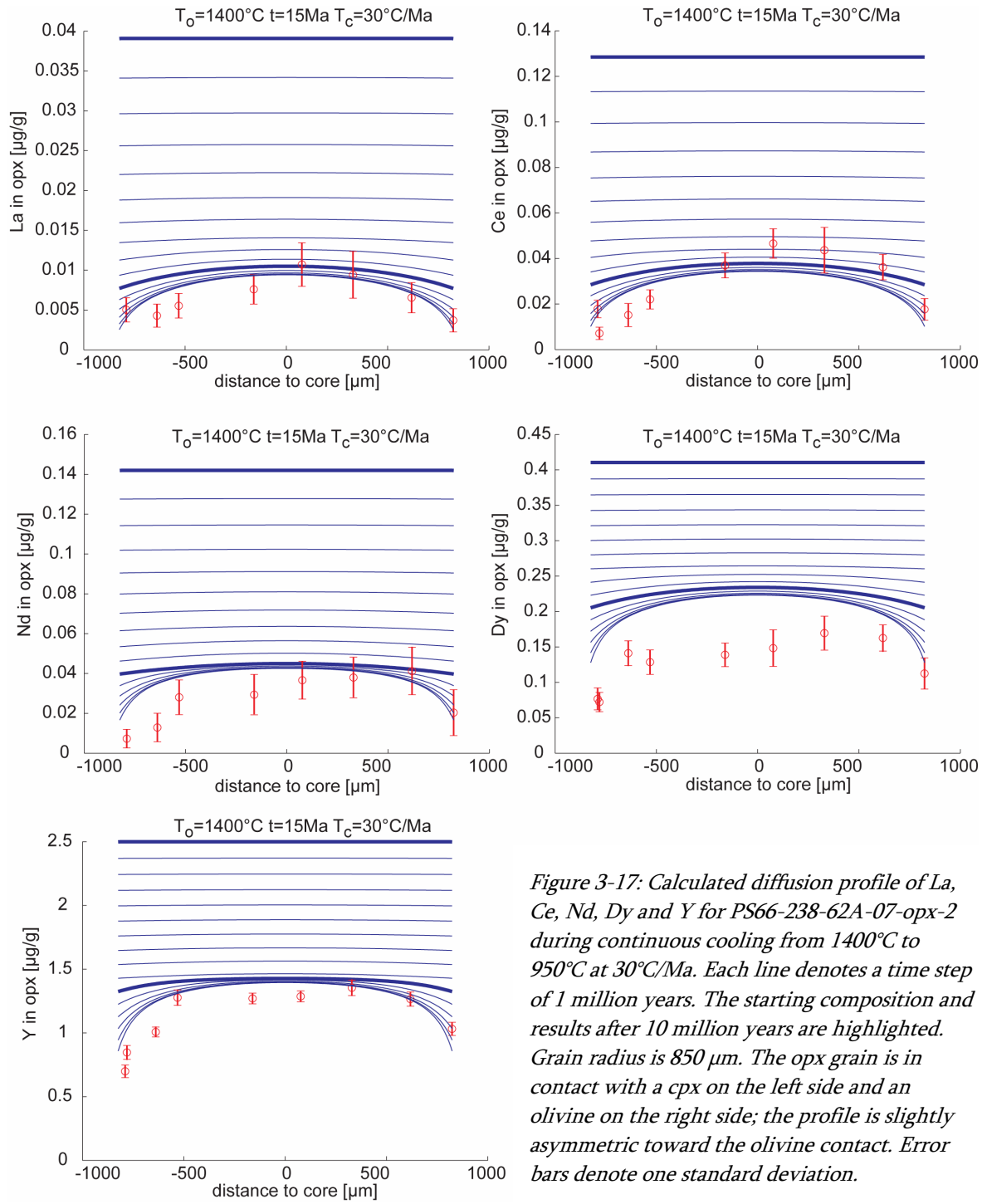


Figure 3-17: Calculated diffusion profile of La, Ce, Nd, Dy and Y for PS66-238-62A-07-opx-2 during continuous cooling from 1400°C to 950°C at 30°C/Ma . Each line denotes a time step of 1 million years. The starting composition and results after 10 million years are highlighted. Grain radius is $850\ \mu\text{m}$. The opx grain is in contact with a cpx on the left side and an olivine on the right side; the profile is slightly asymmetric toward the olivine contact. Error bars denote one standard deviation.

CHAPTER 3

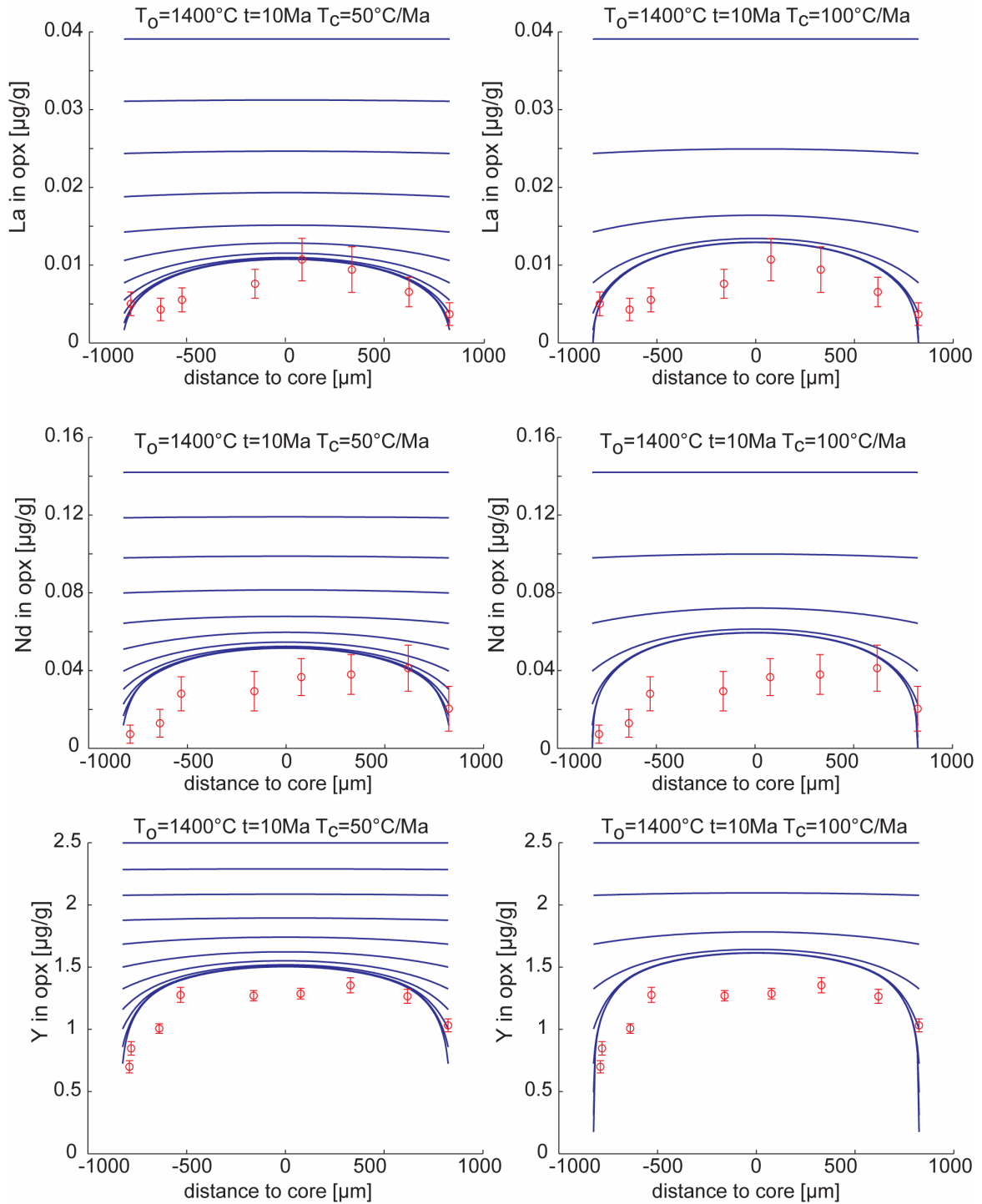


Figure 3-18: Calculated La, Nd and Y diffusion profile for PS66-238-62A-07-opx-2 during continuous cooling of a cpx-opx pair. The system cools down from 1400°C to 900° at 50°C/Ma and down to 400°C at 100°C/Ma. Each line denotes a time step of 1 million years. Starting temperature is always 1400°C, starting composition, calculated to be in equilibrium with 238-25A-cpx at 1400°C. Grain radius of 238-62A-07-opx-2 is 850 µm. Error bars denote one standard deviation.

Overall, the straightforward diffusion model can recreate the shape of the REE zoning patterns in opx but fails to match them, maybe with the exception of La, within the boundary conditions estimated for this sample location.

The strength of this model, its sensitivity to the model parameters, is its disadvantage at the same time. Model results are very sensitive to the chosen starting temperature, or more exactly, to the assumed starting composition. Hence, if the initial conditions are unconstrained, a level of uncertainty is introduced to the model results. For example, if uplift rates are unknown, as in the case of ophiolites, and accordingly the time available for diffusion, the model will not give one definite answer. Ideally, this model approach should be combined with a different approach to calculate cooling rates; a model insensitive to starting compositions.

3.4.2.2 Closure temperature profiles and cooling rates

The concept of closure temperature was introduced by Dodson (1973) and is described as the temperature at which an element species in a mineral stops diffusive exchange with its surroundings. The closure temperature depends on the diffusion parameters, the cooling rate and the effective diffusion radius and hence the grain size. If the rate of volume diffusion in a mineral is decreasing with decreasing temperature, the concentration in the interior begins to lag behind to that at the surface (Dodson, 1986). Dodson (1986) further describes: “Eventually the system “closes”: initially at the centre, and subsequently nearer to the outside, the concentration approaches a limit at which the whole grain is effectively isolated from its surroundings, except for an infinitesimal surface layer”. The resulting concentration variation is then called a closure profile.

A number of different approaches exists using such mineral closure temperature profiles to extract cooling rates, a more recent and more widely applicable comes from Ganguly and Tirone (1999).

CHAPTER 3

The formulation for closure temperature profiles developed by Dodson assumes sufficient diffusion to change core compositions. This will not be true for very slow diffusing elements and/or large grain sizes, and Ganguly and Tirone extended Dodson's equation to include cases with small amounts of diffusion by adding a correction function to it. The modified formulation reads as follows:

$$\frac{E}{R T_c(x)} = \frac{E}{R T_0} + \ln M + G(x) + g(x) \quad (3-6)$$

, where E and R are the activation energy and gas constant, respectively, T_0 the starting temperature and $T_c(x)$ the closure temperature at point x . $G(x)$ is the closure function as defined by Dodson (1986) and $g(x)$ a correction function introduced by Ganguly and Tirone (1999) to account for very small amounts of diffusion. However, their results will converge upon the Dodson's values again when Dodson assumptions for sufficient diffusion are met such as for small grain sizes or high peak temperatures.

The dimensionless parameter M is defined as

$$M = \frac{D(T_0)\tau}{a^2} \quad (3-7)$$

, where $D(T_0)$ is the diffusion coefficient at T_0 , a is the radius of the spherical, cylindrical grain or half thickness of plane sheet, respectively, and τ is the cooling time constant i.e. the time taken for D to diminish by e during cooling.

3.4.2.2.1 Model parameters

The starting temperature T_0 in this model is the temperature at which the diffusion species still has a homogeneous concentration in the grain at the onset of or during cooling (Ganguly and Tirone, 1999). Forward numerical modelling for trace element zoning in orthopyroxene in the previous section showed that grains remain unzoned for almost 200°C after cooling from 1400°C. Therefore, the starting temperature T_0 was set to 1250°C. Nevertheless, the advantage of this method is its relative insensitivity to the chosen starting temperature. A difference of 100°C, such as from 1400°C to 1300°C as starting temperature, results in a decrease in core closure temperature of 3°C and at the rim of 4°C for a grain radius

of 850 μm . The defining variables in this model are the diffusion coefficients and grain size; the latter can be directly measured.

Diffusion coefficients were taken again from Cherniak and Liang (2007):

$$D_{\text{REE, Y}} = 1.2 \times 10^{-7} \exp(-369 [\text{kJ mol}^{-1}] / RT) [\text{m}^2 \text{s}^{-1}]$$

$$D_{\text{Sr}} = D_{\text{Eu}^{2+}} = 6.93 \times 10^{-6} \exp(-384 [\text{kJ mol}^{-1}] / RT) [\text{m}^2 \text{s}^{-1}]$$

Rare earth element zoning profiles are relatively symmetric for most elements except for rims in contact with olivine, as discussed in a previous section. Only half (i.e. rim-core) profiles are shown here and the complementary part of the profile was inverted to increase data density but data points closer than 100 μm to the olivine grain boundary were excluded. Then, closure temperature profiles were calculated for the individual opx profiles using the extension of the Dodson formulation by Ganguly and Tirone (1999) and software developed by these authors.

3.4.2.2.2 Model results

Figure 3-19 shows the results of calculations for the opx profile from PS66-238-25A for La, Ce, Eu and Y. Cooling rates can be very accurately determined by this method for elements with good analytical precision such as yttrium. Closure temperature profiles for La and Ce require high cooling rates of about 100°C/Ma and 70°C/Ma, respectively, whereas Eu and Y rather a cooling rate of 15°C/Ma. This shows the same systematic behaviour as in the previous model, namely that LREE give consistently higher cooling rates relative to HREE. In the case of erbium, cooling rates much lower than 10°C/Ma, even lower than the mantle adiabat are required.

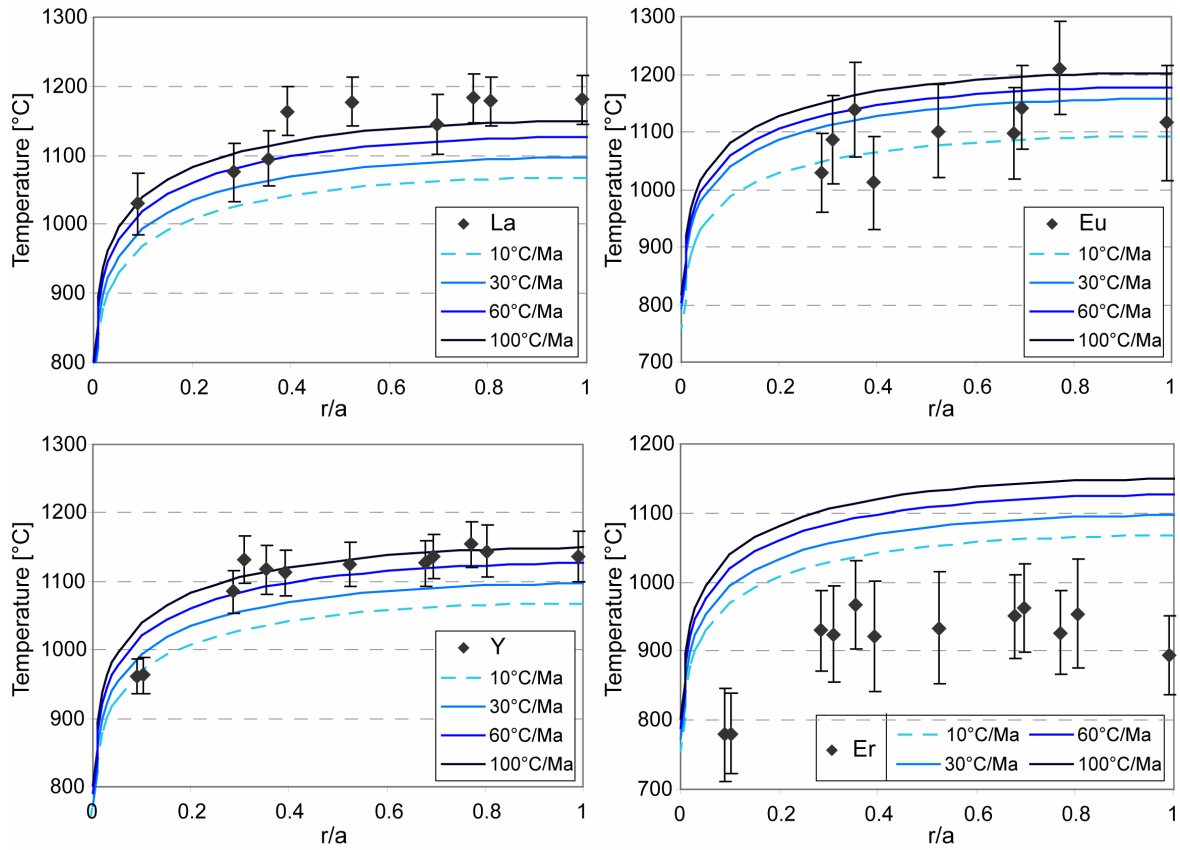


Figure 3-19: Closure temperature profiles calculated for a constant cooling rate of 10°C/Ma, 30°C/Ma, 60°C/Ma and 100°C/Ma for La, Eu, Y and Er. Profile from 238-25A-02-opx-01. Starting temperature is 1250°C. Error bars denote one standard deviation.

Similar calculations were carried out for selected REE, Y and Sr in sample PS66-238-62A (238-62A-07-opx-1) (Figure 3-20). Lanthanum and cerium require highest cooling rates among the REE. In contrast, closure temperatures of europium and erbium require cooling rates lower than 10°C/Ma. Strontium was incorporated in this model as well and the diffusion coefficient was taken to be similar to divalent Eu, as proposed by Cherniak and Liang (2007). Closure temperatures calculated for Sr are very high and no reasonable cooling rate is able to reproduce the closure temperature profiles.

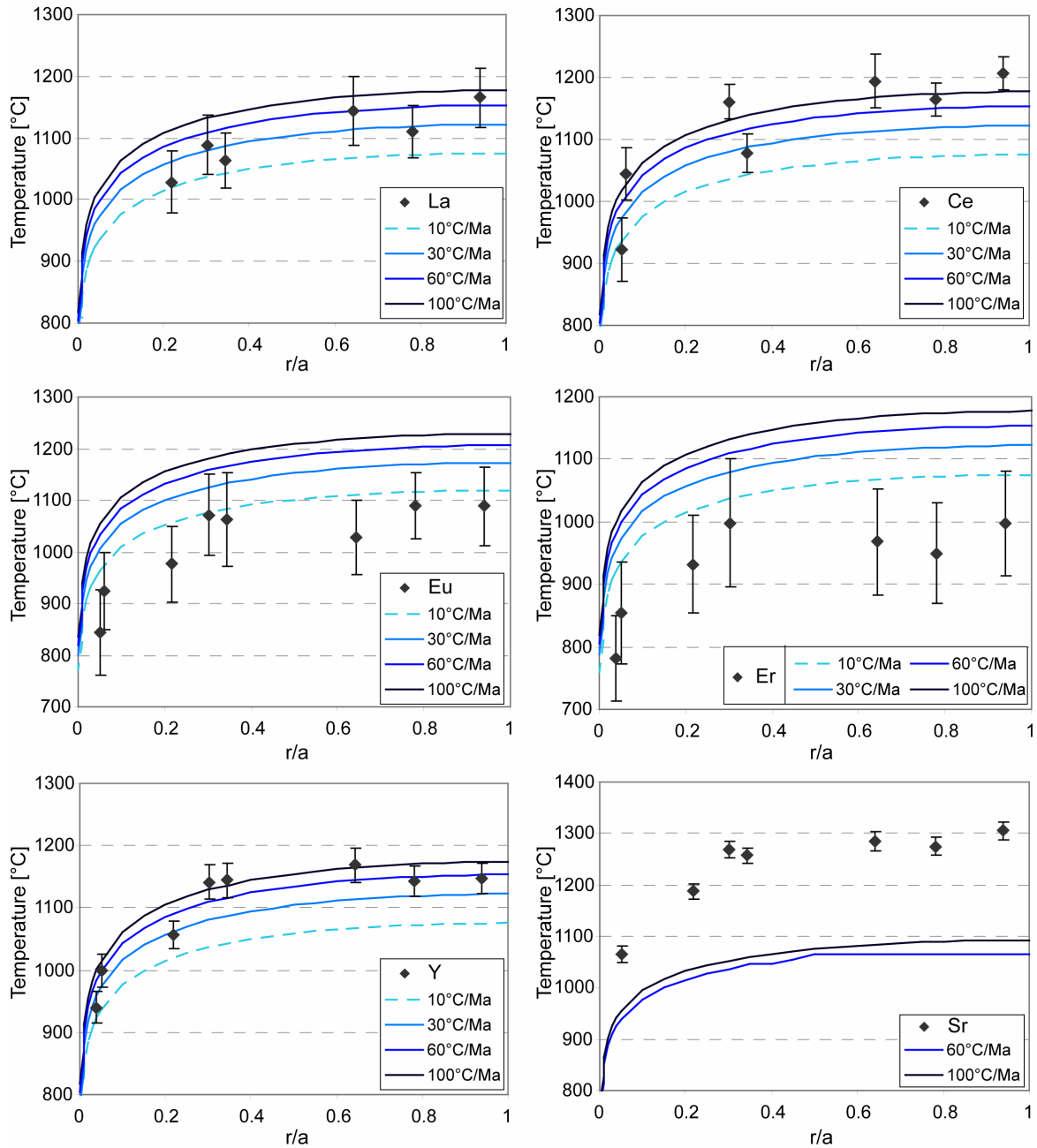


Figure 3-20: Closure temperature profiles of selected REE and Y calculated for a constant cooling rate of 10°C; 30°C/Ma, 60°C/Ma and 100°C/Ma except for Sr that shows only result for 60°C/Ma and 100°C/Ma. Zoning profile: 238-62A-07-opx-02. Starting temperature is 1250°C. Error bars denote one standard deviation.

Modelling of trace element zoning and closure temperature profiles was carried out for REE, Y and Sr in opx from two different samples. Cooling rate estimates for a given element differ slightly between both samples such that profiles in 238-62A-02 consistently record lower cooling rates. This does not indicate that cooling rates differed between the samples but

may be an effect of the cutting plane of the grain. If closure temperatures are not determined at the center of the grain, they will record slower apparent cooling rates.

Modelling results for the complete set of REE, both for element zoning patterns as well as closure temperature profiles, do not give a consistent cooling rate estimate but show an extreme range, well beyond reasonable values. However, results from both models are consistent with each other in that LREE require much higher apparent cooling rates relative to HREE. The two variables that influence closure temperature profiles are the grain size and the diffusion coefficient. The grain size can be directly measured; hence it is possible that the chosen set of diffusion coefficients may not be applicable for mantle orthopyroxenes.

Trace element zoning in opx and their associated closure temperatures allow making qualitative statements about cation diffusion in opx. These results differ significantly from the experimental diffusion data of Cherniak and Liang (2007) and indicate that they cannot be used in this study. The reasons of this will be discussed in the following chapter.

It has been demonstrated that orthopyroxenes are a good recorder of the thermal history of mantle rocks. A new approach to calculate cooling rates from upper mantle peridotites has been presented that utilizes the down-temperature trace element exchange between cpx and opx. Unfortunately, due to the lack of diffusion data, only qualitative statements can be made. Nevertheless, with a more appropriate set of diffusion coefficients, the potential of this new geospeedometer is striking. Cooling rates can be calculated with very good precision. Especially, experimental calibration of diffusion of Sc and Y in opx is highly desirable. The individual temperature interval covered by each individual element will even allow to investigate variable cooling rates. Thus, orthopyroxenes are very good recorders of the cooling history in mantle rocks in a temperature interval previously “invisible” to standard methods.

3.5 SUMMARY

Major and trace elements were obtained from two very fresh spinel peridotites that were recovered from the ultraslow-spreading Gakkel Ridge. The aim of this study is to develop a

CHAPTER 3

new geospeedometer for mantle peridotites that utilizes the down-temperature trace element exchange between cpx and opx.

- Both samples are similar in major element composition and microtextures. While cpx is homogeneous on grain and thin section scale for major and trace elements, opx shows very pronounced core-rim zoning in all incompatible trace elements.
- Trace element zoning profiles in opx show the characteristic mushroom- or bell-shaped pattern typical for diffusive re-equilibration during cooling.
- Equilibrium temperatures were calculated for opx using the trace element geothermometer of Witt-Eickschen and O'Neill (2005). Temperatures for REE range between 1350°C and 760°C.
- Besides cpx, olivine has an important affect on opx composition during cooling. Trace element rim concentrations of opx in contact to olivine are always elevated relative to contacts to cpx. Partition coefficient data for the temperature-dependent exchange between all three minerals corroborates that olivine can induce significant change in opx composition during cooling. This complicates zoning profiles but more importantly will affect opx-cpx trace element geothermometers. Here, small, interstitial grains may record an artificial heating event.
- Straightforward numerical modelling of REE zoning patterns is in agreement with a diffusion process but cannot reproduce the zoning within reasonable boundary conditions.
- Calculations of closure temperature profiles using the formulation of Tirone and Ganguly (1999) suggest an extreme range in cooling rates as well but show the same systematic change in apparent cooling rate as trace element models.
- The recently determined enstatite REE diffusion coefficients cannot give reasonable results in our models and are deemed unsuitable for mantle orthopyroxene.
- Orthopyroxene is an excellent recorder of the thermal history of mantle peridotites in the high temperature range.

3.6 REFERENCES

- Anders, E. and Grevesse, N. (1989). Abundances of the elements - meteoritic and solar. *Geochimica Et Cosmochimica Acta* 53, 197-214.
- Behn, M. D., Boettcher, M. S. and Hirth, G. (2007). Thermal structure of oceanic transform faults. *Geology* 35, 307-310.
- Bertrand, P. and Mercier, J. C. (1985). The mutual solubility of coexisting ortho- and clinopyroxene: Toward an absolute geothermometer for the natural system? *Earth and Planetary Science Letters* 76, 109-122.
- Bonatti, E., Brunelli, D., Fabretti, P., Ligi, M., Portaro, R. A. and Seyler, M. (2001). Steady-state creation of crust-free lithosphere at cold spots in mid-ocean ridges. *Geology* 29, 979-982.
- Bonatti, E., Ligi, M., Brunelli, D., Cipriani, A., Fabretti, P., Ferrante, V., Gasperini, L. and Ottolini, L. (2003). Mantle thermal pulses below the Mid-Atlantic Ridge and temporal variations in the formation of oceanic lithosphere. *Nature* 423, 499-505.
- Brey, G. P. and Köhler, T. (1990). Geothermobarometry in 4-phase lherzolites 2: new thermobarometers, and practical assessment of existing thermobarometers. *Journal of Petrology* 31, 1353-1378.
- Chakraborty, S. (2006). Diffusion modeling as a tool for constraining timescales of evolution of metamorphic rocks. *Mineralogy and Petrology* 88, 7-27.
- Cherniak, D. J. (1998). Pb diffusion in clinopyroxene. *Chemical Geology* 150, 105-117.
- Cherniak, D. J. (2001). Pb diffusion in Cr diopside, augite, and enstatite, and consideration of the dependence of cation diffusion in pyroxene on oxygen fugacity. *Chemical Geology* 177, 381-397.
- Cherniak, D. J. and Liang, Y. (2007). Rare earth element diffusion in natural enstatite. *Geochimica Et Cosmochimica Acta*, doi 10.1016/j.gca.2006.1012.1001.
- Coogan, L. A., Kasemann, S. A. and Chakraborty, S. (2005). Rates of hydrothermal cooling of new oceanic upper crust derived from lithium-geospeedometry. *Earth and Planetary Science Letters* 240, 415-424.
- Crank, J. (1975). *The mathematics of diffusion*. Oxford: Clarendon Press, p.
- Demouchy, S., Jacobsen, S. D., Gaillard, F. and Stern, C. R. (2006). Rapid magma ascents recording by water diffusion profiles in mantle olivine. *Geology* 34, 429-432.
- Detrick, R. S., Buhl, P., Vera, E., Mutter, J., Orcutt, J., Madsen, J. and Brocher, T. (1987). Multichannel seismic imaging of a crustal magma chamber along the East Pacific Rise. *Nature* 326, 35-41.
- Dimanov, A., Jaoul, O. and Sautter, V. (1996). Calcium self-diffusion in natural diopside single crystals. *Geochimica Et Cosmochimica Acta* 60, 4095-4106.
- Dodson, M. H. (1973). Closure temperature in cooling geochronological and petrological systems. *Contributions to Mineralogy and Petrology* 40, 259-274.

CHAPTER 3

- Dodson, M. H. (1986). Closure profiles in cooling systems. *Materials Science Forum* 7, 145-154.
- Doin, M. P. and Fleitout, L. (1996). Thermal evolution of the oceanic lithosphere: an alternative view. *Earth and Planetary Science Letters* 142, 121-136.
- Droop, G. T. R. (1987). A general equation for estimating Fe³⁺ concentrations in ferromagnesian silicates and oxides from microprobe analyses, using stoichiometric criteria. *Mineralogical Magazine* 51, 431-435.
- Eggins, S. M., Rudnick, R. L. and McDonough, W. F. (1998). The composition of peridotites and their minerals: A laser- ablation ICP-MS study. *Earth and Planetary Science Letters* 154, 53-71.
- Fabries, J. (1979). Spinel-olivine geothermometry in peridotites from ultramafic complexes. *Contributions to Mineralogy and Petrology* 69, 329-336.
- Faryad, W. and Chakraborty, S. (2005). Duration of Eo-Alpine metamorphic events obtained from multicomponent diffusion modeling of garnet: A case study from the Eastern Alps. *Contributions to Mineralogy and Petrology* 250, 306-318.
- Ganguly, J. and Tazzoli, V. (1994). Fe²⁺-Mg interdiffusion in ortho-pyroxene - retrieval from the data on intracrystalline exchange-reaction. *American Mineralogist* 79, 930-937.
- Ganguly, J. and Tirone, M. (1999). Diffusion closure temperature and age of a mineral with arbitrary extent of diffusion: theoretical formulation and applications. *Earth and Planetary Science Letters* 170, 131-140.
- Garrido, C. J., Kelemen, P. B. and Hirth, G. (2001). Variation of cooling rate with depth in lower crust formed at an oceanic spreading ridge: Plagioclase crystal size distributions in gabbros from the Oman ophiolite. *Geochemistry Geophysics Geosystems* 2, doi:10.1029/2000GC000136.
- Ghose, I., Cannat, M. and Seyler, M. (1996). Transform fault effect on mantle melting in the MARK area (Mid- Atlantic Ridge south of the Kane transform). *Geology* 24, 1139-1142.
- Green, D. H. and Falloon, T. J. (1998). Pyrolite: a ringwood concept and its current expression. In: Jackson, I. (ed.) *The earth's mantle: composition, structure and evolution*. Cambridge: Cambridge University Press, 311-380.
- Green, D. H. and Ringwood, A. E. (1967). The genesis of basaltic magmas. *Contributions to Mineralogy and Petrology* 15, 103-190.
- Hellebrand, E., Snow, J. E., Hoppe, P. and Hofmann, A. W. (2002). Garnet-field melting and late-stage refertilization in 'residual' abyssal peridotites from the Central Indian Ridge. *Journal of Petrology* 43, 2305-2338.
- Hellebrand, E., Snow, J. E., Mostefaoui, S. and Hoppe, P. (2005). Trace element distribution between orthopyroxene and clinopyroxene in peridotites from the Gakkel Ridge: a SIMS and NanoSIMS study. *Contributions to Mineralogy and Petrology* 150, 486-504.
- Hervig, R. L. and Smith, J. V. (1982). Temperature-dependent distribution of Cr between olivine and pyroxenes in lherzolite xenoliths. *Contributions to Mineralogy and Petrology* 81, 184-189.

CHAPTER 3

- Hirschmann, M. M. (2000). Mantle solidus: Experimental constraints and the effects of peridotite composition. *Geochemistry Geophysics Geosystems* 1, doi:10.1029/2000GC000070.
- Hofmeister, A. M. (1999). Mantle values of thermal conductivity and the geotherm from phonon lifetimes. *Science* 283, 1699-1706.
- Honda, S. and Yuen, D. A. (2001). Interplay of thermal conductivity and thermal expansivity on the thermal structure of oceanic lithosphere. *Geophysical Research Letters* 28, 351-354.
- Jaupart, C. and Mareschal, J. C. (1999). The thermal structure and thickness of continental roots. *Lithos* 48, 93-114.
- Jiang, J. X. and Lasaga, A. C. (1990). The effect of postgrowth thermal events on growth-zoned garnet - Implications for metamorphic P-T history calculations. *Contributions to Mineralogy and Petrology* 105, 454-459.
- Jochum, K. P., Stoll, B., Herwig, K., Willbold, M., Hofmann, A. W., Amini, M., Aarburg, S., Abouchami, W., Hellebrand, E., Mocek, B., Raczek, I., Stracke, A., Alard, O., Bouman, C., Becker, S., Ducking, M., Bratz, H., Klemm, R., de Bruin, D., Canil, D., Cornell, D., de Hoog, C. J., Dalpe, C., Danyushevsky, L., Eisenhauer, A., Premo, W. R., Sun, W. D. D., Tiepolo, M., Vannucci, R., Vennemann, T., Wayne, D. and Woodhead, J. D. (2006). MPI-DING reference glasses for in situ microanalysis: New reference values for element concentrations and isotope ratios. *Geochemistry Geophysics Geosystems* 7, doi:10.1029/2005GC001060.
- Jokat, W., Ritzmann, O., Schmidt-Aursch, M. C., Drachev, S. S., Gauger, S. and Snow, J. E. (2003). Geophysical evidence for reduced melt production on the Arctic ultraslow Gakkel mid-ocean ridge. *Nature* 423, 962-965.
- Lasaga, A. C. (1983). Geospeedometry: An extension of geothermometry. In: Saxena, S. K. (ed.) *Kinetics and equilibrium in mineral reactions*. Advances in Physical Geochemistry 3. 81-114.
- Lasaga, A. C. and Jiang, J. X. (1995). Thermal history of rocks - P-T-T paths from geospeedometry, petrological data, and inverse-theory techniques. *American Journal of Science* 295, 697-741.
- Lee, C. T. A., Harbert, A. and Leeman, W. P. (2007). Extension of lattice strain theory to mineral/mineral rare-earth element partitioning: An approach for assessing disequilibrium and developing internally consistent partition coefficients between olivine, orthopyroxene, clinopyroxene and basaltic melt. *Geochimica Et Cosmochimica Acta* 71, 481-496.
- Li, J. P., Kornprobst, J., Vielzeuf, D. and Fabries, J. (1995). An improved experimental calibration of the olivine-spinel geothermometer. *Chinese Journal of Geochemistry* 14, 68-77.
- Liermann, H. P. and Ganguly, J. (1999). Thermodynamics and kinetics of Fe²⁺-Mg exchange between spinel and orthopyroxene: Experimental determinations and applications to cooling rates. *Meteoritics & Planetary Science* 34, A75-A75.

CHAPTER 3

- Liermann, H. P. and Ganguly, J. (2002). Diffusion kinetics of Fe²⁺ and Mg in aluminous spinel: Experimental determination and applications. *Geochimica Et Cosmochimica Acta* 66, 2903-2913.
- Liermann, H. P. and Ganguly, J. (2003). Fe²⁺-Mg fractionation between orthopyroxene and spinel: experimental calibration in the system FeO-MgO-Al₂O₃-Cr₂O₃-SiO₂, and applications. *Contributions to Mineralogy and Petrology* 145, 217-227.
- Ligi, M., Bonatti, E., Cipriani, A. and Ottolini, L. (2005). Water-rich basalts at mid-ocean ridge cold spots. *Nature* 434, 66-69.
- McKay, G. A. (1986). Crystal liquid partitioning of REE in basaltic systems - extreme fractionation of REE in olivine. *Geochimica Et Cosmochimica Acta* 50, 69-79.
- McKenzie, D., Jackson, J. and Priestley, K. (2005). Thermal structure of oceanic and continental lithosphere. *Earth and Planetary Science Letters* 233, 337-349.
- Morgan, J. P. and Chen, Y. J. (1993). Dependence of ridge-axis morphology on magma supply and spreading rate. *Nature* 364, 706-708.
- Nimis, P. and Trommsdorff, V. (2001). Comment on 'New constraints on the P-T evolution of the Alpe Arami garnet peridotite body (Central Alps, Switzerland)' by Paquin & Altherr (2001). *Journal of Petrology* 42, 1773-1779.
- Niu, Y. L. and Batiza, R. (1994). Magmatic processes at a slow-spreading ridge segment - 26°S Mid-Atlantic Ridge. *Journal of Geophysical Research-Solid Earth and Planets* 99, 19719-19740.
- Ozawa, K. (1983). Evaluation of olivine-spinel geothermometry as an indicator of thermal history for peridotites. *Contributions to Mineralogy and Petrology* 82, 52-65.
- Ozawa, K. (1984). Olivine-spinel geospeedometry - analysis of diffusion-controlled Mg-Fe²⁺ exchange. *Geochimica Et Cosmochimica Acta* 48, 2597-2611.
- Paquin, J. and Altherr, R. (2001). New constraints on the P-T evolution of the Alpe Arami garnet peridotite body (Central Alps, Switzerland). *Journal of Petrology* 42, 1119-1140.
- Parsons, B. and Sclater, J. G. (1977). An analysis of the variation of ocean floor bathymetry and heat flow with age. *Journal of Geophysical Research-Solid Earth and Planets* 82, 803-827.
- Phipps Morgan, J. and Forsyth, D. W. (1988). Three-dimensional flow and temperature perturbations due to a transform offset: Effects on oceanic crust and upper mantle structure. *Journal of Geophysical Research-Solid Earth and Planets* 93, 2955-2966.
- Rampone, E., Bottazzi, P. and Ottolini, L. (1991). Complementary Ti and Zr anomalies in orthopyroxene and clinopyroxene from mantle peridotites. *Nature* 354, 518-520.
- Redfern, S. A. T., Henderson, C. M. B., Wood, B. J., Harrison, R. J. and Knight, K. S. (1996). Determination of cooling rates from metal-cation ordering. *Nature* 381, 407-409.
- Ringwood, A. E. (1966). Chemical evolution of terrestrial planets. *Geochimica Et Cosmochimica Acta* 30, 41-104.
- Rudnick, R. L. and Nyblade, A. A. (1999). The thickness and heat production of the Archean lithosphere: Constraints from xenolith thermobarometry and surface heat flow. In: Fei,

CHAPTER 3

- Y. W., Bertka, C. M. & Mysen, B. O. (eds.) *Mantle petrology: field observations and high pressure experimentation: A tribute to Francis R. (Joe) Boyd*. 6. London: Special Publications of the Geochemical Society, 3-12.
- Schwandt, C. S., Randall, T. C. and Westrich, H. R. (1998). Magnesium self diffusion in orthoenstatite. *Contributions to Mineralogy and Petrology* 130, 390-396.
- Seitz, H. M., Altherr, R. and Ludwig, T. (1999). Partitioning of transition elements between orthopyroxene and clinopyroxene in peridotitic and websteritic xenoliths: New empirical geothermometers. *Geochimica Et Cosmochimica Acta* 63, 3967-3982.
- Seyler, M., Lorand, J. P., Dick, H. J. B. and Drouin, M. (2007). Pervasive melt percolation reactions in ultra-depleted refractory harzburgites at the Mid-Atlantic Ridge, 15° 20' N: ODP Hole 1274A. *Contributions to Mineralogy and Petrology* 153, 303-319.
- Shen, Y. and Forsyth, D. W. (1992). The effects of temperature- and pressure-dependent viscosity on three-dimensional passive flow of the mantle beneath a ridge-transform system. *Journal of Geophysical Research-Solid Earth and Planets* 97, 19717-19728.
- Shen, Y. and Forsyth, D. W. (1995). Geochemical constraints on initial and final depths of melting beneath mid-ocean ridges. *Journal of Geophysical Research-Solid Earth and Planets* 100, 2211-2237.
- Sinha, M. C., Navin, D. A., MacGregor, L. M., Constable, S., Peirce, C., White, A., Heinson, G. and Inglis, M. A. (1997). Evidence for accumulated melt beneath the slow-spreading Mid-Atlantic Ridge. *Philosophical Transactions of the Royal Society of London Series a-Mathematical Physical and Engineering Sciences* 355, 233-253.
- Sleep, N. H. (1975). Formation of oceanic crust: Some thermal constraints. *Journal of Geophysical Research-Solid Earth and Planets* 80, 4037-4042.
- Sneeringer, M., Hart, S. R. and Shimizu, N. (1984). Strontium and samarium diffusion in diopside. *Geochimica Et Cosmochimica Acta* 48, 1589-1608.
- Stein, C. A. and Stein, S. (1992). A model for the global variation in oceanic depth and heat flow with lithospheric age. *Nature* 359, 123-129.
- Stimpfl, M., Ganguly, J. and Molin, G. (2005). Kinetics of Fe²⁺-Mg order-disorder in orthopyroxene: experimental studies and applications to cooling rates of rocks. *Contributions to Mineralogy and Petrology* 150, 319-334.
- Toomey, D. R., Solomon, S. C. and Purdy, G. M. (1988). Microearthquakes beneath median valley of Mid-Atlantic Ridge near 23°N: Tomography and tectonics. *Journal of Geophysical Research-Solid Earth and Planets* 93, 9093-9112.
- Treiman, A. H. (1996). The perils of partition: Difficulties in retrieving magma compositions from chemically equilibrated basaltic meteorites. *Geochimica Et Cosmochimica Acta* 60, 147-155.
- Turcotte, D. L. and Schubert, G. (2002). *Geodynamics*. Cambridge, New York, Melbourne: Cambridge University Press, p. 456.
- van Orman, J. A., Grove, T. L. and Shimizu, N. (1998). Uranium and thorium diffusion in diopside. *Earth and Planetary Science Letters* 160, 505-519.

CHAPTER 3

- van Orman, J. A., Grove, T. L. and Shimizu, N. (2001). Rare earth element diffusion in diopside: influence of temperature, pressure, and ionic radius, and an elastic model for diffusion in silicates. *Contributions to Mineralogy and Petrology* 141, 687-703.
- von der Handt, A., Hellebrand, E. and Snow, J. E. (2005). Contrasting trace element signatures in abyssal peridotites: High temperature refertilization versus cooling-controlled trace element zoning in orthopyroxene. *Eos Trans. AGU* 86, T41-E-1353.
- Watson, E. B. and Baxter, E. F. (2007). Diffusion in solid-Earth systems. *Earth and Planetary Science Letters* 253, 307-327.
- Wells, P. R. A. (1977). Pyroxene thermometry in simple and complex systems. *Contributions to Mineralogy and Petrology* 62, 129-139.
- Witt-Eickschen, G. and O'Neill, H. S. (2005). The effect of temperature on the equilibrium distribution of trace elements between clinopyroxene, orthopyroxene, olivine and spinel in upper mantle peridotite. *Chemical Geology* 221, 65-101.
- Witt-Eickschen, G. and Seck, H. A. (1991). Solubility of Ca and Al in orthopyroxene from spinel peridotite - an improved version of an empirical geothermometer. *Contributions to Mineralogy and Petrology* 106, 431-439.
- Zanetti, A., Tiepolo, M., Oberti, R. and Vannucci, R. (2004). Trace-element partitioning in olivine: modelling of a complete data set from a synthetic hydrous basanite melt. *Lithos* 75, 39-54.

CHAPTER 3

Table 3-1d: Major element composition of spinels in [wt%]

Sample	238-25A	238-25B	238-62A	238-62B
n	108	131	131	67
SiO ₂	0.04 ± 0.01	0.04 ± 0.01	0.04 ± 0.01	0.04 ± 0.01
TiO ₂	0.08 ± 0.02	0.08 ± 0.02	0.07 ± 0.02	0.09 ± 0.03
Cr ₂ O ₃	20.2 ± 1.8	19.5 ± 1.8	18.9 ± 1.7	20.7 ± 2.2
Al ₂ O ₃	47.1 ± 2.0	48.1 ± 1.8	48.8 ± 1.8	46.1 ± 2.9
V ₂ O ₃	0.12 ± 0.02	0.11 ± 0.02	0.10 ± 0.02	0.13 ± 0.03
FeO	13.7 ± 1.4	13.1 ± 0.6	13.2 ± 0.9	14.7 ± 2.3
MgO	17.7 ± 0.6	18.0 ± 0.4	18.1 ± 0.5	17.5 ± 0.9
MnO	0.12 ± 0.02	0.11 ± 0.02	0.11 ± 0.02	0.12 ± 0.02
CaO	0.01 ± 0.02	0.01 ± 0.02	0.01 ± 0.02	0.02 ± 0.02
CoO	0.06 ± 0.01	0.06 ± 0.01	0.07 ± 0.01	0.06 ± 0.01
NiO	0.25 ± 0.03	0.25 ± 0.03	0.25 ± 0.03	0.24 ± 0.03
ZnO	0.22 ± 0.06	0.22 ± 0.05	0.23 ± 0.04	0.25 ± 0.06
Total	99.7 ± 0.3	99.6 ± 0.2	100.0 ± 0.2	100.0 ± 0.3
Cr-number	0.224 ± 0.023	0.214 ± 0.021	0.207 ± 0.021	0.232 ± 0.030
Mg-number	0.697 ± 0.027	0.709 ± 0.014	0.710 ± 0.019	0.680 ± 0.043
FeO*	12.10 ± 0.69215	11.82 ± 0.49167	11.79 ± 0.53361	12.36 ± 0.9214
Fe ₂ O ₃ *	1.81 ± 0.86707	1.44 ± 0.28521	1.58 ± 0.49106	2.66 ± 1.6298

n: number of analyses ±: one standard deviation

*: FeO and Fe₂O₃ calculated after Droop (1987)

Table 3-2: Temperatures from different geothermometers in [°C]

Geothermometers	238-25A	238-25B	238-62A	238-62B	avg
T _{ol-sp} ^a	702	709	702	700	703 ± 4
T _{ol-sp} ^b	815	823	814	812	816 ± 5
T _{Na_cpx/opx} ^c	897	926	901	935	915 ± 18
T _{BKN} ^c	972	945	924	899	935 ± 31
T _{opx-sp} ^d	983	998	994	978	988 ± 9
T _{Ca_opx} EPMA avg ^e	971 ± 43	990 ± 52	981 ± 64	1000 ± 59	985 ± 12
T _{Ca_opx} SIMS avg ^{c,f}					1030 ± 144
avg ^e	1014 ± 60	997 ± 57	1019 ± 74	1026 ± 70	1014 ± 12
T _{pyroxenes} avg	975 ± 6	977 ± 28	966 ± 37	959 ± 53	

a: Fabries (1979)

b: Li et al. (1995)

c: Brey and Köhler (1990)

d: Liermann and Ganguly (2003)

e: Witt-Eickschen and Seck (1991)

f: no sample average because of non-equal number of analyses per sample

CHAPTER 3

Table 3-3a: Average trace element composition of clinopyroxenes in [$\mu\text{g/g}$] measured by SIMS

Sample	238-25A	238-25B	238-62A	238-62B
n	12	4	4	4
Ca	146357 \pm 6879	140889 \pm 6354	133398 \pm 7571	149231 \pm 4431
Na	6403 \pm 655	5775 \pm 497	5003 \pm 231	5829 \pm 221
Sc	54.0 \pm 5.6	51.8 \pm 6.3	52.2 \pm 5.7	53.3 \pm 2.6
Ti	1526 \pm 132	1454 \pm 122	1418 \pm 93	1539 \pm 114
V	251 \pm 16	234 \pm 12	230 \pm 12	247 \pm 10
Cr	7846 \pm 385	7903 \pm 465	7743 \pm 387	8141 \pm 122
Sr	28.9 \pm 1.0	35.3 \pm 1.3	27.4 \pm 1.8	36.5 \pm 3.9
Y	11.1 \pm 0.9	10.6 \pm 0.4	10.6 \pm 0.5	11.3 \pm 0.4
Zr	11.4 \pm 1.0	10.9 \pm 0.4	9.9 \pm 0.5	12.8 \pm 0.9
La	1.04 \pm 0.09	1.26 \pm 0.17	1.02 \pm 0.11	1.45 \pm 0.18
Ce	2.80 \pm 0.21	3.42 \pm 0.34	2.74 \pm 0.09	3.61 \pm 0.30
Pr	0.43 \pm 0.02	0.50 \pm 0.04	0.44 \pm 0.00	0.51 \pm 0.04
Nd	2.02 \pm 0.14	2.38 \pm 0.10	2.00 \pm 0.16	2.47 \pm 0.22
Sm	0.85 \pm 0.09	0.84 \pm 0.04	0.79 \pm 0.04	0.86 \pm 0.06
Eu	0.33 \pm 0.02	0.41 \pm 0.03	0.38 \pm 0.01	0.34 \pm 0.05
Gd	1.34 \pm 0.10	1.23 \pm 0.01	1.23 \pm 0.19	1.47 \pm 0.19
Dy	1.53 \pm 0.18	1.83 \pm 0.15	1.95 \pm 0.22	1.66 \pm 0.13
Er	1.36 \pm 0.11	1.29 \pm 0.09	1.13 \pm 0.15	1.38 \pm 0.05
Yb	1.14 \pm 0.14	1.02 \pm 0.17	1.03 \pm 0.23	1.15 \pm 0.05

n: number of analyses \pm : one standard deviation

Table 3-3b: Average trace element composition of clinopyroxenes in [$\mu\text{g/g}$] measured by LA-ICP-MS

Sample	238-25A	238-25B	238-62B
n	5	4	5
Sc	64 \pm 3	67 \pm 7	61 \pm 3
Ti	1601 \pm 18	1478 \pm 40	1548 \pm 40
Sr	31.9 \pm 3.0	32.7 \pm 3.4	42.2 \pm 6.7
Y	11.5 \pm 0.1	11.9 \pm 0.6	11.7 \pm 0.3
Zr	11.9 \pm 0.5	11.9 \pm 0.5	12.2 \pm 0.9
La	1.19 \pm 0.10	1.20 \pm 0.18	1.63 \pm 0.27
Ce	3.18 \pm 0.35	3.13 \pm 0.38	4.12 \pm 0.56
Pr	0.47 \pm 0.05	0.46 \pm 0.06	0.59 \pm 0.07
Nd	2.31 \pm 0.26	2.32 \pm 0.28	2.83 \pm 0.31
Sm	0.87 \pm 0.09	0.87 \pm 0.10	1.00 \pm 0.06
Eu	0.34 \pm 0.04	0.34 \pm 0.03	0.37 \pm 0.02
Gd	1.32 \pm 0.10	1.36 \pm 0.11	1.42 \pm 0.05
Tb	0.26 \pm 0.01	0.27 \pm 0.02	0.27 \pm 0.01
Dy	1.95 \pm 0.07	2.02 \pm 0.15	2.01 \pm 0.04
Ho	0.44 \pm 0.01	0.47 \pm 0.03	0.44 \pm 0.01
Er	1.31 \pm 0.02	1.40 \pm 0.06	1.32 \pm 0.03
Tm	0.19 \pm 0.01	0.20 \pm 0.01	0.19 \pm 0.01
Yb	1.24 \pm 0.04	1.34 \pm 0.05	1.26 \pm 0.03
Lu	0.17 \pm 0.01	0.19 \pm 0.01	0.18 \pm 0.00

n: number of analyses \pm : one standard deviation

Table 3-4: Trace element composition of orthopyroxene in [mg/g]

Analysis	25A_07-opx-2-1	25A_07-opx-1-1	25A_07-opx-1-2	25A_12-opx-2-1	25A_12-opx-1-1	25A_12-opx-1-2	25A_12-opx-1-3
Ca	14919 ± 432	19987 ± 478	17148 ± 267	22823 ± 2131	20858 ± 433	17686 ± 366	16595 ± 371
Na	193 ± 6	511 ± 19	350 ± 27	569 ± 107	601 ± 64	394 ± 13	286 ± 9
Sc	27 ± 0.5	27 ± 0.4	28 ± 0.4	28 ± 0.7	27 ± 0.4	29 ± 0.3	29 ± 0.3
Ti	444 ± 7	521 ± 7	505 ± 13	518 ± 33	508 ± 14	520 ± 9	548 ± 13
V	122 ± 2	131 ± 2	133 ± 2	130 ± 3	131 ± 3	137 ± 2	143 ± 3
Cr	3220 ± 22	4699 ± 56	5015 ± 66	4975 ± 98	4826 ± 69	4240 ± 64	4053 ± 62
Sr	b.d. ± NaN	0.31 ± 0.016	0.20 ± 0.015	b.d. ± NaN	0.54 ± 0.042	0.28 ± 0.015	0.20 ± 0.018
Y	0.79 ± 0.039	1.22 ± 0.041	1.15 ± 0.068	1.49 ± 0.152	1.39 ± 0.074	1.08 ± 0.064	0.95 ± 0.037
Zr	0.71 ± 0.030	1.39 ± 0.044	1.36 ± 0.054	1.76 ± 0.204	1.50 ± 0.082	1.24 ± 0.042	0.92 ± 0.050
La	b.d. ± 0.000	0.0100 ± 0.003	0.003 ± 0.001	0.023 ± 0.004	0.015 ± 0.002	0.004 ± 0.002	0.005 ± 0.002
Ce	0.004 ± 0.002	0.0242 ± 0.004	0.020 ± 0.006	0.080 ± 0.015	0.050 ± 0.006	0.025 ± 0.004	0.020 ± 0.004
Nd	b.d. ± NaN	0.0392 ± 0.010	0.010 ± 0.005	0.066 ± 0.017	0.071 ± 0.013	0.031 ± 0.008	b.d. ± NaN
Sm	b.d. ± NaN	0.0276 ± 0.008	0.024 ± 0.011	b.d. ± NaN	0.032 ± 0.009	0.014 ± 0.008	0.010 ± 0.005
Eu	0.004 ± 0.002	0.011 ± 0.004	0.011 ± 0.004	0.023 ± 0.005	0.015 ± 0.003	0.004 ± 0.002	0.006 ± 0.002
Gd	0.03 ± 0.010	0.06 ± 0.014	0.05 ± 0.012	0.14 ± 0.050	0.09 ± 0.025	0.05 ± 0.012	0.03 ± 0.011
Dy	0.06 ± 0.013	0.14 ± 0.015	0.12 ± 0.016	0.18 ± 0.036	0.14 ± 0.015	0.11 ± 0.013	0.09 ± 0.012
Er	0.13 ± 0.025	0.19 ± 0.021	0.18 ± 0.020	0.20 ± 0.021	0.19 ± 0.021	0.18 ± 0.020	0.17 ± 0.026
Yb	0.22 ± 0.025	0.26 ± 0.025	0.26 ± 0.030	0.25 ± 0.024	0.25 ± 0.042	0.28 ± 0.034	0.32 ± 0.029
CaO ^a	0.55	1.39	0.92	1.87	1.54	1.01	0.83

b.d. = below detection limit a = recalculated from correlation between EPMA and SIMS analyses

Table 3-4 (continued): Trace element composition of orthopyroxene in [mg/g]

Analysis	25A_12-opx-1-4	25A_12-opx-1-5	25A_12-opx-1-6	25A_12-opx-1-7	25A_12-opx-1-8	25A_12-opx-1-9	25A_12-opx-1-10
Ca	17216 ± 514	19758 ± 587	19219 ± 345	19224 ± 498	17904 ± 283	19932 ± 245	19546 ± 617
Na	254 ± 7	531 ± 36	512 ± 34	466 ± 21	381 ± 22	496 ± 21	462 ± 44
Sc	26 ± 0.5	27 ± 0.5	27 ± 0.4	27 ± 0.4	27 ± 0.4	28 ± 0.4	28 ± 0.4
Ti	473 ± 5	542 ± 12	519 ± 13	536 ± 8	516 ± 11	523 ± 12	535 ± 24
V	117 ± 2	134 ± 3	135 ± 2	135 ± 3	132 ± 3	133 ± 3	136 ± 4
Cr	3623 ± 37	4955 ± 82	4802 ± 69	4602 ± 57	4623 ± 71	4631 ± 75	4831 ± 84
Sr	0.24 ± 0.014	0.48 ± 0.044	0.43 ± 0.019	0.40 ± 0.031	0.33 ± 0.027	0.45 ± 0.034	0.40 ± 0.066
Y	0.92 ± 0.035	1.26 ± 0.043	1.18 ± 0.052	1.22 ± 0.050	1.10 ± 0.039	1.24 ± 0.066	1.22 ± 0.106
Zr	0.86 ± 0.033	1.57 ± 0.085	1.37 ± 0.095	1.34 ± 0.043	1.24 ± 0.053	1.42 ± 0.065	1.51 ± 0.174
La	0.006 ± 0.002	0.014 ± 0.003	0.010 ± 0.002	0.011 ± 0.002	0.009 ± 0.002	0.009 ± 0.002	0.013 ± 0.002
Ce	0.020 ± 0.004	0.037 ± 0.005	0.034 ± 0.005	0.034 ± 0.006	0.018 ± 0.004	0.038 ± 0.009	0.025 ± 0.004
Nd	0.018 ± 0.006	0.042 ± 0.010	0.036 ± 0.011	0.031 ± 0.009	0.016 ± 0.006	0.035 ± 0.009	0.049 ± 0.015
Sm	0.017 ± 0.007	0.008 ± 0.004	0.018 ± 0.007	0.021 ± 0.008	0.015 ± 0.006	0.026 ± 0.011	0.032 ± 0.009
Eu	0.004 ± 0.002	0.011 ± 0.003	0.010 ± 0.003	0.015 ± 0.004	0.010 ± 0.004	0.007 ± 0.002	0.012 ± 0.005
Gd	0.05 ± 0.013	0.07 ± 0.015	0.03 ± 0.010	0.05 ± 0.013	0.04 ± 0.019	0.06 ± 0.014	0.07 ± 0.015
Dy	0.07 ± 0.010	0.12 ± 0.018	0.14 ± 0.015	0.13 ± 0.015	0.12 ± 0.020	0.11 ± 0.014	0.15 ± 0.030
Er	0.12 ± 0.017	0.22 ± 0.023	0.18 ± 0.028	0.18 ± 0.027	0.16 ± 0.038	0.18 ± 0.021	0.20 ± 0.024
Yb	0.18 ± 0.030	0.25 ± 0.025	0.28 ± 0.032	0.25 ± 0.026	0.23 ± 0.026	0.28 ± 0.044	0.30 ± 0.027
CaO ^a	0.93	1.35	1.26	1.27	1.04	1.38	1.32

b.d. = below detection limit a = recalculated from correlation between EPMA and SIMS analyses

Table 3-4 (continued): Trace element composition of orthopyroxene in [mg/g]

Analysis	25A_12-opx-1-11	25A_01-opx-2-1	25A_02-opx-1-1	25A_02-opx-1-2	25A_02-opx-1-3	25A_02-opx-1-4	25A_02-opx-1-5
Ca	19215 ± 273	17318 ± 396	15849 ± 509	18118 ± 373	19093 ± 249	20163 ± 278	17975 ± 344
Na	516 ± 28	333 ± 13	253 ± 2	402 ± 21	443 ± 19	519 ± 22	415 ± 13
Sc	27 ± 0.3	30 ± 0.5	25 ± 0.5	28 ± 0.4	28 ± 0.2	28 ± 0.2	28 ± 0.4
Ti	512 ± 15	535 ± 9	450 ± 5	547 ± 28	541 ± 14	565 ± 23	548 ± 15
V	134 ± 3	138 ± 2	126 ± 2	142 ± 6	135 ± 3	137 ± 5	138 ± 3
Cr	4882 ± 58	4059 ± 58	4847 ± 37	4936 ± 107	4663 ± 82	4811 ± 104	4897 ± 79
Sr	0.39 ± 0.036	0.21 ± 0.013	0.17 ± 0.023	0.29 ± 0.019	0.38 ± 0.021	0.42 ± 0.020	0.36 ± 0.017
Y	1.23 ± 0.041	1.16 ± 0.052	0.78 ± 0.032	1.22 ± 0.063	1.31 ± 0.077	1.34 ± 0.043	1.21 ± 0.066
Zr	1.42 ± 0.095	1.16 ± 0.040	0.82 ± 0.032	1.52 ± 0.148	1.50 ± 0.079	1.55 ± 0.115	1.42 ± 0.072
La	0.010 ± 0.002	0.004 ± 0.001	0.003 ± 0.001	0.007 ± 0.002	0.012 ± 0.002	0.012 ± 0.002	0.011 ± 0.002
Ce	0.034 ± 0.005	0.010 ± 0.003	0.008 ± 0.002	0.027 ± 0.005	0.040 ± 0.006	0.050 ± 0.009	0.028 ± 0.005
Nd	0.047 ± 0.011	b.d. ± NaN	0.013 ± 0.005	0.036 ± 0.009	0.033 ± 0.009	0.047 ± 0.012	0.025 ± 0.010
Sm	0.028 ± 0.011	0.015 ± 0.006	b.d. ± NaN	0.009 ± 0.005	0.023 ± 0.009	0.046 ± 0.011	b.d. ± NaN
Eu	0.015 ± 0.004	0.007 ± 0.002	0.005 ± 0.004	0.015 ± 0.004	0.017 ± 0.004	0.019 ± 0.005	0.009 ± 0.003
Gd	0.07 ± 0.015	0.06 ± 0.014	b.d. ± NaN	0.05 ± 0.012	0.06 ± 0.013	0.07 ± 0.017	0.07 ± 0.015
Dy	0.14 ± 0.015	0.08 ± 0.017	0.09 ± 0.012	0.13 ± 0.024	0.15 ± 0.016	0.12 ± 0.020	0.12 ± 0.014
Er	0.20 ± 0.026	0.17 ± 0.021	0.12 ± 0.018	0.21 ± 0.023	0.20 ± 0.030	0.19 ± 0.021	0.19 ± 0.021
Yb	0.26 ± 0.040	0.29 ± 0.027	0.21 ± 0.035	0.22 ± 0.027	0.22 ± 0.027	0.20 ± 0.031	0.26 ± 0.046
CaO ^a	1.26	0.95	0.70	1.08	1.24	1.42	1.06

b.d. = below detection limit a = recalculated from correlation between EPMA and SIMS analyses

Table 3-4 (continued): Trace element composition of orthopyroxene in [mg/g]

Analysis	25A_02-opx-1-6	25A_02-opx-1-7	25A_02-opx-1-8	25A_02-opx-1-31	25A_02-opx-1-32	25A_02-opx-1-33	25A_02-opx-1-34
Ca	18463 ± 187	20144 ± 230	16879 ± 311	20369 ± 417	20041 ± 431	18178 ± 416	17747 ± 411
Na	350 ± 18	524 ± 22	338 ± 11	619 ± 21	549 ± 13	444 ± 17	392 ± 10
Sc	29 ± 0.2	27 ± 0.3	25 ± 0.4	27 ± 0.4	27 ± 0.4	26 ± 0.3	27 ± 0.4
Ti	540 ± 17	534 ± 11	437 ± 10	548 ± 9	563 ± 10	530 ± 13	535 ± 9
V	140 ± 4	135 ± 2	109 ± 3	137 ± 3	142 ± 3	140 ± 2	142 ± 2
Cr	4778 ± 78	4801 ± 73	4072 ± 73	4804 ± 62	4752 ± 52	5096 ± 54	4215 ± 58
Sr	0.31 ± 0.025	0.45 ± 0.021	0.26 ± 0.014	0.66 ± 0.033	0.51 ± 0.020	0.40 ± 0.022	0.56 ± 0.039
Y	1.22 ± 0.073	1.25 ± 0.047	0.86 ± 0.040	1.25 ± 0.040	1.29 ± 0.068	1.12 ± 0.037	1.12 ± 0.040
Zr	1.48 ± 0.097	1.46 ± 0.047	0.87 ± 0.034	1.57 ± 0.066	1.51 ± 0.044	1.25 ± 0.039	1.20 ± 0.055
La	0.014 ± 0.002	0.012 ± 0.002	0.009 ± 0.002	0.015 ± 0.003	0.012 ± 0.002	0.006 ± 0.002	0.009 ± 0.003
Ce	0.031 ± 0.005	0.038 ± 0.005	0.021 ± 0.005	0.037 ± 0.005	0.033 ± 0.005	0.031 ± 0.005	0.040 ± 0.005
Nd	0.034 ± 0.009	0.032 ± 0.009	0.020 ± 0.006	0.035 ± 0.009	0.032 ± 0.010	0.024 ± 0.009	0.033 ± 0.009
Sm	0.025 ± 0.010	0.030 ± 0.011	0.017 ± 0.006	0.027 ± 0.009	0.019 ± 0.010	0.024 ± 0.009	0.009 ± 0.005
Eu	0.008 ± 0.004	0.013 ± 0.004	0.005 ± 0.002	0.012 ± 0.003	0.013 ± 0.005	0.009 ± 0.003	0.009 ± 0.003
Gd	0.06 ± 0.014	0.09 ± 0.017	0.03 ± 0.009	0.08 ± 0.016	0.07 ± 0.013	0.04 ± 0.011	0.05 ± 0.011
Dy	0.14 ± 0.015	0.13 ± 0.015	0.09 ± 0.014	0.15 ± 0.017	0.17 ± 0.029	0.18 ± 0.018	0.12 ± 0.015
Er	0.16 ± 0.019	0.19 ± 0.031	0.12 ± 0.019	0.20 ± 0.021	0.17 ± 0.019	0.19 ± 0.020	0.16 ± 0.024
Yb	0.29 ± 0.027	0.21 ± 0.023	0.17 ± 0.019	0.32 ± 0.033	0.28 ± 0.029	0.29 ± 0.033	0.30 ± 0.032
CaO ^a	1.14	1.42	0.87	1.46	1.40	1.09	1.02

b.d. = below detection limit a = recalculated from correlation between EPMA and SIMS analyses

Table 3-4 (continued): Trace element composition of orthopyroxene in [mg/g]

Analysis	25A_02-opx-1-35	25A_02-opx-1-36	25A_02-opx-1-37	25A_02-opx-1-38	25A_02-opx-1-39	25A_02-opx-1-41	25A_02-opx-1-42
Ca	19196 ± 448	15757 ± 513	17644 ± 497	20627 ± 477	18558 ± 457	18713 ± 455	19955 ± 407
Na	450 ± 17	245 ± 6	346 ± 5	650 ± 16	497 ± 19	425 ± 12	575 ± 22
Sc	28 ± 0.5	24 ± 0.5	29 ± 0.4	25 ± 0.3	25 ± 0.4	25 ± 0.4	27 ± 0.4
Ti	531 ± 9	427 ± 7	551 ± 10	522 ± 11	502 ± 10	508 ± 7	584 ± 14
V	143 ± 2	114 ± 2	148 ± 2	131 ± 2	129 ± 2	134 ± 2	145 ± 3
Cr	4933 ± 52	4016 ± 39	4806 ± 53	4636 ± 64	4629 ± 50	4512 ± 60	4840 ± 61
Sr	0.41 ± 0.018	0.33 ± 0.020	0.42 ± 0.035	0.72 ± 0.037	0.43 ± 0.032	0.53 ± 0.055	0.52 ± 0.035
Y	1.29 ± 0.040	0.77 ± 0.031	1.19 ± 0.038	1.27 ± 0.055	1.09 ± 0.046	1.06 ± 0.036	1.32 ± 0.062
Zr	1.46 ± 0.057	0.76 ± 0.039	1.38 ± 0.052	1.37 ± 0.056	1.22 ± 0.054	1.27 ± 0.056	1.63 ± 0.063
La	0.010 ± 0.002	0.004 ± 0.001	0.009 ± 0.002	0.017 ± 0.004	0.007 ± 0.002	0.008 ± 0.002	0.010 ± 0.002
Ce	0.032 ± 0.005	0.010 ± 0.003	0.018 ± 0.004	0.044 ± 0.006	0.026 ± 0.005	0.026 ± 0.005	0.046 ± 0.006
Nd	0.033 ± 0.011	0.015 ± 0.006	0.013 ± 0.005	0.051 ± 0.012	0.021 ± 0.007	0.013 ± 0.006	0.050 ± 0.016
Sm	0.030 ± 0.010	b.d. ± NaN	0.009 ± 0.006	0.023 ± 0.012	0.025 ± 0.011	0.012 ± 0.005	0.028 ± 0.009
Eu	0.015 ± 0.004	b.d. ± NaN	0.011 ± 0.004	0.021 ± 0.004	0.010 ± 0.003	0.010 ± 0.003	0.010 ± 0.003
Gd	0.08 ± 0.014	0.02 ± 0.006	0.04 ± 0.015	0.06 ± 0.017	b.d. ± NaN	0.05 ± 0.014	0.09 ± 0.016
Dy	0.14 ± 0.016	0.06 ± 0.013	0.16 ± 0.017	0.18 ± 0.019	0.16 ± 0.017	0.12 ± 0.015	0.20 ± 0.026
Er	0.21 ± 0.023	0.12 ± 0.022	0.17 ± 0.031	0.22 ± 0.022	0.19 ± 0.020	0.14 ± 0.017	0.18 ± 0.020
Yb	0.34 ± 0.027	0.22 ± 0.032	0.34 ± 0.038	0.28 ± 0.034	0.26 ± 0.025	0.26 ± 0.032	0.28 ± 0.026
CaO ^a	1.26	0.69	1.00	1.50	1.15	1.18	1.39

b.d. = below detection limit a = recalculated from correlation between EPMA and SIMS analyses

Table 3-4 (continued): Trace element composition of orthopyroxene in [mg/g]

Analysis	25A_02-opx-1-43	25A_02-opx-1-44	25A_02-opx-1-45	25A_02-opx-1-46	25A_02-opx-1-47	25A_02-opx-1-48	25A_02-opx-1-49
Ca	15503 ± 746	17488 ± 489	15222 ± 461	16747 ± 501	18610 ± 386	16326 ± 454	16859 ± 426
Na	304 ± 7	332 ± 9	228 ± 8	336 ± 8	429 ± 17	290 ± 7	348 ± 13
Sc	21 ± 0.6	29 ± 0.4	22 ± 0.5	24 ± 0.4	26 ± 0.5	26 ± 0.4	27 ± 0.5
Ti	381 ± 5	578 ± 10	375 ± 5	482 ± 11	480 ± 8	442 ± 5	532 ± 11
V	97 ± 1	155 ± 3	106 ± 1	125 ± 3	123 ± 2	123 ± 1	138 ± 3
Cr	3892 ± 28	5377 ± 74	4335 ± 17	4190 ± 60	3864 ± 46	4329 ± 23	3907 ± 61
Sr	0.26 ± 0.033	0.44 ± 0.019	0.21 ± 0.014	0.27 ± 0.028	0.39 ± 0.018	0.24 ± 0.022	0.57 ± 0.055
Y	0.64 ± 0.029	1.18 ± 0.039	0.72 ± 0.032	0.86 ± 0.033	0.99 ± 0.036	0.89 ± 0.036	0.97 ± 0.036
Zr	0.58 ± 0.027	1.59 ± 0.053	0.50 ± 0.033	0.90 ± 0.057	1.00 ± 0.046	0.90 ± 0.037	1.12 ± 0.069
La	0.004 ± 0.001	0.008 ± 0.002	b.d. ± NaN	0.003 ± 0.001	0.011 ± 0.002	0.003 ± 0.001	0.005 ± 0.001
Ce	0.012 ± 0.003	0.031 ± 0.006	0.010 ± 0.003	0.009 ± 0.004	0.027 ± 0.005	0.020 ± 0.004	0.022 ± 0.004
Nd	b.d. ± NaN	0.043 ± 0.011	0.012 ± 0.008	0.011 ± 0.005	0.033 ± 0.009	0.023 ± 0.012	0.014 ± 0.006
Sm	b.d. ± NaN	0.012 ± 0.006	b.d. ± NaN	b.d. ± NaN	0.028 ± 0.009	0.008 ± 0.005	0.013 ± 0.006
Eu	0.006 ± 0.003	0.009 ± 0.003	b.d. ± NaN	0.004 ± 0.002	0.013 ± 0.003	0.011 ± 0.003	0.005 ± 0.002
Gd	0.02 ± 0.008	0.04 ± 0.010	0.02 ± 0.007	0.03 ± 0.012	0.07 ± 0.014	0.03 ± 0.009	0.06 ± 0.017
Dy	0.11 ± 0.023	0.17 ± 0.030	0.09 ± 0.013	0.11 ± 0.015	0.14 ± 0.017	0.09 ± 0.020	0.14 ± 0.017
Er	0.09 ± 0.015	0.21 ± 0.022	0.11 ± 0.016	0.13 ± 0.017	0.17 ± 0.019	0.13 ± 0.018	0.14 ± 0.027
Yb	0.18 ± 0.021	0.28 ± 0.026	0.16 ± 0.020	0.27 ± 0.036	0.21 ± 0.022	0.26 ± 0.035	0.22 ± 0.023
CaO ^a	0.64	0.98	0.60	0.85	1.16	0.78	0.87

b.d. = below detection limit a = recalculated from correlation between EPMA and SIMS analyses

Table 3-4 (continued): Trace element composition of orthopyroxene in [mg/g]

Analysis	25A_02-opx-1-50	25A_02-opx-1-51	25A_02-opx-1-52	25A_02-opx-1-53	25A_02-opx-1-54
Ca	18368 ± 476	18230 ± 527	18454 ± 533	21507 ± 569	20921 ± 409
Na	451 ± 13	477 ± 13	515 ± 17	658 ± 19	766 ± 26
Sc	28 ± 0.4	27 ± 0.4	25 ± 0.3	27 ± 0.6	26 ± 0.4
Ti	555 ± 9	566 ± 12	507 ± 12	590 ± 9	560 ± 13
V	145 ± 2	148 ± 2	129 ± 2	142 ± 2	140 ± 3
Cr	4962 ± 62	4811 ± 54	4641 ± 52	5047 ± 47	5012 ± 55
Sr	0.48 ± 0.033	0.41 ± 0.044	0.58 ± 0.040	0.75 ± 0.057	0.65 ± 0.039
Y	1.27 ± 0.050	1.19 ± 0.058	1.11 ± 0.053	1.43 ± 0.045	1.37 ± 0.045
Zr	1.50 ± 0.046	1.47 ± 0.056	1.28 ± 0.067	1.86 ± 0.052	1.52 ± 0.077
La	0.009 ± 0.002	0.008 ± 0.002	0.007 ± 0.003	0.031 ± 0.004	0.017 ± 0.003
Ce	0.024 ± 0.005	0.032 ± 0.006	0.037 ± 0.006	0.067 ± 0.007	0.048 ± 0.008
Nd	0.031 ± 0.009	b.d. ± NaN	0.019 ± 0.010	0.065 ± 0.022	0.062 ± 0.013
Sm	0.033 ± 0.012	b.d. ± NaN	0.010 ± 0.005	0.040 ± 0.023	0.025 ± 0.012
Eu	0.012 ± 0.004	0.014 ± 0.004	0.009 ± 0.004	0.015 ± 0.004	0.017 ± 0.004
Gd	0.06 ± 0.013	0.06 ± 0.014	0.05 ± 0.011	0.09 ± 0.015	0.08 ± 0.015
Dy	0.15 ± 0.018	0.18 ± 0.023	0.12 ± 0.015	0.21 ± 0.021	0.20 ± 0.020
Er	0.19 ± 0.025	0.18 ± 0.022	0.13 ± 0.025	0.18 ± 0.021	0.16 ± 0.020
Yb	0.24 ± 0.027	0.29 ± 0.029	0.23 ± 0.024	0.27 ± 0.039	0.24 ± 0.025
CaO ^a	1.12	1.10	1.14	1.65	1.55

b. d. = below detection limit a = recalculated from correlation between EPMA and SIMS analyses

Table 3-4 (continued): Trace element composition of orthopyroxene in [mg/g]

Analysis	25B_06-opx-1-01	25B_05-opx-2-01	25B_05-opx-2-02
Ca	17333 ± 529	19725 ± 528	16334 ± 474
Na	355 ± 8	500 ± 12	276 ± 7
Sc	26 ± 0.4	27 ± 0.3	29 ± 0.4
Ti	474 ± 10	535 ± 11	546 ± 16
V	124 ± 2	138 ± 3	148 ± 3
Cr	3791 ± 63	4410 ± 52	3939 ± 82
Sr	0.21 ± 0.023	0.48 ± 0.025	0.23 ± 0.015
Y	0.93 ± 0.054	1.33 ± 0.044	0.95 ± 0.060
Zr	0.88 ± 0.036	1.49 ± 0.053	1.12 ± 0.039
La	0.004 ± 0.001	0.009 ± 0.002	0.003 ± 0.001
Ce	0.013 ± 0.003	0.031 ± 0.006	0.012 ± 0.003
Nd	0.026 ± 0.009	0.044 ± 0.014	0.022 ± 0.007
Sm	b.d. ± NaN	0.027 ± 0.012	b.d. ± NaN
Eu	0.005 ± 0.002	0.012 ± 0.003	0.003 ± 0.002
Gd	0.04 ± 0.011	0.06 ± 0.013	0.03 ± 0.010
Dy	0.10 ± 0.015	0.19 ± 0.020	0.13 ± 0.016
Er	0.11 ± 0.023	0.18 ± 0.026	0.14 ± 0.018
Yb	0.23 ± 0.025	0.26 ± 0.026	0.31 ± 0.028
CaO ^a	0.95	1.35	0.78

b. d. = below detection limit a = recalculated from correlation between EPMA and SIMS analyses

Table 3-4 (continued): Trace element composition of orthopyroxene in [mg/g]

	62A_07-opx-2-01	62A_07-opx-2-02	62A_07-opx-2-03	62A_07-opx-2-04	62A_07-opx-2-05	62A_07-opx-2-06	62A_07-opx-2-07
Ca	19972 ± 415	19161 ± 444	14901 ± 498	16633 ± 475	19869 ± 460	18178 ± 724	19920 ± 404
Na	561 ± 20	509 ± 15	216 ± 6	331 ± 6	502 ± 16	402 ± 17	580 ± 26
Sc	27 ± 0.3	28 ± 0.4	26 ± 0.4	29 ± 0.3	27 ± 0.4	29 ± 0.4	28 ± 0.2
Ti	547 ± 12	556 ± 14	491 ± 10	564 ± 13	553 ± 13	570 ± 7	576 ± 13
V	139 ± 2	145 ± 3	130 ± 2	150 ± 3	143 ± 2	148 ± 2	149 ± 4
Cr	4956 ± 76	4647 ± 73	3927 ± 65	4240 ± 74	4864 ± 65	3780 ± 55	4915 ± 68
Sr	0.59 ± 0.033	0.46 ± 0.021	0.14 ± 0.013	0.27 ± 0.015	0.50 ± 0.029	0.54 ± 0.046	0.49 ± 0.024
Y	1.29 ± 0.043	1.28 ± 0.060	0.85 ± 0.054	1.03 ± 0.052	1.27 ± 0.042	1.13 ± 0.039	1.27 ± 0.056
Zr	1.44 ± 0.062	1.48 ± 0.064	0.81 ± 0.035	1.18 ± 0.044	1.52 ± 0.045	1.24 ± 0.063	1.50 ± 0.075
La	0.011 ± 0.003	0.006 ± 0.002	b.d. ± NaN	0.004 ± 0.001	0.008 ± 0.002	0.012 ± 0.003	0.007 ± 0.002
Ce	0.047 ± 0.006	0.022 ± 0.004	0.007 ± 0.003	0.018 ± 0.005	0.037 ± 0.005	0.037 ± 0.005	0.036 ± 0.006
Nd	0.037 ± 0.010	0.028 ± 0.009	b.d. ± NaN	0.020 ± 0.012	0.029 ± 0.010	0.041 ± 0.012	0.041 ± 0.012
Sm	0.021 ± 0.009	0.020 ± 0.007	b.d. ± NaN	b.d. ± NaN	0.021 ± 0.009	b.d. ± NaN	0.022 ± 0.008
Eu	0.014 ± 0.004	0.013 ± 0.005	0.004 ± 0.002	0.007 ± 0.002	0.014 ± 0.004	0.010 ± 0.004	0.013 ± 0.004
Gd	0.04 ± 0.010	0.06 ± 0.017	0.03 ± 0.009	0.04 ± 0.012	0.07 ± 0.014	0.04 ± 0.011	0.08 ± 0.015
Dy	0.15 ± 0.026	0.13 ± 0.017	0.07 ± 0.014	0.11 ± 0.022	0.14 ± 0.017	0.15 ± 0.017	0.16 ± 0.019
Er	0.18 ± 0.021	0.19 ± 0.039	0.13 ± 0.021	0.19 ± 0.021	0.16 ± 0.020	0.15 ± 0.019	0.18 ± 0.030
Yb	0.26 ± 0.026	0.26 ± 0.035	0.25 ± 0.045	0.30 ± 0.026	0.25 ± 0.027	0.26 ± 0.028	0.32 ± 0.029
CaO ^a	1.39	1.26	0.54	0.83	1.37	1.09	1.38

b.d.= below detection limit a=recalculated from correlation between EPMA and SIMS analyses

Table 3-4 (continued): Trace element composition of orthopyroxene in [mg/g]

	62A_07-opx-2-08	62A_07-opx-2-09	62A_07-opx-2-10
Ca	20420 ± 490	17661 ± 509	15557 ± 518
Na	613 ± 22	452 ± 15	223 ± 5
Sc	27 ± 0.3	27 ± 0.5	24 ± 0.4
Ti	559 ± 12	524 ± 10	413 ± 11
V	145 ± 2	139 ± 3	115 ± 3
Cr	4960 ± 64	4402 ± 53	4229 ± 125
Sr	0.53 ± 0.040	0.31 ± 0.017	0.30 ± 0.026
Y	1.35 ± 0.061	1.01 ± 0.039	0.70 ± 0.049
Zr	1.62 ± 0.079	1.33 ± 0.053	0.62 ± 0.046
La	0.009 ± 0.003	0.004 ± 0.001	0.005 ± 0.002
Ce	0.044 ± 0.010	0.015 ± 0.005	0.018 ± 0.004
Nd	0.038 ± 0.010	0.013 ± 0.007	b.d. ± NaN
Sm	0.017 ± 0.007	b.d. ± NaN	0.013 ± 0.008
Eu	0.011 ± 0.003	0.009 ± 0.003	0.003 ± 0.002
Gd	0.07 ± 0.015	0.06 ± 0.013	0.02 ± 0.010
Dy	0.17 ± 0.024	0.14 ± 0.018	0.08 ± 0.015
Er	0.17 ± 0.022	0.16 ± 0.020	0.10 ± 0.016
Yb	0.27 ± 0.032	0.32 ± 0.029	0.19 ± 0.022
CaO ^a	1.47	1.00	0.65

b.d.= below detection limit a=recalculated from correlation between EPMA and SIMS analyses

Table 3-4 (continued): Trace element composition of orthopyroxene in [mg/g]

	62B_03-opx-2-1	62B_03-opx-2-2	62B_07-opx-2-3	62B_07-opx-2-4	62B_07-opx-2-5	62B_07-opx-2-6	62B_07-opx-2-7
Ca	15607 ± 437	16572 ± 518	21917 ± 606	16294 ± 243	18273 ± 375	21415 ± 215	18492 ± 299
Na	261 ± 7	339 ± 7	476 ± 13	311 ± 14	251 ± 11	512 ± 30	397 ± 25
Sc	26 ± 0.4	28 ± 0.5	27 ± 0.3	27 ± 0.4	25 ± 0.4	27 ± 0.4	28 ± 0.5
Ti	426 ± 11	493 ± 5	516 ± 6	476 ± 6	453 ± 8	502 ± 9	493 ± 9
V	114 ± 3	129 ± 1	128 ± 2	116 ± 2	109 ± 2	129 ± 1	131 ± 2
Cr	3677 ± 52	4169 ± 44	5276 ± 53	3830 ± 51	3843 ± 34	5143 ± 71	4452 ± 52
Sr	0.13 ± 0.011	0.41 ± 0.020	0.75 ± 0.025	0.18 ± 0.012	0.36 ± 0.020	0.57 ± 0.024	0.32 ± 0.015
Y	0.85 ± 0.036	1.09 ± 0.041	1.40 ± 0.043	1.09 ± 0.037	1.04 ± 0.043	1.36 ± 0.079	1.14 ± 0.037
Zr	0.73 ± 0.032	1.18 ± 0.042	1.92 ± 0.049	1.25 ± 0.056	1.10 ± 0.041	1.71 ± 0.053	1.46 ± 0.064
La	b.d. ± NaN	0.014 ± 0.003	0.031 ± 0.005	0.004 ± 0.002	0.014 ± 0.003	0.020 ± 0.003	b.d. ± NaN
Ce	0.004 ± 0.003	0.039 ± 0.010	0.094 ± 0.008	0.014 ± 0.003	0.045 ± 0.006	0.060 ± 0.006	0.026 ± 0.004
Nd	b.d. ± NaN	0.039 ± 0.012	0.099 ± 0.015	0.010 ± 0.005	0.036 ± 0.012	0.076 ± 0.013	0.031 ± 0.008
Sm	b.d. ± NaN	0.032 ± 0.013	0.051 ± 0.011	0.011 ± 0.005	0.027 ± 0.008	0.036 ± 0.009	0.015 ± 0.007
Eu	0.004 ± 0.002	0.006 ± 0.002	0.017 ± 0.004	0.009 ± 0.003	0.011 ± 0.003	0.020 ± 0.004	0.008 ± 0.002
Gd	0.02 ± 0.009	0.02 ± 0.003	0.11 ± 0.018	0.04 ± 0.011	0.07 ± 0.014	0.09 ± 0.020	0.04 ± 0.011
Dy	0.07 ± 0.011	0.11 ± 0.015	0.19 ± 0.021	0.10 ± 0.017	0.12 ± 0.022	0.15 ± 0.015	0.10 ± 0.012
Er	0.16 ± 0.020	0.17 ± 0.033	0.20 ± 0.021	0.14 ± 0.018	0.14 ± 0.018	0.20 ± 0.026	0.17 ± 0.019
Yb	0.21 ± 0.036	0.28 ± 0.029	0.22 ± 0.022	0.25 ± 0.024	0.22 ± 0.023	0.22 ± 0.023	0.26 ± 0.029
CaO ^a	0.66	0.82	1.72	0.78	1.11	1.63	1.14

b.d.= below detection limit a=recalculated from correlation between EPMA and SIMS analyses

Table 3-4 (continued): Trace element composition of orthopyroxene in [mg/g]

	62B_08-opx-2-3	62B_08-opx-1-1	62B_11-opx-3-1	62B_11-opx-3-2
Ca	16983 ± 490	19297 ± 287	18080 ± 356	16846 ± 336
Na	290 ± 11	445 ± 16	415 ± 19	310 ± 14
Sc	26 ± 0.4	28 ± 0.4	29 ± 0.5	30 ± 0.5
Ti	459 ± 5	499 ± 8	543 ± 9	546 ± 8
V	121 ± 1	127 ± 1	140 ± 2	141 ± 2
Cr	4096 ± 48	4291 ± 50	4806 ± 55	4382 ± 45
Sr	0.21 ± 0.013	0.28 ± 0.015	0.36 ± 0.018	0.21 ± 0.012
Y	0.82 ± 0.035	1.14 ± 0.040	1.16 ± 0.040	1.06 ± 0.066
Zr	0.91 ± 0.034	1.18 ± 0.044	1.51 ± 0.042	1.46 ± 0.059
La	0.003 ± 0.001	0.007 ± 0.002	0.005 ± 0.001	0.002 ± 0.001
Ce	0.012 ± 0.003	0.024 ± 0.004	0.028 ± 0.006	0.013 ± 0.005
Nd	0.013 ± 0.006	0.025 ± 0.008	0.024 ± 0.007	0.015 ± 0.007
Sm	0.009 ± 0.005	0.017 ± 0.007	0.022 ± 0.007	0.010 ± 0.005
Eu	0.004 ± 0.002	0.009 ± 0.003	0.007 ± 0.003	0.007 ± 0.003
Gd	0.03 ± 0.009	0.06 ± 0.020	0.07 ± 0.014	0.05 ± 0.015
Dy	0.09 ± 0.015	0.15 ± 0.025	0.12 ± 0.013	0.10 ± 0.012
Er	0.16 ± 0.024	0.18 ± 0.021	0.16 ± 0.022	0.18 ± 0.028
Yb	0.26 ± 0.025	0.22 ± 0.023	0.21 ± 0.021	0.29 ± 0.025
CaO ^a	0.89	1.28	1.07	0.87

b.d.= below detection limit a=recalculated from correlation between EPMA and SIMS analyses

Table 3-5: D_{cpX/opx}

	25A_07-opx-2-1	25A_07-opx-1-1	25A_07-opx-1-2	25A_12-opx-2-1	25A_12-opx-1-1	25A_12-opx-1-2	25A_12-opx-1-3
Na	33.2 ± 3.6	12.5 ± 1.4	18.3 ± 2.4	11.3 ± 2.4	10.7 ± 1.6	16.2 ± 1.7	22.4 ± 2.4
K	3.0 ± 0.6	3.1 ± 0.7	3.2 ± 0.6	3.4 ± 0.6	2.3 ± 0.4	3.2 ± 0.7	2.9 ± 0.6
Sc	2.0 ± 0.2	2.0 ± 0.2	1.9 ± 0.2	2.0 ± 0.2	2.0 ± 0.2	1.8 ± 0.2	1.9 ± 0.2
Ti	3.4 ± 0.3	2.9 ± 0.3	3.0 ± 0.3	2.9 ± 0.3	3.0 ± 0.3	2.9 ± 0.3	2.8 ± 0.3
V	2.1 ± 0.1	1.9 ± 0.1	1.9 ± 0.1	1.9 ± 0.1	1.9 ± 0.1	1.8 ± 0.1	1.8 ± 0.1
Cr	2.4 ± 0.1	1.7 ± 0.1	1.6 ± 0.1	1.6 ± 0.1	1.6 ± 0.1	1.9 ± 0.1	1.9 ± 0.1
Sr	a	92.6 ± 5.7	147.5 ± 12.6	a	53.1 ± 4.5	104.4 ± 6.6	146.4 ± 14.4
Y	14.1 ± 1.3	9.1 ± 0.8	9.7 ± 0.9	7.4 ± 0.9	8.0 ± 0.7	10.3 ± 1.0	11.7 ± 1.0
Zr	16.0 ± 1.6	8.2 ± 0.8	8.4 ± 0.8	6.5 ± 0.9	7.6 ± 0.8	9.2 ± 0.9	12.4 ± 1.3
La	a	103.8 ± 29.4	407.7 ± 230.7	45.2 ± 9.5	69.3 ± 12.8	275.1 ± 120.1	193.7 ± 58.6
Ce	687.2 ± 291.6	115.5 ± 22.0	141.7 ± 44.9	34.8 ± 6.8	56.1 ± 8.0	112.5 ± 20.9	140.3 ± 30.0
Nd	a	51.5 ± 13.2	193.1 ± 91.0	30.5 ± 8.3	28.5 ± 5.5	65.0 ± 18.2	a
Sm	a	30.8 ± 10.0	35.4 ± 16.1	a	26.5 ± 8.0	60.3 ± 36.0	86.6 ± 46.5
Eu	76.8 ± 36.6	29.9 ± 11.1	28.9 ± 11.5	14.5 ± 3.4	21.2 ± 5.0	76.5 ± 37.2	58.6 ± 23.1
Gd	44.7 ± 14.8	22.4 ± 5.6	28.1 ± 7.4	9.3 ± 3.3	15.6 ± 4.8	29.5 ± 7.8	46.8 ± 18.1
Dy	27.7 ± 7.4	11.3 ± 1.8	13.2 ± 2.3	8.5 ± 1.9	11.1 ± 1.8	14.2 ± 2.4	18.0 ± 3.3
Er	10.5 ± 2.2	7.1 ± 1.0	7.5 ± 1.0	7.0 ± 0.9	7.0 ± 1.0	7.7 ± 1.1	8.0 ± 1.4
Yb	5.2 ± 0.8	4.4 ± 0.7	4.3 ± 0.7	4.5 ± 0.7	4.6 ± 1.0	4.1 ± 0.7	3.6 ± 0.5
distance to rim [µm]	108	477	65	761	1056	53	74
nearest mineral	ol	ol	ol	ol	ol	ol	ol

a: opx below detection limit
±: one standard deviation
Italics denote analyses that were not considered for modeling because of their large error

Table 3-5 (continued): D_{cpX/opx}

	25A_12-opx-1-4	25A_12-opx-1-5	25A_12-opx-1-6	25A_12-opx-1-7	25A_12-opx-1-8	25A_12-opx-1-9	25A_12-opx-1-10
Na	25.3 ± 2.7	12.1 ± 1.5	12.5 ± 1.5	13.7 ± 1.5	16.8 ± 2.0	12.9 ± 1.4	13.9 ± 1.9
K	2.5 ± 0.6	3.9 ± 0.7	3.1 ± 0.6	3.5 ± 0.7	1.0 ± 0.2	2.8 ± 0.5	3.0 ± 0.6
Sc	2.1 ± 0.2	2.0 ± 0.2	2.0 ± 0.2	2.0 ± 0.2	2.0 ± 0.2	2.0 ± 0.2	1.9 ± 0.2
Ti	3.2 ± 0.3	2.8 ± 0.3	2.9 ± 0.3	2.8 ± 0.3	3.0 ± 0.3	2.9 ± 0.3	2.9 ± 0.3
V	2.2 ± 0.1	1.9 ± 0.1	1.9 ± 0.1	1.9 ± 0.1	1.9 ± 0.1	1.9 ± 0.1	1.9 ± 0.1
Cr	2.2 ± 0.1	1.6 ± 0.1	1.6 ± 0.1	1.7 ± 0.1	1.7 ± 0.1	1.7 ± 0.1	1.6 ± 0.1
Sr	120.1 ± 8.1	59.6 ± 5.8	66.7 ± 3.8	72.7 ± 6.3	87.0 ± 7.7	63.6 ± 5.3	72.2 ± 12.2
Y	12.0 ± 1.0	8.8 ± 0.7	9.4 ± 0.8	9.1 ± 0.8	10.1 ± 0.9	8.9 ± 0.8	9.1 ± 1.1
Zr	13.2 ± 1.3	7.2 ± 0.7	8.3 ± 0.9	8.5 ± 0.8	9.2 ± 0.9	8.0 ± 0.8	7.5 ± 1.1
La	189.1 ± 56.6	71.8 ± 13.8	108.0 ± 24.5	98.4 ± 21.6	119.1 ± 27.6	121.1 ± 28.6	79.3 ± 15.5
Ce	137.3 ± 28.1	74.8 ± 12.2	82.6 ± 14.0	81.9 ± 15.4	153.8 ± 33.1	72.7 ± 18.4	110.2 ± 60.2
Nd	113.3 ± 41.8	48.6 ± 12.4	56.0 ± 17.2	64.3 ± 18.7	130.3 ± 51.5	57.1 ± 15.5	41.2 ± 12.7
Sm	49.8 ± 21.4	108.0 ± 51.6	47.3 ± 19.1	40.7 ± 15.4	58.7 ± 25.5	33.1 ± 14.7	26.9 ± 8.1
Eu	89.6 ± 42.1	30.3 ± 8.8	33.5 ± 10.1	21.8 ± 5.4	32.4 ± 12.6	45.9 ± 15.9	18.4 ± 4.0
Gd	25.9 ± 6.6	19.4 ± 4.4	39.5 ± 12.0	25.5 ± 6.5	34.4 ± 17.0	22.1 ± 5.3	27.0 ± 10.8
Dy	23.5 ± 4.6	12.8 ± 2.4	11.3 ± 1.8	12.1 ± 2.0	13.1 ± 2.7	14.1 ± 2.4	10.1 ± 2.3
Er	11.0 ± 1.8	6.3 ± 0.9	7.6 ± 1.4	7.7 ± 1.3	8.6 ± 2.2	7.4 ± 1.1	6.8 ± 1.0
Yb	6.2 ± 1.3	4.6 ± 0.7	4.1 ± 0.7	4.5 ± 0.7	5.1 ± 0.8	4.1 ± 0.8	3.8 ± 0.6
distance to rim [µm]	115	1162	702	291	379	392	839
nearest mineral	ol	ol	ol	ol	ol	ol	ol

a: opx below detection limit
±: one standard deviation
Italics denote analyses that were not considered for modeling because of their large error

Table 3-5 (continued): D^{cpx/oxp}

	25A_12-oxp-1-11	25A_01-oxp-2-1	25A_02-oxp-1-1	25A_02-oxp-1-2	25A_02-oxp-1-3	25A_02-oxp-1-4	25A_02-oxp-1-5
Na	12.4 ± 1.4	19.2 ± 2.1	25.3 ± 2.6	15.9 ± 1.8	14.4 ± 1.6	12.3 ± 1.4	15.4 ± 1.7
K	3.0 ± 0.5	1.9 ± 0.4	2.4 ± 0.5	2.3 ± 0.5	2.2 ± 0.4	3.2 ± 0.6	3.3 ± 0.6
Sc	2.0 ± 0.2	1.8 ± 0.2	2.1 ± 0.2	1.9 ± 0.2	1.9 ± 0.2	1.9 ± 0.2	1.9 ± 0.2
Ti	3.0 ± 0.3	2.9 ± 0.3	3.4 ± 0.3	2.8 ± 0.3	2.8 ± 0.3	2.7 ± 0.3	2.8 ± 0.3
V	1.9 ± 0.1	1.8 ± 0.1	2.0 ± 0.1	1.8 ± 0.1	1.9 ± 0.1	1.8 ± 0.1	1.8 ± 0.1
Cr	1.6 ± 0.1	1.9 ± 0.1	1.6 ± 0.1	1.6 ± 0.1	1.7 ± 0.1	1.6 ± 0.1	1.6 ± 0.1
Sr	73.7 ± 7.2	135.1 ± 9.7	174.6 ± 25.0	100.4 ± 7.4	76.6 ± 5.0	69.6 ± 4.1	80.9 ± 4.8
Y	9.0 ± 0.8	9.5 ± 0.8	14.3 ± 1.2	9.0 ± 0.8	8.4 ± 0.8	8.2 ± 0.7	9.2 ± 0.9
Zr	8.0 ± 0.9	9.8 ± 0.9	13.8 ± 1.3	7.5 ± 1.0	7.6 ± 0.8	7.3 ± 0.8	8.0 ± 0.8
La	106.1 ± 24.8	286.5 ± 100.7	351.9 ± 131.1	148.9 ± 37.7	88.3 ± 18.2	86.0 ± 17.4	96.2 ± 20.4
Ce	82.9 ± 14.1	286.3 ± 83.1	337.3 ± 101.8	105.6 ± 20.5	69.5 ± 11.0	55.6 ± 10.8	100.3 ± 18.0
Nd	42.8 ± 10.1	a	159.9 ± 68.5	56.2 ± 14.8	60.7 ± 17.0	43.4 ± 11.8	80.8 ± 32.7
Sm	30.2 ± 12.0	56.2 ± 24.4	a	93.0 ± 50.0	37.5 ± 15.8	18.5 ± 4.8	a
Eu	21.5 ± 5.6	45.5 ± 15.8	64.5 ± 49.0	22.3 ± 6.8	19.5 ± 4.5	17.1 ± 4.6	38.3 ± 13.2
Gd	19.2 ± 4.3	22.1 ± 5.5	a	25.9 ± 6.5	23.8 ± 5.9	18.2 ± 4.3	19.8 ± 4.5
Dy	11.3 ± 1.8	19.8 ± 4.9	17.3 ± 3.0	12.1 ± 2.7	10.0 ± 1.6	12.5 ± 2.5	12.3 ± 2.0
Er	6.9 ± 1.1	8.0 ± 1.2	11.1 ± 1.9	6.6 ± 0.9	6.8 ± 1.2	7.3 ± 1.0	7.3 ± 1.0
Yb	4.5 ± 0.9	4.0 ± 0.6	5.4 ± 1.1	5.2 ± 0.9	5.3 ± 0.9	5.8 ± 1.1	4.4 ± 0.9
distance to rim [µm]	1056	161	65	223	506	484	246
nearest mineral	ol	sp	cpx	cpx	cpx	ol	ol

a: opx below detection limit
±: one standard deviation

Italics denote analyses that were not considered for modeling because of their large error

Table 3-5 (continued): D^{cpx/oxp}

	25A_02-oxp-1-6	25A_02-oxp-1-7	25A_02-oxp-1-8	25A_02-oxp-1-31	25A_02-oxp-1-32	25A_02-oxp-1-33	25A_02-oxp-1-34
Na	18.3 ± 2.1	12.2 ± 1.3	19.0 ± 2.0	10.3 ± 1.1	11.7 ± 1.2	14.4 ± 1.6	16.3 ± 1.7
K	2.8 ± 0.7	3.5 ± 0.8	3.7 ± 0.7	0.6 ± 0.1	0.5 ± 0.1	0.5 ± 0.1	0.7 ± 0.1
Sc	1.9 ± 0.2	2.0 ± 0.2	2.2 ± 0.2	2.0 ± 0.2	2.0 ± 0.2	2.1 ± 0.2	2.0 ± 0.2
Ti	2.8 ± 0.3	2.9 ± 0.3	3.5 ± 0.3	2.8 ± 0.2	2.7 ± 0.2	2.9 ± 0.3	2.9 ± 0.3
V	1.8 ± 0.1	1.9 ± 0.1	2.3 ± 0.2	1.8 ± 0.1	1.8 ± 0.1	1.8 ± 0.1	1.8 ± 0.1
Cr	1.6 ± 0.1	1.6 ± 0.1	1.9 ± 0.1	1.6 ± 0.1	1.7 ± 0.1	1.5 ± 0.1	1.9 ± 0.1
Sr	93.9 ± 8.3	63.7 ± 3.7	110.1 ± 6.9	43.9 ± 2.7	57.0 ± 3.0	71.9 ± 4.7	51.6 ± 4.0
Y	9.1 ± 0.9	8.9 ± 0.8	12.9 ± 1.2	8.8 ± 0.7	8.6 ± 0.8	9.9 ± 0.8	9.9 ± 0.8
Zr	7.7 ± 0.8	7.8 ± 0.7	13.1 ± 1.3	7.3 ± 0.7	7.5 ± 0.7	9.1 ± 0.9	9.4 ± 0.9
La	75.2 ± 14.3	88.9 ± 18.3	114.0 ± 24.6	67.8 ± 12.7	87.0 ± 17.8	170.6 ± 48.5	116.2 ± 38.8
Ce	90.1 ± 15.4	72.7 ± 11.5	136.1 ± 33.9	74.9 ± 12.2	84.2 ± 14.2	91.2 ± 15.8	70.8 ± 11.1
Nd	59.6 ± 16.1	62.6 ± 17.5	101.7 ± 33.6	57.9 ± 15.6	64.0 ± 21.0	82.6 ± 31.9	60.4 ± 17.2
Sm	34.6 ± 14.5	28.0 ± 10.6	49.0 ± 18.5	31.3 ± 11.0	44.5 ± 23.7	35.9 ± 13.5	92.0 ± 47.9
Eu	38.9 ± 16.7	25.9 ± 8.1	70.7 ± 27.9	26.2 ± 7.0	24.4 ± 9.0	35.2 ± 10.5	37.5 ± 11.6
Gd	21.6 ± 5.0	14.4 ± 2.9	49.1 ± 17.2	17.4 ± 3.9	19.3 ± 3.9	31.4 ± 8.5	28.1 ± 6.7
Dy	10.9 ± 1.7	11.5 ± 1.8	16.2 ± 3.1	10.5 ± 1.7	8.9 ± 1.8	8.7 ± 1.3	12.7 ± 2.2
Er	8.4 ± 1.2	7.1 ± 1.3	11.4 ± 2.1	6.8 ± 0.9	7.9 ± 1.1	7.2 ± 1.0	8.5 ± 1.5
Yb	4.0 ± 0.6	5.5 ± 0.9	6.9 ± 1.1	3.6 ± 0.6	4.1 ± 0.7	4.0 ± 0.7	3.8 ± 0.6
distance to rim [µm]	71	581	76	426	463	180	61
nearest mineral	ol	ol	opx	ol	ol/cpx	cpx	ol

a: opx below detection limit
±: one standard deviation

Italics denote analyses that were not considered for modeling because of their large error

Table 3-5 (continued): D^{cpx/oxp}

	25A_02-opx-1-35	25A_02-opx-1-36	25A_02-opx-1-37	25A_02-opx-1-38	25A_02-opx-1-39	25A_02-opx-1-41	25A_02-opx-1-42
Na	14.2 ± 1.6	26.1 ± 2.8	18.5 ± 1.9	9.9 ± 1.0	12.9 ± 1.4	15.1 ± 1.6	11.1 ± 1.2
K	0.4 ± 0.1	0.4 ± 0.1	0.7 ± 0.1	0.4 ± 0.1	0.5 ± 0.1	0.5 ± 0.1	0.6 ± 0.1
Sc	1.9 ± 0.2	2.3 ± 0.2	1.9 ± 0.2	2.1 ± 0.2	2.1 ± 0.2	2.1 ± 0.2	2.0 ± 0.2
Ti	2.9 ± 0.3	3.6 ± 0.3	2.8 ± 0.2	2.9 ± 0.3	3.0 ± 0.3	3.0 ± 0.3	2.6 ± 0.2
V	1.8 ± 0.1	2.2 ± 0.1	1.7 ± 0.1	1.9 ± 0.1	1.9 ± 0.1	1.9 ± 0.1	1.7 ± 0.1
Cr	1.6 ± 0.1	2.0 ± 0.1	1.6 ± 0.1	1.7 ± 0.1	1.7 ± 0.1	1.7 ± 0.1	1.6 ± 0.1
Sr	70.3 ± 3.9	88.0 ± 6.2	69.5 ± 6.3	39.9 ± 2.5	67.5 ± 5.6	64.9 ± 6.0	55.3 ± 4.2
Y	8.6 ± 0.7	14.4 ± 1.2	9.3 ± 0.8	8.7 ± 0.8	10.1 ± 0.9	10.5 ± 0.9	8.4 ± 0.8
Zr	7.8 ± 0.8	15.0 ± 1.5	8.2 ± 0.8	8.3 ± 0.8	9.3 ± 0.9	9.0 ± 0.9	7.0 ± 0.7
La	108.3 ± 28.2	236.1 ± 74.5	116.9 ± 26.9	62.4 ± 17.3	145.2 ± 37.5	134.4 ± 33.0	99.2 ± 23.9
Ce	86.7 ± 14.6	267.2 ± 73.7	156.4 ± 33.9	63.4 ± 9.8	106.0 ± 19.8	106.8 ± 22.4	61.4 ± 9.4
Nd	61.5 ± 21.1	132.3 ± 51.4	154.4 ± 64.8	40.0 ± 9.7	97.7 ± 33.6	153.4 ± 67.1	40.1 ± 12.9
Sm	28.1 ± 9.4	a	92.6 ± 58.6	37.2 ± 19.2	34.6 ± 16.4	73.0 ± 34.1	30.4 ± 9.8
Eu	21.9 ± 5.8	a	29.5 ± 11.4	15.9 ± 3.4	33.4 ± 10.3	31.6 ± 9.0	32.1 ± 9.5
Gd	17.2 ± 3.3	74.7 ± 27.3	32.5 ± 11.9	23.0 ± 7.0	a	29.8 ± 9.5	14.4 ± 2.7
Dy	10.6 ± 1.7	25.6 ± 6.2	9.3 ± 1.5	8.8 ± 1.4	9.6 ± 1.5	12.3 ± 2.1	7.6 ± 1.3
Er	6.6 ± 0.9	11.1 ± 2.2	7.8 ± 1.5	6.3 ± 0.8	7.2 ± 1.0	9.8 ± 1.5	7.7 ± 1.1
Yb	3.4 ± 0.5	5.2 ± 1.0	3.4 ± 0.6	4.2 ± 0.7	4.3 ± 0.7	4.5 ± 0.8	4.1 ± 0.6
distance to rim [µm]	437	57	58	203	346	227	495
nearest mineral	cpx	cpx	ol	opx	ol	ol	ol

a: opx below detection limit
±: one standard deviation
Italics denote analyses that were not considered for modeling because of their large error

Table 3-5 (continued): D^{cpx/oxp}

	25A_02-opx-1-43	25A_02-opx-1-44	25A_02-opx-1-45	25A_02-opx-1-46	25A_02-opx-1-47	25A_02-opx-1-48	25A_02-opx-1-49
Na	21.0 ± 2.2	19.3 ± 2.0	28.1 ± 3.0	19.1 ± 2.0	14.9 ± 1.6	22.1 ± 2.3	18.4 ± 2.0
K	0.7 ± 0.1	0.4 ± 0.1	0.8 ± 0.1	0.6 ± 0.1	0.7 ± 0.1	0.6 ± 0.1	0.3 ± 0.1
Sc	2.6 ± 0.3	1.9 ± 0.2	2.5 ± 0.3	2.2 ± 0.2	2.1 ± 0.2	2.1 ± 0.2	2.0 ± 0.2
Ti	4.0 ± 0.4	2.6 ± 0.2	4.1 ± 0.4	3.2 ± 0.3	3.2 ± 0.3	3.4 ± 0.3	2.9 ± 0.3
V	2.6 ± 0.2	1.6 ± 0.1	2.4 ± 0.2	2.0 ± 0.1	2.0 ± 0.1	2.0 ± 0.1	1.8 ± 0.1
Cr	2.0 ± 0.1	1.5 ± 0.1	1.8 ± 0.1	1.9 ± 0.1	2.0 ± 0.1	1.8 ± 0.1	2.0 ± 0.1
Sr	111.3 ± 14.5	66.0 ± 3.7	134.7 ± 9.9	105.0 ± 11.5	74.9 ± 4.3	122.3 ± 12.3	50.8 ± 5.2
Y	17.3 ± 1.5	9.4 ± 0.8	15.3 ± 1.4	12.9 ± 1.1	11.2 ± 1.0	12.4 ± 1.1	11.4 ± 1.0
Zr	19.5 ± 1.9	7.1 ± 0.7	22.5 ± 2.5	12.7 ± 1.4	11.3 ± 1.1	12.6 ± 1.2	10.2 ± 1.1
La	278.3 ± 96.6	134.5 ± 39.1	276.2 ± 81.7	356.6 ± 139.7	92.6 ± 19.9	315.9 ± 123.7	214.0 ± 67.5
Ce	225.3 ± 63.1	90.8 ± 19.8	166.0 ± 108.4	296.4 ± 115.0	103.8 ± 19.4	138.2 ± 30.5	126.5 ± 26.1
Nd	a	47.6 ± 12.3	166.0 ± 108.4	178.4 ± 82.0	61.1 ± 17.0	86.6 ± 44.7	140.3 ± 58.9
Sm	a	69.7 ± 32.2	a	a	30.2 ± 9.7	106.3 ± 64.0	66.8 ± 31.1
Eu	53.8 ± 24.8	36.7 ± 11.4	a	92.5 ± 51.4	25.8 ± 6.9	30.1 ± 9.0	66.2 ± 32.0
Gd	54.6 ± 17.9	34.4 ± 9.6	80.1 ± 33.7	39.2 ± 14.1	20.6 ± 4.8	45.3 ± 14.8	24.0 ± 7.4
Dy	14.5 ± 3.5	9.1 ± 1.9	17.9 ± 3.4	13.5 ± 2.3	10.9 ± 1.8	16.3 ± 3.9	11.3 ± 1.9
Er	14.8 ± 2.7	6.4 ± 0.9	12.4 ± 2.1	10.2 ± 1.6	8.0 ± 1.1	10.6 ± 1.7	10.0 ± 2.1
Yb	6.3 ± 1.0	4.0 ± 0.6	7.2 ± 1.3	4.3 ± 0.8	5.5 ± 0.9	4.4 ± 0.8	5.3 ± 0.8
distance to rim [µm]	57	43	58	64	43	70	43
nearest mineral	opx	ol	opx	ol	ol	cpx	ol

a: opx below detection limit
±: one standard deviation
Italics denote analyses that were not considered for modeling because of their large error

Table 3-5 (continued): $D^{cpx/ol}$

	25A_02-opx-1-50	25A_02-opx-1-51	25A_02-opx-1-52	25A_02-opx-1-53	25A_02-opx-1-54
Na	14.2 ± 1.5	13.4 ± 1.4	12.4 ± 1.3	9.7 ± 1.0	8.4 ± 0.9
K	0.6 ± 0.1	0.7 ± 0.1	0.5 ± 0.1	0.5 ± 0.1	0.2 ± 0.0
Sc	2.0 ± 0.2	2.0 ± 0.2	2.2 ± 0.2	2.0 ± 0.2	2.1 ± 0.2
Ti	2.7 ± 0.2	2.7 ± 0.2	3.0 ± 0.3	2.6 ± 0.2	2.7 ± 0.2
V	1.7 ± 0.1	1.7 ± 0.1	2.0 ± 0.1	1.8 ± 0.1	1.8 ± 0.1
Cr	1.6 ± 0.1	1.6 ± 0.1	1.7 ± 0.1	1.6 ± 0.1	1.6 ± 0.1
Sr	60.6 ± 4.7	71.3 ± 8.1	50.0 ± 3.9	38.7 ± 3.2	44.5 ± 3.1
Y	8.7 ± 0.8	9.3 ± 0.8	9.9 ± 0.9	7.8 ± 0.6	8.1 ± 0.7
Zr	7.6 ± 0.7	7.7 ± 0.7	8.9 ± 0.9	6.1 ± 0.6	7.5 ± 0.8
La	111.3 ± 26.7	136.7 ± 37.4	157.0 ± 63.8	33.5 ± 5.3	62.7 ± 11.9
Ce	116.1 ± 23.6	87.9 ± 17.2	76.5 ± 13.9	42.1 ± 5.7	58.7 ± 10.3
Nd	65.9 ± 19.7	a	104.8 ± 56.4	31.1 ± 10.5	32.4 ± 7.0
Sm	26.0 ± 10.0	a	84.3 ± 43.9	21.4 ± 12.6	34.4 ± 17.0
Eu	27.4 ± 8.3	23.2 ± 6.4	38.4 ± 16.5	21.8 ± 5.5	19.5 ± 4.8
Gd	23.9 ± 5.7	21.4 ± 5.1	29.3 ± 7.5	15.6 ± 3.0	17.6 ± 3.7
Dy	10.5 ± 1.7	8.7 ± 1.5	13.0 ± 2.2	7.4 ± 1.1	7.8 ± 1.2
Er	7.3 ± 1.2	7.6 ± 1.1	10.1 ± 3.0	7.5 ± 1.0	8.4 ± 1.3
Yb	4.8 ± 0.8	3.9 ± 0.6	5.1 ± 0.8	4.2 ± 0.8	4.8 ± 0.8
distance to rim [μ m]	194	306	346	334	254
nearest mineral	ol	cpx	ol	ol	opx

a: opx below detection limit
±: one standard deviation

italics denote analyses that were not considered for modeling because of their large error

Table 3-5 (continued): $D^{cpx/ol}$

	25B_06-opx-1-01	25B_05-opx-2-01	25B_05-opx-2-02
Na	16.2 ± 1.4	11.6 ± 1.0	20.9 ± 1.9
K	4.8 ± 1.4	2.4 ± 0.7	2.8 ± 0.8
Sc	2.0 ± 0.2	1.9 ± 0.2	1.8 ± 0.2
Ti	3.1 ± 0.3	2.7 ± 0.2	2.7 ± 0.2
V	1.9 ± 0.1	1.7 ± 0.1	1.6 ± 0.1
Cr	2.1 ± 0.1	1.8 ± 0.1	2.0 ± 0.1
Sr	165.3 ± 18.7	73.9 ± 4.7	150.4 ± 11.0
Y	11.4 ± 0.8	8.0 ± 0.4	11.2 ± 0.8
Zr	12.3 ± 0.7	7.3 ± 0.4	9.7 ± 0.5
La	294.1 ± 106.1	134.7 ± 38.5	411.4 ± 181.1
Ce	272.6 ± 77.3	110.2 ± 23.7	276.0 ± 75.9
Nd	90.4 ± 29.6	54.4 ± 17.1	109.1 ± 37.0
Sm	a	31.0 ± 14.1	a
Eu	87.1 ± 41.3	33.8 ± 9.8	122.4 ± 63.1
Gd	33.6 ± 9.8	20.8 ± 4.5	36.6 ± 10.6
Dy	17.5 ± 2.9	9.7 ± 1.3	14.0 ± 2.1
Er	12.1 ± 2.7	7.3 ± 1.2	9.4 ± 1.4
Yb	4.4 ± 0.9	3.8 ± 0.7	3.3 ± 0.6
distance to rim [μ m]	170	288	39
nearest mineral	ol	ol	ol

a: opx below detection limit
±: one standard deviation

italics denote analyses that were not considered for modeling because of their large error

Table 3-5 (continued): $D^{cpx/olpx}$

	62A_07-opx-2-01	62A_07-opx-2-02	62A_07-opx-2-03	62A_07-opx-2-04	62A_07-opx-2-05	62A_07-opx-2-06	62A_07-opx-2-07
Na	8.9 ± 0.3	9.8 ± 0.3	23.2 ± 0.7	15.1 ± 0.3	10.0 ± 0.3	12.4 ± 0.5	8.6 ± 0.4
K	0.8 ± 0.1	1.0 ± 0.2	1.7 ± 0.2	1.2 ± 0.2	1.0 ± 0.2	0.4 ± 0.0	0.7 ± 0.1
Sc	1.9 ± 0.0	1.9 ± 0.0	2.0 ± 0.0	1.8 ± 0.0	1.9 ± 0.0	1.8 ± 0.0	1.9 ± 0.0
Ti	2.6 ± 0.1	2.5 ± 0.1	2.9 ± 0.1	2.5 ± 0.1	2.6 ± 0.1	2.5 ± 0.0	2.5 ± 0.1
V	1.6 ± 0.0	1.6 ± 0.0	1.8 ± 0.0	1.5 ± 0.0	1.6 ± 0.0	1.5 ± 0.0	1.5 ± 0.0
Cr	1.6 ± 0.0	1.7 ± 0.0	2.0 ± 0.0	1.8 ± 0.0	1.6 ± 0.0	2.0 ± 0.0	1.6 ± 0.0
Sr	46.4 ± 2.6	59.5 ± 2.7	190.2 ± 17.7	99.6 ± 5.3	54.2 ± 3.2	50.6 ± 4.3	56.0 ± 2.7
Y	8.3 ± 0.3	8.3 ± 0.4	12.6 ± 0.8	10.3 ± 0.5	8.4 ± 0.3	9.4 ± 0.3	8.4 ± 0.4
Zr	6.8 ± 0.3	6.7 ± 0.3	12.1 ± 0.5	8.3 ± 0.3	6.5 ± 0.2	7.9 ± 0.4	6.6 ± 0.3
La	94.9 ± 24.2	183.4 ± 51.2	a	273.9 ± 107.4	133.7 ± 32.6	86.5 ± 20.0	155.1 ± 44.9
Ce	58.7 ± 8.2	124.1 ± 23.7	384.0 ± 146.9	155.0 ± 41.3	74.0 ± 11.0	73.1 ± 10.6	75.6 ± 11.6
Nd	54.5 ± 14.1	71.1 ± 22.2	a	97.9 ± 55.3	67.9 ± 23.4	48.6 ± 13.8	48.4 ± 13.9
Sm	38.4 ± 16.1	40.1 ± 14.3	a	a	38.2 ± 17.2	a	36.5 ± 13.0
Eu	26.9 ± 8.2	30.0 ± 10.8	93.1 ± 42.3	58.3 ± 21.7	26.8 ± 6.7	37.6 ± 14.2	28.9 ± 9.1
Gd	29.2 ± 7.1	22.2 ± 6.6	41.8 ± 12.7	29.6 ± 8.2	18.3 ± 3.7	27.9 ± 6.8	15.6 ± 3.0
Dy	13.2 ± 2.3	15.2 ± 2.1	27.1 ± 5.1	17.4 ± 3.4	14.1 ± 1.7	12.7 ± 1.4	12.0 ± 1.4
Er	6.1 ± 0.7	5.9 ± 1.2	8.8 ± 1.5	6.1 ± 0.7	6.9 ± 0.8	7.5 ± 1.0	6.1 ± 1.0
Yb	4.0 ± 0.4	3.9 ± 0.5	4.1 ± 0.7	3.5 ± 0.3	4.1 ± 0.4	4.0 ± 0.4	3.3 ± 0.3
distance to rim [µm]	798	292	43	51	663	40	256
nearest mineral	ol	cpx	cpx	ol	cpx	ol	ol

a: opx below detection limit

±: one standard deviation

italics denote analyses that were not considered for modeling because of their large error

Table 3-5 (continued): $D^{cpx/olpx}$

	62A_07-opx-2-08	62A_07-opx-2-09	62A_07-opx-2-10
Na	8.2 ± 0.3	11.1 ± 0.4	22.5 ± 0.5
K	1.1 ± 0.2	0.7 ± 0.1	0.9 ± 0.1
Sc	1.9 ± 0.0	1.9 ± 0.0	2.2 ± 0.0
Ti	2.5 ± 0.1	2.7 ± 0.1	3.4 ± 0.1
V	1.6 ± 0.0	1.7 ± 0.0	2.0 ± 0.1
Cr	1.6 ± 0.0	1.8 ± 0.0	1.8 ± 0.1
Sr	51.7 ± 3.9	87.3 ± 4.7	92.1 ± 8.1
Y	7.9 ± 0.4	10.6 ± 0.4	15.2 ± 1.1
Zr	6.1 ± 0.3	7.4 ± 0.3	15.9 ± 1.2
La	108.0 ± 33.6	236.7 ± 79.6	202.2 ± 61.4
Ce	62.7 ± 14.4	180.5 ± 60.6	153.4 ± 33.3
Nd	52.5 ± 14.1	154.4 ± 85.7	a
Sm	46.4 ± 19.2	a	60.1 ± 28.3
Eu	34.9 ± 10.8	44.6 ± 15.0	147.8 ± 87.7
Gd	16.8 ± 3.4	20.1 ± 4.4	56.3 ± 25.2
Dy	11.5 ± 1.6	13.8 ± 1.7	25.5 ± 5.1
Er	6.6 ± 0.8	7.2 ± 0.9	11.1 ± 1.7
Yb	3.9 ± 0.5	3.3 ± 0.3	5.4 ± 0.6
distance to rim [µm]	545	185	34
nearest mineral	ol	ol	cpx

a: opx below detection limit

±: one standard deviation

italics denote analyses that were not considered for modeling because of their large error

CHAPTER 3

Table 3-5 (continued): $D^{opx/opx}$

	62B_03-opx-2-1	62B_03-opx-2-2	62B_07-opx-2-3	62B_07-opx-2-4	62B_07-opx-2-5	62B_07-opx-2-6	62B_07-opx-2-7
Na	22.4 ± 1.0	17.2 ± 0.7	12.2 ± 0.6	18.7 ± 1.1	23.3 ± 1.3	11.4 ± 0.8	14.7 ± 1.1
K	2.9 ± 1.1	2.6 ± 1.0	3.3 ± 1.2	2.8 ± 1.0	2.8 ± 1.0	3.6 ± 1.3	2.7 ± 1.0
Sc	2.1 ± 0.1	1.9 ± 0.1	1.9 ± 0.1	2.0 ± 0.1	2.1 ± 0.1	2.0 ± 0.1	1.9 ± 0.1
Ti	3.6 ± 0.3	3.1 ± 0.2	3.0 ± 0.2	3.2 ± 0.2	3.4 ± 0.3	3.1 ± 0.2	3.1 ± 0.2
V	2.2 ± 0.1	1.9 ± 0.1	1.9 ± 0.1	2.1 ± 0.1	2.3 ± 0.1	1.9 ± 0.1	1.9 ± 0.1
Cr	2.2 ± 0.0	2.0 ± 0.0	1.5 ± 0.0	2.1 ± 0.0	2.1 ± 0.0	1.6 ± 0.0	1.8 ± 0.0
Sr	271.3 ± 36.6	88.3 ± 10.4	48.4 ± 5.5	202.9 ± 25.6	102.2 ± 12.4	63.8 ± 7.4	113.9 ± 13.4
Y	13.3 ± 0.7	10.4 ± 0.5	8.1 ± 0.4	10.4 ± 0.5	10.9 ± 0.6	8.3 ± 0.6	9.9 ± 0.5
Zr	17.6 ± 1.4	10.8 ± 0.8	6.7 ± 0.5	10.3 ± 0.8	11.6 ± 0.9	7.5 ± 0.6	8.7 ± 0.7
La	a	104.7 ± 28.1	47.0 ± 9.8	393.9 ± 183.7	102.8 ± 23.9	70.7 ± 13.1	a
Ce	942.7 ± 655.8	91.9 ± 23.9	38.4 ± 4.6	264.0 ± 63.2	80.3 ± 12.1	60.4 ± 8.2	137.0 ± 25.8
Nd	a	62.4 ± 19.9	25.0 ± 4.4	242.3 ± 114.9	69.2 ± 24.1	32.6 ± 6.5	79.8 ± 22.0
Sm	a	27.4 ± 11.8	16.9 ± 3.9	77.3 ± 36.5	32.5 ± 10.2	23.9 ± 6.5	56.3 ± 24.5
Eu	84.4 ± 41.2	55.7 ± 21.7	20.4 ± 5.3	39.0 ± 12.8	30.1 ± 9.8	16.6 ± 4.0	40.8 ± 13.4
Gd	62.6 ± 25.6	65.9 ± 12.0	13.8 ± 2.9	39.3 ± 12.1	22.2 ± 5.5	17.1 ± 4.6	32.8 ± 9.1
Dy	23.8 ± 4.3	15.0 ± 2.3	8.7 ± 1.2	16.6 ± 3.1	14.4 ± 3.0	11.1 ± 1.4	16.6 ± 2.4
Er	8.8 ± 1.2	8.1 ± 1.6	6.9 ± 0.8	10.1 ± 1.4	9.7 ± 1.3	7.0 ± 0.9	8.1 ± 0.9
Yb	5.5 ± 1.0	4.1 ± 0.5	5.3 ± 0.6	4.6 ± 0.5	5.1 ± 0.6	5.1 ± 0.6	4.4 ± 0.5
distance to rim [µm]	97	54	1099	100	55	1143	173
nearest mineral	ol	ol	ol	sp	ol	ol	ol

a: opx below detection limit

±: one standard deviation

italics denote analyses that were not considered for modeling because of their large error

Table 3-5 (continued): $D^{opx/opx}$

	62B_08-opx-2-3	62B_08-opx-1-1	62B_11-opx-3-1	62B_11-opx-3-2
Na	20.1 ± 1.1	13.1 ± 0.7	14.1 ± 0.8	18.8 ± 1.1
K	1.6 ± 0.6	0.9 ± 0.4	2.1 ± 0.8	3.9 ± 1.4
Sc	2.0 ± 0.1	1.9 ± 0.1	1.9 ± 0.1	1.8 ± 0.1
Ti	3.4 ± 0.3	3.1 ± 0.2	2.8 ± 0.2	2.8 ± 0.2
V	2.0 ± 0.1	1.9 ± 0.1	1.8 ± 0.1	1.7 ± 0.1
Cr	2.0 ± 0.0	1.9 ± 0.0	1.7 ± 0.0	1.9 ± 0.0
Sr	173.3 ± 21.6	128.2 ± 15.4	102.1 ± 12.1	173.8 ± 21.2
Y	12.3 ± 0.6	10.0 ± 0.5	9.8 ± 0.5	10.7 ± 0.8
Zr	14.0 ± 1.1	10.9 ± 0.8	8.4 ± 0.6	8.8 ± 0.7
La	541.8 ± 211.2	211.8 ± 62.9	297.8 ± 89.1	623.5 ± 254.6
Ce	312.9 ± 82.9	152.7 ± 29.8	130.5 ± 28.4	287.3 ± 124.8
Nd	188.0 ± 81.1	97.8 ± 31.2	102.8 ± 31.5	159.7 ± 71.1
Sm	93.2 ± 51.9	50.2 ± 19.9	39.6 ± 13.1	84.1 ± 39.7
Eu	76.5 ± 34.2	39.7 ± 13.4	45.9 ± 18.3	51.2 ± 26.7
Gd	55.6 ± 20.2	25.2 ± 9.4	21.9 ± 5.2	27.3 ± 8.2
Dy	18.5 ± 3.5	10.8 ± 2.0	14.1 ± 1.9	16.5 ± 2.4
Er	8.8 ± 1.4	7.7 ± 0.9	8.6 ± 1.2	7.8 ± 1.3
Yb	4.4 ± 0.5	5.2 ± 0.6	5.6 ± 0.6	4.0 ± 0.4
distance to rim [µm]	82	281	249	75
nearest mineral	opx	ol	ol	ol

a: opx below detection limit

±: one standard deviation

italics denote analyses that were not considered for modeling because of their large error

Table 3-6: Equilibrium temperatures [°C] calculated after Witt-Eickchen and O'Neill (2005)

	25A_07-opx-2-1	25A_07-opx-1-1	25A_07-opx-1-2	25A_12-opx-2-1	25A_12-opx-1-1	25A_12-opx-1-2	25A_12-opx-1-3	25A_12-opx-1-4
Sc	1178 ± 51	1178 ± 51	1194 ± 52	1191 ± 52	1187 ± 51	1220 ± 53	1217 ± 53	1159 ± 50
Sc ^a	1208 ± 40	1207 ± 40	1220 ± 41	1217 ± 41	1213 ± 40	1240 ± 41	1237 ± 41	1192 ± 39
Ti	879 ± 44	965 ± 51	947 ± 51	962 ± 62	951 ± 51	964 ± 51	994 ± 54	912 ± 46
V ^a	1114 ± 30	1150 ± 32	1158 ± 32	1144 ± 33	1150 ± 33	1170 ± 32	1192 ± 34	1095 ± 29
Cr ^a	1145 ± 96	1145 ± 96	1191 ± 91	1185 ± 95	1163 ± 95	1078 ± 109	1050 ± 115	987 ± 128
Sr	1155 ± 10	1083 ± 13	1197 ± 55	1197 ± 55	1252 ± 16	1136 ± 10	1084 ± 15	1114 ± 10
Y	967 ± 28	1117 ± 32	1092 ± 36	1113 ± 34	1166 ± 38	1071 ± 35	1026 ± 29	1018 ± 28
Zr	930 ± 17	1060 ± 20	1056 ± 21	1300 ± 42	1077 ± 23	1036 ± 20	977 ± 20	965 ± 18
La	1152 ± 48	1152 ± 48	1059 ± 50	1300 ± 42	1220 ± 33	1036 ± 20	1057 ± 45	1061 ± 44
Ce	1091 ± 31	1091 ± 31	1089 ± 50	1313 ± 43	1216 ± 27	1095 ± 30	1061 ± 33	1064 ± 32
Nd	1129 ± 52	1129 ± 52	1089 ± 50	1240 ± 65	1256 ± 46	1085 ± 54	1061 ± 33	989 ± 63
Sm	1120 ± 79	1120 ± 79	1089 ± 113	1259 ± 74	1157 ± 77	1085 ± 54	1061 ± 33	1018 ± 94
Eu	1066 ± 94	1066 ± 94	1074 ± 103	1259 ± 74	1152 ± 64	1085 ± 54	1061 ± 33	852 ± 87
Gd	1088 ± 66	1088 ± 66	1012 ± 65	1207 ± 93	1168 ± 96	1001 ± 64	926 ± 80	1032 ± 65
Dy	1100 ± 55	1100 ± 55	1050 ± 57	1207 ± 93	1106 ± 55	1026 ± 52	958 ± 51	890 ± 49
Er	1075 ± 61	1075 ± 61	1054 ± 59	1085 ± 60	1082 ± 61	1044 ± 59	1026 ± 72	909 ± 55
Yb	994 ± 87	1089 ± 95	1092 ± 103	1065 ± 91	1057 ± 123	1127 ± 111	1220 ± 111	908 ± 95
Ca_in_opx (SIMS)	890	1117	1006	1207	1146	1029	981	1009
distance to rim	108	477	65	761	1056	53	74	115

a: calculated after Seitz et al. (1999)

±: one standard deviation

Table 3-6 (continued): Equilibrium temperatures [°C] calculated after Witt-Eickchen and O'Neill (2005)

	25A_12-opx-1-5	25A_12-opx-1-6	25A_12-opx-1-7	25A_12-opx-1-8	25A_12-opx-1-9	25A_12-opx-1-10	25A_12-opx-1-11	25A_01-opx-2-1
Sc	1179 ± 51	1178 ± 51	1187 ± 51	1174 ± 50	1189 ± 51	1199 ± 52	1185 ± 51	1224 ± 54
Sc ^a	1208 ± 40	1207 ± 40	1214 ± 40	1204 ± 40	1215 ± 40	1223 ± 41	1212 ± 40	1243 ± 42
Ti	988 ± 54	962 ± 52	981 ± 52	959 ± 51	967 ± 52	980 ± 58	955 ± 52	980 ± 52
V ^a	1162 ± 33	1163 ± 32	1165 ± 33	1155 ± 33	1157 ± 32	1167 ± 34	1162 ± 33	1176 ± 32
Cr ^a	1182 ± 94	1160 ± 95	1131 ± 99	1134 ± 100	1135 ± 100	1164 ± 97	1172 ± 93	1051 ± 114
Sr	1231 ± 18	1211 ± 10	1196 ± 15	1165 ± 15	1219 ± 15	1197 ± 30	1193 ± 17	1096 ± 11
Y	1128 ± 33	1104 ± 33	1115 ± 33	1077 ± 30	1123 ± 36	1116 ± 44	1119 ± 32	1097 ± 33
Zr	1088 ± 23	1058 ± 24	1053 ± 20	1037 ± 20	1065 ± 22	1078 ± 33	1065 ± 24	1022 ± 19
La	1214 ± 35	1145 ± 37	1160 ± 37	1130 ± 37	1127 ± 38	1197 ± 34	1148 ± 39	1004 ± 48
Ce	1164 ± 29	1146 ± 30	1148 ± 33	1047 ± 33	1169 ± 46	1197 ± 34	1146 ± 30	1004 ± 48
Nd	1140 ± 53	1113 ± 62	1087 ± 56	1047 ± 33	1109 ± 54	1174 ± 68	1167 ± 51	994 ± 92
Sm	1063 ± 70	1028 ± 89	1059 ± 86	986 ± 91	1104 ± 112	1152 ± 76	1125 ± 102	975 ± 75
Eu	1107 ± 64	1040 ± 71	1144 ± 66	1048 ± 96	974 ± 75	1090 ± 106	1148 ± 71	1072 ± 67
Gd	1107 ± 64	1040 ± 71	1036 ± 65	1053 ± 67	1071 ± 64	1121 ± 61	1109 ± 63	1072 ± 67
Dy	1060 ± 61	1100 ± 56	1077 ± 56	998 ± 101	1141 ± 86	1100 ± 55	1100 ± 55	932 ± 68
Er	1130 ± 65	1047 ± 76	1043 ± 72	1005 ± 89	1058 ± 61	1093 ± 67	1085 ± 70	1028 ± 60
Yb	1053 ± 92	1124 ± 107	1073 ± 94	1005 ± 89	1181 ± 130	1181 ± 104	1074 ± 120	1145 ± 102
Ca_in_opx (SIMS)	1109	1090	1090	1039	1115	1101	1089	1014
distance to rim	1162	702	291	379	392	839	1056	161

a: calculated after Seitz et al. (1999)

±: one standard deviation

Table 3-6 (continued): Equilibrium temperatures [°C] calculated after Witt-Eickchen and O'Neill (2005)

	25A_02-opx-1-1	25A_02-opx-1-2	25A_02-opx-1-3	25A_02-opx-1-4	25A_02-opx-1-5	25A_02-opx-1-6	25A_02-opx-1-7	25A_02-opx-1-8
Sc	1146 ± 49	1201 ± 52	1204 ± 52	1195 ± 51	1202 ± 52	1208 ± 52	1187 ± 51	1137 ± 48
Sc ^a	1181 ± 39	1225 ± 41	1227 ± 41	1220 ± 40	1226 ± 41	1230 ± 41	1214 ± 40	1174 ± 38
Ti	887 ± 44	983 ± 61	987 ± 61	1002 ± 59	995 ± 55	986 ± 55	979 ± 53	872 ± 44
V ^a	1131 ± 30	1189 ± 39	1163 ± 32	1171 ± 36	1175 ± 33	1183 ± 35	1166 ± 32	1064 ± 29
Cr ^a	1166 ± 92	1179 ± 97	1140 ± 100	1161 ± 100	1174 ± 94	1156 ± 97	1160 ± 96	1053 ± 116
Sr	1059 ± 20	1142 ± 12	1187 ± 11	1203 ± 10	1178 ± 10	1153 ± 14	1219 ± 10	1128 ± 10
Y	963 ± 26	1117 ± 35	1144 ± 38	1154 ± 33	1113 ± 36	1116 ± 37	1125 ± 33	995 ± 29
Zr	957 ± 18	1081 ± 29	1078 ± 23	1085 ± 26	1066 ± 22	1074 ± 24	1072 ± 21	967 ± 18
La	978 ± 50	1096 ± 39	1178 ± 35	1183 ± 35	1164 ± 36	1206 ± 34	1177 ± 35	1137 ± 35
Ce	940 ± 40	1105 ± 32	1177 ± 29	1218 ± 37	1114 ± 30	1132 ± 29	1169 ± 28	1065 ± 39
Nd	937 ± 69	1112 ± 52	1097 ± 55	1163 ± 58	1046 ± 77	1101 ± 53	1092 ± 54	1007 ± 57
Sm			1077 ± 101	1250 ± 75		1094 ± 103	1143 ± 98	1021 ± 81
Eu		1138 ± 82	1174 ± 64	1211 ± 80	1011 ± 79	1008 ± 101	1101 ± 81	892 ± 76
Gd		1032 ± 63	1052 ± 65	1124 ± 68	1100 ± 63	1077 ± 63	1193 ± 63	893 ± 73
Dy	970 ± 50	1077 ± 76	1143 ± 57	1067 ± 67	1073 ± 54	1113 ± 55	1095 ± 55	987 ± 56
Er	908 ± 58	1111 ± 64	1097 ± 78	1067 ± 61	1062 ± 60	1006 ± 58	1074 ± 81	898 ± 60
Yb	977 ± 106		939 ± 97		1086 ± 132	1147 ± 102		861 ± 71
Ca_in_opx (SIMS)	943	1047	1085	1123	1041	1061	1122	994
distance to rim	65	223	506	484	246	71	581	76

a: calculated after Seitz et al. (1999)

±: one standard deviation

Table 3-6 (continued): Equilibrium temperatures [°C] calculated after Witt-Eickchen and O'Neill (2005)

	25A_02-opx-1-31	25A_02-opx-1-32	25A_02-opx-1-33	25A_02-opx-1-34	25A_02-opx-1-35	25A_02-opx-1-36	25A_02-opx-1-37	25A_02-opx-1-38
Sc	1171 ± 50	1184 ± 51	1164 ± 50	1179 ± 51	1195 ± 52	1116 ± 47	1209 ± 53	1147 ± 48
Sc ^a	1211 ± 40	1211 ± 40	1196 ± 39	1207 ± 40	1220 ± 41	1157 ± 38	1231 ± 41	1183 ± 38
Ti	995 ± 53	1010 ± 55	974 ± 53	980 ± 52	976 ± 52	861 ± 43	998 ± 54	966 ± 52
V ^a	1171 ± 33	1188 ± 34	1183 ± 32	1188 ± 33	1195 ± 33	1083 ± 29	1210 ± 34	1148 ± 32
Cr ^a	1160 ± 95	1153 ± 95	1203 ± 88	1074 ± 109	1179 ± 91	1045 ± 113	1160 ± 94	1136 ± 99
Sr	1288 ± 12	1239 ± 10	1198 ± 11	1257 ± 15	1202 ± 10	1164 ± 12	1204 ± 16	1307 ± 12
Y	1127 ± 32	1137 ± 37	1085 ± 31	1085 ± 31	1136 ± 32	961 ± 26	1107 ± 31	1132 ± 34
Zr	1087 ± 22	1079 ± 21	1038 ± 20	1031 ± 21	1072 ± 21	942 ± 18	1059 ± 21	1058 ± 21
La	1224 ± 34	1181 ± 35	1075 ± 43	1134 ± 56	1145 ± 43	1030 ± 45	1133 ± 37	1239 ± 53
Ce	1164 ± 29	1143 ± 29	1129 ± 30	1173 ± 28	1138 ± 29	970 ± 38	1044 ± 33	1193 ± 29
Nd	1106 ± 53	1087 ± 64	1042 ± 72	1098 ± 56	1095 ± 68	965 ± 64	942 ± 68	1180 ± 53
Sm	1117 ± 86		1086 ± 89		1143 ± 85			
Eu	1098 ± 68		1029 ± 69		1142 ± 72		1069 ± 98	1232 ± 65
Gd	1136 ± 66		986 ± 64		1140 ± 55	816 ± 67	979 ± 89	1062 ± 82
Dy	1127 ± 58		1194 ± 81		1123 ± 57	869 ± 59	1169 ± 59	1193 ± 62
Er	1093 ± 60		1032 ± 57		1107 ± 64	906 ± 68	1034 ± 82	1130 ± 62
Yb	1224 ± 116		1128 ± 103		1256 ± 112	995 ± 101	1267 ± 129	1119 ± 110
Ca_in_opx (SIMS)	1130	1119	1050	1032	1089	939	1028	1139
distance to rim	426	463	180	61	437	57	58	203

a: calculated after Seitz et al. (1999)

±: one standard deviation

Table 3-6 (continued): Equilibrium temperatures [°C] calculated after Witt-Eickchen and O'Neill (2005)

	25A_02-opx-1-39	25A_02-opx-1-41	25A_02-opx-1-42	25A_02-opx-1-43	25A_02-opx-1-44	25A_02-opx-1-45	25A_02-opx-1-46	25A_02-opx-1-47
Sc	1146 ± 49	1152 ± 49	1187 ± 51	1070 ± 44	1210 ± 53	1081 ± 45	1130 ± 47	1153 ± 49
Sc ^a	1181 ± 39	1186 ± 39	1214 ± 40	1120 ± 36	1232 ± 41	1129 ± 36	1169 ± 38	1187 ± 39
Ti	945 ± 50	951 ± 49	1033 ± 58	808 ± 39	1028 ± 56	801 ± 38	922 ± 48	920 ± 47
V ^a	1143 ± 31	1162 ± 32	1202 ± 34	1018 ± 25	1236 ± 36	1054 ± 27	1127 ± 31	1119 ± 31
Cr ^a	1135 ± 97	1118 ± 101	1165 ± 94	1027 ± 116	1243 ± 85	1092 ± 102	1071 ± 110	1022 ± 119
Sr	1209 ± 15	1246 ± 20	1244 ± 14	1126 ± 21	1213 ± 10	1097 ± 11	1135 ± 17	1191 ± 10
Y	1075 ± 31	1064 ± 30	1148 ± 36	908 ± 25	1104 ± 31	942 ± 26	993 ± 27	1041 ± 29
Zr	1034 ± 20	1041 ± 21	1097 ± 22	897 ± 17	1091 ± 21	873 ± 18	973 ± 21	994 ± 19
La	1099 ± 40	1111 ± 39	1159 ± 41	1008 ± 48	1111 ± 46	873 ± 18	976 ± 52	1170 ± 36
Ce	1105 ± 31	1104 ± 35	1199 ± 29	992 ± 40	1130 ± 38	965 ± 40	1108 ± 31	1108 ± 31
Nd	1013 ± 60		1180 ± 72		1145 ± 54		921 ± 73	1096 ± 54
Sm			1124 ± 79				1125 ± 79	1102 ± 68
Eu	1041 ± 73	1053 ± 68	1050 ± 71	942 ± 100	1020 ± 71	805 ± 77	938 ± 81	1089 ± 63
Gd		998 ± 78	1193 ± 60	872 ± 65	966 ± 64	960 ± 54	1044 ± 55	1114 ± 58
Dy	1158 ± 59	1071 ± 55	1248 ± 73	1021 ± 76	1179 ± 82	872 ± 53	937 ± 54	1025 ± 57
Er	1073 ± 59		1042 ± 58	819 ± 53	1119 ± 62	843 ± 72	1101 ± 113	962 ± 81
Yb	1092 ± 94	1076 ± 105	1123 ± 98	898 ± 75	1139 ± 99	909	988	1067
Ca_in_opx (SIMS)	1065	1071	1116	925	1021	58	64	43
distance to rim	346	227	495	57	43			

a: calculated after Seitz et al. (1999)

±: one standard deviation

Table 3-6 (continued): Equilibrium temperatures [°C] calculated after Witt-Eickchen and O'Neill (2005)

	25A_02-opx-1-48	25A_02-opx-1-49	25A_02-opx-1-50	25A_02-opx-1-51	25A_02-opx-1-52	25A_02-opx-1-53	25A_02-opx-1-54
Sc	1167 ± 50	1180 ± 51	1190 ± 52	1183 ± 51	1142 ± 48	1175 ± 51	1161 ± 50
Sc ^a	1198 ± 39	1209 ± 40	1216 ± 40	1210 ± 40	1178 ± 38	1204 ± 40	1193 ± 39
Ti	878 ± 44	977 ± 52	1002 ± 54	1015 ± 56	950 ± 51	1040 ± 57	1008 ± 55
V ^a	1120 ± 30	1175 ± 33	1202 ± 34	1210 ± 34	1140 ± 32	1189 ± 33	1183 ± 33
Cr ^a	1091 ± 103	1029 ± 120	1183 ± 91	1161 ± 94	1136 ± 97	1196 ± 89	1190 ± 90
Sr	1111 ± 16	1260 ± 19	1228 ± 14	1199 ± 20	1263 ± 15	1313 ± 17	1286 ± 13
Y	1006 ± 28	1036 ± 29	1132 ± 34	1107 ± 34	1082 ± 33	1179 ± 35	1163 ± 34
Zr	974 ± 18	1015 ± 22	1077 ± 21	1073 ± 21	1044 ± 22	1126 ± 22	1080 ± 23
La	992 ± 54	1043 ± 46	1140 ± 39	1108 ± 43	1044 ± 22	1362 ± 34	1238 ± 35
Ce	1063 ± 34	1077 ± 33	1090 ± 33	1136 ± 34	1160 ± 32	1273 ± 28	1208 ± 33
Nd		956 ± 69	1082 ± 58			1236 ± 82	1227 ± 50
Sm		962 ± 96	1161 ± 102				1096 ± 127
Eu	1064 ± 73	904 ± 99	1087 ± 77	1128 ± 73	1010 ± 102	1144 ± 68	1174 ± 69
Gd	908 ± 69	1050 ± 81	1052 ± 61	1079 ± 64	1003 ± 62	1169 ± 59	1133 ± 60
Dy	986 ± 70	1102 ± 58	1128 ± 60	1196 ± 69	1055 ± 56	1262 ± 65	1238 ± 65
Er	922 ± 56		1065 ± 69	1046 ± 62	1055 ± 60	1055 ± 60	1006 ± 58
Yb	1083 ± 110	986 ± 84	1031 ± 93	1159 ± 105	1007 ± 86	1118 ± 120	1038 ± 90
Ca_in_opx (SIMS)	968	993	1057	1052	1061	1167	1148
distance to rim	70	43	194	306	346	334	254

a: calculated after Seitz et al. (1999)

±: one standard deviation

Table 3-6 (continued): Equilibrium temperatures [°C] calculated after Witt-Eickchen and O'Neill (2005)

	25B_06-opx-1-01	25B_05-opx-2-01	25B_05-opx-2-02	62A_07-opx-2-01	62A_07-opx-2-02	62A_07-opx-2-03	62A_07-opx-2-04
Sc	1175 ± 59	1197 ± 60	1229 ± 63	1189 ± 53	1205 ± 55	1177 ± 53	1229 ± 56
Sc ^a	1205 ± 46	1223 ± 47	1248 ± 49	1218 ± 42	1230 ± 43	1208 ± 42	1248 ± 44
Ti	934 ± 48	1004 ± 53	1017 ± 56	1030 ± 45	1040 ± 46	964 ± 40	1050 ± 46
V ^a	1156 ± 27	1210 ± 30	1249 ± 32	1228 ± 29	1250 ± 30	1190 ± 28	1269 ± 32
Cr ^a	1008 ± 149	1098 ± 124	1029 ± 146	1192 ± 93	1146 ± 100	1040 ± 121	1086 ± 111
Sr	1065 ± 16	1191 ± 11	1079 ± 11	1274 ± 16	1228 ± 14	1044 ± 16	1140 ± 13
Y	1033 ± 24	1166 ± 21	1041 ± 25	1148 ± 24	1145 ± 28	999 ± 26	1065 ± 25
Zr	974 ± 11	1081 ± 12	1021 ± 11	1094 ± 15	1099 ± 15	975 ± 12	1050 ± 13
La	1000 ± 50	1110 ± 45	959 ± 59	1165 ± 47	1064 ± 44		
Ce		1098 ± 35	965 ± 37	1206 ± 27	1078 ± 31		
Nd	1026 ± 59	1117 ± 64	994 ± 58	1116 ± 55	1066 ± 61		1044 ± 41
Sm		1119 ± 119		1068 ± 100	1060 ± 82		
Eu		1039 ± 67		1088 ± 77	1062 ± 90	843 ± 83	924 ± 75
Gd	971 ± 68	1085 ± 58	953 ± 66	1046 ± 67	1068 ± 93	922 ± 75	997 ± 78
Dy	966 ± 47	1153 ± 50	1030 ± 46	1139 ± 83	1003 ± 53	853 ± 52	965 ± 65
Er		1062 ± 71	963 ± 54	1140 ± 168	1147 ± 181	984 ± 81	1142 ± 85
Yb	1084 ± 120	1167 ± 133	1278 ± 150	1116	1087	1118 ± 195	1241 ± 189
Ca_in_opx (SIMS)	1014	1108	968	798	292	889	983
distance to rim	170	288	39			43	51

a: calculated after Seitz et al. (1999)

±: one standard deviation

Table 3-6 (continued): Equilibrium temperatures [°C] calculated after Witt-Eickchen and O'Neill (2005)

	62A_07-opx-2-05	62A_07-opx-2-06	62A_07-opx-2-07	62A_07-opx-2-08	62A_07-opx-2-09	62A_07-opx-2-10
Sc	1195 ± 54	1232 ± 57	1204 ± 54	1201 ± 54	1196 ± 54	1136 ± 50
Sc ^a	1222 ± 42	1251 ± 44	1229 ± 42	1227 ± 42	1223 ± 43	1176 ± 40
Ti	1037 ± 45	1057 ± 45	1063 ± 47	1043 ± 45	1002 ± 42	872 ± 35
V ^a	1243 ± 29	1262 ± 30	1265 ± 32	1250 ± 30	1225 ± 30	1129 ± 28
Cr ^a	1178 ± 94	1018 ± 124	1186 ± 93	1192 ± 92	1110 ± 104	1085 ± 123
Sr	1245 ± 16	1258 ± 20	1239 ± 15	1253 ± 18	1162 ± 14	1153 ± 18
Y	1143 ± 24	1097 ± 23	1142 ± 27	1169 ± 28	1057 ± 22	940 ± 25
Zr	1106 ± 13	1061 ± 15	1102 ± 16	1121 ± 16	1076 ± 14	926 ± 16
La	1111 ± 42	1181 ± 44	1089 ± 48	1144 ± 56	1029 ± 51	1050 ± 47
Ce	1164 ± 27	1166 ± 27	1160 ± 28	1194 ± 44	1046 ± 33	
Nd	1074 ± 69	1138 ± 61	1139 ± 62	1123 ± 57		
Sm	1070 ± 110		1080 ± 85	1029 ± 93		
Eu	1090 ± 63	1012 ± 88	1071 ± 79	1028 ± 72	976 ± 73	
Gd	1119 ± 73	1011 ± 72	1165 ± 75	1143 ± 77	1094 ± 75	
Dy	1026 ± 51	1059 ± 52	1076 ± 54	1090 ± 62	1031 ± 52	867 ± 56
Er	1087 ± 80	1047 ± 78	1140 ± 103	1107 ± 85	1068 ± 79	905 ± 68
Yb	1128 ± 167	1137 ± 166	1282 ± 201	1164 ± 181	1279 ± 200	973 ± 134
Ca_in_opx (SIMS)	1113	1050	1115	1132	1028	928
distance to rim	663	40	256	545	185	34

a: calculated after Seitz et al. (1999)

±: one standard deviation

Table 3-6 (continued): Equilibrium temperatures [°C] calculated after Witt-Eickchen and O'Neill (2005)

	62B_03-opx-2-1	62B_03-opx-2-2	62B_07-opx-2-3	62B_07-opx-2-4	62B_07-opx-2-5	62B_07-opx-2-6	62B_07-opx-2-7	62B_08-opx-2-3
Sc	1161 ± 24	1206 ± 26	1179 ± 25	1179 ± 25	1155 ± 24	1180 ± 25	1197 ± 26	1172 ± 25
Sc ^a	1193 ± 19	1229 ± 20	1218 ± 19	1208 ± 19	1189 ± 19	1209 ± 19	1222 ± 20	1203 ± 19
Ti	853 ± 37	927 ± 40	952 ± 42	908 ± 39	884 ± 38	937 ± 42	927 ± 41	890 ± 38
V ^a	1093 ± 21	1150 ± 20	1147 ± 21	1099 ± 19	1074 ± 19	1150 ± 20	1157 ± 21	1119 ± 19
Cr ^a	975 ± 54	1045 ± 42	1201 ± 32	997 ± 50	999 ± 43	1182 ± 37	1085 ± 40	1035 ± 44
Sr	1000 ± 18	1164 ± 20	1270 ± 22	1039 ± 17	1140 ± 19	1220 ± 21	1123 ± 18	1061 ± 18
Y	984 ± 17	1067 ± 18	1161 ± 18	1066 ± 17	1049 ± 18	1149 ± 27	1083 ± 17	1009 ± 16
Zr	915 ± 14	1004 ± 15	1107 ± 17	1014 ± 16	990 ± 15	1081 ± 16	1047 ± 17	954 ± 14
La		1150 ± 45	1282 ± 42		1153 ± 39	1216 ± 33		
Ce		1128 ± 45	1291 ± 25	971 ± 32	1151 ± 26	1202 ± 25	1064 ± 29	949 ± 35
Nd		1091 ± 63	1287 ± 43	878 ± 71	1073 ± 67	1224 ± 46	1047 ± 50	913 ± 67
Sm		1147 ± 115	1274 ± 68	935 ± 93	1108 ± 76	1181 ± 71	993 ± 93	
Eu	861 ± 93	935 ± 80	1160 ± 72	1006 ± 74	1064 ± 81	1218 ± 72	997 ± 72	878 ± 86
Gd	847 ± 81	837 ± 33	1205 ± 67	937 ± 68	1069 ± 66	1140 ± 80	976 ± 64	868 ± 73
Dy	886 ± 45	1010 ± 47	1196 ± 53	979 ± 54	1022 ± 65	1107 ± 45	980 ± 42	950 ± 52
Er	990 ± 51	1023 ± 81	1086 ± 50	937 ± 49	954 ± 47	1083 ± 60	1021 ± 47	990 ± 61
Yb	962 ± 90	1134 ± 72	982 ± 58	1061 ± 62	998 ± 60	997 ± 59	1088 ± 73	1084 ± 65
Ca_in_opx (SIMS)	930	980	1180	966	1053	1164	1062	999
distance to rim	97	54	1099	100	55	1143	173	82

a: calculated after Seitz et al. (1999)

±: one standard deviation

Table 3-6 (continued): Equilibrium temperatures [°C] calculated after Witt-Eickchen and O'Neill (2005)

	62B_08-opx-1-1	62B_11-opx-3-1	62B_11-opx-3-2
Sc	1199 ± 25	1214 ± 26	1233 ± 27
Sc ^a	1224 ± 20	1236 ± 20	1250 ± 21
Ti	933 ± 41	981 ± 45	985 ± 45
V ^a	1142 ± 20	1189 ± 22	1196 ± 22
Cr ^a	1062 ± 42	1135 ± 37	1075 ± 39
Sr	1105 ± 18	1140 ± 19	1060 ± 17
Y	1082 ± 17	1087 ± 17	1056 ± 25
Zr	1003 ± 15	1054 ± 16	1047 ± 17
La	1045 ± 43	999 ± 40	
Ce	1048 ± 30	1071 ± 34	
Nd	1013 ± 56	1004 ± 53	936 ± 72
Sm	1016 ± 85	1064 ± 75	921 ± 91
Eu	1003 ± 76	973 ± 88	
Gd	1038 ± 99	1073 ± 64	1018 ± 75
Dy	1115 ± 65	1029 ± 42	982 ± 43
Er	1041 ± 51	998 ± 55	1034 ± 68
Yb	988 ± 60	957 ± 55	1141 ± 64
Ca_in_opx (SIMS)	1092	1046	993
distance to rim	281	249	75

a: calculated after Seitz et al. (1999)

±: one standard deviation

CHAPTER 3

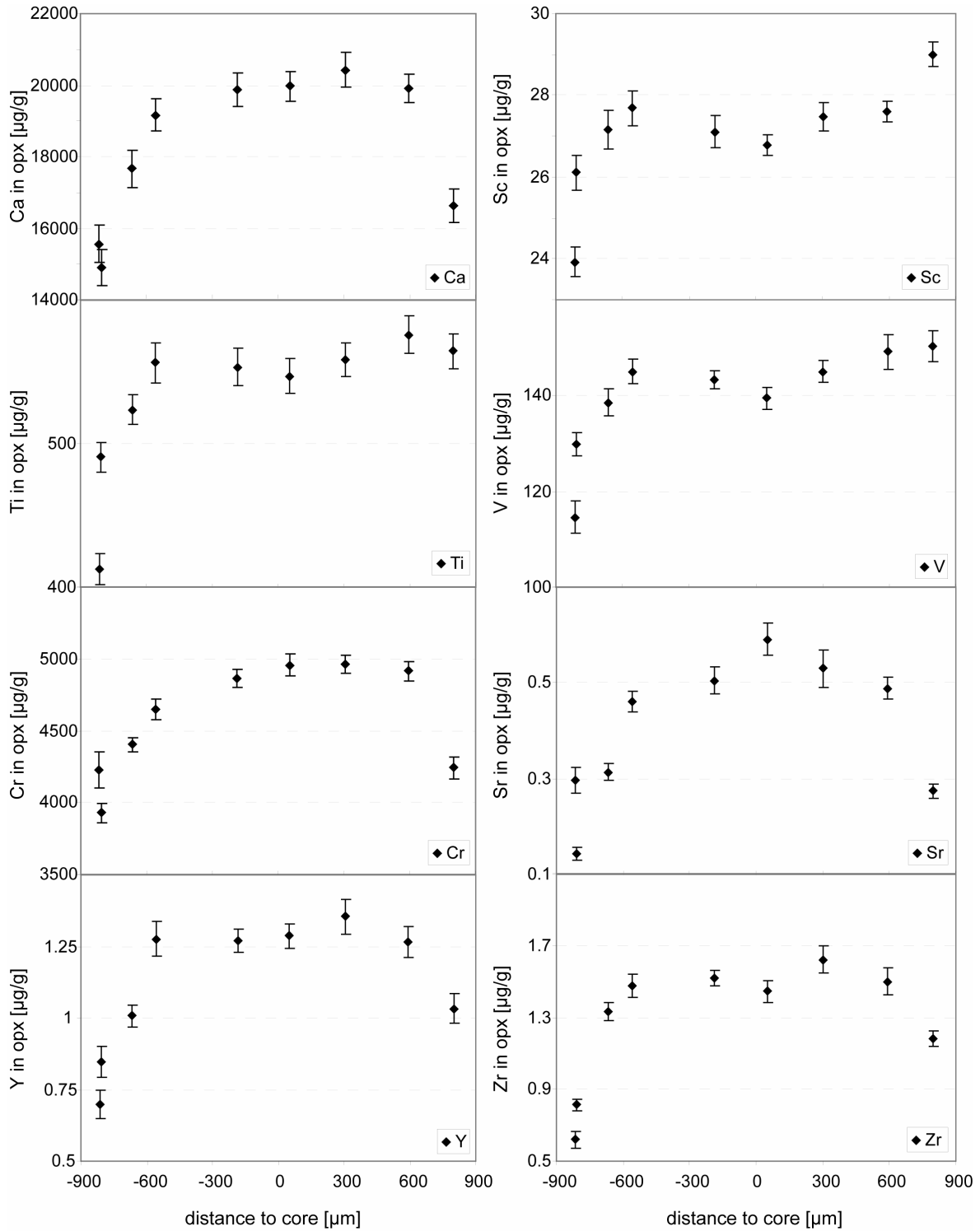


Figure A3-1: Trace element zoning profiles in opx (profile 238-62A-07-opx-2). The opx grain is in contact with cpx on the left side and olivine on the right side. Error bars denote one standard deviation.

CHAPTER 3

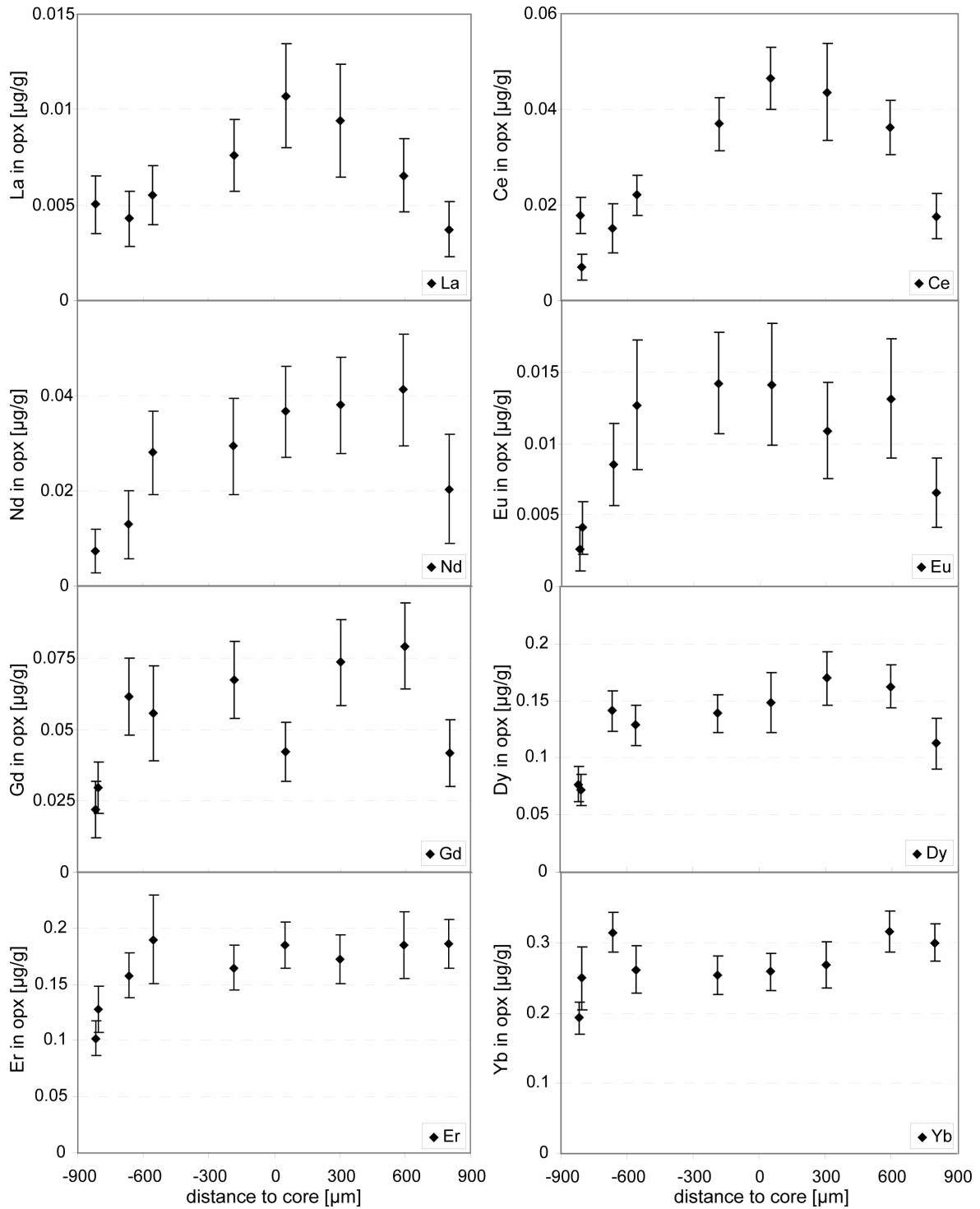


Figure A3-2: REE zoning profiles in opx (profile 238-62A-07-opx-2); Sm is not shown because its concentrations close to the detection limit. The opx grain is in contact with cpx on the left side and olivine on the right side. Error bars denote one standard deviation.

CHAPTER 3

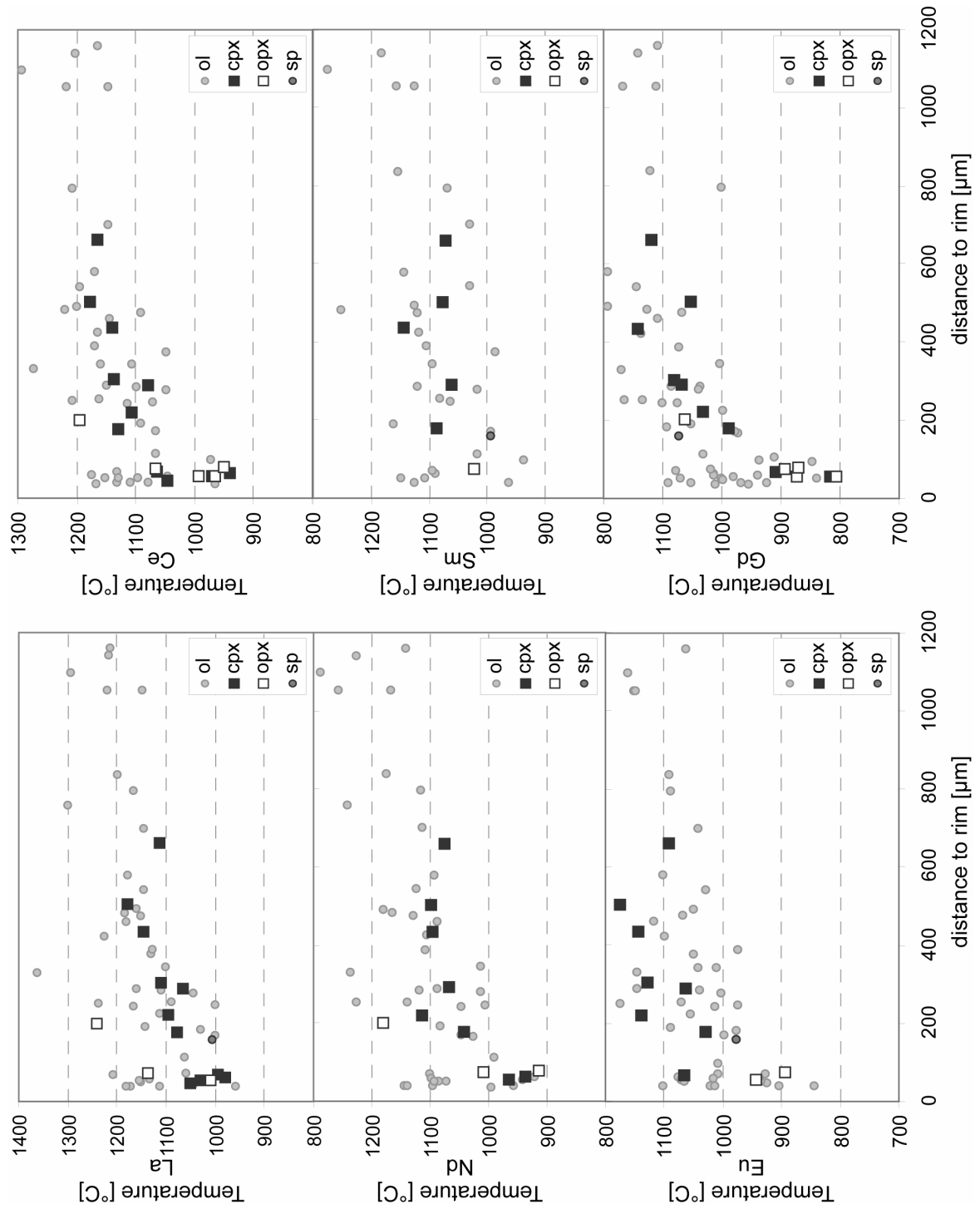


Figure A3-3: Equilibration temperatures of REE in opx versus the distance to the closest rim for the complete data set. The data are grouped depending on what mineral phase is in contact at the nearest rim.

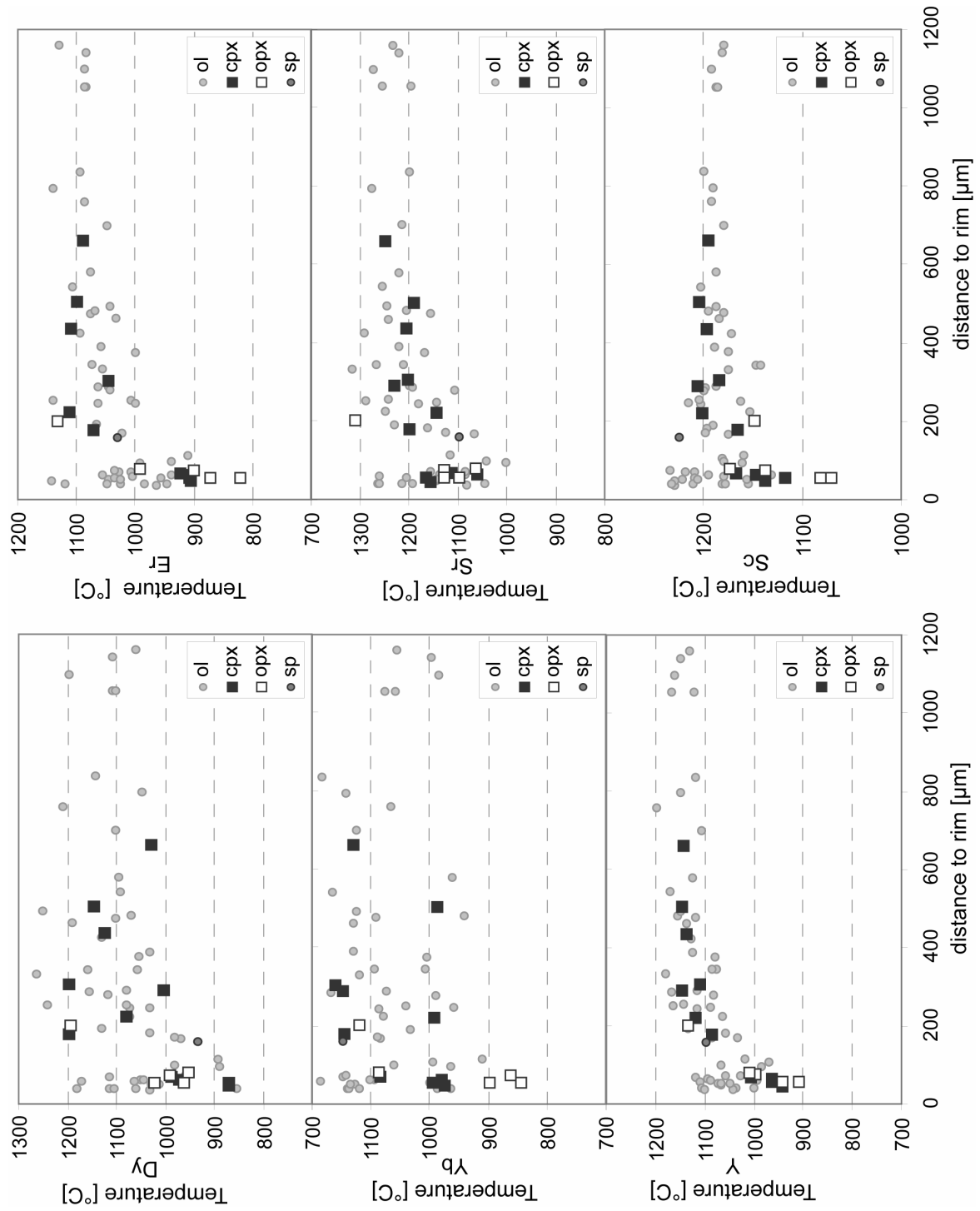


Figure A3-4: Equilibration temperatures of selected REE and trace elements in opx versus the distance to the closest rim for the complete data set. The data are grouped depending on what mineral phase is in contact at the nearest rim.

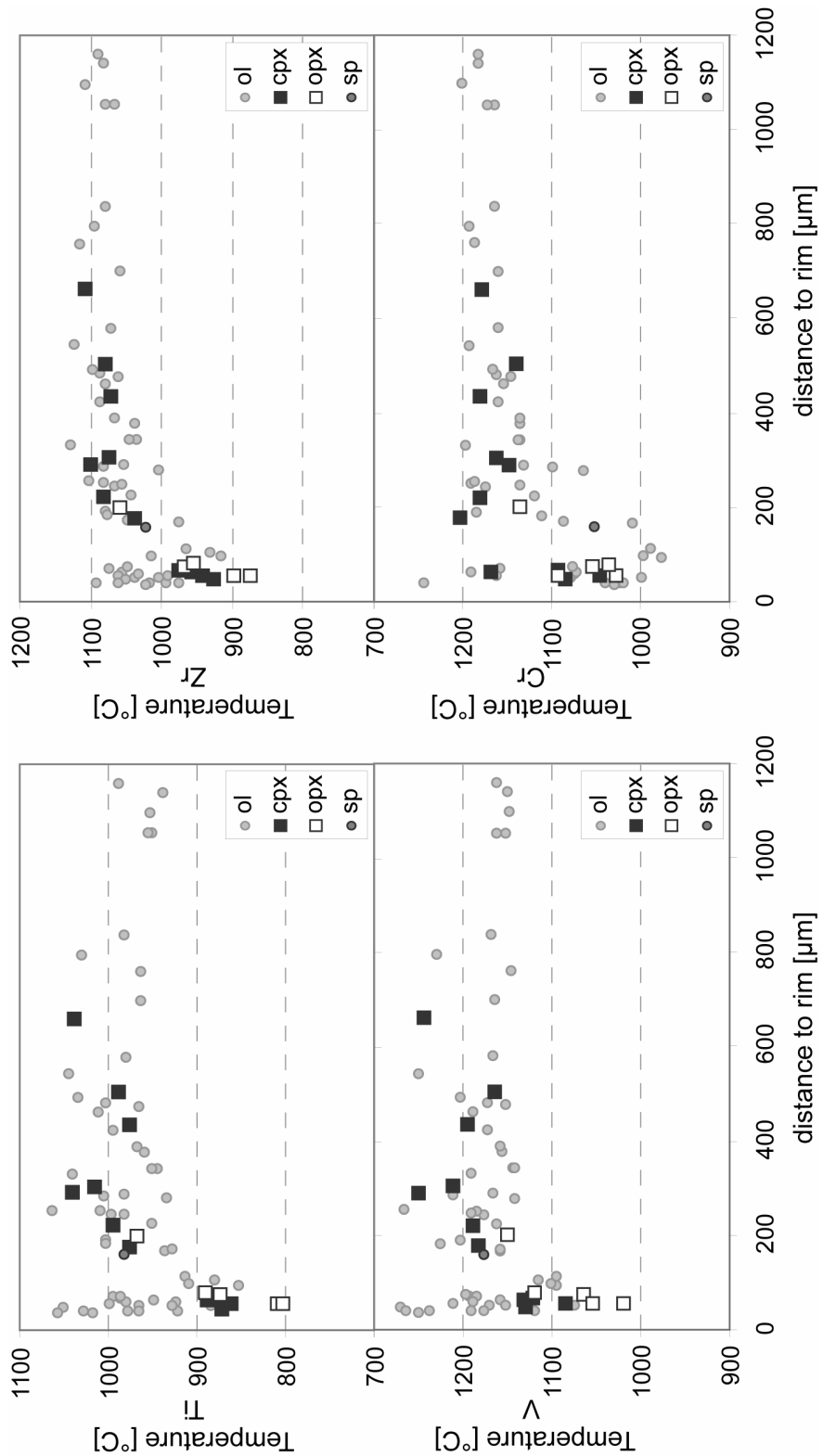


Figure A3-5: Equilibration temperatures of selected trace elements in opx versus the distance to the closest rim for the complete data set. The data are grouped depending on what mineral phase is in contact at the nearest rim.

CHAPTER 3

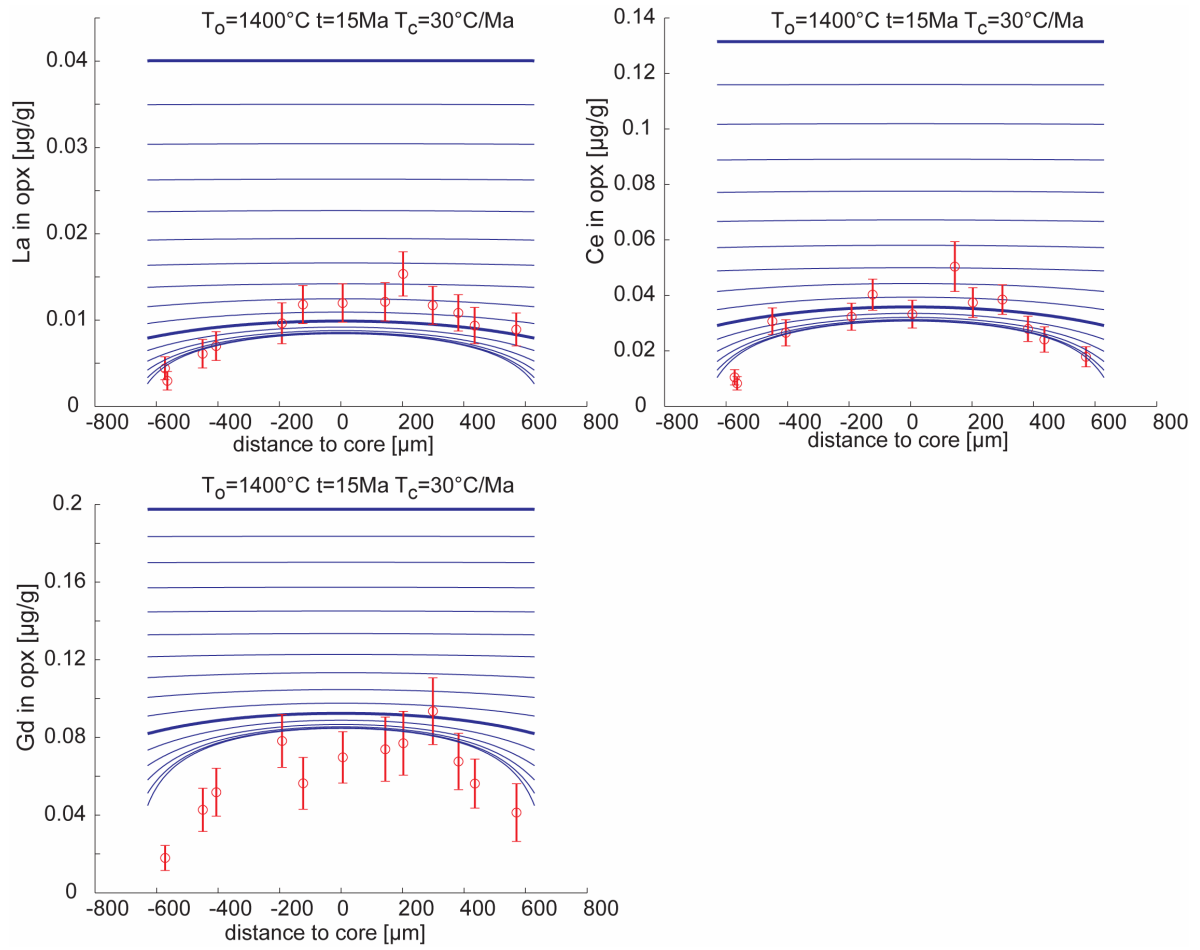


Figure A3-6: Calculated diffusion profile of La, Ce, Y for PS66-238-25A-02-opx-1 during continuous cooling from 1400°C to 950°C at 30°C/Ma. Each line denotes 1 million year increment. The starting composition and results after 10 million years are highlighted. Total time is 15 million years. Grain radius is 850 µm. The opx grain is in contact with cpx on the left side and olivine on the right side; the profile is slightly asymmetric toward the olivine contact. Error bars denote one standard deviation.

CHAPTER 3

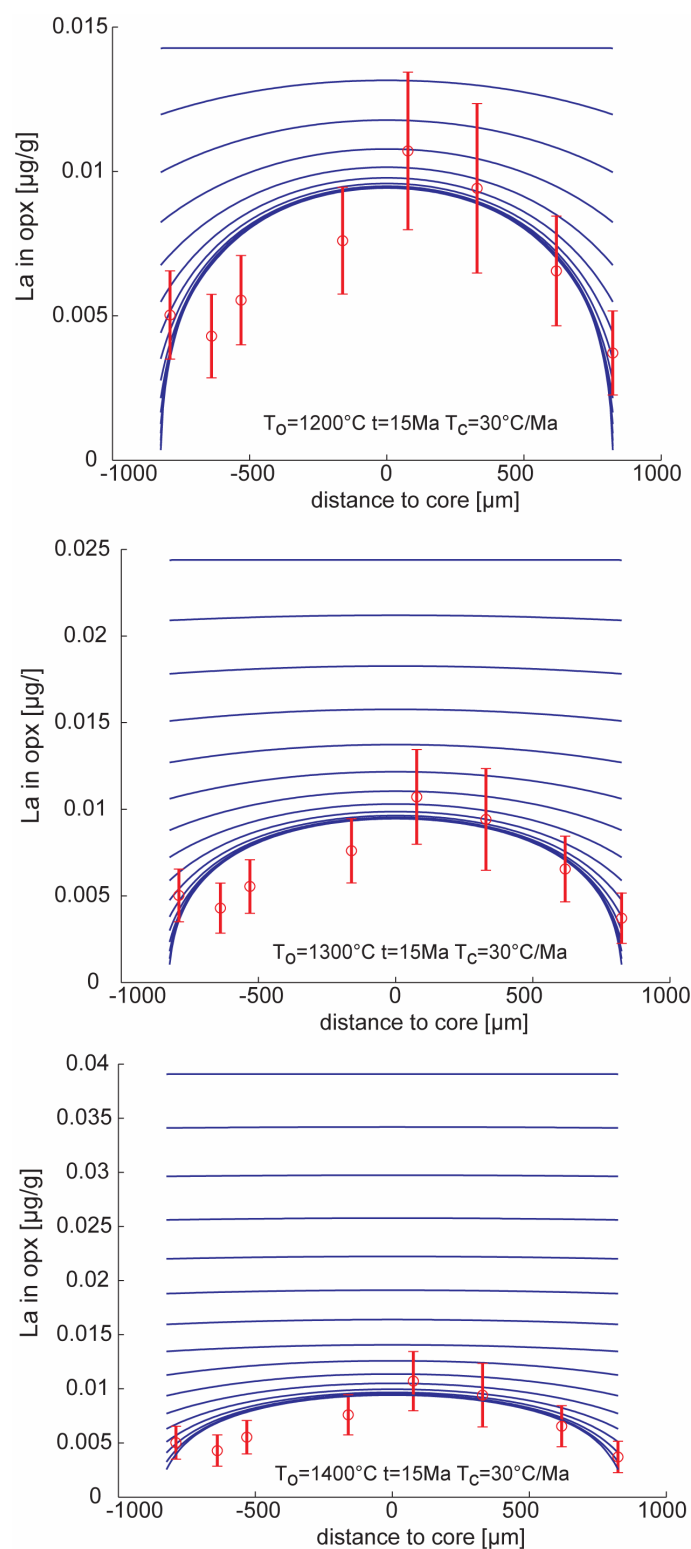


Figure A3-7: Influence of starting temperature on diffusion profiles in opx at a constant cooling rate of 50°C. Starting temperatures are 1200°C, 1300°C and 1400°C, respectively. All profiles are calculated for a total duration of 15 million years. Each line denotes one million year increments. Starting composition of opx is calculated to be in equilibrium with 238-62A-cpx average at the respective starting temperature. Grain radius is 850 μm .

CHAPTER 4

CATION DIFFUSION IN ORTHOPYROXENE

4.1 INTRODUCTION

The interpretation of the petrogenetic and thermal history of terrestrial and meteoritic rocks that involves pyroxenes requires accurate diffusion data for each mineral type (Delaney et al., 1981, Lasaga, 1983, Ganguly et al., 1994). A still growing number of experimental studies exist now on cation volume diffusion in rock-forming minerals. With data covering a wider range of P-T conditions and compositions, different parameters emerge that exert control on relative diffusivities. However, experimentally determined cationic diffusion data for orthopyroxene did not exist until ten years ago (Schwandt et al., 1998) and kinetic modelling, including cooling rate determinations, was subject to significant uncertainty. Since then, diffusion of magnesium (Schwandt et al., 1998), chromium (Ganguly et al., 2007), lead (Cherniak, 2001) and selected rare earth elements (REE) (Cherniak and Liang, 2007) in enstatite has been studied.

This chapter is the result of a study on orthopyroxene zoning in mantle peridotites from Gakkel Ridge with the objective to determine cooling rates through the temperature-dependent trace element partitioning between orthopyroxene (opx) and clinopyroxene (cpx). The results of this study differ from the experimentally determined REE diffusion data set of Cherniak and Liang (2007). Before the results of this study will be presented and discussed, known systematics of diffusion in silicate systems and opx with special emphasis on REE diffusion will be summarized.

4.1.1 Diffusion in silicates

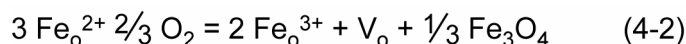
Diffusion in solids may be subdivided into volume, grain boundary and surface diffusion. Solid diffusion systems are often thermally activated and follow an Arrhenius relationship of the form:

$$D = D_0 \times e^{\left(\frac{-E}{RT}\right)} \quad (4-1)$$

where D_0 is the pre-exponential factor, representing the diffusion coefficient at infinitively high temperatures, E stands for the activation energy, R is the gas constant and T the temperature.

Volume diffusion, that is the diffusion through the crystal lattice, takes place via atomic jumps. It commonly occurs either by an interstitial (migration of atoms through interstitial sites) or vacancy mechanism (atoms move by interchanging position with a vacancy); the vacancy mechanism is by far the most important of all diffusion mechanisms (Ganguly, 2002).

Volume diffusion is controlled by external and internal factors. Among the external factors, temperature has the strongest effect on diffusion coefficients (eq. 4-1), as it provides the energy to exceed the energy barrier between the sites. Other factors include pressure and volatile species such as oxygen fugacity (fO_2) and fugacities of water-related species. Although, increasing pressure should reduce the diffusion coefficient, experimental data so far only show a minor effect; in contrast, the importance of oxygen fugacity is strong (Ganguly, 2002). Here, octahedral vacancies are controlled by the oxidation reaction of divalent cations, primarily Fe^{2+} , following the reaction (Ganguly et al., 2007):



with V_o as the vacancy; Fe^{3+} on the M1 site is then compensated by an increase in M2 vacancies and the diffusion coefficient will vary as a function of fO_2 . Diffusion in diopside is commonly a function of the iron content with variation of up to two orders of magnitude at a change from almost nil to 1.5 wt% (Sneeringer et al., 1984, Dimanov et al., 1996, Cherniak, 1998a, Cherniak, 2001). Abundance of other multivalent trace elements will only play an important role for the diffusive process at very low concentrations of transition metals (Chakraborty, 1997).

Diffusion coefficients, similar to partition coefficients, are controlled by crystal lattice parameters. An empirical correlation between pre-exponential factor D_0 and activation energy E has been noted, the so-called “compensation law”, in many materials such as silicates (Hart, 1981), and melts (Hofmann, 1980). This empirical correlation can be linked to a number of physical/crystallographic parameters. Zener (1952) showed that such a correlation is

theoretically expected if a large fraction of the migration entropy is expended during an atomic jump due to the elastic strain of the crystal lattice. Hence, a relation between motion energy and the elastic Young's modulus (a measure for the rigidity of a material) is expected. Such a correlation of diffusion parameters with mineral elastic properties has been noted in a number of minerals (Cherniak, 1998a, Cherniak, 2001). Minerals with a larger Young's modulus generally exhibit larger activation energies which also seems to apply to REE diffusion (Cherniak, 1998c).

In particular, different crystal-chemical parameters influence diffusion rates in silicates and oxides; in the order of decreasing importance, there are (e.g. Dowty, 1980): (1) ionic porosity, (2) electrostatic site energy, (3) cationic charge and (4) ionic radius:

(1) A first order relation exists between diffusivity and ionic porosity (Dowty, 1980, Fortier and Giletti, 1989). Ionic porosity is defined as the fraction of the unit cell volume in a mineral not occupied by an ion. Ionic porosity also proxies for the mean metal-oxygen bond length/strength in minerals. Minerals with a lower ionic porosity and therefore closer packing tend to have higher activation energies for diffusion and lower diffusivities. Higher values indicate more open mineral structures, which would enhance diffusive rates. The relationship with D_0 is less strong.

(2) Electrostatic (Madelung) site energies: The site energy is defined as the work required to bring the ion into the site from an infinite distance, and a rough proportionality is proposed between site energy and activation energy. In a given structure, ions with lower (meaning less negative) site energy will tend to be more mobile (Dowty, 1980).

(3) An important parameter of relative diffusive rate is the cationic charge. Pronounced decreases in relative diffusion rate with increasing cationic charge of the element of interest have been noted in feldspars, zircon and calcite (Cherniak, 1998c). However, the variation in diffusivity also increases with increasing rigidity of the crystal lattice. Therefore, the effect of ionic charge appears to be less important in pyroxenes when compared to zircon, in particular for the trivalent and tetravalent cations (van Orman et al., 1998).

(4) Relative diffusion rates usually increase with decreasing ionic radius (as in diopside, feldspar, zircon, apatite or olivine (Cherniak et al., 1997, van Orman et al., 1998, Cherniak, 2000, Cherniak, 2001, van Orman et al., 2001, Cherniak, 2003), with rare exceptions such as in garnet (van Orman et al., 2002b). Orthopyroxene was found to fall into the latter group despite its mineralogical similarity to diopside (Cherniak and Liang, 2007).

4.1.2 Diffusion in orthopyroxene

The structure of a mineral has important effects on crystallographically controlled processes such as volume diffusion. Magnesium-rich, calcium-poor orthopyroxenes (opx) have crystal structures that belong to the space group *Pbca* (e.g. Cameron and Papike, 1981).

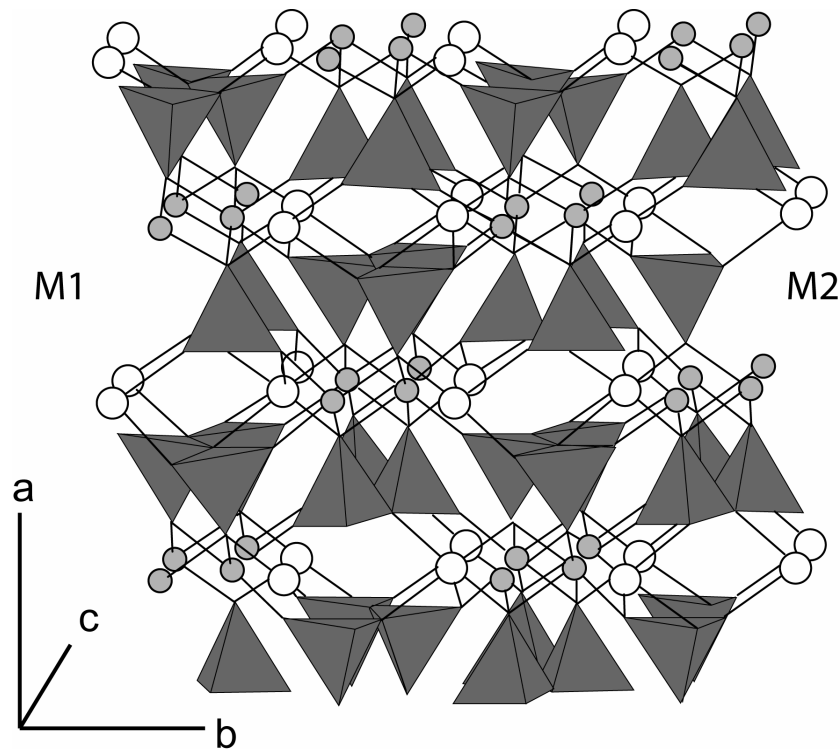


Figure 4-1: Crystal model showing the partial unit cell for orthoenstatite viewed down the *c*-axis. *M1* and *M2* chains extend parallel to the *c*-axis, but are spaced apart along the *b*-axis and separated by tetrahedral layers along the *a*-direction (Schwandt et al., 1998).

In anisotropic crystals, diffusion will vary in different directions because the direction of a crystallographic symmetry axis may coincide with that of a principal diffusion axis. Diffusion

in opx is expected to be anisotropic with the three principal diffusion axes being parallel to the crystallographic axes (Ganguly and Tazzoli, 1994, Schwandt et al., 1998): (1) diffusion parallel to the c-axis along the chains of M1 and M2 octahedral sites, (2) diffusion parallel to the b-axis in the planes of M1 and M2 octahedral sites and (3) diffusion parallel to the a-axis perpendicular to the alternating octahedral and tetrahedral layers (Figure 4-2). Hence, relative diffusivities will decrease in the order: $D//c > D//b > D//a$ (Schwandt et al., 1998). Diffusion anisotropy would be also expected to decrease with increasing temperatures because of the relaxation of the crystal structure with increasing temperatures (Ganguly, 2002).

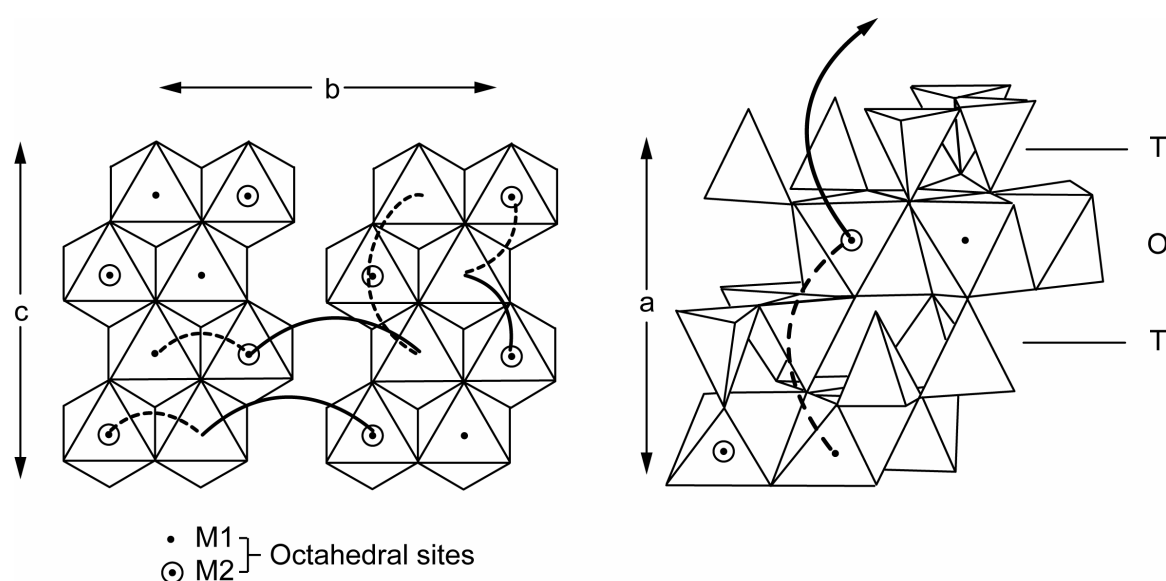


Figure 4-2: Schematic diagram of the stereochemical arrangement of octahedral sites in orthopyroxene along the a, b and c direction. The solid and dashed lines indicate the jump distances. Along a, there is a tetrahedral layer (T) between two successive octahedral layers (O) (Schwandt et al., 1998).

Cation ordering between the M1 and M2 site may also contribute to anisotropy. However, in enstatite, both sites are similar in size and show much less preferred ordering of Mg and Fe^{2+} than in clinopyroxenes (cpx) (Cameron and Papike, 1981, Schwandt et al., 1998). Therefore, no strong crystallographic control is expected in enstatite. So far, only diffusion of Cr has been found to be strongly anisotropic in enstatite (Ganguly et al., 2007), whereas Mg and Pb show only weak dependence on crystallographic direction (Schwandt et al., 1998, Cherniak, 2001).

4.1.3 REE diffusion in orthopyroxene and silicates

Rare earth elements (REE) and Sr are only incorporated in crystallographic sites in rock-forming minerals if Ca²⁺ sites are present. If Ca²⁺ sites are absent, they are incorporated at interstitial sites (Morris, 1975). When a trivalent REE exchanges for the divalent Ca, the excess charge must be compensated via a coupled substitution; REE incorporation into the enstatite structure is achieved by the coupled substitution ${}^{\text{VI}}\text{REE}^{3+} + {}^{\text{IV}}\text{Al}^{3+} \leftrightarrow {}^{\text{VI}}\text{M}^{2+} + {}^{\text{IV}}\text{Si}^{4+}$ (Schwandt and McKay, 1998).

REE diffusion in diopside depends on the relative oxygen fugacity, in agreement with diffusion by a vacancy mechanism (van Orman et al., 2001). Pb diffusion in enstatite also operates via a vacancy mechanism (Cherniak, 2001), while Cr-diffusion in opx operates via a mixture of vacancy and interstitial mechanisms, in proportions depending on the relative oxygen fugacity (Ganguly et al., 2007).

Diffusion of La, Nd, Eu, Gd and Yb in a near-end member enstatite was studied at 850-1250°C and 1bar under reducing (IW buffer) and oxidizing (air) conditions by Cherniak and Liang (2007). No dependence on $f\text{O}_2$ was seen except that diffusion of Eu under IW buffered conditions (in its divalent state) is over an order of magnitude faster than diffusion of Eu in air (when it is trivalent). Diffusion rates of the trivalent REE are essentially identical within error and found to be insensitive to changes in ionic radius within the experimental error. Activation energies are smaller in enstatite relative to diopside, and Cherniak and Liang (2007) suggested that significant fractionation of REE between coexisting pyroxenes occurs during partial melting and melt migration.

Enstatite has a very low ionic porosity (= 33.2, (Dahl, 1997)) but similar to diopside (= 34.3 (Fortier and Giletti, 1989)). Zircon with a slightly lower ionic porosity of 28.8 relative to enstatite shows dramatic fractionation of REE (Cherniak et al., 1997). However, that effect appears to be caused by at least in part by the difference in ionic size between the REE and the Zr-ion for which they substitute in zircon.

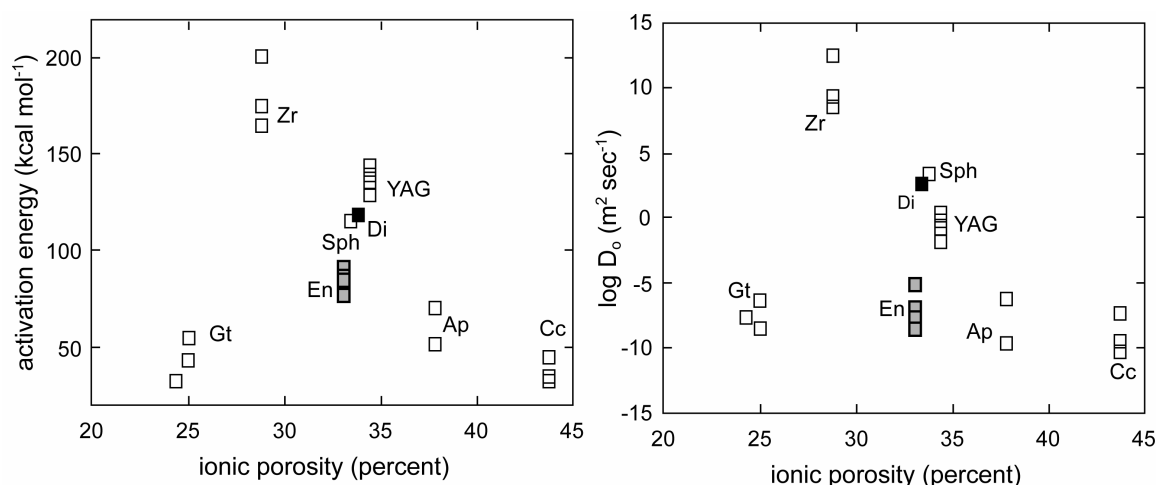


Figure 4-3: Plot of REE diffusion parameters in different minerals (Zr: zircon (Cherniak et al., 1997); Sph: sphene; YAG: yttrium aluminum garnet (Cherniak, 1998b); Di: diopside (van Orman et al., 2001); Ap: apatite (Cherniak, 2000); Cc: calcite (Cherniak, 1998c); Gt: garnet (van Orman et al., 2002b)) versus their ionic porosities (Dahl, 1997). Enstatite REE data from Cherniak and Liang (2007) are shown as grey squares, diopside (van Orman et al., 2001) is shown as a black square.

With the exception of garnet and enstatite, diffusion data of REE in minerals follows a good correlation of ionic porosity versus diffusion parameters (Figure 4-3). The small site energies of divalent cations for which REE substitute in garnet may be the reason for the deviation of garnet from the trend (Cherniak et al., 1997). No clear reason for the deviation of the trend for REE diffusion in enstatite is given.

4.2 METHODS AND RESULTS

This chapter is the result of a trace element partitioning study between orthopyroxene and clinopyroxene in two fresh spinel peridotites from Gakkel Ridge. Clinopyroxene and orthopyroxene trace element concentrations were obtained by SIMS (for analytical conditions and results, see Chapter 3). Both samples are very similar in their major element composition without core-rim zoning. Orthopyroxene, on the other hand, shows systematic core to rim zoning in all incompatible trace elements while clinopyroxene grains are unzoned. The zoning in orthopyroxene is the result of the down-temperature trace element exchange between cpx and opx. Witt-Eickschen and O'Neill (2005) studied the temperature-dependent trace element exchange between cpx and opx on a suite of well equilibrated spinel peridotite xenoliths and

CHAPTER 4

formulated geothermometers based on the opx-cpx partition coefficients. Using these temperature-dependent interpyroxene partition coefficients allows calculation of equilibrium temperatures at any given point in the orthopyroxene grain.

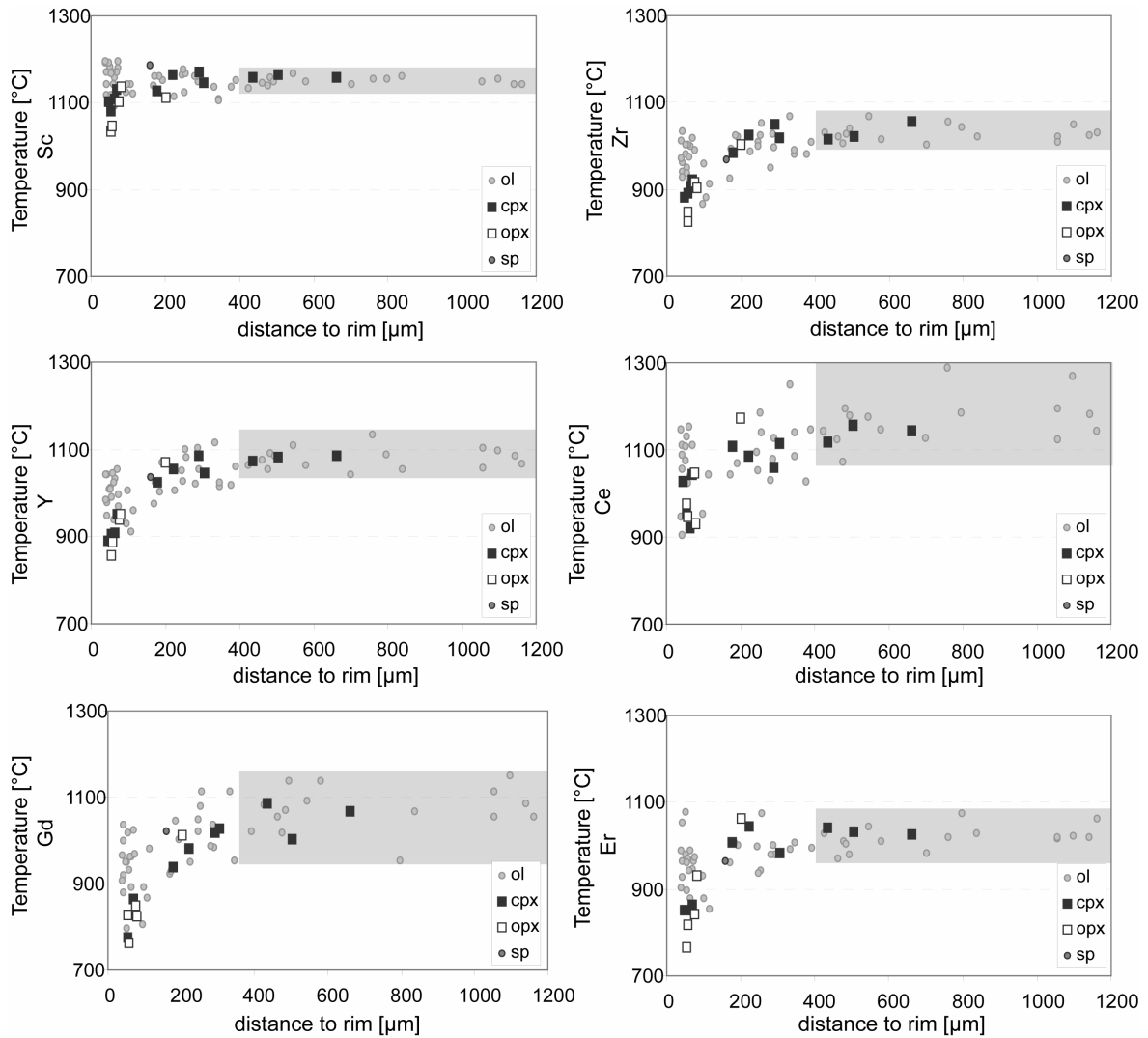


Figure 4-4: Equilibrium closure temperatures for selected TE in opx. At distances of more than 400 μm , the temperatures become constant within analytical error. The data are grouped depending on the nearest mineral in contact. At distances larger than 400 μm , no dependence on mineralogy in contact can be seen. Constant core equilibrium temperatures are shown by all modeled elements and average temperatures are calculated for each element.

Figure 4-4 shows calculated equilibrium temperatures for selected trace and rare earth elements versus their linear distance to the opx grain boundary. At distances further than 400 μm away from the grain boundary, temperatures reach a plateau and become constant within error. This systematic behavior is shown by all modeled elements, and thus, average core

CHAPTER 4

temperatures were calculated. Average equilibrium temperatures in the opx core and their standard deviation are reported in Table 4-1.

Table 4-1a: Average TE core temperatures in orthopyroxene in [°C]

Element	Sc	Sc ^a	Ti	V ^a	Cr ^a	Sr	Y	Zr	Ca_in_opx ^b
Temperature	1187	1214	969	1164	1178	1231	1143	1085	1134
±	7	6	28	25	14	31	29	18	43

a: calculated after Seitz et al. (1999)

b: calculated after Brey and Köhler (1990)

±: one standard deviation

Table 4-1b: Average REE core temperatures in orthopyroxene in [°C]

Element	La	Ce	Nd	Sm	Eu	Gd	Dy	Er	Yb
Temperature	1211	1210	1191	1141	1135	1142	1118	1092	1075
±	56	63	63	80	72	39	55	27	65

±: one standard deviation

The temperature calculated from the equilibrium partition coefficient between cpx and opx represents the “closure” temperature of the element exchange. At high temperatures, diffusion is efficient enough to ensure exchange equilibrium between cpx and opx. During cooling, the diffusion decreases exponentially and equilibrium can no longer be maintained, initially at the core and then proceeding outwards. The system “closes” and a closure profile develops (e.g. Dodson, 1986).

Dodson (1973) formalized the concept of closure temperature and formulated the equation.

$$\frac{E}{RT_c} = \ln \left(- \frac{ART_c^2 D_0}{E (dT/dt) a^2} \right) \quad (4-3)$$

where T_c is the closure temperature, D_0 the pre-exponential factor, E the activation energy, R the gas constant, a is the grain radius, (dT/dt) is the cooling rate and A is a geometric factor related to the grain geometry.

Hence, the closure temperature depends on the diffusion coefficient, the cooling rate and the grain radius. All these parameters control the shape and height of the “dome” of the

CHAPTER 4

closure temperature profile (see also Chapter 3, Figure 3-19 and -20) and the change in “height” in the profile center, ideally coinciding with the core of the grain, provides the highest resolution. The relative difference in core temperatures is then alone a function of either one of the parameters if the other two are fixed. The results of this chapter are based on the following assumptions: (1) both spinel peridotite samples were subject to the same cooling rate. They come from the same sample location, probably very closely spaced, considering their almost identical major and trace element composition. This assumption is also corroborated by forward numerical modeling of trace element profiles and closure temperature profiles (see Chapter 3). (2) each set of individual element closure temperatures is internally consistent. All trace element analyses are obtained from the same measurement spot; hence they share the parameters of grain size and geometry as well as major element composition. Therefore, the relative variation of closure temperatures is a direct expression of the relative diffusivity of the respective element.

Closure temperatures reach a constant value at distances of more than 400 μm from the rim and only vary within error. Averaging over distances more than 400 μm gives an acceptable statistical basis to obtain relative diffusivities for 16 elements. This is of course a generalization over the complete data set and the individual distance was not normalized to the grain size. However, variation in core temperatures because of grain size variation or anisotropy does not appear to be significant within error.

The objective is to obtain relative diffusivities for each element of the data set and this approach is robust at the precision of the temperature estimates. Looking only at relative diffusivities, grain size effects will cancel each other out because they affect each temperature estimate in a similar manner.

Therefore, in the order of decreasing relative diffusivity we obtain:

$$D_{\text{Ti}} \gg D_{\text{Yb}} > D_{\text{Zr}} > D_{\text{Er}} > D_{\text{Dy}} > (D_{\text{Ca}} \approx) D_{\text{Eu}} \approx D_{\text{Sm}} \approx D_{\text{Gd}} \approx D_{\text{Y}} > D_{\text{V}} > D_{\text{Cr}} > D_{\text{Sc}} > D_{\text{Nd}} > D_{\text{Ce}} > D_{\text{La}} > D_{\text{Sc}} > D_{\text{Sr}}.$$

Closure temperatures for the different REE vary systematically. This is unexpected because experimentally determined diffusion coefficients for REE are identical within error

(Cherniak and Liang, 2007) and hence the REE should all record similar closure temperatures. In contrast, closure temperatures for the light rare earth elements lie around 1210°C, whereas the heavy rare earth elements fall at 1080°C. A good correlation (R^2 of 0.96) between REE cationic radius and average core closure temperature can be obtained (Figure 4-5). The standard deviation is relatively large for certain elements but the difference between La and Er is significant. This increase in diffusivity with decreasing ionic radius is similar to what has been observed in clinopyroxene (van Orman et al., 2001). The good fit of Eu relative to its neighboring REE shows that it occurs in its trivalent state.

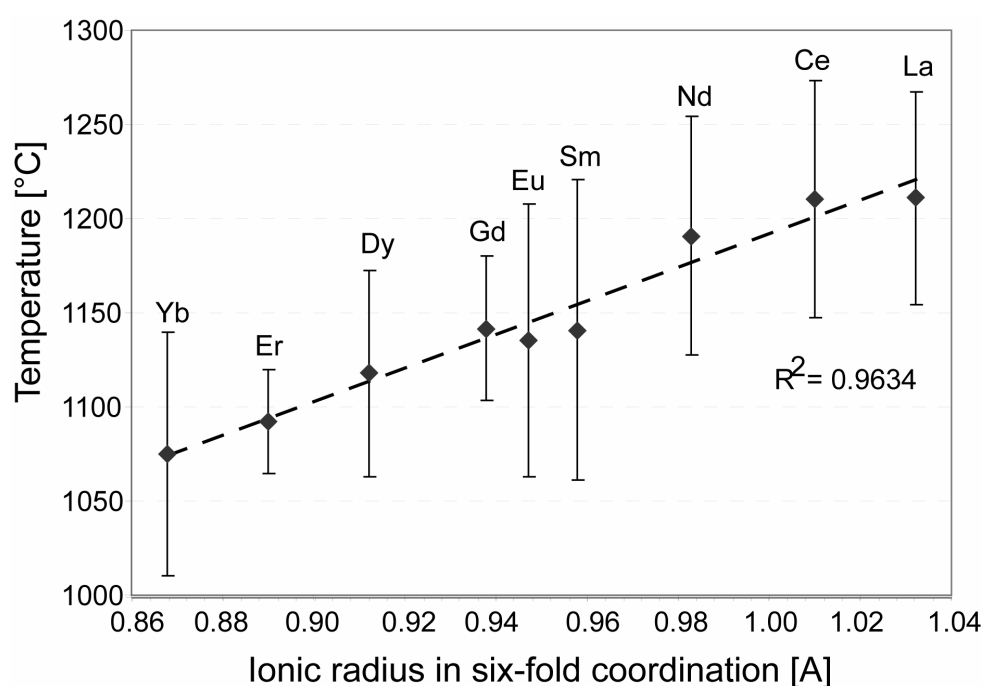


Figure 4-5: Average closure temperatures of REE in orthopyroxene at distances more than 400 μm versus their ionic radius in six-fold coordination (from Shannon, 1976). Error bars denote one standard deviation.

4.3 DISCUSSION

4.3.1 Diffusion of rare earth elements in orthopyroxene

Diffusion of REE in opx shows a clear dependence on ionic radius in this study similar to what is known for diffusion in diopside (van Orman et al., 2001). To further investigate the relative systematics and compare them to REE diffusion in diopside, closure temperatures were calculated for REE at various cooling rates using the REE diffusion coefficients for cpx (van

CHAPTER 4

Orman et al., 2002a) and opx (Cherniak and Liang, 2007). Dodson's formulation of closure temperature assumes sufficiently fast diffusion to change core compositions and is therefore not valid for slow diffusing species. Ganguly and Tirone (1999) extended Dodson's equation to include cases of arbitrary small diffusion (for details, see Chapter 3). Their formulation was applied and core closure temperatures for REE were calculated for different parameters using the software developed by the authors.

Figure 4-6 shows the results of the closure temperature calculations for REE at different cooling rates, temperatures and grain sizes. Closure temperatures calculated with the diffusion coefficients of Cherniak and Liang (2007) result in a flat line and are shown for comparison in Figure 4-6a. A good match with the measured distribution of closure temperatures is obtained for a cooling rate of $10^{\circ}\text{C}/\text{Ma}$ at a starting temperature of 1250°C and grain radius of $1160\ \mu\text{m}$ using the diffusion coefficients from van Orman et al. (2002a). The grain radius of $1160\ \mu\text{m}$ complies with the measurement farthest away from a rim in this data set. The influence of grain size and relative measurement position in the grain on the absolute closure temperature is shown for a grain radius of $580\ \mu\text{m}$ (Figure 4-6b) and for the case that the temperature was not obtained at the grain center but halfway between core and rim (Figure 4-6c). The grain radius has an effect on the absolute closure temperature and smaller grain sizes result in lower closure temperatures in the core. However, the relative fractionation between the REE at a given cooling rate remains the same in both scenarios and it does not seem to affect the average core temperature estimate. Temperatures determined about half-way from the grain center also do not deviate much from the core temperature. Therefore, the generalization over the complete data set will represent a good estimate of the true core temperature within our precision. The closure temperature model is relative insensitive to starting temperature (Figure 4-6d).

CHAPTER 4

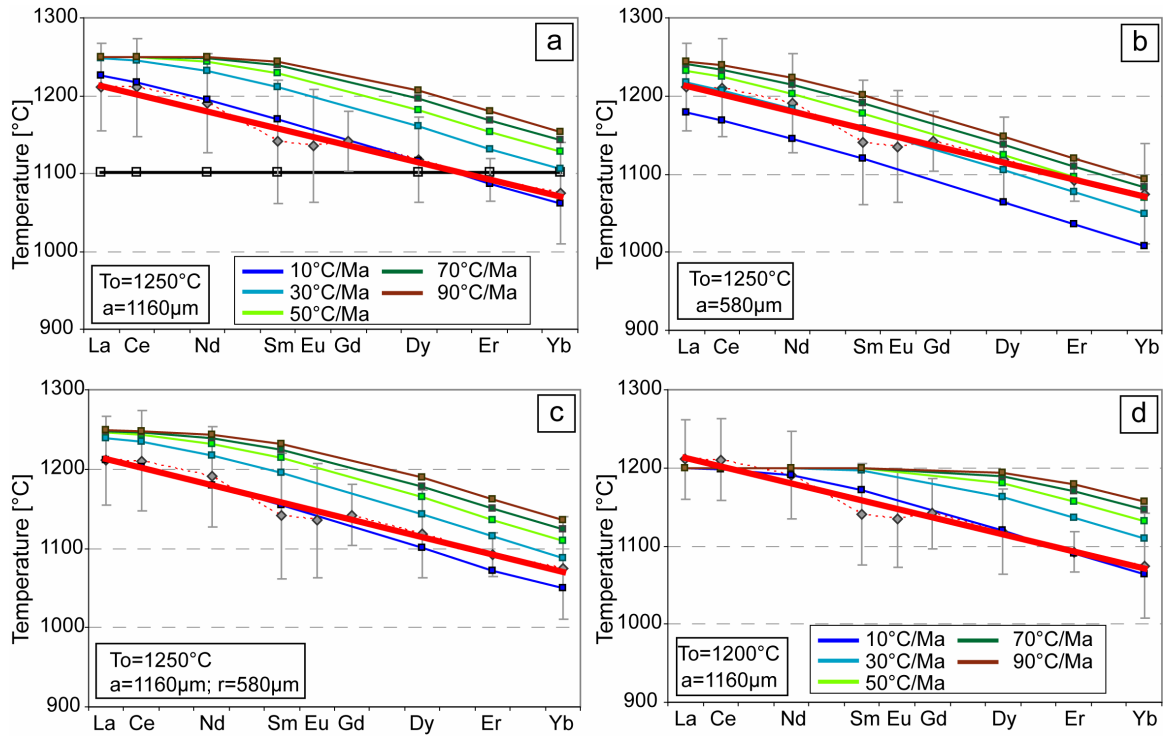


Figure 4-6: Calculated closure temperature for REE at different cooling rates, grain radii 'a' and starting temperatures T_0 . Data of this study are shown in grey in the background with the best fit as bold red line. The black solid line in (a) shows closure temperatures at a cooling rate of 10°C/Ma from diffusion coefficients by Cherniak and Liang (2007). All other closure temperatures are calculated with the diffusion data set for diopside from van Orman et al. (2002a). The best match for closure temperatures in opx is obtained by using diopside diffusion coefficients with a cooling rate of 10°C/Ma, T_0 of 1250°C and a grain radius of 1160 μm . This corroborates that REE diffusion in opx shows the same variation on ionic radius as for diopside at probably higher absolute diffusive velocities.

Diffusion of REE in opx shows a similar increase with decreasing ionic radii as known from diopside and also most other studied silicate minerals. Another question is if the extent of fractionation between cpx and opx differs. Closure temperature correlations using the diopside diffusion coefficients mimic the correlation of the opx temperatures overall well. The best match is obtained for a cooling rate of 10°C/Ma and grain radius of 1160 μm . A cooling rate of 30°C/Ma and grain radius of 580 μm also provide a good match but the temperature data mostly comes from much larger grains, so the cooling rate is likely to be lower. However, the important result is that the relative variation in REE diffusion coefficients between cpx and opx is almost identical. This means that Yb diffuses 35 times faster than La in opx similar to cpx (van Orman et al., 2001), with very similar dependence on ionic radius in cpx and opx. The good match for a cooling rate of 10°C/Ma implies that diffusion has to be faster in opx

than in cpx. Theoretical considerations for this sample location showed that reasonable cooling rates need to be higher than 30°C/Ma. This is corroborated by forward numerical modeling of the diffusion profiles, which requires much faster diffusion than given by the diffusion coefficients from Cherniak and Linag (2007) in order to produce the observed zoning within a given time frame (for discussion, see Chapter 3).

4.3.2 Diffusion systematics and crystal site positions in orthopyroxene

Besides REE, seven other trace elements were investigated. Figure 4-7 shows the average core closure temperatures for all modeled elements versus their ionic radius in six-fold coordination.

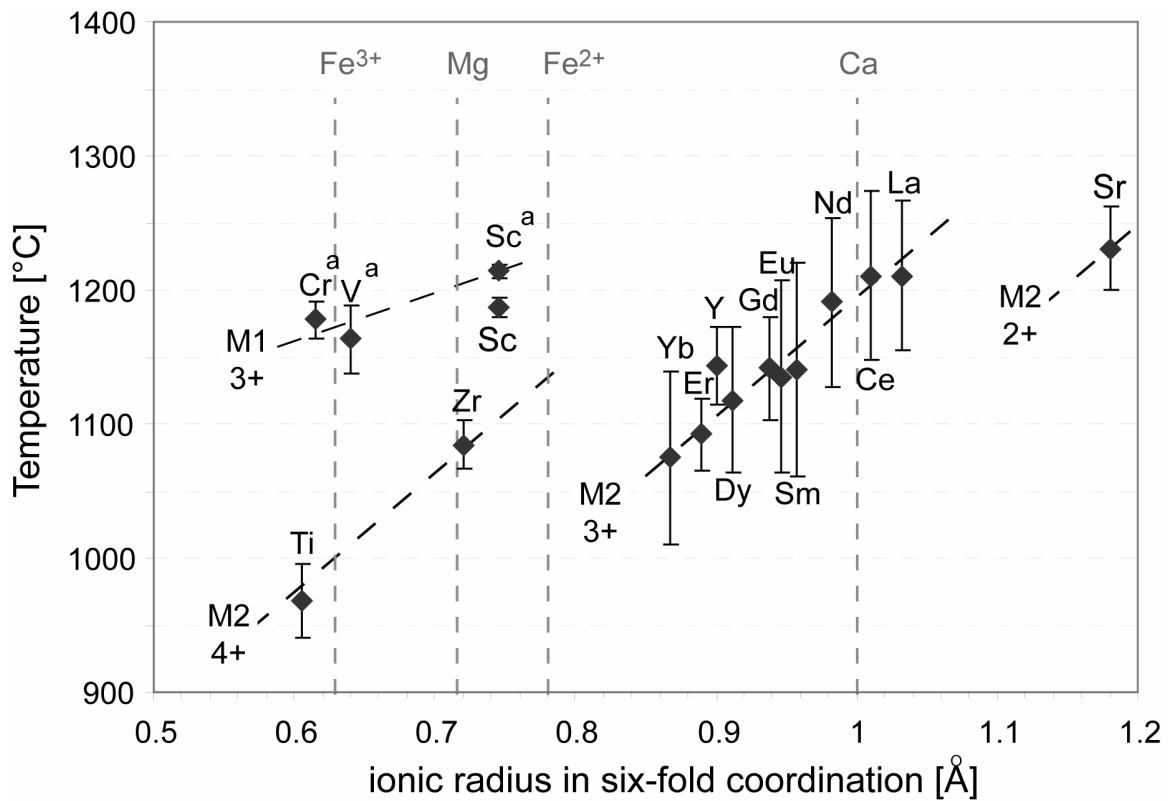


Figure 4-7: Average core closure temperatures versus ionic radii for all analyzed elements. The core temperature is used as a proxy for the relative diffusivity of the elements. With increasing closure temperature, diffusive rates decrease. Cationic radii from Shannon (1976) in six-fold coordination. Temperatures are calculated from partitioning data of Witt-Eickschen and O'Neill (2005), except Cr and V that are calculated after Seitz et al. (1999) (denoted a). Sc temperatures are calculated from both geothermometers. If the partitioning relationship of Witt-Eickschen and O'Neill (2005) holds up, Cr and V should reflect lower equilibration temperatures.

CHAPTER 4

The relative diffusivities allow to assign structural sites in opx to the individual cations based on the systematics of diffusion in silicates. The two octahedral sites in opx have a similar size, so no strong control of ionic radius on cation ordering between both sites is expected.

The trivalent REE are six-fold coordinated in opx and commonly substitute for Ca^{2+} in silicates, similar to Sr. Hence, they all will occupy the M2 site. Sc, Cr, and V are known to occupy the M1 site in opx (Smyth and Ito, 1977, Tazzoli and Domeneghetti, 1987). Chromium occurs in the trivalent state in opx (Ganguly et al., 2007) and vanadium likely as well. They all show a good correlation of decreasing diffusive rate with increasing ionic radius at their individual crystal site.

Zirconium has a diffusive velocity similar to erbium, and titanium is the fastest diffusing element of all of them. The two tetravalent cations show lower diffusivity relative to the trivalent cations in the M1 site, even though they both have similar ionic radii. In general, diffusion in silicates decreases in rate from the divalent cations to the trivalent cations and to the tetravalent cations (e.g. Cherniak and Watson, 2003). If diffusion of Ti and Zr complies with this observation, they must occupy the M2 site where they follow the control of ionic charge on diffusivity of M2 site cations.

The difference in relative diffusivity decreases among isovalent ions with increasing charge, such that the difference between tetravalent ions is less than for trivalent ions in zircon (Cherniak and Watson, 2003). This does not appear to be the case for opx as the slope of correlation between isovalent cations in the M2 site is similar, at least for the trivalent and tetravalent ions. In contrast, the relative change in diffusivity between the trivalent cations in the M1 site is much smaller. Understanding the systematics of diffusion in opx may also help predicting the relative diffusivity of other elements. For instance, it is predicted that diffusion that depends strongly on ionic radius should also strongly depend on the ionic charge (van Orman et al., 2001). Hence, it can be speculated that relative diffusivities of divalent and tetravalent cations in the M1 site will not differ much as well from trivalent cations of similar size.

Tetravalent cations in the M2 site diffuse much faster than trivalent cations in M1, even though they have almost the same ionic radius in six-fold coordination. The difference in diffusion coefficients of trivalent cations in the M1 and M2 site is probably due to the different

site energies of the metal sites in enstatite (M1: -1242 kcal/mol versus M2: -1134 kcal/mol, (Smyth and Bish, 1988)).

As a general summary, the following observations can be made:

(1) Site energy appears to exert the strongest control with isovalent cations showing different diffusivities depending on the metal site in which they reside. Higher site energies should be reflected in higher activation energies for diffusion in the M1 site and diffusion is accordingly slower relative to M2 at a given ionic radius and ionic charge.

(2) Second most important factor is the ionic charge: Among cations residing in the same crystal site and with the same ionic radius, divalent cations will diffuse faster than trivalent than tetravalent.

(3) Ionic radius also exerts some control: For isovalent cations from the same crystal site, the diffusivity decreases with increasing ionic radius. This change in diffusivity is stronger in the M2 site than in the M1 site.

4.3.3 Differences between diffusion in orthopyroxene and clinopyroxene

Given the observed correlation between ionic porosity and pre-exponential factor as well as activation energy, ortho- and clinopyroxene should show similar diffusivities. It has been shown in the previous section that diffusion coefficients of REE in opx decrease with increasing ionic radius in a manner similar to their behavior in cpx. However, REE diffusion in opx must be much faster than in cpx to be consistent with cooling rate estimates for this location (see Chapter 3).

The M2 sites of cpx and opx, in which the REE reside, differ in certain aspects. Site energies for the M1 sites in both pyroxenes are quite similar (-1284 kcal/mol for diopside and -1242 kcal/mol for enstatite), but for the M2 sites they differ greatly between diopside and enstatite (-957 kcal/mol and -1134 kcal/mol, respectively) (Smyth and Bish, 1988). Activation energies should be correspondingly larger for diffusion of REE in opx, which is also predicted by the correlation with ionic porosity. The result would be lower diffusivities for REE

CHAPTER 4

diffusion in opx compared to cpx, seen also for diffusion of Pb in enstatite and diopside (Cherniak, 2001). However, cooling rate estimates for mineral zoning in opx using diffusion coefficients for cpx yield unreasonably low cooling rates for the sample location. Therefore, higher effective REE diffusivities for opx are required relative to cpx. This controversy is probably not due to significantly different crystal lattice controls between cpx and opx but rather the result of different major element chemistry. The diffusion rate is very sensitive to the iron content in the mineral and for example diffusion rates for Sr in diopside increase by two orders of magnitude with an increase of FeO content of 1.5 wt%. The FeO content in diopside in the van Orman (2001) experiments is relatively low (0.70 ± 0.07 wt%) while orthopyroxene in this study contains more than 6 wt% FeO on average. Whether further disparity between opx and cpx in pre-exponential factors exists cannot be resolved.

The question remains whether the similarity in diffusion behavior between opx and cpx also exists for other cations beyond the REE.

An experimental study on natural and synthetic diopside by Sneeringer et al. (1984) investigated the diffusion of Sr at 1 bar and Sr and Sm at 20 kbar. Diffusion of Sr and Sm was found to be similar at high pressures, but a more recent study retrieved much lower, by at least one order of magnitude, diffusion rates for Dy (van Orman et al., 2001). Van Orman and coworkers assumed that difficulties with surface preparation and retrieval may account for the high apparent diffusion rates in the high pressure experiments of Sneeringer et al (1984). Since then, diffusion of Sr has been taken to be orders of magnitude faster than REE in diopside (Cherniak and Liang, 2007), even though that conclusion stems from different experimental studies on different minerals. Diffusion of Sr in opx was also assumed to be very fast relative to the REE (Cherniak and Liang, 2007), but in contrast, Sr is the slowest diffusing element in opx in this study. If diffusion in cpx is similar to opx beyond the behavior of the REE, it is in contradiction with the assumption that Sr diffuses faster than REE in diopside. Of course, it may be possible that the difference in crystal structure and site energy between the M2 sites of the pyroxenes could result in very different relative diffusivities between divalent and trivalent cations in the M2 site.

4.3.4 REE diffusion in orthopyroxene: experimental data and results from Gakkel Ridge peridotites

Experimentally determined diffusion data for REE in opx (Cherniak and Liang, 2007) and diffusion systematics obtained in this study differ strongly. This section will discuss possible reasons for this discrepancy.

A critical point in the application of laboratory experimental data to natural systems is the possible change of diffusion mechanisms from one to another (Ganguly, 2002). On one hand, the diffusion mechanism can change as a function of variables as temperature, pressure or fO_2 . For example, Cr diffusion in opx changes its dominant mechanisms between vacancy and interstitial diffusion depending on fO_2 (Ganguly et al., 2007). However, the experimental temperature range of the enstatite diffusion experiments fits the temperature range seen in this study well. The presence of trivalent europium suggests relatively oxidizing conditions in these samples and no discrepancy to diffusion conditions determined in air should occur. On the other hand, the diffusion mechanism can change due to the use of end member or near-end member mineral composition in laboratory experiments. It has been suggested previously that the dominant diffusion mechanism can change as a function of iron content, and will therefore differ between nominally iron-free minerals and iron-bearing minerals (e.g. Ganguly, 2002). The equilibrium vacancies controlled by the ferric-ferrous equilibrium in an iron-bearing mineral greatly influence its vacancy content. When the FeO content falls below a critical value, the vacancies created by oxidation of FeO play just a minor role in the diffusion process. Chakraborty et al. (1994) suggested that this mechanism is relevant at least for the diffusion in olivine. Only when the iron content in olivine exceeds a threshold value of ~150 ppm, vacancy diffusion dominates, otherwise interstitial diffusion is the dominant mechanism (Ganguly, 2002). A similar behavior has been suggested for spinel (Liermann and Ganguly, 2002) and may be extendable to pyroxenes as well.

The diffusion study of Cherniak and Liang (2007) used a natural near-end member enstatite of the stoichiometric composition $Mg_{1.926}Fe_{0.016}Ca_{0.001}Al_{0.047}Si_{1.992}O_6$. Its FeO content (0.59 wt%) is comparable to the FeO content in van Orman's (2001) experiments (0.70 ± 0.07 wt%). If FeO contents are the key controlling factor for the diffusion mechanism it should have affected van Orman's results as well. The difference in FeO content between the

experimental material and opx from mantle peridotites can therefore only explain differences in absolute diffusion rates, not changes in the control of ionic radius.

Coupled substitution reactions may also affect diffusion processes. Incorporation of trivalent REE into the crystal lattice of opx requires a coupled substitution to balance the exchange with a divalent cation. Several coupled substitutions for minor elements in pyroxenes are possible (e.g. Cameron and Papike, 1981), the most likely for REE in opx being ${}^{\text{VI}}\text{REE}^{3+} + {}^{\text{IV}}\text{Al}^{3+}$ for ${}^{\text{VI}}\text{M}^{2+} + {}^{\text{IV}}\text{Si}^{4+}$ (Schwandt and McKay, 1998).

In the Cherniak and Liang experiments (2007), the tracer layer consisted of a mix of synthetic enstatite powder and microcrystalline rare earth aluminate garnet. Therefore, exchange elements for a Mg-Tschermak-type substitution were present in the experiment. Cherniak and Liang (2007) also conjecture that the cation vacancy concentration control in their enstatite is controlled by Al^{3+} rather than Fe^{3+} . Thereby, the coupled charge balance is explained by Al^{3+} substitution for Si^{4+} to compensate for REE^{3+} exchange with Mg^{2+} . If coupled REE+Al diffusion occurs, the diffusion is likely rate limited by the trivalent aluminum than the trivalent REE and major differences between REE diffusivities would be unlikely. This scenario has been discussed by Cherniak and coworkers for REE diffusion in zircon (Cherniak et al., 1997) and by van Orman for REE in diopside. Van Orman stated that Tschermak-substitution (REEAl-CaSi) would lead to diffusion profiles of equal length for all REE^{3+} and no detectable variation in diffusive rates among them (van Orman et al., 2001). This is exactly what has been observed in enstatite REE diffusion experiments experiments.

In contrast, the tracer source in the van Orman experiment consisted of an aqueous solution of REE-oxides and accordingly no exchange element for a substitution reaction was available in the tracer layer. The introduction of REE into the diopside was suggested to involve an Eskola-type exchange where the charge balance was achieved through formation of vacancies on the M1 or M2 site. Hence, it was concluded that REE diffusion in the experiment was rate limited by the mobility of the REE elements only (van Orman et al., 2001).

Al-diffusion in diopside has been measured only at one temperature (Sautter et al., 1988), yet their data match the REE diffusion data from Cherniak and Liang (2007) at the same

temperature (Figure 4-8). There is no definite reason to assume that Al diffusivity in enstatite is the same as in diopside but the coincidence is remarkable.

In summary, it is suggested that REE diffusion in the experiments of Cherniak and Liang was rate-limited by the coupled substitution with aluminum. Hence, the obtained diffusion coefficients may rather reflect the diffusivity of Al. Ganguly and Tirone (2001) obtained a single measurement for Nd diffusion in enstatite at 827°C at 1 bar under reducing conditions (IW-buffer). Extrapolating the Nd diffusion data in diopside to this temperature shows that diffusion of Nd in enstatite is three orders of magnitude faster than diffusion in diopside and similar to diffusion of Mg^{2+} in enstatite (Cherniak and Liang, 2007). If diffusion of divalent cations in the M1 site does not differ significantly from the trivalent cations as suggested before, we would also obtain a similar diffusivity for magnesium as for Nd in Figure 4-7. This assertion rests on many assumptions and unfortunately, not enough data exists to obtain an Arrhenian relationship for diffusion of Nd. Nevertheless, if the similarity between Mg and Nd diffusivity holds true, diffusion data of magnesium in enstatite could be used as proxy for the MREE.

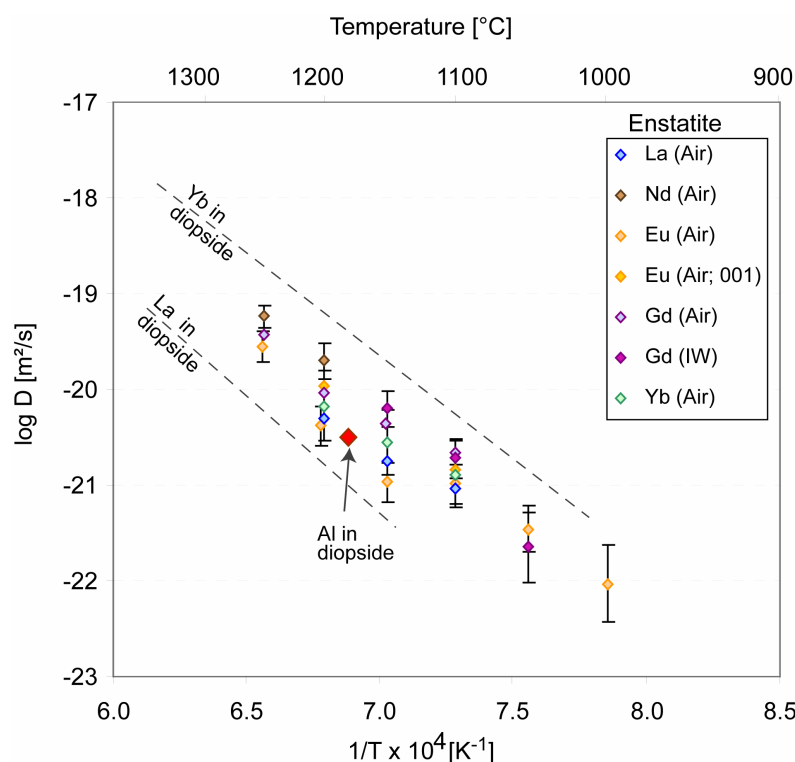


Figure 4-8: Arrhenius-plot for REE diffusion data in opx from Cherniak and Liang (2007). Diopside diffusion data for La and Yb from van Orman (2001) are added for comparison with their respective trends as stippled lines. Al diffusion datum in diopside from Sautter et al. (1988) is added for comparison.

4.4 SUMMARY

Diffusion in opx has been studied through opx zoning in two spinel peridotites from Gakkel Ridge. Application of the geothermometers of Witt-Eickschen and O'Neill (Witt-Eickschen and O'Neill, 2005) allows the calculation of closure temperatures for 16 elements (REE and other TE) in opx. Constant closure temperatures in the opx cores are assumed to be good proxies for their relative diffusivities, and based on known diffusion systematics in silicates their crystal site position could be assigned. The following observations have been made:

- REE diffusion rates in orthopyroxene decreases with increasing ionic radius with $D_{La} \ll D_{Yb}$. Furthermore, REE diffusion in opx follows very closely a similar relationship as REE diffusion in cpx, suggesting that Yb diffuses 35 times faster than La.
- Relative diffusivities between isovalent cations is lower in the M1 site compared to the M2 site, most likely because of the higher site energies of M1. Therefore, the most important control of diffusion in opx is the crystal site energy.
- Diffusion of cation occupying the M2 site is also strongly controlled by cationic charge, followed by ionic radius.
- Influence of ionic radius on relative diffusivities is stronger in the M2 site than in M1.
- Diffusion of REE in opx is much faster compared to cpx, probably because of the higher iron content.
- Experimentally determined diffusion data for REE in opx from Cherniak and Liang (2007) are potentially affected by the coupled substitution with aluminum and are not applicable for diffusion processes in natural systems.

4.5 REFERENCES

- Cameron, M. and Papike, J. J. (1981). Crystal chemistry of silicate pyroxenes. In: Prewitt, C. T. (ed.) *Pyroxenes*. Reviews in Mineralogy 7. Mineralogical Society of America, 5-92.
- Chakraborty, S. (1997). Rates and mechanisms of Fe-Mg interdiffusion in olivine at 980°-1300°C. *Journal of Geophysical Research-Solid Earth and Planets* 102, 12317-12331.
- Chakraborty, S., Farver, J. R., Yund, R. A. and Rubie, D. C. (1994). Mg tracer diffusion in synthetic forsterite and San-Carlos olivine as a function of P, T and fo₂. *Physics and Chemistry of Minerals* 21, 489-500.
- Cherniak, D. J. (1998a). Pb diffusion in clinopyroxene. *Chemical Geology* 150, 105-117.
- Cherniak, D. J. (1998b). Rare earth element and gallium diffusion in yttrium aluminum garnet. *Physics and Chemistry of Minerals* 26, 156-163.
- Cherniak, D. J. (1998c). REE diffusion in calcite. *Earth and Planetary Science Letters* 160, 273-287.
- Cherniak, D. J. (2000). Rare earth element diffusion in apatite. *Geochimica Et Cosmochimica Acta* 64, 3871-3885.
- Cherniak, D. J. (2001). Pb diffusion in Cr diopside, augite, and enstatite, and consideration of the dependence of cation diffusion in pyroxene on oxygen fugacity. *Chemical Geology* 177, 381-397.
- Cherniak, D. J. (2003). REE diffusion in feldspar. *Chemical Geology* 193, 25-41.
- Cherniak, D. J., Hanchar, J. M. and Watson, E. B. (1997). Rare-earth diffusion in zircon. *Chemical Geology* 134, 289-301.
- Cherniak, D. J. and Liang, Y. (2007). Rare earth element diffusion in natural enstatite. *Geochimica Et Cosmochimica Acta*, doi 10.1016/j.gca.2006.1012.1001.
- Cherniak, D. J. and Watson, E. B. (2003). Diffusion in zircon. *Reviews in Mineralogy & Geochemistry* 53. 113-143.
- Dahl, P. S. (1997). A crystal-chemical basis for Pb retention and fission track annealing systematics in U-bearing minerals, with implications for geochronology. *Earth and Planetary Science Letters* 150, 277-290.
- Delaney, J. S., Nehru, C. S., Prinz, M. and Harlow, G. E. (1981). Metamorphism in mesosiderites. *Proceedings of Lunar and Planetary Science* 12, 1315-1342.
- Dimanov, A., Jaoul, O. and Sautter, V. (1996). Calcium self-diffusion in natural diopside single crystals. *Geochimica Et Cosmochimica Acta* 60, 4095-4106.
- Dodson, M. H. (1973). Closure temperature in cooling geochronological and petrological systems. *Contributions to Mineralogy and Petrology* 40, 259-274.
- Dodson, M. H. (1986). Closure profiles in cooling systems. *Materials Science Forum* 7, 145-154.
- Dowty, E. (1980). Crystal-chemical factors affecting mobility of ions in minerals. *American Mineralogist* 65, 174-182.

CHAPTER 4

- Fortier, S. M. and Giletti, B. J. (1989). An empirical model for predicting diffusion coefficients in silicate minerals. *Science* 245, 1481-1484.
- Ganguly, J. (2002). Diffusion kinetics in minerals: Principles and applications to tectono-metamorphic processes. In: Gramaccioli, C. M. (ed.) *EMU Notes in Mineralogy*. 4. Budapest: Eötvös University Press, 271-309.
- Ganguly, J., Ito, M. and Zhang, X. (2007). Cr diffusion in orthopyroxene: Experimental determination, ^{53}Mn - ^{53}Cr thermochronology, and planetary applications. *Geochimica Et Cosmochimica Acta* 71, 3915-3925.
- Ganguly, J. and Tazzoli, V. (1994). Fe $^{2+}$ -Mg interdiffusion in ortho-pyroxene - retrieval from the data on intracrystalline exchange-reaction. *American Mineralogist* 79, 930-937.
- Ganguly, J., Yang, H. X. and Ghose, S. (1994). Thermal history of mesosiderites - quantitative constraints from compositional zoning and Fe-Mg ordering in orthopyroxenes. *Geochimica Et Cosmochimica Acta* 58, 2711-2723.
- Hart, S. R. (1981). Diffusion compensation in natural silicates. *Geochimica Et Cosmochimica Acta* 45, 200-215.
- Hofmann, A. W. (1980). Diffusion in natural silicate melts: a critical review. In: Hargraves, E. B. (ed.) *Physics of magmatic processes*. Princeton: Princeton University Press, 385-417.
- Lasaga, A. C. (1983). Geospeedometry: An extension of geothermometry. In: Saxena, S. K. (ed.) *Kinetics and equilibrium in mineral reactions*. Advances in Physical Geochemistry 3. 81-114.
- Liermann, H. P. and Ganguly, J. (2002). Diffusion kinetics of Fe $^{2+}$ and Mg in aluminous spinel: Experimental determination and applications. *Geochimica Et Cosmochimica Acta* 66, 2903-2913.
- Morris, R. V. (1975). Electron paramagnetic resonance study of the site preferences of Gd $^{3+}$ and Eu $^{2+}$ in polycrystalline silicate and aluminate minerals. *Geochimica Et Cosmochimica Acta* 39, 621-634.
- Sautter, V., Jaoul, O. and Abel, F. (1988). Aluminium diffusion in diopside using the $^{27}\text{Al}(p, \gamma)^{28}\text{Si}$ nuclear reaction: preliminary results. *Earth and Planetary Science Letters* 89, 109-114.
- Schwandt, C. S. and McKay, G. A. (1998). Rare earth element partition coefficients from enstatite/melt synthesis experiments. *Geochimica Et Cosmochimica Acta* 62, 2845-2848.
- Schwandt, C. S., Randall, T. C. and Westrich, H. R. (1998). Magnesium self diffusion in orthoenstatite. *Contributions to Mineralogy and Petrology* 130, 390-396.
- Seitz, H. M., Altherr, R. and Ludwig, T. (1999). Partitioning of transition elements between orthopyroxene and clinopyroxene in peridotitic and websteritic xenoliths: New empirical geothermometers. *Geochimica Et Cosmochimica Acta* 63, 3967-3982.
- Shannon, R. D. (1976). Revised effective ionic radii and systematic studies of interatomic distances in halides and chalcogenides. *Acta Crystallographica A* 32, 751-763.

CHAPTER 4

- Smyth, J. R. and Bish, D. L. (1988). *Crystal structures and cation sites of the rock forming minerals*. Winchester: Allen and Unwin, p. 332.
- Smyth, J. R. and Ito, J. (1977). The synthesis and crystal structure of a magnesium-lithium-scandium protopyroxene. *American Mineralogist* 62, 1252-1257.
- Sneeringer, M., Hart, S. R. and Shimizu, N. (1984). Strontium and samarium diffusion in diopside. *Geochimica Et Cosmochimica Acta* 48, 1589-1608.
- Tazzoli, V. and Domeneghetti, M. C. (1987). Crystal-chemistry of natural and heated aluminous orthopyroxenes. *Physics and Chemistry of Minerals* 15, 131-139.
- van Orman, J. A., Grove, T. L. and Shimizu, N. (1998). Uranium and thorium diffusion in diopside. *Earth and Planetary Science Letters* 160, 505-519.
- van Orman, J. A., Grove, T. L. and Shimizu, N. (2001). Rare earth element diffusion in diopside: influence of temperature, pressure, and ionic radius, and an elastic model for diffusion in silicates. *Contributions to Mineralogy and Petrology* 141, 687-703.
- van Orman, J. A., Grove, T. L. and Shimizu, N. (2002a). Diffusive fractionation of trace elements during production and transport of melt in Earth's upper mantle. *Earth and Planetary Science Letters* 198, 93-112.
- van Orman, J. A., Grove, T. L., Shimizu, N. and Layne, G. D. (2002b). Rare earth element diffusion in a natural pyrope single crystal at 2.8 GPa. *Contributions to Mineralogy and Petrology* 142, 416-424.
- Witt-Eickschen, G. and O'Neill, H. S. (2005). The effect of temperature on the equilibrium distribution of trace elements between clinopyroxene, orthopyroxene, olivine and spinel in upper mantle peridotite. *Chemical Geology* 221, 65-101.
- Zener, C. (1952). Theory of diffusion. In: Shockley, W., Hollomon, J. H., Maurer, R. & Seitz, F. (eds.) *Imperfections in nearly perfect crystals*. New York: Wiley, 289-314.

CHAPTER 5

PLAGIOCLASE PERIDOTITES FROM GAKKEL RIDGE: ON STAGNANT REACTIVE POROUS FLOW AND SILICA ACTIVITY

5.1 INTRODUCTION

Plagioclase-bearing peridotites are an abundant lithology among the ultramafic rocks; according to dredge statistics, they account for about 30% of abyssal peridotites dredged along the mid-ocean ridges (Dick, 1989). Plagioclase peridotites occur in a variety of oceanic settings, but mostly in magma-starved environments like slow-spreading ridges, transform faults or ocean-continent transition zones. Despite the ubiquitous presence of plagioclase peridotite at mid-ocean ridges and ophiolites, their origin is still a matter of debate. Two contrasting theories have been put forward to explain their petrogenesis: (1) they are the product of metamorphic breakdown of spinel peridotites at low pressures (Hamlyn and Bonatti, 1980, Kornprobst and Tabit, 1988, Vissers et al., 1991, Rampone et al., 1993, Strating et al., 1993, Cannat and Seyler, 1995, Rampone et al., 2005); (2) they are products of impregnation by either an indigenous or exotic melt (Menzies and Allen, 1974, Boudier and Nicolas, 1985, Nicolas, 1986, Dick, 1989, Cannat et al., 1990, Girardeau and Francheteau, 1993, Rampone et al., 1997, Dijkstra et al., 2001, Tartarotti et al., 2002, Barth et al., 2003, Dijkstra et al., 2003, Müntener et al., 2004, Piccardo et al., 2007).

Despite the small number of studies on abyssal plagioclase peridotites relative to their residual spinel counterparts, plagioclase peridotites play an important role in the theoretical framework of many studies. In the following, I will briefly summarize the significance of either origin of plagioclase peridotites within the framework of mid-ocean ridge studies.

5.1.1 Significance of the spinel to plagioclase phase transformation

The role of metamorphic phase transitions in the oceanic crust is of importance to several fields of investigation:

1. Effect on basin subsidence/buoyancy: The plagioclase-spinel transition has been invoked as an influential control on basin subsidence (Wood and Yuen, 1983, Petrini et al., 2001, Kaus et al., 2005). In this model, all uplifted spinel peridotite transforms to plagioclase peridotite during rifting and crustal thinning. After rifting ceases, mantle cools and plagioclase lherzolite transforms back into spinel lherzolite. The density change associated with the spinel- to plagioclase-facies transition is then thought to result in more post-rift subsidence and less syn-rift subsidence.

2. Effect on rheology: Localization of strain in deforming rocks is believed to be of essential importance in controlling the dynamics of lithosphere. Field observations in mylonites (Furusho and Kanagawa, 1999, Newman et al., 1999) and experimental studies (de Ronde et al., 2004, de Ronde et al., 2005) find a close relationship between the spinel- to plagioclase-transition reaction and strain localization. Grain size reduction and nucleation of new phases during the spinel- to plagioclase-phase transition is believed to cause localized rheological weakening and formation of shear zones (e.g. De Bresser et al., 2001, Yamasaki, 2004).

3. Effect on melt productivity: The effect of pressure-induced solid-solid phase transitions has been invoked to cause changes in melt productivity during partial melting. Experimental data give positive Clapeyron slopes for the spinel- to plagioclase-facies transition (CMAS: Presnall et al., 1979, Walter and Presnall, 1994), while thermodynamic calculations show a negative clapeyron slope (for CMASNF: Asimow et al., 1995). This will either lead to an increase in melt productivity or decrease, respectively. Asimow et al. (1995) using the original MELTS-package predicted a cessation of melt production for fractional-type melting and complete freezing for batch-type melting, However, the relative importance seems to change with the applied model formulation and replication of the calculation of Asimow et al. (1995) with the new PMELTS-package reduced the effect (Presnall et al., 2002).

5.1.2 Significance of melt migration and melt stagnation processes

Melt migration and melt stagnation processes have several important effect on ridge structures and dynamics.

1. Effect on buoyancy-driven mantle flow: Melt migration and melt retention exerts a strong effect on buoyancy-driven mantle flow because of the density contrast between melt and mantle. Depending on the amount of melt present in the granular network, the decreased aggregate density will lead to more vigorous mantle upwelling that will be focused into a narrow zone. This effect also depends on the melt viscosity (e.g. Jha et al., 1994, Barnouin-Jha et al., 1997).

2. Effect of advection of heat by melt migration: Advection of heat during melt migration is believed to raise the isotherms above the melting regime and decrease the minimum and average pressure of melting. The additional heat brought into the melting regime will further increase the melt production rate at shallower depths. However, the effect of advection of heat via melt migration is smaller in numerical models than the effect of latent heat release during melting.

3. Effect of melt freezing on the thermal mantle structure and melt flow: At the depth of the thermal boundary layer (TBL), temperatures drop below the melt liquidus and crystallization will begin, reducing the permeability by the crystallized phases. Crystallization of melt at entering the conductively cooled lithosphere is thought to produce a permeability barrier that halts porous flow and leads to melt focusing toward the segment center (Sparks and Parmentier, 1991, Spiegelman, 1993c, Kelemen et al., 1997b, Magde and Sparks, 1997). Melt “freezing” is not gradual, but will be completed soon after the melt temperature dropped below the solidus (Korenaga and Kelemen, 1997, Kelemen and Aharonov, 1998). Here, the maximum freezing rate is about ten times greater than the highest melting rate (Cordery and Morgan, 1992). As result, the crystallization region is expected to be a narrow band above the melting regime that mimics the overall shape of the isotherms near the ridge axis while the melting regime spans a broad region of many kilometers.

Evidently, plagioclase peridotites play an important role in the field of mid-ocean ridge studies either because of solid state transitions or manifestation of low pressure porous flow. Thus, it is even more surprising that they have received relatively little attention relative to their importance and abundance.

However, the study of plagioclase peridotites from mid-ocean ridges has been strongly hampered by their generally high degree of alteration. The severe and often almost complete alteration of abyssal peridotites has too often restricted analyses to cores of minerals, plagioclase generally not among those. The recovery of very fresh abyssal peridotites in the Sparsely Magmatic Zone of Gakkel Ridge allows a systematic study of the processes responsible for the formation of plagioclase in mantle peridotites.

5.2 SAMPLE DESCRIPTION AND METHODS

The aim of this study is to investigate in detail the geochemical modifications that occur with formation of plagioclase in Gakkel Ridge peridotites, assuming that they are representative of other plagioclase-bearing abyssal peridotites. In order to accomplish such a detailed study, only two plagioclase-bearing samples were chosen for careful investigation with micro-analytical techniques. Two spinel peridotites from the same dredge haul were added to study the unreacted analogue for comparison.

5.2.1 Modal analyses

Modal amounts of the different phases were determined by point counting with 500-600 points on average. Each thin section was point counted three times to ensure good representative results. Plagioclase is often very heterogeneously distributed and the large standard deviation of plagioclase peridotites represents spatial heterogeneity rather than the error of the method. Sample 235-134 has two extremely modally different parts (Table 5-1 and Figure 5-1) and the point counting results for the two respective parts are shown separately. Here, 134a-I represents the pyroxene-rich part and 134a-II the olivine-rich part.

CHAPTER 5

Table 5-1: Modal analyses of the studied samples.

sample name	ol	opx	cpx	sp	plag
235-17	61.2 ± 1.1	28.0 ± 0.5	10.2 ± 0.8	0.4 ± 0.1	0.0 ± 0.0
235-19	61.3 ± 1.0	24.1 ± 0.9	7.9 ± 0.3	0.5 ± 0.4	5.7 ± 0.5
235-20	73.6 ± 0.9	17.9 ± 0.1	7.3 ± 0.9	1.0 ± 0.3	0.0 ± 0.0
235-134a-I	37.5 ± 0.4	53.2 ± 0.5	2.6 ± 0.3	0.4 ± 0.2	6.1 ± 0.4
235-134a-II	73.7 ± 0.3	15.3 ± 1.2	6.7 ± 0.8	0.9 ± 0.2	3.1 ± 0.5

±: one standard deviation

For comparison, the average abyssal plagioclase-free spinel peridotite is estimated to contain 75% olivine, 21% enstatite, 3.5% diopside and 0.5% spinel. The typical abyssal plagioclase peridotite contains roughly 2.5% plagioclase and slightly more pyroxene relative to olivine than spinel peridotites do (Dick, 1989). The highest abundance of plagioclase in mantle peridotite at mid-ocean ridges known to date occurs at the Romanche Fracture Zone, Mid-Atlantic Ridge, with up to 17% plagioclase (Dick, 1989, Seyler and Bonatti, 1997, Tartarotti et al., 2002).

5.2.2 Petrography

Sample 235-17 and 235-20 are coarse-grained spinel lherzolites. They display a protogranular texture, following the terminology of Mercier and Nicolas (1975). Olivines show weak deformation with subgrains, undulose extinction and swallowtail kink-bands. Pyroxenes show weak deformation with undulose extinction, while orthopyroxenes additionally developed kink-bands. Fine exsolution lamellae of the complementary pyroxene (i.e. cpx in opx and opx in cpx) are well developed. Orthopyroxenes are very coarse grained (up to 15 mm in length). Clinopyroxenes occur in smaller grain sizes (< 7 mm) and also as interstitial grains between olivines. Light brown spinels can be found, often associated with pyroxenes.

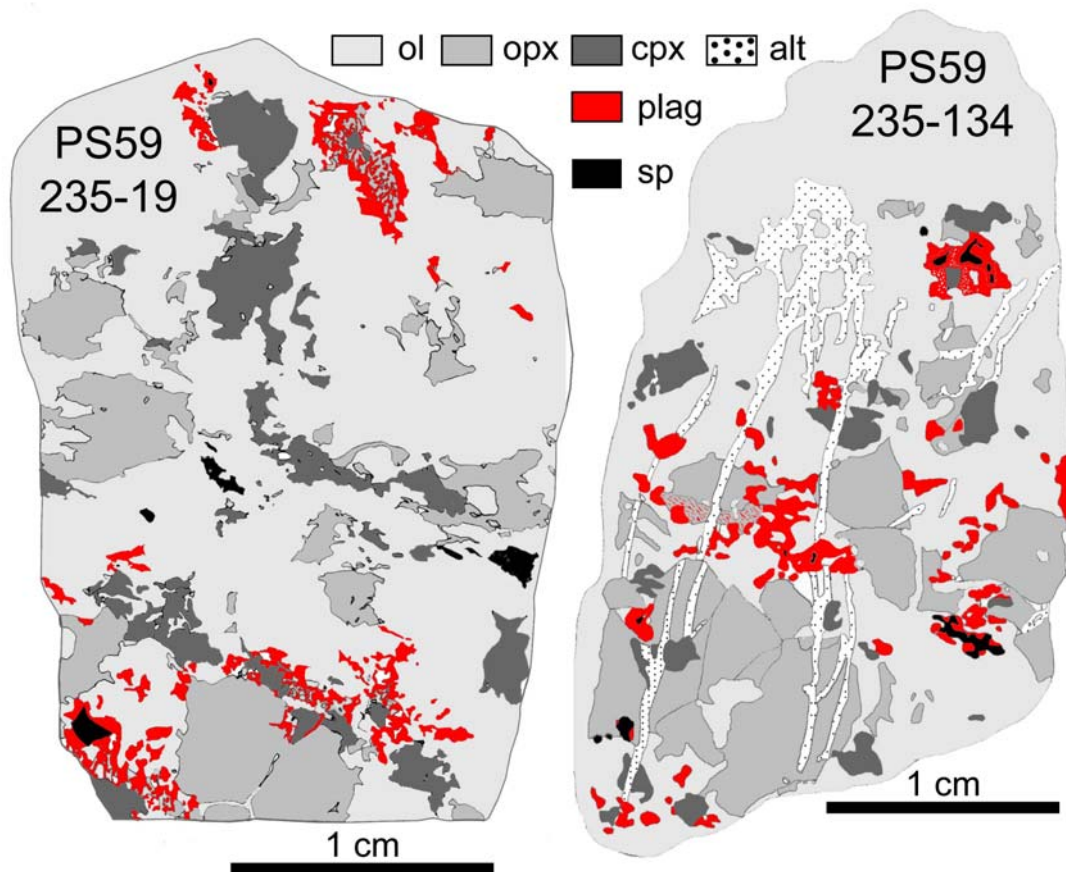


Figure 5-1: Sketches of the distribution of mineral phases in plagioclase peridotites 235-19 and 235-134, redrawn after microscope pictures in combination with element maps and individual spot analyses.

Plagioclase peridotites 235-19 and 235-134 both contain around 6% and 4% plagioclase on average, respectively. Plagioclase is heterogeneously distributed in the samples, specifically in 235-19. Modal composition of 235-134 dominantly varies in its pyroxene distribution with very high abundance of orthopyroxene in one part and an olivine-rich other half. The texture of plagioclase-bearing sample 235-19 is protogranular to porphyroclastic. Olivines show weak deformation with swallowtail kink-bands, sub-grains and undulose extinction. Pyroxenes show undulose extinction and kink-bands; fine exsolution lamellae of the complementary pyroxene are developed. Clinopyroxenes are aligned in the lower and middle part of the thin section and are partly very coarse with grain sizes up to 3 mm. Orthopyroxenes are dispersed in the thin section and can reach up to 4 mm in size.

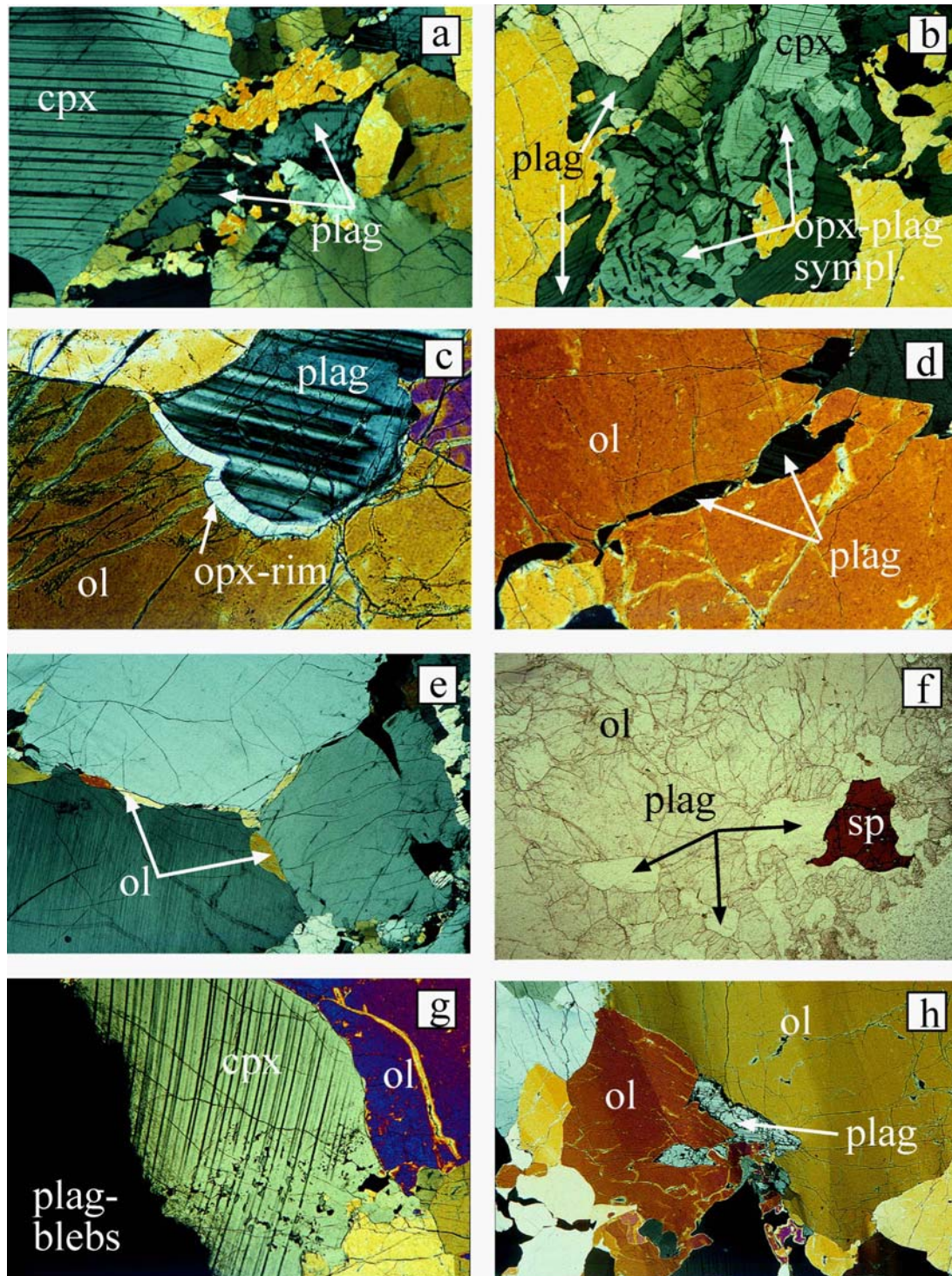


Figure 5-2: Photomicrographs of 235-19 with crossed-nicols (except f with plane-polarized light): a) plag in contact to a large cpx porphyroblast within an ol-matrix (fov: 5 mm); b) small cpx grain surrounded by an opx-plag symplectite. On both sides coarse plag-blebs occur in an ol-matrix (fov: 2.6 mm); c) plag in an ol-matrix. Between plag and ol, a contact rim has developed consisting dominantly by opx and less of secondary ol (fov: 0.65 mm); d) plag crosscutting mantle ol (fov: 1.3 mm); e) secondary ol-veins occur along grain boundaries (fov: 1.3 mm); f) plag as blebs in an ol-matrix and as a corona around spinel (fov: 5 mm); g) plag-blebs in a cpx porphyroblast (fov: 2.6 mm); h) plag along grain boundaries and crosscutting ol (fov: 5 mm).

CHAPTER 5

Plagioclase is restricted to the lower and upper area of the thin section where it seems to follow a lineation and usually occurs as rims around spinels (Figure 5-2f) and blebs in olivine (Figure 5-2d, f). Two opx-plag symplectites around cpx can be found in thin section, where plagioclase forms rods in the orthopyroxene matrix. Plagioclase can also occur as blebs in clinopyroxenes (Figure 5-2g), but no plagioclase exsolutions could be identified. Plagioclase develops sometimes swallow-tail deformation-lamellae indicating further deformation after formation. A reaction rim consisting of orthopyroxene and minor olivine is sometimes present at contacts between olivine and plagioclase (Figure 5-2c). Spinel is usually rimmed by plagioclase but not in the plagioclase-void central part of the thin section. There, it is rather elongated and vermicular in shape and appears to follow the lineation.

In contrast to the previously described samples, plagioclase peridotite 235-134 shows minor amount of alteration, mostly serpentine and chlorite. These phases occur in either veins crosscutting minerals or more pervasively at grain boundaries. Similar to plagioclase peridotite 235-19, this sample shows a protogranular to porphyroclastic texture. Olivines are weakly deformed with formation of subgrains and undulose extinction. Pyroxenes are also weakly deformed with undulose extinction and rare kinkbands. Fine exsolution lamellae of the complementary pyroxene are developed in both pyroxenes. Olivines and pyroxenes occur in two grain sizes: very coarse grains (orthopyroxenes can reach up to 8 mm) and smaller ones (< 1 mm). Plagioclase in sample 235-19 occurs texturally in blebs in olivines and clinopyroxenes (Figure 5-3c), as veins crosscutting mantle olivines, around spinel (Figure 5-3b) and in symplectites. A symplectitic intergrowth of orthopyroxene and plagioclase can be found in the middle part of the thin section. A combined opx-plag/ol-plag symplectite (Figure 5-3f) is present in the thin section as well and will be separately described. In places, plagioclase has developed swallowtail deformation-lamellae. Similar to sample 235-19, reaction rims of orthopyroxene form at contacts between olivine and plagioclase. Spinel is always associated with plagioclase, except for two minute grains, which are associated with olivine. All sorts of spinel shapes occur: oval, holly-leaf as well as vermicular spinel grains. They usually have light brown colors and show no alteration. Sulphides are frequently identified in thin section, associated usually with clinopyroxenes (Figure 5-3c). Several small veins can be identified along grain boundaries of olivine and orthopyroxenes. They consist of olivine and plagioclase, sometimes fading into another.

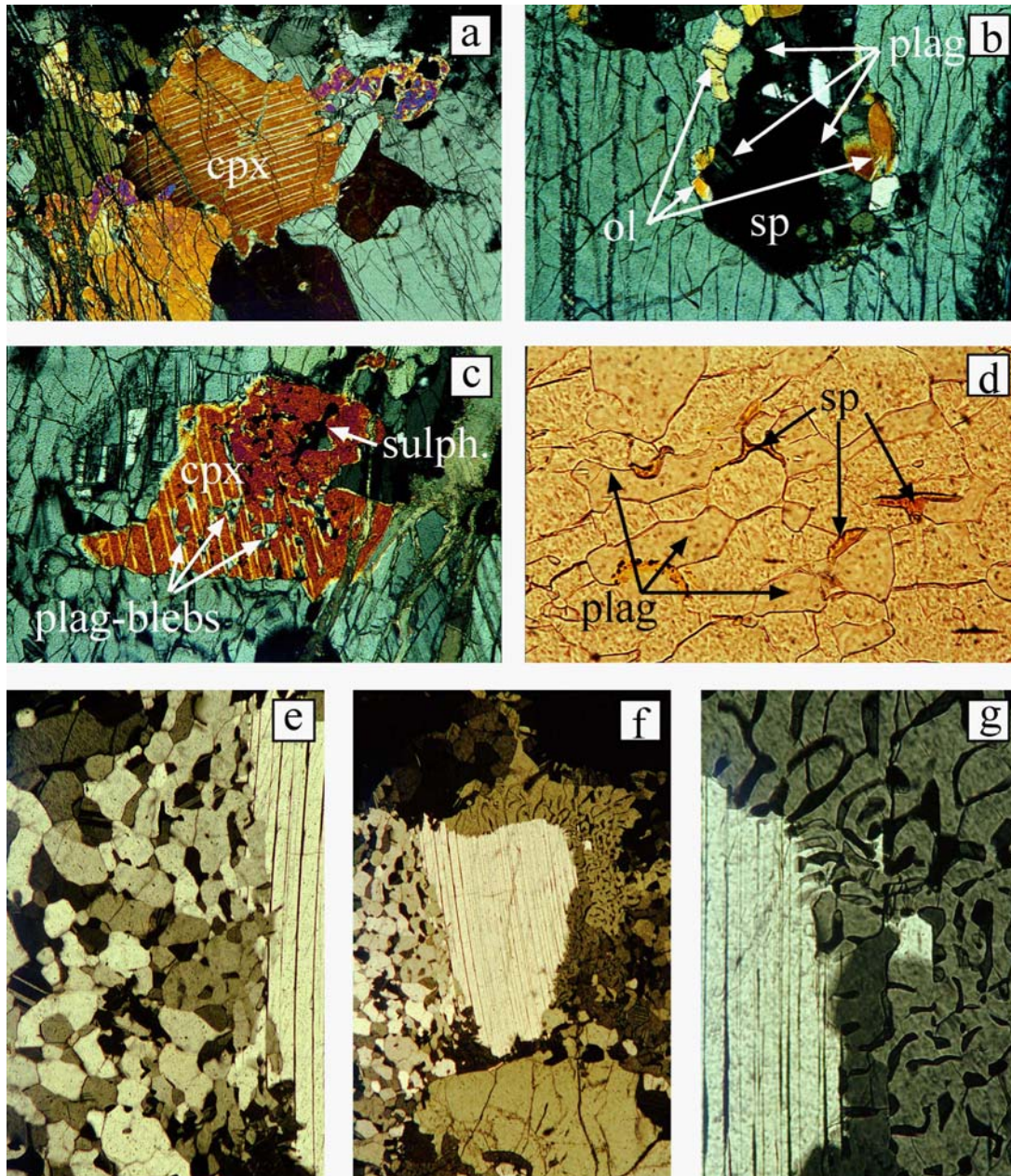


Figure 5-3: Photomicrographs of 235-234 with crossed-nicols, except d) with plane-polarized light: a) cpx with opx-exsolutions and proximal plagioclase (fov: 2.6 mm); b) spinel grain surrounded by ol and plag in an opx (fov: 1.3 mm); c) poikiloblastic cpx with plag-blebs and sulphides (fov: 1.3 mm); d) minute sp-grains in interstices of the ol-plag symplectite (fov: 0.26 mm); e) left left part of f) showing the ol-plag symplectite (fov: 0.65 mm); f) ol-plag and opx-symplectite around cpx-grain; for details see Figure 5-4 (fov: 1.3 mm); g) right part of the cpx of f) with opx-plag symplectite. Two crystallographic orientations of the opx and a dismembered cpx can be seen (fov: 0.65 mm).

An important textural feature can be found in plagioclase-bearing sample 235-134. There, an ol-plag symplectite has formed on one side of a clinopyroxene and on the other side an opx-plag symplectite. Two generations of olivines are recognized in the symplectitic area: a

first generation of porphyroclastic mantle olivines with undulose extinction (1) and strain free symplectitic olivine (2). A clinopyroxene grain acts as core for the symplectite formation (3); it has a narrow system of orthopyroxene lamellae and exhibits undulose extinction. A small part of the clinopyroxene, dismembered as a result of symplectite formation can still be seen in the upper left part (Figure 5-3g; 4).

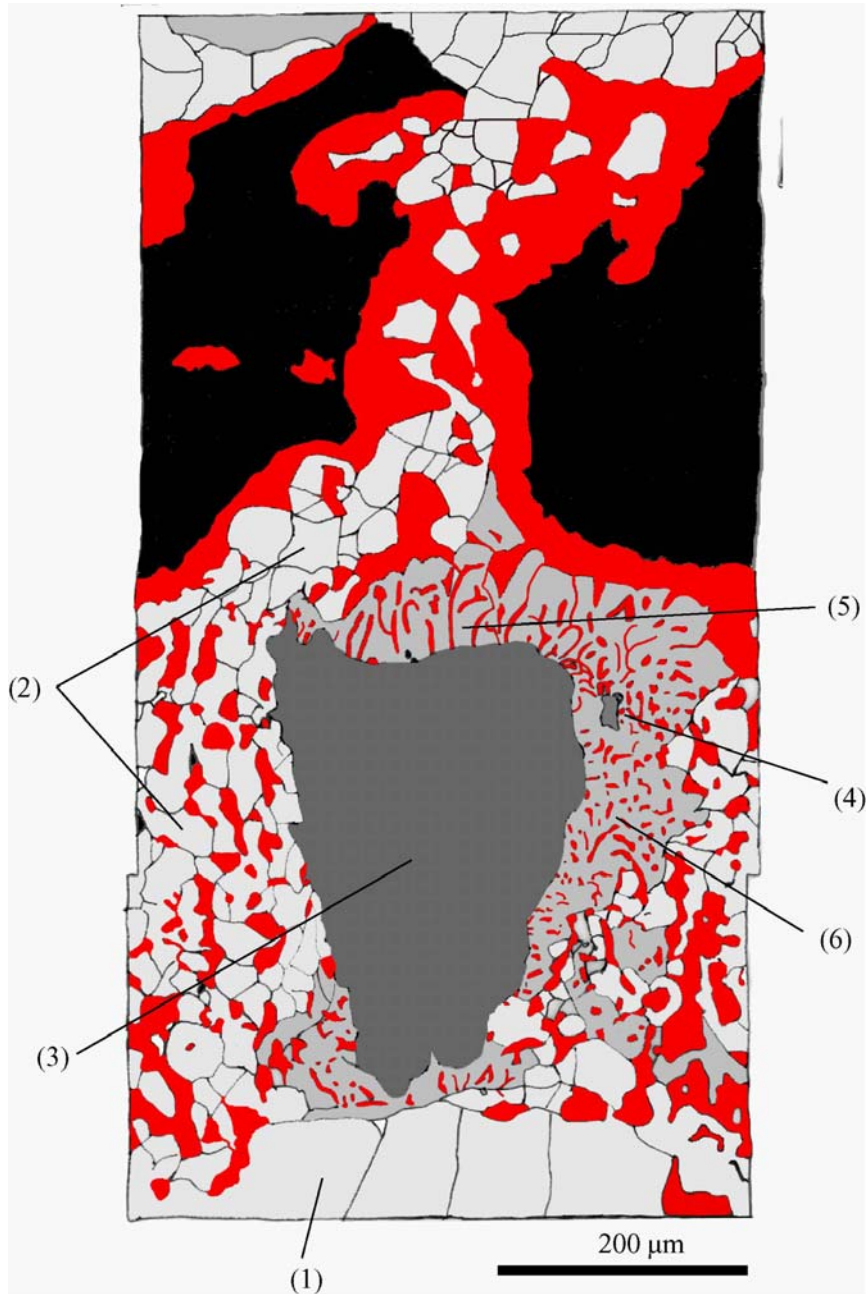


Figure 5-4: Sketch of the symplectitic area in 235-134, see text for numbers; legend as in Figure 5-1.

In places, plagioclase in the symplectite shows deformation lamellae and their texture depends on the symplectite type. In the opx-plag symplectite, the plagioclase forms elongated rods in an opx-matrix but their shape depends on their orientation. Parallel to the cpx lamellae, they are straight and rather elongated (5), perpendicular to the cpx lamellae, they become shorter and more roundish (6), indicating reduced diffusion conditions. In the ol-plag symplectite, the plagioclase has the form of round blebs between and along grain boundaries of the olivines (Figure 5-3e). Minute spinel grains also occur (Figure 5-3d). Plagioclase also forms coronas with changing crystallographic orientations around the large spinel grains. The orthopyroxene in the symplectite shows two crystallographic orientations as observed by different extinction angles (Figure 5-3g). The areas of ol-plag assemblages and opx-plag assemblages are not symmetrical to each other and interfinger in some areas. A spinel train of four coarse spinel grains can be found above the symplectite. They have light-brown colors, show holly-leaf shape and are completely surrounded by plagioclase.

5.2.3 Methods

Major element compositions of the mineral phases were analyzed with a five spectrometer electron microanalyzer (JEOL Superprobe 8900) at the University of Mainz. For pyroxenes and plagioclase an accelerating voltage of 15 kV and a beam current of 12 nA at a beam size of 2 μm were used. Standard counting times were 15s for Si, Mg, Fe, Ca, Cr, Mn and 20s for Al, Ti, Na, K and Ni. For spinels, an accelerating voltage of 20 kV and beam current of 20 nA were used. Standard counting times were 40s for Ca, Ti; 35s for Mg, Al; 30s for Cr, Fe, Mn, Co, Ni, Zn, and 20s for Si. Olivines were measured using a long counting program with 120s on Ni to obtain high quality data. Natural and synthetic mineral and element standards were employed. Total FeO is assumed to be ferrous except for spinel. Fe^{3+} -content of spinel was calculated based on stoichiometry (Droop, 1987).

In addition to quantitative analyses, qualitative element distribution maps were produced from different symplectites and spinels in contact with plagioclase. The selected elements were Al, Mg, Fe, Ti and Cr for spinels and Al, Ca, Cr, Ti and Mg for silicates. The measurement parameters used were: accelerating potential: 15 kV; beam current: 20 nA; beam size: 1 μm ; dwell time: 200 ms; step width: 1 μm .

Pyroxenes and plagioclase were analyzed in-situ in polished thin sections for REE, Ti, Sc, V, Cr, Sr, Y and Zr by secondary ion mass spectrometry (SIMS) using a modified Cameca IMS-3f ion probe (SIMS) at the Max-Planck-Institute for Chemistry in Mainz. The primary beam of ^{16}O -ions was focused to a spot of 10 nA corresponding to a spot size of 20 μm . A high energy offset of -80eV was used to reduce molecular interferences. Additional interference corrections were performed offline, where mass/ ^{30}Si ratios were corrected for overlaps at Eu, Gd, Dy, Er and Yb. Each measurement consisted of 6 cycles. REE were measured in each cycle for 60s except Ce, Gd, Er and Yb for 40s, Dy, Sr and Zr for 20s, Y for 8s, Ti and Sc for 5s and all of the remaining elements for 1s. Detailed analytical conditions are reported in Hellebrand et al. (2002). The overall accuracy is better than 20% for all REE and better than 12% for all other trace elements. Sensitivity factors were monitored by continuous analysis of the MPI-DING glasses GOR132-G and KL2-G (Jochum et al., 2006).

5.3 RESULTS

This study focuses on major and trace elements in four samples. Several areas representative of each sample were chosen after microscopic investigation for more detailed measurements. The purpose of the geochemical analyses was (a) to resolve spatial heterogeneities, (b) to trace compositional variations accompanying the plagioclase formation and (c) to highlight the differences between spinel and plagioclase peridotites.

5.3.1 *Spinel*

Spinel of spinel peridotites 235-17 and 235-20 have uniform compositions, showing just small scatter around an average Cr-number (molar $\text{Cr}/(\text{Cr}+\text{Al})$) of 0.14 and 0.16, respectively. In contrast, both plagioclase peridotites exhibit large variations in spinel Cr-number, which almost cover the entire compositional field of abyssal peridotites (Figure 5-5b). Sample 235-134 exhibits the widest intra-sample range with Cr-numbers from 0.10 to 0.43, whereas 235-19 only covers Cr-numbers from 0.20 to 0.42. This heterogeneity is also reflected in intra-grain variations, where Cr-number can vary from 0.10 to 0.33 within a single grain and similarly from one grain to the next. Such large scale heterogeneities in spinel

compositions characterize spinels rimmed by plagioclase, but smaller scale variation can also be detected in grains without surrounding plagioclase. Even though in the latter texture, spinel shows similar zoning patterns, the variation lies within a much narrower range (± 0.03). In addition to their variation in aluminum content, plagioclase peridotites have much higher TiO_2 contents relative to spinel peridotites. Here, TiO_2 concentration is usually correlated with Cr-number forming different trends for each sample (Figure 5-5a). TiO_2 -contents in spinels of 235-19 are consistently higher (up to 70%) than 235-134 spinels at a given Cr-number. All other minor elements show no distinct behavior, displaying a similar range for spinel and plagioclase peridotites.

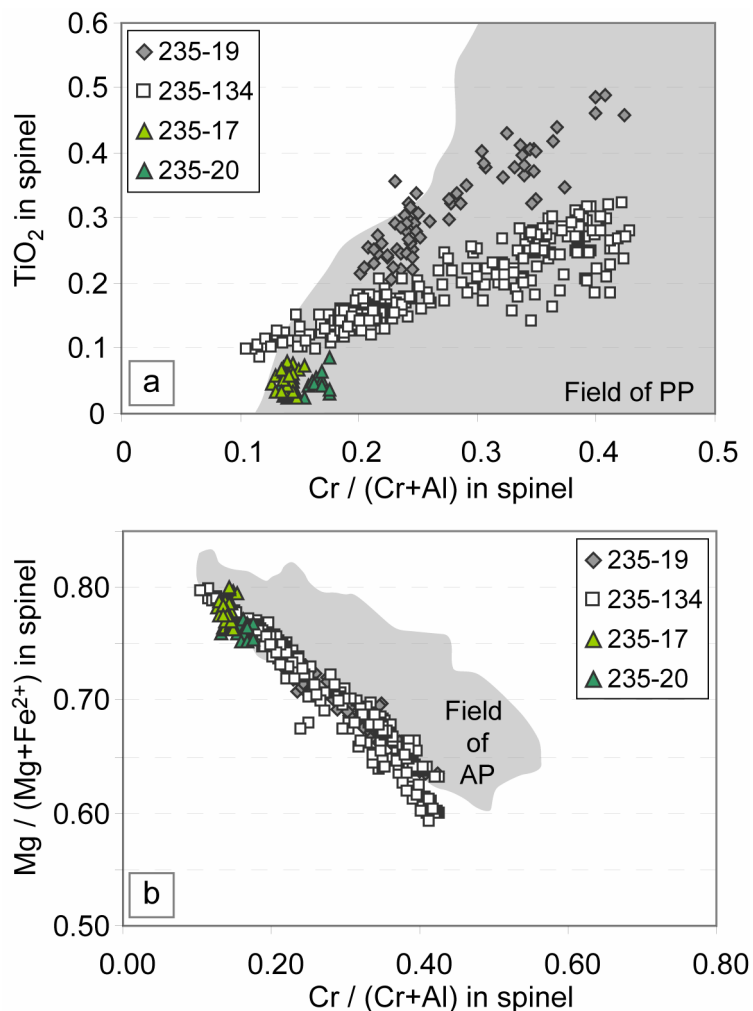


Figure 5-5: (a) TiO_2 against Cr-number in spinel. Spinel in spinel peridotites show little compositional variation and have very low TiO_2 -contents. Spinel in plagioclase-bearing peridotites show higher TiO_2 -contents which correlate with Cr-number. The compositional field of plagioclase peridotites (PP) is shown for comparison; (b) Mg-number versus Cr-number in spinel. The compositional field of abyssal peridotites (AP) from Dick and Bullen (1984) is shown for comparison.

A tight correlation between Cr-number and Mg-number (molar $\text{Mg}/(\text{Mg}+\text{Fe}^{2+})$) in the spinels can be observed, slightly shifted toward lower Mg-numbers off the melting trend of Dick and Bullen (1984) (Figure 5-5b). This has previously been reported for plagioclase peridotites by Dick and Bullen (1984), but only at high Cr-numbers of 0.5 to 0.6.

This compositional range in spinel shows up in elemental maps as strong zonation in all major elements, in places asymmetric. Zones of equal composition can run almost parallel to each other, whereas neighboring grains can have very different composition. It is a common feature that small neighboring grains show distinctly different compositions even at distances of 50 μm or less. Spinel grain apophyses are often characterized by very low aluminum contents. The details of the spinel composition in the light of a larger sample set will be discussed in the following chapter.

5.3.2 Clinopyroxene

Clinopyroxenes in the samples are Cr-diopsides. Clinopyroxenes in spinel peridotites show relatively high uniform Al_2O_3 contents of around 6 wt%. Clinopyroxene in plagioclase peridotites show a large range in aluminum contents between 7.3 wt% and 3.4 wt% for 235-19 and between 6.8 wt% and 1.8 wt% for 235-134. Clinopyroxene grains without direct contact to plagioclase show less variation in Al_2O_3 contents compared to grains sharing grain boundaries with plagioclase. The Na_2O contents of cpx in 235-20 and 235-17 are higher than in plagioclase peridotites (Figure 5-5a). The cores of cpx porphyroclasts are generally characterized by higher aluminum and sodium as well as lower chromium and titanium contents. Sample 235-19 cpx shows higher TiO_2 contents by a factor 0.7 compared to 235-134 (Figure 5-5b) similar to the spinel data. In contrast, spinel peridotite 235-20 has relatively low TiO_2 concentrations (< 0.28 wt %) as expected for a residual cpx. For all other major elements, no distinct behavior can be recognized between the samples.

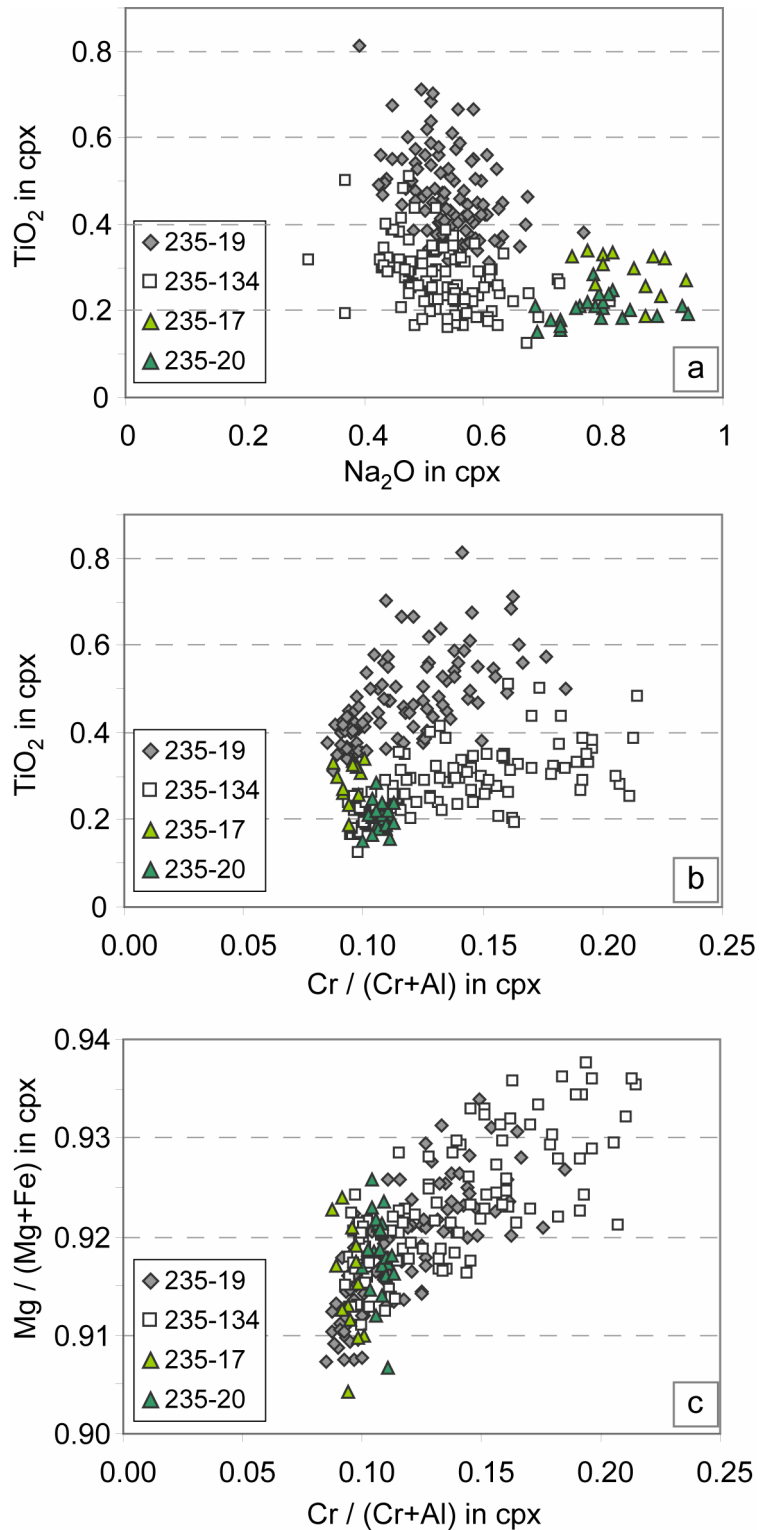


Figure.5-6: (a) Na_2O versus TiO_2 in clinopyroxene. Plagioclase-bearing peridotites (235-19 and -134) contain less Na_2O but more TiO_2 relative to plagioclase-free peridotites (17 and 20). (b) Cr -number versus TiO_2 in clinopyroxene. 235-19 cpx contains more TiO_2 relative to 235-134 at a given Cr -number similar to spinel compositions in the respective samples. (c) Cr -number versus Mg -number in cpx. At low Cr -numbers, cpx in plagioclase-bearing peridotites cover a similar range as plagioclase-free peridotites, but cpx rims in plagioclase-bearing peridotites show increasing Cr -number and Mg -number relative to their cores.

CHAPTER 5

Rare earth element (REE) and trace element concentrations of clinopyroxenes have been obtained by SIMS and are reported in Table 5-3. Clinopyroxenes in spinel lherzolites 235-17 and -20 show homogeneous trace element compositions without apparent negative Eu-anomaly, but have a slight negative Sr-anomaly of about 0.8. Rare earth patterns are steep with low $(La/Yb)_N$ of 0.14 and 0.04 for 235-20 and 235-17, respectively. Negative Ti- and Zr anomalies which are typical for mantle clinopyroxenes (Rampone et al., 1991), are prominent in PS59-235 samples (Figure 5-7).

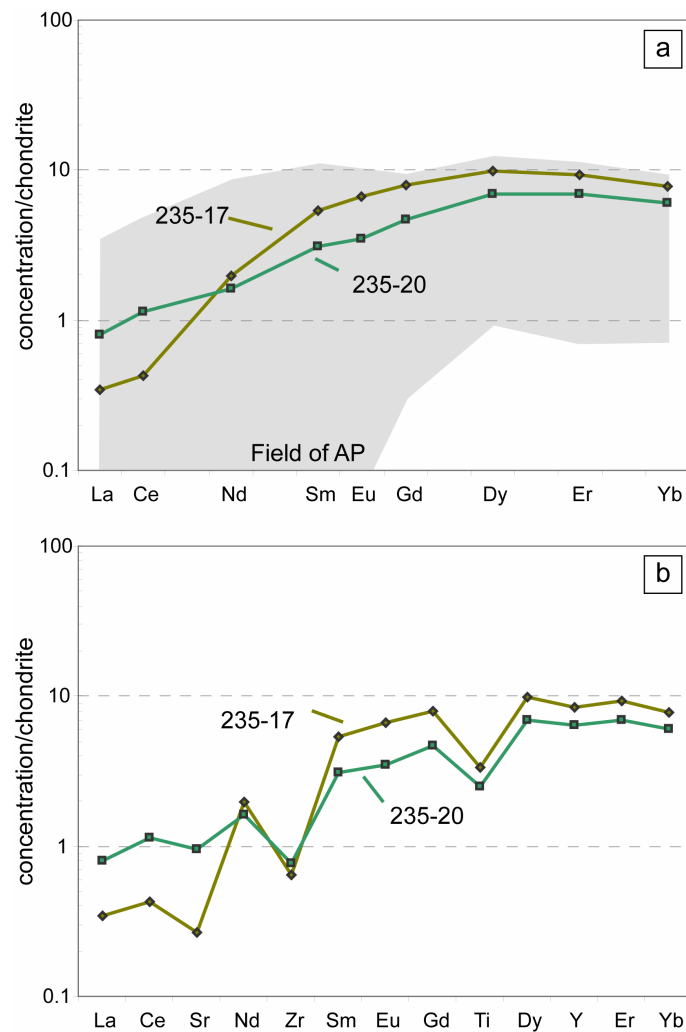


Figure 5- 7: (a) Chondrite-normalized REE and (b) trace element abundances of average cpx in PS59-235 spinel peridotites. The compositional field of global abyssal peridotites (AP) from Johnson et al. (1990) is shown for comparison.

Clinopyroxenes in plagioclase peridotites show a large range in composition with lower LREE and higher MREE to HREE relative to the spinel peridotites from the same dredge

haul. They also have very pronounced negative Sr-anomalies and develop with increasing $(La/Yb)_N$ a negative Eu-anomaly.

The variation of clinopyroxene trace element patterns in plagioclase peridotite 235-19 is closely related to its textural context. Clinopyroxenes without direct contact to plagioclase show little or no core-rim variation, the negative Sr-anomaly is not very pronounced and a negative Eu-anomaly along the rim is rare. Close contact to plagioclase has a clear effect on cpx compositions. Core-rim variations can be observed, a negative Sr-anomaly is more pronounced and an enrichment in MREE and HREE along the rim together with a negative Eu-anomaly forms.

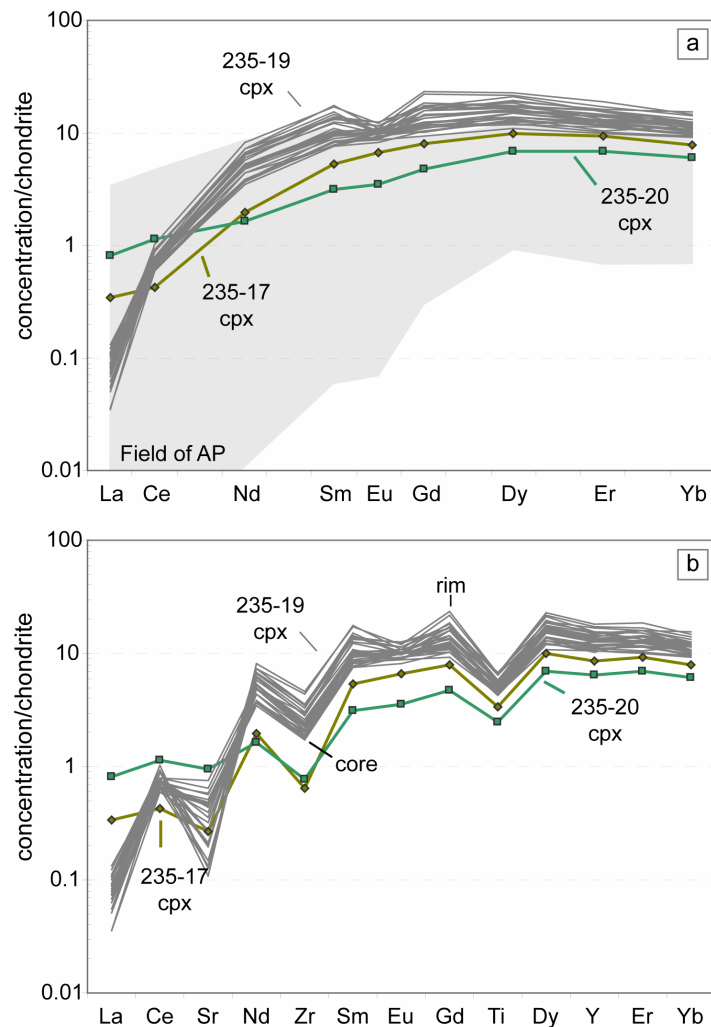


Figure 5-8: (a) Chondrite-normalized REE and (b) trace element abundances of cpx in plagioclase peridotites PS59-235-19. The composition of cpx in spinel peridotites from this study and the range of abyssal peridotites (AP) from Johnson et al., (1990) (grey field) is shown for comparison. Clinopyroxenes from 235-19 show a wide range in composition with highest and lowest contents occurring as core-rim zoning in large porphyroclasts.

CHAPTER 5

Clinopyroxene grains in contact with plagioclase show a systematic decrease in Al, Sr, Eu and increase in REE, Cr, Ti, V and Sc toward the rim (Figure 5-9). This trace element zoning is mirrored by their major element composition, most notably aluminum (not shown) which results in systematic increase in Cr-number and Mg-number toward the rim.

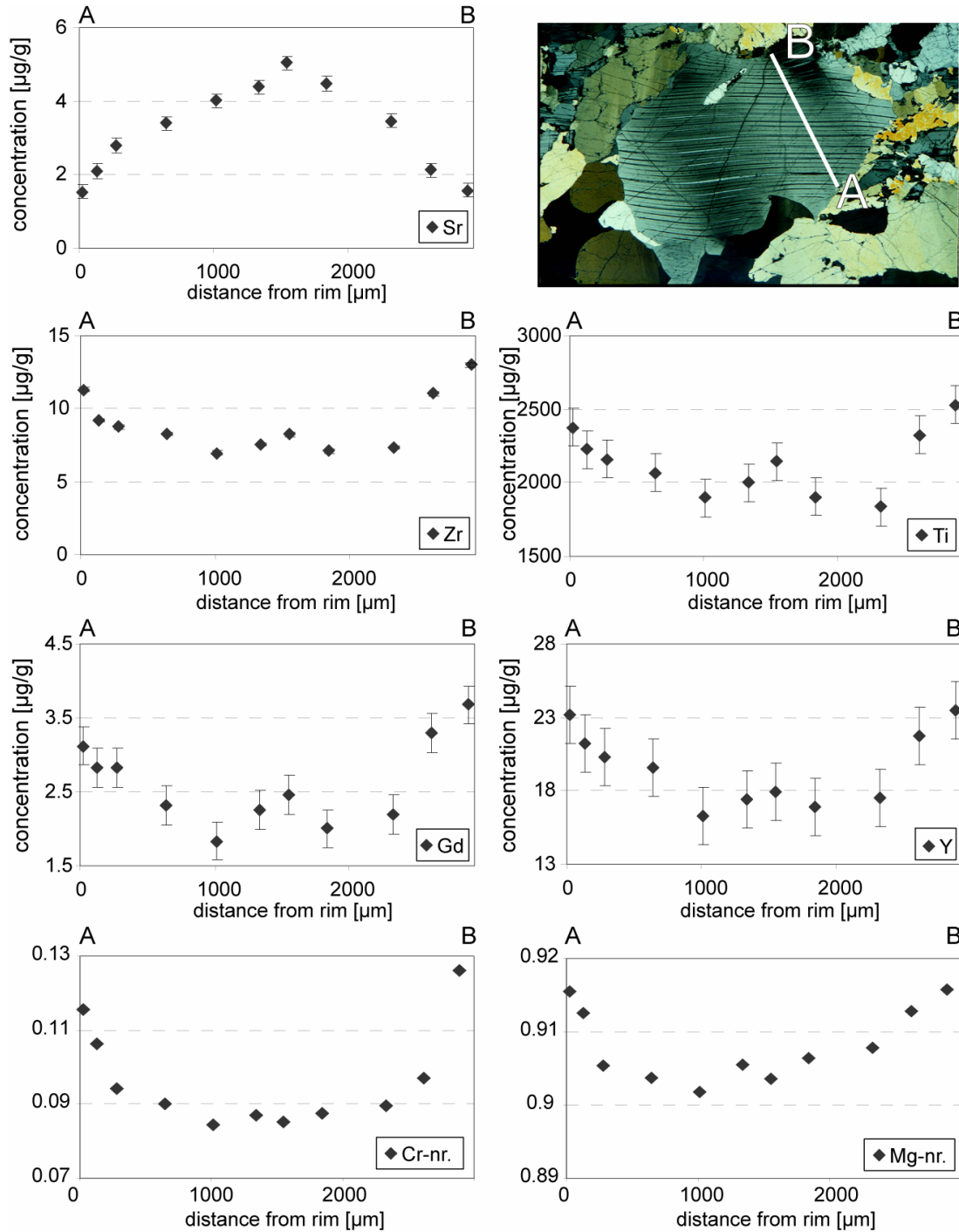


Figure 5-9: Rim to rim profile of a clinopyroxene grain (235-19-0) in contact to plagioclase for selected trace elements (SIMS) and Mg- and Cr-number (EPMA). Error bars denote one standard deviation.

CHAPTER 5

Clinopyroxenes from sample 235-134 show slightly lower MREE to HREE and higher La concentrations relative to 235-19. Clinopyroxenes rimmed by opx-plag symplectites generally show very pronounced enrichment in MREE to HREE on the rim relative to the core. In contrast to 235-19, sample 235-134 contains another generation of clinopyroxene grains, distinct in composition and texture. These cpx grains differ in their trace element composition from large porphyroclasts by their homogeneous composition (no core-rim variation), pronounced negative Sr- and Eu-anomalies and highest enrichment in MREE to HREE at the rim. In addition, the highest Cr-numbers occur here. They also differ in textures as they often lack opx exsolutions. They appear to be the most melt influenced and are termed “magmatic” in the further on.

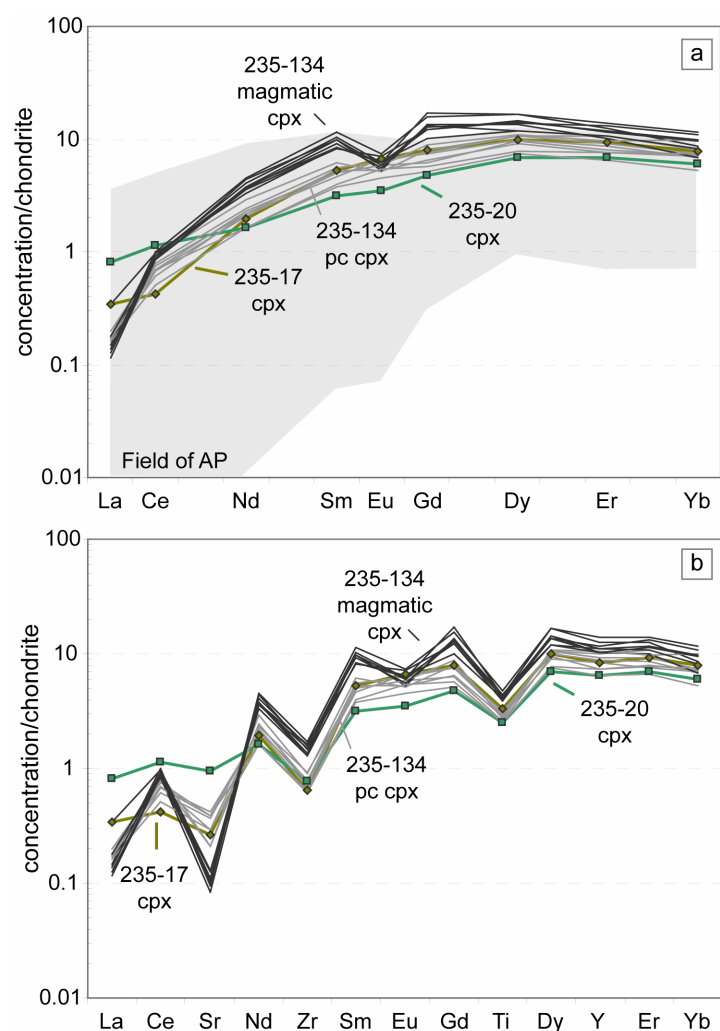


Figure 5-10: Chondrite-normalized REE (a) and trace element abundances (b) of cpx in plagioclase peridotites PS59-235-134. Two distinct types of cpx can be found, zoned porphyroclasts (pc) and homogeneous “magmatic” cpx. The range of cpx in abyssal peridotites (AP) from Johnson et al., 1990 (grey field) is reported for comparison.

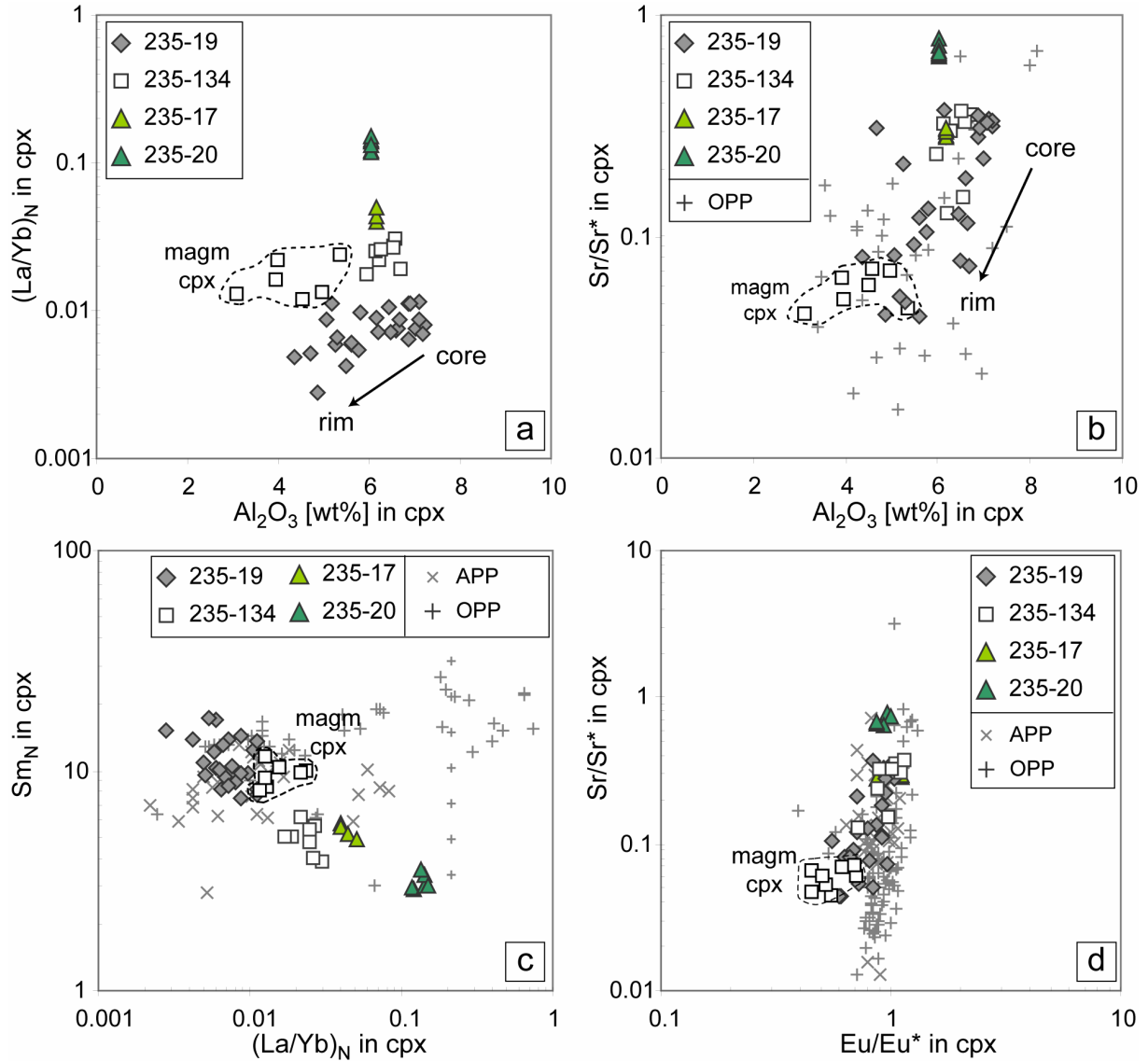


Figure 5-11: (a) Al_2O_3 versus chondrite-normalized $(La/Yb)_N$ in clinopyroxene. Major and trace element analyses come from the same position. A weak correlation of Al_2O_3 -content and $(La/Yb)_N$ exists for each plagioclase-bearing peridotite. The variation occurs in 235-19 cpx mostly as core-rim zoning while in 235-134, lower Al_2O_3 -contents found in the unzoned magmatic cpx; (b) Al_2O_3 versus Sr/Sr^* in cpx. The extent of the negative Sr-anomaly shows a weak correlation with Al_2O_3 -content with more pronounced negative Sr-anomalies; (c) $(La/Yb)_N$ versus Sm_N in cpx. A good negative correlation between $(La/Yb)_N$ and Sm_N ; (d) Eu/Eu^* versus Sr/Sr^* in cpx. While cpx in plagioclase peridotites often show no to only weak negative Eu-anomalies, their negative Sr-anomalies are very pronounced in most cases. Cpx from this study deviate slightly from the trend shown by other abyssal plagioclase peridotites (APP, Seyler and Bonatti (1997) and own unpubl. results) and from orogenic lherzolites and ophiolites (OPP) towards more pronounced negative Eu-anomalies. Abyssal plagioclase peridotites (APP) and plagioclase peridotites from orogenic lherzolites and ophiolites (OPP) are shown for comparison. Subscript N denotes chondrite-normalized after Anders and Grevesse (1989); $Sr^* = (Ce_N * Nd_N)^{1/2}$, $Eu^* = (Sm_N * Gd_N)^{1/2}$.

Aluminum contents and $(La/Yb)_N$ are correlated in clinopyroxene from plagioclase peridotites (Figure 5-11a); there appears to be a correlation between aluminum and Sr-

anomaly as well (Figure 5-11b). Clinopyroxene in plagioclase peridotites often show only weak negative Eu-anomalies or none at all while negative Sr-anomalies are very pronounced. Clinopyroxene from this study deviate slightly from the trend shown by other abyssal plagioclase peridotites (Figure 5-11d). In contrast, spinel peridotites show little variation in cpx composition. Clinopyroxene in 235-17 are very similar in composition to core composition of 235-134 cpx, except for LREE.

5.3.3 Orthopyroxene

Orthopyroxene in the peridotites is enstatite; Mg-numbers show a similar range for plagioclase peridotites (0.901 – 0.913), and a slightly narrower range for spinel peridotites (0.904 ± 0.003).

In contrast to spinel and clinopyroxene, orthopyroxenes show only moderate increase in TiO₂ toward the rims. CaO contents vary between 0.47 and 1.94 wt%. Systematic core-rim variations are only observed for Ca, Al, Cr and rarely Mg.

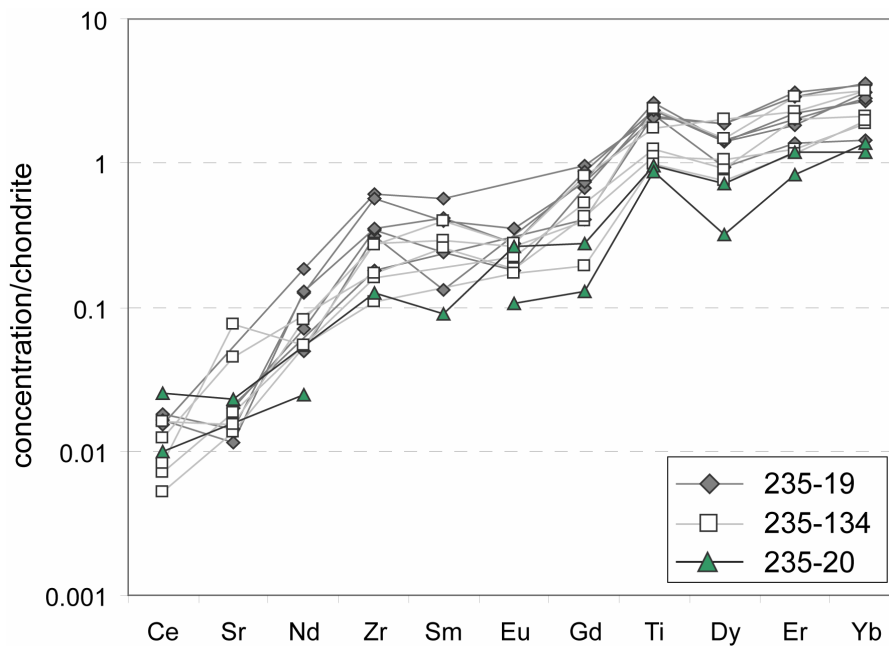
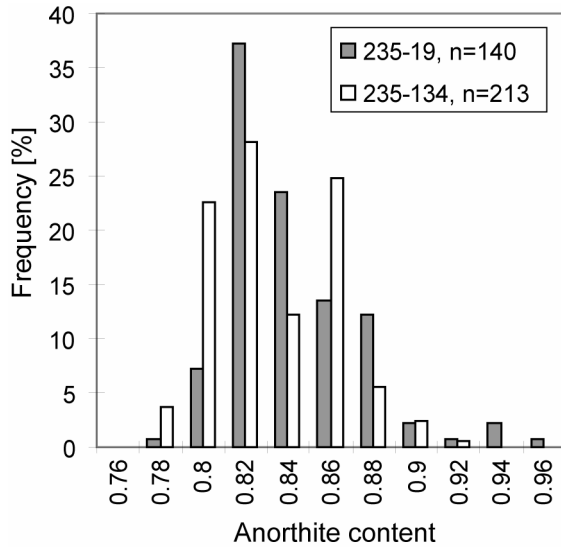


Figure 5-12: Chondrite-normalized trace element abundances of orthopyroxenes.

5.3.4 Plagioclase



Plagioclase of 235-19 and 235-134 cover a wide range of calcic compositions, ranging from An77 to An95, with an average around An82. Plagioclase grains are variable in composition and are often zoned although without a consistent systematic behavior. In broad generalization, most common is reverse zoning.

Figure 5-13: Frequency distribution of anorthite contents in plagioclase peridotites.

A weak correlation between plagioclase composition and texture can be observed. Low anorthite contents between 75 and 80 occur in plagioclase crosscutting mantle olivine while high anorthite contents (>85) occur in spinel coronae and symplectites. Very calcic plagioclase usually occurs in opx-plagioclase symplectites.

Plagioclase trace element compositions vary in both samples, most notably in 235-134. Both samples are characterized by their very low LREE concentration with strong positive Eu-anomalies but only weak positive Sr-anomalies. Lowest Sr-concentrations of 2.38 and 2.99 $\mu\text{g/g}$ occur in the ol-plag/opx-plag-symplectite of 235-134, creating even a slightly negative Sr-anomaly in plagioclase trace element patterns.

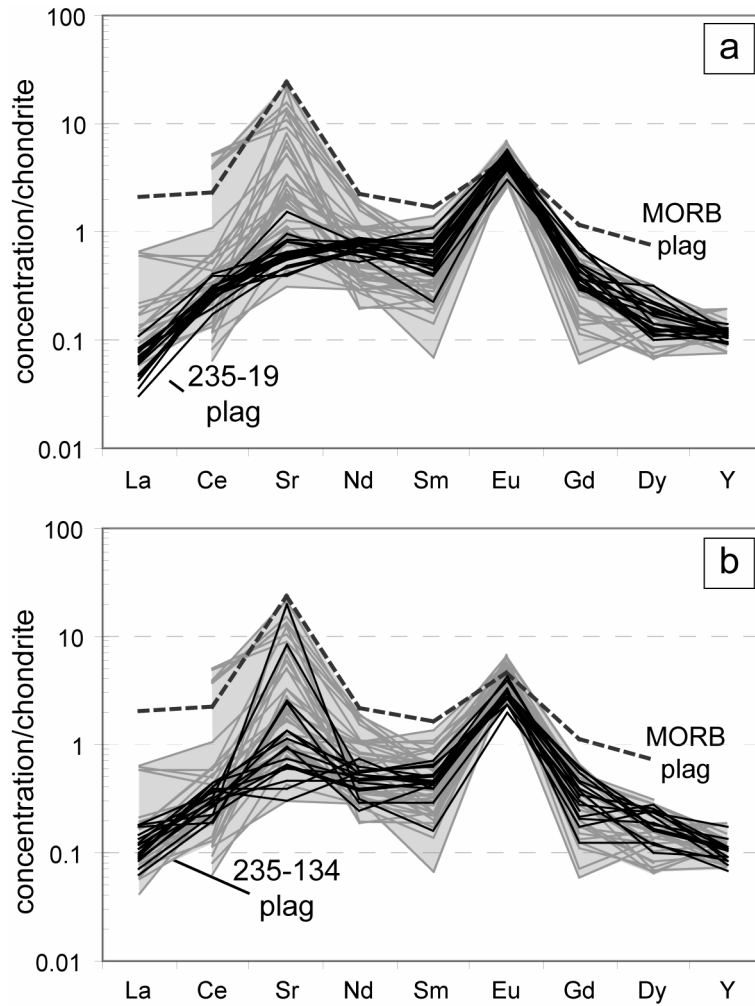


Figure 5-14: Chondrite-normalized REE, Y and Sr abundances of plagioclase in (a) PS56-235-19 and (b) PS59-235-134. In grey, the field of plagioclase compositions from peridotites is shown for comparison (data from Rampone et al., 1993, Rampone et al., 1995, Rampone et al., 1997, Dijkstra et al., 2003, Piccardo et al., 2007). Also shown is a plagioclase of An₈₀ in equilibrium with an average N-MORB composition (from Hofmann, 1988).

Only few analyses of 235-19 show weak positive Sr-anomalies, while Sr concentrations in plagioclase of 235-134 covers a wider range. No clear coupling between Sr- and Eu-anomalies in plagioclase can be observed. Similar observations can be also made for Eu-anomaly and Sr-anomaly against La-concentrations, respectively. Furthermore, no correlation with major element compositions such as anorthite contents exists, indicating that the trace element variability is not the result of trace element partitioning coefficients on major element components.

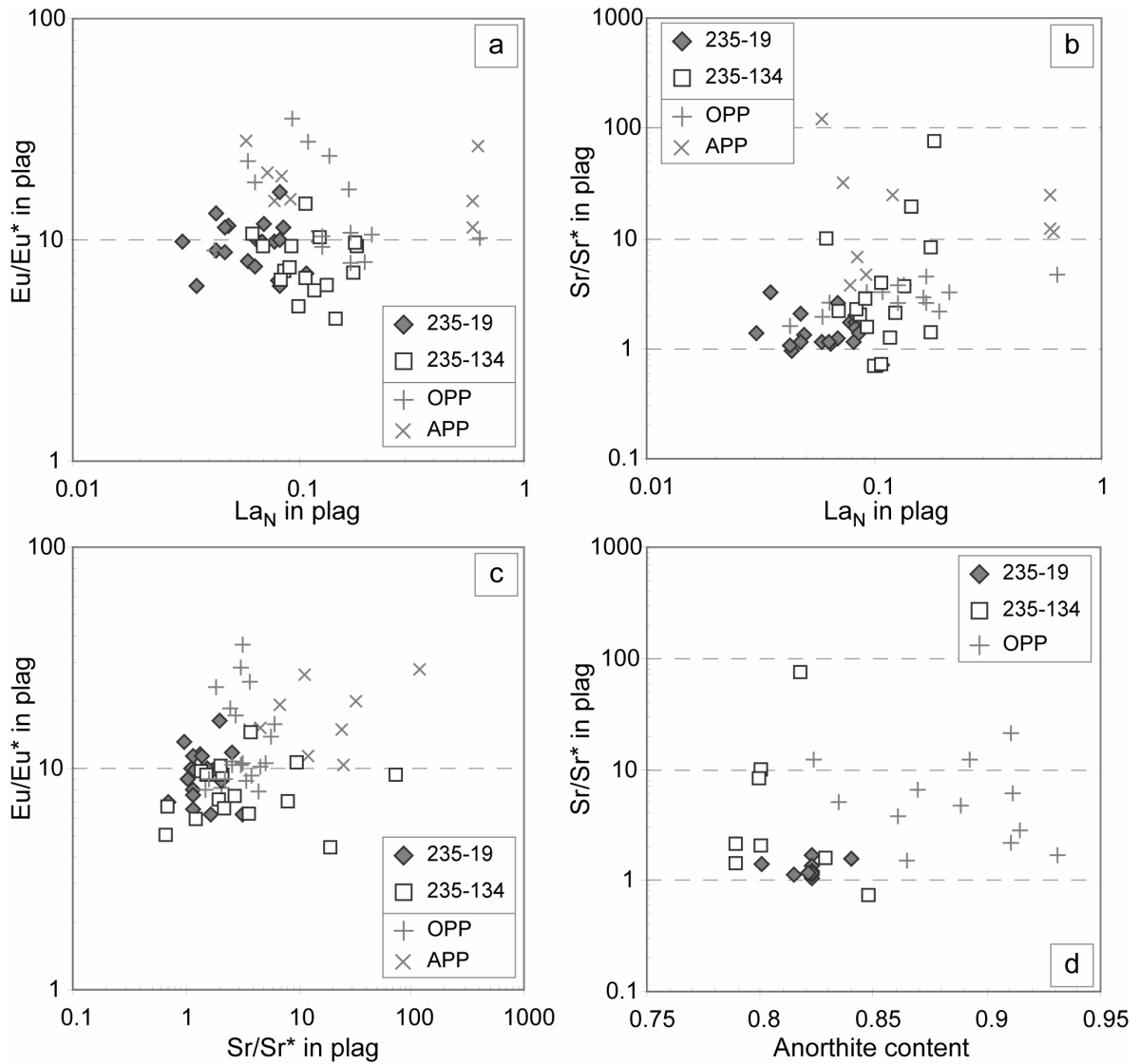


Figure 5-15: (a) La_N versus Eu/Eu^* in plag; (b) La_N versus Sr/Sr^* in plag; (c) Sr/Sr^* versus Eu/Eu^* in plag; (d) anorthite content versus Sr/Sr^* in plag. No clear correlation between major and trace elements is present. Data for comparison from abyssal plagioclase peridotites (APP; SWIR; own data) and from orogenic lherzolites and ophiolites (OPP: Rampone et al., 1997, Dijkstra et al., 2003, Rampone et al., 2005, Piccardo et al., 2007) is shown. Subscript N denotes chondrite-normalized after Anders and Grevesse (1989); $Sr^* = (Ce_N * Nd_N)^{1/2}$, $Eu^* = (Sm_N * Gd_N)^{1/2}$.

5.3.5 Olivine

Olivines from the spinel peridotites display a similar wide range in Mg-numbers as plagioclase peridotites, which ranges from 0.898 to 0.918. Olivines in plagioclase peridotites have almost no overlap in NiO contents, while olivines from spinel peridotites plot in between.

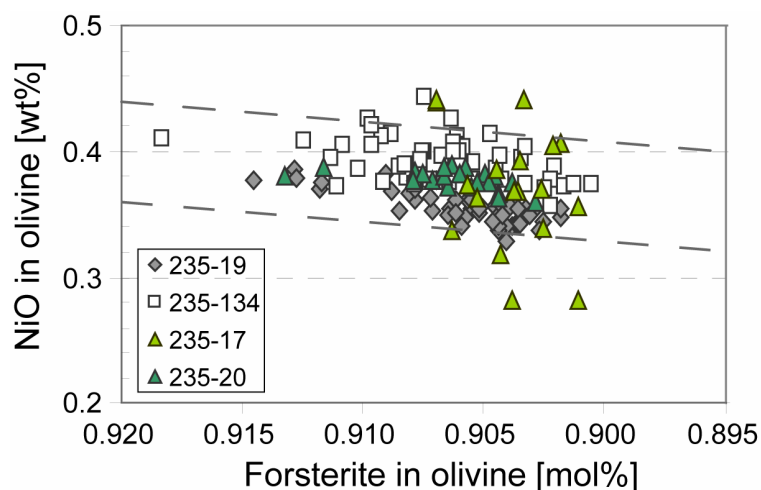


Figure 5-16: Forsterite content against NiO in olivine. The scatter in the Ni-data of 235-17 is an analytical artifact.

5.4 MODELS

There is no consensus on the formation of plagioclase in peridotites. Three different hypotheses for its origin in mantle peridotites have been proposed: (1) subsolidus breakdown of spinel during the transition from spinel- to plagioclase-facies conditions (Hamlyn and Bonatti, 1980, Kornprobst and Tabit, 1988, Vissers et al., 1991, Rampone et al., 1993, Strating et al., 1993, Cannat and Seyler, 1995, Canil et al., 2003), (2) crystallization of an in-situ formed melt (Menzies, 1973, Menzies and Allen, 1974, Boudier and Nicolas, 1985) and (3) crystallization of a transient exotic melt (Dick and Bullen, 1984, Dick, 1989, Barth et al., 2003, Dijkstra et al., 2003, Piccardo et al., 2007). The first two processes are closed-system processes whereas the third should have open system characteristics and it should be possible to narrow down the origin of plagioclase on certain characteristics of these processes. Hence, three different endmember models are usually contemplated: (1) metamorphic formation during the spinel- to plagioclase facies transition; (2) trapped melt crystallization and (3) fractional crystallization and will be discussed in the following.

Textural evidence in the samples provides no conclusive evidence for either of the aforementioned processes. Symplectites often occur in plagioclase-bearing peridotites, either as opx-plag or ol-plag phase assemblages around cpx. Symplectites are mineral intergrowths, believed to form by solid-state reactions and their presence is generally thought to indicate

chemical disequilibrium (Ashworth and Chambers, 2000). An olivine-plagioclase symplectite, replacing cpx in sample 235-134 could indicate accordingly subsolidus transition from spinel- to plagioclase-facies conditions. In contrast, the more ubiquitous opx-plag symplectites require an open system formation with SiO₂-addition. Corona textures such as plagioclase around spinel are typical for transport-controlled reactions such as solid-solid transformations (e.g. Fisher, 1978). On the other hand, grain boundaries between olivine and spinel have high surface energies and are preferential sites of melt movement (Schäfer and Foley, 2002); often, spinels develop plagioclase coronae when they were originally in contact with olivine.

Clinopyroxenes in the plagioclase peridotites show a wide range of trace element composition that may be indicative for either processes of plagioclase formation. Hence, different models are carried out to reproduce the observed trace element patterns (see Appendix for model parameters, partition coefficients and boundary conditions). Furthermore, volume diffusion in plagioclase is known to be very sluggish, particularly for more calcic compositions because of the stronger rigidity of the calcic plagioclase structure (Blundy and Wood, 1991). Therefore, it can be assumed that the plagioclase trace element composition has not substantially changed by volume diffusion but reflects its original composition at the time of formation (see also discussion below).

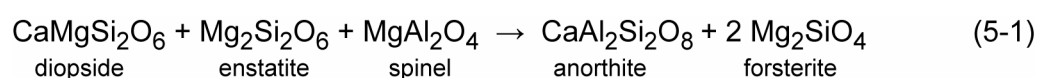
5.4.1 Closed-system breakdown

Plagioclase is only stable in the mantle at low pressures and the upper stability of plagioclase in experimental runs shows a range of 8 to 12 kb at 1200°C (Green and Hibberson, 1970) or 6 to 10 kbar (Kushiro and Yoder, 1966), and the amount of plagioclase decreases with increasing pressures. P-T estimates in natural systems place the transition at about 6.4 kbar at 715°C (Frost, 1976), which is also in agreement with the extrapolation from the work of Kushiro and Yoder (1966). The phase transition has a very steep slope in P-T space and should therefore mostly depend on the change in pressure, regardless of variations in geothermal gradient (Kushiro and Yoder, 1966, Herzberg, 1972). The transition from plagioclase- to spinel-peridotite facies stabilities is strongly composition dependent, and the stability of plagioclase lherzolite increases with the addition of sodium and iron (Herzberg, 1972). The reaction is univariant in the CaO-MgO-Al₂O₃-SiO₂ (CMAS) system, but becomes divariant or

CHAPTER 5

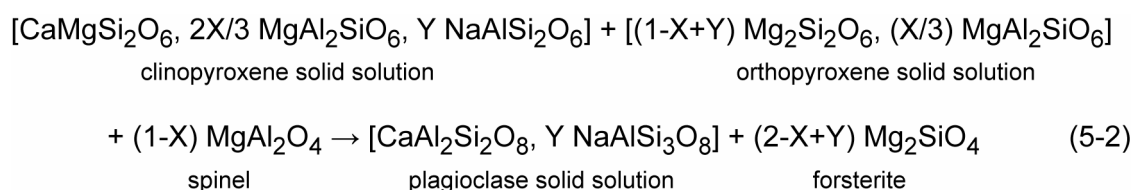
multivariant with the presence of other components (most notably Na₂O, Cr₂O₃, FeO and Fe₂O₃). Therefore, spinel and plagioclase are both stable over a P-T range and can coexist. Furthermore, the facies boundary in natural samples will differ from those predicted by experiments (Frost, 1976). This fits to the observation that spinel usually is still present in plagioclase peridotites.

The transition from spinel to plagioclase facies in the ultramafic CMAS system may be described as



This represents a very simple approach on the reaction and does not take into account the importance of Na and Cr to the system.

A more realistic approach to a natural system may be the following equation (Takazawa et al., 1996):



with $0 < X < 1$; $0 < Y < 1$

This approach takes into account the Mg-Tschermak (MgTs) component in cpx and opx and the jadeite component in cpx, both of which have a strong effect on the modal amount of plagioclase that can be formed by this reaction. Anorthite contents of the resulting plagioclase can be varied as well.

All plagioclase peridotites contain some Cr-spinel, and the complete reaction until spinel-out is not found in natural peridotites. Therefore, the model incorporates a reacting spinel 1 with a Cr-number of 0.1, similar to the lowest Cr-number in PS59-235 spinel peridotites, and produces a spinel 2 of a Cr-number of 0.5, which represents the upper limit of spinel in plagioclase peridotites. No exchange with a kosmochlor component of clinopyroxene was taken into account. This assumption is realistic because increasing chromium contents in

cpx suggest a passive increase by cpx volume decrease. Trace element partition coefficients of plagioclase vary strongly as a function of major element composition (Blundy and Wood, 1991, Bindeman et al., 1998, Bindeman and Davis, 2000, Bedard, 2006) and the formulation of Bedard (2006) has been used accordingly in the model.

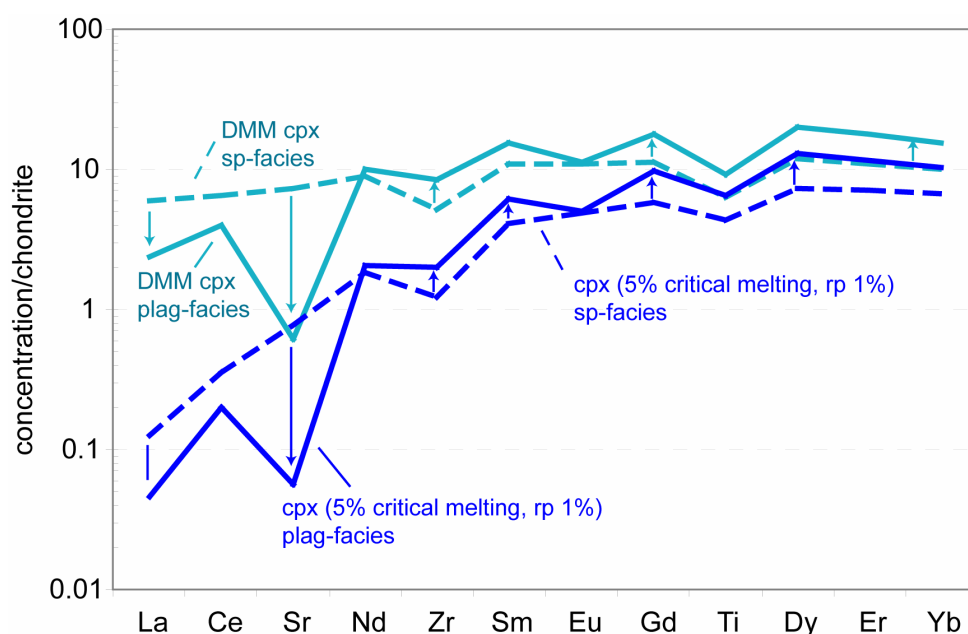


Figure 5-17: Equilibrium trace element redistribution in cpx as a result of the formation of metamorphic plagioclase in a DMM-like mantle composition (Workman and Hart, 2005) and a residual cpx after 5% of critical melting at 1% residual porosity. HREE concentrations in cpx increase as a result of cpx mass reduction. The decrease in LREE and strongly negative Sr-anomalies results from incorporation of these elements into the plagioclase lattice. Metamorphic plagioclase is An_{80} (Model parameters: $X=0.25$ and $Y=0.25$).

Figure 5-17 shows the effect of the spinel- to plagioclase-facies transition on cpx trace element compositions. Two different residual cpx in the spinel facies are shown, one in equilibrium with a DMM mantle composition from Workman and Hart (2005) and the other after 5% critical melting in the spinel stability field and a residual porosity of 1% (see appendix for details). Trace element re-distribution during the formation of metamorphic plagioclase generally results in a strong decrease in LREE and increase in MREE to HREE concentration in cpx and formation of negative Eu- and Sr -anomalies relative to spinel facies cpx.

The effects of the spinel- to plagioclase-facies transition on cpx- and plagioclase composition were modeled for a DMM mantle composition after different degrees of partial

melting. Spinel peridotites from PS59-235 show indicators of high-temperature refertilization (for discussion see Chapter 2) and the protolith of the plagioclase peridotites 235-19 and 235-134 was probably affected by refertilization as well. Therefore, both spinel peridotites 235-17 and -20 are included in the calculations for a more realistic range in spinel peridotite compositions. In the model, the anorthite content of the plagioclase and the MgTs-component in the reacting cpx are varied. These parameters are important, both for the maximal amount of plagioclase formed and trace element composition of the plag-facies cpx and plagioclase itself.

The results of this calculation are shown in Figure 5-18. The amount of plagioclase formed during the spinel- to plagioclase-facies transition is strongly controlled by the amount of spinel present in the sample and to a lesser extent by the pyroxene content. The fertile DMM mantle composition of Workman and Hart (2005) can produce around 13.7% plagioclase, while 235-20 and 235-17 can only form 6.0% and 3.1%, respectively (for anorthite contents typical of the sample set (An_{83}) and a MgTs-component of 0.17). Lower anorthite contents in plagioclase allow the formation of higher abundance of plagioclase but only in pyroxene-rich peridotites. Otherwise pyroxene-out is reached before spinel-out.

Clinopyroxene trace element zoning pattern in PS59-235 plagioclase peridotites show decrease of LREE and increase of MREE to HREE together with negative Eu- and Sr-anomalies as described before. The slope of the REE pattern is strongly controlled by the depletion of the spinel-facies composition. With higher anorthite contents, the plagioclase-facies clinopyroxenes contain more LREE at a less pronounced negative Eu- and Sr-anomaly but similar HREE relative to lower anorthite contents in the associated plagioclase. Incomplete reaction of clinopyroxene may lead to zoning profiles similar as is observed in plagioclase peridotite clinopyroxenes.

Calculated plagioclase compositions are very uniform in their trace element concentrations with little variation between different anorthite contents. Also, the influence of MgTs-component of cpx on plagioclase composition is negligible; the strongest influence is the residual depletion of the protolith, which is reflected in the final LREE abundances. With increasing anorthite contents, plagioclase has much lower MREE and HREE contents but similar LREE and Sr content. With higher anorthite contents, the Sr-anomaly increases as a

result of decreasing Nd-concentrations, rather than changes in Sr content. Theoretically, metamorphic plagioclase only forms a positive Sr-anomaly in the most fertile DMM composition at high anorthite contents and no addition of MgTs-component. In summary, the most dominant control is the contribution of the MgTs-component, and on second order, the effect of decrease of the $D_{\text{plag/liq}}$ for Sr at increasing anorthite contents.

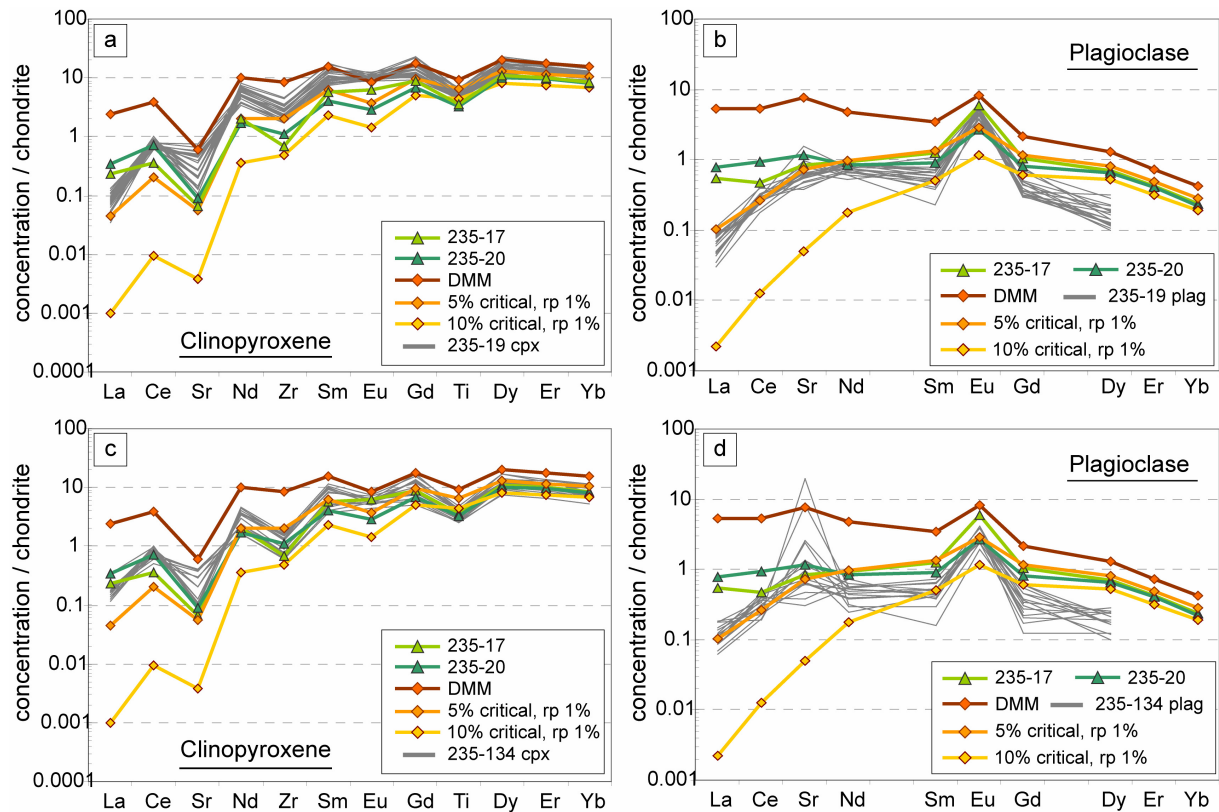


Figure 5-18: Results of closed system spinel- to plagioclase-facies breakdown models for cpx and plagioclase. Also shown are trace element abundances of plagioclase peridotite samples 235-19 (a; b) and 235-134 (c; d). In this model, the produced plagioclase has an anorthite content of 80 and the consumed cpx participated with 0.08 MgTs-component (Model parameters: $X=0.25$, $Y=0.12$). The calculation was carried out for different starting compositions: 235-17 and 235-20 spinel peridotite reconstructed bulk composition; a DMM mantle composition after Workmann and Hart (2005) and after 5% and 10% critical melting (*rp*: residual porosity). Plagioclase from depleted compositions generally shows no or only weak positive Sr-anomalies.

None of the spinel peridotites compositions assumed in this model can exactly reproduce trace element patterns seen in the plagioclase peridotite samples. In order to further explore the systematics of trace element redistribution occurring during the spinel to

plagioclase facies transition, a number of diagrams are constructed that may be useful for fingerprinting this process and will be discussed below.

Figure 5-19 and 5-20 inspect two distinctive element and element ratios, respectively, of plagioclase-facies clinopyroxene compositions. Figure 5-19 displays the formation of a strong negative Sr-anomaly at a minor decrease in LREE/HREE ratio. The reaction trajectories are essentially parallel for cpx compositions with increasing bulk depletion in the spinel field but negative Sr-anomalies increase slightly in more refractory compositions. The anorthite content in the associated plagioclase has only a minor impact on the cpx composition. Calculated plagioclase-facies cpx composition cannot explain the range in negative Sr-anomalies in the samples of this study. Clinopyroxene rim compositions should show the most pronounced signature of any process. However, none of the model parameters can reproduce the pronounced negative Sr-anomaly exhibited by clinopyroxenes in plagioclase peridotites. Using reconstructed bulk compositions of spinel peridotites from this study as starting composition does not change this conclusion (not shown). Breakdown of sample 235-20 will follow the compositional trend of a DMM composition, only shifted downwards in the Figure 5-18a, but not sufficiently to explain the cpx compositions of the plagioclase peridotites. Breakdown of sample 235-17 will actually result in decreasing Sr-anomalies with increasing depletion. This is the result of the low modal amount of spinel in 235-17 that only allows the formation of small amounts of plagioclase. The lower the amount of plagioclase formed the less impact its formation has on clinopyroxene composition naturally. No reasonable set of model parameter allows enclosing all the cpx composition from plagioclase peridotites.

CHAPTER 5

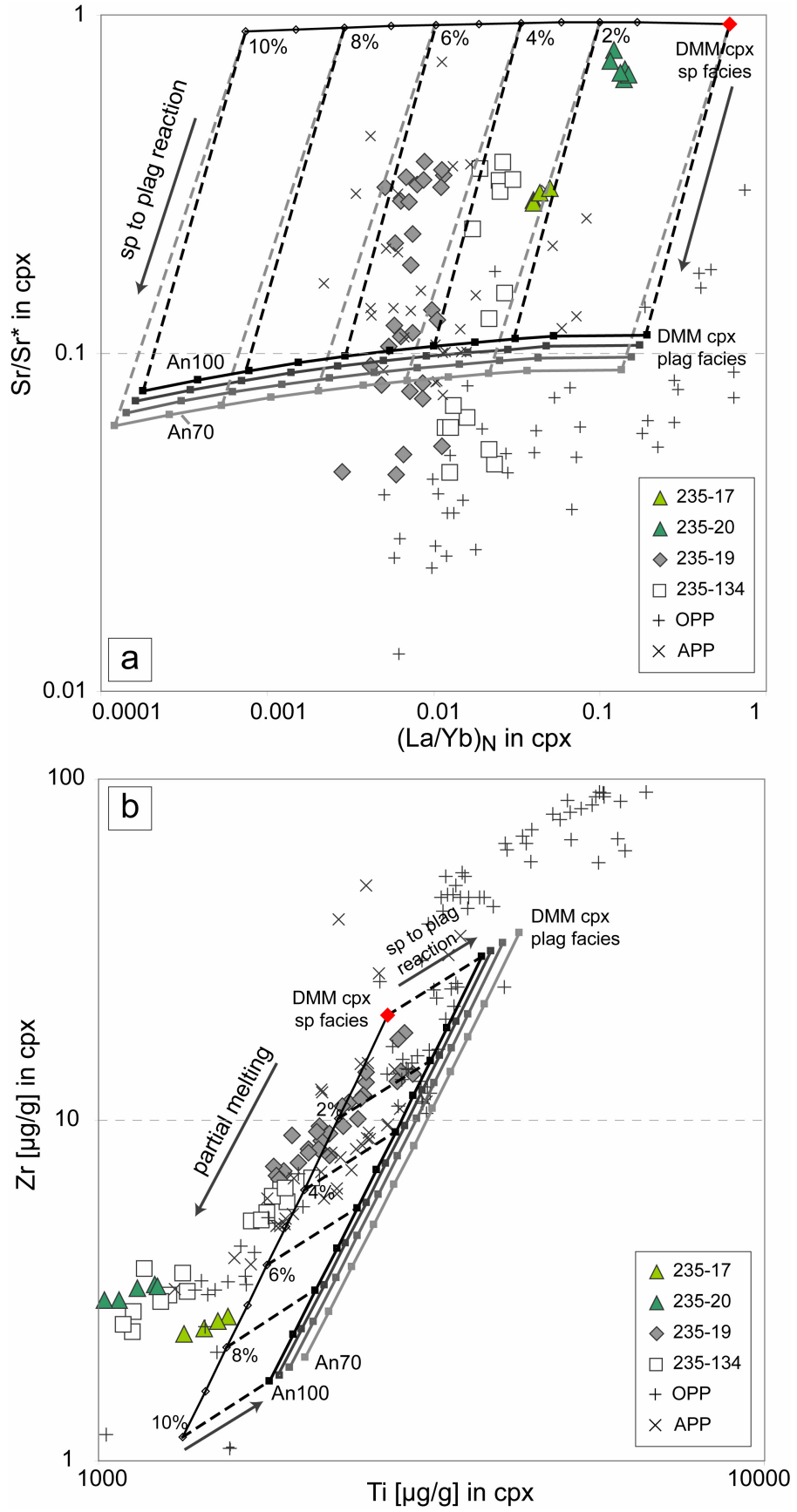


Figure 5-19: Results of the spinel to plagioclase facies transition model for clinopyroxene compositions. Starting composition is a DMM mantle composition at increasing degrees of depletion after critical melting at 1% residual porosity. This composition is then subjected to a complete breakdown reaction of spinel to plagioclase facies. Anorthite contents in plagioclase in equilibrium are varied between An70 and An100 ($Y = 0.438 - 0$) but the MgTs-component in the pyroxenes is constant ($X = 0.12$). Data from abyssal plagioclase peridotites (APP, SWIR own data) and plagioclase peridotites from orogenic lherzolites and ophiolites (Frey et al., 1991, Barth et al., 2003, Müntener et al., 2004, Piccardo et al., 2007) are shown for comparison; (a) $(La/Yb)_N$ versus Sr/Sr^ . The spinel to plagioclase facies transition leads to a minor decrease in $(La/Yb)_N$ and a strong increase in negative Sr-anomaly in plagioclase-facies cpx relative to its spinel-facies composition. Decreasing anorthite contents in the equilibrium plagioclase shift the $(La/Yb)_N$ ratio toward lower values. (b) Ti- versus Zr-concentration in clinopyroxene. The spinel to plagioclase facies transition shifts concentrations in clinopyroxene to higher Ti- and Zr-concentration which results in a shift away from the melting trend.*

Figure 5-19 explores how two other useful trace elements in cpx, Ti and Zr are affected by the formation of metamorphic plagioclase in peridotites. Titanium and zirconium in cpx are often used as indicator for the degree of melting as proposed by Johnson et al. (1990). The spinel to plagioclase-facies transition shifts cpx from the melting trend toward higher Ti- and Zr-content relative to its spinel facies counterpart. The lower the anorthite content in the newly formed plagioclase, the more plagioclase is formed, and accordingly the stronger this shift will be. Neither the breakdown of a residue after partial melting of DMM nor of either the spinel peridotites can explain the observed compositional range. The variation in Ti-Zr in each sample is too steep with respect to the reaction trajectory in the Ti-Zr compositional space to comply with a spinel to plagioclase transformation process.

The range in plagioclase compositions formed by this reaction is even more restricted as can be seen in Figure 5-20. Metamorphic plagioclase formed in peridotites should only show a narrow range in positive Eu- and Sr-anomalies, which are much smaller than commonly seen in plagioclase peridotites. Decreasing anorthite contents will only result in slightly lower Eu- and Sr- anomalies. The LREE in plagioclase can change strongly but only reflect the spinel facies depletion of the bulk rock. A purely metamorphic origin of plagioclase cannot explain the range of positive Sr-anomalies seen in the sample set and also plagioclase composition from other locations.

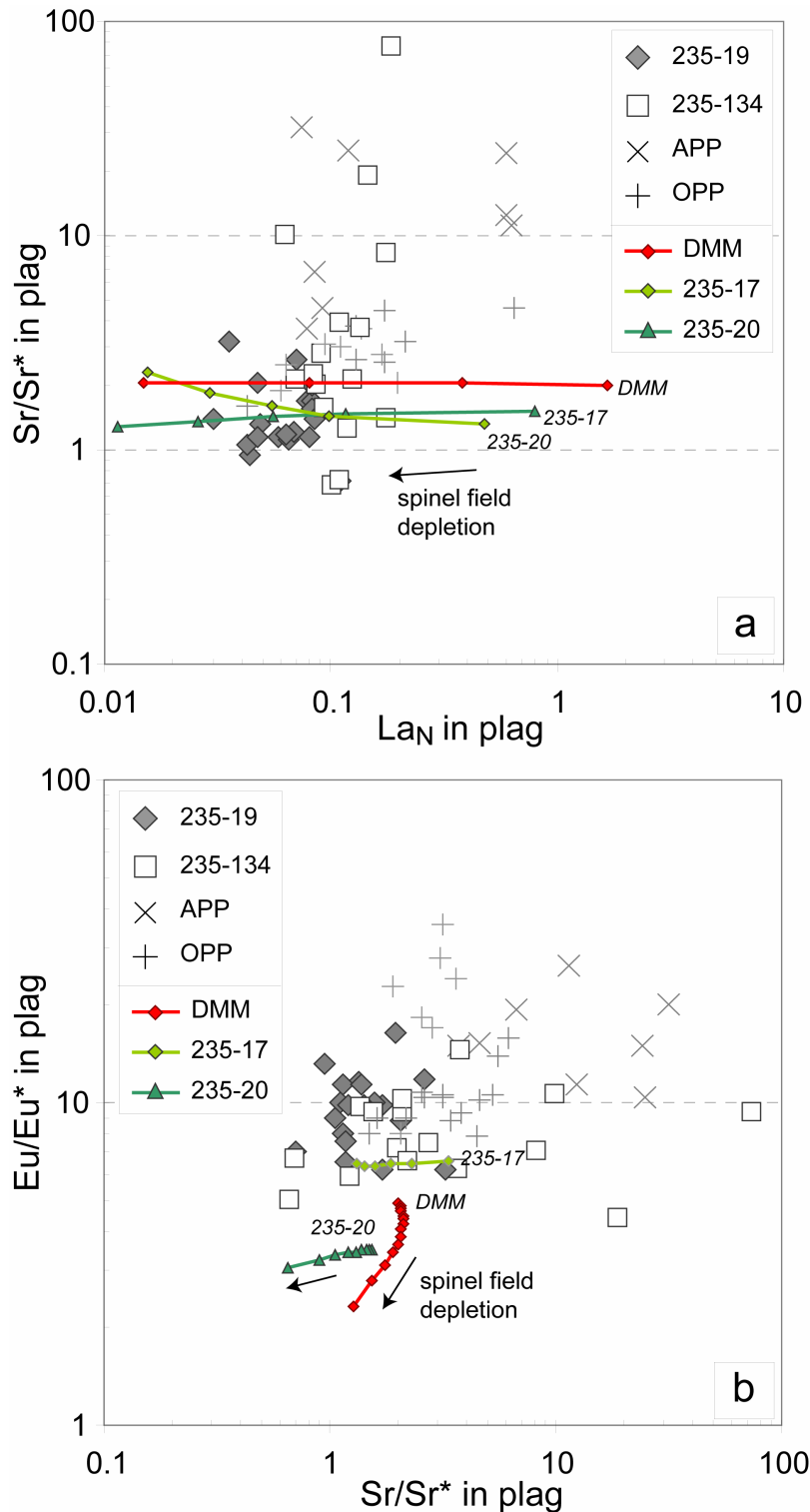


Figure 5-20: Results of the spinel to plagioclase facies transition model for plagioclase. In both models, anorthite contents in plagioclase are An_{90} ($Y=0.11$) and the $MgTs$ component in the pyroxenes is constant ($X=0.12$). The change in plagioclase compositions due to variable anorthite contents is only barely visible in the log-spaced diagram. Starting composition is a DMM mantle composition at increasing degrees of depletion after critical melting at 1% residual porosity. This composition is then subjected to a complete breakdown reaction of spinel to plagioclase facies. Data from abyssal plagioclase peridotites (APP, SWIR own data) and plagioclase peridotites from orogenic lherzolites and ophiolites

CHAPTER 5

(Rampone et al., 1993, Rampone et al., 2005, Piccardo et al., 2007) are shown for comparison; (a) Sr/Sr versus Eu/Eu* in plagioclase. Composition of metamorphic plagioclase is almost constant, facies transition leads to a minor decrease in (La/Yb)_N and a strong increase in negative Sr-anomaly in plagioclase-facies cpx relative to its spinel-facies composition. Decreasing anorthite contents in the equilibrium plagioclase shift the (La/Yb)_N ratio toward lower values. (b) Chondrite-normalized La versus Sr/Sr* in plagioclase. The spinel to plagioclase facies transition shifts concentrations in clinopyroxene to higher Ti- and Zr-concentration which results in a shift away from the melting trend.*

In summary, while the core-rim zoning of cpx appears to be in qualitative agreement with trace element redistribution expected during the spinel- to plagioclase-facies transition, a purely metamorphic origin of the plagioclase peridotites from Gakkel Ridge can be ruled out. However, cpx and plagioclase in the olivine-plagioclase symplectite in sample 235-134 can be explained well by a closed system breakdown of spinel. Figure 5-21 shows the composition of plagioclase and clinopyroxene formed as the products of the spinel to plagioclase facies transition, respectively. Two possible protoliths are shown: a DMM mantle composition after 5% of critical melting (residual porosity 1%) and spinel peridotites 235-17 from the same dredge haul. The pronounced negative Ti- and Zr-anomalies in the spinel peridotite from Gakkel Ridge make them a more likely precursor for plagioclase peridotite 235-134. An almost perfect match is achieved for PS59-235-17. Minor differences in composition may be either explained by slight differences in starting composition, incomplete reaction of the clinopyroxene and differences in partition coefficients.

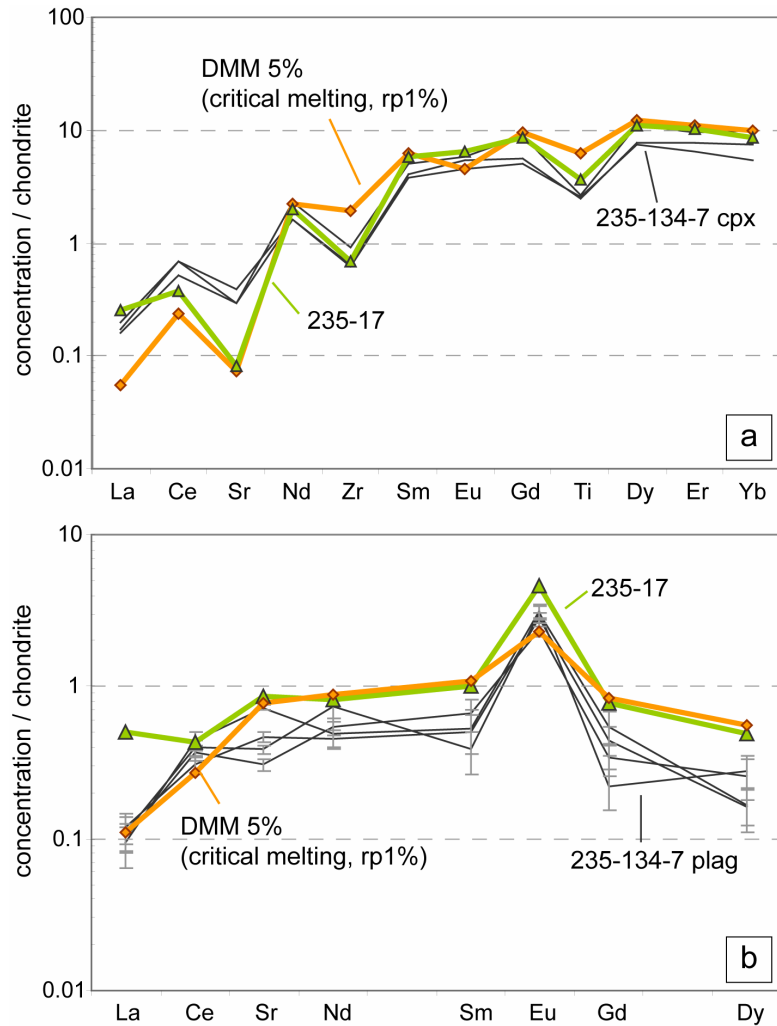


Figure 5-21: Results of spinel- to plagioclase-facies breakdown models for cpx and plagioclase and the respective trace element abundances from the olivine-plagioclase symplectite in samples 235-134. In this model, the produced plagioclase has an anorthite content of 90 and the consumed cpx participated with 0.08 MgTs-component (Model parameters: $X=0.11$, $Y=0.12$). The calculation was carried out for different starting compositions: (1) DMM mantle composition after Workmann and Hart (2005) after 5% critical melting (rp : residual porosity); (2) 235-17 spinel peridotite.

5.4.2 Melt impregnation

Melt refertilization is a ubiquitous process in the upper oceanic mantle (Dick, 1989, Elthon, 1992, Seyler and Bonatti, 1997, Hellebrand et al., 2002, Niu, 2004, Brunelli et al., 2006, Le Roux et al., 2007). In particular, if melts migrate by porous flow and enter the conductively cooled mantle lithosphere, partial crystallization and formation of impregnated peridotites is expected (e.g., (Ceuleneer et al., 1988, Dick, 1989, Ceuleneer and Rabinowicz, 1992, Elthon, 1992, Spiegelman, 1993c, Seyler and Bonatti, 1997). This should occur primarily in areas of

increased lithospheric thickness like fracture zones or slow-spreading ridges. Theoretical calculations suggest that the thermal boundary layer (TBL) beneath most or all slow-spreading ridges could extend deeper than 15 km (Sleep, 1975, Sleep and Barth, 1997) or as much as 20 km at half-spreading rates of ~ 10 mm/year (Sleep, 1975, Reid and Jackson, 1981, Braun et al., 2000, White et al., 2001). It may be even thicker at Gakkel Ridge near the sample location with its half-spreading rate of 6 mm/year (Montesi and Behn, 2007).

Melts entering the TBL may reach saturation in plagioclase and/or orthopyroxene and subsequent crystallization will then result in reduction of pore space. The saturation of low Ca-opx in the melt and crystallization will further create another permeability barrier by the “choking” effect of opx. Orthopyroxene is known to impede melt migration due to its wetting angle effect based on laboratory experiments on melt migration in olivine and ol+opx aggregates (Fujii et al., 1986, Toramaru and Fujii, 1986, Daines and Kohlstedt, 1993, Schäfer and Foley, 2002, Dijkstra et al., 2003).

Reaction between peridotite and crystallizing liquid below the temperature of plagioclase saturation ($\sim 1240^\circ\text{C}$) nearly doubles the rate of crystallization compared to cooling alone (Kelemen and Aharonov, 1998) and is predicted to quickly reduce porosity and permeability (Kelemen et al., 1997b, Korenaga and Kelemen, 1997). Cooling of olivine-saturated liquids similar to parental MORB in the forsterite-anorthite-diopside system leads to minor olivine crystallization, followed by co-saturation in ol+plag, and then olivine+plag+cpx. At the eutectic in the simple system, all of the magma is consumed by crystallization at constant temperature before cooling can continue. Crystallization rates of up to tens of percent of their liquid mass are predicted to occur over a 20-40°C interval at temperatures below the ol+plag (+cpx) saturation. In the natural system of course, olivine+ plag+ cpx saturation is not truly eutectic, but the analogy with the simple system explains the large decrease in magma mass over a narrow cooling interval (Kelemen and Aharonov, 1998, Asimow, 2002). As a result, impregnation of peridotite by a basaltic melt may vary between a localized complete crystallization as trapped melt and the formation of cumulus minerals from transient melts.

In the sections below, the chemical effects of these two end-member models on the trace element signatures of plagioclase are evaluated. The principles of these mass balance

calculations have been described in detail for spinel peridotites by Elthon (1992), Hellebrand et al. (2002) and Brunelli et al. (2005).

5.4.2.1 Trapped melt model

The origin of plagioclase and cpx in plagioclase peridotites by a trapped melt in plagioclase peridotites has been suggested before (Dick, 1989, Rampone et al., 1997). A “cryptic trapped melt fraction” was also suggested to explain the relatively enriched character of cumulus phases. In particular the variation in cpx-HREE in plagioclase peridotites was suggested to be related to the equilibration of cpx with a trapped melt fraction (Dijkstra et al., 2003), that will lead to an increase in the MREE and HREE, the so-called “trapped liquid shift” (Barnes, 1986).

Accordingly, a trapped melt model after Elthon (1992) was modeled. This model simulates entrapment of small amounts of melt in a residual peridotite matrix, followed by crystallization and equilibrium trace element redistribution as a function of the mineral/liquid partition coefficients. By varying the input parameters (initial whole-rock composition and mineral modes, composition of the infiltrating melt and crystallization mode), the possible range of compositional variation can be explored.

Residual rock compositions were calculated after 1%, 5%, 10% and 15% (cpx out) of critical melting of a DMM mantle composition (Workman and Hart, 2005). Melt increments at corresponding degrees of critical melting were calculated and linearly mixed with the whole-rock at varying proportions. Only crystallization of plagioclase and clinopyroxene was assumed in proportions of 10:90, 50:50 and 90:10. Pure plagioclase crystallization is unlikely as plagioclase crystallizes along cotectics with olivine and/or clinopyroxene. Crystallization of olivine and/or orthopyroxene will not significantly change the trace element budget because of their low relative trace element concentrations. The mineral proportions are chosen to explore a wide range of compositions and are not intended to reflect commonly accepted cotectic ratios.

The maximum amount of trapped melt that can be held in peridotite matrix before disaggregation occurs is still open to debate. The suggested range of trapped melt fractions in

mantle peridotites varies from few percent (Seyler et al., 2001, Hellebrand et al., 2002, Brunelli et al., 2006) over 10-15% (Elthon, 1992, Rampone et al., 1997, Takahashi, 2001, Dijkstra et al., 2003) to as much as 30% (Dick, 1989). The latter is in agreement with the maximum estimate for porosity waves in the mantle (Khodakovskii et al., 1995) and experimental data (Renner et al., 2000) and may represent an extreme upper limit. On the other hand, melt migration by porous flow is thought to not exceed a few percent of the total melt flux (Korenaga and Kelemen, 1998) and the total amount of trapped melt in the peridotite may be the result of accumulation of many small melt increments. Furthermore, melt production rates at Gakkel Ridge are supposed to be very low (Michael et al., 2003).

Figure 5-22 shows the effect of trapped melt on the composition of residual cpx in a peridotite matrix. Unsurprisingly, cpx compositions in highly refractory peridotites are affected the most by impregnation by a more fertile melt. At less than one percent of melt fraction added, easily overlooked in serpentinized peridotites, the $(La/Yb)_N$ ratio of cpx increases drastically. Simultaneously, the associated negative Sr-anomaly even decreases at high cpx/plag ratios or stay constant at very low cpx/plag ratios. Only when the amount of trapped melt exceeds 1%, will the negative Sr-anomaly increase at small change in $(La/Yb)_N$ until melt/rock ratios of several percent are reached.

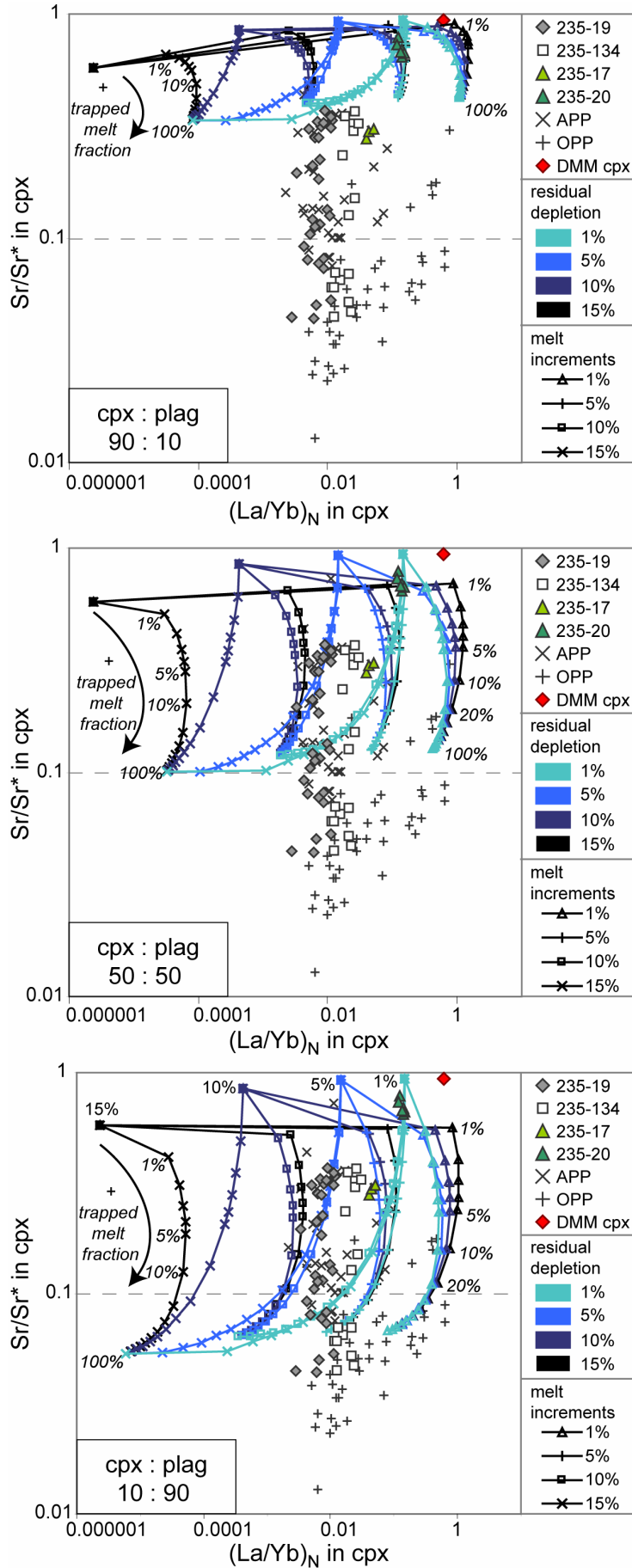


Figure: 5-22: Chondrite-normalized (La/Yb) ratio versus Sr/Sr^* in cpx. Trapped melt model with the combination of different degrees of the depletion of DMM-like mantle (Workman and Hart, 2005) and corresponding melt increments produced at a residual porosity of 1%. The trapped melt fraction crystallized cpx and plag in different proportions (10:90; 50:50; 90:10). Data from abyssal plagioclase peridotites (APP: SWIR: own data) and plagioclase peridotites from ophiolites and orogenic lherzolites (OPP: (Frey et al., 1991, Barth et al., 2003, Müntener and Piccardo, 2003, Müntener et al., 2004, Piccardo et al., 2007)). This figure basically shows the effect of increasing amounts of plagioclase in a peridotite matrix on cpx compositions. The trapped melt fraction ranges between nil and 100% (shown in italics). With increasing amount of plagioclase, the strength of the negative Sr anomaly increases. $Sr^* = (Ce_N^*/Nd_N)^{1/2}$.

CHAPTER 5

For most combinations of melt-rock compositions, LREE/HREE ratios and Sr-anomaly vary in a similar order of magnitude respectively. Only high trace element concentrations and initial cpx mode in fertile mantle compositions buffer the REE budget and cpx predominantly varies in its Sr-content until a large amount of plagioclase is trapped. In general, negative Sr-anomalies in cpx increase with increasing plagioclase crystallization in the matrix while $(La/Yb)_N$ ratios typically change at very high melt/rock ratios.

The reactive textures between residual minerals and new phases preclude an origin from an in-situ formed equilibrium melt by incipient melting. Furthermore, in order to explain the core-rim variation seen in cpx in the plagioclase peridotites, 235-19 and -134, the impregnating melt has to be more refractory relative to the residual peridotite. This suggests that these clinopyroxenes would still reflect their melting history in the LREE/HREE ratio at low melt-rock ratios and would correspond to a degree of depletion between 5% and 10% for the plagioclase peridotites prior impregnation. However, even in the unrealistic scenario of 100% trapped melt fraction (which would rather be anorthosite with xenocrysts) the range of negative Sr- anomalies cannot be reproduced by this trapped melt model.

Figure 5-23 explores the effect of melt entrapment in the Ti-Zr compositional space of cpx. The variation in Ti- and Zr-concentrations in cpx is often used to estimate the degree of partial melting as proposed by Johnson et al. (1990). This may be applicable to residual peridotites, However it can be seen from Figure 5-23 that the Ti-Zr ratio in cpx is easily disturbed by melt-rock reaction. Trapped melt is capable to increase Ti- and Zr-concentration at small amounts of trapped melt. The range in cpx composition that can be produced by trapped melt with dominantly plagioclase crystallization is very large and covers both the measured data as well as the global range of plagioclase peridotites. In most cases, melt fractions of around 10% would be sufficient.

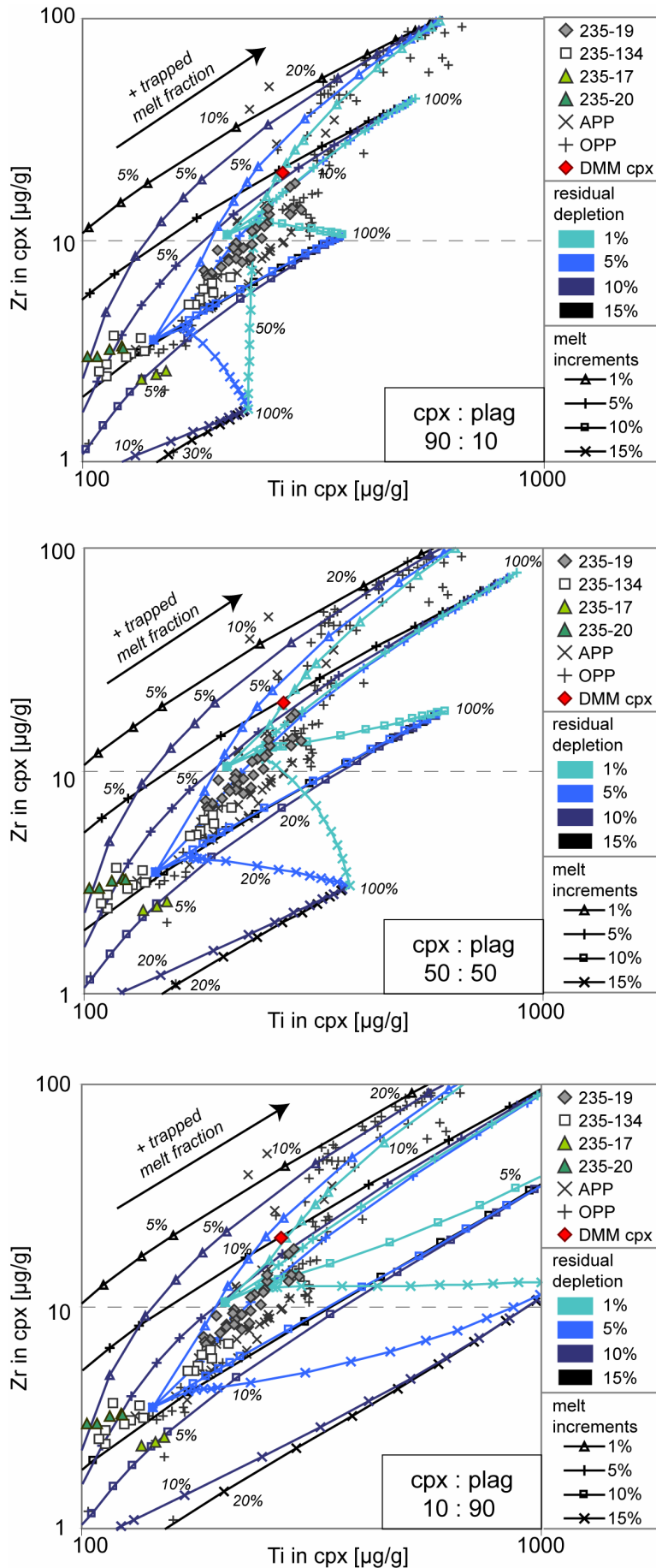


Figure 5-23: Ti-content versus Zr in cpx. Trapped melt model with the combination of different degrees of the depletion of DMM-like mantle (Workman and Hart, 2005) and corresponding melt increments produced at a residual porosity of 1%. The trapped melt fraction crystallized cpx and plag in different proportions (10:90; 50:50; 90:10). Data from abyssal plagioclase peridotites (APP: SWIR: own data) and plagioclase peridotites from ophiolites and orogenic lherzolites (OPP: (Frey et al., 1991, Barth et al., 2003, Müntener and Piccardo, 2003, Müntener et al., 2004, Piccardo et al., 2007)). This figure shows the effect of increasing amounts of plagioclase in a peridotite matrix on cpx compositions. The trapped melt fraction ranges between nil and 100% (shown in italics). With increasing amount of plagioclase increases the strength of the negative Sr anomaly.

Similar to Figure 5-22, a residual depletion between 5% and 10% is suggested by the Ti- and Zr-contents for the plagioclase peridotites. Nevertheless, the large range of negative Sr-anomalies cannot be explained by pure trapped melt model even at high melt-rock ratios. Furthermore, trace element patterns cannot be reproduced by this model.

In summary, simple entrapment of discrete melt increments in a spinel peridotite and equilibration cannot explain the compositional range seen in the clinopyroxenes from the plagioclase peridotites.

5.4.2.2 Fractional crystallization model

High anorthite contents in plagioclase and Mg-numbers in cpx have been suggested to be the product of (fractional) crystallization from a melt rather than frozen-in melt pockets. Similar compositions have been found in cumulate minerals in oceanic gabbros (Ross and Elthon, 1993, Coogan et al., 2000, Natland and Dick, 2001) and gabbroic sills in peridotites from the Oman ophiolite (Kelemen et al., 1997a, Benoit et al., 1999, Koga et al., 2001). They are also often described in plagioclase-bearing peridotites from ophiolites (Rampone et al., 1996, Rampone et al., 1997, Dijkstra et al., 2003). In all instances, they have been interpreted as the product of fractional crystallization from depleted melts, the crystals representing only a small fraction of the parental liquid mass.

Clinopyroxenes in plagioclase peridotite sample 235-134 form two distinct groups in textures and composition. Their characteristics (no core-rim zoning; high Cr-numbers and REE abundances; most pronounced negative Sr- and Eu-anomalies) suggest that they are crystallized from the melt as a final step. Accordingly, two magmatic phases need to be considered in sample PS59-235-134, magmatic cpx and plagioclase.

Information on the geochemical signature of the impregnating melt, can be obtained by the trace element composition of the magmatic phases using mineral/melt partition coefficients. Calculation of individual equilibrium liquids for plagioclase and magmatic cpx in sample 235-134 shows that both phases are in apparent disequilibrium. Equilibrium liquids for clinopyroxene are shifted to much higher concentrations relative to parental melts from

plagioclase. Furthermore, the parental melt of clinopyroxene shows significant negative anomalies for Sr, Ti, Eu and Zr (Figure 5-24).

However, such calculations are strongly dependent on the appropriate partition coefficient set and melt structure has been shown to have significant control on trace element partitioning (Ewart and Griffin, 1994). Experiments indicate that the influence of melt structure increases as the degree of melting decreases and is significant at low pressures (10 - 15 kbar) (Gaetani, 2004). Melt structure does not change the compatibility from one REE to another (Ellison and Hess, 1989) but can proportionally increase or decrease the partition coefficients (Gaetani, 2004). However, trace elements with low to charge to radius ratios are concentrated in highly polymerized melts while smaller, highly charged cations partition preferentially into depolymerized melts. Therefore, alkalis, HFSE and REE can be fractionated (Gaetani, 2004). Orthopyroxene crystallization suggests high silica saturation of the melt and the role of high $D^{cpx/l}$ for plagioclase peridotites has been recently pointed out (Piccardo and Vissers, 2007, Piccardo et al., 2007). Therefore, partition coefficients from Vannucci et al. (1998), estimated from clinopyroxenes in equilibrium with glasses in a range of SiO₂ contents, were applied. Discrepancies between parental melts calculated from clinopyroxene and plagioclase could be resolved by application of partition coefficients for a SiO₂ content of 52 wt% in the melt. In addition, the extent of negative anomalies in the melt was either eliminated or at least reduced (Figure 5-24).

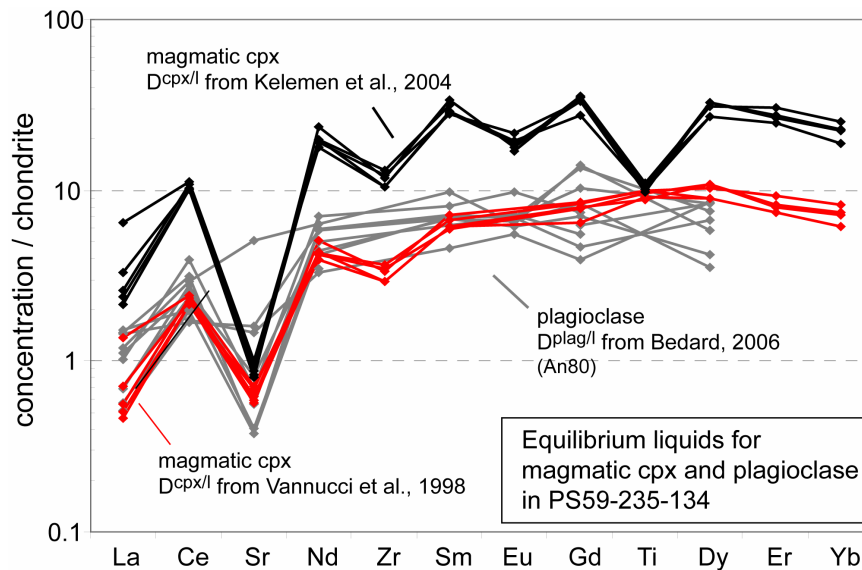


Figure 5-24: Chondrite-normalized parental melts for PS59-235-134 plagioclase (excluding plagioclase from the olivine-plagioclase symplectite) calculated with $D^{plag/l}$ calculated from Bedard (2006) in grey, and magmatic clinopyroxene calculated with $D^{cpx/l}$ from Kelemen et al. (2004) and Vannucci et al. (1998).

CHAPTER 5

This suggests that the distinctive MREE to HREE enrichment that usually occurs at cpx rims in plagioclase peridotites is at least partly due to melt structure modified $D^{cpx/l}$ partition coefficients.

It also further corroborates that post-crystallization REE-redistribution between plagioclase and clinopyroxene was negligible. Generally, the preference of pyroxenes for HREE while plagioclase for LREE and Eu^{2+} would result only in a slight rotation of their respective REE-pattern (Loucks, 1996, Papike et al., 1996, Treiman, 1996). Thus, plagioclase and 235-134 magmatic cpx composition are used as the best estimate for the composition of the infiltrating melt.

The pronounced negative Sr-anomalies in the equilibrium liquids indicate significant plagioclase fractionation. Equilibrium melts plagioclase grains in sample 235-134 show progressive plagioclase fractionation with increasing negative Sr-anomalies. Relating the equilibrium liquid compositions to a fractional crystallization model yields good results although no excellent match was achieved. Only equilibrium liquids to plagioclase were considered and only plagioclase fractionation was assumed. Crystallization of orthopyroxene, obvious in thin section, did not change significantly liquid trace element composition because of its low trace element content. Furthermore, major and trace element compositions of magmatic cpx indicate that it crystallized late in the sequence, probably as final stage. However, significant plagioclase crystallization (as much as 80%) is required to produce the negative Sr-anomalies in the parental liquid. Best fit to calculated liquid compositions was achieved by impregnation of a melt increment of 235-20. However, although fractional crystallization provides the best agreement for the compositional variation in plagioclase peridotites, it could not explain all distinctive features of plagioclase peridotites.

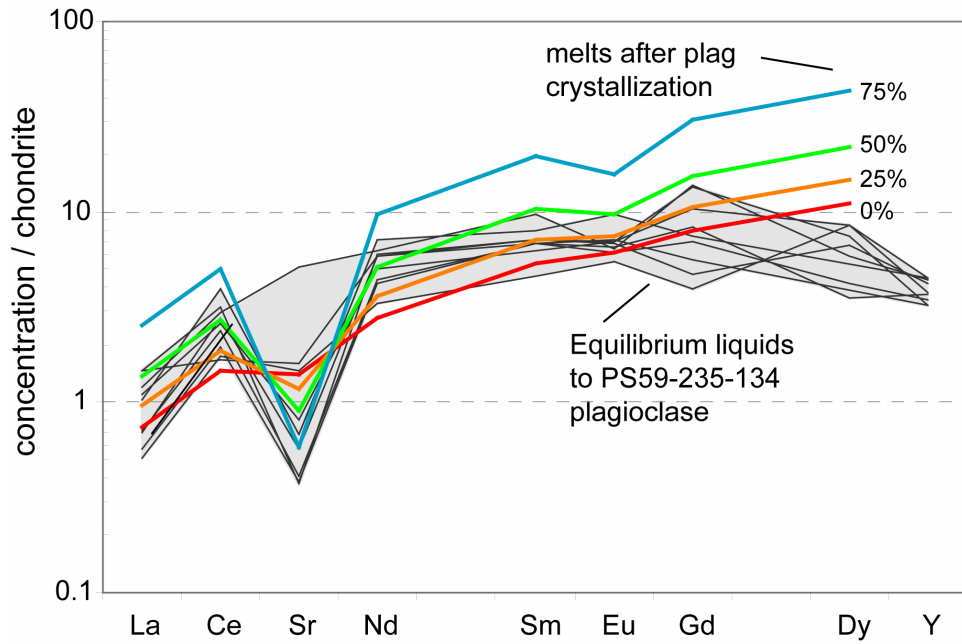


Figure 5-25: Fractional crystallization model for chondrite-normalized parental melts for PS59-235-134 plagioclase calculated with $D^{plag/l}$ calculated from Bedard (2006).

5.5 DISCUSSION

Three mutually non-exclusive models have been proposed to explain the occurrence of plagioclase in abyssal peridotites: (1) subsolidus breakdown of spinel during the spinel- to plagioclase facies transition (5.4.1), (2) trapped melt crystallization (5.4.2.1) and (3) fractional crystallization (5.4.2.2). Despite the relative fertility of spinel peridotites at Gakkel Ridge (high modal cpx, high Na_2O in cpx, low spinel Cr-number), the range of composition in plagioclase peridotites from Gakkel Ridge cannot be explained by closed system breakdown of spinel alone. Instead the dominant process was interaction with a transient melt and only minor contribution of subsolidus phase transformation. Hence, plagioclase formation in peridotites at extensional settings can be due to both, melt impregnation and metamorphic recrystallization from spinel- to plagioclase-facies conditions. Both processes are likely concomitant, and not easily distinguishable in their petrological signature. Major and trace element variation in clinopyroxene are not conclusively indicative of either process, especially when the impregnating melts have a trace element depleted composition (Rampone et al., 2005). Rather, plagioclase compositions and Sr-concentrations in cpx and plagioclase are important indicators

in the discrimination of the different processes while Eu-anomalies in clinopyroxene are often not developed.

5.5.1 Parental melts to plagioclase peridotites – ambiguous

Plagioclase peridotites from Gakkel Ridge are dominantly produced by a migrating exotic melt, however, compositional characteristics of the impregnating melt appear to contradict commonly accepted facts on peridotite melting.

In examining the possible processes responsible for the formation of plagioclase peridotites, several observations must be accounted for and explained. These are (1) LREE-depleted plagioclase and clinopyroxene composition, (2) high anorthite plagioclase, (3) higher Cr- and Mg-number at pyroxene rims than cores and (4) dissolution of clinopyroxene and olivine and formation of orthopyroxene and plagioclase (\pm cpx).

Different processes have been taken into consideration to explain the parental melt characteristics indicated by plagioclase peridotites. Depleted signature in melts are thought to be the result of (1) (shallow) melting of a refractory source (Sobolev and Shimizu, 1993, Kelemen et al., 1997a, Barth et al., 2003, Dijkstra et al., 2003), sometimes under the assistance of water (Benoit et al., 1999, Nonnotte et al., 2005) or (2) chromatographic equilibration with a depleted mantle column (Godard et al., 1995, Batanova et al., 1998, Reiners, 1998, Suhr et al., 1998).

The high anorthite contents in plagioclase, ubiquitous in plagioclase peridotites and abyssal gabbros (Elthon et al., 1992, Ross and Elthon, 1993, Natland and Dick, 2001) are either produced by shallow crystallization of refractory melt (Cannat et al., 1990, Dijkstra et al., 2003) or crystallization from a hydrous melt (Sisson and Grove, 1993, Panjasawatwong et al., 1995, Takagi et al., 2005).

High Mg-numbers in pyroxenes coupled with rather low trace element concentrations in pyroxenes and plagioclase suggest a rather unfractionated signature of the parental melt. However, primitive MORBs are undersaturated in orthopyroxene with respect to the equilibrium cotectic melt composition at pressures of the crust-mantle transition zone (1-2

kbar) (O'Hara, 1965, Stolper, 1980, Elthon, 1989). Secondary formation of orthopyroxene in the continental mantle has been usually explained by interaction with high-silica melts derived either by low degrees of melting of eclogite (formed after subducted basalts or sediments in an arc environment) (Boyd, 1989, Kelemen et al., 1992, Kelemen et al., 1998) or silica- and alkali-rich near-solidus melts (Baker et al., 1995, Falloon et al., 1997, Pin et al., 2001, Laporte et al., 2004). In contrast, in mid-ocean ridge settings, extensive melt-wall rock reaction through continuous dissolution of pyroxenes and crystallization of olivine has been suggested to bring melts close to orthopyroxene saturation (Kelemen, 1990, Kelemen and Dick, 1995, Kelemen et al., 1995b, Dijkstra et al., 2003). The latter process has been frequently used to explain the concomitant crystallization of orthopyroxene and plagioclase in plagioclase peridotites from many Mediterranean ophiolitic peridotites (Rampone et al., 1997, Dijkstra et al., 2001, Barth et al., 2003, Dijkstra et al., 2003, Müntener et al., 2004, Piccardo et al., 2004a, Piccardo et al., 2004b, Piccardo et al., 2007).

However, there are many caveats in suggesting a similar origin for Gakkel Ridge plagioclase peridotites. The melt-wall rock reaction process is most efficient at low pressures to reach orthopyroxene-saturation. The olivine-orthopyroxene phase boundary only becomes an incongruent reaction boundary at pressures of less than 5 kbar in the CaO-MgO-SiO₂ system (Bowen and Andersen, 1914, Andersen, 1915, Boyd et al., 1964, Hudon et al., 2005). Although the addition of water or alkalis can extend this process to higher pressures (Kushiro et al., 1968, Taylor, 1973), high silica enrichments are less likely as only bulk dissolution of orthopyroxene is expected to occur. Also, the melt flux required to exhaust orthopyroxene from peridotites increases with pressure (Asimow and Stolper, 1999). To reach pyroxene-saturation, a given melt mass must convert an equal mass of peridotite (containing 30% pyroxenes) into dunite during its adiabatic ascent from 90 km (Kelemen et al., 1997a). Small amounts of melt can only produce dunite through melt-rock reaction if melting continues down to pressures of 1 bar (Asimow and Stolper, 1999). Furthermore, at low melt-rock ratios, melts and solid will maintain the same temperature and the orthopyroxene dissolution reaction is unlikely to be important over long vertical distances (more than a temperature interval of 40°C in the TBL) (Kelemen et al., 1998).

At Gakkel Ridge, it has been suggested the TBL extends to depths of around 30 km, ca. 10 kbar, at the sample location (Montesi and Behn, 2007). The ultraslow-spreading rates, absence of magmatic crust or gabbros (Michael et al., 2003, Jokat and Schmidt-Aursch, 2007) and generally anhydrous conditions (Peslier et al., 2007) of the sample location makes the production of significant melt fluxes unreasonable. Furthermore, increasing Mg-numbers toward pyroxene rims and highly calcic plagioclase are not sufficiently explained by such a process.

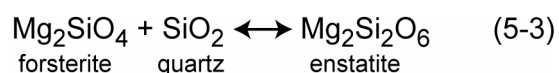
Concurrent crystallization of orthopyroxene and plagioclase is a common and most remarkable signature of plagioclase peridotites. By trying to fit all geochemical characteristics of parental melts to known liquid lines of descent in basaltic systems, sometimes large stretches of imagination are necessary. I will show that the formation of plagioclase peridotites with the aforementioned characteristics can also be the result of a simple equilibration process between melt and wall rock peridotite that does neither require extensive crystal fractionation, nor melting of refractory mantle or hydrous conditions.

5.5.2 Coupled flow and reaction in the mantle - A conceptual model for the formation of plagioclase peridotites and melt-rock reaction in the mantle

In the following, I propose a model for reactive melt percolation in which all textural and compositional features of plagioclase peridotites comply with an equilibration reaction of the peridotite system toward higher silica activity.

5.5.2.1 Silica activity in the mantle

The silica activity in the Earth's mantle is fixed by the co-existence of olivine and Ca-poor pyroxene. Equilibrium between liquid, olivine and orthopyroxene is maintained by the reaction:



At low to intermediate degrees of partial melting, changes in modal proportion of olivine and orthopyroxene in mantle peridotite are small. Accordingly, changes in silica activity of magnesian peridotite and associated melt fractions will be modest during partial melting at constant pressure until cpx-out (Hirschmann et al., 1998). However, as soon as a critical melt mass is exceeded during partial melting, melts migrate up because of their density contrast to the peridotite. In such a dynamic melting model, a larger range of silica activity can be produced from a single-starting composition, such as MORB pyrolite, relative to batch melting because of the escape of incremental melt fractions and the subsequent change of the peridotite bulk composition (Falloon et al., 1988). The silica activity of melts can be affected by many variables during their ascent to the surface. Decreasing temperatures will cause a small decrease in silica activity of the melt and hence of the SiO₂-content (Sack and Ghiorso, 1989) while decreasing pressures will result in an increase of polymerization because of decreasing MgO contents (e.g. Stolper, 1980). Increasing water contents in contrast will lead to depolymerization of melts shifting the stability of olivine to higher pressures (Gaetani and Grove, 1998, Gaetani et al., 2003). Fractionation and dissolution processes that affect the silica content of the liquid must be compensated by changes in liquid composition to maintain equilibrium with the surrounding peridotite. This can be achieved by concentration variations of minor components in the melt (Kushiro, 1975, Ryerson, 1985, Baker et al., 1995). Here, highly charged cations such as titanium increase the stability of orthopyroxene at the expense of olivine which causes a decrease in SiO₂ of liquids (Xirouchakis et al., 2001), while alkalis have the opposite effect (Hirschmann et al., 1998, Draper and Green, 1999, Pickering-Witter and Johnston, 2000). As a result, increases in the silica-content of the melt are always accompanied by an increase in Na₂O-content as well (Hirschmann et al., 1998, Robinson et al., 1998, Longhi, 2002). This effect is pressure-dependent and even though its importance diminishes at equilibration pressures higher than 15 kbar (Blundy et al., 1995, Hirschmann et al., 1998), it gains importance toward lower pressures: 1 wt% increase in alkalis will increase SiO₂ by 1 wt% at 10 kbar (Hirschmann et al., 1998). The variation in alkali content is usually accompanied by variations in other oxide concentrations as well. As a consequence, melts will continuously change their composition by equilibration with peridotite or will affect the mineralogy of the peridotite.

5.5.2.2 Melt-rock reaction and the silica activity space

Continuous porous flow throughout the melting column is emphasized in many melt extraction models for the oceanic mantle (McKenzie, 1984, Spiegelman, 1993a, Spiegelman, 1993b, Aharonov et al., 1995, Niu, 1997, Dijkstra et al., 2003). Porous flow along grain boundaries will bring two different systems, residual peridotite and melt, into contact that may be out of chemical equilibrium at the given pressure and temperature. Already Bowen (1922) stated that if liquid and solid phases are out of equilibrium, they will react, regardless of the melting temperature of the pure solid phases. Hence, during melt-rock reaction between liquids and peridotite that are equilibrated at different silica activities, the system will attempt to equilibrate toward a new stable phase assemblage at either higher or lower silica activity depending on the relative composition.

The importance of silica activity has been recognized before in fluid-rock reaction processes (Manning, 1995b, Manning, 1995a, Frost and Beard, 2007) but has not been extended to melt-rock reaction processes in the mantle yet. While many theories on melt-rock reaction adequately describe and explain changes in mineralogy, they rest strongly on the position of liquidus surfaces and often require substantial melt-rock ratios as well as crystal fractionation. This places certain limits on those processes that makes them more likely to areas of high melt production or low pressures, often not entirely in accordance with the actual tectonic environment. Furthermore, most assimilation models assume assimilation as melt (e.g. Spera and Bohron, 2001) placing thermal limitations whereas this model proposes that the assimilant stays mostly solid and the actual transformation occurs in a series of incongruent dissolution reactions. This silica-activity driven process, referred to in the following as “SAE”- (silica activity equilibration-) process shares resemblance with the “hydration crystallization” process of Beard (2004) with the non-isochemical replacement by incongruent melting reactions of one mineral assemblage by another.

5.5.2.3 Phase relations in systems of variable silica activity

Kushiro and Yoder (1966) and Green and Ringwood (1967) studied the basalt to eclogite transition in a series of experiments on variable basaltic compositions. Their results give an overview over phase changes that occur with increasing pressure and temperature in systems of variable silica saturation. While Kushiro and Yoder (1966) studied the relative simple CaO-MgO-Al₂O₃-SiO₂ (CMAS) system, a broader experimental study was carried out by Green and Ringwood (1967) on natural basaltic compositions. The latter study also included the influence of alkali contents, Mg/Fe ratio and oxygen fugacity on the mineralogy. Nevertheless, the simple CMAS system encompasses the four principal components of basalts, eclogites and peridotites and describes the compositional range of 80% of most basalts and eclogites and about 90% of peridotites. The results of Kushiro and Yoder (1966) and Green and Ringwood (1967) are in good agreement with each other, although it is shown that other solid solution components in natural minerals have a stabilizing or more reactive effect on stability fields (Green and Ringwood, 1967). Bultitude and Green (1970) studied the variation in mineralogy of olivine nephelinite as a function of pressure and temperature.

These experimental studies are still the most comprehensive and detailed on the mineralogy of the upper mantle at different silica activity and dry conditions to date. The graphical portrayal and emphasis of the results differs in both studies and will be used accordingly in the following discussion. Neither of the studies is a realistic representation of the silica-undersaturated peridotite system and reactions relevant for refractory peridotites cannot be quantitatively described. However, their results can serve highlighting the systematic of the proposed process. The important factor to be shown is that mineralogical changes are not only to be expected during (closed system) adiabatic uplift but also by (open system) changes in the silica saturation. A short overview of the three experimental studies is given in the appendix of this chapter.

The interpretation of the SAE-process is based on the experimental studies of Kushiro and Yoder (1966), Green and Ringwood (1967) and Bultitude and Green (1970). Figure 5-26 shows the phase diagrams from Kushiro and Yoder (1966), transformed into three-dimensional spaces of pressure, temperature and silica activity. Two different scenarios are shown, one

CHAPTER 5

depicting the equilibration toward lower silica activity and the other toward higher silica activity.

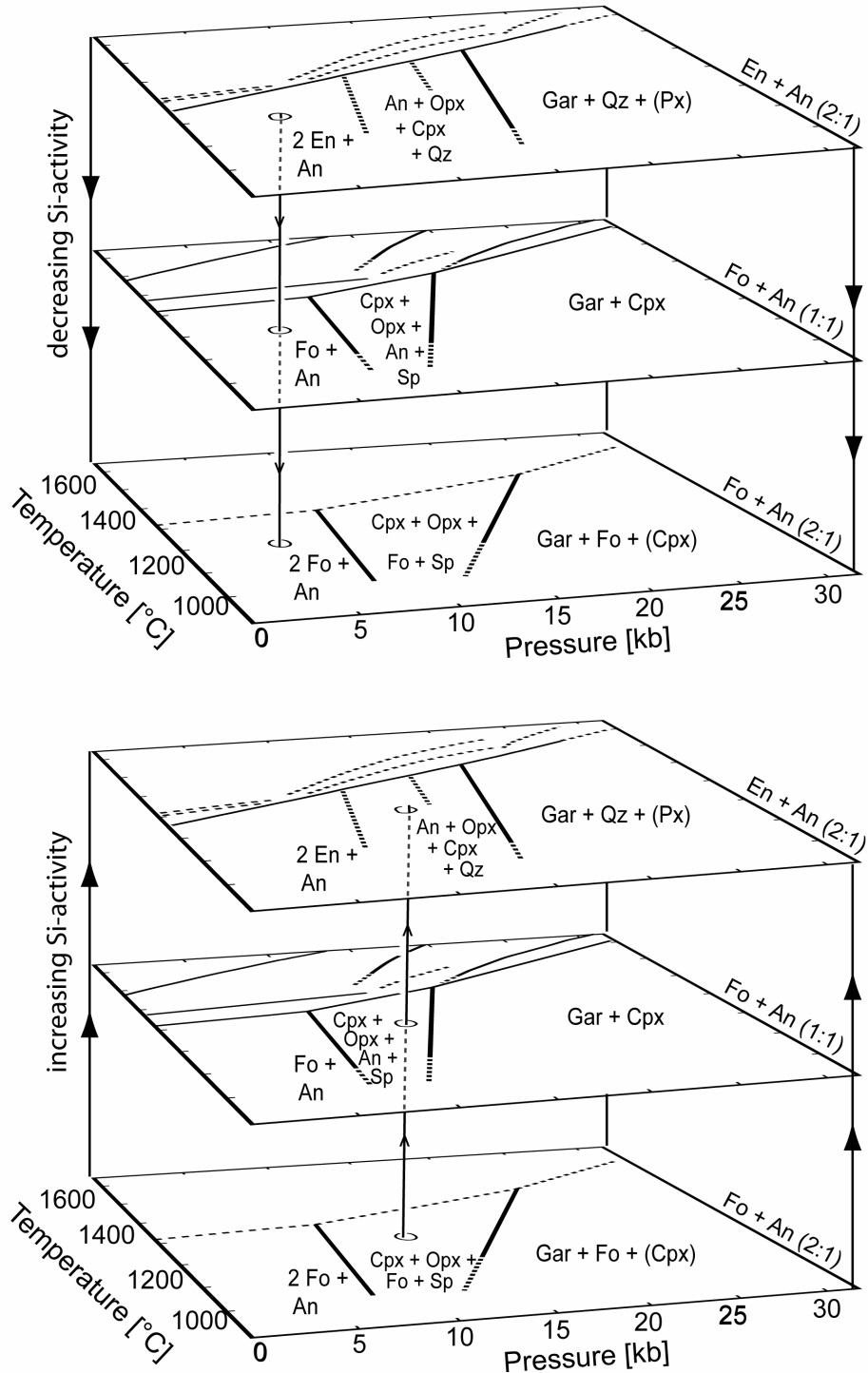


Figure 5-26: Conceptual model of melt-rock reaction processes in the mantle. Interaction between melts and wall rock peridotite at different degrees of silica activity leads to open system phase transformation until the system is stabilized at the equilibrium silica saturation.

5.5.2.3.1 Reaction toward lower silica activity

The upper part of Figure 5-26 depicts the SAE-reaction between a silica-rich peridotite (e.g. lherzolite) with a relatively more silica-undersaturated melt (e.g. olivine tholeiite) at around 5 kbar and 1200°C. In the most extreme case in this system, the original assemblage would consist of anorthite and enstatite (Figure 5-26). Infiltration of a liquid at lower silica activity will require reaction with the peridotite and equilibration of the peridotite to lower silica activity relative to the initial composition. The stable mineralogy in the silica undersaturated end-member in the system of Kushiro and Yoder (1967) consists of anorthite and forsterite. Hence, equilibration toward lower silica activity would lead to de-stabilizing of enstatite for the benefit of forsterite and the system would move toward a more olivine-rich composition. The relative difference in silica activity of melt and peridotite and the relative proportions will control the final silica activity and thus the amount of orthopyroxene transformed into olivine. If plagioclase is not yet present in the system, small amounts will be formed. If plagioclase is already present, its composition and amount will change.

Green and Ringwood (1967) investigated a wide range of natural basaltic compositions in their experimental study on the subsolidus mineralogy at conditions of the upper mantle. Their study is the only one that gives a graphic portrayal of the changing mineralogy of two basaltic compositions at different silica activity as a function of pressure (see Appendix, Figure A5-2-1 and A5-2-2).

Figure 5-27 is based on their results and shows the change in modal abundances at fixed temperature and pressure during such a change in silica activity. Shown are pressures of 5 and 10 kbar, relevant for plagioclase peridotites, higher pressures are shown in the Appendix of the chapter. Both basaltic compositions (alkali basalt and quartz tholeiite) are not representative for peridotite compositions but showcase the effects of changing bulk compositions on phase assemblages. At 5 kbar, reaction toward lower silica activity would lead to drastic stabilization and therefore production of olivine and to a lesser extent of clinopyroxene and spinel at the expense of enstatite and feldspar (if present); comparing the phase assemblages at 5 kbar and 10 kbar shows the effect of pressure and temperature on the mineralogy. Melt-rock reaction by similar reactants but at 10 kbar would result in an increase of the stability of clinopyroxene and spinel and in slightly higher orthopyroxene/olivine ratios

CHAPTER 5

in the solid assemblage relative to 5 kbar. Therefore, the final stable assemblage is controlled by the pressure, temperature and the difference in chemistry of both reactants. Reactive melt-rock at even higher pressures in the presence of garnet would lead to the production of olivine at the expense of clinopyroxene (see Appendix Figure A5-2-2).

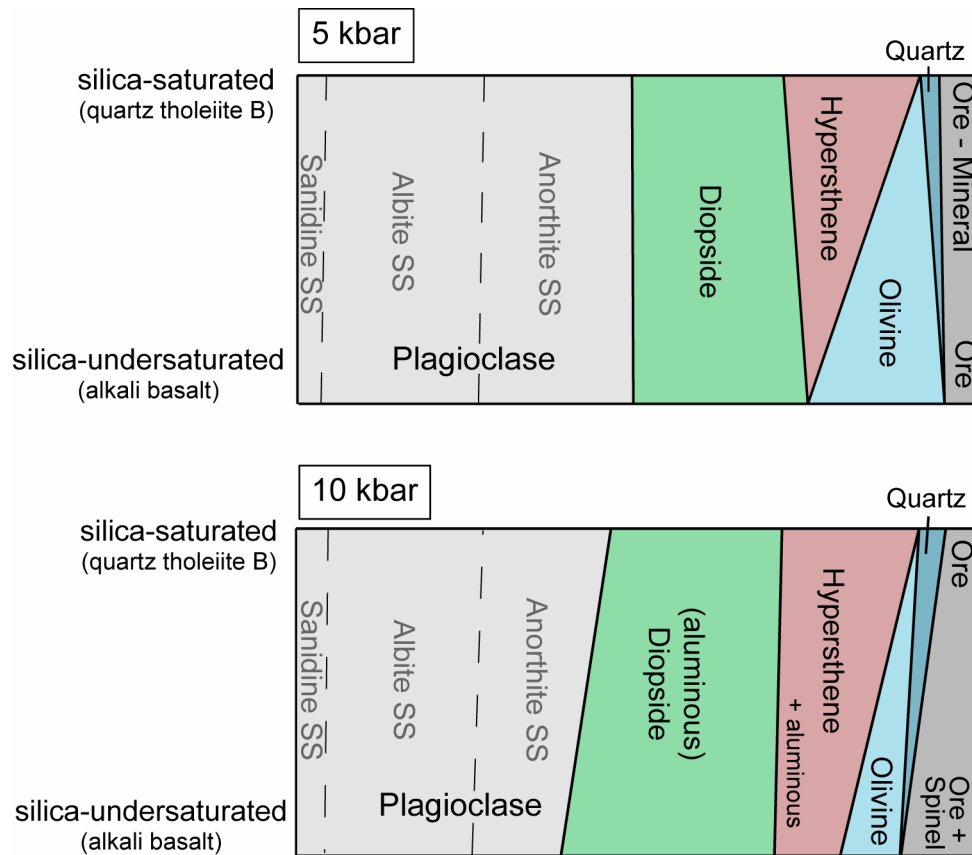


Figure 5-27: Diagrammatic representation of the change in mineralogy between two basalts with different silica-activity at 1100°C and 5 and 10 kbar, respectively. The proportions are taken from Figure 5 and 6 of Green and Ringwood (1967) (see also Figure A5-2-1 in the Appendix). The depicted phase assemblages are not representative for ultramafic compositions and most probable overestimate the presence of plagioclase and diopside and underestimate olivine phase proportions in the mantle. Nevertheless, the change in modal mineralogy is obvious.

In a natural, silica-undersaturated composition (olivine nephelinite), more similar to an olivine tholeiite, the stable phase assemblage at around 5 kbar and 1100°C consists of (in the order of abundance) olivine, clinopyroxene, (calcic) plagioclase and spinel (Bultitude and Green, 1970). Hence, the reaction would progress toward a strong decrease in orthopyroxene mode and production of olivine and subordinately clinopyroxene and plagioclase. Spinel

would be theoretically formed in this process as well, but may change strongly its composition to be stable at this pressure.

5.5.2.3.2 Reaction toward higher silica activity

Melt-rock reaction in the mantle can of course occur as well by reaction with silica-rich melts and equilibration towards higher silica activity. The reaction will then essentially progress in the opposite direction and results in the consumption of clinopyroxene, olivine and spinel while enstatite and plagioclase will be produced. At higher pressures, the process would produce garnet and consume olivine instead. Again, modal abundances and composition of the final assemblage will be a combination of the relative difference in silica activity of the reactants and their proportions as well as pressure and temperature of their reaction.

An SAE-process toward higher silica activity is in agreement with textures (olivine and clinopyroxene consumption and orthopyroxene and plagioclase production) seen in plagioclase peridotites from this study. Nevertheless, plagioclase in peridotites can be formed by either “direction” of the SAE-process but will occur at different pressure and temperature and with different final phase assemblages. Interaction of peridotite with a melt of lower silica activity will form plagioclase at lower pressures and temperatures because of the relative position and slope of the plagioclase-out reaction at the given bulk silica activity (see also Figure 5-27 or Figure A5-2-1). In this case, the new assemblage would consist of plagioclase, clinopyroxene and olivine while orthopyroxene would be consumed. Also, the produced anorthite contents should be intermediate because of the preferential consumption of orthopyroxene and formation of clinopyroxene and plagioclase (dissolution of clinopyroxene will increase the Ca/Al ratio of the melt, while dissolution of opx will decrease the Ca/Al-ratio). The stability of spinel decreases toward systems of higher silica activity and will strongly react with the melt. Toward lower silica activity, its stability should actually increase but as closed system kinetic reactions are sluggish (Rubie, 1990, Rubie, 1998), it may be possible that it lags behind in equilibration (i.e. spinel to plagioclase facies transition) and the melt will act as catalyst.

In summary, the extent of the SAE-process and hence the final mineralogy will depend on the final silica activity, temperature and pressure of the melt-rock reaction. At moderate chemical disequilibrium, the process may only result in a change in solid solution components.

For example, at equilibration toward higher silica activity, the diopside component in clinopyroxene might decrease while the enstatite component will be less affected.

Reactive melt-rock reaction will continue until either equilibrium is achieved or complete consumption of the melt mass. At very small melt mass, the melt will probably completely react-out - stagnate - and with sufficient equilibration resemble melt entrapment although without cotectic phase proportion crystallization. If final equilibrium is achieved before the melt mass is entirely consumed, the melt will continue its ascent. When the SAE occurs in the TBL, it might start to fractionate mineral phases in which the liquid is saturated. The presence of “magmatic” clinopyroxene in plagioclase peridotite PS59-235-134 probably marks that transition in the reaction process.

This very simplistic view does not account for Mg/Fe ratios. Because fayalitic olivine can also coexist with quartz, the equilibrium silica activity is connected through the presence of magnetite with oxygen fugacity and also depends on the Fe/Mg-ratio (see Chapter 6 for further discussion). Andersen et al. (1993) showed that for this silica-buffer (eq. 5-3), only a difference of 0.02 log units in silica activity exists between the pure magnesian system and a typical mantle olivine with Mg-number of 0.9. However, it might still affect phase boundaries and will likely contribute to changes in Mg/Fe ratios.

5.5.2.4 Evidence from experiments and nature: melt-rock reaction and crystal dissolution

Experimental studies on the interaction between melts and peridotite provide vital clues on reaction processes in the upper mantle (Kelemen et al., 1990, Yaxley and Green, 1998, Morgan and Liang, 2003, Morgan and Liang, 2005, Shaw and Dingwell, 2008). A growing number of dissolution experiments add further information. Melt-rock reaction experiments commonly use finely ground rock powders, which ensure good reactivity (i.e. presence of nucleation cores) and balance-out the small experiment charge sizes required for high pressure-experiments. However, melt-rock reaction is not studied in the range of natural grain sizes of several millimeters and the role of kinetics might not be adequately addressed.

5.5.2.4.1 Textures

Reaction zones around minerals in xenoliths have been reported from many localities worldwide (e.g. Shaw et al., 2006). A common feature in ultramafic xenoliths is the occurrence of glass-bearing “sieve”-textured rims of clinopyroxene and spinel and reaction rims around orthopyroxene (Shaw et al., 2006).

Shaw and Dingwell (2008) recently studied the interaction between lherzolite and leucitite melt at 1 atm and 1200°C and 1156°C. The experimental set-up at atmospheric pressure allowed the use of a cored disk from a natural peridotite sample (lherzolite xenolith) rather than rock powders. Mineral grain sizes of several millimeters allowed the study of zoning profiles and as a result of kinetic processes.

Melt-peridotite reaction processes based on experiments (Shaw and Dingwell, 2008) and mantle xenoliths (Shaw et al., 2006) are reported to proceed in a two-step process. Generally, distinct reaction textures, the aforementioned “sieve texture”, develop around the reacting minerals. Initially, interaction of the silica-undersaturated melt with orthopyroxene yields a silica- and alkali-enriched melt and olivine. In addition, in long experimental runs, a zonation in reactant assemblages of ol+cpx – ol+glass – glass develops away from the orthopyroxene interface. In a second step, this melt migrates along grain boundaries further into the peridotite and causes incongruent dissolution of clinopyroxene and spinel. This second reaction step involves complete dissolution of clinopyroxene and spinel followed by the nucleation and growth of a second generation of clinopyroxene. Crystals that are not in contact with the melt show no sign of reaction (Shaw and Dingwell, 2008).

This “sieve texture” is typical for mantle xenoliths but only in xenoliths that contain orthopyroxene (e.g. Shaw et al., 2006, Shaw and Dingwell, 2008). This texture is also strikingly similar to the orthopyroxene-plagioclase symplectites around clinopyroxene that are often observed in plagioclase peridotites (Figure 5-28) (e.g. Piccardo et al., 2007).

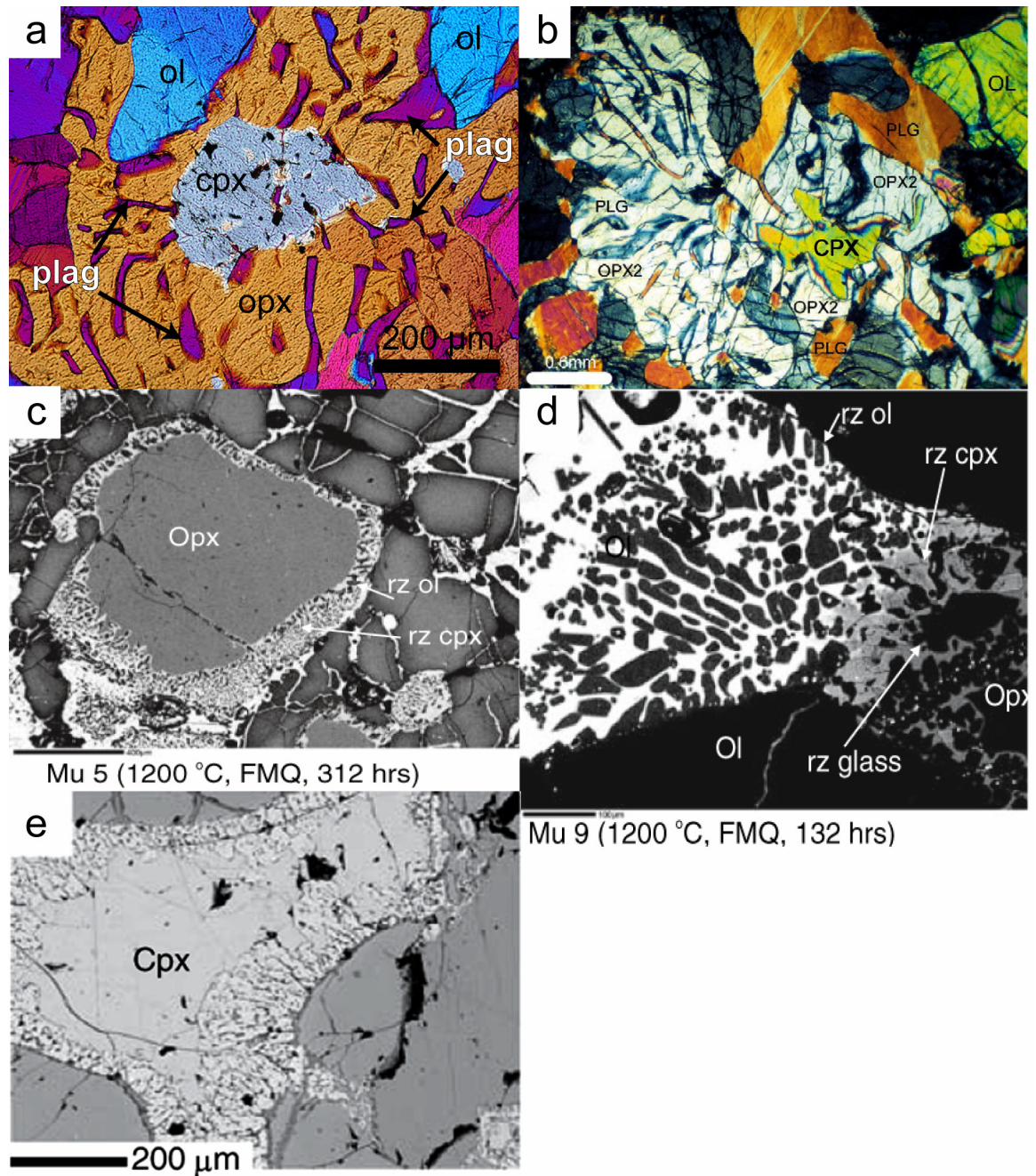


Figure 5-28: Textures from plagioclase peridotites (a-b), melt-rock reaction experiments (c-d) and a mantle xenolith (e); a) cpx replaced by plagioclase and orthopyroxene in plagioclase peridotite PS59-235-19; b) cpx replaced by plagioclase and orthopyroxene in plagioclase peridotite from Lanzo South (Piccardo et al. 2007) c) "sieve textured" orthopyroxene surrounded by an intergrowth of olivine and clinopyroxene; d) reaction zone around orthopyroxene consisting of olivine and clinopyroxene and olivine and glass; replaced orthopyroxene is at the lower right hand of the picture; e) clinopyroxene surrounded by intergrowth of clinopyroxene and olivine (c-e: Shaw and Dingwell, 2008).

5.5.2.4.2 Reaction progress: Dissolution reactions and their influence

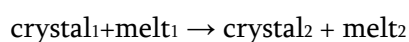
The main processes of mass transfer in solid/liquid systems include diffusive exchange and dissolution-reprecipitation (Liang, 2003). Mantle xenoliths and peridotites from massifs show evidence for both processes (Bodinier et al., 1990, Godard et al., 1995, Shaw and Dingwell, 2008). However, it is important to distinguish between both as they can attain equilibrium at different time scales. Trace element exchange via dissolution and precipitation is thought to occur much faster than volume diffusion (Navon and Stolper, 1987, Lundstrom et al., 1995).

Two types of dissolution can occur (Tsuchiyama, 1985):

- Type A dissolution (simple dissolution) with the complete resorption of the mineral in a melt, leaving a melt with a distinctly different composition from the reacting melt.



- Type B dissolution (partial dissolution) with resorption of a mineral and formation of secondary minerals and melt phase, both different in composition to the original melt and mineral.



The reaction products seen in experiments and also proposed here are best explained by partial dissolution, which is described as initial congruent dissolution of the margin of the crystal that is followed by the nucleation and crystallization of the stable phase(s) in the melt (Shaw and Dingwell, 2008).

The kinetics of the dissolution process has important implications for the chemical variability generated by the SAE-process that is also evident in the plagioclase peridotites in this study. Even though the SAE-process is essentially an assimilation-fractional crystallization process (AFC) (cf. DePaolo, 1981), the AFC path is controlled by the rate of assimilation reactions. Generally, a number of possible rate-controlling processes occurs during mineral

dissolution reactions, but only two are considered important for silicate minerals: (1) interface reaction kinetics and (2) cation diffusion away from the interface (c.f. Shaw, 2000). In melts of geological interest, only diffusion will be the rate controlling factor (Zhang et al., 1989, Liang, 1999) at least in high viscosity systems (Jackson and Mills, 1997, Shaw, 2004).

Nevertheless, reaction rates can differ with each mineral-melt pair in a complicated manner. It has been shown that the relative rate of dissolution is proportional to the “affinity” for the reaction, representing the degree of disequilibrium between a crystal and a melt or the stability of that phase at a specific P and T (Edwards and Russell, 1996 and references herein). In general, relative mineral dissolution rates in basaltic melt decrease in the order garnet > cpx = opx > olivine > spinel over the range of 5 – 30 kbar (Brearley and Scarfe, 1986). However, dissolution rates essentially follow an Arrhenian relationship at least for superliquidus conditions, resulting in changes of the relative order in dissolution rates in multicomponent materials at different P and T (Edwards and Russell, 1996). Polymerization also seems to affect dissolution rates and experiments of quartz dissolution showed that at equal silica activities, dissolution rates are greater in lower viscosity melts (Shaw, 2006). Here, quartz solubility is directly correlated with temperature and the solvent NBO/T and to a lesser extent with temperature (Shaw, 2006).

The strong chemical variability seen in plagioclase peridotites suggests that dissolution kinetics are very important, dissolution rates are much faster than diffusive re-equilibration and the often inferred “local equilibrium” will be reduced to the μm -scale. Dissolution processes are further complicated by uphill diffusion; that is diffusion of components up their own concentration gradients. In dissolution experiments with andesitic melt, it has been found that uphill diffusion is the rule rather than the exception, particularly during olivine dissolution (Zhang et al., 1989). Cation diffusivities in the melt depend on the degree of polymerization of the melt and olivine dissolution has an important effect, as the change in melt SiO_2 by dissolution of other minerals is often balanced by network-forming components such as Al_2O_3 (Zhang et al., 1989). Major element diffusion uphill and downhill often follows gradients in the polymerization of melt during dissolution processes (Zhang et al., 1989). As a result, the melt gains extra components through diffusive separation in addition to the mixing

of the mineral component with the melt. Hence, dissolution kinetics can significantly complicate inferring melt composition from mineral composition. Zhang et al. (1989) reported that to explain the compositional variation in a melt that was generated experimentally by diffusive olivine dissolution alone, by linear mixing required “nontrivial” amounts of clinopyroxene, orthopyroxene and plagioclase in addition to olivine.

This variability in melt composition and mineral zoning is also reported in melt-peridotite experiments from Shaw and Dingwell (2008). Also, a similar extent in chemical variation and dependence on the interface is seen in reaction experiments between spinel lherzolite and amphibolite (Sen and Dunn, 1994).

Early studies on high pressure hybridization of peridotite by silica-rich melt showed that the composition of the produced silicic liquid cannot be modeled as a simple linear mixing weighed by their relative proportions (Wyllie and Sekine, 1982) and is not dramatically modified as well (Wyllie and Sekine, 1982, Sekine and Wyllie, 1983, Carroll and Wyllie, 1989). Silicic to intermediate liquids equilibrated or having reacted with mantle minerals usually all display lower FeO/MgO, increasing MgO and Na₂O.

In experiments of Shaw and Dingwell (2008), different melt compositions are found in the experiment that vary depending on their textural context but are relatively homogeneous within their textural context. They found: (1) a low silica leucitite melt in veins in the peridotite; (2) high silica, quartz-normative melt in reaction zones around orthopyroxene and (3), also quartz-normative, but alumina-poor and CaO-rich melt in association with reacted clinopyroxene. The most silica-rich melt was immobile in the experiments.

5.5.3 Mineral compositions in plagioclase peridotites

If the SAE-reaction toward higher silica activity occurs in the plagioclase stability field, clinopyroxene, olivine and spinel will be unstable while enstatite and plagioclase will be precipitated. The trace element and major element composition of the melt will be mostly modified by the clinopyroxene dissolution (and the plagioclase precipitation).

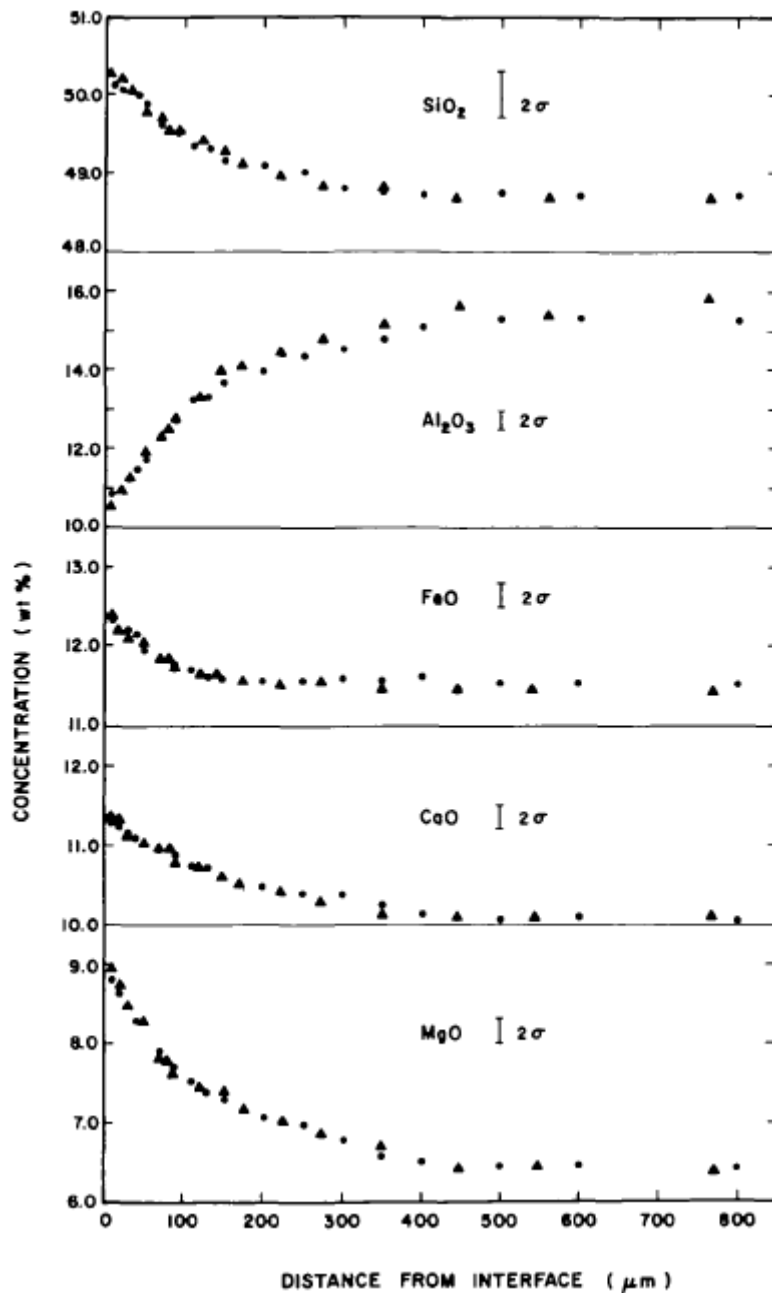


Figure 5- 29: Dissolution of clinopyroxene in an alkali basalt. Shown is the change in melt composition with distance from the crystal/melt interface. Experiments made at 5 kb and 1250°C. Filled circles represent experiments of 30 min durations, triangles of 60 min duration. (Figure 7 from Brearley and Scarfe, 1986).

Figure 5-29 shows the compositional gradients developed in alkali basalt during dissolution of diopside. Dissolution of diopside changes the melt composition at the interface to high Ca/Al, SiO₂ and higher Mg-number. Panjasawatwong et al. (1995) showed that the anorthite content of magmatic plagioclase is controlled by the Ca/Al-ratio of the melt.

Remarkably, highest anorthite contents in each thin section in this study occur in opx-plag symplectites around clinopyroxene. Hence, high anorthite contents of the plagioclase peridotites are well explained by this process without requiring a refractory melt composition. Dissolution of clinopyroxene and crystallization of orthopyroxene will also move the melt towards higher Mg-number while concomitant crystallization of plagioclase will only affect the Cr-number of the melt but not the Mg-number. This is also in excellent agreement with pyroxene-rim compositions in plagioclase peridotites.

As a result of the dissolution reactions, plagioclase REE composition will not only depend on the melt composition, but will be strongly controlled by the contributing clinopyroxene composition. Inherently, this clinopyroxene will be part of a refractory assemblage and thus be LREE-depleted. This may be another reason that plagioclase patterns generally mimic clinopyroxene patterns in plagioclase peridotites. Furthermore, the LREE depletion in the melt will be enhanced by melt structure dependent cpx/liquid partitioning (see also 5.4.2.2). Models of closed-system formation of plagioclase (5.4.1) have shown that Sr-concentrations of plagioclase are a function of participation of the MgTs component of clinopyroxene. Here, anorthite showed positive Sr-anomalies when the entire clinopyroxene solid solution was consumed in the reaction while the positive Sr-anomaly decreased with increasing additional MgTs component. This is essentially the difference between the case of simple dissolution and partial dissolution and if this holds true, would also explain low Sr-concentrations in plagioclase. Remarkably, clinopyroxenes from plagioclase peridotites in this study always develop core-rim zoning in MgTs component.

5.5.4 Differences to current models of melt-rock reaction processes

Dunites are generally believed to form by reactive dissolution as olivine-normative basalts percolate through a harzburgitic or lherzolitic matrix (Quick, 1981, Kelemen, 1990, Kelemen et al., 1992, Kelemen and Dick, 1995, Kelemen et al., 1995a, Asimow and Stolper, 1999). This process has been described to preferentially dissolve pyroxenes and precipitate olivine, finally producing dunite channels that will allow MORB melts to retain their high pressure chemical signature during ascent. The reactive porous flow process and its final products resemble the SAE-process described in the previous section.

However, melt-rock reaction by reactive porous flow predicts dissolution processes and crystallization products based on liquidus saturation surfaces. The predictions for reactions between olivine tholeiite and peridotite agree well with many mineralogical changes in the mantle but require increasingly extensive reaction steps to account for orthopyroxene crystallization at low pressures. Orthopyroxene crystallization in the mantle is either explained by high pressure crystallization or extensive melt-wall rock reaction followed by crystallization or water-assisted melting.

The SAE-process is controlled by the stable subsolidus mineralogy and in return entirely controlled by phase equilibria, dominantly the silica activity. New phase assemblages that are produced by this process depend on the pressure and temperature conditions and the bulk composition of the melt+peridotite system. The reaction process occurs by incongruent dissolution and precipitation and the produced minerals might be different from predicted crystallization series of liquidus phases from primary/non-fractionated melts. The SAE-process might also only involve changes in solid-solution composition, resulting in a “cryptic” rather than “patent” metasomatism. However, many predictions for reactive porous flow sensu “Kelemen” will also apply for the SAE-process with only minor modifications depending on the system variables. The SAE-process toward silica-undersaturation will also reduce the pyroxene content and increase the olivine content of peridotites. Though, depending on the final silica activity and pressure and temperature of equilibration, olivine-rich rocks will still contain a small amount of clinopyroxene (\pm plagioclase). The melt mass will also increase depending on the reaction coefficients of opx and ol+cpx during the process. Melt involved in SAE-reaction toward higher silica activity will decrease in mass and presumably react out and stagnate before reaching the surface, thus not contribute strongly to MORB.

The most distinctive difference between these processes is that bulk composition equilibrium controls SAE-produced phase assemblages, rather than cotectic relationships.

5.5.5 Origin of silica-rich melts in the oceanic mantle

During the adiabatic upwelling of the oceanic mantle, melting occurs when the geotherm intersects the solidus. Subsequently, melts form in the peridotite framework at triple points until a critical melt mass is exceeded and melts migrate up because of their density contrast to the peridotite. Continuous porous flow throughout the melting column is emphasized in many melt extraction models for the oceanic mantle (McKenzie, 1984, Spiegelman, 1993a, Spiegelman, 1993b, Aharonov et al., 1995, Dijkstra et al., 2003). However, it has been shown that melt migration in a grain scale porous network will lead to rapid equilibration (e.g. Spiegelman and Kenyon, 1992). Chemical disequilibrium between extracted MORB melts and peridotites suggest chemical isolation between these two at lower pressures, indicating melt transport in fractures.

The occurrence of silica-enriched melts at mid-ocean ridges is generally not expected. In contrast to the well-established interaction between slab-derived melt and mantle peridotites in subduction zones, melts at mid-ocean ridges settings are generally silica-undersaturated.

In the following, four different scenarios are envisaged, that might lead to interaction between peridotite and silica-rich melts. However it is important to keep in mind that the SAE reaction process is driven by *differences* in silica activity not by high silica contents sensu-stricto. Partition coefficients $D^{\text{cpx/liq}}$ for clinopyroxene composition in plagioclase peridotites suggest a melt SiO_2 content of 52 wt% (see 5.5.4.2), only slightly higher than average N-MORB (50.45 wt%: Hofmann, 1988).

Hence, possible processes could involve (1) melt-rock reaction that changes the melt composition toward higher silica activity by dissolution of orthopyroxene. In that scenario, plagioclase peridotites would represent the second step in melt-rock reaction processes of originally silica-undersaturated melts. However, the reaction will probably occur on local scales then. Dissolution experiments on orthopyroxene showed that high silica melts are easily produced by this process (Shaw et al., 1998, Shaw, 1999); (2) interaction with near-solidus melts. Liquids produced by near-solidus melting are expected to be very silica-rich (Johnson and Kushiro, 1992, Baker et al., 1995, Laporte et al., 2004). They would be highly reactive upon further migration away from their site of production. Evidence for low-degree melts has

been also suggested based on trace element composition of cpx and textures in spinel peridotites from the same sample location (see Chapter 1); (3) variability of melt migration. Melt migration rates depend on the permeability, the rheology and the mineralogy of the partial molten rocks through which the melt is migrating. Under hydrostatic stresses, the distribution of melt depends on the dihedral angle (Holness and Siklos, 2000). Changes in permeability because of precipitation of pyroxenes can cause low permeability zones next to high permeability zones and flow to become diffuse and uniform (Aharonov et al., 1997). Here, alternating “patchy” regions of low and high permeability form along the main flow direction (Aharonov et al., 1997); (4) ancient depletion and/or existing regions of depletion. It has been suggested that a certain part of the mantle column consists of refractory peridotites, also on Gakkel Ridge (Seyler et al., 2003, Hellebrand et al., 2006, Liu et al., in press). The depleted portion of the mantle would not partake in melting processes below the ridge but provide zones of preferred melt migration because of their pyroxene-poor mineralogy. Additionally, collapse of dunite channels at the crust-mantle boundary and leaking of melts in the surrounding mantle would be a feasible process at low pressures. Here, the high reactivity of the high-pressure melts with the depleted shallow peridotite expected by the SAE-process would strongly contribute to stagnation of significant amounts of melt in the upper mantle and lower crust.

5.6 SUMMARY

Fresh plagioclase peridotites have been recovered in the Sparsely Magmatic Zone at Gakkel Ridge. Their lack of alteration allowed systematic in-situ analyses of all phases that contributed to the detection of significant compositional heterogeneity. Plagioclase peridotites in this dredge haul are very heterogeneous in major and trace element composition and modal abundances. The high modal amount of orthopyroxene in plagioclase peridotites, often intergrown with plagioclase, suggests concomitant formation of orthopyroxene and plagioclase. Furthermore, olivine and clinopyroxene dissolution textures in sample 235-19 indicate clearly that clinopyroxene was not stable during the formation of plagioclase peridotites. In general, plagioclase has low LREE and Sr contents and high anorthite contents. Models for subsolidus closed system formation of plagioclase by breakdown of spinel showed

that although it is possible to form plagioclase without positive Sr-anomaly by this process but generally failed to reproduce the trace element variation of the sample set. Major element (such as low Al₂O₃ contents) and trace element composition (e.g. strong negative Sr- and Eu-anomaly) of a distinct type of clinopyroxene in sample 235-134 and cpx rim compositions evidence interaction with melts. Nevertheless, trapped melt and fractional crystallization models also could not explain features of plagioclase peridotites.

Based on the petrological characteristics of plagioclase peridotites, their formation by a reactive melt migration and stagnation process was proposed. The process is active along gradients in silica activity and continues through a series of equilibration reactions of incongruent dissolution. This process was termed “silica activity equilibration” (SAE) process. The course of events predicted to occur during SAE-processes is based on recent melt-rock reaction experiments and established knowledge on phase equilibria in the upper mantle. The SAE process is capable to explain the textures and petrological variation of plagioclase peridotites in this study. Trace element variation in clinopyroxene and calculated parental melt compositions show the effect of melt structure on $D^{cpx/l}$ and suggest a melt silica-content of 52 wt%.

The occurrence of the process at relatively shallow levels and the anomalous thick lithosphere at Gakkel Ridge has most likely contributed to the preservation of the reaction details that would have been erased at higher temperatures. Hence, plagioclase peridotites from Gakkel Ridge provide a unique “window” into upper mantle processes of reactive melt migration and melt stagnation.

5.7 REFERENCES

- Aharonov, E., Spiegelman, M. and Kelemen, P. (1997). Three-dimensional flow and reaction in porous media. *Journal of Geophysical Research* 102, 14821-14834.
- Aharonov, E., Whitehead, J. A., Kelemen, P. B. and Spiegelman, M. (1995). Channeling instability of upwelling melt in the mantle. *Journal of Geophysical Research-Solid Earth and Planets* 100, 20433-20450.
- Anders, E. and Grevesse, N. (1989). Abundances of the elements - meteoritic and solar. *Geochimica Et Cosmochimica Acta* 53, 197-214.

CHAPTER 5

- Andersen, D. J., Lindsley, D. H. and Davidson, P. M. (1993). A PASCAL program to assess equilibria among Fe, Mg, Mn, Ti oxides, pyroxenes, olivine, and quartz. *Computers & Geosciences* 19, 1333-1350.
- Andersen, O. (1915). The system anorthite-forsterite-silica. *American Journal of Science* 39, 407-454.
- Ashworth, J. R. and Chambers, A. D. (2000). Symplectic reaction in olivine and the controls of intergrowth spacing in symplectites. *Journal of Petrology* 41, 285-304.
- Asimow, P. D. (2002). Steady-state mantle-melt interactions in one dimension: II. Thermal interactions and irreversible terms. *Journal of Petrology* 43, 1707-1724.
- Asimow, P. D., Hirschmann, M. M., Ghiorso, M. S., Ohara, M. J. and Stolper, E. M. (1995). The effect of pressure-induced solid-solid phase-transitions on decompression melting of the mantle. *Geochimica Et Cosmochimica Acta* 59, 4489-4506.
- Asimow, P. D. and Stolper, E. M. (1999). Steady-state mantle-melt interactions in one dimension: I. Equilibrium transport and melt focusing. *Journal of Petrology* 40, 475-494.
- Baker, M. B., Hirschmann, M. M., Ghiorso, M. S. and Stolper, E. M. (1995). Compositions of near-solidus peridotite melts from experiments and thermodynamic calculations. *Nature* 375, 308-311.
- Barnes, S. J. (1986). The effect of trapped liquid crystallization on cumulus mineral compositions in layered intrusions. *Contributions to Mineralogy and Petrology* 93, 524-531.
- Barnouin-Jha, K., Parmentier, E. M. and Sparks, D. W. (1997). Buoyant mantle upwelling and crustal production at oceanic spreading centers: On axis segmentation and off-axis melting. *Journal of Geophysical Research-Solid Earth and Planets* 102, 11979-11989.
- Barth, M. G., Mason, P. R. D., Davies, G. R., Dijkstra, A. H. and Drury, M. R. (2003). Geochemistry of the Othris Ophiolite, Greece: Evidence for refertilization? *Journal of Petrology* 44, 1759-1785.
- Batanova, V. G., Suhr, G. and Sobolev, A. V. (1998). Origin of geochemical heterogeneity in the mantle peridotites from the Bay of Islands ophiolite, Newfoundland, Canada: Ion probe study of clinopyroxenes. *Geochimica Et Cosmochimica Acta* 62, 853-866.
- Beard, J. S., Ragland, P. C. and Rushmer, T. (2004). Hydration crystallization reactions between anhydrous minerals and hydrous melt to yield amphibole and biotite in igneous rocks: Description and implications. *Journal of Geology* 112, 617-621.
- Bedard, J. H. (2006). Trace element partitioning in plagioclase feldspar. *Geochimica Et Cosmochimica Acta* 70, 3717-3742.
- Benoit, M., Ceuleneer, G. and Polve, M. (1999). The remelting of hydrothermally altered peridotite at mid-ocean ridges by intruding mantle diapirs. *Nature* 402, 514-518.
- Bindeman, I. N. and Davis, A. M. (2000). Trace element partitioning between plagioclase and melt: investigation of dopant influence on partition behavior. *Geochimica Et Cosmochimica Acta* 64, 2863-2878.

CHAPTER 5

- Bindeman, I. N., Davis, A. M. and Drake, M. J. (1998). Ion microprobe study of plagioclase-basalt partition experiments at natural concentration levels of trace elements. *Geochimica Et Cosmochimica Acta* 62, 1175-1193.
- Blundy, J. D., Falloon, T. J., Wood, B. J. and Dalton, J. A. (1995). Sodium partitioning between clinopyroxene and silicate melts. *Journal of Geophysical Research-Solid Earth and Planets* 100, 15501-15515.
- Blundy, J. D. and Wood, B. J. (1991). Crystal-chemical controls on the partitioning of Sr and Ba between plagioclase feldspar, silicate melts, and hydrothermal solutions. *Geochimica Et Cosmochimica Acta* 55, 193-209.
- Bodinier, J. L., Vasseur, G., Vernieres, J., Dupuy, C. and Fabries, J. (1990). Mechanisms of mantle metasomatism - geochemical evidence from the Lherz orogenic peridotite. *Journal of Petrology* 31, 597-628.
- Boudier, F. and Nicolas, A. (1985). Harzburgite and lherzolite subtypes in ophiolitic and oceanic environments. *Earth and Planetary Science Letters* 76, 84-92.
- Bowen, N. L. (1922). The behavior of inclusions in igneous magmas. *Journal of Geology* 30, 177-198.
- Bowen, N. L. and Andersen, O. (1914). The binary system MgO-SiO₂. *American Journal of Science* 37, 447-500.
- Boyd, F. R. (1989). Compositional distinction between oceanic and cratonic lithosphere. *Earth and Planetary Science Letters* 96, 15-26.
- Boyd, F. R., England, J. L. and Davis, B. T. C. (1964). Effects of pressure on the melting and polymorphism of enstatite, MgSiO₃. *Journal of Geophysical Research-Solid Earth and Planets* 69, 2101-2109.
- Braun, M. G., Hirth, G. and Parmentier, E. M. (2000). The effects of deep damp melting on mantle flow and melt generation beneath mid-ocean ridges. *Earth and Planetary Science Letters* 176, 339-356.
- Brearley, M. and Scarfe, C. M. (1986). Dissolution rates of upper mantle minerals in an alkali basalt melt at high pressure: An experimental study and implications for ultramafic xenolith survival. *Journal of Petrology* 27, 1157-1182.
- Brunelli, D., Seyler, M., Cipriani, A., Ottolini, L. and Bonatti, E. (2006). Discontinuous melt extraction and weak refertilization of mantle peridotites at the Vema Lithospheric Sections (Mid-Atlantic Ridge). *Journal of Petrology* 47, 745-771.
- Bultitude, R. J. and Green, D. H. (1970). Highly undersaturated rocks in upper mantle conditions. *Nature* 226, 748-749.
- Canil, D., Johnston, S. T., Evers, K., Shellnutt, J. G. and Creaser, R. A. (2003). Mantle exhumation in an early proterozoic passive margin, Northern Cordillera, Yukon. *Journal of Geology* 111, 313-327.
- Cannat, M., Bideau, D. and Hebert, R. (1990). Plastic-deformation and magmatic impregnation in serpentinized ultramafic rocks from the Garrett Transform-Fault (East Pacific Rise). *Earth and Planetary Science Letters* 101, 216-232.

CHAPTER 5

- Cannat, M. and Seyler, M. (1995). Transform tectonics, metamorphic plagioclase and amphibolitization in ultramafic rocks of the Vema Transform-Fault (Atlantic-Ocean). *Earth and Planetary Science Letters* 133, 283-298.
- Carroll, M. R. and Wyllie, P. J. (1989). Experimental phase relations in the system tonalite-peridotite-H₂O at 15 kb: Implications for assimilation and differentiation processes near the crust-mantle boundary. *Journal of Petrology* 30, 1351-1382.
- Ceuleneer, G., Nicolas, A. and Boudier, F. (1988). Mantle flow patterns at an oceanic spreading center - the Oman Peridotites record. *Tectonophysics* 151, 1-26.
- Ceuleneer, G. and Rabinowicz, M. (1992). Mantle flow and melt migration beneath oceanic ridges: Models derived from observations in ophiolites. In: Phipps Morgan, J., Blackman, D. K. & Sinton, J. M. (eds.) *Mantle flow and melt generation at mid-ocean ridges*. 71. Washington: American Geophysical Union, 123-154.
- Coogan, L. A., Kempton, P. D., Saunders, A. D. and Norry, M. J. (2000). Melt aggregation within the crust beneath the Mid-Atlantic Ridge: evidence from plagioclase and clinopyroxene major and trace element compositions. *Earth and Planetary Science Letters* 176, 245-257.
- Cordery, M. J. and Morgan, J. P. (1992). Melting and mantle flow beneath a midocean spreading center. *Earth and Planetary Science Letters* 111, 493-516.
- Daines, M. J. and Kohlstedt, D. L. (1993). A laboratory study of melt migration. *Philosophical Transactions of the Royal Society of London Series a-Mathematical Physical and Engineering Sciences* 342, 43-52.
- De Bresser, J. H. P., Ter Heege, J. H. and Spiers, C. J. (2001). Grain size reduction by dynamic recrystallization: can it result in major rheological weakening? *International Journal of Earth Sciences* 90, 28-45.
- de Ronde, A. A., Heilbronner, R., Stünitz, H. and Tullis, J. (2004). Spatial correlation of deformation and mineral reaction in experimentally deformed plagioclase-olivine aggregates. *Tectonophysics* 389, 93-109.
- de Ronde, A. A., Stünitz, H., Tullis, J. and Heilbronner, R. (2005). Reaction-induced weakening of plagioclase-olivine composites. *Tectonophysics* 409, 85-106.
- DePaolo, D. J. (1981). Trace element and isotopic effects of combined wallrock assimilation and fractional crystallization. *Earth and Planetary Science Letters* 53, 189-202.
- Dick, H. J. B. (1989). Abyssal peridotites, very slow spreading ridges and ocean ridge magmatism. In: Saunders, A. D. & Norry, M. J. (eds.) *Magmatism in the ocean basins*. Geol. Soc. London Spec. Pub. 42. 71-105.
- Dick, H. J. B. and Bullen, T. (1984). Chromian spinel as a petrogenetic indicator in abyssal and alpine-type peridotites and spatially associated lavas. *Contributions to Mineralogy and Petrology* 86, 54-76.
- Dijkstra, A. H., Barth, M. G., Drury, M. R., Mason, P. R. D. and Vissers, R. L. M. (2003). Diffuse porous melt flow and melt-rock reaction in the mantle lithosphere at a slow-spreading ridge: A structural petrology and LA-ICP-MS study of the Othris Peridotite Massif (Greece). *Geochemistry Geophysics Geosystems* 4, doi:10.1029/2001GC000278.

CHAPTER 5

- Dijkstra, A. H., Drury, M. R. and Vissers, R. L. M. (2001). Structural petrology of plagioclase peridotites in the west Othris mountains (Greece): Melt impregnation in mantle lithosphere. *Journal of Petrology* 42, 5-24.
- Draper, D. S. and Green, T. H. (1999). P-T phase relations of silicic, alkaline, aluminous liquids: new results and applications to mantle melting and metasomatism. *Earth and Planetary Science Letters* 170, 255-268.
- Droop, G. T. R. (1987). A general equation for estimating Fe³⁺ concentrations in ferromagnesian silicates and oxides from microprobe analyses, using stoichiometric criteria. *Mineralogical Magazine* 51, 431-435.
- Edwards, B. R. and Russell, J. K. (1996). A review and analysis of silicate mineral dissolution experiments in natural silicate melts. *Chemical Geology* 130, 233-245.
- Ellison, A. J. G. and Hess, P. C. (1989). Solution properties of rare earth elements in silicate melts: Inferences from immiscible liquids. *Geochimica Et Cosmochimica Acta* 53, 1965-1974.
- Elthon, D. (1989). Pressure of origin of primary mid-ocean ridge basalts. In: Saunders, A. D. & Norry, M. J. (eds.) *Magmatism in the ocean basins*. 42. Geol. Soc. London Spec. Pub., 125-136.
- Elthon, D. (1992). Chemical trends in abyssal peridotites - refertilization of depleted suboceanic mantle. *Journal of Geophysical Research-Solid Earth and Planets* 97, 9015-9025.
- Elthon, D., Stewart, M. and Ross, D. K. (1992). Compositional trends of minerals in oceanic cumulates. *Journal of Geophysical Research-Solid Earth and Planets* 97, 15189-15199.
- Ewart, A. and Griffin, W. L. (1994). Application of proton-microprobe data to trace-element partitioning in volcanic rocks. *Chemical Geology* 117, 251-284.
- Falloon, T. J., Green, D. H., Hatton, C. J. and Harris, K. L. (1988). Anhydrous partial melting of a fertile and depleted peridotite from 2kb to 30kb and application to basalt petrogenesis. *Journal of Petrology* 29, 1257-1282.
- Falloon, T. J., Green, D. H., O'Neill, H. S. and Hibberson, W. O. (1997). Experimental tests of low degree peridotite partial melt compositions: implications for the nature of anhydrous near- solidus peridotite melts at 1 GPa. *Earth and Planetary Science Letters* 152, 149-162.
- Fisher, G. W. (1978). Rate laws in metamorphism. *Geochimica Et Cosmochimica Acta* 42, 1035-1050.
- Frey, F. A., Shimizu, N., Leinbach, A., Obata, M. and Takazawa, E. (1991). Compositional variations within the lower layered zone of the Horoman peridotite, Hokkaido, Japan: Constraints on models for melt-solid segregation. *Journal of Petrology* 32, 211-227.
- Frost, B. R. (1976). Limits to the assemblage forsterite-anorthite as inferred from peridotite hornfels, Icicle Creek, Washington. *American Mineralogist* 61, 732-750.
- Frost, B. R. and Beard, J. S. (2007). On silica activity and serpentinization. *Journal of Petrology* 48, 1351-1368.

- Fujii, N., Osamura, K. and Takahashi, E. (1986). Effect of water saturation on the distribution of partial melt in olivine-pyroxene-plagioclase system. *Journal of Geophysical Research-Solid Earth and Planets* 91, 9253-9259.
- Furusho, M. and Kanagawa, K. (1999). Transformation-induced strain localization in a lherzolite mylonite from the Hidaka metamorphic belt of central Hokkaido, Japan. *Tectonophysics* 313, 411-432.
- Gaetani, G. A. (2004). The influence of melt structure on trace element partitioning near the peridotite solidus. *Contributions to Mineralogy and Petrology* 147, 511-527.
- Gaetani, G. A. and Grove, T. L. (1998). The influence of water on melting of mantle peridotite. *Contributions to Mineralogy and Petrology* 131, 323-346.
- Gaetani, G. A., Kent, A. J. R., Grove, T. L., Hutcheon, I. D. and Stolper, E. M. (2003). Mineral/melt partitioning of trace elements during hydrous peridotite partial melting. *Contributions to Mineralogy and Petrology* 145, 391-405.
- Girardeau, J. and Francheteau, J. (1993). Plagioclase-wehrlites and peridotites on the East Pacific Rise (Hess Deep) and the Mid-Atlantic Ridge (DSDP Site 334) - evidence for magma percolation in the oceanic upper mantle. *Earth and Planetary Science Letters* 115, 137-149.
- Godard, M., Bodinier, J. L. and Vasseur, G. (1995). Effects of mineralogical reactions on trace-element redistributions in mantle rocks during percolation processes - a chromatographic approach. *Earth and Planetary Science Letters* 133, 449-461.
- Green, D. H. and Hibberson, W. O. (1970). The instability of plagioclase in peridotite at high pressure. *Lithos* 3, 209-221.
- Green, D. H. and Ringwood, A. E. (1967). An experimental investigation of gabbro to eclogite transformation and its petrological applications. *Geochimica Et Cosmochimica Acta* 31, 767-833.
- Hamlyn, P. R. and Bonatti, E. (1980). Petrology of mantle-derived ultramafics from the Owen Fracture-Zone, Northwest Indian-Ocean - implications for the nature of the oceanic upper mantle. *Earth and Planetary Science Letters* 48, 65-79.
- Hellebrand, E., Snow, J. E., Dick, H. J. B. and von der Handt, A. (2006). Inherited depletion in the oceanic mantle inferred from peridotite composition and distribution along Gakkel Ridge. *Ophioliti* 31, 60-61.
- Hellebrand, E., Snow, J. E., Hoppe, P. and Hofmann, A. W. (2002). Garnet-field melting and late-stage refertilization in 'residual' abyssal peridotites from the Central Indian Ridge. *Journal of Petrology* 43, 2305-2338.
- Herzberg, C. T. (1972). Stability fields of plagioclase- and spinel-lherzolite. In: Biggar, G. M. (ed.) *Progress in experimental petrology*. London: Nat Environ Res Counc Publ, 145-148.
- Hirschmann, M. M., Baker, M. B. and Stolper, E. M. (1998). The effect of alkalis on the silica content of mantle-derived melts. *Geochimica Et Cosmochimica Acta* 62, 883-902.

- Hofmann, A. W. (1988). Chemical differentiation of the earth - the relationship between mantle, continental-crust, and oceanic-crust. *Earth and Planetary Science Letters* 90, 297-314.
- Holness, M. B. and Siklos, S. T. C. (2000). The rates and extent of textural equilibration in high-temperature fluid-bearing systems. *Chemical Geology* 162, 137-153.
- Hudon, P., Jung, I. H. and Baker, D. R. (2005). Experimental investigation and optimization of thermodynamic properties and phase diagrams in the systems CaO-SiO₂, MgO-SiO₂, CaMgSi₂O₆-SiO₂ and CaMgSi₂O₆-Mg₂SiO₄ to 1.0 GPa. *Journal of Petrology* 45, 1859-1880.
- Jackson, M. J. and Mills, B. (1997). Dissolution of quartz in vitrified ceramic materials. *Journal of Material Science* 32, 5295-5304.
- Jha, K., Parmentier, E. M. and Morgan, J. P. (1994). The role of mantle-depletion and melt-retention buoyancy in spreading-center segmentation. *Earth and Planetary Science Letters* 125, 221-234.
- Jochum, K. P., Stoll, B., Herwig, K., Willbold, M., Hofmann, A. W., Amini, M., Aarburg, S., Abouchami, W., Hellebrand, E., Mocek, B., Raczek, I., Stracke, A., Alard, O., Bouman, C., Becker, S., Dücking, M., Bratz, H., Klemd, R., de Bruin, D., Canil, D., Cornell, D., de Hoog, C. J., Dalpe, C., Danyushevsky, L., Eisenhauer, A., Premo, W. R., Sun, W. D. D., Tiepolo, M., Vannucci, R., Vennemann, T., Wayne, D. and Woodhead, J. D. (2006). MPI-DING reference glasses for in situ microanalysis: New reference values for element concentrations and isotope ratios. *Geochemistry Geophysics Geosystems* 7, doi:10.1029/2005GC001060.
- Johnson, K. T. M., Dick, H. J. B. and Shimizu, N. (1990). Melting in the oceanic upper mantle - an ion microprobe study of diopsides in abyssal peridotites. *Journal of Geophysical Research-Solid Earth and Planets* 95, 2661-2678.
- Johnson, K. T. M. and Kushiro, I. (1992). Segregation of high pressure partial melts from peridotite using aggregates of diamond: A new experimental approach. *Geophysical Research Letters* 19, 1703-1706.
- Jokat, W. and Schmidt-Aursch, M. C. (2007). Geophysical characteristics of the ultraslow spreading Gakkel Ridge, Arctic Ocean. *Geophysical Journal International* 168, 983-998.
- Kaus, B. J. P., Connolly, J. A. D., Podladchikov, Y. Y. and Schmalholz, S. M. (2005). Effect of mineral phase transitions on sedimentary basin subsidence and uplift. *Earth and Planetary Science Letters* 233, 213-228.
- Kelemen, P. B. (1990). Reaction between ultramafic rock and fractionating basaltic magma .1. phase-relations, the origin of calc-alkaline magma series, and the formation of discordant dunite. *Journal of Petrology* 31, 51-98.
- Kelemen, P. B. and Aharonov, E. (1998). Periodic formation of magma fractures and generation of layered gabbros in the lower crust beneath oceanic spreading centers. In: Buck, W. R., Delaney, P. T., Karson, J. A. & Lagabriele, Y. (eds.) *Faulting and Magmatism at Mid-Ocean Ridges*. AGU Monograph Series 106. American Geophysical Union, 267-289.

- Kelemen, P. B. and Dick, H. J. B. (1995). Focused melt flow and localized deformation in the upper-mantle - juxtaposition of replacive dunite and ductile shear zones in the Josephine Peridotite, SW Oregon. *Journal of Geophysical Research-Solid Earth and Planets* 100, 423-438.
- Kelemen, P. B., Dick, H. J. B. and Quick, J. E. (1992). Formation of harzburgite by pervasive melt rock reaction in the upper mantle. *Nature* 358, 635-641.
- Kelemen, P. B., Hart, S. R. and Bernstein, S. (1998). Silica enrichment in the continental upper mantle via melt/rock reaction. *Earth and Planetary Science Letters* 164, 387-406.
- Kelemen, P. B., Hirth, G., Shimizu, N., Spiegelman, M. and Dick, H. J. B. (1997a). A review of melt migration processes in the adiabatically upwelling mantle beneath oceanic spreading ridges. *Philosophical Transactions of the Royal Society of London Series a-Mathematical Physical and Engineering Sciences* 355, 283-318.
- Kelemen, P. B., Joyce, D. B., Webster, J. D. and Holloway, J. R. (1990). Reaction between ultramafic rock and fractionating basaltic magma II. Experimental investigation of reaction between olivine tholeiite and harzburgite at 1150-1050°C and 5 kb. *Journal of Petrology* 31, 99-134.
- Kelemen, P. B., Koga, K. and Shimizu, N. (1997b). Geochemistry of gabbro sills in the crust-mantle transition zone of the Oman ophiolite: Implications for the origin of the oceanic lower crust. *Earth and Planetary Science Letters* 146, 475-488.
- Kelemen, P. B., Shimizu, N. and Salters, V. J. M. (1995a). Extraction of mid-ocean-ridge basalt from the upwelling mantle by focused flow of melt in dunite channels. *Nature* 375, 747-753.
- Kelemen, P. B., Whitehead, J. A., Aharonov, E. and Jordahl, K. A. (1995b). Experiments on flow focusing in soluble porous-media, with applications to melt extraction from the mantle. *Journal of Geophysical Research-Solid Earth and Planets* 100, 475-496.
- Khodakovskii, G., Rabinowicz, M., Ceuleneer, G. and Trubitsyn, V. P. (1995). Melt percolation in a partially molten mantle mush - Effect of a variable viscosity. *Earth and Planetary Science Letters* 134, 267-281.
- Koga, K. T., Kelemen, P. B. and Shimizu, N. (2001). Petrogenesis of the crust-mantle transition zone and the origin of lower crustal wehrlite in the Oman ophiolite. *Geochemistry Geophysics Geosystems* 2, doi:10.1029/2000GC000132.
- Korenaga, J. and Kelemen, P. B. (1997). Origin of gabbro sills in the Moho transition zone of the Oman ophiolite: Implications for magma transport in the oceanic lower crust. *Journal of Geophysical Research-Solid Earth and Planets* 102, 27729-27749.
- Korenaga, J. and Kelemen, P. B. (1998). Melt migration through the oceanic lower crust: a constraint from melt percolation modeling with finite solid diffusion. *Earth and Planetary Science Letters* 156, 1-11.
- Kornprobst, J. and Tabit, A. (1988). Plagioclase-bearing ultramafic tectonites from the Galicia Margin (Leg 103, Site 637): comparison of their origin and evolution with low-pressure ultramafic bodies in Western Europe. In: Boillot, G. & Winterer, E. L. (eds.)

CHAPTER 5

- Proceedings of the Ocean Drilling Program, Scientific Results*. 103. College Station, Texas: Ocean Drilling Program, 253-268.
- Kushiro, I. (1975). On the nature of silicate melt and its significance in magma genesis: Regularities in the shift of the liquidus boundaries involving olivine, pyroxene and silica minerals. *American Journal of Science* 275, 411-311.
- Kushiro, I. and Yoder, H. S. (1966). Anorthite-forsterite and anorthite-enstatite reactions and their bearing on basalt-eclogite transformation. *Journal of Petrology* 7, 337-362.
- Kushiro, I., Yoder, H. S. and Nishikawa, M. (1968). Effect of water on the melting of enstatite. *Geological Society of America Bulletin* 79, 1685-1692.
- Laporte, D., Toplis, M. J., Seyler, M. and Devidal, J. L. (2004). A new experimental technique for extracting liquids from peridotite at very low degrees of melting: application to partial melting of depleted peridotite. *Contributions to Mineralogy and Petrology* 146, 463-484.
- Le Roux, V., Bodinier, J. L., Tommasi, A., Alard, O., Dautria, J. M., Vauchez, A. and Riches, A. J. V. (2007). The Lherz spinel lherzolite: Refertilized rather than pristine mantle. *Earth and Planetary Science Letters* 259, 599-612.
- Liang, Y. (1999). Diffusive dissolution in ternary systems: Analysis with applications to quartz and quartzite dissolution in molten silicates. *Geochimica Et Cosmochimica Acta* 63, 3983-3995.
- Liang, Y. (2003). Kinetics of crystal-melt reaction in partially molten silicates: 1. Grain scale processes. *Geochemistry Geophysics Geosystems* 4, doi:10.1029/2002GC000375.
- Liu, C., Snow, J. E., Hellebrand, E., Brüggmann, G., Von der Handt, A., Büchl, A. and Hofman, A. W. (in press). Ancient, highly heterogeneous mantle beneath Gakkel Ridge, Arctic Ocean. *Nature*.
- Longhi, J. (2002). Some phase equilibrium systematics of lherzolite melting: I. *Geochemistry Geophysics Geosystems* 3, doi:10.1029/2001GC000204.
- Loucks, R. R. (1996). Restoration of the elemental and stable-isotopic compositions of diffusionally altered minerals in slowly cooled rocks. *Contributions to Mineralogy and Petrology* 124, 346-358.
- Lundstrom, C. C., Gill, J., Williams, Q. and Perfit, M. R. (1995). Mantle melting and basalt extraction by equilibrium porous flow. *Science* 270, 1958-1961.
- Magde, L. S. and Sparks, D. W. (1997). Three-dimensional mantle upwelling, melt generation, and melt migration beneath segment slow spreading ridges. *Journal of Geophysical Research-Solid Earth and Planets* 102, 20571-20583.
- Manning, C. E. (1995a). Coupled reaction and flow in subduction zones: Silica metasomatism in the mantle wedge. In: Jamtveit, B. & Yardley, B. (eds.) *Fluid flow and transport in rocks: Mechanisms and effects*. London: Chapman & Hall, 139-148.
- Manning, C. E. (1995b). Phase-equilibrium controls on SiO₂ metasomatism by aqueous fluid in subduction zones: Reaction at constant pressure and temperature. *International Geology Review* 37, 1074-1093.

CHAPTER 5

- McKenzie, D. (1984). The generation and compaction of partially molten rock. *Journal of Petrology* 25, 713-765.
- Menzies, M. (1973). Mineralogy and partial melt textures within an ultramafic-mafic body, Greece. *Contributions to Mineralogy and Petrology* 42, 273-285.
- Menzies, M. and Allen, C. (1974). Plagioclase lherzolite-residual mantle relationships within 2 eastern mediterranean ophiolites. *Contributions to Mineralogy and Petrology* 45, 197-213.
- Mercier, J.-C. C. and Nicolas, A. (1975). Textures and fabrics of upper-mantle xenoliths as illustrated by xenoliths from basalts. *Journal of Petrology* 16, 454-487.
- Michael, P. J., Langmuir, C. H., Dick, H. J. B., Snow, J. E., Goldstein, S. L., Graham, D. W., Lehnert, K., Kurras, G. J., Jokat, W., Mühe, R. and Edmonds, H. N. (2003). Magmatic and anagmatic seafloor generation at the ultraslow-spreading Gakkel Ridge, Arctic Ocean. *Nature* 423, 956-961.
- Montesi, L. G. J. and Behn, M. D. (2007). Mantle flow and melting underneath oblique and ultraslow mid-ocean ridges. *Geophysical Research Letters* 34, doi:10.1029/2007GL031067.
- Morgan, Z. and Liang, Y. (2003). An experimental and numerical study of the kinetics of harzburgite reactive dissolution with applications to dunite dike formation. *Earth and Planetary Science Letters* 214, 59-74.
- Morgan, Z. and Liang, Y. (2005). An experimental study of the kinetics of lherzolite reactive dissolution with applications to melt channel formation. *Contributions to Mineralogy and Petrology* 150, 369-385.
- Müntener, O., Pettke, T., Desmurs, L., Meier, M. and Schaltegger, U. (2004). Refertilization of mantle peridotite in embryonic ocean basins: trace element and Nd isotopic evidence and implications for crust-mantle relationships. *Earth and Planetary Science Letters* 221, 293-308.
- Müntener, O. and Piccardo, G. B. (2003). Melt migration in ophiolitic peridotites: the message from Alpine-Apennine peridotites and implication for embryonic ocean basins. In: Dilek, Y. & Robinson, P. T. (eds.) *Ophiolites in Earth history*. 218. London: Geological Society, 69-89.
- Natland, J. H. and Dick, H. J. B. (2001). Formation of the lower ocean crust and the crystallization of gabbroic cumulates at a very slowly spreading ridge. *Journal of Volcanology and Geothermal Research* 110, 191-233.
- Navon, O. and Stolper, E. (1987). Geochemical consequences of melt percolation - the upper mantle as a chromatographic column. *Journal of Geology* 95, 285-307.
- Newman, J., Lamb, W. M., Drury, M. R. and Vissers, R. L. M. (1999). Deformation processes in a peridotite shear zone: reaction-softening by an H₂O-deficient, continuous net transfer reaction. *Tectonophysics* 303, 193-222.
- Nicolas, A. (1986). A melt extraction model based on structural studies in mantle peridotites. *Journal of Petrology* 27, 999-1022.

- Niu, Y. L. (1997). Mantle melting and melt extraction processes beneath ocean ridges: Evidence from abyssal peridotites. *Journal of Petrology* 38, 1047-1074.
- Niu, Y. L. (2004). Bulk-rock major and trace element compositions of abyssal peridotites: Implications for mantle melting, melt extraction and post-melting processes beneath mid-ocean ridges. *Journal of Petrology* 45, 2423-2458.
- Nonnotte, P., Ceuleneer, G. and Benoit, M. (2005). Genesis of andesitic-boninitic magmas at mid-ocean ridges by melting of hydrated peridotites: Geochemical evidence from DSDP Site 334 gabbro-norites. *Earth and Planetary Science Letters* 236, 632-653.
- O'Hara, M. J. (1965). Primary magmas and the origin of basalts. *Scot. J. Geol.* 1, 19-40.
- Panjasawatwong, Y., Danyushevsky, L. V., Crawford, A. J. and Harris, K. L. (1995). An experimental study of the effects of melt composition on plagioclase - melt equilibria at 5 and 10 kbar: implications for the origin of magmatic high-An plagioclase. *Contributions to Mineralogy and Petrology* 118, 420-432.
- Papike, J. J., Fowler, G. W., Shearer, C. K. and Layne, G. D. (1996). Ion microprobe investigation of plagioclase and orthopyroxene from lunar Mg-suite norites: Implications for calculating parental melt REE concentrations and for assessing postcrystallization REE redistribution. *Geochimica Et Cosmochimica Acta* 60, 3967-3978.
- Peslier, A. H., Snow, J. E., Hellebrand, E. and von der Handt, A. (2007). Low water contents in minerals from Gakkel ridge abyssal peridotites, Arctic Ocean. *Geochimica Et Cosmochimica Acta* 71, A779.
- Petrini, K., Connolly, J. A. D. and Podladchikov, Y. Y. (2001). A coupled petrological-tectonic model for sedimentary basin evolution: The influence of metamorphic reactions on basins subsidence. *Terra Nova* 13, 354-359.
- Piccardo, G. B., Müntener, O., Zanetti, A. and Pettke, T. (2004a). Ophiolitic peridotites of the Alpine-Apennine system: Mantle processes and geodynamic relevance. *International Geology Review* 46, 1119-1159.
- Piccardo, G. B., Müntener, O., Zanetti, A., Romairone, A., Bruzzone, S., Poggi, E. and Spagnolo, G. (2004b). The Lanzo South peridotite: Melt/peridotite interaction in the mantle lithosphere of the Jurassic Ligurian Tethys. *Ofioliti* 29, 37-62.
- Piccardo, G. B. and Vissers, R. L. M. (2007). The pre-oceanic evolution of the Erro-Tobbio peridotite (Voltri Massif, Ligurian Alps, Italy). *Journal of Geodynamics* 43, 417-449.
- Piccardo, G. B., Zanetti, A. and Müntener, O. (2007). Melt/peridotite interaction in the Southern Lanzo peridotite: Field, textural and geochemical evidence. *Lithos* 94, 181-209.
- Pickering-Witter, J. and Johnston, A. D. (2000). The effects of variable bulk composition on the melting systematics of fertile peridotitic assemblages. *Contributions to Mineralogy and Petrology* 140, 190-211.
- Pin, C., Paquette, J. L., Monchoux, P. and Hammouda, T. (2001). First field-scale occurrence of Si-Al-Na-rich low-degree partial melts from the upper mantle. *Geology* 29, 451-454.

CHAPTER 5

- Presnall, D. C., Dixon, J. R., Odonnell, T. H. and Dixon, S. A. (1979). Generation of mid-ocean ridge tholeiites. *Journal of Petrology* 20, 3-35.
- Presnall, D. C., Gudfinnsson, G. H. and Walter, M. J. (2002). Generation of mid-ocean ridge basalts at pressures from 1 to 7 GPa. *Geochimica Et Cosmochimica Acta* 66, 2073-2090.
- Quick, J. E. (1981). The origin and significance of large, tabular dunite bodies in the Trinity Peridotite, Northern California. *Contributions to Mineralogy and Petrology* 78, 413-422.
- Rampone, E., Bottazzi, P. and Ottolini, L. (1991). Complementary Ti and Zr anomalies in orthopyroxene and clinopyroxene from mantle peridotites. *Nature* 354, 518-520.
- Rampone, E., Hofmann, A. W., Piccardo, G. B., Vannucci, R., Bottazzi, P. and Ottolini, L. (1995). Petrology, mineral and isotope geochemistry of the external liguride peridotites (Northern Apennines, Italy). *Journal of Petrology* 36, 81-105.
- Rampone, E., Hofmann, A. W., Piccardo, G. B., Vannucci, R., Bottazzi, P. and Ottolini, L. (1996). Trace element and isotope geochemistry of depleted peridotites from an N-MORB type ophiolite (Internal Liguride, N Italy). *Contributions to Mineralogy and Petrology* 123, 61-76.
- Rampone, E., Piccardo, G. B., Vannucci, R. and Bottazzi, P. (1997). Chemistry and origin of trapped melts in ophiolitic peridotites. *Geochimica Et Cosmochimica Acta* 61, 4557-4569.
- Rampone, E., Piccardo, G. B., Vannucci, R., Bottazzi, P. and Ottolini, L. (1993). Subsolidus reactions monitored by trace-element partitioning - the spinel-facies to plagioclase-facies transition in mantle peridotites. *Contributions to Mineralogy and Petrology* 115, 1-17.
- Rampone, E., Romairone, A., Abouchami, W., Piccardo, G. B. and Hofmann, A. W. (2005). Chronology, petrology and isotope geochemistry of the Erro-Tobbio peridotites (Ligurian Alps, Italy): Records of Late Palaeozoic lithospheric extension. *Journal of Petrology* 46, 799-827.
- Reid, M. R. and Jackson, I. (1981). Oceanic spreading rate and crustal thickness. *Marine Geophysical Research* 5, 165-172.
- Reiners, P. W. (1998). Reactive melt transport in the mantle and geochemical signatures of mantle-derived magmas. *Journal of Petrology* 39, 1039-1061.
- Renner, J., Evans, B. and Hirth, G. (2000). On the rheologically critical melt fraction. *Earth and Planetary Science Letters* 181, 585-594.
- Robinson, J. A. C., Wood, B. J. and Blundy, J. D. (1998). The beginning of melting of fertile and depleted peridotite at 1.5 GPa. *Earth and Planetary Science Letters* 155, 97-111.
- Ross, K. and Elthon, D. (1993). Cumulates from strongly depleted mid-ocean-ridge basalt. *Nature* 365, 826-829.
- Rubie, D. C. (1990). Role of kinetics in the formation and preservation of eclogites. In: Carswell, D. A. (ed.) *Eclogite facies rocks*. Glasgow: Blackie, 111-140.

- Rubie, D. C. (1998). Disequilibrium during metamorphism: the role of nucleation kinetics. In: Treloar, P. J. & O'Brien, P. J. (eds.) *What drives metamorphism and metamorphic reactions*. 138. London: Geological Society, 199-214.
- Ryerson, F. J. (1985). Oxide solution mechanism in silicate melts: Systematic variations in the activity coefficient of SiO. *Geochimica Et Cosmochimica Acta* 49, 637-649.
- Sack, R. O. and Ghiorso, M. S. (1989). Importance of considerations of mixing properties in establishing an internally consistent thermodynamic database - Thermochemistry of minerals in the system Mg₂SiO₄-Fe₂SiO₄-SiO₂. *Contributions to Mineralogy and Petrology* 102, 41-68.
- Schäfer, F. N. and Foley, S. F. (2002). The effect of crystal orientation on the wetting behaviour of silicate melts on the surfaces of spinel peridotite minerals. *Contributions to Mineralogy and Petrology* 143, 254-261.
- Sekine, T. and Wyllie, P. J. (1983). Experimental simulation of mantle hybridization in subduction zones. *Journal of Geology* 91, 511-528.
- Sen, C. and Dunn, T. (1994). Experimental modal metasomatism of a spinel lherzolite and the production of amphibole-bearing peridotite. *Contributions to Mineralogy and Petrology* 119, 422-4323.
- Seyler, M. and Bonatti, E. (1997). Regional-scale melt-rock interaction in lherzolitic mantle in the Romanche Fracture Zone (Atlantic Ocean). *Earth and Planetary Science Letters* 146, 273-287.
- Seyler, M., Cannat, M. and Mevel, C. (2003). Evidence for major-element heterogeneity in the mantle source of abyssal peridotites from the Southwest Indian Ridge (52° to 68°E). *Geochemistry Geophysics Geosystems* 4, doi:10.1029/2002GC000305.
- Seyler, M., Toplis, M. J., Lorand, J. P., Luguët, A. and Cannat, M. (2001). Clinopyroxene microtextures reveal incompletely extracted melts in abyssal peridotites. *Geology* 29, 155-158.
- Shaw, C. S. J. (1999). Dissolution of orthopyroxene in basanitic magma between 0.4 and 2 GPa: Further implications for the origin of Si-rich alkaline glass inclusions in mantle xenoliths. *Contributions to Mineralogy and Petrology* 135, 114-132.
- Shaw, C. S. J. (2000). The effect of experiment geometry on the mechanism and rate of dissolution of quartz in basanite at 0.5 GPa and 1350°C. *Contributions to Mineralogy and Petrology* 139, 509-525.
- Shaw, C. S. J. (2004). Mechanisms and rates of quartz dissolution in melts in the CMAS (CaO-MgO-Al₂O₃-SiO₂) system. *Contributions to Mineralogy and Petrology* 148, 180-200.
- Shaw, C. S. J. (2006). Effects of melt viscosity and silica activity on the rate and mechanism of quartz dissolution in melts of the CMAS and CAS systems. *Contributions to Mineralogy and Petrology* 151, 665-680.
- Shaw, C. S. J. and Dingwell, D. B. (2008). Experimental peridotite-melt reaction at one atmosphere: A textural and chemical study. *Contributions to Mineralogy and Petrology* 155, 199-214.

- Shaw, C. S. J., Heidelbach, F. and Dingwell, D. B. (2006). The origin of reaction textures in mantle peridotite xenoliths from Sal Island, Cape Verde: The case for "metasomatism" by the host lava. *Contributions to Mineralogy and Petrology* 151, 681-697.
- Shaw, C. S. J., Thibault, Y., Edgar, A. D. and Lloyd, F. E. (1998). Mechanisms of orthopyroxene dissolution in silica-undersaturated melts at 1 atmosphere and implications for the origin of silica-rich glass in mantle xenoliths. *Contributions to Mineralogy and Petrology* 132, 354-370.
- Sisson, T. W. and Grove, T. L. (1993). Experimental investigations of the role of H₂O in calc-alkaline differentiation and subduction zone magmatism. *Contributions to Mineralogy and Petrology* 113, 143-166.
- Sleep, N. H. (1975). Formation of oceanic crust: Some thermal constraints. *Journal of Geophysical Research-Solid Earth and Planets* 80, 4037-4042.
- Sleep, N. H. and Barth, G. A. (1997). The nature of oceanic lower crust and shallow mantle emplaced at low spreading rates. *Tectonophysics* 279, 181-191.
- Sobolev, A. V. and Shimizu, N. (1993). Ultra-depleted primary melt included in an olivine from the Mid-Atlantic Ridge. *Nature* 363, 151-154.
- Sparks, D. W. and Parmentier, E. M. (1991). Melt extraction from the mantle beneath spreading centers. *Earth and Planetary Science Letters* 105, 368-377.
- Spera, F. J. and Bohron, W. A. (2001). Energy-constrained open-system magmatic processes I: General model and energy-constrained assimilation and fractional crystallization (EC-AFC) formulation. *Journal of Petrology* 42, 999-1018.
- Spiegelman, M. (1993a). Flow in deformable porous media. Part 1: Simple analysis. *Journal of Fluid Mechanics* 247, 17-38.
- Spiegelman, M. (1993b). Flow in deformable porous media. Part 2: Numerical analysis - the relationship between shock waves and solitary waves. *Journal of Fluid Mechanics* 247, 39-63.
- Spiegelman, M. (1993c). Physics of melt extraction - theory, implications and applications. *Philosophical Transactions of the Royal Society of London Series a-Mathematical Physical and Engineering Sciences* 342, 23-41.
- Spiegelman, M. and Kenyon, P. (1992). The requirements for chemical disequilibrium during magma migration. *Earth and Planetary Science Letters* 109, 611-620.
- Stolper, E. (1980). A phase diagram for mid-ocean ridge basalts: Preliminary results and implications for petrogenesis. *Contributions to Mineralogy and Petrology* 74, 13-27.
- Strating, E. H. H., Rampone, E., Piccardo, G. B., Drury, M. R. and Vissers, R. L. M. (1993). Subsolidus emplacement of mantle peridotites during incipient oceanic rifting and opening of the Mesozoic Tethys (Voltri Massif, NW Italy). *Journal of Petrology* 34, 901-927.
- Suhr, G., Seck, H. A., Shimizu, N., Gunther, D. and Jenner, G. (1998). Infiltration of refractory melts into the lowermost oceanic crust: evidence from dunite- and gabbro-hosted

- clinopyroxenes in the Bay of Islands ophiolite. *Contributions to Mineralogy and Petrology* 131, 136-154.
- Takagi, D., Sato, H. and Nakagawa, M. (2005). Experimental study of a low-alkali tholeiite at 1–5 kbar: optimal condition for the crystallization of high-An plagioclase in hydrous arc tholeiite. *Contributions to Mineralogy and Petrology* 149, 527-540.
- Takahashi, N. (2001). Origin of plagioclase lherzolite from the Nikanbetsu peridotite complex, Hokkaido, northern Japan: Implications for incipient melt migration and segregation in the partially molten upper mantle. *Journal of Petrology* 42, 39-54.
- Takazawa, E., Frey, F., Shimizu, N. and Obata, M. (1996). Evolution of the Horoman Peridotite (Hokkaido, Japan): Implications from pyroxene compositions. *Chemical Geology* 134, 3-26.
- Tartarotti, P., Susini, S., Nimis, P. and Ottolini, L. (2002). Melt migration in the upper mantle along the Romanche Fracture Zone (Equatorial Atlantic). *Lithos* 63, 125-149.
- Taylor, H. C. J. (1973). Melting relations in the system MgO-Al₂O₃-SiO₂ at 15 kb. *Geological Society of America Bulletin* 84, 1334-1348.
- Toramaru, A. and Fujii, N. (1986). Connectivity of melt phase in a partially molten peridotite. *Journal of Geophysical Research-Solid Earth and Planets* 91, 9239-9252.
- Treiman, A. H. (1996). The perils of partition: Difficulties in retrieving magma compositions from chemically equilibrated basaltic meteorites. *Geochimica Et Cosmochimica Acta* 60, 147-155.
- Tsuchiyama, A. (1985). Dissolution kinetics of plagioclase in the melt of the system diopside-albite-anorthite, and the origin of dusty plagioclase in andesites. *Contributions to Mineralogy and Petrology* 89, 1-16.
- Vannucci, R., Bottazzi, P., Wulff-Pedersen, E. and Neumann, E. R. (1998). Partitioning of REE, Y, Sr, Zr and Ti between clinopyroxene and silicate melts in the mantle under La Palma (Canary Islands): implications for the nature of the metasomatic agents. *Earth and Planetary Science Letters* 158, 39-51.
- Vissers, R. L. M., Drury, M. R., Strating, E. H. H. and Vanderwal, D. (1991). Shear zones in the upper mantle - a case-study in an alpine lherzolite massif. *Geology* 19, 990-993.
- Walter, M. J. and Presnall, D. C. (1994). Melting behavior of simplified lherzolite in the system CaO-MgO-Al₂O₃-SiO₂-Na₂O from 7 to 35 Kbar. *Journal of Petrology* 35, 329-359.
- White, R. S., Minshull, T. A., Bickle, M. J. and Robinson, C. J. (2001). Melt generation at very slow-spreading oceanic ridges: constraints from geochemical and geophysical data. *Journal of Petrology* 42, 1171-1196.
- Wood, B. J. and Yuen, D. A. (1983). The role of lithospheric phase-transitions on seafloor flattening at old ages. *Earth and Planetary Science Letters* 66, 303-314.
- Workman, R. K. and Hart, S. R. (2005). Major and trace element composition of the depleted MORB mantle (DMM). *Earth and Planetary Science Letters* 231, 53-72.
- Wyllie, P. J. and Sekine, T. (1982). The formation of mantle phlogopite in subduction zone hybridization. *Contributions to Mineralogy and Petrology* 79, 375-380.

CHAPTER 5

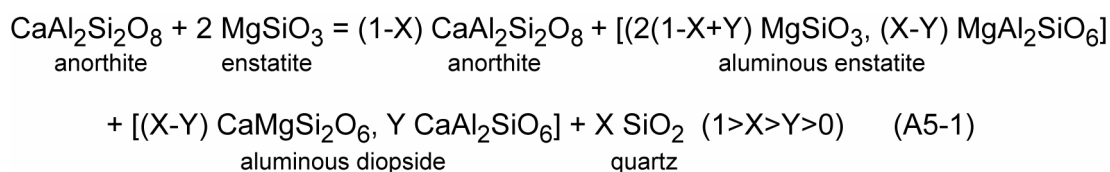
- Xirouchakis, D., Hirschmann, M. M. and Simpson, J. A. (2001). The effect of titanium on the silica content and on mineral-liquid partitioning of mantle-equilibrated melts. *Geochimica Et Cosmochimica Acta* 65, 2201-2217.
- Yamasaki, T. (2004). Localized rheological weakening by grain-size reduction during lithospheric extension. *Tectonophysics* 386, 117-145.
- Yaxley, G. M. and Green, D. H. (1998). Reactions between eclogite and peridotite: Mantle refertilisation by subduction of oceanic crust. *Schweizerische Mineralogische Und Petrographische Mitteilungen* 78, 243-255.
- Zhang, Y., Walker, D. and Lesher, C. E. (1989). Diffusive crystal dissolution. *Contributions to Mineralogy and Petrology* 102, 492-513.

A5.1: RESULTS OF THE EXPERIMENTAL STUDY OF KUSHIRO AND YODER (1966)

In the following, I will give a short overview over the experimental results of Kushiro and Yoder (1966) (Figure A5-1-1) in the order of decreasing silica saturation in the basaltic system.

A5.1.1 *The system enstatite and anorthite in the ratio 2:1*

At low pressures, anorthite and enstatite are the stable assemblage at silica-saturated conditions. With increasing pressure, enstatite becomes aluminous and small amounts of aluminous diopside and quartz begin to appear, while more diopside and enstatite solid solution increase in the complimentary pyroxene. At pressures less than 10 kb the amounts of diopside solid solution and quartz are very small. The amount of diopside solid solution increases rapidly with increasing pressure at the expense of anorthite and close to curve A (Figure A5-1-1a) anorthite is almost completely consumed at temperatures near 1400°C. Between curve A and B, the assemblage becomes aluminous diopside and aluminous enstatite with or without quartz. On the higher pressure side of curve B garnet appears, and the assemblage evolves to garnet + orthopyroxene and clinopyroxene with or without quartz up to 24 kb (eq. A5-1). At higher pressures, only clinopyroxene occurs which also decreases with increasing pressures.

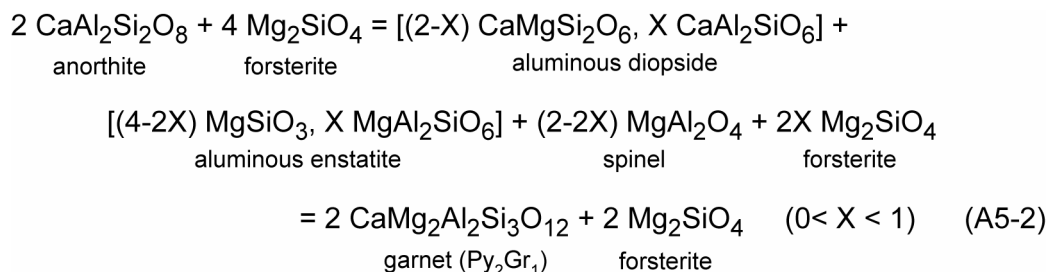


A5.1.2 *The system forsterite and anorthite in the ratio 2:1*

In the system of forsterite to anorthite ratio of 2:1, anorthite is consumed by reaction (eq. A5-2) at curve C (Figure A5-1-1b) and no forsterite would remain as well if only pure diopside and enstatite would be produced. The pyroxenes are presumed to be aluminous in natural systems and a considerable amount of forsterite is still present on the higher pressure side of curve C. The assemblage pyroxenes + spinel + forsterite is stable up to curve D, at which

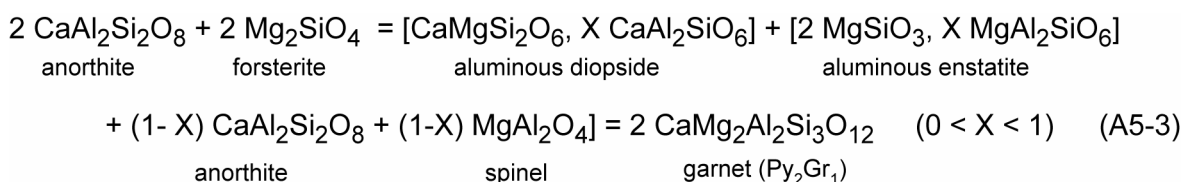
CHAPTER 5

garnet appears and the stable assemblage evolves to garnet + forsterite + clinopyroxene with or without orthopyroxene and spinel. It is believed that pyroxenes and spinel are metastable, and forsterite and garnet are stable.

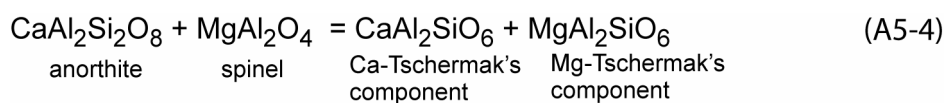


A5.1.3 The system forsterite and anorthite in the ratio 1:1

The anorthite+ forsterite assemblage is stable up to curve E (Figure A5-1-1c) at which the forsterite disappears and pyroxenes and spinel appear (eq. A5-3). This new stable assemblage pyroxenes + anorthite + spinel is stable up to curve F where garnet appears and the assemblage consists of garnet + clinopyroxene. Between curves E and F the relative amounts of pyroxenes to anorthite and spinel change with pressure as well as the composition of pyroxenes changes.



With increasing pressure, the Tschermak-component in pyroxenes increases (pyroxenes become more aluminous). whereas the amounts of spinel and anorthite decrease (eq. A5-4).



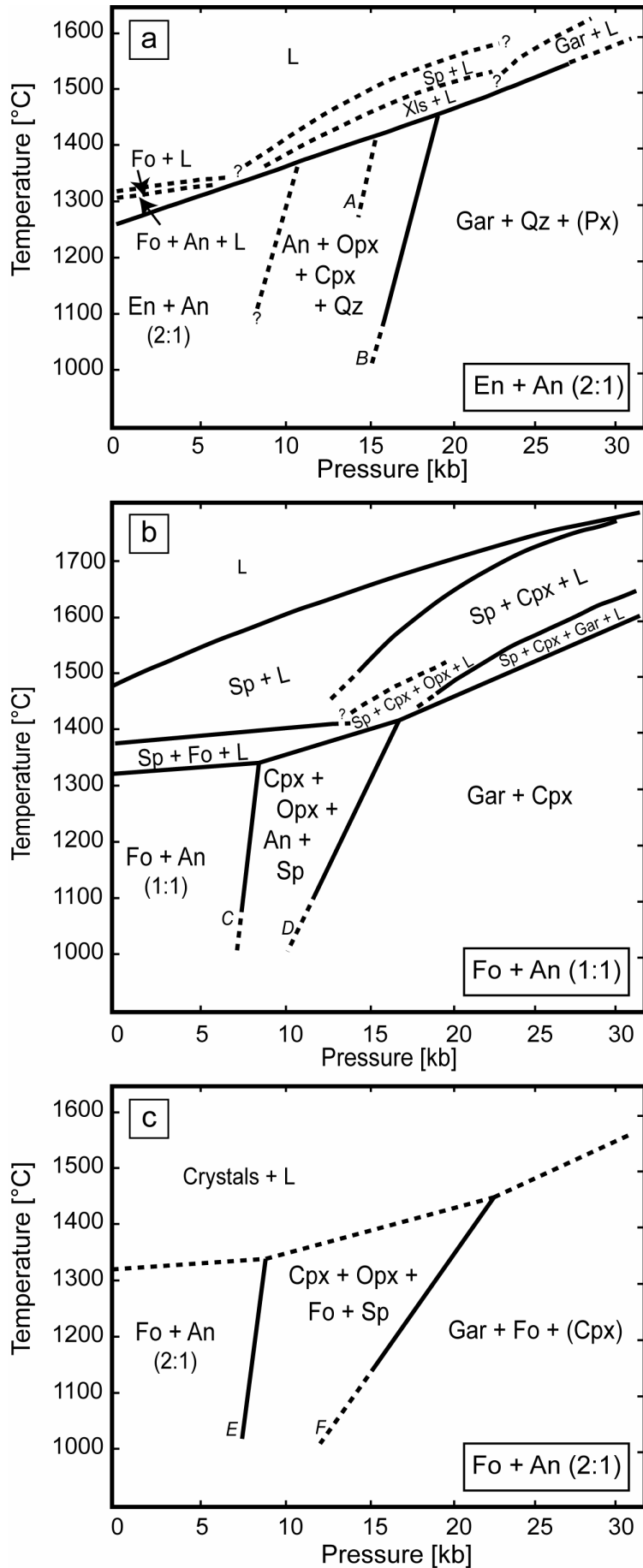


Figure A5-1-1: Pressure-temperature plane for silica-saturated and -undersaturated basaltic systems in the CMAS-system (from Kushiro and Yoder, 1966).

L: liquid; An: anorthite; Cpx: clinopyroxene solid solution; Opx: orthopyroxene solid solution; Sp: spinel; Gar: garnet; Fo: forsterite; Xls: various crystals.

A5.2: RESULTS OF THE EXPERIMENTAL STUDY OF GREEN AND RINGWOOD (1967)

Green and Ringwood (1967) studied the mineralogy of a range of natural basaltic compositions as a function of pressure, temperature, composition and oxygen fugacity. The most notable difference in results between the CMAS-system of Kushiro and Yoder (1966) and natural compositions of Green and Ringwood are the influence of iron as a major component to enable garnet to appear at lower pressures; the presence of albite as a major component to stabilize plagioclase up to pressures at which albite begins to form jadeite solid solution in diopside and that plagioclase becomes more sodic with increasing pressure (Green and Ringwood, 1967). They represent the only study known to me that give a graphic representation of the changing mineralogy with pressure.

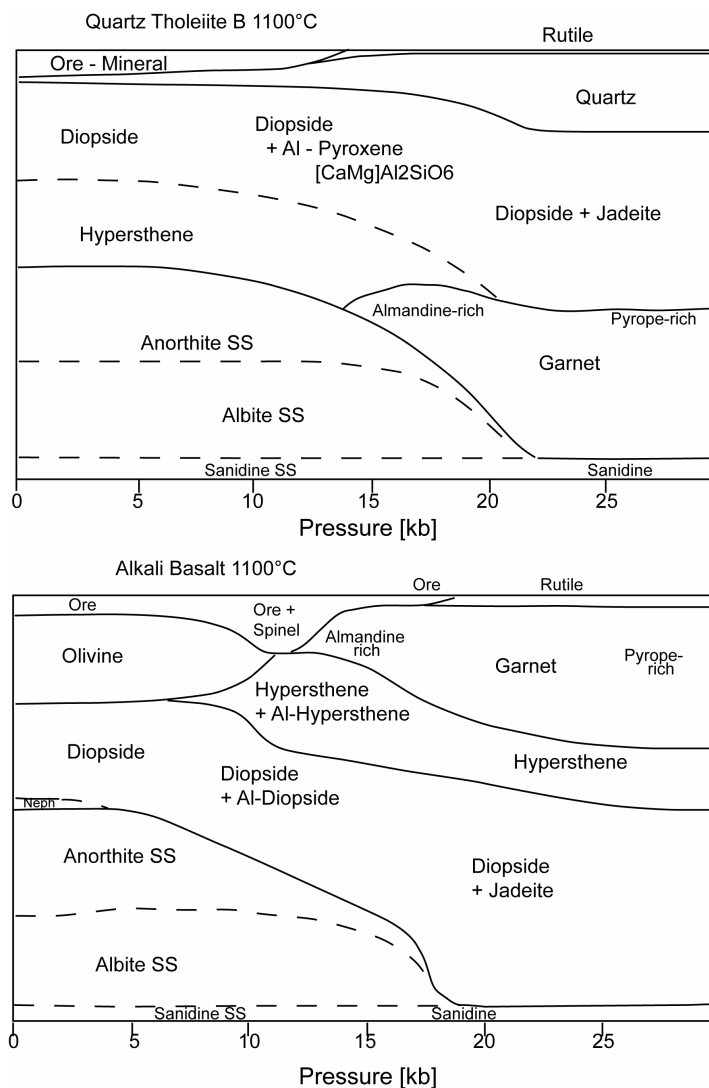


Figure A5-2-1: Diagrammatic representation of the change in mineralogy with pressure at 1100°C in the a quartz tholeiite and an alkali basalt composition (Figure 6 and 7 from Green and Ringwood, 1967).

CHAPTER 5

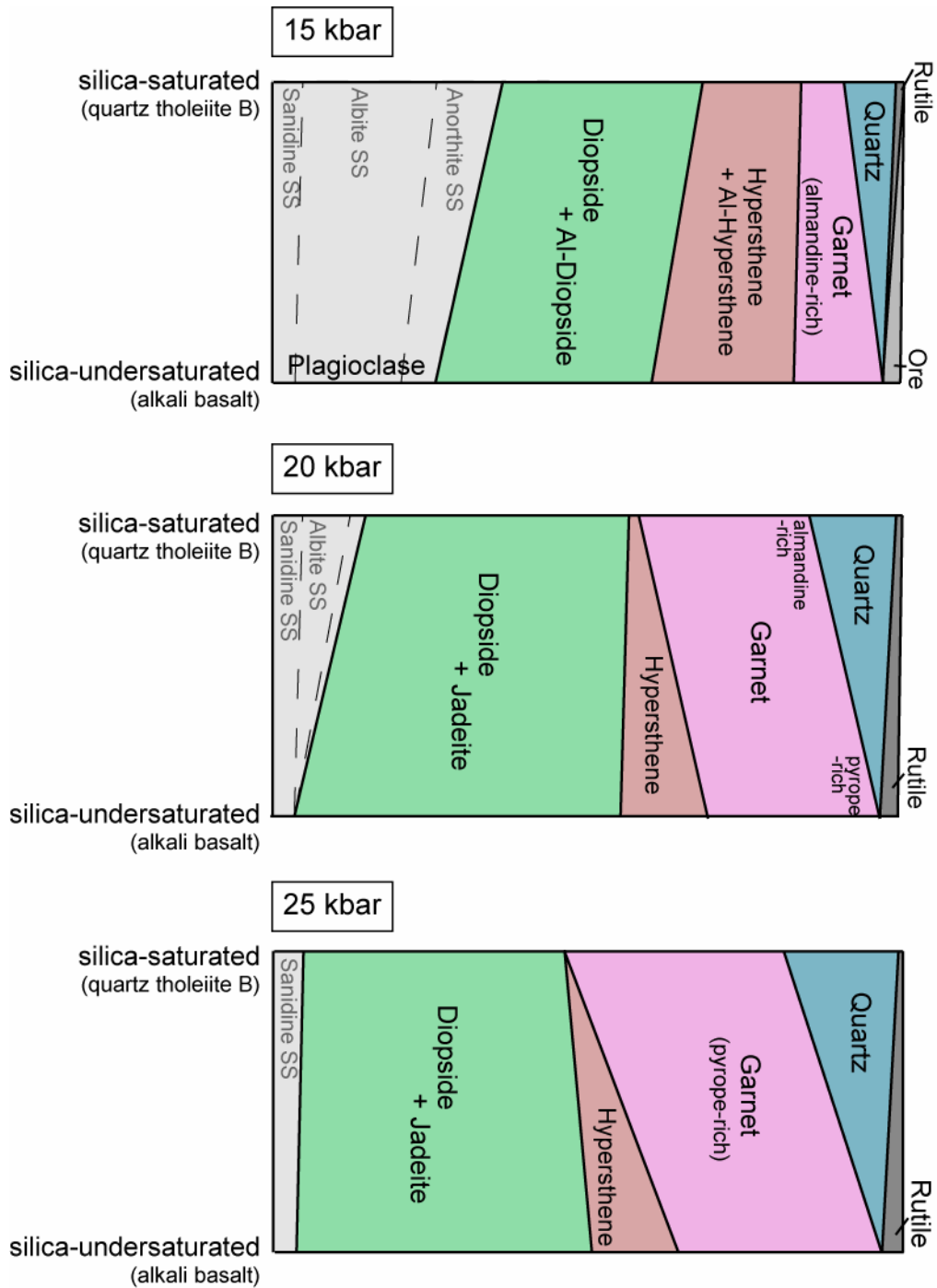


Figure A5-2-2: Diagrammatic representation of the change in mineralogy at changes in silica-saturation at 1100°C and 15, 20 and 25 kbar in two basaltic compositions. The proportions are taken from Figure A5-2-1. The phase assemblages are not representative for silica-undersaturated systems but will overestimate the presence of plagioclase and diopside and underestimate olivine phase proportions in the mantle.

A5.3: RESULTS OF THE EXPERIMENTAL STUDY OF BULTITUDE AND GREEN (1970)

Table 2. MINERAL ASSEMBLAGES FORMED BY REACTION OF OLIVINE NEPHELINE COMPOSITION AT 1,100° C AT VARIOUS PRESSURES

Pressure (kilobars)	Temperature (° C)	Time (h)	Phases present	Comments
1 atmosphere	1,100	4	Ol + Cpx + Pl + glass	Minor plagioclase Minor spinel. Possible incipient melting Less olivine than at 4.5 kilobars Possible incipient melting Minor olivine, spinel increased from 9 kilobars Rare olivine, spinel increased from 13.5 kilobars Olivine not detected, minor mica Large euhedral garnet Minor olivine and spinel, rare mica
1 atmosphere	1,000	24	Ol + Cpx + Pl	
4.5	1,100	2	Ol + Cpx + Pl + Sp + ? glass	
9.0	1,100	4	Ol + Cpx + Pl + Sp + ? glass	
13.5	1,100	4	Ol + Cpx + Sp	
18.0	1,100	4	Ol + Cpx + Sp	
22.5	1,100	4	Cpx + Sp + mica	
24.8	1,100	4	Cpx + Sp + mica	
27.0	1,100	4	Cpx + Sp + Ga + mica	
36.0	1,100	4	Ol + Cpx + Sp + Ga + mica	

Experimental conditions are given in the first column; the mineralogy produced is listed in the fourth column.

Ol, Olivine; Cpx, clinopyroxene; Ga, garnet; Sp, spinel.

Bultitude and Green (1970) investigated the variation of mineralogy of a highly silica-undersaturated rock as a function of pressure and temperature. The starting material was transitional between olivine nephelinite and nepheline-rich basanite.

All phase assemblages reported come from experiments at 1100°C. At atmospheric pressure, phases present were olivine, clinopyroxene and plagioclase. With increasing pressures modal abundance of plagioclase and olivine decrease while spinel and clinopyroxene increase. Plagioclase disappears between 9 and 13.5 kbar. Olivine decreases further in abundance in favour of spinel with increasing pressure until olivine-out between 18 and 22.5 kbar; Mica appears (as suggested due to presence of minor water in the experiment) and the phase assemblage consists of clinopyroxene, spinel and mica. At 27 kbar, garnet occurs and increases with increasing pressures at the expense of clinopyroxene and spinel.

Table A5-3-1: Results of the experimental study on nepheline-normative basalt from Bultitude and Green (1970).

Table 5-2: Clinopyroxene major element composition in [wt%]

Sample	235-19	235-19	235-19	235-19	235-19	235-19	235-19	235-19
Comment	0-cpx-1	0-cpx-2	0-cpx-3	0-cpx-4	0-cpx-5	0-cpx-6	0-cpx-7	0-cpx-8
n	3	3	3	3	3	3	3	3
SiO ₂	50.1 ± 0.3	50.2 ± 0.4	50.5 ± 0.1	49.4 ± 0.1	50.3 ± 0.3	49.4 ± 0.8	49.2 ± 0.2	49.2 ± 0.4
TiO ₂	0.33 ± 0.03	0.44 ± 0.03	0.47 ± 0.01	0.35 ± 0.01	0.39 ± 0.05	0.38 ± 0.01	0.38 ± 0.07	0.36 ± 0.07
Cr ₂ O ₃	0.98 ± 0.08	1.04 ± 0.05	1.07 ± 0.07	0.98 ± 0.02	1.03 ± 0.00	1.02 ± 0.01	1.03 ± 0.03	1.02 ± 0.02
Al ₂ O ₃	7.11 ± 0.07	5.61 ± 0.64	5.49 ± 0.13	6.88 ± 0.08	5.79 ± 0.10	6.60 ± 0.11	7.00 ± 0.14	7.20 ± 0.09
FeO	3.03 ± 0.21	2.98 ± 0.26	2.71 ± 0.17	2.85 ± 0.04	2.74 ± 0.16	2.84 ± 0.11	3.04 ± 0.04	2.95 ± 0.15
MgO	15.6 ± 0.8	16.7 ± 0.9	16.5 ± 0.3	15.5 ± 0.2	16.1 ± 0.3	15.2 ± 0.0	16.0 ± 0.3	15.9 ± 0.4
MnO	0.12 ± 0.03	0.13 ± 0.03	0.11 ± 0.05	0.08 ± 0.01	0.13 ± 0.03	0.10 ± 0.08	0.11 ± 0.03	0.10 ± 0.04
CaO	21.1 ± 0.9	20.8 ± 0.8	21.3 ± 0.4	21.4 ± 0.2	21.5 ± 0.4	22.0 ± 0.0	20.9 ± 0.1	21.0 ± 0.6
NiO	0.09 ± 0.07	0.03 ± 0.05	0.04 ± 0.02	0.04 ± 0.02	0.06 ± 0.05	0.01 ± 0.01	0.04 ± 0.04	0.04 ± 0.05
Na ₂ O	0.53 ± 0.05	0.48 ± 0.06	0.52 ± 0.01	0.54 ± 0.03	0.52 ± 0.05	0.51 ± 0.05	0.48 ± 0.06	0.54 ± 0.02
K ₂ O	0.00 ± 0.01	0.00 ± 0.01	0.01 ± 0.01	0.00 ± 0.00	0.01 ± 0.01	0.02 ± 0.00	0.00 ± 0.00	0.01 ± 0.01
Total	98.9 ± 0.2	98.4 ± 0.3	98.7 ± 0.0	98.0 ± 0.3	98.5 ± 0.2	98.2 ± 0.8	98.2 ± 0.0	98.2 ± 0.3
Cr-number	0.085 ± 0.007	0.112 ± 0.014	0.115 ± 0.009	0.088 ± 0.001	0.106 ± 0.002	0.094 ± 0.000	0.090 ± 0.004	0.087 ± 0.002
Mg-number	0.902 ± 0.002	0.909 ± 0.005	0.915 ± 0.004	0.906 ± 0.000	0.913 ± 0.003	0.905 ± 0.003	0.904 ± 0.001	0.905 ± 0.002

±: one standard deviation

n: number of analyses

Table 5-2 (continued): Clinopyroxene major element composition in [wt%]

Sample	235-19	235-19	235-19	235-19	235-19	235-19	235-19	235-19
Comment	0-cpx-9	0-cpx-10	0-cpx-12	0-cpx-13	1-cpx-1	1-cpx-2	1-cpx-3	1-cpx-4
n	3	3	3	3	3	3	3	3
SiO ₂	49.7 ± 0.4	49.5 ± 0.5	50.4 ± 0.6	49.6 ± 0.0	49.6 ± 0.1	49.9 ± 0.6	50.0 ± 0.3	49.8 ± 0.5
TiO ₂	0.39 ± 0.04	0.37 ± 0.02	0.49 ± 0.05	0.42 ± 0.02	0.37 ± 0.09	0.50 ± 0.06	0.42 ± 0.03	0.48 ± 0.03
Cr ₂ O ₃	1.00 ± 0.05	1.01 ± 0.08	1.08 ± 0.04	1.03 ± 0.08	1.07 ± 0.03	1.19 ± 0.12	1.07 ± 0.01	1.09 ± 0.00
Al ₂ O ₃	7.19 ± 0.04	6.87 ± 0.07	5.08 ± 0.62	6.45 ± 0.13	6.65 ± 0.06	5.60 ± 0.43	6.49 ± 0.16	5.77 ± 0.07
FeO	3.05 ± 0.23	2.77 ± 0.10	2.64 ± 0.21	2.63 ± 0.06	2.68 ± 0.13	2.71 ± 0.13	2.73 ± 0.07	2.85 ± 0.21
MgO	16.0 ± 0.4	15.3 ± 0.2	16.1 ± 0.2	15.5 ± 0.2	15.7 ± 0.4	16.0 ± 0.0	16.0 ± 0.4	16.1 ± 0.3
MnO	0.13 ± 0.03	0.11 ± 0.01	0.12 ± 0.03	0.08 ± 0.02	0.09 ± 0.03	0.09 ± 0.02	0.13 ± 0.01	0.12 ± 0.01
CaO	20.9 ± 0.6	21.9 ± 0.3	21.8 ± 0.3	21.8 ± 0.1	21.7 ± 0.4	21.5 ± 0.2	21.6 ± 0.5	21.5 ± 0.2
NiO	0.00 ± 0.00	0.08 ± 0.02	0.04 ± 0.03	0.06 ± 0.03	0.06 ± 0.06	0.04 ± 0.01	0.06 ± 0.05	0.01 ± 0.00
Na ₂ O	0.51 ± 0.01	0.55 ± 0.00	0.50 ± 0.05	0.55 ± 0.03	0.51 ± 0.03	0.50 ± 0.02	0.46 ± 0.04	0.49 ± 0.00
K ₂ O	0.01 ± 0.01	0.01 ± 0.01	0.00 ± 0.01	0.01 ± 0.01	0.00 ± 0.00	0.00 ± 0.01	0.01 ± 0.01	0.01 ± 0.00
Total	98.8 ± 0.3	98.5 ± 0.5	98.2 ± 0.1	98.1 ± 0.3	98.5 ± 0.1	98.0 ± 0.7	98.9 ± 0.8	98.2 ± 0.2
Cr-number	0.085 ± 0.004	0.090 ± 0.007	0.126 ± 0.016	0.087 ± 0.006	0.097 ± 0.003	0.125 ± 0.020	0.100 ± 0.002	0.113 ± 0.001
Mg-number	0.904 ± 0.004	0.908 ± 0.002	0.916 ± 0.006	0.913 ± 0.002	0.913 ± 0.003	0.913 ± 0.004	0.912 ± 0.004	0.910 ± 0.004

±: one standard deviation

n: number of analyses

Table 5-2: Clinopyroxene major element composition in [wt%]

Sample	235-19	235-19	235-19	235-19	235-19	235-19	235-19	235-19	235-19
Comment	2-cpx-1	2-cpx-2	2-cpx-3	4-cpx-02	4-cpx-01	4-cpx-02	4-cpx-02	5-cpx-2	5-cpx-3
n	3	3	3	3	3	3	3	3	3
SiO ₂	49.7 ± 0.1	50.4 ± 0.6	50.7 ± 0.8	50.3 ± 0.2	49.3 ± 0.2	51.2 ± 0.8	51.2 ± 0.8	49.7 ± 0.1	50.6 ± 0.1
TiO ₂	0.38 ± 0.05	0.39 ± 0.03	0.47 ± 0.06	0.38 ± 0.04	0.37 ± 0.03	0.42 ± 0.03	0.42 ± 0.03	0.39 ± 0.02	0.56 ± 0.06
Cr ₂ O ₃	1.08 ± 0.05	1.02 ± 0.05	1.05 ± 0.05	1.05 ± 0.01	0.99 ± 0.03	1.00 ± 0.06	1.00 ± 0.06	1.04 ± 0.05	1.12 ± 0.03
Al ₂ O ₃	6.90 ± 0.13	5.27 ± 0.62	4.69 ± 0.74	6.19 ± 0.09	7.08 ± 0.24	5.10 ± 0.08	5.10 ± 0.08	6.14 ± 0.01	4.86 ± 0.11
FeO	2.80 ± 0.20	2.68 ± 0.14	2.64 ± 0.19	2.74 ± 0.06	2.92 ± 0.14	2.51 ± 0.06	2.51 ± 0.06	2.81 ± 0.13	2.66 ± 0.05
MgO	15.1 ± 0.2	16.0 ± 0.7	16.5 ± 0.1	15.6 ± 0.2	15.6 ± 0.3	16.4 ± 0.2	16.4 ± 0.2	16.0 ± 0.4	16.4 ± 0.3
MnO	0.06 ± 0.00	0.13 ± 0.01	0.12 ± 0.04	0.12 ± 0.03	0.12 ± 0.03	0.08 ± 0.05	0.08 ± 0.05	0.10 ± 0.04	0.08 ± 0.03
CaO	21.9 ± 0.2	21.8 ± 0.7	21.7 ± 0.5	22.0 ± 0.1	21.8 ± 0.3	22.4 ± 0.5	22.4 ± 0.5	21.9 ± 0.3	22.0 ± 0.1
NiO	0.03 ± 0.02	0.04 ± 0.03	0.09 ± 0.01	0.05 ± 0.01	0.04 ± 0.04	0.02 ± 0.02	0.02 ± 0.02	0.05 ± 0.07	0.06 ± 0.03
Na ₂ O	0.59 ± 0.01	0.53 ± 0.03	0.50 ± 0.05	0.58 ± 0.01	0.54 ± 0.05	0.51 ± 0.09	0.51 ± 0.09	0.52 ± 0.03	0.47 ± 0.01
K ₂ O	0.00 ± 0.01	0.01 ± 0.01	0.00 ± 0.00	0.00 ± 0.00	0.00 ± 0.01	0.00 ± 0.00	0.00 ± 0.00	0.01 ± 0.00	0.00 ± 0.00
Total	98.6 ± 0.3	98.3 ± 0.4	98.5 ± 0.5	99.0 ± 0.2	98.9 ± 0.3	99.6 ± 1.4	99.6 ± 1.4	98.6 ± 0.3	98.8 ± 0.1
Cr-number	0.095 ± 0.008	0.116 ± 0.009	0.133 ± 0.017	0.102 ± 0.002	0.086 ± 0.004	0.116 ± 0.007	0.116 ± 0.007	0.102 ± 0.004	0.134 ± 0.000
Mg-number	0.906 ± 0.005	0.914 ± 0.004	0.918 ± 0.006	0.910 ± 0.001	0.905 ± 0.002	0.921 ± 0.002	0.921 ± 0.002	0.910 ± 0.002	0.917 ± 0.003

±: one standard deviation

n: number of analyses

Table 5-2 (continued): Clinopyroxene major element composition in [wt%]

Sample	235-19	235-19	235-19	235-19
Comment	6-cpx-2-1	6-cpx-2-2	6-cpx-2-3	6-cpx-2-4
n	3	3	3	3
SiO ₂	50.7 ± 0.1	50.3 ± 0.2	49.3 ± 0.1	50.6 ± 0.4
TiO ₂	0.43 ± 0.04	0.48 ± 0.01	0.43 ± 0.04	0.49 ± 0.03
Cr ₂ O ₃	1.02 ± 0.07	1.17 ± 0.09	1.02 ± 0.04	1.11 ± 0.04
Al ₂ O ₃	4.36 ± 0.32	5.28 ± 0.43	6.66 ± 0.05	5.18 ± 0.49
FeO	2.87 ± 0.09	2.86 ± 0.17	2.89 ± 0.17	2.69 ± 0.19
MgO	17.6 ± 0.2	16.6 ± 0.7	16.2 ± 0.7	17.0 ± 0.9
MnO	0.10 ± 0.03	0.07 ± 0.02	0.13 ± 0.05	0.08 ± 0.04
CaO	20.9 ± 0.2	21.3 ± 0.8	21.3 ± 0.8	21.1 ± 0.6
NiO	0.04 ± 0.04	0.02 ± 0.00	0.01 ± 0.01	0.09 ± 0.03
Na ₂ O	0.41 ± 0.01	0.45 ± 0.02	0.47 ± 0.03	0.49 ± 0.05
K ₂ O	0.00 ± 0.00	0.01 ± 0.01	0.01 ± 0.01	0.01 ± 0.01
Total	98.4 ± 0.2	98.6 ± 0.4	98.4 ± 0.1	98.9 ± 0.4
Cr-number	0.136 ± 0.001	0.130 ± 0.017	0.093 ± 0.003	0.126 ± 0.013
Mg-number	0.916 ± 0.002	0.912 ± 0.001	0.909 ± 0.001	0.918 ± 0.003

±: one standard deviation

n: number of analyses

Table 5-2: Clinopyroxene major element composition in [wt%]

Sample	235-134	235-134	235-134	235-134	235-134	235-134	235-134	235-134	235-134
Comment	1-cpx-1	1-cpx-2	3-cpx-1-1	3-cpx-1-2	5-cpx-1	5-cpx-2	5-cpx-3	5-cpx-1	5-cpx-3
n	3	3	3	3	3	3	3	3	3
SiO ₂	49.8 ± 0.3	49.8 ± 0.3	51.0 ± 0.5	51.6 ± 0.4	50.1 ± 0.1	51.3 ± 0.5	49.9 ± 0.2	50.1 ± 0.1	49.9 ± 0.2
TiO ₂	0.21 ± 0.00	0.24 ± 0.05	0.33 ± 0.05	0.34 ± 0.04	0.22 ± 0.03	0.21 ± 0.02	0.203 ± 0.02	0.22 ± 0.03	0.203 ± 0.02
Cr ₂ O ₃	1.15 ± 0.00	1.15 ± 0.03	1.24 ± 0.15	0.89 ± 0.19	1.08 ± 0.01	1.06 ± 0.07	1.150 ± 0.08	1.08 ± 0.01	1.150 ± 0.08
Al ₂ O ₃	6.56 ± 0.21	6.23 ± 0.27	3.95 ± 0.69	3.11 ± 0.73	6.71 ± 0.12	4.96 ± 0.76	6.277 ± 0.53	6.71 ± 0.12	6.277 ± 0.53
FeO	2.76 ± 0.22	2.83 ± 0.10	2.51 ± 0.26	2.63 ± 0.20	2.68 ± 0.12	2.80 ± 0.17	2.827 ± 0.14	2.68 ± 0.12	2.827 ± 0.14
MgO	16.0 ± 0.2	16.6 ± 0.2	16.9 ± 0.8	17.2 ± 0.6	15.3 ± 0.1	17.4 ± 0.8	16.4 ± 0.3	15.3 ± 0.1	16.4 ± 0.3
MnO	0.11 ± 0.04	0.13 ± 0.02	0.13 ± 0.03	0.09 ± 0.02	0.13 ± 0.03	0.12 ± 0.03	0.106 ± 0.04	0.13 ± 0.03	0.106 ± 0.04
CaO	21.5 ± 0.3	21.0 ± 0.7	22.0 ± 1.1	22.1 ± 0.2	22.0 ± 0.0	20.9 ± 1.0	21.3 ± 1.0	22.0 ± 0.0	21.3 ± 1.0
NiO	0.04 ± 0.02	0.01 ± 0.01	0.06 ± 0.05	0.07 ± 0.04	0.06 ± 0.04	0.04 ± 0.04	0.050 ± 0.05	0.06 ± 0.04	0.050 ± 0.05
Na ₂ O	0.49 ± 0.03	0.51 ± 0.01	0.51 ± 0.04	0.43 ± 0.06	0.69 ± 0.02	0.61 ± 0.02	0.607 ± 0.09	0.69 ± 0.02	0.607 ± 0.09
K ₂ O	0.01 ± 0.02	0.01 ± 0.01	0.00 ± 0.00	0.01 ± 0.00	0.00 ± 0.00	0.01 ± 0.01	0.014 ± 0.01	0.00 ± 0.00	0.014 ± 0.01
Total	98.6 ± 0.1	98.5 ± 0.5	98.7 ± 0.4	98.5 ± 0.1	99.0 ± 0.2	99.4 ± 0.6	98.8 ± 0.5	99.0 ± 0.2	98.8 ± 0.5
Cr-number	0.105 ± 0.003	0.110 ± 0.007	0.176 ± 0.029	0.165 ± 0.047	0.097 ± 0.002	0.126 ± 0.011	0.110 ± 0.007	0.097 ± 0.002	0.110 ± 0.007
Mg-number	0.912 ± 0.006	0.913 ± 0.002	0.923 ± 0.005	0.921 ± 0.008	0.911 ± 0.003	0.917 ± 0.005	0.912 ± 0.002	0.911 ± 0.003	0.912 ± 0.002

±: one standard deviation

n: number of analyses

Table 5-2 (continued): Clinopyroxene major element composition in [wt%]

Sample	235-134	235-134	235-134	235-134	235-134	235-134	235-134
Comment	7-cpx-2	7-cpx-3	7-cpx-4	11-cpx-1-1	11-cpx-1-2	11-cpx-1-3	11-cpx-2-1c
n	3	3	3	3	3	3	1
SiO ₂	49.79 ± 0.08	50.10 ± 0.25	50.08 ± 0.07	51.67 ± 0.46	50.94 ± 0.16	50.97 ± 0.69	50.61
TiO ₂	0.20 ± 0.03	0.24 ± 0.05	0.19 ± 0.02	0.33 ± 0.01	0.32 ± 0.04	0.29 ± 0.06	0.31
Cr ₂ O ₃	1.08 ± 0.03	1.10 ± 0.11	1.01 ± 0.02	1.17 ± 0.08	1.19 ± 0.07	1.15 ± 0.08	1.19
Al ₂ O ₃	6.59 ± 0.13	5.97 ± 0.30	6.54 ± 0.30	3.98 ± 0.41	4.99 ± 0.38	4.53 ± 0.76	4.60
FeO	2.95 ± 0.01	2.75 ± 0.15	2.59 ± 0.16	2.52 ± 0.19	2.72 ± 0.12	2.60 ± 0.07	2.57
MgO	16.48 ± 0.46	16.42 ± 0.62	16.40 ± 0.80	16.84 ± 0.51	16.36 ± 0.14	16.46 ± 0.53	16.41
MnO	0.13 ± 0.04	0.09 ± 0.04	0.11 ± 0.01	0.10 ± 0.02	0.09 ± 0.03	0.09 ± 0.03	0.08
CaO	20.99 ± 0.58	21.38 ± 0.88	21.13 ± 0.99	22.15 ± 0.86	21.95 ± 0.38	22.24 ± 0.24	22.03
NiO	0.07 ± 0.03	0.03 ± 0.04	0.09 ± 0.07	0.05 ± 0.00	0.07 ± 0.06	0.04 ± 0.04	0.00
Na ₂ O	0.54 ± 0.01	0.48 ± 0.03	0.55 ± 0.06	0.50 ± 0.00	0.56 ± 0.01	0.55 ± 0.04	0.47
K ₂ O	0.00 ± 0.00	0.01 ± 0.01	0.00 ± 0.00	0.01 ± 0.01	0.01 ± 0.01	0.00 ± 0.00	0.01
Total	98.8 ± 0.1	98.6 ± 0.3	98.7 ± 0.5	99.3 ± 0.2	99.2 ± 0.1	98.9 ± 0.2	98.3
Cr-number	0.099 ± 0.000	0.111 ± 0.015	0.094 ± 0.002	0.165 ± 0.005	0.138 ± 0.010	0.147 ± 0.018	0.149
Mg-number	0.909 ± 0.002	0.914 ± 0.002	0.919 ± 0.001	0.923 ± 0.003	0.915 ± 0.003	0.919 ± 0.003	0.919

±: one standard deviation

n: number of analyses

Table 5-3: Clinopyroxene trace element composition in [$\mu\text{g/g}$]

Sample Comment position	235-19 0-cpx-1		235-19 0-cpx-2		235-19 0-cpx-3		235-19 0-cpx-4		235-19 0-cpx-5		235-19 0-cpx-6		235-19 0-cpx-7		235-19 0-cpx-8	
	core	rim	core	rim	core	rim	intermediate	rim	intermediate	rim	intermediate	rim	intermediate	rim	intermediate	core
Na	2628 ± 32	2829 ± 89	2969 ± 100	2555 ± 73	2666 ± 54	2628 ± 69	2804 ± 74	2819 ± 82								
Sc	47.9 ± 0.8	61.4 ± 0.3	58.3 ± 0.6	48.1 ± 0.6	55.2 ± 0.6	54.2 ± 0.5	51.1 ± 0.4	49.2 ± 0.6								
Ti	1898 ± 22	2505 ± 24	2378 ± 13	1903 ± 15	2225 ± 15	2160 ± 22	2067 ± 17	2002 ± 124								
V	186 ± 2	226 ± 41	221 ± 2	185 ± 3	219 ± 2	209 ± 4	194 ± 3	192 ± 2								
Cr	5854 ± 19	6383 ± 76	6198 ± 30	5904 ± 69	6120 ± 15	6115 ± 35	6101 ± 56	6088 ± 31								
Sr	4.01 ± 0.13	2.09 ± 0.07	1.54 ± 0.06	4.48 ± 0.11	2.09 ± 0.06	2.79 ± 0.08	3.40 ± 0.08	4.39 ± 0.09								
Y	16.31 ± 0.40	20.86 ± 0.32	23.17 ± 0.51	16.93 ± 0.35	21.20 ± 0.60	20.29 ± 0.40	19.56 ± 0.39	17.46 ± 0.28								
Zr	6.98 ± 0.13	11.9 ± 0.2	11.3 ± 0.3	7.11 ± 0.13	9.20 ± 0.16	8.75 ± 0.14	8.27 ± 0.17	7.55 ± 0.13								
La	0.025 ± 0.004	0.017 ± 0.003	0.013 ± 0.004	0.026 ± 0.004	0.026 ± 0.004	0.020 ± 0.004	0.021 ± 0.004	0.022 ± 0.004								
Ce	0.38 ± 0.03	0.47 ± 0.03	0.48 ± 0.03	0.42 ± 0.04	0.45 ± 0.04	0.46 ± 0.03	0.45 ± 0.03	0.44 ± 0.03								
Nd	1.66 ± 0.13	2.87 ± 0.18	2.60 ± 0.14	1.74 ± 0.19	2.42 ± 0.13	2.27 ± 0.14	2.25 ± 0.14	1.98 ± 0.12								
Sm	1.22 ± 0.09	1.79 ± 0.13	2.04 ± 0.12	1.15 ± 0.10	1.44 ± 0.09	1.47 ± 0.09	1.43 ± 0.09	1.31 ± 0.09								
Eu	0.49 ± 0.03	0.55 ± 0.03	0.57 ± 0.03	0.56 ± 0.04	0.57 ± 0.03	0.61 ± 0.04	0.57 ± 0.03	0.56 ± 0.03								
Gd	1.83 ± 0.12	3.11 ± 0.16	3.12 ± 0.23	2.00 ± 0.16	2.83 ± 0.15	2.83 ± 0.21	2.31 ± 0.13	2.26 ± 0.13								
Dy	2.63 ± 0.18	4.16 ± 0.23	4.74 ± 0.24	3.15 ± 0.20	3.96 ± 0.21	3.83 ± 0.26	2.89 ± 0.18	3.29 ± 0.19								
Er	1.57 ± 0.18	2.30 ± 0.12	2.51 ± 0.13	1.85 ± 0.11	2.02 ± 0.15	2.29 ± 0.12	2.04 ± 0.11	1.67 ± 0.10								
Yb	1.50 ± 0.10	2.04 ± 0.13	2.14 ± 0.10	1.60 ± 0.08	1.84 ± 0.09	1.88 ± 0.10	1.91 ± 0.09	1.88 ± 0.15								

±: one standard deviation

Table 5-3 (continued): Clinopyroxene trace element composition in [$\mu\text{g/g}$]

Sample Comment position	235-19 0-cpx-9		235-19 0-cpx-10		235-19 0-cpx-11		235-19 0-cpx-12		235-19 0-cpx-13		235-19 1-cpx-1		235-19 1-cpx-2		235-19 1-cpx-3		235-19 1-cpx-4	
	core	rim	intermediate	rim	intermediate	rim	intermediate	rim	intermediate	rim	core	rim	intermediate	rim	intermediate	rim	intermediate	rim
Na	2760 ± 58	2538 ± 85	2908 ± 112	2771 ± 107	2486 ± 70	2753 ± 60	2969 ± 88	2688 ± 86										
Sc	51.5 ± 0.6	49.4 ± 0.4	60.3 ± 0.4	54.2 ± 0.4	53.0 ± 0.5	68.3 ± 0.6	63.1 ± 0.5	62.8 ± 0.8										
Ti	2146 ± 20	1836 ± 23	2530 ± 17	2325 ± 29	1958 ± 30	2886 ± 25	2525 ± 24	2821 ± 15										
V	197 ± 3	187 ± 2	221 ± 2	214 ± 5	200 ± 3	259 ± 3	242 ± 4	247 ± 4										
Cr	6235 ± 33	5774 ± 36	6324 ± 43	6274 ± 61	5797 ± 79	7099 ± 41	6477 ± 39	6909 ± 20										
Sr	5.05 ± 0.10	3.47 ± 0.08	1.57 ± 0.05	2.12 ± 0.06	1.63 ± 0.09	1.00 ± 0.05	1.52 ± 0.06	2.08 ± 0.12										
Y	17.89 ± 0.29	17.48 ± 0.42	23.47 ± 0.32	21.77 ± 0.31	18.87 ± 0.30	28.49 ± 0.38	26.21 ± 0.46	27.14 ± 0.38										
Zr	8.26 ± 0.14	7.33 ± 0.19	13.0 ± 0.2	11.0 ± 0.2	9.04 ± 0.20	18.1 ± 0.2	13.8 ± 0.2	17.3 ± 0.2										
La	0.017 ± 0.005	0.015 ± 0.003	0.023 ± 0.004	0.031 ± 0.004	0.021 ± 0.004	0.021 ± 0.004	0.026 ± 0.007	0.018 ± 0.003										
Ce	0.48 ± 0.04	0.39 ± 0.03	0.54 ± 0.03	0.47 ± 0.03	0.40 ± 0.03	0.62 ± 0.03	0.56 ± 0.03	0.53 ± 0.04										
Nd	2.18 ± 0.14	1.73 ± 0.19	3.05 ± 0.23	2.74 ± 0.16	2.26 ± 0.15	3.72 ± 0.18	3.06 ± 0.19	3.30 ± 0.15										
Sm	1.37 ± 0.09	1.22 ± 0.09	2.12 ± 0.11	1.84 ± 0.16	1.54 ± 0.13	2.51 ± 0.13	2.03 ± 0.13	2.57 ± 0.12										
Eu	0.56 ± 0.03	0.56 ± 0.05	0.58 ± 0.04	0.64 ± 0.04	0.58 ± 0.05	0.67 ± 0.04	0.69 ± 0.04	0.61 ± 0.03										
Gd	2.46 ± 0.17	2.19 ± 0.13	3.67 ± 0.20	3.29 ± 0.16	2.38 ± 0.21	4.56 ± 0.20	3.28 ± 0.16	4.31 ± 0.21										
Dy	3.33 ± 0.20	2.90 ± 0.18	4.24 ± 0.22	4.11 ± 0.21	3.32 ± 0.20	5.52 ± 0.37	4.63 ± 0.24	5.22 ± 1.08										
Er	1.99 ± 0.11	1.79 ± 0.11	2.51 ± 0.13	2.51 ± 0.12	1.98 ± 0.11	2.99 ± 0.19	2.56 ± 0.13	2.70 ± 0.56										
Yb	1.71 ± 0.08	1.58 ± 0.13	1.86 ± 0.11	2.04 ± 0.09	1.97 ± 0.09	2.39 ± 0.10	2.50 ± 0.10	2.28 ± 0.46										

±: one standard deviation

Table 5-3 (continued): Clinopyroxene trace element composition in [$\mu\text{g/g}$]

Sample Comment position	235-19		235-19		235-19		235-19		235-19		235-19		235-19	
	2-cpx-1 core	2-cpx-2 rim	2-cpx-3 rim	4-cpx-01 core	4-cpx-02 rim	5-cpx-2 core	5-cpx-3 rim	6-cpx-1-1 core	235-19 core	235-19 rim	235-19 core	235-19 rim	235-19 core	235-19 rim
Na	2820 ± 56	2863 ± 69	2637 ± 102	3605 ± 151	3151 ± 154	4128 ± 304	3441 ± 134	4365 ± 388						
Sc	45.9 ± 0.5	63.2 ± 0.3	61.0 ± 0.5	49.0 ± 2.6	53.9 ± 0.6	54.9 ± 0.5	61.9 ± 1.3	54.1 ± 0.9						
Ti	1851 ± 10	2452 ± 11	2223 ± 24	1869 ± 36	2071 ± 25	2147 ± 23	2971 ± 22	2333 ± 82						
V	181 ± 3	229 ± 4	224 ± 3	203 ± 19	228 ± 4	228 ± 5	256 ± 4	234 ± 8						
Cr	5887 ± 34	6102 ± 38	6190 ± 60	5891 ± 31	6059 ± 34	6130 ± 48	6701 ± 25	6142 ± 101						
Sr	3.79 ± 0.08	3.10 ± 0.09	3.58 ± 0.08	3.73 ± 0.08	3.54 ± 0.08	5.86 ± 0.76	0.83 ± 0.07	1.66 ± 0.14						
Y	16.54 ± 0.31	21.39 ± 0.30	19.93 ± 0.29	15.84 ± 2.39	20.16 ± 0.55	20.81 ± 0.43	24.01 ± 0.51	19.91 ± 0.54						
Zr	6.90 ± 0.13	10.2 ± 0.0	7.90 ± 0.12	6.75 ± 1.05	8.08 ± 0.13	9.66 ± 0.20	13.7 ± 0.3	9.62 ± 0.29						
La	0.025 ± 0.004	0.016 ± 0.003	0.013 ± 0.003	0.021 ± 0.005	0.020 ± 0.004	0.025 ± 0.006	0.008 ± 0.003	0.017 ± 0.004						
Ce	0.38 ± 0.02	0.41 ± 0.03	0.36 ± 0.03	0.38 ± 0.04	0.43 ± 0.03	0.48 ± 0.04	0.48 ± 0.04	0.45 ± 0.04						
Nd	1.74 ± 0.12	2.37 ± 0.13	1.69 ± 0.10	1.56 ± 0.22	1.67 ± 0.16	2.35 ± 0.19	3.28 ± 0.22	2.19 ± 0.14						
Sm	1.21 ± 0.08	1.52 ± 0.09	1.39 ± 0.13	1.11 ± 0.38	1.26 ± 0.09	1.43 ± 0.13	2.24 ± 0.20	1.50 ± 0.16						
Eu	0.50 ± 0.03	0.49 ± 0.03	0.56 ± 0.04	0.52 ± 0.05	0.51 ± 0.03	0.54 ± 0.04	0.54 ± 0.06	0.60 ± 0.05						
Gd	2.31 ± 0.15	2.84 ± 0.20	2.40 ± 0.14	2.04 ± 0.50	2.18 ± 0.15	2.66 ± 0.20	3.42 ± 0.23	2.63 ± 0.13						
Dy	2.97 ± 0.29	3.76 ± 0.21	3.67 ± 0.19	3.00 ± 1.54	3.64 ± 0.25	3.95 ± 0.35	4.51 ± 0.38	3.85 ± 0.16						
Er	1.62 ± 0.09	2.20 ± 0.11	1.99 ± 0.10	1.98 ± 0.71	2.05 ± 0.11	2.04 ± 0.16	2.11 ± 0.19	2.20 ± 0.10						
Yb	1.53 ± 0.08	1.86 ± 0.08	1.73 ± 0.10	1.64 ± 1.20	1.97 ± 0.09	1.98 ± 0.14	2.03 ± 0.13	1.87 ± 0.08						

±: one standard deviation

Table 5-3 (continued): Clinopyroxene trace element composition in [$\mu\text{g/g}$]

Sample Comment position	235-19		235-19		235-19	
	6-cpx-2-1 interstitial	6-cpx-2-2 rim	6-cpx-2-3 core	6-cpx-2-4 rim	235-19 core	235-19 rim
Na	3508 ± 160	3845 ± 170	2721 ± 73	3533 ± 44		
Sc	59.6 ± 0.5	61.4 ± 0.6	49.7 ± 1.3	59.1 ± 1.1		
Ti	2482 ± 22	2850 ± 29	2129 ± 20	2816 ± 20		
V	245 ± 4	259 ± 5	219 ± 3	260 ± 4		
Cr	6161 ± 16	6870 ± 35	6018 ± 19	7178 ± 46		
Sr	1.15 ± 0.05	1.00 ± 0.08	1.04 ± 0.05	1.02 ± 0.08		
Y	20.09 ± 0.36	24.04 ± 0.65	18.72 ± 0.49	22.26 ± 0.45		
Zr	11.6 ± 0.2	13.9 ± 0.2	9.27 ± 0.19	13.0 ± 0.2		
La	0.012 ± 0.003	0.019 ± 0.005	0.019 ± 0.004	0.029 ± 0.009		
Ce	0.42 ± 0.03	0.54 ± 0.04	0.39 ± 0.03	0.56 ± 0.03		
Nd	2.21 ± 0.16	3.27 ± 0.17	2.35 ± 0.14	2.98 ± 0.21		
Sm	1.59 ± 0.12	1.94 ± 0.15	1.44 ± 0.10	2.00 ± 0.12		
Eu	0.49 ± 0.03	0.70 ± 0.04	0.56 ± 0.05	0.64 ± 0.04		
Gd	3.14 ± 0.17	3.33 ± 0.19	2.13 ± 0.14	3.59 ± 0.18		
Dy	4.05 ± 0.24	5.10 ± 0.27	3.40 ± 0.21	4.18 ± 0.26		
Er	1.94 ± 0.13	2.41 ± 0.13	1.86 ± 0.15	2.25 ± 0.13		
Yb	1.67 ± 0.09	1.94 ± 0.10	1.55 ± 0.15	1.76 ± 0.10		

±: one standard deviation

Table 5-3 (continued): Clinopyroxene trace element composition in [$\mu\text{g/g}$]

Sample Comment position	235-134 1-cpx-1 core		235-134 3-cpx-1-1 symplectite		235-134 3-cpx-1-2 rim		235-134 5-cpx-1 core		235-134 5-cpx-2 rim		235-134 5-cpx-3 rim		235-134 6-cpx-2 rim	
	Na	2761 ± 22	3487 ± 166	3825 ± 225	3336 ± 139	3009 ± 18	2928 ± 22	3123 ± 29	3765 ± 206	49.9 ± 0.3	46.7 ± 0.4	49.9 ± 0.3	3123 ± 29	3765 ± 206
Sc	51.6 ± 0.4	48.0 ± 0.9	57.8 ± 1.3	52.8 ± 0.6	45.0 ± 0.3	46.7 ± 0.4	49.9 ± 0.3	49.2 ± 0.7	1281 ± 9	1245 ± 11	1363 ± 9	1363 ± 9	1796 ± 12	1796 ± 12
Ti	175 ± 2	199 ± 2	242 ± 5	271 ± 5	172 ± 2	178 ± 3	186 ± 2	224 ± 4	175 ± 2	178 ± 3	186 ± 2	186 ± 2	224 ± 4	224 ± 4
V	6357 ± 20	6796 ± 32	7290 ± 52	7184 ± 47	6454 ± 24	6456 ± 36	6587 ± 37	7940 ± 41	6357 ± 20	6456 ± 36	6587 ± 37	6587 ± 37	7940 ± 41	7940 ± 41
Sr	14.42 ± 0.28	15.68 ± 0.29	19.75 ± 0.44	21.64 ± 0.28	11.36 ± 0.25	13.05 ± 0.26	13.90 ± 0.33	16.10 ± 0.52	14.42 ± 0.28	13.05 ± 0.26	13.90 ± 0.33	13.90 ± 0.33	16.10 ± 0.52	16.10 ± 0.52
Y	3.07 ± 0.09	3.57 ± 0.13	6.27 ± 0.13	6.78 ± 0.12	2.75 ± 0.09	2.95 ± 0.09	3.14 ± 0.09	5.37 ± 0.13	3.07 ± 0.09	2.95 ± 0.09	3.14 ± 0.09	3.14 ± 0.09	5.37 ± 0.13	5.37 ± 0.13
Zr	0.046 ± 0.007	0.041 ± 0.006	0.032 ± 0.005	0.035 ± 0.005	0.032 ± 0.005	0.041 ± 0.009	0.041 ± 0.006	0.038 ± 0.006	0.046 ± 0.007	0.041 ± 0.009	0.041 ± 0.006	0.041 ± 0.006	0.038 ± 0.006	0.038 ± 0.006
La	0.48 ± 0.03	0.55 ± 0.04	0.56 ± 0.03	0.61 ± 0.02	0.41 ± 0.03	0.37 ± 0.03	0.46 ± 0.04	0.51 ± 0.03	1.10 ± 0.10	0.99 ± 0.12	0.99 ± 0.15	0.99 ± 0.15	1.71 ± 0.14	1.71 ± 0.14
Ce	0.82 ± 0.08	0.90 ± 0.08	1.52 ± 0.26	1.68 ± 0.15	0.73 ± 0.07	0.78 ± 0.08	0.69 ± 0.07	1.45 ± 0.16	0.36 ± 0.03	0.30 ± 0.03	0.37 ± 0.03	0.37 ± 0.03	0.30 ± 0.03	0.30 ± 0.03
Nd	0.36 ± 0.03	0.29 ± 0.02	0.34 ± 0.10	0.41 ± 0.03	0.33 ± 0.03	0.30 ± 0.03	0.37 ± 0.03	0.30 ± 0.03	1.48 ± 0.12	1.28 ± 0.11	1.47 ± 0.12	1.47 ± 0.12	2.64 ± 0.25	2.64 ± 0.25
Sm	2.58 ± 0.19	2.56 ± 0.19	4.07 ± 0.76	4.06 ± 0.17	2.33 ± 0.49	2.22 ± 0.19	2.41 ± 0.27	3.30 ± 0.23	1.47 ± 0.10	1.20 ± 0.09	1.38 ± 0.10	1.38 ± 0.10	1.60 ± 0.12	1.60 ± 0.12
Gd	1.47 ± 0.10	1.70 ± 0.11	2.00 ± 0.40	2.21 ± 0.11	1.27 ± 0.26	1.20 ± 0.09	1.38 ± 0.10	1.60 ± 0.12	1.19 ± 0.08	1.14 ± 0.07	1.11 ± 0.07	1.11 ± 0.07	1.11 ± 0.08	1.11 ± 0.08
Dy	1.19 ± 0.08	1.31 ± 0.08	1.40 ± 0.09	1.89 ± 0.08	1.16 ± 0.24	1.14 ± 0.07	1.11 ± 0.07	1.11 ± 0.08						
Yb														

±: one standard deviation

Table 5-3 (continued): Clinopyroxene trace element composition in [$\mu\text{g/g}$]

Sample Comment position	235-134 7-cpx-2 core		235-134 7-cpx-3 rim		235-134 7-cpx-4 rim		235-134 11-cpx-1-1 rim		235-134 11-cpx-1-2 core		235-134 11-cpx-1-3 rim		235-134 11-cpx-2-1 core		235-134 11-cpx-3-1 core	
	Na	2302 ± 17	2003 ± 25	2160 ± 15	3472 ± 131	3645 ± 165	3873 ± 161	3689 ± 125	2535 ± 44	41.9 ± 0.3	59.4 ± 0.4	47.3 ± 0.3	49.4 ± 0.4	46.7 ± 0.6	45.2 ± 0.3	1760 ± 12
Sc	1128 ± 10	1175 ± 11	1091 ± 14	1922 ± 19	1703 ± 27	1832 ± 12	1910 ± 24	1760 ± 12	1128 ± 10	1175 ± 11	1091 ± 14	1832 ± 12	1910 ± 24	1760 ± 12	1760 ± 12	1760 ± 12
Ti	165 ± 3	197 ± 2	168 ± 2	229 ± 5	232 ± 6	224 ± 2	239 ± 3	272 ± 3	165 ± 3	197 ± 2	168 ± 2	224 ± 2	239 ± 3	272 ± 3	272 ± 3	272 ± 3
V	5860 ± 25	6240 ± 29	6036 ± 37	6741 ± 66	6603 ± 64	6620 ± 44	7044 ± 54	7326 ± 44	5860 ± 25	6240 ± 29	6036 ± 37	6620 ± 44	7044 ± 54	7326 ± 44	7326 ± 44	7326 ± 44
Sr	2.30 ± 0.07	2.30 ± 0.08	3.03 ± 0.12	0.80 ± 0.08	0.97 ± 0.04	0.83 ± 0.03	0.87 ± 0.05	1.00 ± 0.15	2.30 ± 0.07	2.30 ± 0.08	3.03 ± 0.12	0.83 ± 0.03	0.87 ± 0.05	1.00 ± 0.15	1.00 ± 0.15	1.00 ± 0.15
Y	10.13 ± 0.27	16.55 ± 0.36	11.40 ± 0.29	17.29 ± 0.28	15.82 ± 0.21	17.10 ± 0.29	18.21 ± 0.36	15.96 ± 0.13	10.13 ± 0.27	16.55 ± 0.36	11.40 ± 0.29	17.10 ± 0.29	18.21 ± 0.36	15.96 ± 0.13	15.96 ± 0.13	15.96 ± 0.13
Zr	2.40 ± 0.12	3.67 ± 0.15	2.53 ± 0.10	5.78 ± 0.13	5.07 ± 0.11	5.99 ± 0.12	6.33 ± 0.15	5.11 ± 0.14	2.40 ± 0.12	3.67 ± 0.15	2.53 ± 0.10	5.99 ± 0.12	6.33 ± 0.15	5.11 ± 0.14	5.11 ± 0.14	5.11 ± 0.14
La	0.038 ± 0.007	0.040 ± 0.007	0.047 ± 0.007	0.042 ± 0.009	0.030 ± 0.006	0.027 ± 0.004	0.033 ± 0.008	0.081 ± 0.013	0.038 ± 0.007	0.040 ± 0.007	0.047 ± 0.007	0.027 ± 0.004	0.033 ± 0.008	0.081 ± 0.013	0.081 ± 0.013	0.081 ± 0.013
Ce	0.31 ± 0.03	0.42 ± 0.03	0.41 ± 0.03	0.54 ± 0.02	0.52 ± 0.02	0.52 ± 0.02	0.56 ± 0.03	0.58 ± 0.05	0.31 ± 0.03	0.42 ± 0.03	0.41 ± 0.03	0.52 ± 0.02	0.56 ± 0.03	0.58 ± 0.05	0.58 ± 0.05	0.58 ± 0.05
Nd	0.73 ± 0.10	1.04 ± 0.16	0.74 ± 0.10	1.99 ± 0.12	1.69 ± 0.10	1.62 ± 0.11	1.67 ± 0.15	1.51 ± 0.10	0.73 ± 0.10	1.04 ± 0.16	0.74 ± 0.10	1.99 ± 0.12	1.67 ± 0.15	1.51 ± 0.10	1.51 ± 0.10	1.51 ± 0.10
Sm	0.56 ± 0.09	0.74 ± 0.10	0.59 ± 0.08	1.43 ± 0.11	1.23 ± 0.10	1.20 ± 0.10	1.35 ± 0.13	1.23 ± 0.09	0.56 ± 0.09	0.74 ± 0.10	0.59 ± 0.08	1.43 ± 0.11	1.35 ± 0.13	1.23 ± 0.09	1.23 ± 0.09	1.23 ± 0.09
Eu	0.25 ± 0.03	0.33 ± 0.03	0.31 ± 0.03	0.33 ± 0.03	0.35 ± 0.04	0.40 ± 0.03	0.31 ± 0.03	0.36 ± 0.03	0.25 ± 0.03	0.33 ± 0.03	0.31 ± 0.03	0.33 ± 0.03	0.31 ± 0.03	0.36 ± 0.03	0.36 ± 0.03	0.36 ± 0.03
Gd	1.01 ± 0.10	1.73 ± 0.15	1.11 ± 0.16	2.61 ± 0.13	2.41 ± 0.12	2.40 ± 0.13	2.54 ± 0.12	1.99 ± 0.15	1.01 ± 0.10	1.73 ± 0.15	1.11 ± 0.16	2.40 ± 0.13	2.54 ± 0.12	1.99 ± 0.15	1.99 ± 0.15	1.99 ± 0.15
Dy	1.81 ± 0.17	2.65 ± 0.22	1.88 ± 0.34	2.90 ± 0.17	3.49 ± 0.16	3.49 ± 0.17	3.33 ± 0.22	2.89 ± 0.12	1.81 ± 0.17	2.65 ± 0.22	1.88 ± 0.34	3.49 ± 0.16	3.33 ± 0.22	2.89 ± 0.12	2.89 ± 0.12	2.89 ± 0.12
Er	1.04 ± 0.13	1.54 ± 0.12	1.22 ± 0.11	1.69 ± 0.13	1.81 ± 0.09	1.88 ± 0.09	2.10 ± 0.10	n.d.	1.04 ± 0.13	1.54 ± 0.12	1.22 ± 0.11	1.88 ± 0.09	2.10 ± 0.10	n.d.	n.d.	n.d.
Yb	0.87 ± 0.21	1.61 ± 0.10	1.22 ± 0.11	1.32 ± 0.07	1.55 ± 0.07	1.59 ± 0.07	1.76 ± 0.08	n.d.	0.87 ± 0.21	1.61 ± 0.10	1.22 ± 0.11	1.59 ± 0.07	1.76 ± 0.08	n.d.	n.d.	n.d.

±: one standard deviation

Table 5-3 (continued): Clinopyroxene trace element composition in [$\mu\text{g/g}$]

Sample	235-20	235-17
n	6	4
Na	4239 \pm 284	3982 \pm 195
Sc	50 \pm 10	47 \pm 3
Ti	1087 \pm 149	1467 \pm 96
V	189 \pm 16	187 \pm 8
Cr	6177 \pm 498	5982 \pm 270
Sr	7.5 \pm 0.6	2.1 \pm 0.1
Y	9.98 \pm 0.66	13.19 \pm 0.71
Zr	3.05 \pm 0.30	2.52 \pm 0.13
La	0.19 \pm 0.01	0.08 \pm 0.01
Ce	0.69 \pm 0.04	0.26 \pm 0.03
Nd	0.74 \pm 0.05	0.89 \pm 0.03
Sm	0.46 \pm 0.04	0.79 \pm 0.06
Eu	0.20 \pm 0.02	0.37 \pm 0.05
Gd	0.93 \pm 0.11	1.56 \pm 0.17
Dy	1.7 \pm 0.2	2.4 \pm 0.2
Er	1.1 \pm 0.1	1.5 \pm 0.1
Yb	1.0 \pm 0.1	1.3 \pm 0.1

\pm : one standard deviation

n: number of analyses

Table 5-4: Orthopyroxene trace element composition in [$\mu\text{g/g}$]

Sample Comment Position	235-19		235-19		235-19		235-19		235-19	
	0-opx-1 core	6-opx-1 rim	6-opx-2 core	6-opx-2 rim	6-opx-3 core	6-opx-3 rim	6-opx-4 core	6-opx-4 rim	6-opx-5 core	6-opx-5 rim
Na	82 ± 2	b.d. ± NaN	b.d. ± NaN	289 ± 7	289 ± 7	373 ± 7	373 ± 7	308 ± 6	308 ± 6	308 ± 6
Sc	26.2 ± 0.3	31.1 ± 1.7	34.8 ± 2.1	28.7 ± 0.3	28.7 ± 0.3	34.6 ± 0.2	34.6 ± 0.2	29.7 ± 0.3	29.7 ± 0.3	29.7 ± 0.3
Ti	943 ± 7	1132 ± 67	918 ± 65	1010 ± 23	1010 ± 23	894 ± 17	894 ± 17	1011 ± 21	1011 ± 21	1011 ± 21
V	102 ± 2	137 ± 9	164 ± 12	145 ± 2	145 ± 2	165 ± 4	165 ± 4	128 ± 3	128 ± 3	128 ± 3
Cr	2589 ± 14	4371 ± 290	4709 ± 333	4716 ± 77	4716 ± 77	4689 ± 75	4689 ± 75	3910 ± 53	3910 ± 53	3910 ± 53
Sr	0.16 ± 0.02	b.d. ± NaN	b.d. ± NaN	0.16 ± 0.04	0.16 ± 0.04	0.11 ± 0.02	0.11 ± 0.02	0.090 ± 0.011	0.090 ± 0.011	0.090 ± 0.011
Y	1.41 ± 0.07	2.29 ± 0.12	3.24 ± 0.27	2.41 ± 0.14	2.41 ± 0.14	2.95 ± 0.08	2.95 ± 0.08	2.53 ± 0.09	2.53 ± 0.09	2.53 ± 0.09
Zr	0.71 ± 0.04	1.24 ± 0.80	2.41 ± 1.34	1.36 ± 0.05	1.36 ± 0.05	2.25 ± 0.07	2.25 ± 0.07	1.37 ± 0.05	1.37 ± 0.05	1.37 ± 0.05
Ce	b.d. ± NaN	b.d. ± NaN	0.009 ± 0.007	b.d. ± NaN	b.d. ± NaN	0.011 ± 0.005	0.011 ± 0.005	0.010 ± 0.003	0.010 ± 0.003	0.010 ± 0.003
Nd	b.d. ± NaN	0.022 ± 0.013	0.084 ± 0.038	0.032 ± 0.012	0.032 ± 0.012	0.057 ± 0.016	0.057 ± 0.016	0.059 ± 0.014	0.059 ± 0.014	0.059 ± 0.014
Sm	b.d. ± NaN	0.020 ± 0.007	0.084 ± 0.015	0.035 ± 0.017	0.035 ± 0.017	0.058 ± 0.016	0.058 ± 0.016	0.061 ± 0.020	0.061 ± 0.020	0.061 ± 0.020
Eu	b.d. ± NaN	b.d. ± NaN	b.d. ± NaN	0.010 ± 0.005	0.010 ± 0.005	0.020 ± 0.005	0.020 ± 0.005	0.016 ± 0.004	0.016 ± 0.004	0.016 ± 0.004
Gd	0.079 ± 0.023	0.15 ± 0.02	0.19 ± 0.02	0.13 ± 0.02	0.13 ± 0.02	0.15 ± 0.02	0.15 ± 0.02	0.17 ± 0.03	0.17 ± 0.03	0.17 ± 0.03
Dy	0.23 ± 0.05	0.34 ± 0.03	0.46 ± 0.08	0.34 ± 0.05	0.34 ± 0.05	0.46 ± 0.04	0.46 ± 0.04	0.35 ± 0.03	0.35 ± 0.03	0.35 ± 0.03
Er	0.22 ± 0.03	0.29 ± 0.03	0.49 ± 0.06	0.35 ± 0.03	0.35 ± 0.03	0.46 ± 0.06	0.46 ± 0.06	0.32 ± 0.04	0.32 ± 0.04	0.32 ± 0.04
Yb	0.23 ± 0.03	0.50 ± 0.06	0.57 ± 0.06	0.43 ± 0.07	0.43 ± 0.07	0.58 ± 0.05	0.58 ± 0.05	0.46 ± 0.04	0.46 ± 0.04	0.46 ± 0.04

±: one standard deviation

Table 5-4 (continued): Orthopyroxene trace element composition in [$\mu\text{g/g}$]

Sample Comment Position	235-134		235-134		235-134		235-134		235-20	
	3-opx-1-3 core	7-opx-1 rim	7-opx-2 core	12-opx-1-1 rim	12-opx-1-2 core	12-opx-1-2 rim	1-opx-1 core	1-opx-1 rim	1-opx-2 core	1-opx-2 rim
Na	127 ± 4	424 ± 90	668 ± 73	239 ± 10	351 ± 13	351 ± 13	520 ± 9	520 ± 9	273 ± 2	273 ± 2
Sc	30.0 ± 0.2	25.6 ± 0.4	25.1 ± 0.3	30.8 ± 0.4	27.8 ± 0.3	27.8 ± 0.3	29.5 ± 0.2	29.5 ± 0.2	30.2 ± 0.2	30.2 ± 0.2
Ti	1031 ± 13	480 ± 9	429 ± 5	762 ± 14	543 ± 8	543 ± 8	415 ± 4	415 ± 4	384 ± 4	384 ± 4
V	175 ± 2	b.d. ± NaN	112 ± 2	164 ± 2	148 ± 2	148 ± 2	121 ± 2	121 ± 2	122 ± 1	122 ± 1
Cr	4970 ± 47	3448 ± 13	3658 ± 39	5017 ± 50	4518 ± 36	4518 ± 36	4757 ± 31	4757 ± 31	3073 ± 15	3073 ± 15
Sr	0.11 ± 0.02	0.35 ± 0.06	0.59 ± 0.11	0.12 ± 0.01	0.15 ± 0.01	0.15 ± 0.01	0.18 ± 0.01	0.18 ± 0.01	b.d. ± NaN	b.d. ± NaN
Y	2.96 ± 0.08	1.98 ± 0.08	1.46 ± 0.07	2.67 ± 0.11	1.95 ± 0.07	1.95 ± 0.07	1.28 ± 0.05	1.28 ± 0.05	b.d. ± NaN	b.d. ± NaN
Zr	1.09 ± 0.04	0.67 ± 0.05	0.43 ± 0.04	1.07 ± 0.05	0.63 ± 0.04	0.63 ± 0.04	0.50 ± 0.03	0.50 ± 0.03	b.d. ± NaN	b.d. ± NaN
Ce	0.003 ± 0.001	0.008 ± 0.005	0.005 ± 0.003	0.010 ± 0.003	0.004 ± 0.002	0.004 ± 0.002	0.015 ± 0.005	0.015 ± 0.005	0.006 ± 0.003	0.006 ± 0.003
Nd	0.024 ± 0.010	b.d. ± NaN	0.024 ± 0.013	0.037 ± 0.014	b.d. ± NaN	b.d. ± NaN	b.d. ± NaN	b.d. ± NaN	0.011 ± 0.006	0.011 ± 0.006
Sm	0.043 ± 0.014	0.038 ± 0.016	b.d. ± NaN	0.059 ± 0.022	b.d. ± NaN	b.d. ± NaN	0.013 ± 0.006	0.013 ± 0.006	b.d. ± NaN	b.d. ± NaN
Eu	0.015 ± 0.004	0.010 ± 0.004	0.010 ± 0.004	0.015 ± 0.005	0.012 ± 0.005	0.012 ± 0.005	0.015 ± 0.004	0.015 ± 0.004	0.006 ± 0.003	0.006 ± 0.003
Gd	0.077 ± 0.018	0.083 ± 0.022	0.038 ± 0.015	0.16 ± 0.03	0.10 ± 0.02	0.10 ± 0.02	0.054 ± 0.013	0.054 ± 0.013	0.025 ± 0.008	0.025 ± 0.008
Dy	0.36 ± 0.05	0.26 ± 0.04	0.19 ± 0.03	0.49 ± 0.07	0.22 ± 0.04	0.22 ± 0.04	0.17 ± 0.02	0.17 ± 0.02	0.08 ± 0.01	0.08 ± 0.01
Er	0.46 ± 0.04	0.20 ± 0.03	0.19 ± 0.03	0.36 ± 0.05	0.32 ± 0.04	0.32 ± 0.04	0.19 ± 0.02	0.19 ± 0.02	0.13 ± 0.02	0.13 ± 0.02
Yb	0.52 ± 0.06	0.30 ± 0.04	0.32 ± 0.04	0.52 ± 0.05	0.34 ± 0.03	0.34 ± 0.03	0.20 ± 0.02	0.20 ± 0.02	0.22 ± 0.02	0.22 ± 0.02

±: one standard deviation

Table 5-5: Plagioclase major element composition in [wt%]

Sample Comment n	235-19			235-19			235-19			235-19			235-19		
	0-plag-1-1	0-plag-1-2	0-plag-1-3	1-plag-1-4	1-plag-1-5	1-plag-1-6	1-plag-1-7	1-plag-1-8	1-plag-1-9	1-plag-1-10	1-plag-1-11	1-plag-1-12	1-plag-1-13	1-plag-1-14	1-plag-1-15
SiO ₂	45.5 ± 0.1	45.6 ± 0.2	44.9 ± 0.5	45.5 ± 0.1	46.0 ± 0.1	47.2	46.6 ± 0.2	47.0 ± 0.2	46.3 ± 0.2	46.9 ± 0.1	46.4 ± 0.1	46.8 ± 0.3	46.8 ± 0.3	46.6 ± 0.2	46.8 ± 0.3
TiO ₂	0.01 ± 0.02	0.00 ± 0.01	0.01 ± 0.02	0.01 ± 0.02	0.01 ± 0.01	0.00	0.02 ± 0.03	0.04 ± 0.02	0.02 ± 0.01	0.01 ± 0.01	0.02 ± 0.03	0.03 ± 0.01	0.03 ± 0.01	0.03 ± 0.01	0.04 ± 0.02
Cr ₂ O ₃	0.06 ± 0.02	0.01 ± 0.01	0.05 ± 0.05	0.06 ± 0.02	0.02 ± 0.03	0.00	0.02 ± 0.02	0.02 ± 0.02	0.02 ± 0.02	0.02 ± 0.03	0.00	0.03 ± 0.02	0.03 ± 0.02	0.02 ± 0.02	0.02 ± 0.00
Al ₂ O ₃	33.5 ± 0.2	32.6 ± 0.3	33.0 ± 0.3	33.5 ± 0.2	32.7 ± 0.1	33.0	32.7 ± 0.1	32.3 ± 0.2	32.9 ± 0.1	32.7 ± 0.1	32.7 ± 0.1	32.9 ± 0.1	32.9 ± 0.1	32.4 ± 0.2	32.3 ± 0.2
FeO	0.16 ± 0.02	0.06 ± 0.03	0.11 ± 0.01	0.16 ± 0.02	0.12 ± 0.02	0.07	0.12 ± 0.02	0.05 ± 0.03	0.08 ± 0.04	0.08 ± 0.04	0.07	0.11 ± 0.03	0.11 ± 0.03	0.08 ± 0.04	0.05 ± 0.03
MgO	0.02 ± 0.01	0.02 ± 0.01	0.02 ± 0.02	0.02 ± 0.02	0.02 ± 0.01	0.06	0.02 ± 0.01	0.01 ± 0.01	0.01 ± 0.01	0.02 ± 0.01	0.06	0.02 ± 0.01	0.02 ± 0.01	0.01 ± 0.01	0.01 ± 0.01
MnO	0.00 ± 0.00	0.01 ± 0.01	0.02 ± 0.02	0.00 ± 0.00	0.00 ± 0.01	0.00	0.00 ± 0.01	0.03 ± 0.02	0.01 ± 0.01	0.00	0.00	0.01 ± 0.01	0.02 ± 0.02	0.01 ± 0.01	0.01 ± 0.01
CaO	17.3 ± 0.3	16.8 ± 0.2	17.4 ± 0.3	17.3 ± 0.3	16.6 ± 0.1	16.9	16.6 ± 0.1	16.3 ± 0.1	16.3 ± 0.2	16.9	16.6 ± 0.1	16.9 ± 0.2	16.9 ± 0.2	16.3 ± 0.2	16.3 ± 0.1
NiO	0.02 ± 0.03	0.01 ± 0.01	0.01 ± 0.01	0.02 ± 0.03	0.01 ± 0.01	0.00	0.01 ± 0.01	0.02 ± 0.03	0.03 ± 0.04	0.02 ± 0.03	0.00	0.03 ± 0.04	0.02 ± 0.03	0.03 ± 0.04	0.02 ± 0.03
Na ₂ O	1.49 ± 0.09	1.84 ± 0.04	1.48 ± 0.13	1.49 ± 0.09	1.83 ± 0.02	2.02	1.83 ± 0.02	2.18 ± 0.02	2.11 ± 0.07	2.02	2.02	2.11 ± 0.07	2.18 ± 0.02	2.11 ± 0.07	2.18 ± 0.02
K ₂ O	0.02 ± 0.01	0.01 ± 0.01	0.03 ± 0.01	0.02 ± 0.01	0.01 ± 0.01	0.02	0.01 ± 0.01	0.01 ± 0.01	0.01 ± 0.01	0.02	0.02	0.01 ± 0.01	0.01 ± 0.01	0.01 ± 0.01	0.01 ± 0.01
Total	98.1 ± 0.3	97.0 ± 0.9	97.0 ± 0.1	98.1 ± 0.3	97.3 ± 0.0	99.4	97.3 ± 0.0	98.0 ± 0.5	97.7 ± 0.3	99.4	99.4	97.7 ± 0.3	98.0 ± 0.5	97.7 ± 0.3	98.0 ± 0.5
An	0.865 ± 0.008	0.835 ± 0.002	0.867 ± 0.012	0.865 ± 0.008	0.834 ± 0.002	0.822	0.834 ± 0.002	0.806 ± 0.001	0.811 ± 0.007	0.822	0.822	0.811 ± 0.007	0.806 ± 0.001	0.811 ± 0.007	0.806 ± 0.001

±: one standard deviation

n: number of analyses

An: (molar Ca/(Ca+Na))

Table 5-5 (continued): Plagioclase major element composition in [wt%]

Sample Comment n	235-19			235-19			235-19			235-19			235-19		
	1-plag-1-9	1-plag-1-10	3-plag-1-1	4-plag-1-1	5-plag-1-1	5-plag-1-2	5-plag-1-3	5-plag-1-4	5-plag-1-5	5-plag-1-6	5-plag-1-7	5-plag-1-8	5-plag-1-9	5-plag-1-10	5-plag-1-11
SiO ₂	46.3 ± 0.2	46.9 ± 0.1	47.4	47.2	46.6 ± 0.1	46.4 ± 0.1	46.4 ± 0.1	46.3 ± 0.2	46.6 ± 0.1	46.4 ± 0.1	46.4 ± 0.1	46.8 ± 0.3	46.8 ± 0.3	46.6 ± 0.1	46.8 ± 0.3
TiO ₂	0.02 ± 0.01	0.04 ± 0.02	0.00	0.02	0.02 ± 0.02	0.02 ± 0.03	0.02 ± 0.03	0.02 ± 0.03	0.02 ± 0.02	0.02 ± 0.03	0.02 ± 0.03	0.03 ± 0.01	0.03 ± 0.01	0.03 ± 0.01	0.04 ± 0.02
Cr ₂ O ₃	0.07 ± 0.02	0.03 ± 0.02	0.03	0.00	0.02 ± 0.00	0.01 ± 0.01	0.01 ± 0.01	0.01 ± 0.01	0.02 ± 0.00	0.01 ± 0.01	0.01 ± 0.01	0.03 ± 0.02	0.03 ± 0.02	0.02 ± 0.02	0.02 ± 0.00
Al ₂ O ₃	32.6 ± 0.1	32.5 ± 0.0	33.0	32.5	32.9 ± 0.1	32.7 ± 0.1	32.7 ± 0.1	32.9 ± 0.1	32.7 ± 0.1	32.7 ± 0.1	32.7 ± 0.1	32.9 ± 0.1	32.9 ± 0.1	32.4 ± 0.2	32.3 ± 0.2
FeO	0.12 ± 0.04	0.09 ± 0.01	0.16	0.10	0.06 ± 0.04	0.14 ± 0.09	0.14 ± 0.09	0.11 ± 0.03	0.08 ± 0.04	0.08 ± 0.04	0.07	0.11 ± 0.03	0.11 ± 0.03	0.08 ± 0.04	0.05 ± 0.03
MgO	0.01 ± 0.01	0.00 ± 0.00	0.05	0.02	0.02 ± 0.02	0.01 ± 0.01	0.01 ± 0.01	0.02 ± 0.02	0.01 ± 0.01	0.02 ± 0.02	0.01 ± 0.01	0.02 ± 0.02	0.02 ± 0.02	0.01 ± 0.01	0.01 ± 0.01
MnO	0.00 ± 0.01	0.00 ± 0.00	0.02	0.02	0.00 ± 0.02	0.00 ± 0.00	0.00 ± 0.00	0.01 ± 0.01	0.00 ± 0.00	0.00 ± 0.00	0.00 ± 0.00	0.01 ± 0.01	0.02 ± 0.02	0.01 ± 0.01	0.01 ± 0.01
CaO	16.2 ± 0.4	16.4 ± 0.1	16.3	16.3	16.7 ± 0.1	16.6 ± 0.1	16.6 ± 0.1	16.9 ± 0.2	16.6 ± 0.1	16.6 ± 0.1	16.6 ± 0.1	16.9 ± 0.2	16.9 ± 0.2	16.3 ± 0.2	16.3 ± 0.1
NiO	0.01 ± 0.02	0.01 ± 0.01	0.02	0.00	0.01 ± 0.00	0.02 ± 0.04	0.02 ± 0.04	0.03 ± 0.04	0.02 ± 0.03	0.02 ± 0.03	0.02 ± 0.03	0.03 ± 0.04	0.02 ± 0.03	0.03 ± 0.04	0.02 ± 0.03
Na ₂ O	2.18 ± 0.22	2.11 ± 0.04	2.25	2.13	1.97 ± 0.03	2.06 ± 0.02	2.06 ± 0.02	1.97 ± 0.14	1.97 ± 0.03	2.06 ± 0.02	2.06 ± 0.02	1.97 ± 0.14	1.97 ± 0.14	2.11 ± 0.07	2.18 ± 0.02
K ₂ O	0.01 ± 0.01	0.00 ± 0.00	0.01	0.01	0.00 ± 0.01	0.01 ± 0.01	0.01 ± 0.01	0.01 ± 0.01	0.00 ± 0.01	0.01 ± 0.01	0.01 ± 0.01	0.01 ± 0.01	0.01 ± 0.01	0.01 ± 0.01	0.01 ± 0.01
Total	97.5 ± 0.2	98.1 ± 0.2	99.2	98.3	98.3 ± 0.4	97.9 ± 0.1	97.9 ± 0.1	98.8 ± 0.3	98.3 ± 0.4	97.9 ± 0.1	97.9 ± 0.1	98.8 ± 0.3	98.8 ± 0.3	97.7 ± 0.3	98.0 ± 0.5
An	0.804 ± 0.019	0.812 ± 0.003	0.800	0.809	0.824 ± 0.003	0.816 ± 0.003	0.816 ± 0.003	0.826 ± 0.012	0.824 ± 0.003	0.816 ± 0.003	0.816 ± 0.003	0.826 ± 0.012	0.826 ± 0.012	0.811 ± 0.007	0.806 ± 0.001

±: one standard deviation

n: number of analyses

An: (molar Ca/(Ca+Na))

Table 5-5: Plagioclase major element composition in [wt%]

Sample Comment n	235-134			235-134			235-134			235-134		
	1-plag-1-1	1-plag-1-2	3-plag-1-1	3-plag-1-2	3-plag-1-1	3-plag-1-2	3-plag-2-1	3-plag-2-2	4-plag-1-1	4-plag-1-1	4-plag-2-1	235-134
SiO ₂	46.9 ± 0.5	47.1 ± 0.1	46.7 ± 0.1	46.7 ± 0.4	46.5 ± 0.3	46.5 ± 0.3	46.5 ± 0.3	47.8	47.1 ± 0.3	47.1 ± 0.3	47.6 ± 0.1	47.6 ± 0.1
TiO ₂	0.03 ± 0.03	0.00 ± 0.01	0.04 ± 0.02	0.03 ± 0.05	0.00 ± 0.01	0.00 ± 0.01	0.00 ± 0.01	0.00	0.00 ± 0.01	0.00 ± 0.01	0.02 ± 0.02	0.02 ± 0.02
Cr ₂ O ₃	0.04 ± 0.03	0.06 ± 0.07	0.12 ± 0.06	0.03 ± 0.05	0.02 ± 0.03	0.02 ± 0.03	0.02 ± 0.03	0.11	0.00 ± 0.01	0.00 ± 0.01	0.02 ± 0.02	0.02 ± 0.02
Al ₂ O ₃	32.8 ± 0.4	32.4 ± 0.1	32.5 ± 0.1	32.5 ± 0.1	32.7 ± 0.2	32.7 ± 0.2	32.7 ± 0.2	32.8	32.3 ± 0.2	32.3 ± 0.2	32.4 ± 0.2	32.4 ± 0.2
FeO	0.06 ± 0.03	0.10 ± 0.02	0.17 ± 0.08	0.15 ± 0.09	0.05 ± 0.05	0.05 ± 0.05	0.05 ± 0.05	0.12	0.08 ± 0.03	0.08 ± 0.03	0.07 ± 0.04	0.07 ± 0.04
MgO	0.02 ± 0.02	0.02 ± 0.00	0.01 ± 0.01	0.02 ± 0.01	0.02 ± 0.01	0.02 ± 0.01	0.02 ± 0.01	0.03	0.03 ± 0.01	0.03 ± 0.01	0.02 ± 0.01	0.02 ± 0.01
MnO	0.01 ± 0.01	0.04 ± 0.02	0.02 ± 0.01	0.01 ± 0.01	0.02 ± 0.03	0.02 ± 0.03	0.02 ± 0.03	0.00	0.01 ± 0.01	0.01 ± 0.01	0.01 ± 0.01	0.01 ± 0.01
CaO	16.6 ± 0.4	16.3 ± 0.3	16.3 ± 0.1	16.5 ± 0.2	16.6 ± 0.2	16.6 ± 0.2	16.6 ± 0.2	16.4	16.2 ± 0.3	16.2 ± 0.3	16.1 ± 0.2	16.1 ± 0.2
NiO	0.04 ± 0.03	0.02 ± 0.03	0.01 ± 0.02	0.02 ± 0.02	0.00 ± 0.00	0.00 ± 0.00	0.00 ± 0.00	0.11	0.02 ± 0.02	0.02 ± 0.02	0.00 ± 0.00	0.00 ± 0.00
Na ₂ O	2.02 ± 0.15	2.30 ± 0.08	2.19 ± 0.07	2.20 ± 0.07	2.05 ± 0.13	2.05 ± 0.13	2.05 ± 0.13	2.26	2.31 ± 0.13	2.31 ± 0.13	2.37 ± 0.04	2.37 ± 0.04
K ₂ O	0.01 ± 0.01	0.01 ± 0.00	0.01 ± 0.02	0.00 ± 0.00	0.01 ± 0.01	0.01 ± 0.01	0.01 ± 0.01	0.01	0.01 ± 0.01	0.01 ± 0.01	0.01 ± 0.01	0.01 ± 0.01
Total	98.5 ± 0.2	98.3 ± 0.4	98.0 ± 0.0	98.1 ± 0.3	98.0 ± 0.3	98.0 ± 0.3	98.0 ± 0.3	99.6	98.1 ± 0.0	98.1 ± 0.0	98.6 ± 0.4	98.6 ± 0.4
An	0.819 ± 0.015	0.796 ± 0.008	0.804 ± 0.006	0.805 ± 0.007	0.818 ± 0.011	0.818 ± 0.011	0.818 ± 0.011	0.800	0.795 ± 0.011	0.795 ± 0.011	0.790 ± 0.002	0.790 ± 0.002

±: one standard deviation

n: number of analyses

An: (molar Ca/(Ca+Na))

Table 5-5 (continued): Plagioclase major element composition in [wt%]

Sample Comment n	235-134			235-134			235-134			235-134		
	6-plag-1-1	7-plag-1-1	7-plag-1-2	7-plag-1-4	7-plag-1-5	10-plag-1-1	7-plag-1-4	7-plag-1-5	10-plag-1-1	7-plag-1-4	7-plag-1-5	10-plag-1-1
SiO ₂	47.3 ± 0.0	47.1 ± 0.6	46.0 ± 0.4	46.0 ± 0.4	46.0 ± 0.6	46.8 ± 0.5	46.0 ± 0.4	46.0 ± 0.6	46.8 ± 0.5	46.0 ± 0.4	46.0 ± 0.6	46.8 ± 0.5
TiO ₂	0.00 ± 0.00	0.01 ± 0.01	0.00 ± 0.00	0.00 ± 0.01	0.00 ± 0.01	0.02 ± 0.03	0.00 ± 0.01	0.00 ± 0.01	0.02 ± 0.03	0.00 ± 0.01	0.00 ± 0.01	0.02 ± 0.03
Cr ₂ O ₃	0.04 ± 0.01	0.03 ± 0.00	0.03 ± 0.04	0.03 ± 0.03	0.02 ± 0.04	0.02 ± 0.02	0.03 ± 0.03	0.02 ± 0.04	0.02 ± 0.02	0.02 ± 0.04	0.02 ± 0.04	0.02 ± 0.02
Al ₂ O ₃	32.5 ± 0.1	32.3 ± 0.6	33.6 ± 0.3	33.1 ± 0.2	33.3 ± 0.3	32.6 ± 0.1	33.1 ± 0.2	33.3 ± 0.3	32.6 ± 0.1	33.3 ± 0.3	32.6 ± 0.1	32.6 ± 0.1
FeO	0.11 ± 0.01	0.04 ± 0.02	0.13 ± 0.07	0.09 ± 0.01	0.08 ± 0.03	0.05 ± 0.04	0.09 ± 0.01	0.08 ± 0.03	0.05 ± 0.04	0.08 ± 0.03	0.05 ± 0.04	0.05 ± 0.04
MgO	0.01 ± 0.00	0.01 ± 0.00	0.02 ± 0.01	0.01 ± 0.01	0.02 ± 0.01	0.01 ± 0.01	0.01 ± 0.01	0.02 ± 0.01	0.01 ± 0.01	0.02 ± 0.01	0.01 ± 0.01	0.01 ± 0.01
MnO	0.01 ± 0.01	0.03 ± 0.01	0.05 ± 0.05	0.02 ± 0.03	0.01 ± 0.01	0.01 ± 0.01	0.02 ± 0.03	0.01 ± 0.01	0.01 ± 0.01	0.01 ± 0.01	0.01 ± 0.01	0.01 ± 0.01
CaO	16.35 ± 0.04	16.3 ± 0.4	17.5 ± 0.5	17.2 ± 0.4	17.3 ± 0.4	16.3 ± 0.2	17.2 ± 0.4	17.3 ± 0.4	16.3 ± 0.2	17.3 ± 0.4	16.3 ± 0.2	16.3 ± 0.2
NiO	0.03 ± 0.03	0.02 ± 0.01	0.00 ± 0.01	0.02 ± 0.02	0.01 ± 0.01	0.00 ± 0.00	0.02 ± 0.02	0.01 ± 0.01	0.00 ± 0.00	0.01 ± 0.01	0.00 ± 0.00	0.00 ± 0.00
Na ₂ O	2.31 ± 0.02	2.35 ± 0.45	1.58 ± 0.22	1.71 ± 0.18	1.61 ± 0.19	2.18 ± 0.16	1.71 ± 0.18	1.61 ± 0.19	2.18 ± 0.16	1.61 ± 0.19	2.18 ± 0.16	2.18 ± 0.16
K ₂ O	0.01 ± 0.01	0.01 ± 0.00	0.01 ± 0.01	0.02 ± 0.01	0.00 ± 0.00	0.01 ± 0.01	0.02 ± 0.01	0.00 ± 0.00	0.01 ± 0.01	0.00 ± 0.00	0.01 ± 0.01	0.01 ± 0.01
Total	98.7 ± 0.2	98.2 ± 0.0	98.8 ± 0.3	98.2 ± 0.1	98.4 ± 0.1	98.0 ± 0.4	98.2 ± 0.1	98.4 ± 0.1	98.0 ± 0.4	98.1 ± 0.0	98.6 ± 0.4	98.6 ± 0.4
An	0.797 ± 0.002	0.794 ± 0.035	0.859 ± 0.020	0.847 ± 0.016	0.856 ± 0.017	0.805 ± 0.013	0.847 ± 0.016	0.856 ± 0.017	0.805 ± 0.013	0.856 ± 0.017	0.805 ± 0.013	0.805 ± 0.013

±: one standard deviation

n: number of analyses

An: (molar Ca/(Ca+Na))

Table 5-6: Plagioclase trace element composition in [µg/g]

Sample	235-19		235-19		235-19		235-19		235-19		235-19		235-19	
	0-plag-1-1	0-plag-1-2	0-plag-1-3	1-plag-1-1	1-plag-1-2	1-plag-1-3	1-plag-1-4	1-plag-1-5	1-plag-1-6	1-plag-1-7	1-plag-1-8	1-plag-1-9	1-plag-1-10	1-plag-1-11
Na	9831 ± 230	9752 ± 3542	11259 ± 425	13402 ± 631	12726 ± 705	11554 ± 665	10968 ± 2943	9657 ± 381						
Sc	7.1 ± 0.2	7.3 ± 0.4	7.2 ± 0.4	7.9 ± 0.4	7.3 ± 0.3	6.4 ± 0.4	7.5 ± 0.5	7.0 ± 0.3						
Sr	12.03 ± 0.56	3.22 ± 0.86	6.66 ± 0.41	4.32 ± 0.24	4.42 ± 0.25	3.63 ± 0.11	5.10 ± 0.33	5.03 ± 0.20						
Y	0.141 ± 0.006	0.219 ± 0.032	0.151 ± 0.013	0.198 ± 0.011	0.196 ± 0.010	0.168 ± 0.008	0.185 ± 0.013	0.180 ± 0.013						
La	0.008 ± 0.001	0.010 ± 0.006	0.018 ± 0.005	0.019 ± 0.006	0.010 ± 0.004	0.014 ± 0.002	0.019 ± 0.009	0.015 ± 0.006						
Ce	0.178 ± 0.013	0.166 ± 0.066	0.184 ± 0.028	0.176 ± 0.022	0.194 ± 0.019	0.151 ± 0.015	0.168 ± 0.033	0.246 ± 0.029						
Pr	0.040 ± 0.004	0.049 ± 0.009	0.063 ± 0.009	0.036 ± 0.006	0.040 ± 0.005	0.041 ± 0.004	0.049 ± 0.009	0.059 ± 0.007						
Nd	0.352 ± 0.043	0.307 ± 0.041	0.368 ± 0.064	0.352 ± 0.044	0.404 ± 0.062	0.297 ± 0.027	0.240 ± 0.038	0.367 ± 0.065						
Sm	0.158 ± 0.031	0.075 ± 0.026	0.115 ± 0.030	0.106 ± 0.025	0.096 ± 0.018	0.080 ± 0.020	0.103 ± 0.034	0.128 ± 0.027						
Eu	0.304 ± 0.016	0.288 ± 0.059	0.324 ± 0.027	0.217 ± 0.030	0.289 ± 0.021	0.208 ± 0.017	0.241 ± 0.048	0.287 ± 0.042						
Gd	0.139 ± 0.024	0.058 ± 0.015	0.088 ± 0.022	0.097 ± 0.015	0.100 ± 0.016	0.077 ± 0.014	0.133 ± 0.027	0.060 ± 0.018						
Dy	0.068 ± 0.020	0.043 ± 0.013	0.027 ± 0.014	0.029 ± 0.011	0.055 ± 0.011	0.024 ± 0.010	0.045 ± 0.014	0.030 ± 0.015						

±: one standard deviation

nd: not determined

Table 5-6 (continued): Plagioclase trace element composition in [µg/g]

Sample	235-19		235-19		235-19		235-19		235-19		235-19		235-19	
	1-plag-1-6	1-plag-1-7	1-plag-1-8	1-plag-1-9	1-plag-1-10	3-plag-1-1	3-plag-1-2	3-plag-1-3	3-plag-1-4	3-plag-1-5	3-plag-1-6	3-plag-1-7	3-plag-1-8	3-plag-1-9
Na	11590 ± 671	11228 ± 584	11469 ± 4474	12400 ± 580	14908 ± 676	16463 ± 418	7518 ± 191	11406 ± 533						
Sc	6.8 ± 0.4	6.8 ± 0.4	6.8 ± 0.4	7.2 ± 0.4	7.3 ± 0.4	7.5 ± 0.1	8.6 ± 0.1	7.7 ± 0.4						
Sr	4.59 ± 0.33	4.63 ± 0.19	4.32 ± 1.04	4.90 ± 0.21	4.73 ± 0.21	3.81 ± 0.16	2.99 ± 0.13	6.38 ± 0.27						
Y	0.183 ± 0.013	0.189 ± 0.013	0.179 ± 0.039	0.168 ± 0.014	0.185 ± 0.013	0.188 ± 0.013	0.176 ± 0.012	0.160 ± 0.013						
La	0.012 ± 0.005	0.016 ± 0.004	0.011 ± 0.007	0.015 ± 0.006	0.019 ± 0.007	0.007 ± 0.001	0.026 ± 0.004	0.011 ± 0.005						
Ce	0.149 ± 0.023	0.162 ± 0.030	0.168 ± 0.074	0.194 ± 0.030	0.118 ± 0.023	0.106 ± 0.014	0.238 ± 0.032	0.144 ± 0.022						
Pr	0.053 ± 0.011	0.048 ± 0.007	0.058 ± 0.013	0.034 ± 0.006	0.034 ± 0.006	0.033 ± 0.005	0.033 ± 0.005	nd						
Nd	0.359 ± 0.057	0.398 ± 0.054	0.377 ± 0.054	0.407 ± 0.050	0.345 ± 0.073	0.313 ± 0.033	0.331 ± 0.034	0.303 ± 0.037						
Sm	0.066 ± 0.019	0.086 ± 0.024	0.108 ± 0.020	0.107 ± 0.038	0.087 ± 0.025	0.097 ± 0.026	0.057 ± 0.015	0.059 ± 0.021						
Eu	0.257 ± 0.045	0.277 ± 0.039	0.309 ± 0.064	0.218 ± 0.021	0.251 ± 0.028	0.257 ± 0.021	0.172 ± 0.014	0.273 ± 0.026						
Gd	0.069 ± 0.015	0.086 ± 0.024	0.062 ± 0.022	0.073 ± 0.021	0.066 ± 0.018	0.066 ± 0.012	0.096 ± 0.017	0.152 ± 0.045						
Dy	0.076 ± 0.019	0.046 ± 0.016	0.034 ± 0.010	0.052 ± 0.015	0.034 ± 0.013	0.026 ± 0.007	0.041 ± 0.011	0.035 ± 0.010						

±: one standard deviation

nd: not determined

Table 5-6 (continued): Plagioclase trace element composition in [$\mu\text{g/g}$]

Sample	235-19		235-19		235-19	
	5-plag-1-1	5-plag-1-2	5-plag-1-2	5-plag-2-1	5-plag-2-1	5-plag-2-1
Na	11764 ± 441	11826 ± 169	11826 ± 169	15406 ± 4544	15406 ± 4544	15406 ± 4544
Sc	7.5 ± 0.3	7.4 ± 0.3	7.4 ± 0.3	7.4 ± 0.5	7.4 ± 0.5	7.4 ± 0.5
Sr	6.18 ± 0.14	7.59 ± 0.62	7.59 ± 0.62	4.87 ± 0.57	4.87 ± 0.57	4.87 ± 0.57
Y	0.14 ± 0.03	0.20 ± 0.05	0.20 ± 0.05	0.17 ± 0.02	0.17 ± 0.02	0.17 ± 0.02
La	0.020 ± 0.005	0.016 ± 0.004	0.016 ± 0.004	0.020 ± 0.011	0.020 ± 0.011	0.020 ± 0.011
Ce	0.16 ± 0.02	0.14 ± 0.02	0.14 ± 0.02	0.16 ± 0.04	0.16 ± 0.04	0.16 ± 0.04
Pr	nd	nd	nd	0.047 ± 0.005	0.047 ± 0.005	0.047 ± 0.005
Nd	0.27 ± 0.06	0.27 ± 0.06	0.27 ± 0.06	0.34 ± 0.03	0.34 ± 0.03	0.34 ± 0.03
Sm	0.034 ± 0.018	0.071 ± 0.026	0.071 ± 0.026	0.077 ± 0.021	0.077 ± 0.021	0.077 ± 0.021
Eu	0.24 ± 0.03	0.28 ± 0.03	0.28 ± 0.03	0.26 ± 0.04	0.26 ± 0.04	0.26 ± 0.04
Gd	0.059 ± 0.036	0.071 ± 0.039	0.071 ± 0.039	0.061 ± 0.012	0.061 ± 0.012	0.061 ± 0.012
DY	0.032 ± 0.023	0.030 ± 0.022	0.030 ± 0.022	0.047 ± 0.011	0.047 ± 0.011	0.047 ± 0.011

±: one standard deviation

nd: not determined

Table 5-6 (continued): Plagioclase trace element composition in [$\mu\text{g/g}$]

Sample	235-134		235-134		235-134		235-134		235-134		235-134	
	1-plag-1-1	1-plag-1-2	3-plag-1-1	3-plag-1-2	3-plag-1-3	3-plag-2-1	3-plag-2-2	3-plag-2-1	3-plag-2-2	3-plag-2-1	3-plag-2-2	4-plag-1-1
Na	14877 ± 598	9739 ± 90	9312 ± 517	11187 ± 397	11953 ± 423	11482 ± 450	23642 ± 514	12903 ± 694	12903 ± 694	12903 ± 694	12903 ± 694	12903 ± 694
Sc	7.4 ± 0.4	8.4 ± 0.2	6.5 ± 0.4	6.3 ± 0.2	7.1 ± 0.3	8.4 ± 0.4	7.5 ± 0.1	7.2 ± 0.3	7.5 ± 0.1	7.2 ± 0.3	7.2 ± 0.3	7.2 ± 0.3
Sr	5.2 ± 0.2	4.8 ± 0.3	8.7 ± 0.5	7.2 ± 1.0	10.4 ± 1.5	155.6 ± 7.8	18.8 ± 2.1	4.8 ± 0.2	18.8 ± 2.1	4.8 ± 0.2	18.8 ± 2.1	4.8 ± 0.2
Y	0.13 ± 0.01	0.12 ± 0.01	0.17 ± 0.01	0.17 ± 0.01	0.12 ± 0.01	0.27 ± 0.03	0.14 ± 0.01	0.16 ± 0.01	0.14 ± 0.01	0.16 ± 0.01	0.14 ± 0.01	0.16 ± 0.01
La	0.020 ± 0.004	0.016 ± 0.006	0.029 ± 0.006	0.020 ± 0.004	0.032 ± 0.010	0.043 ± 0.009	0.015 ± 0.006	0.042 ± 0.006	0.015 ± 0.006	0.042 ± 0.006	0.015 ± 0.006	0.042 ± 0.006
Ce	0.17 ± 0.02	0.14 ± 0.03	0.27 ± 0.02	0.19 ± 0.02	0.18 ± 0.02	0.14 ± 0.03	0.12 ± 0.04	0.22 ± 0.02	0.12 ± 0.04	0.22 ± 0.02	0.12 ± 0.04	0.22 ± 0.02
Pr	0.023 ± 0.004	0.017 ± 0.004	0.039 ± 0.005	0.024 ± 0.004	0.025 ± 0.005	0.019 ± 0.004	0.014 ± 0.004	0.032 ± 0.005	0.014 ± 0.004	0.032 ± 0.005	0.014 ± 0.004	0.032 ± 0.005
Nd	0.18 ± 0.03	0.17 ± 0.04	0.29 ± 0.05	0.24 ± 0.03	0.20 ± 0.03	0.14 ± 0.03	0.13 ± 0.03	0.24 ± 0.03	0.13 ± 0.03	0.24 ± 0.03	0.13 ± 0.03	0.24 ± 0.03
Sm	0.064 ± 0.016	0.065 ± 0.019	0.076 ± 0.017	0.067 ± 0.023	0.058 ± 0.022	0.023 ± 0.014	0.043 ± 0.017	0.068 ± 0.027	0.043 ± 0.017	0.068 ± 0.027	0.043 ± 0.017	0.068 ± 0.027
Eu	0.15 ± 0.01	0.17 ± 0.02	0.24 ± 0.02	0.17 ± 0.01	0.17 ± 0.03	0.11 ± 0.01	0.13 ± 0.02	0.17 ± 0.02	0.13 ± 0.02	0.17 ± 0.02	0.13 ± 0.02	0.17 ± 0.02
Gd	0.061 ± 0.013	0.048 ± 0.015	0.064 ± 0.012	0.090 ± 0.016	0.12 ± 0.02	0.054 ± 0.017	0.034 ± 0.013	0.041 ± 0.010	0.034 ± 0.013	0.041 ± 0.010	0.034 ± 0.013	0.041 ± 0.010
Dy	0.029 ± 0.011	nd	nd	0.058 ± 0.015	0.052 ± 0.014	0.058 ± 0.016	0.059 ± 0.016	0.046 ± 0.011	0.059 ± 0.016	0.046 ± 0.011	0.059 ± 0.016	0.046 ± 0.011

± denotes one standard deviation

nd: not determined

Table 5-6 (continued): Plagioclase trace element composition in [$\mu\text{g/g}$]

Sample	235-134		235-134		235-134		235-134		235-134		235-134	
	4-plag-2-1	6-plag-1-1	7-plag-1-1	7-plag-1-2	7-plag-1-3	7-plag-1-4	7-plag-1-5	7-plag-1-4	7-plag-1-5	7-plag-1-5	10-plag-1-1	10-plag-1-1
Na	9871 ± 308	17204 ± 277	9124 ± 137	7518 ± 116	7050 ± 72	7266 ± 143	6978 ± 86	8326 ± 62	6978 ± 86	8326 ± 62	8326 ± 62	8326 ± 62
Sc	7.3 ± 0.1	6.9 ± 0.3	7.8 ± 0.2	8.6 ± 0.2	7.7 ± 0.1	7.7 ± 0.2	7.6 ± 0.1	6.6 ± 0.2	7.6 ± 0.1	6.6 ± 0.2	6.6 ± 0.2	6.6 ± 0.2
Sr	20.3 ± 2.8	65.1 ± 9.5	2.4 ± 0.2	3.0 ± 0.2	10.4 ± 0.4	3.6 ± 0.2	5.7 ± 0.2	7.6 ± 0.3	5.7 ± 0.2	7.6 ± 0.3	7.6 ± 0.3	7.6 ± 0.3
Y	0.14 ± 0.01	0.17 ± 0.01	0.18 ± 0.01	0.18 ± 0.01	0.21 ± 0.02	0.17 ± 0.01	0.13 ± 0.01	0.11 ± 0.01	0.13 ± 0.01	0.11 ± 0.01	0.13 ± 0.01	0.11 ± 0.01
La	0.042 ± 0.009	0.034 ± 0.006	0.024 ± 0.004	0.026 ± 0.007	0.022 ± 0.007	0.028 ± 0.006	0.022 ± 0.007	0.026 ± 0.007	0.022 ± 0.007	0.026 ± 0.007	0.022 ± 0.007	0.026 ± 0.007
Ce	0.12 ± 0.02	0.20 ± 0.03	0.22 ± 0.03	0.24 ± 0.03	0.25 ± 0.03	0.18 ± 0.03	0.27 ± 0.04	0.16 ± 0.05	0.27 ± 0.04	0.16 ± 0.05	0.27 ± 0.04	0.16 ± 0.05
Pr	0.021 ± 0.004	0.049 ± 0.016	0.025 ± 0.008	0.033 ± 0.010	0.036 ± 0.011	0.018 ± 0.004	0.037 ± 0.011	0.025 ± 0.005	0.037 ± 0.011	0.025 ± 0.005	0.037 ± 0.011	0.025 ± 0.005
Nd	0.24 ± 0.03	0.26 ± 0.04	0.25 ± 0.03	0.33 ± 0.05	0.25 ± 0.04	0.21 ± 0.03	0.22 ± 0.04	0.11 ± 0.03	0.22 ± 0.04	0.11 ± 0.03	0.22 ± 0.04	0.11 ± 0.03
Sm	0.064 ± 0.019	0.093 ± 0.023	0.098 ± 0.024	0.057 ± 0.018	0.107 ± 0.042	0.075 ± 0.022	0.078 ± 0.025	0.063 ± 0.022	0.078 ± 0.025	0.063 ± 0.022	0.078 ± 0.025	0.063 ± 0.022
Eu	0.16 ± 0.02	0.15 ± 0.02	0.13 ± 0.01	0.17 ± 0.02	0.22 ± 0.02	0.16 ± 0.02	0.18 ± 0.02	0.19 ± 0.02	0.18 ± 0.02	0.19 ± 0.02	0.18 ± 0.02	0.19 ± 0.02
Gd	0.073 ± 0.031	0.12 ± 0.03	0.067 ± 0.016	0.11 ± 0.03	0.075 ± 0.018	0.088 ± 0.019	0.043 ± 0.013	0.024 ± 0.009	0.043 ± 0.013	0.024 ± 0.009	0.043 ± 0.013	0.024 ± 0.009
Dy	0.024 ± 0.011	0.040 ± 0.020	0.062 ± 0.019	0.041 ± 0.011	0.043 ± 0.013	0.039 ± 0.013	0.068 ± 0.017	0.030 ± 0.011	0.068 ± 0.017	0.030 ± 0.011	0.068 ± 0.017	0.030 ± 0.011

± denotes one standard deviation

nd: not determined

CHAPTER 6

SPINEL AS PETROGENETIC INDICATOR: INFLUENCE OF REACTIVE MELT-ROCK REACTION AND THE ROLE OF OXYGEN FUGACITY

6.1 INTRODUCTION

Chromian spinel is a ubiquitous accessory phase in peridotites and basalts and known as a useful petrogenetic indicator for various processes affecting peridotites (Irvine, 1965, Sack, 1982, Dick and Bullen, 1984, Allan et al., 1988, Arai, 1994, Hellebrand et al., 2001). Although typically a minor phase, spinel is important because of its wide range of compositional variation of di-, tri- and quadrivalent cations.

The stoichiometry of spinel is of the type AB_2O_4 with one tetrahedral site, denoted A, and two octahedral sites, denoted B, per formula unit. The structure can accommodate a very large number of different cations of different valences of which many can also fit in both (octahedral and tetrahedral) sites (O'Neill and Navrotsky, 1984). Depending on the distribution of cations between the crystal sites, normal, intermediate and inverse spinels can be distinguished. This results in a wide range of solid solutions exhibited by the spinel group. The chromite spinels may be expressed in terms of the theoretical end members (Table 6-1).

Table 6-1: Typical spinel end members

Mineral name	Composition	Structure
Magnetite	$Fe^{3+}[Fe^{2+}Fe^{3+}]O_4$	Inverse
Magnesioferrite	$Fe^{3+}[Mg^{2+}Fe^{3+}]O_4$	Inverse
Chromite	$Fe^{2+}[Cr_2^{3+}]O_4$	Normal
Magnesiochromite	$Mg^{2+}[Cr_2^{3+}]O_4$	Normal
Spinel	$Mg^{2+}[Al_2^{3+}]O_4$	7/8 Inverse
Hercynite	$Fe^{2+}[Al_2^{3+}]O_4$	Normal
Ulvöspinel	$Fe^{2+}[Fe^{2+}, Ti^{4+}]O_4$	Inverse

CHAPTER 6

The wide range in spinel compositions from massif and abyssal peridotites is thought to reflect variations in the degree of partial melting (Dick and Bullen, 1984). The diagram of Cr-number (molar $\text{Cr}/(\text{Cr}+\text{Al})$) against Ti-content in spinel has been suggested to be particularly effective in distinguishing between partial melting and melt-rock interaction (Arai, 1992, Zhou et al., 1996, Parkinson and Pearce, 1998, Pearce et al., 2000). Trends to higher Ti-concentrations are thought to be the consequence of melt-rock reaction or melt impregnation (Kelemen et al., 1995, Edwards et al., 1996, Edwards and Malpas, 1996). In addition, changes in spinel composition also occur in the vicinity of gabbroic intrusions or veins (e.g. Cannat and Casey, 1995), due to tectonic stress (Ozawa, 1989) or cooling related exchange with olivine (Ozawa, 1984, Ballhaus et al., 1991, Liermann and Ganguly, 2003); hydrothermal alteration may affect spinel compositions too (Kimball, 1990, Mellini et al., 2005).

Plagioclase peridotites usually contain spinels that show higher Cr-number, TiO_2 and Fe_2O_3 contents relative to plagioclase-free samples (Figure 6-1) (e.g. Dick et al., 1984, Dick, 1989). This has been either attributed to volume reduction of spinel during the spinel- to plagioclase-facies transition (Hamlyn and Bonatti, 1980, Obata, 1980, Ballhaus and Frost, 1994) or interaction with melt (Dick, 1989, Cannat et al., 1990, Pearce et al., 2000, Tartarotti et al., 2002). Detailed studies on the compositional relationships of spinels in plagioclase peridotites have not been carried out to date.

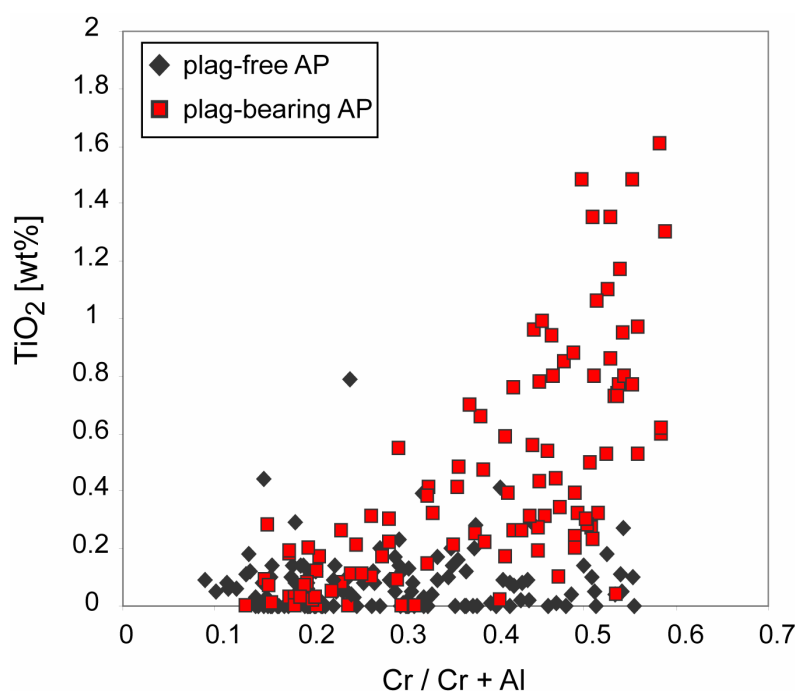


Figure 6-1: Overview of spinel compositions in abyssal peridotite (Hamlyn and Bonatti, 1980, Kornprobst and Tabit, 1988, Dick, 1989, Cannat and Seyler, 1995, Seyler and Bonatti, 1997, Pearce et al., 2000, Tartarotti et al., 2002).

6.2 METHODS AND PETROGRAPHY

The sample set was extended relative to Chapter 5 to enclose a larger range in plagioclase contents. This shall allow the systematic study of the variation in spinel composition in plagioclase-bearing mantle peridotites and the different intrinsic and extrinsic controls on composition.

6.2.1 Sample description and petrography

This study consists of three spinel lherzolites and nine plagioclase peridotites (lherzolites and harzburgites) from dredge haul PS59-235 at the ultraslow-spreading Gakkel Ridge. This dredge haul is located in the Sparsely Magmatic Zone (SMZ), a 100 km long ridge section, where only mantle rocks were recovered. During the ARK XX-2 cruise in 2004, seven out of ten dredge hauls recovered plagioclase peridotites in the SMZ. In this study, the modal amount of plagioclase in the samples ranges from trace levels (~0.1%) to almost 11%, which is close to the maximum amount found to date at a mid-ocean ridge (16.4% at the Romanche Fracture Zone, Mid-Atlantic Ridge: Tartarotti et al., 2002). Some of the samples are very heterogeneous in their modal composition and multiple thin sections (denoted a, b, respectively) were cut from the same piece. Furthermore, sample 235-134 showed such a large range in composition that two more thin sections were cut from the same block (denoted a, b and c).

The majority of the selected samples are fresh, with only few showing minor alteration. Their alteration never exceeds 5% and did not interfere with analyses or point counting. Spinel peridotites and plagioclase-bearing samples from dredge haul PS59-235 usually show almost equigranular textures. The overall degree of deformation is moderate with undulatory extinction in olivine and rare kink-bands in pyroxene. No high-temperature lineation could be observed. Equilibration textures imply a long residence in a cool thermal regime that allowed the formation of 120° angles. Plagioclase often occurs as coronas around spinels, but not invariably (Figure 6-2). Plagioclase is also texturally often found along grain boundaries and crosscutting mantle olivines. Furthermore, two types of symplectites occur in

the plagioclase-bearing samples, dominantly orthopyroxene-plagioclase and once olivine-plagioclase assemblages both surrounding and replacing clinopyroxene grains.

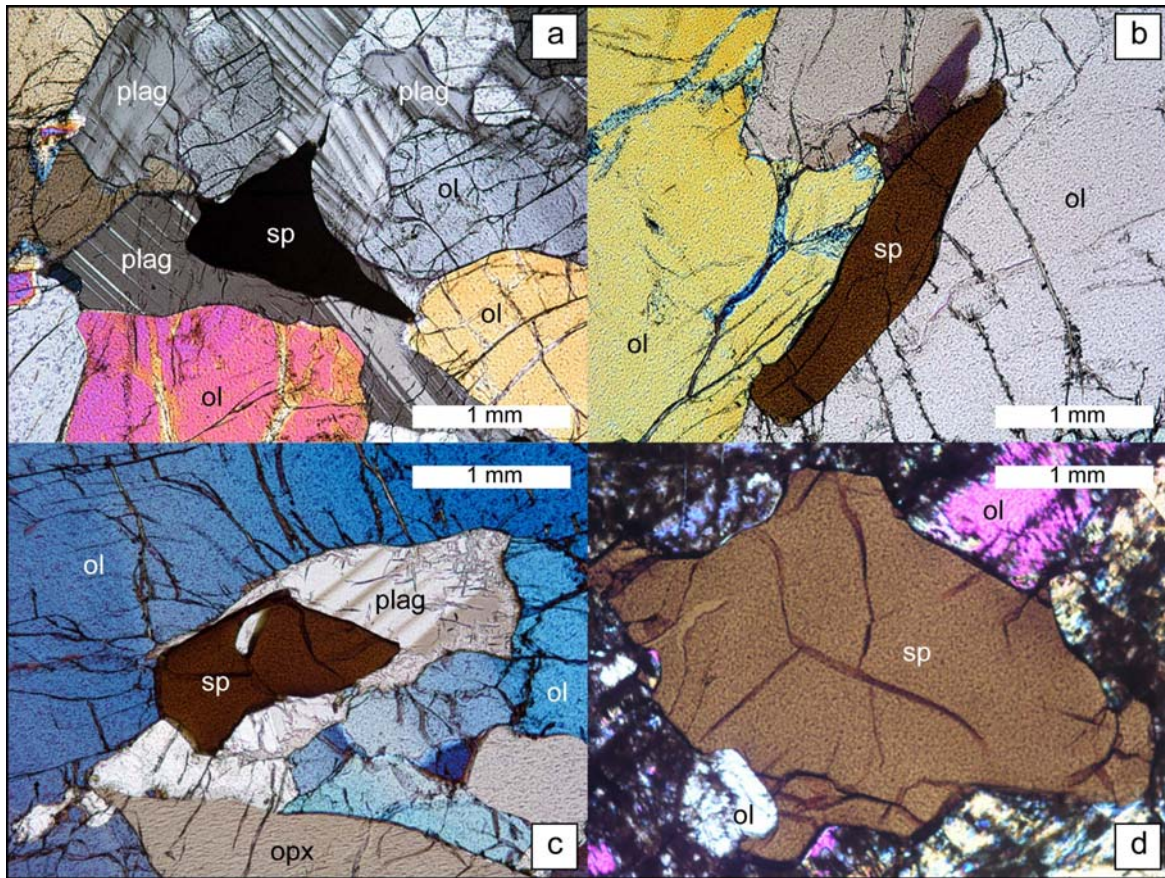


Figure 6-2: Photomicrographs from spinels in plagioclase-bearing samples; a) plagioclase corona around spinel; b) elongated spinel surrounded by olivine; c) plagioclase in contact with spinel; d) large spinel grain in olivine matrix.

6.2.2 Modal proportions

Modal proportions were determined by point counting with 500-600 points on average per thin section, repeated three times to ensure good statistics. Plagioclase is usually heterogeneously distributed and the large standard deviation reported in Table 6-2 for some plagioclase peridotites reflects rather the spatial heterogeneity than the error of the method. Sample 235-134a is divided into two modal domains, one olivine-rich, one pyroxene-poor (see Table 6-2 and Figure A6-1). Point counting results for both areas are listed individually and spinel compositions are further on reported and discussed for the part in which they occur.

CHAPTER 6

Table 6-2: Modal composition of the samples

sample name	ol	opx	cpx	sp	plag
235-2a	66.8 ± 0.8	27.4 ± 0.9	5.2 ± 0.3	0.3 ± 0.1	0.2 ± 0.1
235-2b	59.0 ± 1.9	27.0 ± 1.6	9.0 ± 0.8	0.0 ± 0.0	4.9 ± 0.7
235-4	54.7 ± 1.9	25.5 ± 1.0	13.0 ± 1.8	0.5 ± 0.3	5.9 ± 0.6
235-9	65.4 ± 0.6	28.9 ± 0.3	4.9 ± 0.6	0.5 ± 0.3	0.1 ± 0.1
235-11	69.1 ± 1.6	22.0 ± 2.0	7.6 ± 0.9	1.2 ± 0.2	0.0 ± 0.0
235-12	73.2 ± 1.0	17.5 ± 0.5	5.7 ± 0.8	0.4 ± 0.2	2.9 ± 0.6
235-17	61.2 ± 1.1	28.0 ± 0.5	10.2 ± 0.8	0.4 ± 0.1	0.0 ± 0.0
235-18	54.0 ± 1.2	33.8 ± 1.8	5.5 ± 1.0	0.2 ± 0.1	6.3 ± 1.2
235-19	61.3 ± 1.0	24.1 ± 0.9	7.9 ± 0.3	0.5 ± 0.4	5.7 ± 0.5
235-20	73.6 ± 0.9	17.9 ± 0.1	7.3 ± 0.9	1.0 ± 0.3	0.0 ± 0.0
235-24	61.8 ± 3.3	20.0 ± 2.0	7.6 ± 0.4	0.5 ± 0.0	9.8 ± 1.9
235-27	56.6 ± 2.6	30.2 ± 3.2	2.2 ± 0.2	0.1 ± 0.1	10.6 ± 0.8
235-134a-I	37.5 ± 0.4	53.2 ± 0.5	2.6 ± 0.3	0.4 ± 0.2	6.1 ± 0.4
235-134a-II	73.7 ± 0.3	15.3 ± 1.2	6.7 ± 0.8	0.9 ± 0.2	3.1 ± 0.5
235-134b	65.1 ± 0.5	29.4 ± 0.6	4.8 ± 0.1	0.4 ± 0.2	0.4 ± 0.3
235-134c	61.8 ± 1.3	33.3 ± 1.1	2.0 ± 0.2	0.2 ± 0.2	2.5 ± 0.4

±: one standard deviation

6.2.3 Methods

Spinel major element measurements were carried out on a JEOL 8900 microprobe at the University of Mainz. The accelerating voltage was 20 kV and a beam current of 20 nA was used. Standard counting times were 40s for Ca and Ti; 35s for Mg and Al; 30s for Cr, Fe, Mn, Co, Ni, Zn and 20s for Si. Beam size is 2 μm . Fe^{3+} -contents were calculated based on stoichiometry after the method of Droop (1987). Additionally, olivine analyses were carried out at the JEOL electron microprobe analyzer (EPMA) at the Max-Planck Institute for Chemistry, Mainz, to allow calculation of oxygen fugacity using the oxybarometer of Ballhaus et al. (Ballhaus, 1991, Ballhaus et al., 1991, Ballhaus et al., 1994). Accelerating voltage was 20 kV, and a beam current of 300 nA and beam size of 2 μm were used, following the conditions reported by Sobolev et al. (2007). Sample average compositions for spinel and olivine are reported in Table 6-2 and Table 6-3, respectively, individual analyses can be found in the electronic appendix.

Several element maps were produced by EPMA from selected spinel grains in plagioclase peridotites 235-134 and 235-19. Acceleration voltage was 20 kV, beam current 30

nA and beam size 1 μm ; dwell time 200 ms and step width 1 μm . Spectrometer configuration used was: 1Tap: Al, 2Tap: Mg, 3Pet: Ti, 4Pet: Cr and 5LIFH: Fe.

6.3 RESULTS

6.3.1 Spinel compositions

Spinel lherzolites contain spinels with Cr-numbers between 0.12 and 0.16, which places them at the very fertile end of spinel compositions in abyssal peridotites (e.g. Hellebrand et al., 2001). In places, spinels in spinel peridotites show a slight depletion in aluminum towards the rim but are otherwise homogeneous. Based on the worldwide correlation between the heavy rare earth elements (HREE) in clinopyroxene and spinel Cr-number (Hellebrand et al., 2001), the degree of partial melting was estimated to range between 3 and 6%, low compared to most abyssal peridotites (see also Chapter 2). Spinel peridotites have low TiO_2 -contents of about 0.05 wt%, attesting to their residual nature.

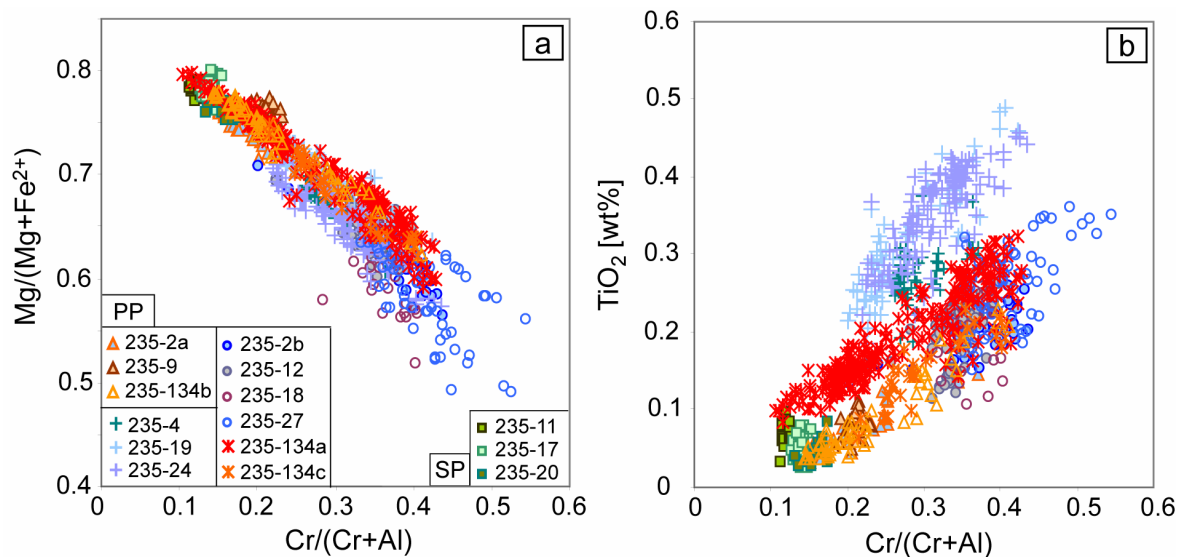


Figure 6-3: Spinel compositions in spinel and plagioclase peridotites from PS59-235 (a) Cr-number against TiO_2 (b) Cr-number against Mg-number.

Spinel compositions of the plagioclase-bearing samples vary considerably between the dredged samples and within individual grains. This is best illustrated in a plot of Cr-number against Mg-number (Figure 6-3a) and against Ti concentration (Figure 6-3b). Spinel in

plagioclase peridotites show a range in Cr-number between 0.10 and 0.54, which is almost the entire range of residual abyssal peridotite spinels as given by Dick and Bullen (1984). Cr-number is also correlated with TiO₂-contents but the slope of the correlation can vary for each sample.

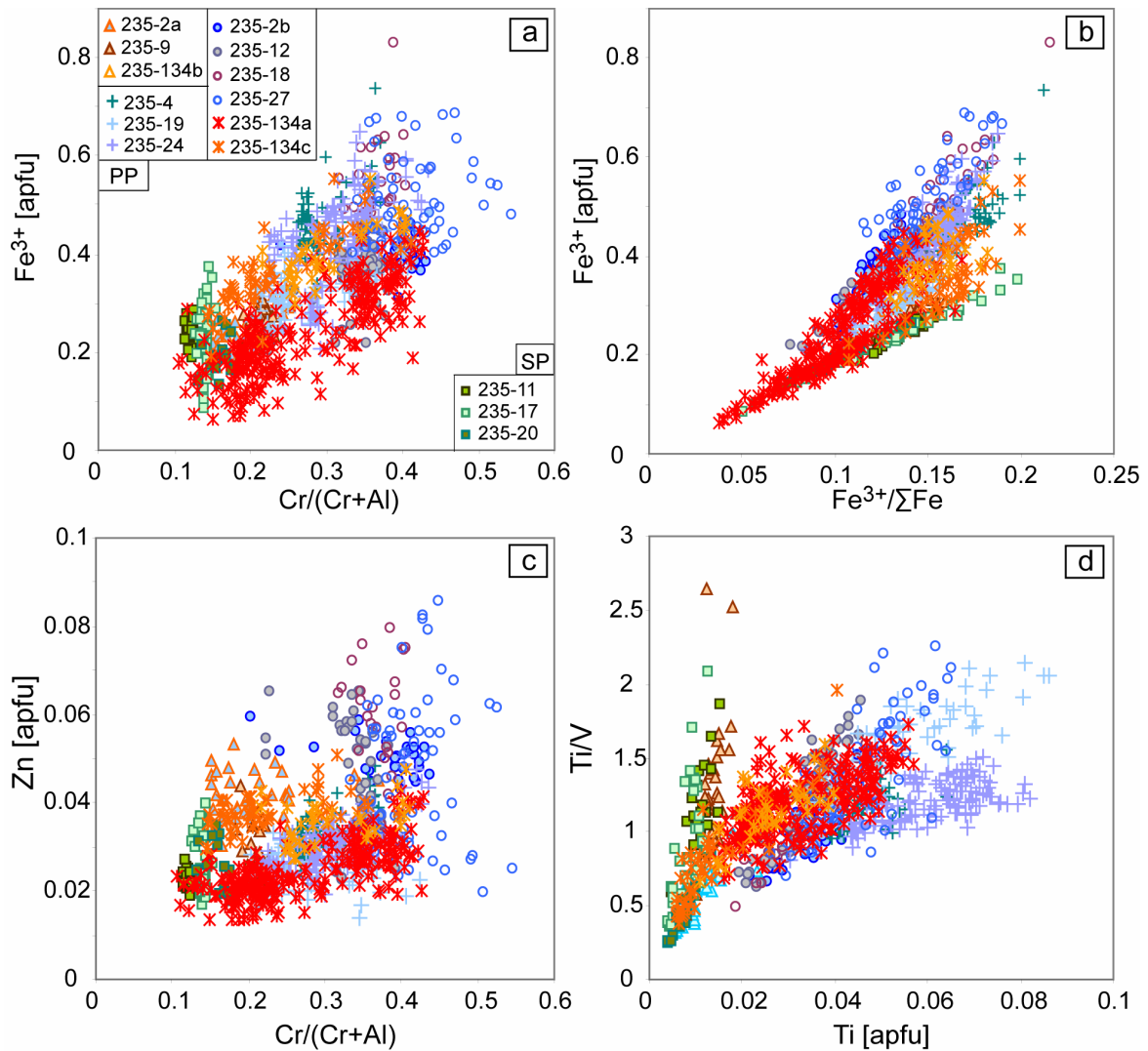


Figure 6-4: Spinel compositions in spinel and plagioclase peridotites from PS59-235. a) Cr-number against ferric iron, b) Fe³⁺/ΣFe against ferric iron, c) Cr-number against Zn, d) Ti against Ti/V (cations per 12 oxygen formula unit).

The compositional range is formed by two components: the variation within single grains and their spatial distribution in thin section. A systematic change in composition can often be observed within the thin section where the average Cr-number of single spinel grains

increases from one side of the thin section to the other. The correlation between Cr-number and Mg-number (molar $\text{Mg}/(\text{Mg}+\text{Fe}^{2+})$) is tight except for samples 235-18 and 235-24, both of which are very plagioclase-rich samples. The largest range in composition is seen in sample 235-134, which is also modally very heterogeneous.

In general, spinel lherzolites always form an end member in the compositional range in major element variation diagrams and but plot away from plagioclase peridotites in element ratio variation diagrams. Samples with only trace amounts of plagioclase show a narrower compositional range and spinel compositions from the plagioclase-free area usually overlap with the compositional field of spinel lherzolites (e.g. 235-134b).

6.3.2 Spinel zoning

Compositional variation in spinel Cr-number within one grain can be as large as 0.11 to 0.33. Thus, in addition to single spot analyses, several EPMA element maps were produced to compliment the data set and to allow the investigation of the spatial extent of zoning.

Spinel grains show a previously unreported asymmetric and apparently unsystematic zoning in composition. Unlike concentric core-rim gradients, expected from melting or reaction processes, flat to steep rim-to-rim gradients can be observed sometimes with parallel domains of equal composition (Figure 6-5). This zoning occurs on very small scales; for example, the Cr-number can change by as much as a factor of three (0.11 – 0.27) within 50 μm . Some rim regions of the grains have even higher Al-concentrations than their cores. Higher even than the spinel peridotites in this study, while the opposite rim can be as Cr-rich as spinels from depleted harzburgites. Element zoning patterns are independent of grain shape, orientation or any other textural relationship.

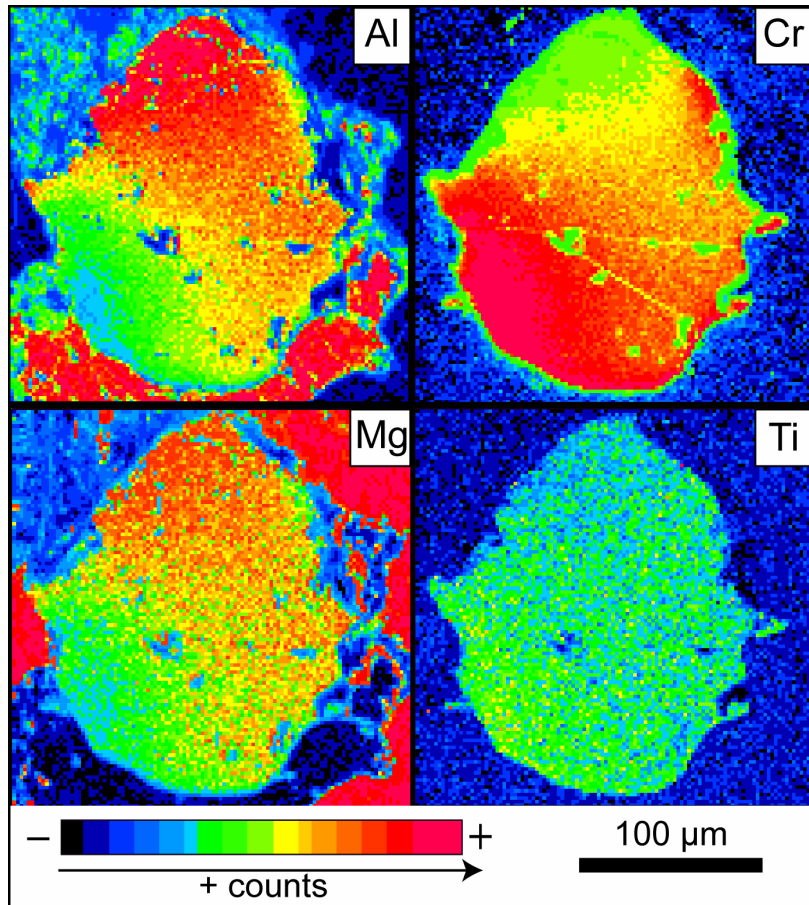


Figure 6-5: Round spinel grain surrounded by plagioclase in sample 235-19.

Figure 6-6 shows two maps for Al-concentration and a synthetic Cr-number of two different spinel grains (labeled I and II) surrounded by plagioclase in PS59-235-134a. The larger spinel grain “I” has a pronounced asymmetric variation in major elements, with the highest Al-concentrations (14.1 wt%) measured along one rim; the small neighboring grain “II”, only 30 μm apart from grain “I”, exhibits high chromium content. This is a typical feature of plagioclase peridotites: small neighboring grains that show distinctly different major element compositions. Figure 6-7 shows element maps from different spinel grains from the same sample, which are rimmed by plagioclase within an olivine matrix. Again, a non-systematic distribution in major element composition can be seen with abrupt changes in Cr-number on a micrometer scale.

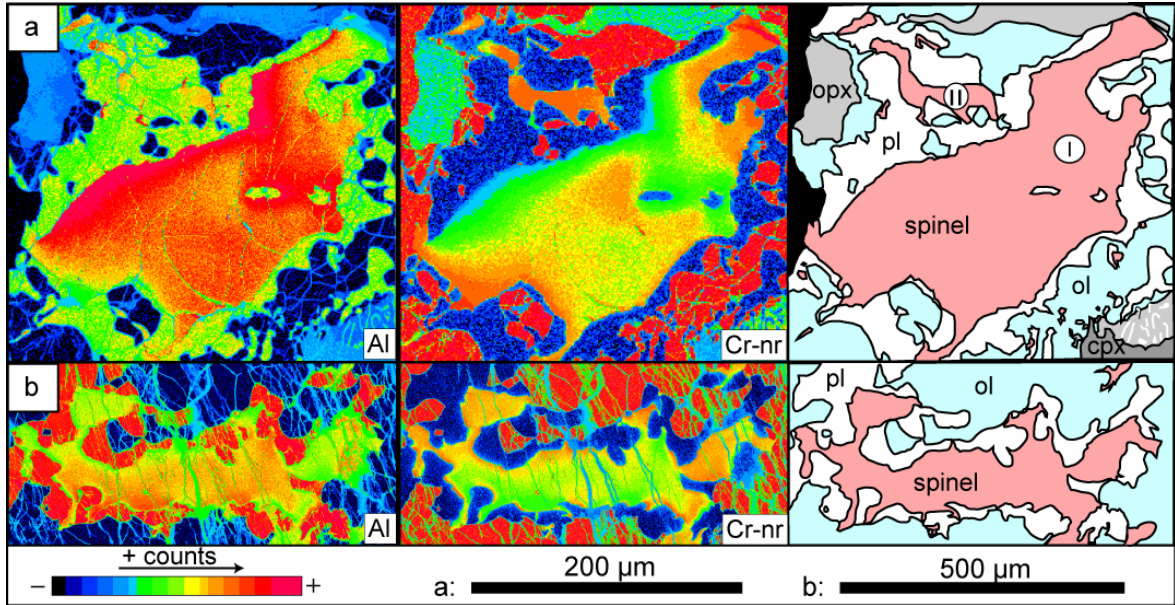


Figure 6-6: Element concentration maps for spinel grains in PS59-134a. From left to right: Map of Al-concentrations - Map of Cr-number - Sketch map (pink: spinel; white: plagioclase; light blue: olivine; light gray: orthopyroxene; dark gray: clinopyroxene).

Figure 6-7 shows a train of spinels highlighting the non-systematic behavior of zoning. The element map of a train of spinels corroborates that there is no preferred orientation of zoning that would imply an influence of stress or another simple external cause. Aluminum-rich rims face in the same direction as chromium-rich rims. Compositional gradients change from gentle to steep. No systematic dependence on the importance of the mineral phase in contact could be found.

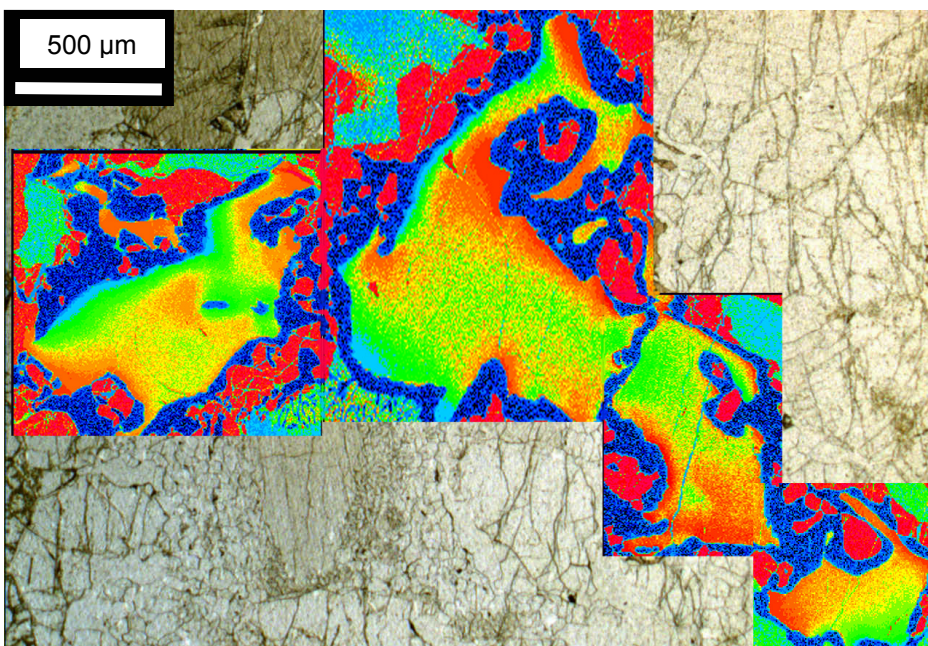


Figure 6-7: Synthetic map of Cr-numbers in spinel for a train of spinels in 235-134a-II.

6.3.3 Sample systematics

Spinels in this study can be separated into different groups based on their major element composition (Figure 6-8):

- Group S1: Spinels from plagioclase-free peridotites (samples 235-11, 235-17 and 235-20). They are homogeneous in composition and contain only low amounts of TiO₂.
- Group P1: Spinels from peridotites with modal amounts of plagioclase between 0.1% and 1% (samples 235-2a, 235-9 and 235-134b). Their spinels overlap with spinel peridotite compositions in plagioclase-free areas of the thin section. However, they usually show a small, but distinct relative difference in major element composition.
- Group P2: Peridotites exceeding 1% modal plagioclase. Two different sub-groups of plagioclase-bearing peridotites can be distinguished here based on their major element composition.
 - Group P2-A (samples 235-4, 235-19 and 235-24): Spinels from Group P2-A are higher in TiO₂, Al₂O₃, MgO, NiO-content and Mg-number relative to Group P2-B.
 - Group P2-B (samples 235-2b, 235-12, 235-18, 235-27, 235-134a and 235-134c): Spinels from Group P2-B are higher in Cr₂O₃, FeO, Fe₂O₃, MnO, ZnO-content and Cr-number relative to Group P2-A.

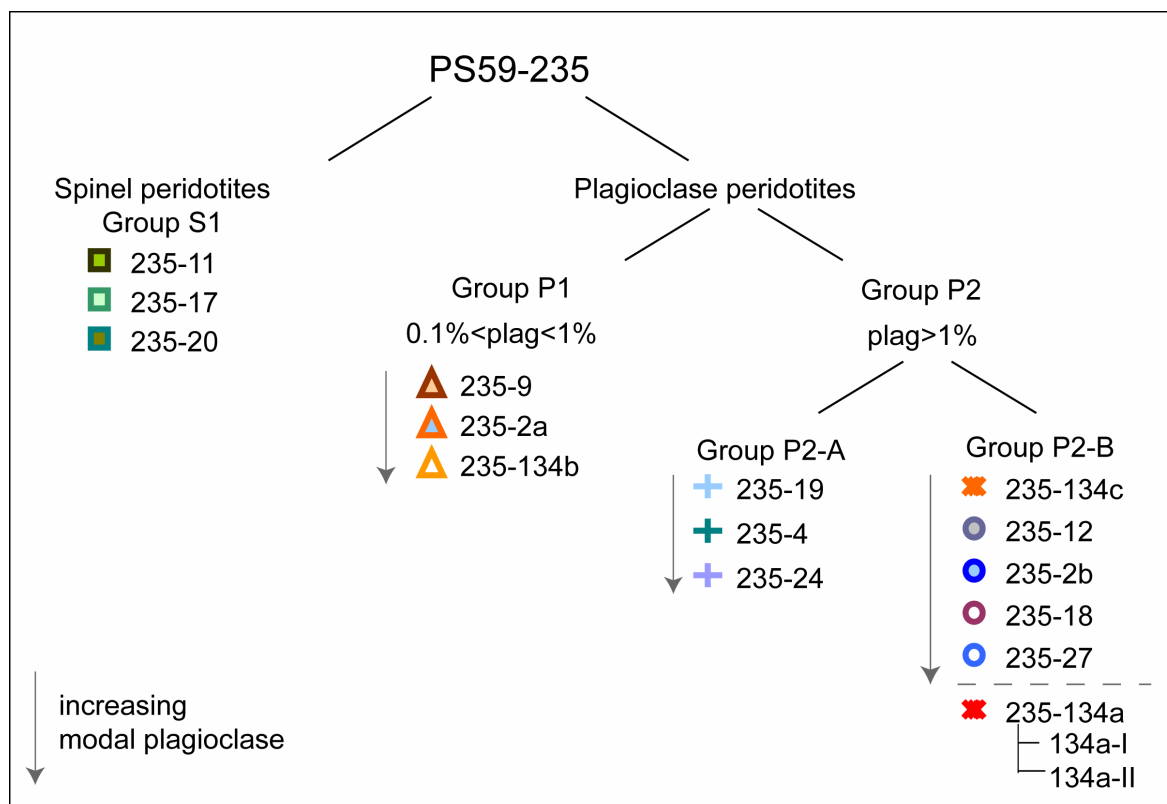


Figure 6-8: Systematics of PS59-235 peridotites in this study. Plagioclase peridotites fall into different groups based on their plagioclase-content and their major element characteristics. Symbols as used in plots.

Spinel from plagioclase peridotite sample 235-134a, part of Group P2-B, show the most extensive range in composition within the entire sample set. The sample is very heterogeneous both modally and compositionally. Textures and clinopyroxene trace element composition suggest that plagioclase was formed dominantly by melt-rock reaction (see Chapter 5 for discussion) but a minor amount of metamorphic plagioclase was formed by the closed-system reaction from spinel- to plagioclase-facies conditions. Figure 6-9 shows the distinct compositional difference between a train of spinels in the olivine-rich part (134a-II) of the thin section and the very pyroxene-rich part (134a-I). Spinel in 134a-II are part of a phase assemblage, interpreted to have formed during the subsolidus transition from spinel to plagioclase facies conditions. Spinel in 134a-I show elevated Fe^{3+} contents relative to spinel peridotites from Group S1 and in agreement with compositions of Group P2 plagioclase peridotites. In contrast, spinel compositions in 134a-II overlap with spinels from Group S1 and plot toward lower Fe^{3+} contents relative to other plagioclase-bearing samples. Spinel compositions from 134a-I and 134a-II are plotted and discussed separately further on.

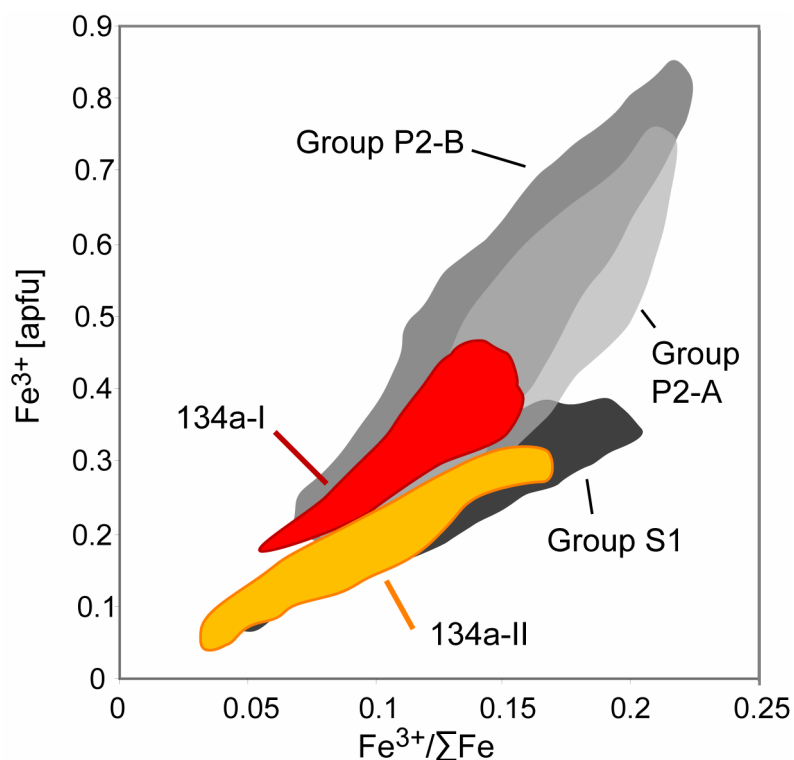


Figure 6-9: $Fe^{3+}/\Sigma Fe$ -ratio against Fe^{3+} in spinel. Sample 235-234a shows two very different populations of spinels in its respective part of the thin section further on labeled as 134a-I (shown in red) and 134a-II (shown in orange). Black: spinel peridotites group S1. Light grey: Group P2-A spinels, dark grey: Group P2-B spinels.

6.3.4 Oxygen fugacities

Oxygen fugacities (fO_2) were calculated using the oxygen barometer of Ballhaus and coworkers (1991, 1991, 1994). The results of calculations are given in Table A6-3, quoted as log units relative to the FMQ (fayalite-magnetite-quartz) buffer. Fe^{3+} contents in spinels were calculated stoichiometrically from EPMA analyses, a method accepted to be reasonably accurate (Canil and O'Neill, 1996, Woodland et al., 2006). Pressure of equilibration was assumed to be 1 GPa. The oxygen barometer is independent of temperature at a given $\Delta \log(fO_2)$ and its dependence on pressure is negligible in the range of interest. Here, an increase in 1 GPa translates only into a decrease of 0.3 to 0.4 log bar units in fO_2 relative to FMQ (Ballhaus et al., 1991).

Spinel peridotites plot between $\Delta\log(fO_2)_{FMQ}$ of -2 and -1 but cluster close to -1, in agreement with values for the upper mantle (Ballhaus et al., 1990). In general, plagioclase peridotites show higher relative oxygen fugacities up to $\Delta\log(fO_2)_{FMQ} + 1$. Higher oxidation of plagioclase peridotites and metasomatized xenoliths has been previously reported and attributed to interaction with an oxidized melt (e.g. Dyar et al., 1989, Ballhaus et al., 1990, McGuire et al., 1991). In contrast, calculated oxygen fugacities in sample PS59-134a extend to extremely reduced values, also lower than seen in the spinel peridotites.

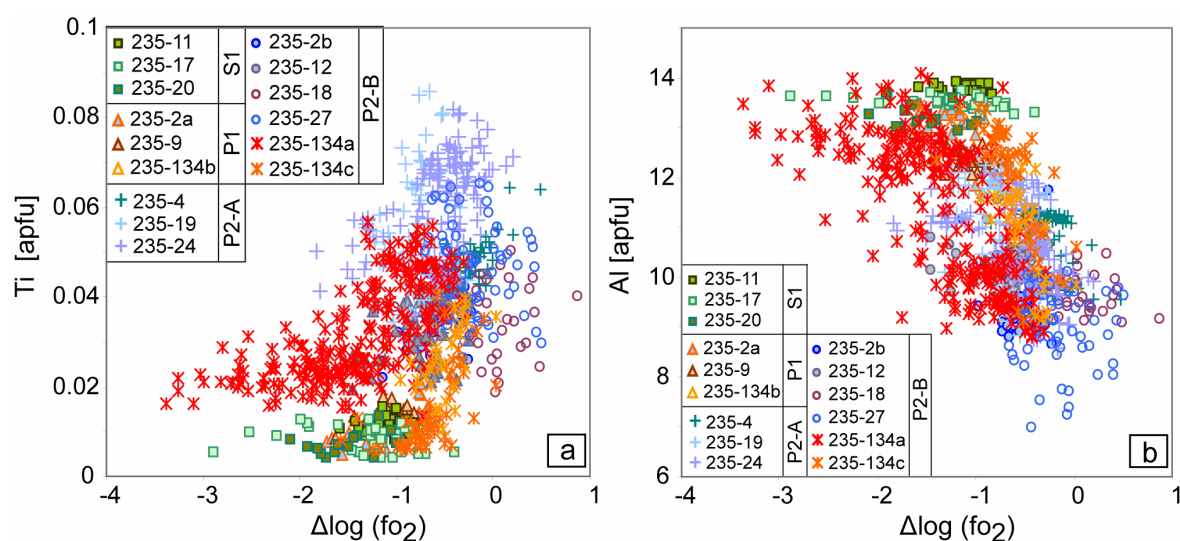


Figure 6-10: Variation of major elements with oxygen fugacity a) Ti (a) and (b) Al [apfu] in spinel versus calculated oxygen fugacity relative to FMQ after Ballhaus (1991). Note the trend of increasing Ti and decreasing Al with increasing oxygen fugacity (cations per 12 oxygen formula unit).

In general, spinel compositions seem to be correlated with oxygen fugacity (Figure 6-10). Here, Al, Mg and Ni decrease and Cr, Fe (both Fe^{2+} and Fe^{3+}), Ti, V and Zn increase with increasing fO_2 , although no tight linear trends are formed. The oxygen barometer from Ballhaus et al. (1991) is based on equilibria between olivine, orthopyroxene and spinel, all of which have variable composition in plagioclase peridotites. Olivine compositions show some variability in plagioclase peridotites (Table 6-4) and it is possible that an even larger compositional range remained undetected. Furthermore, pyroxenes also show zoning in Mg-numbers (Chapter 5). Therefore, compositional variability of the plagioclase peridotites may introduce uncertainty in calculated oxygen fugacities, supposedly responsible for the variation.

The $V/(Cr+Al)$ ratio in spinel has been found to be sensitive to changes in oxygen fugacity as well because D^V is a function of fO_2 (Papike et al., 2004, Papike et al., 2005). The advantage of this ratio is its ability to monitor changes in relative oxygen fugacity by a single mineral indicator, thus unaffected by zoning in the mineral assemblage. As shown in Figure 6-11, calculated oxygen fugacities agree with $V/(Cr+Al)$ and correlate even better with ferric iron. Therefore, the $V/(Cr+Al)$ ratio will be used to trace changes in relative oxygen fugacity and compliment the Ballhaus oxygen barometer.

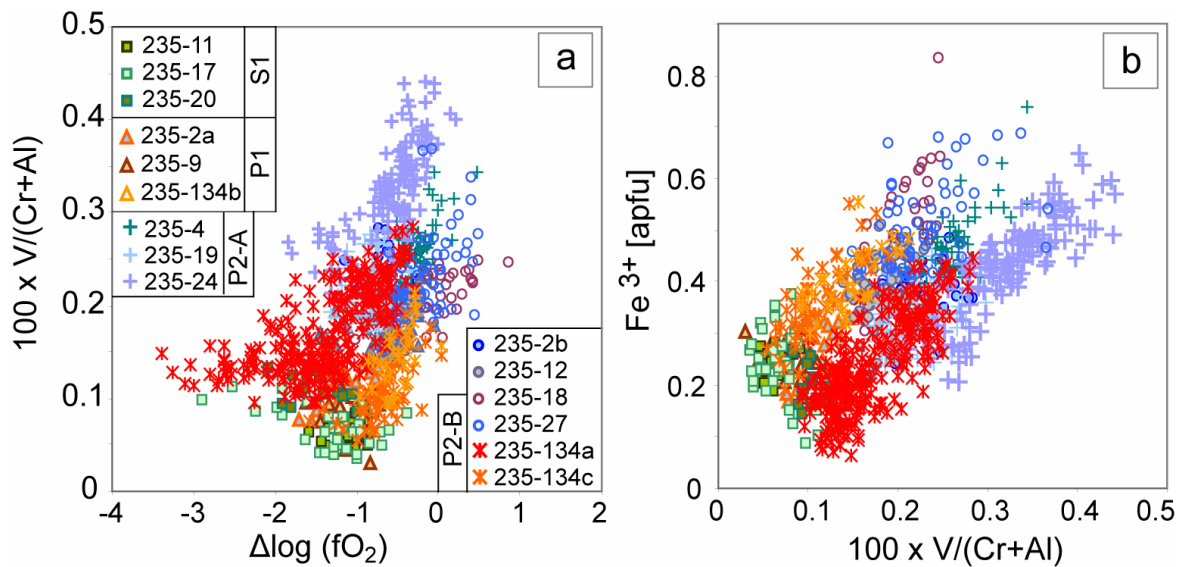


Figure 6-11: Correlation of calculated oxygen fugacity relative to FMQ versus the $V/(Cr+Al)$ ratio, a different indicator of relative oxygen fugacity (a) and the $V/(Cr+Al)$ ratio against ferric iron (cations per 12 oxygen formula unit).

6.4 DISCUSSION

Elevated titanium contents in spinel (up to 2 wt%) and pyroxenes of plagioclase peridotites are commonly observed and have been even suggested as a discrimination tool to separate them from “normal” residual lithologies (Dick and Bullen, 1984, Dick, 1989). The diagram of Cr-number against Ti-content in spinels has been also suggested to be particularly effective in distinguishing between partial melting and melt-rock interaction (Arai, 1992, Zhou et al., 1996, Parkinson and Pearce, 1998, Pearce et al., 2000). Trends to higher Ti-concentrations are usually interpreted as the consequence of melt-rock reaction or melt

impregnation and to reflect the titanium-concentration of the melt (Dick, 1989, Cannat et al., 1990, Suhr and Robinson, 1994, Kelemen et al., 1995, Edwards et al., 1996, Edwards and Malpas, 1996). Moreover, during the spinel- to plagioclase-facies transition, increasing titanium concentrations are thought to reflect volume reduction of titanium-bearing minerals and hence passive increase in titanium (Kornprobst and Tabit, 1988, Woodland et al., 1992, Rampone et al., 1993).

6.4.1 Gakkel Ridge plagioclase peridotites - Variation between spinel composition and plagioclase abundance

Spinel in plagioclase peridotites from Gakkel Ridge show a large compositional range in individual samples as well as grains; most notably is the correlation between spinel Cr-number and titanium. The sample set was separated into different groups based on spinel composition and modal plagioclase content. Although the variation in each thin section can be very large, the variation becomes systematic when sample averages are plotted. Here, spinel compositions vary consistently with plagioclase content within their respective group. Plagioclase-free peridotites from Group S1 plot at the Cr-poor, Al-rich end in spinel compositions (Figure 6-12 a and b), with samples with only trace amounts of plagioclase of Group P1 relatively close-by. Group P2-A and Group P2-B spinels follow two separate trends with almost no overlap at equal amounts of plagioclase. Also systematically spinels in olivine-rich part 134a-II (red diamond) usually plot away from the other groups while spinels from the pyroxene-rich part 134a-I (blue diamond with red outline) plot with Group P2-B spinels (Figure 6-12).

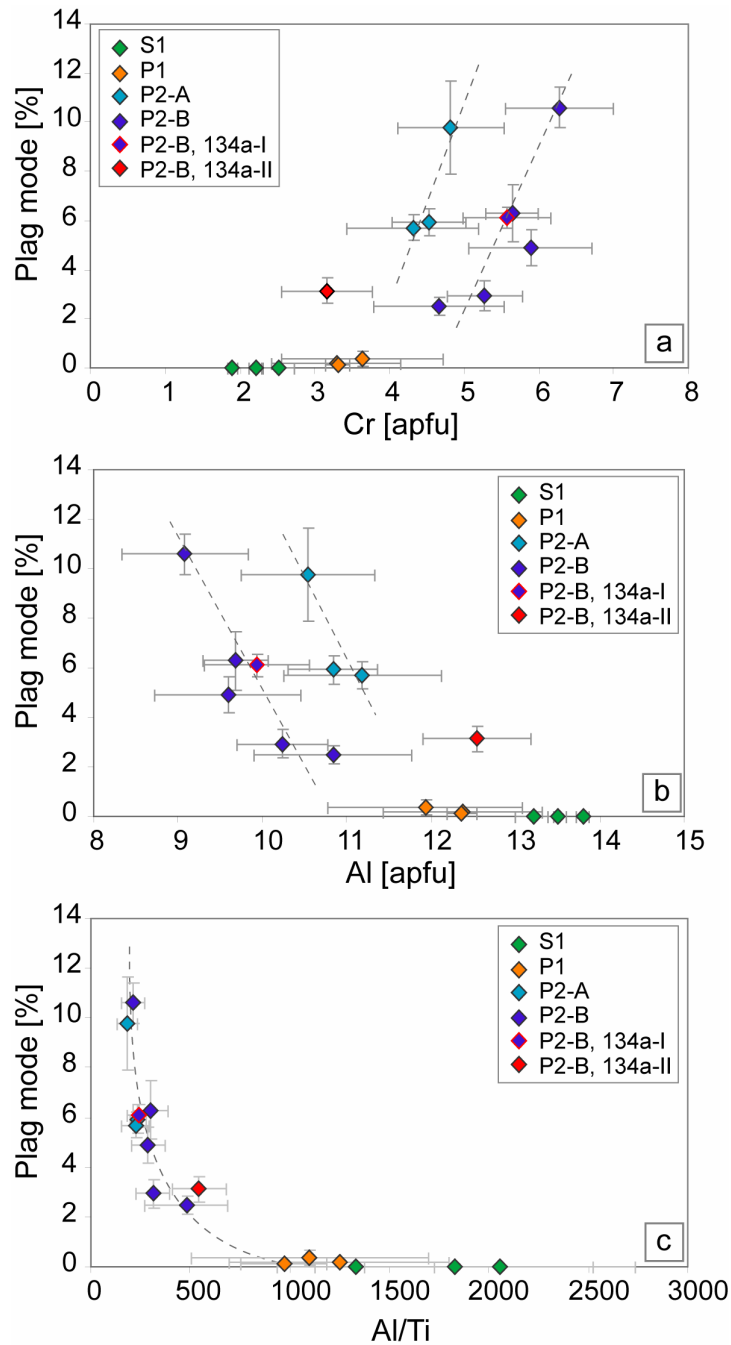


Figure 6-12: Cr, Al and Al/Ti (cations per 12 oxygen formula unit) of the spinel sample averages versus the respective average modal plagioclase abundance. Error bars denote one standard deviation.

Group P2-A spinels show consistently higher Ti-concentrations compared to Group P2-B at a given Cr-number and theoretically, two different melts could be invoked. However, the Al/Ti-ratio (Figure 6-12c) suggests no such difference between the individual groups but instead that Ti-concentrations are controlled by the same process.

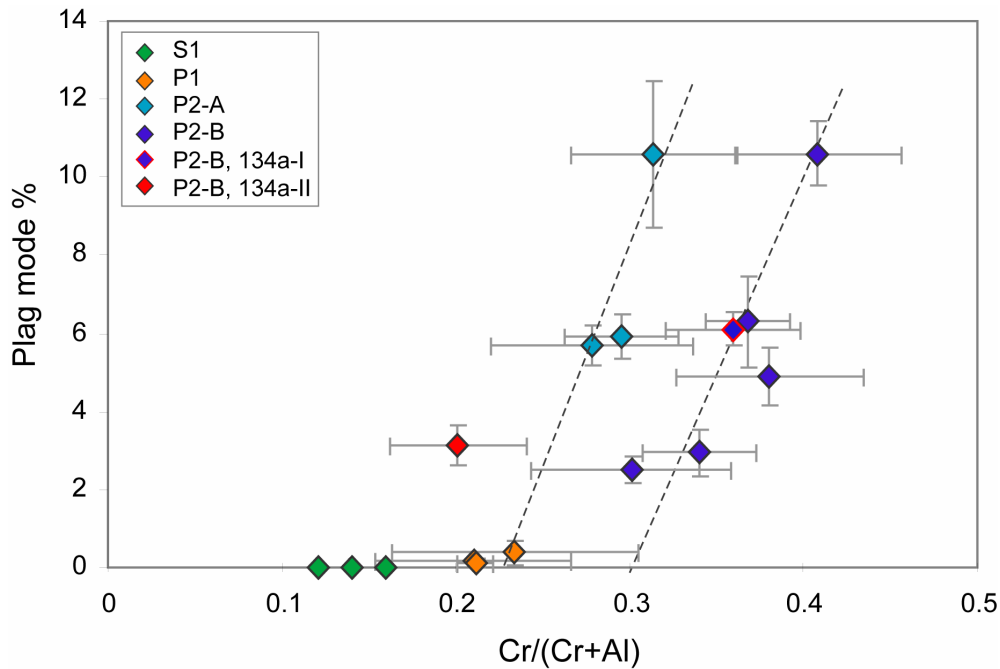


Figure 6-13: Cr-number in spinel versus plagioclase abundance. Shown are sample averages, error bars denote variability within the sample, not analytical uncertainty. Samples are color coded depending on their group.

In this context, a general correlation also exists between spinel Cr-number and amount of plagioclase with samples from Group P2-A and P2-B forming separate trends. Projecting the respective trends back toward a plagioclase-free composition suggests that P2-A plagioclase peridotites and P2-B plagioclase peridotites are produced from different source rocks. Here, group P2-A had a more fertile (i.e. lower Cr-number) spinel peridotite as protolith whereas Group P2-B samples stem from a more refractory peridotite, supposedly with a residual spinel Cr-number around 0.3.

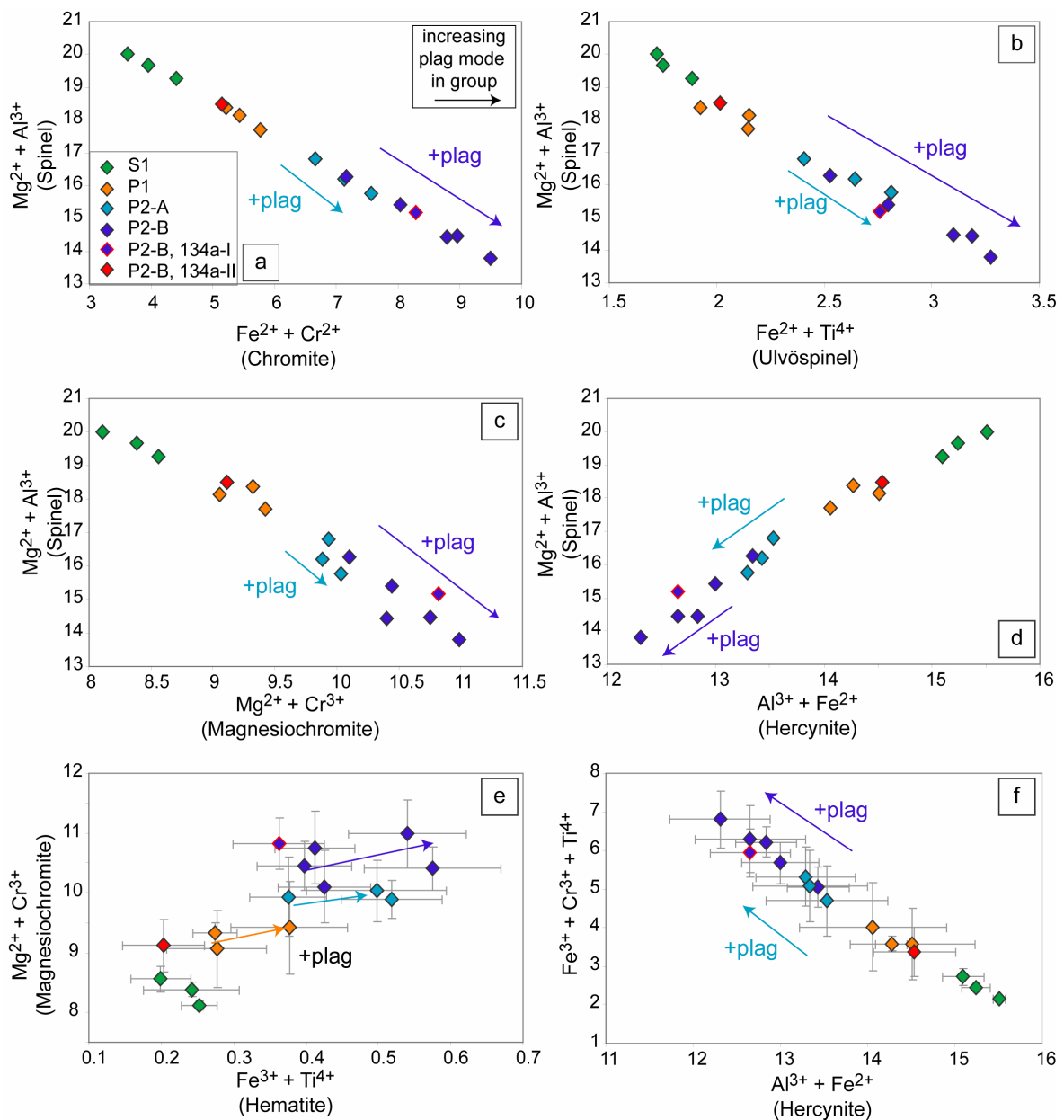
Similar correlations can be found between modal plagioclase and other elements. Plagioclase exerts the dominant effect on spinel chemistry and no further correlation with pyroxene or spinel was found. Moreover, even trace amounts of plagioclase, easily overlooked at higher degrees of alteration, can exert a noticeable change in spinel composition.

Projection of spinel compositions in X-Y diagrams accounts for atomic proportions of Fe^{3+} , Al and Cr but not for Ti and the commonly used ratio plots of the form $\text{Cr}/(\text{Cr}+\text{Al})$ versus $\text{Fe}^{2+}/(\text{Fe}^{2+}+\text{Mg})$ can be misleading for titanian spinels (Pasteris, 1982). This is because titanian

CHAPTER 6

spinel is 2-4 spinels, of the form $X_2^{2+}Y_4^{3+}O_4$, different to the 2-3 spinels of the form $X_2^{2+}Y_3^{3+}O_4$. Therefore, it is more practical to study the solid solution series.

Figure 6-14 shows correlations between different solid solution members for the sample set. Again, only sample averages are plotted, color-coded depending on their respective group. Figure 6-14 a-d shows the correlation between the spinel component and four other dominant solid solution members in spinel. In general, the spinel component decreases with increasing modal plagioclase. Again, Group P2-A and P2-B are relatively shifted in composition with P2-B being further down the solid-solution correlation.



CHAPTER 6

Figure 6-14: Solid solutions (SS) of spinel highlighting the systematic (cations per 12 oxygen formula unit). The color code reflects the individual sample group. Arrows show the increase in modal plagioclase within the individual group. a) SS between chromite and (sensu strictu) spinel; b) SS between ulvöspinel and spinel; SS between magnesiochromite and spinel; d) SS between hercynite and (sensu strictu) spinel; e) correlation between hematite and magnesiochromite; f) correlation between hercynite and the sum of mole of ferric iron, chromium and titanium. Arrows indicate increasing plagioclase abundance within the relative sample group.

The good correlation between the different spinel solid solutions precludes that the variation in spinel composition is the result of insufficient diffusive equilibration. Even though P2-A spinels record the highest Ti-concentrations for a given Cr-number, they contain less ulvöspinel component compared to P2-B in the solid solution series. P2-A and P2-B show similar abundances of plagioclase but P2-B spinel compositions are always shifted further down solid-solution series relative to P2-A spinels.

6.4.2 The role of melt-rock reaction

Compositional variation in spinels from plagioclase peridotites has been previously reported (Hamlyn and Bonatti, 1980, Cannat and Seyler, 1995, Hellebrand et al., 1998, Tartarotti et al., 2002, Sen et al., 2003, von der Handt et al., 2004). The origin of plagioclase in these samples has been either attributed to trapped melt, fractional crystallization or metamorphic breakdown of spinel to plagioclase facies conditions.

Although either of these processes may be capable producing compositional variation in spinels, it is difficult to account for the compositional range of the sample set by them. Crystal fractionation from a melt would be the most likely process to produce a wide range in spinel composition, but will also greatly affect the Mg-number in the associated olivine (e.g. Dick and Bullen, 1984, Barnes and Roeder, 2001). Increasing Ti contents in spinel by crystal fractionation should cause Mg-number variation in olivine between 0.91 to less than 0.83 (Natland and Dick, 2001).

In the previous chapter, the formation of plagioclase and orthopyroxene and dissolution of olivine, clinopyroxene and spinel in two plagioclase peridotites (PS59-235-19

CHAPTER 6

and -134a) have been interpreted as the product of a reactive melt-rock reaction process between two systems of different silica-saturation. Here, peridotite is infiltrated by a melt at higher silica activity and its phase assemblage and composition re-equilibrates through incongruent dissolution reactions toward the higher silica activity. The previous section has shown that spinel composition is related to modal abundances of plagioclase in a thin section. Hereby, the general trend is that of decreasing MgAl_2O_4 component with increasing plagioclase content.

MgAl_2O_4 , spinel *sensu stricto*, is unstable in even moderately silica-rich environments because of its dependence on the bulk Al/Si-ratio (Irvine, 1967). Thayer (1956) suggested that during melt-rock reaction, spinel will react with melt following the reaction:

- spinel + melt \rightarrow olivine + plagioclase

or in systems of higher silica activity:

- spinel + melt \rightarrow orthopyroxene + plagioclase

The decrease of spinel stabilities across reaction zones of increasing silica activities have been reported for instance by Kriegsman and Hensen (1998) and Beard and Tracy (2002).

Nicholls (1977) calculated equilibrium mantle compositions from two different bulk compositions at different silica saturation by Gibbs free energy minimization. At a given pressure and temperature, mineral compositions and abundances differed significantly between the two mantle compositions. Largest differences were found in the minor element contents of the pyroxene, the composition of spinels and the relative proportions of the two pyroxenes; he concluded that the variation must arise by differences in bulk composition alone (Nicholls, 1977).

Figure 6-15 shows Cr-number and Mg-number of spinels that are stable in the two mantle compositions. At identical pressure and temperatures, both spinel compositions are markedly different in Cr-number, a similar range as seen in the variability of spinel compositions in this study.

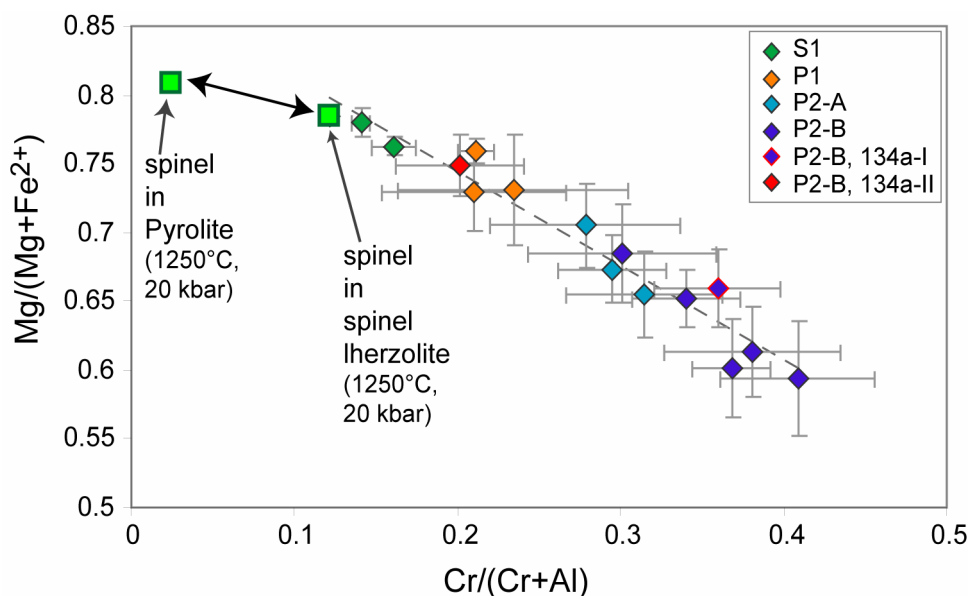


Figure 6-15: Cr-number against Mg-number in spinel for thin section averages. Error bars denote sample variation. Spinel in equilibrium with a Pyrolite composition after Ringwood (1975) and spinel lherzolite from Baja, California, calculated by Nicholls (1977) at temperature of 1250°C and 20 kbar.

Melt-rock reaction with a melt at higher silica activity would lead to the extraction of the MgAl_2O_4 component from chromite-spinel and would hereby enrich the spinel in its other components. The Mg-number in spinel is related to the Mg-number in olivine by equipotential surfaces at a given temperature (Irvine, 1965). This essentially restricts spinel in its major element variation and the only “independent” major element variation can occur in its Cr-Al ratio (Irvine, 1967). Hence, a decrease in MgAl_2O_3 in spinel has to be counterbalanced by an increase in FeCr_2O_3 and therefore spinel composition will move along the equipotential surface between Mg-number and Cr-number during melt-rock reaction.

During melt-rock reaction, the chromium content in spinel is controlled by the host rock because of the low Cr-solubility in melts (Roeder and Reynolds, 1991). Group P2-A and Group P2-B samples contain similar amounts of plagioclase but their spinels differ in Cr-number. The most notable feature of spinels in plagioclase peridotites is their correlation of Ti-content with Cr-number, which varies at a given Cr-number for each sample. This has been usually attributed to different titanium contents in the reacting melt. Titanium in spinel occurs as ulvöspinel or titanomagnetite component. The increase in Ti-concentration seems to be moderated by increasing Fe^{3+} concentration. Trivalent iron substitutes preferentially for Al with increasing availability (Lavina et al., 2005). On a crystallographic level, the $\text{Fe}^{3+} - \text{Fe}^{2+}$

CHAPTER 6

distribution in spinel is strongly temperature (Trestman-Matts et al., 1983) and composition dependent (O'Neill and Navrotsky, 1983) but redistribution of Fe^{2+} and Fe^{3+} between the octahedral (M) and tetrahedral (T) site is very fast (O'Neill and Navrotsky, 1984).

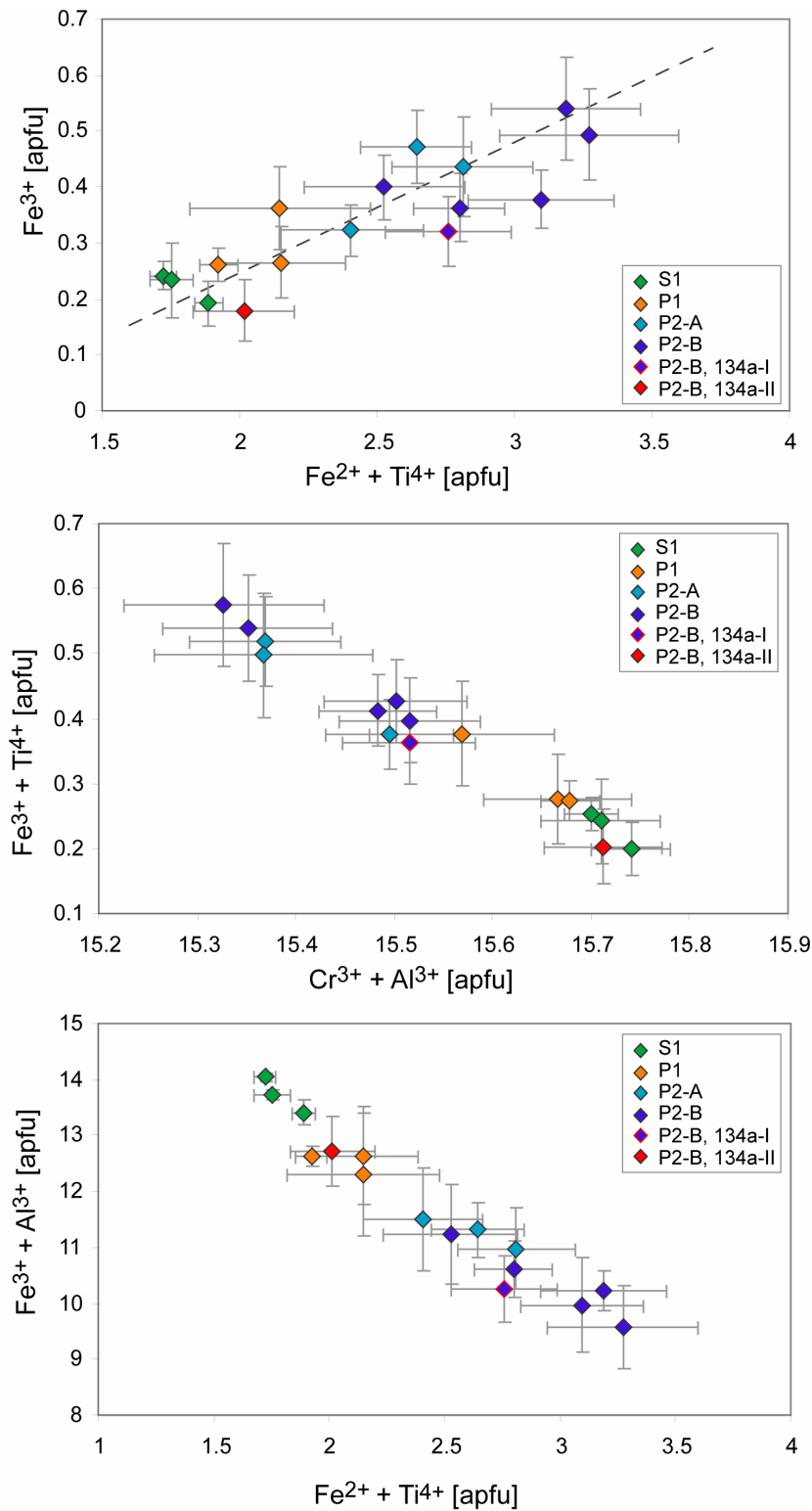


Figure 6-16: Average spinel compositions (cations per 12 oxygen formula unit); a) ulvöspinel against magnetite suggesting $\text{Fe}^{2+} + \text{Ti}^{4+} - 2 \text{Fe}^{3+}$, b) titanomaghemite against the Cr-number following the reaction: $2(\text{Cr}^{3+}, \text{Al}^{3+}) \leftrightarrow \text{Fe}^{2+} + \text{Ti}^{4+}$; c) ulvöspinel against trivalent

Al and iron.

Spinel is the only mineral that can incorporate significant amounts of Cr and Fe³⁺ in ultramafic rocks. Hence, the amount of these elements is not buffered by any equilibrium within the phase assemblage and is primarily controlled by the content of Cr and Fe³⁺ of the bulk rock. The Fe³⁺ is controlled then by fO₂ (Evans and Frost, 1975).

6.4.3 Oxygen fugacity

Oxygen fugacity is an important parameter in the upper mantle and controls partial melting together with temperature, pressure and composition (Mattioli and Wood, 1986, Taylor and Green, 1988, Canil et al., 1994). It is also an important parameter for mantle rheology (Bai et al., 1991, Bai and Kohlstedt, 1992). The upper mantle is believed to be heterogeneous over several log units in terms of oxygen fugacity (Mattioli and Wood, 1986, Wood et al., 1990, Ballhaus, 1993, Canil et al., 1994). Most studies indicate that the fO₂ of the upper mantle lies between the iron-wüstite buffer (IW, Fe_{Metal} + 1/2 = FeO) and the fayalite-magnetite-quartz buffer (FMQ; 3 Fe₂SiO₄ + O₂ = 2 Fe₃O₄ + 3 SiO₂).

Oxygen fugacity is known to have a strong control on spinel compositions (Hill and Roeder, 1974, Roeder and Reynolds, 1991, Toppani and Libourel, 2003). Ballhaus and coworkers produced spinel Cr-numbers of as much as 0.68 in oxidation experiments from low Cr-numbers in the starting mix (Ballhaus et al., 1991). “Cosmic spinels” from meteorites differ from terrestrial spinels by their high Ni and Fe³⁺ contents and show large variations in their composition that can be expressed as a function of temperature, time and oxygen fugacity (Toppani and Libourel, 2003). The ratio of Fe²⁺ to Fe³⁺ is sensitive to variations in oxygen fugacity (fO₂) and used as an oxybarometer (Mattioli and Wood, 1986, Ballhaus et al., 1991) and the ferrous/ferric ratio of spinel is independent of melt composition and only controlled by the oxygen fugacity (Hill and Roeder, 1974).

Ferric iron is moderately incompatible during partial melting in the mantle and the bulk Fe₂O₃-content decreases with increasing MgO (Woodland et al., 2006). Basaltic melts are more oxidized relative to their mantle sources (Ballhaus and Frost, 1994) and their oxidation state is a function of the (1) degree of melting, (2) depth of first melting and (3) fractionation

CHAPTER 6

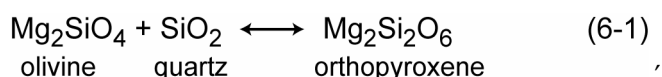
of mineral phases with lower $\text{Fe}^{3+}/\Sigma\text{Fe}$ than the melt (such as olivine or opx) (Ballhaus, 1993). Infiltration of small amounts of fluids or melts can change the $f\text{O}_2$ of peridotites by as much as two log units (Wood et al., 1990). Furthermore, any reaction that either consumes or produces a ferric iron-bearing phase in a phase transition will lower or raise relative $f\text{O}_2$ (Ballhaus, 1995).

Spinel represents the major host for Fe^{3+} in plagioclase peridotites in spite of its low abundance (Woodland et al., 2006). Hence, they should react more sensitively to changes in oxygen fugacity compared to spinel lherzolites. Plagioclase peridotites are usually more oxidized relative to spinel peridotites (Ballhaus et al., 1990) and they often have higher ferric/ferrous iron ratios compared to spinel peridotites (Dick and Bullen, 1984, Ballhaus et al., 1991, Woodland et al., 1992, Woodland et al., 1996).

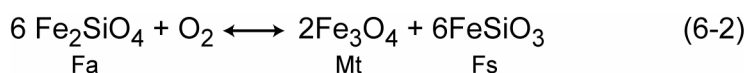
6.4.3.1 Reactive melt-rock reaction and oxygen fugacity – Evidence for oxidation?

Calculation of oxygen fugacities with the oxygen barometer from Ballhaus (1991, 1993) suggests a large range of increased oxygen fugacities up to FMQ+1 for the plagioclase peridotites. It has to be checked if this reflects a true oxidation event.

In the upper mantle, silica activity is effectively buffered by the equilibrium:



Oxygen fugacity in the mantle is at least in part determined by ferric-ferrous iron equilibria such as



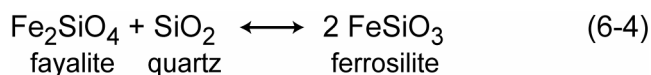
which forms the basis for the spinel-olivine-orthopyroxene oxygen barometer (Fa: fayalite, Mt: magnetite and Fs: ferrosilite). At constant temperature and pressure the oxygen fugacity is then determined by (Irvine 1965, 1967):

CHAPTER 6

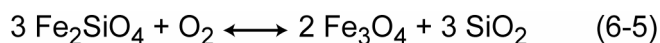
$$f(\text{O}_2) = \frac{(a_{\text{Mt}})^2 (a_{\text{Fs}})^6}{K (a_{\text{Fa}})^6} \quad (6-3)$$

where K is the equilibrium constant and a_i the activity of i . and thus the function of the magnetite, ferrosilite and fayalite activity.

Ferrosilite and fayalite are related through the silica activity by the following equilibrium:



Hence, if magnetite is present, an inverse relation between oxygen fugacity and silica activity exists



that relates oxygen fugacity to silica activity. With increasing silica activity, the fayalite activity will decrease and that of ferrosilite increase if the magnetite activity stays constant. As a result, the oxygen activity will increase. However, at constant oxygen fugacity, the magnetite activity must decrease as well during increases in silica activity.

Because all phases occur in solid solution, most phase assemblages are more tightly constrained than expected from the formal phase rule variance. Five phase assemblages are completely fixed by temperature, pressure, oxygen fugacity and silica activity at which they equilibrate (Lindsley and Frost, 1992). In most rocks, oxygen fugacity is monitored by mineral phase equilibria and thus does not entirely depend on the ferric/ferrous ratio. Frost et al. (1988) pointed out that $f\text{O}_2$ is not only reflected in the composition of coexisting ferromagnesian silicates, but also in the composition of Fe-Ti oxides. In Mg-bearing systems, a whole series of oxide-silicate equilibria occurs that relate the composition of Fe-Ti oxides to that of orthopyroxene. Addition of Ti^{4+} reduces the activity of Fe_3O_4 and stabilizes spinel relative to wüstite, thereby progressively lowering the equilibrium $f\text{O}_2$ (Woodland and Wood, 1994).

CHAPTER 6

Decrease in MgAl_2O_4 and increase in FeCr_2O_4 component will result in an increase of the total FeO . At constant oxygen fugacity the $\text{Fe}^{3+}/\Sigma\text{Fe}$ ratio is buffered and consequently Fe^{3+} has to increase. Fe^{3+} preferentially exchanges with Al^{3+} in the octahedral site. The correlation between $\text{Fe}^{2+} + \text{Ti}^{4+} \rightarrow 2\text{Fe}^{3+}$ implies that their exchange is coupled, a common exchange reaction in oxides (Lindsley, 1991).

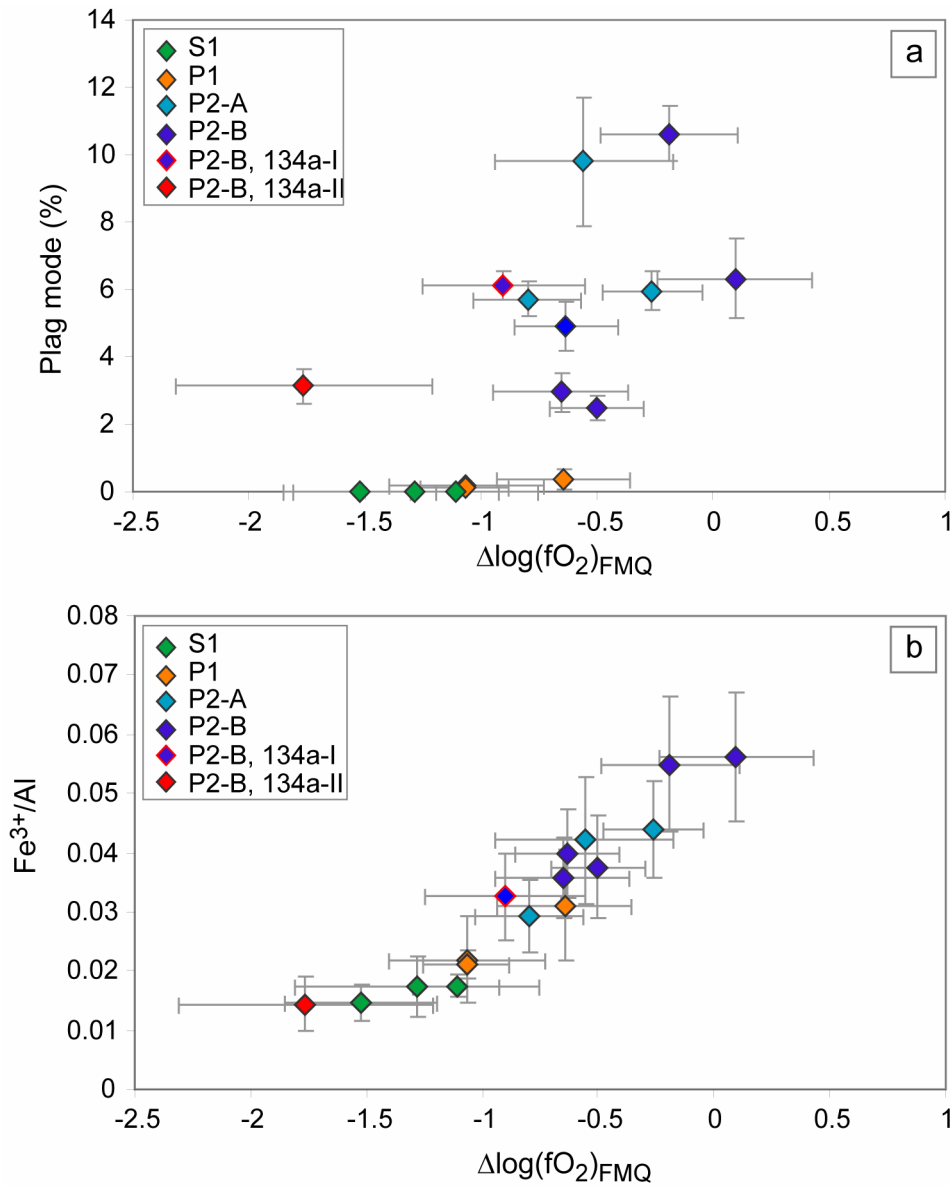


Figure 6-17: Change in oxygen fugacity relative to FMQ calculated after Ballhaus (1991, 1993) against plagioclase abundance (a) and the ferric iron/aluminum ratio (cations per 12 oxygen formula unit).

CHAPTER 6

No variation between plagioclase abundance and the relative change of oxygen fugacity is visible (Figure 6-17a). Instead, a good correlation exists between the calculated oxygen fugacity and the ferric iron/aluminum ratio in spinel. Spinel compositions in plagioclase peridotites are a function of the residual spinel composition and the melt composition thus P2-A spinels generally contain more titanium while P2-B spinels contain more Fe^{3+} . However, this obscures the relationship between oxygen fugacity and plagioclase abundance. By the melt-rock reaction process, described in Chapter 5, the Fe^{3+} passively increases by the decrease in MgAl_2O_3 component in spinel. Therefore, the increase in silica activity in the system can be recorded by the oxygen barometer by plotting calculated values against the Fe^{3+}/Al ratio. Figure 6-17b suggests that P2-B spinels are most affected by this process. In the previous section, it has been inferred based on the correlation between plagioclase abundance and spinel Cr-number that the degree of depletion of the source rock increases from P1 and P2-A to P2-B. During the reaction between a melt of higher silica activity (relative to peridotite) and variably depleted peridotite, the relative increase in silica activity will be larger for more refractory samples.

The $V/(\text{Cr}+\text{Al})$ ratio in spinel has been found to be a good indicator for relative changes in oxygen fugacity as well (Papike et al., 2004, Papike et al., 2005). Figure 6-18a shows the good correlation between $V/(\text{Cr}+\text{Al})$ and titanium in spinel. This diagram suggests that P2-A spinels are more oxidized than P2-B. However, vanadium shows the same partitioning behavior in spinels as titanium and P2-A spinels also contain more TiO_2 compared to P2-B and the relative concentration of Ti is a function of the variables in the melt-rock reaction process. While the partition coefficients for Ti and V between spinel and melt are $f\text{O}_2$ dependent as well (Canil, 2002, Toppani and Libourel, 2003), no significant change in partitioning between the samples can be found (Figure 6-18b) and also no correlation with plagioclase abundance (Figure 6-18c). Therefore, an active oxidation event by melt impregnation cannot be confirmed but it is suggested that increasing oxygen fugacities seen by the oxybarometer are rather the result of the changing spinel composition in response to increasing silica activity than record an active oxidation event.

CHAPTER 6

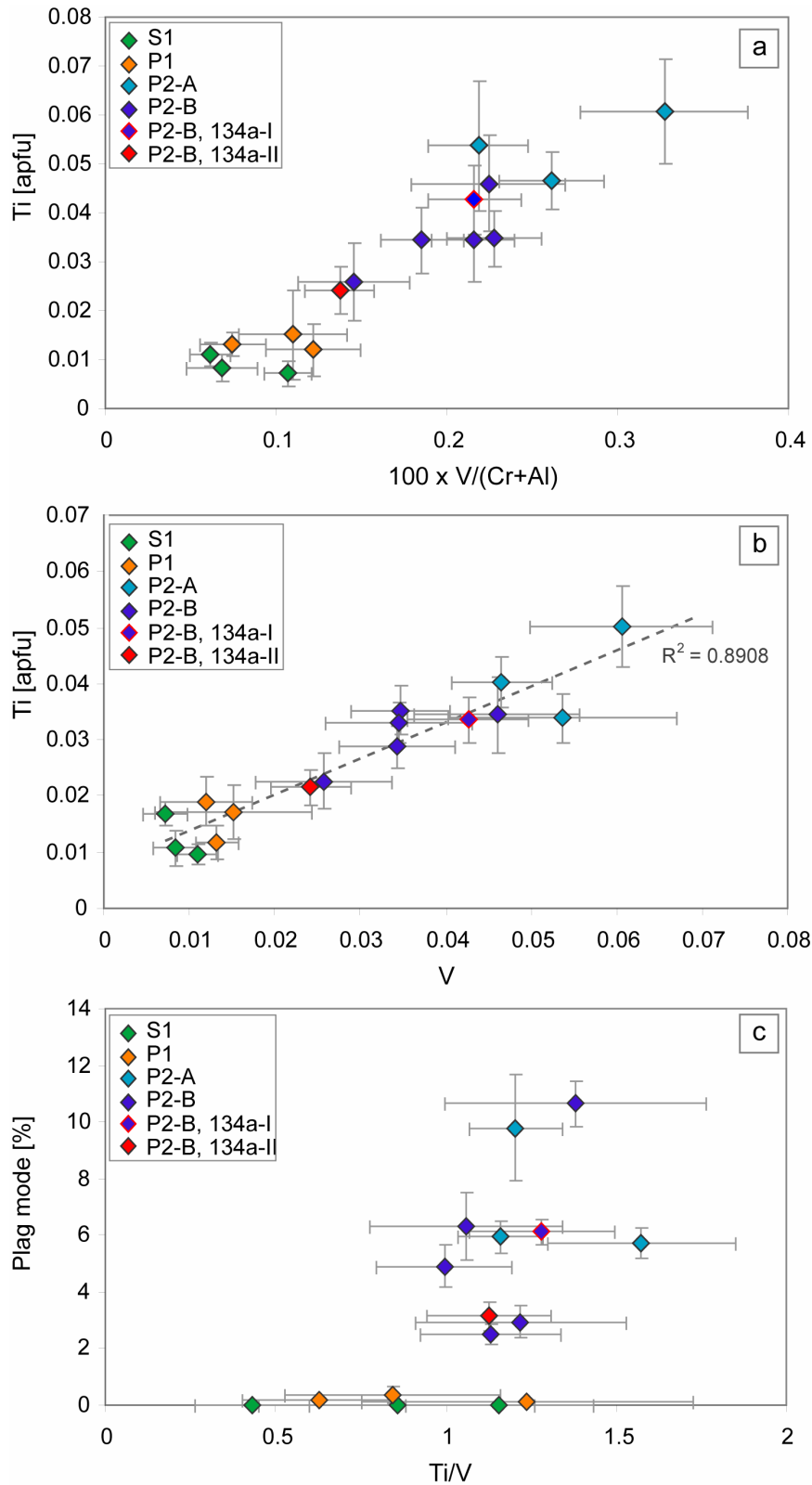


Figure 6-18: a) Correlation of $V/(Cr+Al)$, an indicator for relative oxygen fugacity, b) vanadium against titanium and c) the Ti/V ratio against plagioclase abundance (cations per 12 oxygen formula unit).

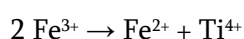
6.4.3.2 The effect of closed-system breakdown of spinel

Spinel compositions show systematic variation with plagioclase abundances in this study with the exception of spinels in plagioclase peridotite 235-134a. 235-134a consists of a pyroxene-rich part 134a-I and an olivine-rich part 134a-II. The difference between spinels in 134a-I and 134a-II is not a function of their different modal composition because 235-12 is very similar in this respect to 134a-II but plots consistently close to 134a-I in spinel composition diagrams. The most striking difference between both parts is seen in Fe^{3+} content in which 134a-II spinels follow the trend of the residual spinels and 134a-I spinels plot toward higher Fe^{3+} contents together with other plagioclase peridotites (Figure 6-9). Modal, textural and geochemical evidence supports that two end-member types of spinel are present in sample 235-134. In the olivine-rich part of the sample (134a-II), spinel compositions are dominated by the spinel- to plagioclase-peridotite facies breakdown reaction, while the spinels of 134a-I are more affected by melt-rock reaction.

Olivine can only host negligible amounts of Fe^{3+} (Canil and O'Neill, 1996) and the olivine-rich, pyroxene-poor part of sample 235-134a should be affected more strongly by the infiltration of an oxidizing melt because of its poor buffering capability. In contrast, the subsolidus breakdown reaction of spinel in 134a-II even seems to exert a reducing effect compared to its spinel counterparts in 134a-I and shows different oxygen fugacities in both areas. Spinel from 134a-II contain too much Ti^{4+} for their given Fe^{3+} compared to the correlation that all other spinels exhibit in this study. This suggests a different substitution mechanism (Figure 6-19).

Two different processes may play a role:

(1) During the spinel to plagioclase transition, TiO_2 is compatible in neither plagioclase nor olivine and TiO_2 concentration increases in spinel. This results in a relative reduction by the substitution reaction:



As a result, the $\text{Fe}^{2+}/\text{Fe}^{3+}$ ratio will increase at an increase of titanium by 0.01.

CHAPTER 6

(2) During melt-rock reaction, ΣFe increases and Al^{3+} decreases, the latter being replaced by Fe^{3+} , which requires again a charge balancing reaction with Ti. As a result, the Ti-content increases more than the $\text{Fe}^{2+}/\text{Fe}^{3+}$ ratio by either reaction:

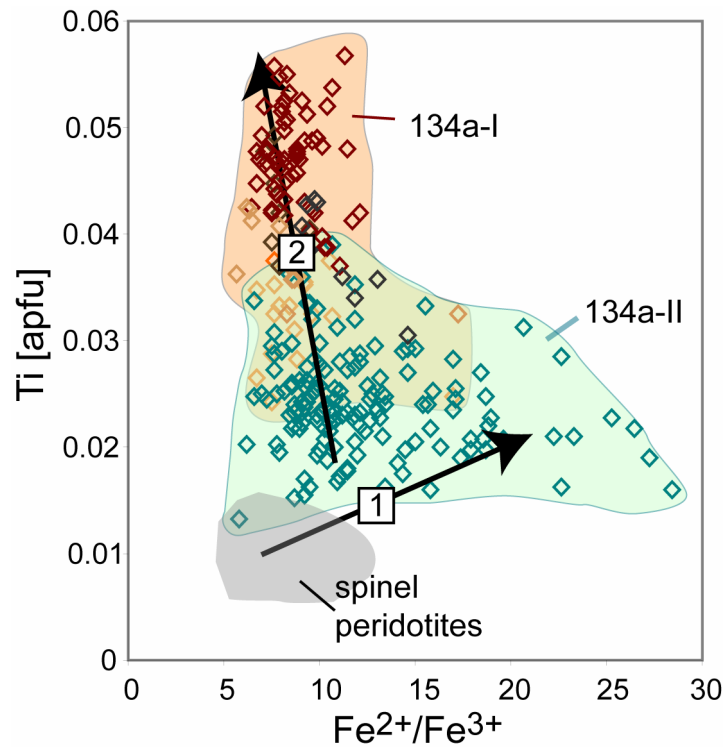
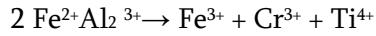
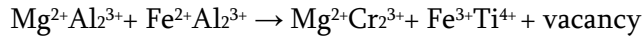


Figure 6-19: Ferric/ferrous iron ratio versus Ti [apfu] of spinels from sample 235-134a (cations per 12 oxygen formula unit).

It is also remarkable that 134a-II spinels usually plot in a similar range as samples with only trace amounts of plagioclase but away from the sample's real modal amount of plagioclase. This suggests that the smaller relative increase in Fe^{3+} and Cr^{3+} reflects only molar changes during the volume reduction while the larger relative change in Al is used for the production of plagioclase. If this holds true, it would imply that about 1% of plagioclase in this area is formed by the metamorphic reaction, while the other 5% are formed by melt-rock reaction. This further corroborates the assertion suggested in Chapter 5 that the reaction from spinel- to plagioclase-facies conditions is triggered by the presence of melt.

6.5 SUMMARY

Spinel in plagioclase peridotites from Gakkel Ridge show a large range in composition, both within samples as well as within grains.

- Major element composition allows separating them into different groups.
- In general, sample averages are a function of the plagioclase abundance in the thin section.
- Spinel is in reaction with a higher silica melt that leads to the de-stabilization of the $MgAl_2O$ component in spinel and therefore progressive depletion. Titanium contents are part of a substitution reaction in response to changing silica activity and oxygen fugacity.
- Major element composition and solid-solution series of spinel suggest that the actual reaction progress is the same in both groups, and the extent of reaction is shown by the abundance of plagioclase.
- Initial spinel composition controls the final relative position within the reaction series of solid solutions.
- Therefore, the final spinel composition not only depends on the melt chemistry but is also strongly dependant on the host rock composition. The melt-rock reaction process then moves the spinel composition along the equilibrium reaction surface.

6.6 REFERENCES

- Allan, J. F., Sack, R. O. and Batiza, R. (1988). Cr-Rich spinels as petrogenetic indicators - Morb-type lavas from the Lamont Seamount Chain, Eastern Pacific. *American Mineralogist* 73, 741-753.
- Arai, S. (1992). Chemistry of chromian spinel in volcanic rocks as a potential guide to magma chemistry. *Mineralogical Magazine* 56, 173-184.
- Arai, S. (1994). Characterization of spinel peridotites by olivine-spinel compositional relationships: Review and interpretation. *Chemical Geology* 113, 191-204.

CHAPTER 6

- Bai, Q. and Kohlstedt, D. L. (1992). High-temperature creep of olivine single crystals. 2. Dislocation structures. *Tectonophysics* 206, 1-29.
- Bai, Q., Mackwell, S. J. and Kohlstedt, D. L. (1991). High-temperature creep of olivine single crystals. 1. Mechanical results for buffered samples. *Journal of Geophysical Research-Solid Earth and Planets* 96, 2441-2463.
- Ballhaus, C. (1991). Correction - High-pressure experimental calibration of the olivine-orthopyroxene-spinel oxygen geobarometer - Implications for the oxidation-state of the upper-mantle. *Contributions to Mineralogy and Petrology* 108, 384-384.
- Ballhaus, C. (1993). Redox states of lithospheric and asthenospheric upper-mantle. *Contributions to Mineralogy and Petrology* 114, 331-348.
- Ballhaus, C. (1995). Is the upper-mantle metal-saturated. *Earth and Planetary Science Letters* 132, 75-86.
- Ballhaus, C., Berry, R. F. and Green, D. H. (1990). Oxygen fugacity controls in the Earth's upper mantle. *Nature* 348, 437-440.
- Ballhaus, C., Berry, R. F. and Green, D. H. (1991). High-pressure experimental calibration of the olivine-ortho-pyroxene-spinel oxygen geobarometer - Implications for the oxidation-state of the upper mantle. *Contributions to Mineralogy and Petrology* 107, 27-40.
- Ballhaus, C., Berry, R. F. and Green, D. H. (1994). High-pressure experimental calibration of the olivine-ortho-pyroxene-spinel oxygen geobarometer - Implications for the oxidation-state of the upper-mantle (Vol 107, Pg 27, 1991). *Contributions to Mineralogy and Petrology* 118, 109-109.
- Ballhaus, C. and Frost, B. R. (1994). The generation of oxidized CO₂-bearing basaltic melts from reduced CH₄-bearing upper-mantle sources. *Geochimica Et Cosmochimica Acta* 58, 4931-4940.
- Barnes, S. J. and Roeder, P. L. (2001). The range of spinel compositions in terrestrial mafic and ultramafic rocks. *Journal of Petrology* 42, 2279-2302.
- Beard, J. S. and Tracy, R. J. (2002). Spinels and other oxides in Mn-rich rocks from the Hutter Mine, Pittsylvania County, Virginia, U.S.A.: Implications for miscibility and solvus relations among jacobsonite, galaxite, and magnetite. *American Mineralogist* 87, 690-698.
- Canil, D. (2002). Vanadium in peridotites, mantle redox and tectonic environments: Archean to present. *Earth and Planetary Science Letters* 195, 75-90.
- Canil, D., O'Neill, H. S., Pearson, D. G., Rudnick, R. L., McDonough, W. F. and Carswell, D. A. (1994). Ferric iron in peridotites and mantle oxidation states. *Earth and Planetary Science Letters* 123, 205-220.
- Canil, D. and O'Neill, H. S. C. (1996). Distribution of ferric iron in some upper-mantle assemblages. *Journal of Petrology* 37, 609-635.
- Cannat, M., Bideau, D. and Hebert, R. (1990). Plastic-deformation and magmatic impregnation in serpentinized ultramafic rocks from the Garrett Transform-Fault (East Pacific Rise). *Earth and Planetary Science Letters* 101, 216-232.

CHAPTER 6

- Cannat, M. and Casey, J. F. (1995). An ultramafic lift at the Mid-Atlantic Ridge: successive stages of magmatism in serpentinized peridotites from the 15°N region. In: Vissers, R. L. M. & Nicolas, A. (eds.) *Mantle and lower crust exposed in oceanic ridges and in ophiolites*. 6. Dordrecht/Boston/London: Kluwer Academic Publishers, 5-34.
- Cannat, M. and Seyler, M. (1995). Transform tectonics, metamorphic plagioclase and amphibolitization in ultramafic rocks of the Vema Transform-Fault (Atlantic-Ocean). *Earth and Planetary Science Letters* 133, 283-298.
- Dick, H. J. B. (1989). Abyssal peridotites, very slow spreading ridges and ocean ridge magmatism. In: Saunders, A. D. & Norry, M. J. (eds.) *Magmatism in the ocean basins*. Geol. Soc. London Spec. Pub. 42. 71-105.
- Dick, H. J. B. and Bullen, T. (1984). Chromian spinel as a petrogenetic indicator in abyssal and alpine-type peridotites and spatially associated lavas. *Contributions to Mineralogy and Petrology* 86, 54-76.
- Dick, H. J. B., Fisher, R. L. and Bryan, W. B. (1984). Mineralogic variability of the uppermost mantle along mid-ocean ridges. *Earth and Planetary Science Letters* 69, 88-106.
- Droop, G. T. R. (1987). A general equation for estimating Fe³⁺ concentrations in ferromagnesian silicates and oxides from microprobe analyses, using stoichiometric criteria. *Mineralogical Magazine* 51, 431-435.
- Dyar, M. D., McGuire, A. V. and Ziegler, R. D. (1989). Redox equilibria and crystal-chemistry of coexisting minerals from spinel Iherzolite mantle xenoliths. *American Mineralogist* 74, 969-980.
- Edwards, S. J., Falloon, T. J., Malpas, J. and Pedersen, R. B. (1996). A review of the petrology of harzburgites at Hess Deep and Garrett Deep: implications for mantle processes beneath segments of the East Pacific Rise. In: MacLeod, C. J., Tyler, P. A. & Walker, C. L. (eds.) *Tectonic, hydrothermal and biological segmentation of Mid Ocean Ridges*. 118. London: Geological Society of London Special Publication, 143-156.
- Edwards, S. J. and Malpas, J. (1996). Melt-peridotite interactions in shallow mantle at the East Pacific rise: Evidence from ODP site 895 (Hess deep). *Mineralogical Magazine* 60, 191-206.
- Evans, B. W. and Frost, B. R. (1975). Chrome spinel in progressive metamorphism - a preliminary analysis. *Geochimica Et Cosmochimica Acta* 39, 959-972.
- Hamlyn, P. R. and Bonatti, E. (1980). Petrology of mantle-derived ultramafics from the Owen Fracture-Zone, Northwest Indian-Ocean - implications for the nature of the oceanic upper mantle. *Earth and Planetary Science Letters* 48, 65-79.
- Hellebrand, E., Snow, J. E., Dick, H. J. B. and Hofmann, A. W. (2001). Coupled major and trace elements as indicators of the extent of melting in mid-ocean-ridge peridotites. *Nature* 410, 677-681.
- Hellebrand, E. W., Snow, J. E., Devey, C. W., Haase, K. M. and Hofmann, A. W. (1998). Cumulate trace element signature in diopsides from plagioclase peridotites from Molloy Ridge, MAR 79°N. *AGU Spring Meeting*. Boston: Eos Transactions, V41A-04.

CHAPTER 6

- Hill, R. and Roeder, P. L. (1974). The crystallization of spinel from basaltic liquid as a function of oxygen fugacity. *Journal of Geology* 80, 709-729.
- Irvine, T. N. (1965). Chromian spinel as a petrogenetic indicator. Part 1. Theory. *Canadian Journal of Earth Sciences* 2, 648-672.
- Irvine, T. N. (1967). Chromian spinel as petrogenetic indicator. Part 2. Petrological applications. *Canadian Journal of Earth Sciences* 4, 71-103.
- Kelemen, P. B., Shimizu, N. and Salters, V. J. M. (1995). Extraction of mid-ocean-ridge basalt from the upwelling mantle by focused flow of melt in dunite channels. *Nature* 375, 747-753.
- Kimball, K. L. (1990). Effects of hydrothermal alteration on the composition of chromian spinels. *Contributions to Mineralogy and Petrology* 105, 337-346.
- Kornprobst, J. and Tabit, A. (1988). Plagioclase-bearing ultramafic tectonites from the Galicia Margin (Leg 103, Site 637): comparison of their origin and evolution with low-pressure ultramafic bodies in Western Europe. In: Boillot, G. & Winterer, E. L. (eds.) *Proceedings of the Ocean Drilling Program, Scientific Results*. 103. College Station, Texas: Ocean Drilling Program, 253-268.
- Kriegsman, L. M. and Hensen, B. J. (1998). Back reaction between restite and melt: Implications for geothermobarometry and pressure-temperature paths. *Geology* 26, 1111-1114.
- Lavina, B., Princivalle, F. and Della Giusta, A. (2005). Controlled time-temperature oxidation reaction in a synthetic Mg-hercynite. *Physics and Chemistry of Minerals* 32, 83-88.
- Liermann, H. P. and Ganguly, J. (2003). Fe²⁺-Mg fractionation between orthopyroxene and spinel: experimental calibration in the system FeO-MgO-Al₂O₃-Cr₂O₃-SiO₂, and applications. *Contributions to Mineralogy and Petrology* 145, 217-227.
- Lindsley, D. H. (1991). Experimental studies of oxide minerals. *Reviews in Mineralogy* 25, 69-106.
- Lindsley, D. H. and Frost, B. R. (1992). Equilibria among Fe-Ti oxides, pyroxenes, olivine, and quartz: Part I. Theory. *American Mineralogist* 77, 987-1003.
- Mattioli, G. S. and Wood, B. J. (1986). Upper mantle fugacity recorded by spinel lherzolites. *Nature* 322, 626-628.
- McGuire, A. V., Dyar, M. D. and Nielson, J. E. (1991). Metasomatic oxidation of upper mantle peridotite. *Contributions to Mineralogy and Petrology* 109, 252-264.
- Mellini, M., Rumori, C. and Viti, C. (2005). Hydrothermally reset magmatic spinels in retrograde serpentinites: formation of "ferritchromit" rims and chlorite aureoles. *Contributions to Mineralogy and Petrology* 149, 266-275.
- Natland, J. H. and Dick, H. J. B. (2001). Formation of the lower ocean crust and the crystallization of gabbroic cumulates at a very slowly spreading ridge. *Journal of Volcanology and Geothermal Research* 110, 191-233.
- Nicholls, I. A. (1977). The calculation of mineral compositions and modes of olivine-two pyroxene-spinel assemblages. *Contributions to Mineralogy and Petrology* 60, 199-142.

CHAPTER 6

- O'Neill, H. S. C. and Navrotsky, A. (1983). Simple spinels - crystallographic parameters, cation radii, lattice energies, and cation distribution. *American Mineralogist* 68, 181-194.
- O'Neill, H. S. C. and Navrotsky, A. (1984). Cation distributions and thermodynamic properties of binary spinel solid-solutions. *American Mineralogist* 69, 733-753.
- Obata, M. (1980). The Ronda Peridotite - garnet-lherzolite, spinel-lherzolite, and plagioclase-lherzolite facies and the P-T trajectories of a high-temperature mantle intrusion. *Journal of Petrology* 21, 533-572.
- Ozawa, K. (1984). Olivine-spinel geospeedometry - analysis of diffusion-controlled Mg-Fe²⁺ exchange. *Geochimica Et Cosmochimica Acta* 48, 2597-2611.
- Ozawa, K. (1989). Stress-induced Al-Cr-zoning of spinel in deformed peridotites. *Nature* 338, 141-144.
- Papike, J. J., Karner, J. M. and Shearer, C. K. (2004). Comparative planetary mineralogy: V/(Cr+Al) systematics in chromite as an indicator of relative oxygen fugacity. *American Mineralogist* 89, 1557-1560.
- Papike, J. J., Karner, J. M. and Shearer, C. K. (2005). Comparative planetary mineralogy: Valence state partitioning of Cr, Fe, Ti, and V among crystallographic sites in olivine, pyroxene, and spinel from planetary basalts. *American Mineralogist* 90, 277-290.
- Parkinson, I. J. and Pearce, J. A. (1998). Peridotites from the Izu-Bonin-Mariana forearc (ODP Leg 125): Evidence for mantle melting and melt-mantle interaction in a supra-subduction zone setting. *Journal of Petrology* 39, 1577-1618.
- Pasteris, J. D. (1982). Representation of compositions in complex titanian spinels and application to the De Beers kimberlite. *American Mineralogist* 67, 244-250.
- Pearce, J. A., Barker, P. F., Edwards, S. J., Parkinson, I. J. and Leat, P. T. (2000). Geochemistry and tectonic significance of peridotites from the South Sandwich arc-basin system, South Atlantic. *Contributions to Mineralogy and Petrology* 139, 36-53.
- Rampone, E., Piccardo, G. B., Vannucci, R., Bottazzi, P. and Ottolini, L. (1993). Subsolidus reactions monitored by trace-element partitioning - the spinel-facies to plagioclase-facies transition in mantle peridotites. *Contributions to Mineralogy and Petrology* 115, 1-17.
- Ringwood, A. E. (1975). *Composition and petrology of the earth's mantle*. New York: McGraw-Hill Book Co., p. 618.
- Roeder, P. L. and Reynolds, I. (1991). Crystallization of chromite and chromium solubility in basaltic melts. *Journal of Petrology* 32, 909-934.
- Sack, R. O. (1982). Spinel as petrogenetic indicators: Activity-composition relations at low pressure. *Contributions to Mineralogy and Petrology* 71, 169-186.
- Sen, G., Yang, H. J. and Ducea, M. (2003). Anomalous isotopes and trace element zoning in plagioclase peridotite xenoliths of Oahu (Hawaii): implications for the Hawaiian plume. *Earth and Planetary Science Letters* 207, 23-38.

CHAPTER 6

- Seyler, M. and Bonatti, E. (1997). Regional-scale melt-rock interaction in lherzolitic mantle in the Romanche Fracture Zone (Atlantic Ocean). *Earth and Planetary Science Letters* 146, 273-287.
- Sobolev, A. V., Hofmann, A. W., Kuzmin, D. V., Yaxley, G. M., Arndt, N. T., Chung, S.-L., Danyushevsky, L. V., Elliott, T., Frey, F. A., Garcia, M. O., Gurenko, A. A., Kamenetsky, V. S., Kerr, A. C., Krivolutszkaya, N. A., Matvienkov, V. V., Nikogosian, I. K., Rocholl, A., Sigurdsson, I. A., Sushchevskaya, N. M. and Teklay, M. (2007). The amount of recycled crust in sources of mantle-derived melts. *Science* 316, 412-417.
- Suhr, G. and Robinson, P. T. (1994). Origin of mineral chemical stratification in the mantle section of the Table Mountain Massif (Bay of Islands Ophiolite, Newfoundland, Canada). *Lithos* 31, 81-102.
- Tartarotti, P., Susini, S., Nimis, P. and Ottolini, L. (2002). Melt migration in the upper mantle along the Romanche Fracture Zone (Equatorial Atlantic). *Lithos* 63, 125-149.
- Taylor, W. R. and Green, D. H. (1988). Measurement of reduced peridotite C-O-H solidus and implications for redox melting of the mantle. *Nature* 332, 349-352.
- Thayer, T. P. (1956). Mineralogy and geology of chromium. In: Udy, M. J. (ed.) *Chromium*. American Chemical Society Monograph 132.
- Toppani, A. and Libourel, G. (2003). Factors controlling compositions of cosmic spinels: application to atmospheric entry conditions of meteoritic materials. *Geochimica Et Cosmochimica Acta* 67, 4621-4638.
- Trestman-Matts, A., Dorris, S. E., Kumarakrishnan, S. and Mason, T. O. (1983). Thermoelectric determination of cation distributions in $\text{Fe}_3\text{O}_4\text{-Fe}_2\text{TiO}_4$. *Journal of the American Ceramic Society* 66, 829-834.
- von der Handt, A., Seyler, M., Snow, J. E. and Hellebrand, E. (2004). Geochemistry of plagioclase peridotites from the Southwest Indian Ridge (63° - 65°). *Geochimica Et Cosmochimica Acta* 68, A706.
- Wood, B. J., Bryndzia, L. T. and Johnson, K. E. (1990). Mantle oxidation state and its relationship to tectonic environment and fluid speciation. *Science* 248, 337-344.
- Woodland, A. B., Kornprobst, J., McPherson, E., Bodinier, J. L. and Menzies, M. A. (1996). Metasomatic interactions in the lithospheric mantle: Petrologic evidence from the Lherz massif, French Pyrenees. *Chemical Geology* 134, 83-112.
- Woodland, A. B., Kornprobst, J. and Tabit, A. (2006). Ferric iron in orogenic lherzolite massifs and controls of oxygen fugacity in the upper mantle. *Lithos* 89, 222-241.
- Woodland, A. B., Kornprobst, J. and Wood, B. J. (1992). Oxygen thermobarometry of orogenic lherzolite massifs. *Journal of Petrology* 33, 203-230.
- Woodland, A. B. and Wood, B. J. (1994). Fe_3O_4 activities in Fe-Ti spinel solid-solutions. *European Journal of Mineralogy* 6, 23-37.
- Zhou, M. F., Robinson, P. T., Malpas, J. and Li, Z. (1996). Podiform chromitites in the Luobusa Ophiolite (Southern Tibet): Implications for melt-rock interaction and chromite segregation in the upper mantle. *Journal of Petrology* 37, 3-21.

Table 6-2: Representative EPMA analyses of PS59-235-spinels in [wt%]

Sample	235-2a		235-2b		235-4		235-9		235-11		235-12		235-17		235-18		235-19		
	Group	P1	P2-B	P2-A	P1	P2-B	P1	S1	P2-B	S1	P2-B	S1	P2-B	S1	P2-B	S1	P2-B	S1	
n	34	30	58	32	22	74	36	28	67	36	28	36	28	67	36	28	67	36	
SiO ₂	0.06 ± 0.02	0.07 ± 0.02	0.06 ± 0.01	0.05 ± 0.01	0.06 ± 0.01	0.05 ± 0.01	0.07 ± 0.01	0.06 ± 0.01	0.06 ± 0.01	0.06 ± 0.01	0.05 ± 0.01	0.07 ± 0.01	0.06 ± 0.01	0.07 ± 0.01	0.06 ± 0.01	0.05 ± 0.01	0.06 ± 0.01	0.07 ± 0.01	0.06 ± 0.01
TiO ₂	0.07 ± 0.03	0.20 ± 0.03	0.27 ± 0.03	0.08 ± 0.01	0.07 ± 0.02	0.20 ± 0.04	0.05 ± 0.02	0.07 ± 0.02	0.20 ± 0.04	0.05 ± 0.02	0.20 ± 0.04	0.05 ± 0.02	0.20 ± 0.04	0.05 ± 0.02	0.20 ± 0.04	0.05 ± 0.02	0.20 ± 0.04	0.05 ± 0.02	0.20 ± 0.04
Cr ₂ O ₃	19.2 ± 4.5	32.0 ± 4.0	25.5 ± 2.4	19.5 ± 0.9	11.5 ± 0.4	29.2 ± 2.5	13.3 ± 0.5	11.5 ± 0.4	29.2 ± 2.5	13.3 ± 0.5	30.8 ± 1.7	13.3 ± 0.5	30.8 ± 1.7	13.3 ± 0.5	30.8 ± 1.7	13.3 ± 0.5	30.8 ± 1.7	13.3 ± 0.5	30.8 ± 1.7
Al ₂ O ₃	48.7 ± 4.6	35.2 ± 4.0	40.9 ± 2.5	48.7 ± 0.9	56.1 ± 0.5	38.1 ± 2.5	54.3 ± 0.6	56.1 ± 0.5	38.1 ± 2.5	54.3 ± 0.6	35.4 ± 1.8	54.3 ± 0.6	35.4 ± 1.8	54.3 ± 0.6	35.4 ± 1.8	54.3 ± 0.6	35.4 ± 1.8	54.3 ± 0.6	35.4 ± 1.8
V ₂ O ₃	0.11 ± 0.02	0.19 ± 0.02	0.22 ± 0.02	0.07 ± 0.02	0.06 ± 0.01	0.16 ± 0.02	0.06 ± 0.02	0.06 ± 0.01	0.16 ± 0.02	0.06 ± 0.02	0.18 ± 0.02	0.06 ± 0.02	0.18 ± 0.02	0.06 ± 0.02	0.18 ± 0.02	0.06 ± 0.02	0.18 ± 0.02	0.06 ± 0.02	0.18 ± 0.02
FeO _{tot}	13.3 ± 1.3	17.7 ± 1.2	16.3 ± 1.1	12.1 ± 0.4	11.2 ± 0.3	16.4 ± 0.9	11.2 ± 0.4	11.2 ± 0.3	16.4 ± 0.9	11.2 ± 0.3	19.0 ± 1.6	11.2 ± 0.4	19.0 ± 1.6	11.2 ± 0.3	19.0 ± 1.6	11.2 ± 0.4	19.0 ± 1.6	11.2 ± 0.3	19.0 ± 1.6
MgO	17.9 ± 1.0	14.1 ± 1.0	16.0 ± 0.8	18.7 ± 0.3	20.0 ± 0.2	15.2 ± 0.7	19.6 ± 0.3	20.0 ± 0.2	15.2 ± 0.7	19.6 ± 0.3	13.8 ± 1.0	19.6 ± 0.3	13.8 ± 1.0	19.6 ± 0.3	13.8 ± 1.0	19.6 ± 0.3	13.8 ± 1.0	19.6 ± 0.3	13.8 ± 1.0
MnO	0.12 ± 0.03	0.19 ± 0.03	0.17 ± 0.02	0.11 ± 0.01	0.10 ± 0.01	0.17 ± 0.02	0.09 ± 0.01	0.10 ± 0.01	0.17 ± 0.02	0.09 ± 0.01	0.20 ± 0.02	0.09 ± 0.01	0.20 ± 0.02	0.09 ± 0.01	0.20 ± 0.02	0.09 ± 0.01	0.20 ± 0.02	0.09 ± 0.01	0.20 ± 0.02
CaO	0.02 ± 0.01	0.03 ± 0.03	0.01 ± 0.01	0.01 ± 0.01	0.01 ± 0.01	0.02 ± 0.02	0.01 ± 0.01	0.01 ± 0.01	0.02 ± 0.02	0.01 ± 0.01	0.02 ± 0.03	0.01 ± 0.01	0.02 ± 0.03	0.01 ± 0.01	0.02 ± 0.03	0.01 ± 0.01	0.02 ± 0.03	0.01 ± 0.01	0.02 ± 0.03
CoO	0.03 ± 0.02	0.04 ± 0.01	0.03 ± 0.01	0.03 ± 0.01	0.03 ± 0.01	0.04 ± 0.01	0.03 ± 0.01	0.03 ± 0.01	0.04 ± 0.01	0.03 ± 0.01	0.04 ± 0.02	0.03 ± 0.01	0.04 ± 0.02	0.03 ± 0.01	0.04 ± 0.02	0.03 ± 0.01	0.04 ± 0.02	0.03 ± 0.01	0.04 ± 0.02
NiO	0.25 ± 0.05	0.12 ± 0.04	0.21 ± 0.03	0.26 ± 0.02	0.35 ± 0.02	0.16 ± 0.03	0.33 ± 0.02	0.35 ± 0.02	0.16 ± 0.03	0.33 ± 0.02	0.13 ± 0.02	0.33 ± 0.02	0.13 ± 0.02	0.33 ± 0.02	0.13 ± 0.02	0.33 ± 0.02	0.13 ± 0.02	0.33 ± 0.02	0.13 ± 0.02
ZnO	0.26 ± 0.03	0.29 ± 0.03	0.20 ± 0.03	0.17 ± 0.03	0.15 ± 0.01	0.24 ± 0.07	0.18 ± 0.04	0.15 ± 0.01	0.24 ± 0.07	0.18 ± 0.04	0.32 ± 0.08	0.18 ± 0.04	0.32 ± 0.08	0.18 ± 0.04	0.32 ± 0.08	0.18 ± 0.04	0.32 ± 0.08	0.18 ± 0.04	0.32 ± 0.08
Total	100.0 ± 0.3	100.1 ± 0.3	99.9 ± 0.2	99.8 ± 0.3	99.6 ± 0.5	99.9 ± 0.3	99.3 ± 0.2	99.6 ± 0.5	99.9 ± 0.3	99.3 ± 0.2	100.2 ± 0.3	99.3 ± 0.2	100.2 ± 0.3	99.3 ± 0.2	100.2 ± 0.3	99.3 ± 0.2	100.2 ± 0.3	99.3 ± 0.2	100.1 ± 0.4
Cr/(Cr+Al)	0.210 ± 0.056	0.381 ± 0.054	0.295 ± 0.033	0.211 ± 0.011	0.121 ± 0.004	0.340 ± 0.033	0.141 ± 0.006	0.121 ± 0.004	0.340 ± 0.033	0.141 ± 0.006	0.368 ± 0.024	0.141 ± 0.006	0.368 ± 0.024	0.141 ± 0.006	0.368 ± 0.024	0.141 ± 0.006	0.368 ± 0.024	0.141 ± 0.006	0.368 ± 0.024
Mg/(Mg+Fe ²⁺)	0.730 ± 0.029	0.614 ± 0.033	0.673 ± 0.025	0.759 ± 0.009	0.784 ± 0.006	0.651 ± 0.021	0.780 ± 0.010	0.784 ± 0.006	0.651 ± 0.021	0.780 ± 0.010	0.602 ± 0.035	0.780 ± 0.010	0.602 ± 0.035	0.780 ± 0.010	0.602 ± 0.035	0.780 ± 0.010	0.602 ± 0.035	0.780 ± 0.010	0.602 ± 0.035
FeO*	11.81 ± 0.99	15.77 ± 1.07	13.80 ± 0.85	10.61 ± 0.37	9.81 ± 0.25	14.47 ± 0.73	9.89 ± 0.45	9.81 ± 0.25	14.47 ± 0.73	9.89 ± 0.45	16.25 ± 1.26	9.89 ± 0.45	16.25 ± 1.26	9.89 ± 0.45	16.25 ± 1.26	9.89 ± 0.45	16.25 ± 1.26	9.89 ± 0.45	16.25 ± 1.26
Fe ₂ O ₃ *	1.62 ± 0.36	2.16 ± 0.27	2.79 ± 0.36	1.61 ± 0.18	1.54 ± 0.16	2.11 ± 0.35	1.47 ± 0.41	1.54 ± 0.16	2.11 ± 0.35	1.47 ± 0.41	3.09 ± 0.51	1.47 ± 0.41	3.09 ± 0.51	1.47 ± 0.41	3.09 ± 0.51	1.47 ± 0.41	3.09 ± 0.51	1.47 ± 0.41	3.09 ± 0.51

±: one standard deviation n: number of analyses

*: FeO and Fe₂O₃ calculated after Droop (1987)

Table 6-2 (continued): Representative EPMA analyses of PS59-235-spinels in [wt%]

Sample	235-20		235-24		235-27		235-134a-I		235-134a-II		235-134b		235-134c	
	Group	S1	P2-A	P2-B	P1	P2-B	P1	P2-B	P2-B	P1	P2-B	P1	P2-B	P2-B
n	14	132	71	109	60	148	60	148	32	60	32	60	32	
SiO ₂	0.09 ± 0.01	0.06 ± 0.01	0.06 ± 0.02	0.10 ± 0.02	0.05 ± 0.01	0.09 ± 0.01	0.05 ± 0.01	0.09 ± 0.01	0.05 ± 0.01	0.05 ± 0.01	0.05 ± 0.01	0.05 ± 0.01	0.05 ± 0.01	
TiO ₂	0.05 ± 0.02	0.35 ± 0.06	0.26 ± 0.05	0.25 ± 0.04	0.09 ± 0.05	0.15 ± 0.03	0.09 ± 0.05	0.15 ± 0.03	0.09 ± 0.05	0.15 ± 0.03	0.09 ± 0.05	0.15 ± 0.03	0.09 ± 0.05	
Cr ₂ O ₃	15.1 ± 1.2	26.7 ± 3.5	33.6 ± 3.2	30.8 ± 2.8	20.8 ± 5.5	18.6 ± 3.3	20.8 ± 5.5	18.6 ± 3.3	20.8 ± 5.5	18.6 ± 3.3	26.1 ± 4.2	20.8 ± 5.5	26.1 ± 4.2	
Al ₂ O ₃	53.1 ± 1.2	39.2 ± 3.6	32.8 ± 3.3	37.0 ± 2.9	46.3 ± 5.7	49.5 ± 3.3	46.3 ± 5.7	49.5 ± 3.3	46.3 ± 5.7	49.5 ± 3.3	40.9 ± 4.4	46.3 ± 5.7	40.9 ± 4.4	
V ₂ O ₃	0.10 ± 0.01	0.27 ± 0.04	0.18 ± 0.03	0.18 ± 0.02	0.10 ± 0.02	0.12 ± 0.02	0.10 ± 0.02	0.12 ± 0.02	0.10 ± 0.02	0.12 ± 0.02	0.12 ± 0.03	0.10 ± 0.02	0.12 ± 0.03	
FeO _{tot}	11.7 ± 0.2	16.7 ± 1.4	18.9 ± 1.6	15.9 ± 1.1	13.6 ± 1.7	12.0 ± 0.9	13.6 ± 1.7	12.0 ± 0.9	13.6 ± 1.7	12.0 ± 0.9	15.4 ± 1.4	13.6 ± 1.7	15.4 ± 1.4	
MgO	19.2 ± 0.2	15.3 ± 1.0	13.5 ± 1.2	15.4 ± 0.9	17.7 ± 1.4	18.6 ± 0.8	17.7 ± 1.4	18.6 ± 0.8	17.7 ± 1.4	18.6 ± 0.8	16.2 ± 1.2	17.7 ± 1.4	16.2 ± 1.2	
MnO	0.11 ± 0.01	0.16 ± 0.02	0.19 ± 0.03	0.15 ± 0.02	0.11 ± 0.02	0.11 ± 0.02	0.11 ± 0.02	0.11 ± 0.02	0.11 ± 0.02	0.11 ± 0.02	0.12 ± 0.02	0.11 ± 0.02	0.12 ± 0.02	
CaO	0.01 ± 0.01	0.02 ± 0.03	0.01 ± 0.01	0.04 ± 0.03	0.02 ± 0.02	0.06 ± 0.02	0.02 ± 0.02	0.06 ± 0.02	0.02 ± 0.02	0.06 ± 0.02	0.01 ± 0.01	0.02 ± 0.02	0.01 ± 0.01	
CoO	0.05 ± 0.01	0.03 ± 0.01	0.04 ± 0.01	0.06 ± 0.02	0.03 ± 0.01	0.04 ± 0.02	0.03 ± 0.01	0.04 ± 0.02	0.03 ± 0.01	0.04 ± 0.02	0.04 ± 0.02	0.03 ± 0.01	0.04 ± 0.02	
NiO	0.31 ± 0.02	0.20 ± 0.04	0.13 ± 0.03	0.15 ± 0.03	0.24 ± 0.06	0.24 ± 0.05	0.24 ± 0.06	0.24 ± 0.05	0.24 ± 0.06	0.24 ± 0.05	0.19 ± 0.04	0.24 ± 0.06	0.19 ± 0.04	
ZnO	0.16 ± 0.04	0.18 ± 0.03	0.26 ± 0.09	0.18 ± 0.03	0.23 ± 0.02	0.13 ± 0.02	0.23 ± 0.02	0.13 ± 0.02	0.23 ± 0.02	0.13 ± 0.02	0.21 ± 0.03	0.23 ± 0.02	0.21 ± 0.03	
Total	100.0 ± 0.3	99.2 ± 0.2	99.8 ± 0.3	100.2 ± 0.3	99.3 ± 0.3	99.7 ± 0.3	99.3 ± 0.3	99.7 ± 0.3	99.3 ± 0.3	99.7 ± 0.3	99.4 ± 0.4	99.3 ± 0.3	99.4 ± 0.4	
Cr/(Cr+Al)	0.160 ± 0.014	0.314 ± 0.048	0.408 ± 0.048	0.360 ± 0.039	0.234 ± 0.071	0.202 ± 0.039	0.234 ± 0.071	0.202 ± 0.039	0.234 ± 0.071	0.202 ± 0.039	0.301 ± 0.057	0.234 ± 0.071	0.301 ± 0.057	
Mg/(Mg+Fe ²⁺)	0.762 ± 0.006	0.655 ± 0.031	0.594 ± 0.042	0.659 ± 0.028	0.731 ± 0.040	0.749 ± 0.022	0.731 ± 0.040	0.749 ± 0.022	0.731 ± 0.040	0.749 ± 0.022	0.685 ± 0.036	0.731 ± 0.040	0.685 ± 0.036	
FeO*	10.65 ± 0.29	14.38 ± 1.03	16.36 ± 1.36	14.21 ± 0.97	11.59 ± 1.39	11.06 ± 0.81	11.59 ± 1.39	11.06 ± 0.81	11.59 ± 1.39	11.06 ± 0.81	13.24 ± 1.20	11.59 ± 1.39	13.24 ± 1.20	
Fe ₂ O ₃ *	1.21 ± 0.25	2.54 ± 0.49	2.78 ± 0.44	1.86 ± 0.34	2.18 ± 0.39	1.11 ± 0.33	2.18 ± 0.39	1.11 ± 0.33	2.18 ± 0.39	1.11 ± 0.33	2.35 ± 0.30	2.18 ± 0.39	2.35 ± 0.30	

±: one standard deviation n: number of analyses

*: FeO and Fe₂O₃ calculated after Droop (1987)

Table 6-3: Representative EPMA analyses of PS59-235-olivines in [wt%]

Sample	235-2a	235-2b	235-4	235-9	235-11	235-12	235-17	235-18	235-19
Group	P1	P2-B	P2-A	P1	S1	P2-B	S1	P2-B	P2-A
n	9	9	12	9	9	9	16	9	51
SiO ₂	40.8 ± 0.1	40.7 ± 0.1	40.6 ± 0.1	40.8 ± 0.1	40.6 ± 0.1	40.8 ± 0.1	40.2 ± 0.2	40.6 ± 0.2	40.8 ± 0.2
Al ₂ O ₃	0.01 ± 0.01	0.00 ± 0.01	0.01 ± 0.01	0.01 ± 0.01	0.01 ± 0.01	0.00 ± 0.00	0.01 ± 0.01	0.00 ± 0.00	0.01 ± 0.01
Cr ₂ O ₃	0.00 ± 0.00	0.01 ± 0.00	0.00 ± 0.00	0.01 ± 0.01	0.01 ± 0.00	0.00 ± 0.00	0.02 ± 0.02	0.00 ± 0.00	0.03 ± 0.02
FeO	9.25 ± 0.10	9.43 ± 0.15	9.78 ± 0.16	8.89 ± 0.12	9.37 ± 0.04	9.24 ± 0.14	9.50 ± 0.18	9.06 ± 0.13	9.08 ± 0.27
MgO	49.3 ± 0.1	49.2 ± 0.1	48.9 ± 0.2	49.6 ± 0.1	49.2 ± 0.1	49.4 ± 0.1	50.1 ± 0.2	49.2 ± 0.1	49.0 ± 0.4
MnO	0.13 ± 0.00	0.14 ± 0.00	0.15 ± 0.01	0.13 ± 0.01	0.14 ± 0.00	0.14 ± 0.00	0.15 ± 0.03	0.13 ± 0.00	0.14 ± 0.01
CaO	0.04 ± 0.01	0.05 ± 0.02	0.03 ± 0.01	0.05 ± 0.01	0.06 ± 0.01	0.04 ± 0.01	0.05 ± 0.02	0.03 ± 0.01	0.04 ± 0.01
NiO	0.38 ± 0.00	0.38 ± 0.01	0.36 ± 0.01	0.37 ± 0.01	0.37 ± 0.01	0.38 ± 0.01	0.37 ± 0.04	0.37 ± 0.00	0.35 ± 0.01
Total	99.9 ± 0.2	99.9 ± 0.2	99.8 ± 0.1	99.9 ± 0.1	99.8 ± 0.2	99.9 ± 0.1	100.4 ± 0.4	99.4 ± 0.4	99.5 ± 0.3
Mg/(Mg+Fe)	0.905 ± 0.001	0.903 ± 0.002	0.899 ± 0.002	0.909 ± 0.001	0.903 ± 0.000	0.905 ± 0.001	0.904 ± 0.002	0.906 ± 0.001	0.906 ± 0.003
Fe/(Fe+Mg)	0.095 ± 0.001	0.097 ± 0.002	0.101 ± 0.002	0.091 ± 0.001	0.097 ± 0.000	0.095 ± 0.001	0.096 ± 0.002	0.094 ± 0.001	0.094 ± 0.003

±: one standard deviation n: number of analyses

Table 6-3 (continued): Representative EPMA analyses of PS59-235-olivines in [wt%]

Sample	235-20	235-24	235-27	235-134a-I	235-134a-II	235-134b	235-134c
Group	S1	P2-A	P2-B	P2-B	P2-B	P1	P2-B
n	23	9	9	39	11	9	9
SiO ₂	40.9 ± 0.2	40.6 ± 0.4	40.6 ± 0.1	40.8 ± 0.2	40.6 ± 0.2	40.6 ± 0.1	40.6 ± 0.1
Al ₂ O ₃	0.01 ± 0.00	0.00 ± 0.01	0.01 ± 0.01	0.01 ± 0.02	0.04 ± 0.09	0.00 ± 0.00	0.00 ± 0.01
Cr ₂ O ₃	0.02 ± 0.01	0.01 ± 0.00	0.01 ± 0.01	0.04 ± 0.04	0.03 ± 0.01	0.00 ± 0.00	0.01 ± 0.00
FeO	9.00 ± 0.27	10.44 ± 0.11	9.34 ± 0.06	9.05 ± 0.29	8.75 ± 0.14	9.42 ± 0.10	9.37 ± 0.10
MgO	48.6 ± 0.3	48.6 ± 0.3	49.1 ± 0.1	48.9 ± 0.4	49.1 ± 0.2	49.1 ± 0.1	49.1 ± 0.2
MnO	0.13 ± 0.01	0.16 ± 0.01	0.13 ± 0.00	0.13 ± 0.02	0.14 ± 0.01	0.14 ± 0.00	0.14 ± 0.00
CaO	0.04 ± 0.01	0.04 ± 0.01	0.04 ± 0.03	0.04 ± 0.01	0.06 ± 0.03	0.05 ± 0.01	0.04 ± 0.01
NiO	0.38 ± 0.01	0.37 ± 0.01	0.39 ± 0.02	0.39 ± 0.02	0.39 ± 0.01	0.38 ± 0.01	0.38 ± 0.01
Total	99.1 ± 0.3	100.2 ± 0.7	99.6 ± 0.1	99.4 ± 0.4	99.1 ± 0.3	99.7 ± 0.2	99.6 ± 0.3
Mg/(Mg+Fe)	0.906 ± 0.003	0.892 ± 0.001	0.904 ± 0.001	0.906 ± 0.003	0.909 ± 0.001	0.903 ± 0.001	0.903 ± 0.001
Fe/(Fe+Mg)	0.094 ± 0.003	0.108 ± 0.001	0.096 ± 0.001	0.094 ± 0.003	0.091 ± 0.001	0.097 ± 0.001	0.097 ± 0.001

±: one standard deviation n: number of analyses

CHAPTER 7

SPINELS IN PLAGIOCLASE PERIDOTITES AS RECORDER OF DISEQUILIBRIUM MELT MIGRATION

7.1 INTRODUCTION

In the previous chapter, it was suggested that the dominant factor for the change in spinel composition is the reactive interaction with a melt. The accompanying equilibration reaction toward higher silica activity at contribution of oxygen fugacity buffer leads to charge balancing reactions in the spinel structure. To a lesser extent, closed-system breakdown of spinel occurs as well, resulting in distinct compositional signatures in spinels expressed by their ferric iron/cation ratios. However, that does not explain the asymmetric zoning seen in spinel. Resetting of trivalent cations is sluggish even at near liquidus temperatures (Ballhaus et al., 1991). The combination of the low lithospheric level of melt stagnation and subsequent fast cooling preserved probably the exact conditions of melt-rock interaction. If the majority of the compositional change in spinel is caused by the reactive interaction with a melt, what does that tell us about melt migration?

At shallow levels, melt transport is considered to take place mostly in melt conduits that isolate the passing melt from surrounding country rock (Spiegelman and Kenyon, 1992). Nevertheless, diffuse porous flow is still active in the upper mantle, either as non-channelized high pressure melt or low pressure melts that are produced close to the crust-mantle boundary (Dijkstra et al., 2003). A variety of models on melt migration and melt-wall rock reactions in the mantle exist, most of which are based on the assumption of an instantaneous local equilibrium (e.g. Kelemen et al., 1992). These local equilibrium models have been thought to provide the most realistic outline for future investigations. The applicability of experimental data (e.g. Kinzler and Grove, 1992, Baker and Stolper, 1994, Baker et al., 1995) as well as computer calculations (e.g. Hirschmann et al., 1999) are based on the assumption of general equilibrium. So far, few observations indicating disequilibrium have been reported in natural

mid-ocean ridge samples, which generally reflect the homogeneous compositions found in plagioclase-free peridotite samples (e.g. Dick, 1989, Hellebrand et al., 2002b).

7.2 DISCUSSION

Plagioclase-bearing abyssal peridotites provide evidence that migrating melts can wet the mantle mineral assemblage even at low pressures. The diffusely dispersed plagioclase in the matrix is generally held to originate from the crystallization of a percolating melt. Since 30 % of all dredged abyssal peridotites contain plagioclase (Dick, 1989), diffuse porous flow appears to be a ubiquitous process at shallow levels. Hence, plagioclase peridotites represent a good opportunity to investigate porous flow in the mantle at low pressures. Here, observations of heterogeneous mineral compositions in abyssal plagioclase peridotites are reported that cast doubt on the assumption of general or local mantle equilibrium during porous melt flow.

Why are these heterogeneities preserved? The steep mineral chemical gradients show that volume diffusion was too slow to equilibrate the minerals on even small scales. This implies relatively rapid uplift rates that are in apparent contradiction to the ultraslow-spreading rate of Gakkel Ridge. Quantitative modelling of the related time scales is not feasible at the current state of research, as interdiffusion coefficients for Cr-Al in spinel are not determined yet and Mg-Fe interdiffusion is strongly dependent on spinel Cr-number (molar $\text{Cr}/(\text{Cr}+\text{Al})$) and oxygen fugacity ($f\text{O}_2$) (Liermann and Ganguly, 2002, Ganguly et al., 2003). Tectonic uplift along fault planes may be one explanation, but time-scales for diffusive homogenization are known experimentally to be in the range of hours (Roeder et al., 2001). The cold thermal regime predicted in most of the slow-spreading environments (Cannat, 1993, Cannat, 1996) and specifically at the sample location (Montesi and Behn, 2007) may cool the country rock sufficiently to prevent efficient re-equilibration.

Melt reaction effects are easier to observe within the plagioclase stability field than at higher pressures. Melt stagnation at spinel-facies conditions has been described based on textures (Seyler et al., 2001, Brunelli et al., 2006) and hump-shaped rare earth element patterns in interstitial clinopyroxene (Hellebrand et al., 2002a). However, in most cases no chemical

gradient to the composition of the wall rock is present (Seyler et al., 2001). In contrast, the preference of plagioclase for light rare earth elements over the heavy rare earth elements as well as for Al enhance the chemical and mineralogical differences with the original residual peridotite and make disequilibrium features more readily observable.

These features suggest the existence of a disequilibrium zone at least at the top of the mid-ocean ridge melting column, which may be of particular importance at (ultra) slow-spreading ridges. It occurs at the transition from the melt-generating asthenosphere to the conductively cooled, brittle lithosphere. In this region, sharp gradients in porosity, permeability and temperature lead to melt stagnation, which sets the conditions for widespread disequilibrium reactive flow.

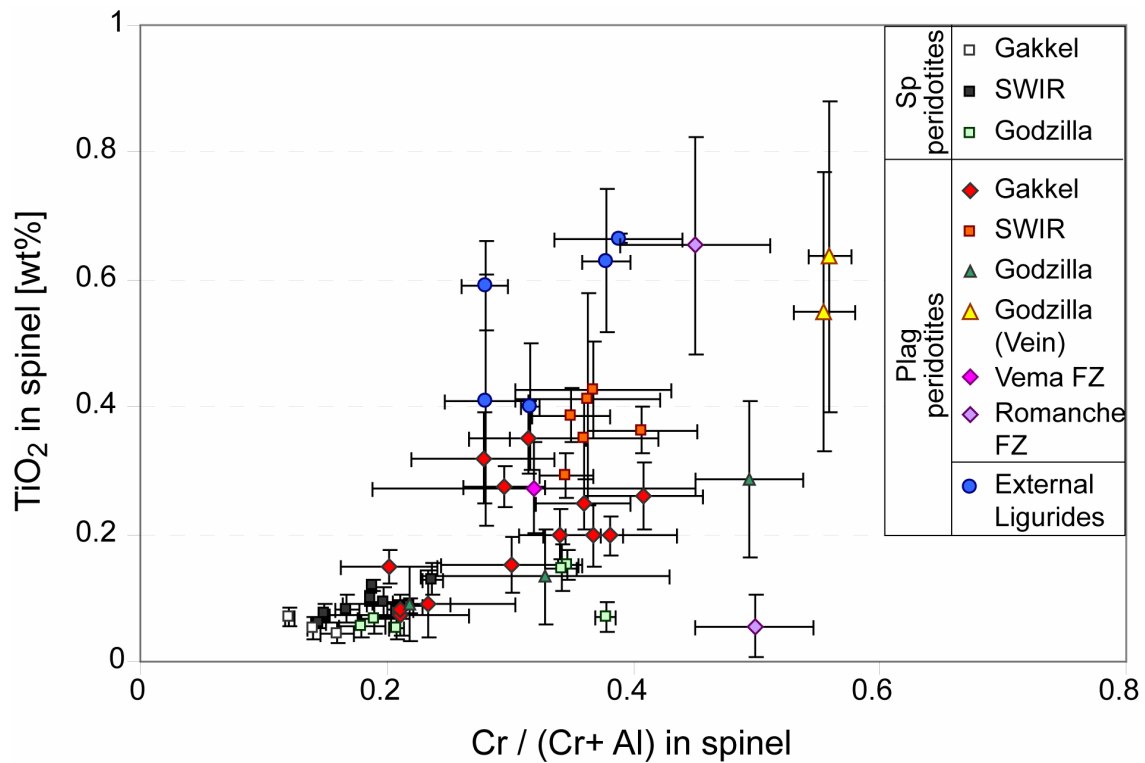


Figure 7-1: Spinel-Cr-numbers (molar $Cr/(Cr+Al)$) versus TiO_2 for spinel and plagioclase peridotites. Error bars denote within-sample variation. Spinel in plagioclase peridotites shows larger compositional variability than spinel peridotites. Two samples from Godzilla Megamullion were influenced by a magmatic vein that pervasively crystallized plagioclase in the peridotite matrix. Data sources: Gakkel Ridge (This study); Southwest Indian Ridge (own unpublished results); Godzilla Megamullion, Parece Vela Basin (unpublished); Vema Fracture Zone (Cannat and Seyler, 1995); Romanche Transform (Tartarotti et al., 2002); External Ligurides (Rampone et al., 1993, Rampone et al., 1995).

Disequilibrium phenomena such as those reported here only have general significance if they are widespread and not local effects. Intra-grain variations of Cr-numbers of spinel in abyssal plagioclase peridotites have been seen in (partly unpublished) studies from the Owen Fracture Zone (Hamlyn and Bonatti, 1980), Romanche Fracture Zone (Tartarotti et al., 2002, not reported but present in the data table), Molloy Deep (Hellebrand et al., 1998), Mariana's back arc (Snow et al., 2003 and unpublished data), the eastern tip of the Southwest Indian Ridge (von der Handt et al., 2004) and a xenolith from Oahu, Hawaii (Sen et al., 2003) (Figure 7-1). Plagioclase-bearing peridotite mylonites from the Vema Transform Fault show compositional heterogeneities (Cannat and Seyler, 1995), but these may be deformation related as described by Ozawa (1989).

Overall, however, mineral compositions reported in the literature are limited to sample averages, plagioclase peridotites tend to be left for later study, and data for heterogeneous grains have a tendency not to be reported at all. Nevertheless, all plagioclase-bearing peridotites from different locations I have analyzed so far show the described compositional heterogeneities.

Therefore, I suggest that the most important, distinctive and common characteristic of plagioclase peridotites is their compositional variability on grain scale rather than other indicators that they can share with other lithologies (i.e. elevated Ti-contents in spinel (Dick, 1989)).

The observations are explained best by a disequilibrium reaction between mantle and migrating melts. The ubiquity of plagioclase-bearing peridotites in the exposed oceanic mantle suggests that this is a worldwide phenomenon. Additional evidence for disequilibrium during melt transport exists from melt inclusions in primitive phases in mid-ocean ridge basalts (Sobolev et al., 2000). While most of these represent aggregated melts that have mixed, the existence of melt inclusions with exotic and highly variable compositions can be explained best by a disequilibrium melting or reaction process. Such compositions could most likely be generated in a reaction zone such as the one studied here.

Thus, the uppermost part of the oceanic mantle is not a simple migration pathway for ascending basaltic melts, but instead is the region of the mantle in between the cessation of melting and the channelization of melts into brittle cracks. In areas of low melt supply, like sparsely magmatic sections of mid-ocean ridges and fracture zones, melt migration is still diffuse rather than channelized. The observed scales of disequilibrium show that the melt-wall rock interaction happens without sufficient diffuse mass transport to equilibrate the grains on a micrometer scale. For these reasons, we infer that chemical disequilibrium is widespread beneath mid-ocean ridges, and is a ubiquitous aspect of the melt generation process, just one that has been overlooked to a certain extent.

7.3 REFERENCES

- Baker, M. B., Hirschmann, M. M., Ghiorso, M. S. and Stolper, E. M. (1995). Compositions of near-solidus peridotite melts from experiments and thermodynamic calculations. *Nature* 375, 308-311.
- Baker, M. B. and Stolper, E. M. (1994). Determining the composition of high-pressure mantle melts using diamond aggregates. *Geochimica Et Cosmochimica Acta* 58, 2811-2827.
- Brunelli, D., Seyler, M., Cipriani, A., Ottolini, L. and Bonatti, E. (2006). Discontinuous melt extraction and weak refertilization of mantle peridotites at the Vema Lithospheric Sections (Mid-Atlantic Ridge). *Journal of Petrology* 47, 745-771.
- Cannat, M. (1993). Emplacement of mantle rocks in the sea-floor at midocean ridges. *Journal of Geophysical Research-Solid Earth and Planets* 98, 4163-4172.
- Cannat, M. (1996). How thick is the magmatic crust at slow spreading oceanic ridges? *Journal of Geophysical Research-Solid Earth and Planets* 101, 2847-2857.
- Cannat, M. and Seyler, M. (1995). Transform tectonics, metamorphic plagioclase and amphibolitization in ultramafic rocks of the Vema Transform-Fault (Atlantic-Ocean). *Earth and Planetary Science Letters* 133, 283-298.
- Dick, H. J. B. (1989). Abyssal peridotites, very slow spreading ridges and ocean ridge magmatism. In: Saunders, A. D. & Norry, M. J. (eds.) *Magmatism in the ocean basins*. Geol. Soc. London Spec. Pub. 42. 71-105.
- Dijkstra, A. H., Barth, M. G., Drury, M. R., Mason, P. R. D. and Vissers, R. L. M. (2003). Diffuse porous melt flow and melt-rock reaction in the mantle lithosphere at a slow-spreading ridge: A structural petrology and LA-ICP-MS study of the Othris Peridotite Massif (Greece). *Geochemistry Geophysics Geosystems* 4, doi:10.1029/2001GC000278.
- Ganguly, J., Cheng, W. and Ducea, M. (2003). Time scales of metamorphic processes: Records in diffusion modification of mineral compositions and ages. *Goldschmidt Conference*, A116.

- Hamlyn, P. R. and Bonatti, E. (1980). Petrology of mantle-derived ultramafics from the Owen Fracture-Zone, Northwest Indian-Ocean - implications for the nature of the oceanic upper mantle. *Earth and Planetary Science Letters* 48, 65-79.
- Hellebrand, E., Snow, J. E., Hoppe, P. and Hofmann, A. W. (2002a). Garnet-field melting and late-stage refertilization in 'residual' abyssal peridotites from the Central Indian Ridge. *Journal of Petrology* 43, 2305-2338.
- Hellebrand, E., Snow, J. E. and Muhe, R. (2002b). Mantle melting beneath Gakkel Ridge (Arctic Ocean): abyssal peridotite spinel compositions. *Chemical Geology* 182, 227-235.
- Hellebrand, E. W., Snow, J. E., Devey, C. W., Haase, K. M. and Hofmann, A. W. (1998). Cumulate trace element signature in diopsides from plagioclase peridotites from Molloy Ridge, MAR 79°N. *AGU Spring Meeting*. Boston: Eos Transactions, V41A-04.
- Hirschmann, M. M., Ghiorso, M. S. and Stolper, E. M. (1999). Calculation of peridotite partial melting from thermodynamic models of minerals and melts. II. Isobaric variations in melts near the solidus and owing to variable source composition. *Journal of Petrology* 40, 297-313.
- Kelemen, P. B., Dick, H. J. B. and Quick, J. E. (1992). Formation of harzburgite by pervasive melt rock reaction in the upper mantle. *Nature* 358, 635-641.
- Kinzler, R. J. and Grove, T. L. (1992). Primary magmas of midocean ridge basalts .1. Experiments and methods. *Journal of Geophysical Research-Solid Earth and Planets* 97, 6885-6906.
- Liermann, H. P. and Ganguly, J. (2002). Diffusion kinetics of Fe²⁺ and Mg in aluminous spinel: Experimental determination and applications. *Geochimica Et Cosmochimica Acta* 66, 2903-2913.
- Montesi, L. G. J. and Behn, M. D. (2007). Mantle flow and melting underneath oblique and ultraslow mid-ocean ridges. *Geophysical Research Letters* 34, doi:10.1029/2007GL031067.
- Ozawa, K. (1989). Stress-induced Al-Cr-zoning of spinel in deformed peridotites. *Nature* 338, 141-144.
- Rampone, E., Hofmann, A. W., Piccardo, G. B., Vannucci, R., Bottazzi, P. and Ottolini, L. (1995). Petrology, mineral and isotope geochemistry of the external liguride peridotites (Northern Apennines, Italy). *Journal of Petrology* 36, 81-105.
- Rampone, E., Piccardo, G. B., Vannucci, R., Bottazzi, P. and Ottolini, L. (1993). Subsolidus reactions monitored by trace-element partitioning - the spinel-facies to plagioclase-facies transition in mantle peridotites. *Contributions to Mineralogy and Petrology* 115, 1-17.
- Roeder, P. L., Poustovetov, A. and Oskarsson, N. (2001). Growth forms and composition of chromian spinel in morb magma: Diffusion-controlled crystallization of chromian spinel. *Canadian Mineralogist* 39, 397-416.

CHAPTER 7

- Sen, G., Yang, H. J. and Ducea, M. (2003). Anomalous isotopes and trace element zoning in plagioclase peridotite xenoliths of Oahu (Hawaii): implications for the Hawaiian plume. *Earth and Planetary Science Letters* 207, 23-38.
- Seyler, M., Toplis, M. J., Lorand, J. P., Luguët, A. and Cannat, M. (2001). Clinopyroxene microtextures reveal incompletely extracted melts in abyssal peridotites. *Geology* 29, 155-158.
- Snow, J. E., Ohara, Y., Hellebrand, E., K., O. and Ishii, T. (2003). Heterogeneous melting of intermediate/fast spreading backarc peridotites, Parece-Vela Rift, Marianas backarc. *AGU Fall meeting*. San Francisco.
- Sobolev, A. V., Hofmann, A. W. and Nikogosian, I. K. (2000). Recycled oceanic crust observed in 'ghost plagioclase' within the source of Mauna Loa lavas. *Nature* 404, 986-990.
- Spiegelman, M. and Kenyon, P. (1992). The requirements for chemical disequilibrium during magma migration. *Earth and Planetary Science Letters* 109, 611-620.
- Tartarotti, P., Susini, S., Nimis, P. and Ottolini, L. (2002). Melt migration in the upper mantle along the Romanche Fracture Zone (Equatorial Atlantic). *Lithos* 63, 125-149.
- von der Handt, A., Seyler, M., Snow, J. E. and Hellebrand, E. (2004). Geochemistry of plagioclase peridotites from the Southwest Indian Ridge (63° - 65°). *Geochimica Et Cosmochimica Acta* 68, A706.

CHAPTER 8

SYNTHESIS AND OUTLOOK

8.1 INTRODUCTION

There is growing evidence that mid-ocean ridges undergo fundamental changes in their structure when their spreading rate drops below 20 mm/yr (Chen, 1992, Cannat, 1996, White et al., 2001). The increasing importance of a thicker thermal lid leads then to either decreasing shallow melting (White et al., 2001) or incomplete melt extraction (Cannat, 1996) or both.

Numerical models suggest that for half-rifting velocities of <6 mm/yr, mantle exhumation and serpentinization occurs before melting can occur (Pérez-Gussinyé et al., 2006). Sleep and Barth (1997) report that, predicted by thermal calculations, the upwelling melt freezes within 10 km of the seafloor if the spreading rate falls below a critical value. Cannat (1996) suggested that up to 25% of the crust may stagnate in the mantle and models for non-volcanic margins show that about 3 km of crustal-thickness-equivalent-melt could be trapped in the mantle (Pérez-Gussinyé et al., 2006). Numerical models have strengthened that the decrease in spreading rate from slow- to ultraslow-spreading coincides with inefficient melt extraction rather than decreasing melt production (Montesi and Behn, 2007). As a result, melt extraction efficiency rather than melting is controlled by spreading rate (Lizarralde et al., 2004, Montesi and Behn, 2007).

At slow-spreading rates, buoyant flow becomes more important relative to passive upwelling (Jha et al., 1994). Buoyant flow is driven by density differences due to (1) melt depletion, (2) melt retention, and (3) thermal expansion. At slow-spreading rates, buoyant flow has a large effect on flow geometry and upwelling rates. The mixing of depleted and undepleted material below mid-ocean ridges is of greater importance at very slow spreading rates because of thermal buoyancy effects (Su et al., 1994).

Gakkal Ridge is the end member for ultraslow-spreading in the system of mid-ocean ridges; the sample location at 3°E has been referred to as the type locality of ultraslow-

spreading (Montesi and Behn, 2007). Therefore, Gakkel Ridge is a natural laboratory to study the processes of low degree melting, melt stagnation and mantle heterogeneity.

The aim of my thesis was the investigation of petrological and geochemical changes that affect abyssal peridotite compositions after melting has ceased. The results, even though only on a limited number of samples, may allow supplementing these predictions.

8.2 MELT EXTRACTION AT GAKKEL RIDGE

None of the samples in this study represent true melt residua. Despite the apparent magmatic nature of the 3°E region, textures and mineral compositions in spinel and plagioclase peridotites indicate significant melt-rock reaction and melt addition. Chapter 2 carried out an investigation on spinel peridotites. Their textures suggest orthopyroxene addition and olivine dissolution. Trace element compositions could be modeled by entrapment of few percents of low-degree melts.

In places, plagioclase peridotites show evidence for metamorphic production of plagioclase but this process is volumetrically very insignificant. Instead, plagioclase peridotites are formed by melt-rock reaction. The reaction process, based on textures and element zoning, is a reactive melt-rock reaction process that operates toward gradients in silica activity through a series of dissolution reactions. This process has been termed SAE (silica activity equilibration)-process and has been described in detail in Chapter 5. During the SAE-process, the peridotite system equilibrates toward a new silica activity. Mineral compositions and abundances of plagioclase peridotites are fixed by subsolidus phase equilibria and are thus a function of pressure and temperature of the interaction and the relative difference in composition between melt and peridotite. Plagioclase peridotites may be formed by equilibration either toward higher or lower silica activity but the final phase assemblage will be indicative of the reaction gradient. Formation of plagioclase peridotite by low-silica melts will produce the assemblage ol+cpx+plag while high silica melts will produce opx+plag. In addition, either process will have different P-T stability fields and will differ systematically in major and trace element composition.

It is possible that the spinel peridotites in this study have been subjected to the same SAE-process rather than melt entrapment as modeled in Chapter 2. When the SAE-process occurs at high temperatures, diffusive equilibration will be fast enough to erase all indicative major and trace element zoning and mineral compositions will appear characteristic of melt entrapment. The SAE-process, however, results in the formation of non-cotectic phase assemblages. Melt composition inferred through mineral-melt partition coefficients will have been modified, too.

Chapter 6 showed that the spinel compositions are also strongly modified by the SAE-process as the MgAl_2O_4 component in spinel is destabilized during the process. By the application of oxygen barometers (based on olivine-spinel-orthopyroxene equilibria), it might be possible to even quantify this reaction due to the relation between silica activity and oxygen fugacity.

It has been usually assumed that melt-rock reaction dominantly proceeds toward olivine addition and pyroxene-dissolution (lherzolite \rightarrow dunite) beneath mid-ocean ridges, and pyroxene addition and olivine dissolution (harzburgites \rightarrow pyroxenite) in the subarc- and continental mantle. Textures and composition of plagioclase peridotites strongly suggest that they are the low pressure equivalent of melt-rock reaction with melts of higher silica activity. Hence, both processes may be active in all tectonic environments at all times but, depending on the relative environment, vary in importance.

8.3 MANTLE HETEROGENEITY AT GAKKEL RIDGE:

8.3.1 Pre-existing heterogeneity

Even though peridotites in the 3°E region are very “fertile” in major element composition and clinopyroxene abundance, results of major and trace element models rather point to refractory host rocks before melt infiltration.

The estimated degree of partial melting for the residual protolith of the spinel peridotites ranges between 4% and 8% and melting occurred entirely (?) in the spinel stability field. Clinopyroxene trace element composition in plagioclase peridotites further suggests a source rock, depleted after 5 to 10% of partial melting in the spinel stability field. The systematic

variation of spinel composition in plagioclase peridotites with plagioclase abundance allowed the back-calculation to a plagioclase-free composition at spinel Cr-numbers of approx. 0.23 and 0.3. This translates to a degree of melting after Hellebrand et al. (2001) of around 9 and 12%, respectively. 10% of partial melting from a DMM source of Workmann and Hart (2005) produces a peridotite at the transition from lherzolite to harzburgite (placed at 5% cpx). In contrast, infiltrating melts seem to be produced from more fertile sources. Two samples from dredge haul PS66-238 suggest even impregnation by melts produced at very low degrees of melting (around 1%); textures in all samples suggest reaction with melts at higher silica activity.

Major and trace element systematics of peridotites throughout the Sparsely Magmatic Zone indicate up to 25% of previously depleted mantle material in the melting column at Gakkel Ridge (Hellebrand et al., 2006). This is also corroborated by an Os-isotopic study of samples from the same sample location (Liu et al., in press) that found very old melt depletion ages in harzburgites. Hence, a pre-existing depletion in parts of the mantle section at Gakkel Ridge may exist. Evidently, the situation at Gakkel Ridge is much more complex than initially assumed.

8.3.2 Heterogeneity at Gakkel Ridge: produced by melt-rock reaction

Textures in spinel and plagioclase peridotites show reactive dissolution of olivine and crystallization of orthopyroxene, which is supported by modal estimates. Melt-rock reaction via SAE-process will change the mineralogy of mantle peridotite as a function of pressure, temperature and difference in composition of the reactants. All samples in this study showed evidence of the SAE-process toward higher silica activity. However, there is no reason why the SAE-process toward lower silica activity should not occur at Gakkel Ridge as well. In a tectonic environment of highly isolated melt production or pre-existing heterogeneity, the reaction may proceed subsequently in both directions as the difference in relative silica activity is the driving force. Hence, reactive melt-rock reaction can create small scale modal variation in the mantle.

8.4 MELT PRODUCTION AT GAKKEL RIDGE

In Chapter 1, it was said that the order of chapters is meant to follow a hypothetical uplift of a mantle parcel below Gakkell Ridge (see also Figure 8-1). Figure 8-1 also includes the position of solidus after Hirschmann (2000). The assumption of a continuous, uniform solidus poses certain restrictions on the order of processes and assumes a homogeneous mantle source. The importance of peridotite composition on the solidus location depends strongly on the competing effects of increased abundance of melt-enhancing components (alkalis, lower Mg-number) and the effect of increased compatibility of those components (cpx mode) (Hirschmann, 2000). The process of hybridization of peridotite by the addition of some percents of basalt lowers the solidus and compress the solidus-liquidus interval during adiabatic uplift (Yaxley, 2000). The addition of basaltic melt to peridotite mixtures in experiments and numerical calculations has been assumed to occur as bulk addition. The SAE-process described in Chapter 5 consumes clinopyroxene, while adding alkali to the residual composition. Reaction temperatures such as the solidus temperature and the temperature of cpx-out are strongly sensitive to the modal abundance of cpx (Wasylenki et al., 2003, Laporte et al., 2004). Hereby, enriching in alkali/cpx modal ratio relative to upper mantle peridotite is likely to lower the solidus relative to that of typical mantle. The liquid mass is supposed to be consumed quickly by this reaction but may nevertheless introduce localized variation in melt production.

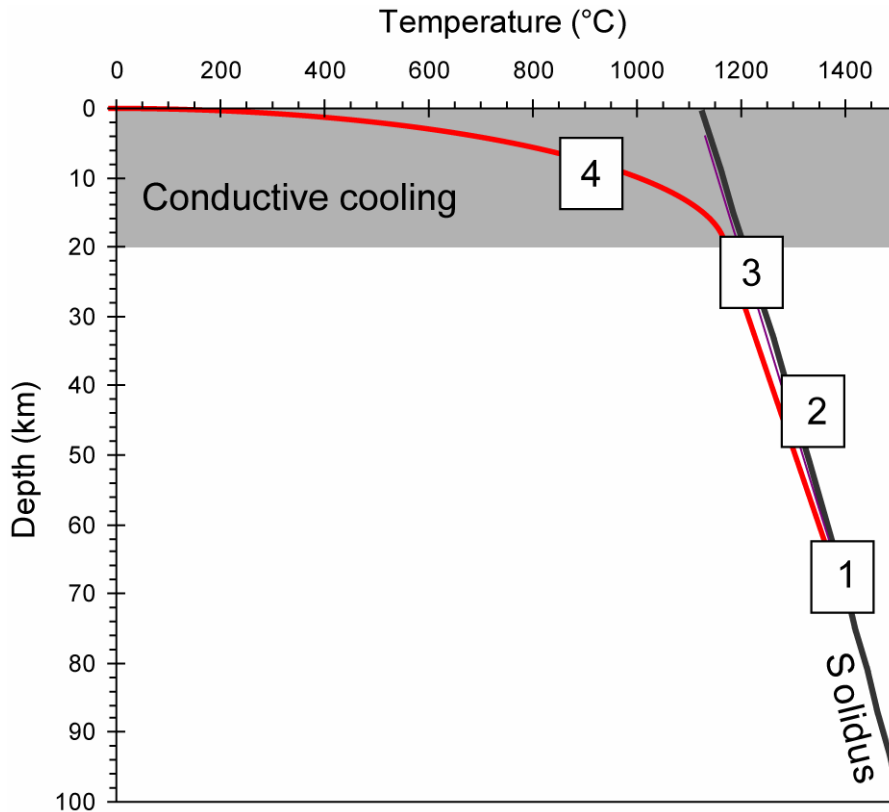


Figure 8-1: Schematic order of processes at 3°E Gakkel Ridge: (1) Melting in the spinel stability field; (2) High temperature refertilization of spinel peridotites (and cooling); (3) Melt stagnation and formation of plagioclase peridotites and (4) Cooling and further uplift..

8.5 HETEROGENEITY OF MELTS

High-silica melts have a much higher viscosity relative to MORB-type melts (Baker et al., 1995). This type of melt would probably never reach the surface because of its high viscosity and high reactivity. Instead, it would lead to (initial) refertilization of depleted peridotites and contribute to the heterogeneity of the mantle. Small differences in modal composition due to preceding depletion or refertilization would result in different onsets and degrees of melting.

Furthermore, unusual basaltic composition found at the South Atlantic Ridge are attributed to the influence of continental crust in the melting process (Kamenetsky et al., 2001). Their chemical composition may also agree with melts formed by SAE-melt-rock reaction. If such melts are pooled and erupted, this process may contribute to global MORB chemical diversity.

Furthermore, reactive melt transport associated with mineralogical changes imparts a strong geochemical signature of the product mineral assemblage to emerging melts (Reiners, 1998). Depending on the produced phase assemblage, melts affected by reactive melt transport might show trace element characteristics of an apparent (silica-undersaturated) pyroxenitic source or high pressure orthopyroxene fractionation.

The SAE-process is essentially an equilibration process, however it has been shown in experiments (Shaw and Dingwell, 2008) that the scale of equilibrium during melt-rock reaction processes is very limited. Dissolution rates and kinetics result in a variably polymerized melt in which uphill diffusion and diffusive fractionation processes are common (Zhang et al., 1989, Shaw and Dingwell, 2008). Zoning in spinel from plagioclase peridotites is a recorder of this process. At low melt-rock ratios, effective disequilibrium during melt migration may be the result, at least in the uppermost mantle. Hence, it may contribute to the compositional range seen in melt inclusions.

8.6 COOLING BELOW GAKKEL RIDGE

The thermal structure below mid-ocean ridges is of great importance to melt production and melt migration processes. The temperature-dependent trace element partition coefficient between clinopyroxene and orthopyroxene was responsible for zoning profiles in orthopyroxene from Gakkal Ridge and equilibration temperatures were found to span a range between 1380 and 760°C. Chapter 3 attempted quantification of cooling rates at Gakkal Ridge by modelling the zoning patterns and temperature profiles in orthopyroxene. However, trace element diffusion coefficients for orthopyroxene did not yield reasonable results and no conclusion could be derived. In the future, experimental estimates on trace element diffusion in orthopyroxene of similar composition may allow the calculation of diffusivities for all other elements and calculation of uplift rates.

8.7 SUMMARY

Low degree melting and melt refertilization outside of the plagioclase stability field is not easily detectable in peridotites. Evidence for such processes is given by the occurrence of queer major element composition (e.g. high Na₂O contents in cpx (Elthon, 1992, Hellebrand and Snow, 2003)) and discrete modal variation (Seyler et al., 2001, Brunelli et al., 2006). The SAE-process is probably not important at high rock-melt ratios at fast-spreading ridges. It might only occur as a “preconditioning” stage before preferred melt migration pathways (i.e. dunites) are established. However, it may play a significant role in areas of low melt production and contribute to mantle heterogeneity and melt stagnation in the mantle.

8.8 REFERENCES

- Baker, M. B., Hirschmann, M. M., Ghiorso, M. S. and Stolper, E. M. (1995). Compositions of near-solidus peridotite melts from experiments and thermodynamic calculations. *Nature* 375, 308-311.
- Brunelli, D., Seyler, M., Cipriani, A., Ottolini, L. and Bonatti, E. (2006). Discontinuous melt extraction and weak refertilization of mantle peridotites at the Vema Lithospheric Sections (Mid-Atlantic Ridge). *Journal of Petrology* 47, 745-771.
- Cannat, M. (1996). How thick is the magmatic crust at slow spreading oceanic ridges? *Journal of Geophysical Research-Solid Earth and Planets* 101, 2847-2857.
- Chen, Y. J. (1992). Oceanic crustal thickness versus spreading rate. *Geophysical Research Letters* 19, 753-756.
- Elthon, D. (1992). Chemical trends in abyssal peridotites - refertilization of depleted suboceanic mantle. *Journal of Geophysical Research-Solid Earth and Planets* 97, 9015-9025.
- Hellebrand, E. and Snow, J. E. (2003). Deep melting and sodic metasomatism underneath the highly oblique-spreading Lena Trough (Arctic Ocean). *Earth and Planetary Science Letters* 216, 283-299.
- Hellebrand, E., Snow, J. E., Dick, H. J. B. and Hofmann, A. W. (2001). Coupled major and trace elements as indicators of the extent of melting in mid-ocean-ridge peridotites. *Nature* 410, 677-681.
- Hellebrand, E., Snow, J. E., Dick, H. J. B. and von der Handt, A. (2006). Inherited depletion in the oceanic mantle inferred from peridotite composition and distribution along Gakkel Ridge. *Ophioliti* 31, 60-61.

CHAPTER 8

- Hirschmann, M. M. (2000). Mantle solidus: Experimental constraints and the effects of peridotite composition. *Geochemistry Geophysics Geosystems* 1, doi:10.1029/2000GC000070.
- Jha, K., Parmentier, E. M. and Morgan, J. P. (1994). The role of mantle-depletion and melt-retention buoyancy in spreading-center segmentation. *Earth and Planetary Science Letters* 125, 221-234.
- Kamenetsky, V. S., Maas, R., Sushevskaya, N. M., Norman, M. D., Cartwright, I. and Peyve, A. A. (2001). Remnants of Gondwana continental lithosphere in oceanic upper mantle: Evidence from the South Atlantic Ridge. *Geology* 29, 243-246.
- Laporte, D., Toplis, M. J., Seyler, M. and Devidal, J. L. (2004). A new experimental technique for extracting liquids from peridotite at very low degrees of melting: application to partial melting of depleted peridotite. *Contributions to Mineralogy and Petrology* 146, 463-484.
- Liu, C., Snow, J. E., Hellebrand, E., Brüggmann, G., Von der Handt, A., Büchl, A. and Hofman, A. W. (in press). Ancient, highly heterogeneous mantle beneath Gakkel Ridge, Arctic Ocean. *Nature*.
- Lizarralde, D., Gaherty, J. B., Collins, J. A., Hirth, G. and Kim, S. D. (2004). Spreading-rate dependence of melt extraction at mid-ocean ridges from mantle seismic refraction data. *Nature* 432, 744-747.
- Montesi, L. G. J. and Behn, M. D. (2007). Mantle flow and melting underneath oblique and ultraslow mid-ocean ridges. *Geophysical Research Letters* 34, doi:10.1029/2007GL031067.
- Pérez-Gussinyé, M., Phipps Morgan, J., Reston, T. J. and Ranero, C. R. (2006). The rift to drift transition at non-volcanic margins: Insights from numerical modelling. *Earth and Planetary Science Letters* 244, 458-473.
- Reiners, P. W. (1998). Reactive melt transport in the mantle and geochemical signatures of mantle-derived magmas. *Journal of Petrology* 39, 1039-1061.
- Seyler, M., Toplis, M. J., Lorand, J. P., Lugué, A. and Cannat, M. (2001). Clinopyroxene microtextures reveal incompletely extracted melts in abyssal peridotites. *Geology* 29, 155-158.
- Shaw, C. S. J. and Dingwell, D. B. (2008). Experimental peridotite-melt reaction at one atmosphere: A textural and chemical study. *Contributions to Mineralogy and Petrology* 155, 199-214.
- Sleep, N. H. and Barth, G. A. (1997). The nature of oceanic lower crust and shallow mantle emplaced at low spreading rates. *Tectonophysics* 279, 181-191.
- Su, W. S., Mutter, C. Z., Mutter, J. C. and Buck, W. R. (1994). Some theoretical predictions on the relationships among spreading rate, mantle temperature, and crustal thickness. *Journal of Geophysical Research-Solid Earth and Planets* 99, 3215-3227.
- Wasylenki, L. E., Baker, M. B., Kent, A. J. R. and Stolper, E. M. (2003). Near-solidus melting of the shallow upper mantle: partial melting experiments on depleted peridotite. *Journal of Petrology* 44, 1163-1191.

CHAPTER 8

- White, R. S., Minshull, T. A., Bickle, M. J. and Robinson, C. J. (2001). Melt generation at very slow-spreading oceanic ridges: constraints from geochemical and geophysical data. *Journal of Petrology* 42, 1171-1196.
- Workman, R. K. and Hart, S. R. (2005). Major and trace element composition of the depleted MORB mantle (DMM). *Earth and Planetary Science Letters* 231, 53-72.
- Yaxley, G. M. (2000). Experimental study of the phase and melting relations of homogeneous basalt plus peridotite mixtures and implications for the petrogenesis of flood basalts. *Contributions to Mineralogy and Petrology* 139, 326-338.
- Zhang, Y., Walker, D. and Leshner, C. E. (1989). Diffusive crystal dissolution. *Contributions to Mineralogy and Petrology* 102, 492-513.

APPENDIX

Constant mineral/melt distribution coefficients D were used for all minerals over the entire range of melting with the exception of plagioclase. The internally consistent partition coefficient compilation from Kelemen et al. (2004) was adopted because of their large range in elements and the interpartition coefficients for cpx and opx agreed with magmatic temperatures calculated with (Witt-Eickschen and O'Neill, 2005). Trace element partition coefficients between melt and plagioclase strongly depend on the major element composition of plagioclase (Bedard, 2006, Bindeman et al., 1998, Blundy and Wood, 1991) and the semi-empirical parametrization of Bedard (2006) has been used in all models.

Different source compositions were assumed in the models, a DMM mantle composition from Workman and Hart (2005) as well as two spinel peridotites from the same sample location (PS59-235-17 and -20). Melt modes are from Kinzler and Grove (1992). Table A-1 summarizes all model parameters.

A: PARTIAL MELTING

Partial melting has been modeled using a critical melting model (Maaloe, 1982). Critical melting is similar to fractional melting except that that it accounts for residual melt porosity with an interstitial melt. Melt is extracted when a critical fraction is reached which is assumed to remain constant throughout the melting process. The critical melt fraction in the mantle is assumed to vary between 0.001 and 0.03 (Brunelli et al., 2006, Forsyth et al., 1998, Johnson et al., 1990) and the critical melt fraction in the models was varied within these values until a good match was achieved.

At melt fractions below the critical porosity, the system is closed and the melting process can be described by batch melting equations (c.f. Shaw, 1970). However, when the critical porosity is exceeded, a melt fraction is extracted from the residual solid and melt; the melt fraction retained in the residue buffers the LREE budget at high melting increments.

APPENDIX

For an increment of melting $F \geq \alpha/(\alpha+1)$ with α as residual porosity, the extracted melt composition can be described as follows

$$C_L = \left[\frac{C_o}{D_o + (1-P) \frac{\alpha}{\alpha+1}} \right] \left[\frac{(D_o + \alpha) - (P + \alpha) F}{(D_o + \alpha) - (P + \alpha) \frac{\alpha}{\alpha+1}} \right]^{\frac{(1-P)}{(P+\alpha)}} \quad (A1)$$

The relative concentration in the residue is given by

$$C_{res} = C_L \left(\frac{D_o - PF}{1 - F} \right) \quad (A2)$$

and the cpx in the residue has the composition

$$C_{cpx} = C_{res} \left(\frac{D_{cpx/liq}}{D_{bulk}} \right) \quad (A3)$$

C_{res} is the trace element concentration in the residue; C_o is the trace element concentration in the source; D_o is the initial bulk distribution coefficient:

$$D_o = \sum (D^{i/liq} M_{o,i}) \quad (A4)$$

where $M_{o,i}$ is the mode of the phase i in the source; P is the weighted partition coefficient:

$$P = \sum (D^{i/liq} p_i) \quad (A5)$$

where p_i is the melting mode of the phase i . With the chosen melt and start mode of a DMM source as given in Table A1, clinopyroxene is exhausted in the source at 15% partial melting.

B: TRAPPED MELT MODEL

Refertilization by melt entrapment has been calculated by adding a variable amount of melt to the residual bulk rock. Both, the melt and the residual bulk rock were calculated by

APPENDIX

critical melting as described in Appendix A. The trapped melt model follows the formulation by Hellebrand et al. (2002).

Melt entrapment on a residual peridotite is derived in four simple steps. First, the new whole rock composition after linear mixing is calculated:

$$C_{wr} = C_o(1-X) + C_{liq}X \quad (B1)$$

, where X is the melt fraction added to the residual peridotite and C_{wr} and C_o are the new and initial whole rock compositions, respectively. After addition of a melt with concentration C_{liq} , trace elements are redistributed, assuming the newly formed minerals that crystallized from the melt attain equilibrium with pre-existing phases of the peridotite. The new mode M of phase j can be expressed as a function of X :

$$M_j = M_o(1-X) + Z_jX \quad (B2)$$

where Z_j is the crystallization mode which describes the proportion of new minerals that crystallize from the melt.

Using these new mineral modes, the new bulk distribution coefficient D_{bulk} can be calculated:

$$D_{bulk} = \sum(D^{i/liq} M_j) \quad (B3)$$

The concentration in the re-equilibrated cpx after melt addition depends on the modified bulk distribution coefficient and is identical to equation (A4).

C: FRACTIONAL CRYSTALLIZATION

Fractional crystallization of a melt was calculated as follows:

The concentration of an element in the residual melt fraction is:

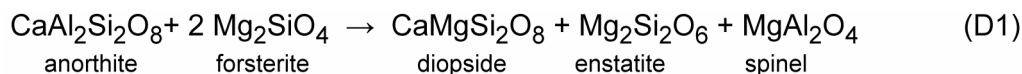
$$C_{liq} = C_o X^{(D_{bulk}-1)} \quad (C1)$$

, where C_o is the concentration in the initial liquid, X the fraction of the cumulate produced and D_{bulk} the bulk partition coefficient of the crystallizing phases.

APPENDIX

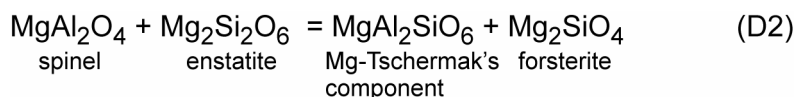
D: TRANSITION FROM SPINEL TO PLAGIOCLASE FACIES CONDITION

The sub-solidus formation of two pyroxenes and spinel from the reaction between anorthite and olivine (Kushiro and Yoder, 1966) in the CaO-MgO-Al₂O₃-SiO₂ system can be written as:

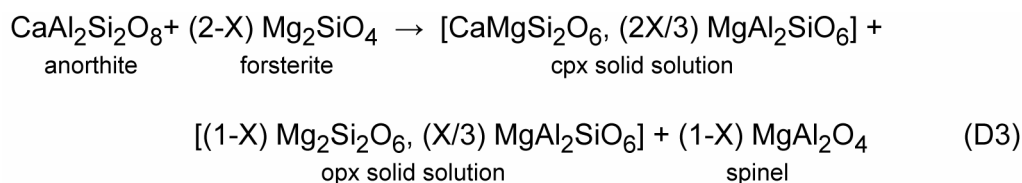


This simplified system does not take into account the pyroxene and plagioclase solid solutions. Henceforth, the spinel to plagioclase facies transition was modeled following the formulation of Takazawa et al. (1996). This formulation allows for the variation of the anorthite component in plagioclase and Mg-Tschermak- (MgTs) and jadeite-components in the pyroxenes.

The MgTs-component in pyroxene is formed by:



If we assume that MgTs is partitioned in a 2:1 ratio between clinopyroxene and orthopyroxene, combination of Eq. (D1) and Eq. (D2) leads to:



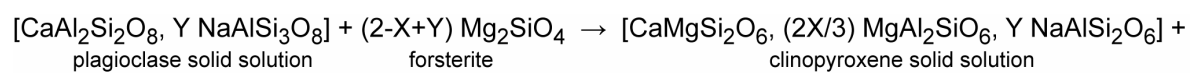
, where $0 < X < 1$.

The reaction forming from albite component of plagioclase can be described as:



APPENDIX

Eq. (D3) and Eq. (D4) can then be combined to give:



where Y represents albite molar fraction in plagioclase ($0 < Y < 1$). It was assumed that all the jadeite component is incorporated into cpx.

Table A-1: Source composition, modes and partition coefficients used in models

	Partition coefficients and modes					Source compositions [$\mu\text{g/g}$]					
	ol ^a	opx ^a	cpx ^a	cpx ^b	sp ^a	pl ^c	DMM cpx ^d	DMIM ^d	235-17 ^e	235-20 ^e	Cl ^f
SM_DMIM ^d	0.57	0.28	0.13		0.02		1.41	0.19	0.00861	0.0143	0.2347
SM_235-17	0.61	0.28	0.10		0.004		3.93	0.55	0.0286	0.0543	0.603
SM_235-20	0.74	0.18	0.07		0.010		56.11	7.66	0.225	0.577	7.8
MM ^g	-0.3	0.4	0.82		0.08		4.04	0.58	0.103	0.0605	0.4524
La	0.000007	0.001	0.0536	0.25	0.0006	0.12	20.28	5.08	0.536	0.490	3.94
Ce	0.00001	0.003	0.0858	0.4	0.0006	0.11	1.59	0.24	0.0965	0.0401	0.1471
Sr	0.00001	0.003	0.1283	0.18	0	1.63	0.61	0.10	0.0485	0.0180	0.056
Nd	0.00007	0.009	0.1873	0.86	0.0006	0.09	2.21	0.36	0.209	0.0883	0.1966
Zr	0.004	0.04	0.1234	0.44	0.07	0.00	2714.6	716.3	337.7	188.0	436
Sm	0.0007	0.02	0.291	1.36	0.0006	0.06	2.92	0.51	0.350	0.174	0.2427
Eu	0.00095	0.03	0.33	1.38	0.0006	0.31	1.73	0.35	0.257	0.140	0.1589
Gd	0.0012	0.04	0.37	1.55	0.0006	0.04	1.62	0.36	0.256	0.152	0.1625
Ti	0.015	0.15	0.4	0.44	0.15	0.04					
Dy	0.004	0.06	0.442	1.33	0.0015	0.03					
Er	0.009	0.09	0.43	1.43	0.003	0.02					
Yb	0.023	0.1	0.43	1.32	0.0045	0.01					

^a: from Kelemen et al. (2004)

^c: calculated after Bedard (2006), shown is An80 for example

^b: from Vannucci et al. (1998) for PAT2-42

^d: from Workman and Hart (2005)

^e: reconstructed from mineral compositions and mineral modes

^f: chondrite normalization values from Anders and Grevesse (1989)

^g: from Kinzler and Grove (1992)

SM: source mode

MM: melt mode

APPENDIX

REFERENCES

- Bedard, J. H. (2006). Trace element partitioning in plagioclase feldspar. *Geochimica Et Cosmochimica Acta* 70, 3717-3742.
- Bindeman, I. N., Davis, A. M. and Drake, M. J. (1998). Ion microprobe study of plagioclase-basalt partition experiments at natural concentration levels of trace elements. *Geochimica Et Cosmochimica Acta* 62, 1175-1193.
- Blundy, J. D. and Wood, B. J. (1991). Crystal-chemical controls on the partitioning of Sr and Ba between plagioclase feldspar, silicate melts, and hydrothermal solutions. *Geochimica Et Cosmochimica Acta* 55, 193-209.
- Brunelli, D., Seyler, M., Cipriani, A., Ottolini, L. and Bonatti, E. (2006). Discontinuous melt extraction and weak refertilization of mantle peridotites at the Vema Lithospheric Sections (Mid-Atlantic Ridge). *Journal of Petrology* 47, 745-771.
- Forsyth, D. W., Scheirer, D. S., Webb, S. C., Dorman, L. M., Orcutt, J. A., Harding, A. J., Blackman, D. K., Morgan, J. P., Detrick, R. S., Shen, Y., Wolfe, C. J., Canales, J. P., Toomey, D. R., Sheehan, A. F., Solomon, S. C. and Wilcock, W. S. D. (1998). Imaging the deep seismic structure beneath a mid-ocean ridge: The MELT experiment. *Science* 280, 1215-1218.
- Hellebrand, E., Snow, J. E., Hoppe, P. and Hofmann, A. W. (2002). Garnet-field melting and late-stage refertilization in 'residual' abyssal peridotites from the Central Indian Ridge. *Journal of Petrology* 43, 2305-2338.
- Johnson, K. T. M., Dick, H. J. B. and Shimizu, N. (1990). Melting in the oceanic upper mantle - an ion microprobe study of diopsides in abyssal peridotites. *Journal of Geophysical Research-Solid Earth and Planets* 95, 2661-2678.
- Kelemen, P. B., Yogodzinski, G. M. and Scholl, D. W. (2004). Along-strike variation in lavas of the Aleutian island arc: implications for the genesis of high Mg# andesite and the continental crust. In: Eiler, J. (ed.) *Inside the subduction factory*. AGU Monograph 138. Washington, DC: AGU, 223-276.
- Kinzler, R. J. and Grove, T. L. (1992). Primary magmas of midocean ridge basalts .1. Experiments and methods. *Journal of Geophysical Research-Solid Earth and Planets* 97, 6885-6906.
- Kushiro, I. and Yoder, H. S. (1966). Anorthite-forsterite and anorthite-enstatite reactions and their bearing on basalt-eclogite transformation. *Journal of Petrology* 7, 337-362.
- Maaloe, S. (1982). Geochemical aspects of permeability controlled partial melting and fractional crystallization. *Geochimica Et Cosmochimica Acta* 46, 43-57.
- Shaw, D. M. (1970). Trace element fractionation during anatexis. *Geochimica Et Cosmochimica Acta* 34, 237-243.
- Takazawa, E., Frey, F., Shimizu, N. and Obata, M. (1996). Evolution of the Horoman Peridotite (Hokkaido, Japan): Implications from pyroxene compositions. *Chemical Geology* 134, 3-26.

APPENDIX

Witt-Eickschen, G. and O'Neill, H. S. (2005). The effect of temperature on the equilibrium distribution of trace elements between clinopyroxene, orthopyroxene, olivine and spinel in upper mantle peridotite. *Chemical Geology* 221, 65-101.

CURRICULUM VITAE

Anette Katharina Marie Nora von der Handt

Date of birth: 05/22/1975

Place of birth: Düsseldorf, Germany

e-mail: avdhandt@mpch-mainz.mpg.de

Education

- since 11/2003 Graduate student at the Max-Planck Institute for Chemistry, Geochemistry Division.
- 09/2003 Diplom (MSc) in Geology, University of Bonn
Diplom thesis: *Impregnation-triggered breakdown: a case study of plagioclase peridotites from the Gakkel Ridge, Arctic Ocean* at the Max-Planck-Institute for Chemistry, Mainz, Supervisor Dr. Jonathan Snow
- 03/2001 – 05/2001 Sedimentological Mapping Survey in the Tacchi-Area of Central Sardinia. Title: *Evolution of the Permian basin of Perdasdefogu and the Jurassic transgression at the Tacco di Perdalonga*. In cooperation with the Dipartimento Scienze della Terra, University of Cagliari.
- 01/2001 – 03/2001 Internship at the Alfred-Wegener-Institute for Polar and Marine Research, Bremerhaven
- 09/1999 Vordiplom (Intermediate Diploma)
- 10/1996 – 09/2003 Studies of Geology at the University of Bonn
- 10/1994 – 09/1996 Studies of German and comparative linguistics at the University of the Saarland, Saarbrücken
- 07/1994 Abitur, Lessing-Gymnasium Frankfurt am Main

Cruise Participation

- 11/2004 – 01/2005 IODP Leg 304: Oceanic Core Complex, Atlantis Massif; Co-Chief Scientists: D.K. Blackmann and B.E. John, Position: Igneous Petrologist
- 07/2004 – 08/2004 ARK XX-2: Petrology of Lena Trough, Arctic Ocean, RV Polarstern, Chief Petrologist: J.E. Snow, Position: Shiftleader Sample Curation
- 08/2001 – 10/2001 ARK XVII-2: Arctic Mid-Ocean Ridge Expedition to Gakkel Ridge, Arctic Ocean, International two-ship cruise with RV Polarstern and USGC Healy, Chief Petrologist: J.E. Snow, Position: Shiftleader Sample Curation

Publications

C. Liu, J.E. Snow, E. Hellebrand, G. Brügmann, **A. von der Handt**, A. Büchl, A. Hofmann (2008): Ancient highly heterogeneous mantle beneath Gakkel Ridge, Arctic Ocean. *Nature*, accepted.

B. Ildefonse, D.K. Blackmann, B.E. John, Y. Ohara, D.J. Miller, C.J. MacLeod, N. Abe, M. Abratis, E.S. Andal, M. Andréani, S. Awaji, J.S. Beard, D. Brunelli, A.B. Charney, D.M. Christie, A.G. Delacour, H. Delius, M. Drouin, F. Einaudi, J. Escartin, B.R. Frost, P.B. Fryer, J.S. Gee, M. Godard, C.B. Grimes, A. Halfpenny, H-E. Hansen, A.C. Harris, N.W. Hayman, E. Hellebrand, T. Hirose, J.G. Hirth, S. Ishimaru, K.T.M. Johnson, G.D. Karner, M. Linek, J. Maeda, O.U. Mason, A.M. McCaig, K. Michibayashi, A. Morris, T. Nakagawa, T. Nozaka, M. Rosner, R.C. Searle, G. Suhr, A. Tamura, M. Tominaga, **A. von der Handt**, T. Yamasaki, X. Zhao. (2007): Oceanic core complexes and crustal accretion at slow-spreading ridges. *Geology* 35, 623–626.

Y. Gao, J. Hoefs, E. Hellebrand, **A. von der Handt**, J.E. Snow (2007): Trace element zoning in pyroxenes from ODP Hole 735B gabbros: diffusive exchange or synkinematic crystal fractionation? *Contributions to Mineralogy and Petrology* 153, 429–442.

Shipboard Scientific Party IODP Expeditions 304 and 305 (incl. **A.von der Handt**) (2005): Oceanic Core Complex Formation, Atlantis Massif. *Scientific Drilling Journal*, 1, 28–31, doi: 10.2204/iodp.sd.1.05.2005.

Reports

Blackman, D.K., Ildefonse, B., John, B.E., Ohara, Y., Miller, D.J., MacLeod, C.J., and the Expedition 304/305 Scientists (incl. **A. von der Handt**) (2006): Proc. IODP, 304/305: College Station TX (Integrated Ocean Drilling Program Management International, Inc.). doi:10.2204/iodp.proc.304305.2006

Expedition Scientific Party (incl. **A. von der Handt**) (2005): Oceanic core complex formation, Atlantis Massif—oceanic core complex formation, Atlantis Massif, Mid-Atlantic Ridge: drilling into the footwall and hanging wall of a tectonic exposure of deep, young oceanic lithosphere to study deformation, alteration, and melt generation. IODP Prel. Rept., 304.

J. Snow, M. Biegler, R. Eckardt, S. Feig, H. Feldmann, Y. Gao, **A. von der Handt**, E. Hellebrand, Z. Jovanovic, T. Liesenfeld, J. Morgan, F. Nauret, S. Schmitt, S. Turini, K. Wiegler (2004): Cruise Report ARK XX-2: Petrologic and tectonic evolution of the Lena Trough and western Gakkel Ridge. In: Lemke, P. (ed) (2004) Cruise report, ARK XX-2, Reports on Polar Research.

A. von der Handt (2003): Impregnation-triggered breakdown: a case study of plagioclase peridotites from the Gakkel Ridge (Arctic Ocean) (in english). Diplom-Thesis. University of Bonn. 117 p.

A. von der Handt (2003): Die Evolution des Permischen Beckens von Perdasdefogu und die Jurassische Transgression im Bereich des Tacco di Perdalonga, Sardinien (in german). Mapping Survey Report. University of Bonn. 92 p.

Snow, J. E. and Petrology Group (incl. **A. von der Handt**), ARK VXII-2 (2002) ARK XVII/2 Petrology cruise report: Petrogenesis of magmatic and amagmatic crust along the world's slowest spreading mid-ocean ridge. In: Thiede, J. (ed.) (2002) Cruise report, ARK XVII/2, Reports on Polar Research.